EXTENSIONAL REGIME DATA BASE

Presentation by
Paul Spudich, U.S. Geological Survey, Menlo Park, CA

Ground Motion Workshop #2 -
Methods, Models, and Preliminary Interpretations

Doubletree Hotel
Salt Lake City, UT

January 9, 1997

1028

9704010133- Part 3

COLLECTION OF GROUND MOTION DATA

Extensional regimes from which we obtained data:

- US Intermountain region (e.g. Basin and Range, Long Valley CA, Yellowstone)
- Salton Trough, CA
- shallow volcanic regions of Central America
- western Europe, Italy, Greece
- New Zealand
- Turkey (extensional jogs in Anatolian fault)
- *(n.b. -extensional regimes have normal and strike-slip earthquakes. We used both because there are strike-slip events that might affect Yucca Mountain and because there was not much normal faulting data.)*

Data criteria:

- available in digitized form
- recorded in small structures (fewer than 3 stories, not from deeply embedded basements, etc)
- triggered before S wave arrival
- moment magnitude ≥ 5.0
- distance ≤ 105 km

Table 7. List of candidate, relevant, and used earthquakes

An earthquake is a "candidate" if it has been suggested for any reason to be possibly relevant to this project.
An earthquake is "relevant" if it is in an extensional regime, has moment magnitude >=5.0, and has usable strong motion d
GRAY signifies irrelevant event

Explanation of columns:

Year ... hr:mn	Approximate earthquake origin time
Approx MAG	Approx MAG is ML, Ms, Mw, or other estimates, w/o references; italic is moment magnitude
Rlvnt?	Rlvnt is our current opinion of whether this event is relevant for further study
W&S	This event was studied by Westaway and Smith (1989)
used\tot stns	number of usable stations\total number of stations we know about

Year	Month	day	hr:mn	NAME or LOCATION	Approx MAG	Rlvnt?	why	W&S	used\tot recs	used here?
1935	10	31	18:38	Helena, Mt	6.2	n	1 rec in 5 story bldg	*		
1935	10	31	1918	Helena, Mt		n	1 rec in 4 story bldg			
1935	11	21	20:58	Helena, Mt	5.8	n	1 rec in 4 story bldg			
1935	11	28	7:42	Helena, Mt	5.8	n	1 rec in 4 story bldg	*		
1938	6	6	2:42	Imperial Valley, CA	5	n	extens (16); only rec is Strig		0\1	
1940	5	19	4:37	Imperial Valley, CA	*6.87*	Y	IV extens (16)		1\1	y
1949	4	13	19:55	Western Washington	7.1, 6.7	n	too deep (10)	*		
1951	1	24	7:17	Imperial Valley, CA	5.6	n	extens (16); only rec is Strig		0\1	
1953	6	14	4:17	Imperial Valley, CA	5.5	Y	IV extens (16)		1\1	
1955	12	17	6:07	Imperial Valley, CA	5.4	n	extens (16); only rec is Strig		0\1	
1959	8	18	5:37	Hebgen Lake, Mt	7	Y	/S89; stns > 100km, no dig	*	1\2	
1962	8	30	13:35	Cache Valley, UT	ML5.7,Ms5.7(W&S)	n	1 rec in 3 story bldg	*		
1972	12	23	6:29	Managua	*6.2*	Y	extensional (26)		1\1	y
1972	12	23	7:17	Managua	5	n	extensional (26) bad data			
1972	12	23	7:19	Managua	5.2	Y	extensional (26)		1\1	
1972	2	6	21:44	Ancona, Italy	3.5, 4.4	n	too small(1)	*		
1972	2	8	12:19	Ancona, Italy	3.9, 4.6	n	too small(1)	*		
1972	6	14	18:55	Ancona, Italy	4.6, 4.7	n	too small(1)	*		
1972	6	14	21:01	Ancona, Italy	3.3, 4.7	n	too small(1)	*		
1972	6	21	15:06	Ancona, Italy	2.7, 4.0	n	too small(1)	*		
1974	1	29	15:12	Patras, Greece	3.5, 4.4	n	too small(1)	*		
1975	4	4	5:16	Patras, Greece	4.6, 5.1	n	in WS89; too deep (26)	*	1\1	
1975	5	13	0:22	Xylokastron, Greece	3.9, 4.6	n	too small(1)	*		
1975	10	12	8:23	Corinth, Greece	4.5, 4.6	n	too small(1)	*		
1975	8	1	20:02	Oroville, CA	5.7	n	only digital rec is S trig	*	0\5	

71

Table 7 p 1/7

Year	Month	day	hr:mn	NAME or LOCATION	Approx MAG	Rlvnt?	why	W&S	used\tot recs	used here?
1975	8	2	20:22	Oroville, CA	*5*	Y	in WS89	*	1\2	
1975	8	2	20:59	Oroville, CA	4.4, 5.2	n	in WS89; too small	*	3\3	
1975	8	3	1:03	Oroville, CA	4.5,4.8	n	too small(1)	*		
1975	8	3	2:47	Oroville, CA	3.7, 4.3	n	too small(1)	*		
1975	8	6	3:05	Oroville, CA	4.0, 4.7	n	too small(1)	*		
1975	8	8	7:00	Oroville, CA	4.5, 4.6	n	too small(1)	*		
1975	8	11	6:11	Oroville, CA	4.3, 4.4	n	too small(1)	*		
1975	8	16	5:48	Oroville, CA	3.3, 4.1	n	too small(1)	*		
1975	9	26	2:31	Oroville, CA	2.9, 4.2	n	too small(1)	*		
1975	9	27	22:34	Oroville, CA	Mw 4.67 (21)	n	too small	*		
1976	8	19	1:12	Denizli, Turkey	4.9	n	too small(1)			
1977	12	9	15:33	Izmir, Turkey	4.3, 4.9	n	too small(1)	*		
1977	12	16	7:37	Izmir, Turkey	4.9, 5.3	Y	in WS89	*	1\1	
1978	6	20	20:03	Thessaloniki, Greece	Ms 6.5	n	tensional (25), 1 rec lrg bl	*		
1978	7	4		Thessaloniki, Greece	Ms 5.1	n	tensional (25), 1 rec lrg bldg			
1979	7	18	13:12	Dursunbey, Turkey	4.9, 5.2	Y	in WS89	*	1\1	
1979	9	19	21:35	Valnerina, Italy	*5.9*	Y	in WS89	*	3\7	y
1979	10	15	23:16	Imperial Valley, CA	*6.5*	Y	IV extens (16)		33\35	y
1979	10	15	23:19	Imperial Valley, CA	*4.8*	n	IV extens (16)		16\16	
1979	10	16	6:58	Imperial Valley, CA	5.5	Y	IV extens (16)		1\1	
1980	5	25	16:34	Mammoth Lakes, CA	*6.2*	Y	extensional (17)	3	2\3	y
1980	5	25	16:36	Mammoth Lakes, CA	ML 5.0	n	borderline, only 1 rec - tch		?\1	
1980	5	25	16:49	Mammoth Lakes, CA	*5.8*	Y	extensional (17)	*	2\3	y
1980	5	25	19:44	Mammoth Lakes, CA	*5.8*	Y	extensional (17)	*	2\4	y
1980	5	25	20:35	Mammoth Lakes, CA	*5.7*	Y	extensional (17)		2\4	y
1980	5	25	20:59	Mammoth Lakes, CA	Mb4.2 ML5.5(20)	Y	extensional (17)		?	
1980	5	26	1:19	Mammoth Lakes, CA	Mb4.4 ML4.7(20)	Y	extensional (17)		?	
1980	5	26	12:24	Mammoth Lakes, CA	Mb4.7 ML5.6(20)	Y	extensional (17)		?	
1980	5	26	18:57	Mammoth Lakes, CA	5.8, 6.1	Y	extensional (17)		1\2	
1980	5	27	14:50	Mammoth Lakes, CA	*6*	Y	extensional (17)	*	4\6	y
1980	5	27	19:01	Mammoth Lakes, CA	Mm=4.6, TCH 6/23	n	extensional (17), too small	*	6\6	
1980	5	28	4:03	Mammoth Lakes, CA	2.6, 4.0	n	too small(1)	*		
1980	5	28	5:16	Mammoth Lakes, CA	3.7, 4.9	n	too small(1)	*		
1980	5	31	0:58	Mammoth Lakes, CA	2.7, 4.4	n	too small(1)	*		
1980	5	31	10:11	Mammoth Lakes, CA	3.0, 4.2	n	too small(1)	*		
1980	5	31	15:16	Mammoth Lakes, CA	, 4.9,ML4.9 Mb4.1(	n	too small(1)	*		
1980	5	31	15:02	Mammoth Lakes, CA	2.9, 4.0	n	too small(1)	*		

72

Table 7 p 2/7

Year	Month	day	hr:mn	NAME or LOCATION	Approx MAG	Rlvnt?	why	W&S	used\tot recs	used here?
1980	6	5	19:41	Mammoth Lakes, CA	2.4, 4.3	n	too small(1)	*		
1980	6	9	3:28	Victoria, Mexico	*6.32*	Y	IV extens (16)		2\7	y
1980	6	9	3:30	Victoria, Mexico	not in PDE	n	bogus event			
1980	6	9	10:00	Mexicali VAlley	Mb4.4, ML4.5 (15)	n	too small			
1980	6	9	23:33	Mexicali Valley	ML4.2(pas)	n	too small			
1980	6	11	4:41	Mammoth Lakes, CA	Mm=4.0 TCH 6/23	n	extensional (17), too small		7\9	
1980	7	16		Volos, Greece	Ms 4.9	n	extensional (25), too small			
1980	8	11		Volos, Greece	Ms5.2, ML4.7		extensional (25)		1\1	
1980	9	26		Volos, Greece	Ms 4.8	n	extensional (25), too small			
1980	11	23	18:34	Campania (Irpinia), Italy	*6.9*	Y	in WS89	*	9\19	y
1980	11	23	18:35	Campania (Irpinia), Italy	*6.2*	Y	in WS89	*	10\10	y
1980	11	24	0:23	Campania (Irpinia), Italy	4.7	n	too small(1)	*		
1980	12	1	19:04	Campania (Irpinia), Italy	4.6	n	too small(1)	*		
1981	1	16	0:37	Campania (Irpinia), Italy	4.7	n	too small(1)	*		
1981	2	24	20:53	Corinth, Greece	6.7	Y	in WS89	*	1\1	
1981	2	25	2:35	Corinth, Greece	6.4	Y	in WS89	*	1\1	
1981	3	4	21:58	Corinth, Greece	Ms6.4(12)	Y	normal (12)		1\1	
1981	4	26	12:09	Westmorland, CA (11)	*5.8*	Y	IV extens (16)		6\6	y
1981	9	30	11:53	Mammoth Lakes, CA	b5.6 Ms5.8 ML5.8(2	Y	extensional (17)		?	
1981	9	30	13:06	Mammoth Lakes, CA	Mb4.7 ML4.6(20)	Y	extensional (17)		?	
1983	1	7	1:38	Mammoth Lakes, CA	Ms5.0 (15) ML5.0	Y	extensional (17)		1\1	
1983	1	7	3:24	Mammoth Lakes, CA	Ms5.0 (15) ML5.4	Y	extensional (17)		1\1	
1983	1	17		Argostoli, Greece (mainsh	Ms 7.0	n	not extensional (25)			
1983	1	17		Argostoli, Greece (aftersh	Ms 5.3	n	not extensional (25)			
1983	1	19		Argostoli, Greece (aftersh	Ms 5.7	n	not extensional (25)			
1983	1	31		Argostoli, Greece (aftersh	Ms 5.3	n	not extensional (25)			
1983	2	2		Zakynthos, Greece	Ms 5.4	n	not extensional (25)			
1983	3	16		Lefkada, Greece (mainsh)	Ms 5.2	n	not extensional (25)			
1983	3	23		Lefkada, Greece (aftersh)	Ms 5.2	n	not extensional (25)			
1983	3	23		Argostoli, Greece (aftersh	Ms 6.2	n	not extensional (25)			
1983	3	24		Argostoli, Greece (aftersh	Ms 5.5	n	not extensional (25)			
1983	7	5	12:01	Biga, Turkey	5.8, 6.1	Y	in WS89	*	≤1\5	
1983	8	6	15:43	North Aegean, Greece	*6.74*	Y	extensional (25)		1\1	y
1983	8	26		Ouranopolis, Greece	Ms4.9	n	too small			
1983	10	28	14:06	Borah Peak, ID	*6.9*	Y	in WS89	*	2\8	y
1983	10	29	23:29	Borah Peak, ID	*5.1*	Y	in WS89	*	3\5	y
1983	10	29	23:39	Borah Peak, ID	Mm=4.8 (23)	n	in WS89	*		

73

Table 7 p 3/7

Year	Month	day	hr:mn	NAME or LOCATION	Approx MAG	Rlvnt?	why	W&S	used\tot recs	used here?
1983	10	30	1:24	Borah Peak, ID	3.5, 4.8	n	too small(1)	*		
1983	10	30	1:59	Borah Peak, ID	3.1, 4.7	n	too small(1)	*		
1983	11	2	23:43	Borah Peak, ID	3.5, 4.2	n	too small(1)	*		
1983	11	6	21:04	Borah Peak, ID	3.3, 4.6	n	too small(1)	*		
1983	11	8		Liege, Belgium	5.1	n?	no d<100 km?		?	
1984	2	19		Poligiros, Greece	Ms 4.9	n	ensional (25), too small, S trig			
1984	3	5	2:07	South Taupo, NZ	5.5	?		*	1\1	
1984	4	29	5:02	Umbria, Italy	5.0, 5.6	Y	in WS89	*	?\6	
1984	5	7	17:49	Lazio-Abruzzo, Italy	*5.8*	Y	in WS89	*	5\16	y
1984	5	11	10:41	Lazio-Abruzzo, Italy	5.2, 5.5	Y	in WS89	*	?\10	
1984	5	11	10:05	Lazio-Abruzzo, Italy	4.2	n	too small(1)	*		
1984	5	11	11:26	Lazio-Abruzzo, Italy	4.2	n	too small(1)	*		
1984	5	11	13:14	Lazio-Abruzzo, Italy	4.3	n	too small(1)	*		
1984	5	11	13:39	Lazio-Abruzzo, Italy	4.1	n	too small(1)	*		
1984	5	11	16:39	Lazio-Abruzzo, Italy	4.3	n	too small(1)	*		
1984	5	11	23:35	Lazio-Abruzzo, Italy	4.1	n	too small(1)	*		
1984	6	24		Granada, Spain	5	?			1\6	
1984	7	9		Edessa, Greece	Ms5.3, ML4.8	n	nsional (25), 2 recs in big bldgs		1\1	
1984	10	4		Zakynthos, Greece	Ms 5.0	n	not extensional (25)			
1984	10	10		Pelekanada, Greece	Ms5.0, ML4.5	Y	extensional (25)		≥1\2	
1984	11	23	18:08	Round Valley, CA	5.6 Ms5.7 ML6.2(2	Y	extensional (17)		?	
1984	11	23	19:12	Bishop, (Round Valley), CA	4.8 Ms4.7 ML5.4(2	Y	extensional (17)		1\1	
1985	3	3		Amfilochia (main shock)	Ms4.5	n	not extensional (25)			
1985	3	3		Amfilochia (aftersh)	Ms4.5	n	not extensional (25)			
1985	8	31		Lefkada, Greece	Ms 5.2	n	not extensional (25)			
1985	11	9		Drama, Greece	Ms5.5, ML5.0	Y	extensional (25)		2\2	
1986	2	18		Edessa, Greece	Ms 5.0	Y	extensional (25)		?	
1986	7	20	14:29	Chalfant Valley, CA	*5.8*	Y	extensional(18)		5\5	y
1986	7	21	14:42	Chalfant Valley, CA	*6.3*	Y	extensional(18)		10\11	y
1986	7	21	14:51	Chalfant Valley, CA	*5.6*	Y	extensional(18)		3\3	y
1986	7	31	7:22	Chalfant Valley, CA	*5.8*	Y	extensional(18)		2\2	y
1986	9	13	17:24	Kalamata, Greece (mainsh	Ms6.2	n	in WS89; 1 rec in big bldg	*	1\1	
1986	9	15	11:41	Kalamata, Greece (aftersh	Ms5.4	n	in WS89; too small	*	3\3	
1986	10	10	17:49	San Salvador, El Salvador	*5.76*				2\9	y
1987	2	7	3:45	Cerro Prieta, Mexico	Ml=5.4	Y	IV extens (16)		1\1	
1987	3	2	1:35	Edgecomb, New Zeleand	5.2	Y	in WS89	*	?\1	
1987	3	2	1:42	Edgecomb, New Zeleand	*6.6*	Y	in WS89	*	2\3	y

24

Table 7 p 4/7

Year	Month	day	hr:mn	NAME or LOCATION	Approx MAG	Rlvnt?	why	W&S	used\tot recs	used here?
1987	3	2	1:51	Edgecomb, New Zeleand	*5.8*	Y	in WS89	*	1\2	y
1987	11	24	1:54	Elmore Ranch, CA	*6.2*	Y	IV extens (16)		1\1	y
1987	11	24	13:15	Superstition Hills, CA	*6.6*	Y	IV extens (16)		2\3	y
1988	8	14	20:03	San Rafael Swell, UT	5.21(27)		West US probably extensional		?	
1988	10	16		Kyllini, Greece (mainsh)	Ms 5.9	n	not extensional (25)			
1988	10	17		Kyllini, Greece (aftersh)	Ms 4.4	n	not extensional (25)			
1988	10	20		Kyllini, Greece (aftersh)	Ms 4.1	n	not extensional (25)			
1988	10	22		Kyllini, Greece (aftersh)	Ms 4.5	n	not extensional (25)			
1988	10	23		Kyllini, Greece (aftersh)	Ms 4.3	n	not extensional (25)			
1988	10	23		Kyllini, Greece (aftersh)	Ms 4.5	n	not extensional (25)			
1988	10	23		Kyllini, Greece (aftersh)	Ms ?	n	not extensional (25)			
1988	10	28		Kyllini, Greece (aftersh)	Ms 4.4	n	not extensional (25)			
1988	10	31		Kyllini, Greece (aftersh)	Ms 4.3	n	not extensional (25)			
1988	10	17		Kyllini, Greece (aftersh)	Ms 4.4	n	not extensional (25)			
1988	11	11		Kyllini, Greece (aftersh)	Ms 4.3	n	not extensional (25)			
1989	1	30	4:06	So Wasatch Plateau, UT	5.12 (27)		West US probably extensional		?	
1990	10	24	6:15	Lee Vining, CA	5.29 (27)		West US probably extensional		?	
1990	12	21		Griva, Greece	Ms5.9	Y	extensional (25)		2\2	
1991	2	24		Korinth, Greece	Ms 6.7	n	not extensional (25)			
1991	12	3	17:54	Mexicali, Mexico	5.18 (27)		IV/Baja probably extensional		?	
1992	3	13	17:19	Erzincan, Turkey	*6.7*	Y	extensional(6)		1\2	y
1992	4	12	1:02	Roermond, Holland	*5.31*				3\19	y
1992	6	22	17:43	Matata, NZ	5.7	?			1\2	
1992	6	28	11:58	Landers, CA		n	not extens(19)			
1992	6	28		Big Bear, CA	Mw=5.3 (7)	n	not extens(19)			
1992	6	29	10:14	Little Skull Mtn, NV	*5.7*	Y	normal (7)		8\24	y
1992	9	2	10:26	St. George, UT	Mw=5.5 (7)	n	no good records			
1992	10	11	13:09	Dahshur, Egypt	Ml=5.9	n	no records			
1993	3	26		Pyrgos, Greece (aftersh)	Ms 5.0	n	not extensional (25)			
1993	3	26		Pyrgos, Greece (aftersh)	Ms 5.1	n	not extensional (25)			
1993	3	26		Pyrgos, Greece (mainsh)	Ms 5.2	n	not extensional (25)			
1993	3	26		Pyrgos, Greece (aftersh)	Ms 4.9	n	ɔo small, not extensional (25)			
1993	3	26		Pyrgos, Greece (aftersh)	Ms 4.7	n	ɔo small, not extensional (25)			
1993	4	29		Pyrgos, Greece (aftersh)	Ms 4.8	n	o small, not extensional (25)			
1993	4	29	8:21	Cataract Creek, AZ	5.27 (27)		West US probably extensional		?	
1993	5	17		Eureka Valley, CA	Mw=6.0 (7)	n	3 analog, no digital recs			
1993	7	14		Patras, Greece	Ms 5.4	n	ıxtensional (25), poor digitiz			

75

Table 7 p 5/7

Year	Month	day	hr:mn	NAME or LOCATION	Approx MAG	Rlvnt?	why	W&S	used\tot recs	used here?
1993	9	21	3:28	Klammath Falls, OR	Mw=6.0 (7)	Y	normal (7)		?	
1993	9	21	5:45	Klammath Falls, OR	Mw=6.0 (7)	Y	normal (7)		?	
1993	12	4	22:15	Klammath Falls, OR	Mw=5.5 (9)	Y	normal (9)		?	
1994	2	3	9:05	Drainey Peak, ID	Mw=5.7 (7)	Y?	normal (7)		?	
1994	6	7	13:30	Near Borah Peak, ID	5.01-5.12 (28)		West US probably extensional		?	
1994	9	12	12:23	Double Springs Flat	*5.9*	Y			1\5	y
1994	9	12	23:57	Double Springs Flat	(brk)5.0, Md-reno	n	no digital records, too small			
1995	4	14	0:32	Western Texas	5.62 (27)		West US probably extensional		?	
1995	5	4		Thesaloniki(?), Greece	Ms 5.8	n	data withheld till mid?1996		?	
1995	5	13	8:47	Kozani, Greece	Ms=6.6 (30)	Y	normal (30)		1\1	
1995	5	15	4:13	Kozani, Greece af A	Ms=5.5 (30)	Y	aftershock, prob extensional		1\1	
1995	5	17	4:14	Kozani, Greece af B	Ms=5.4 (30)	Y	aftershock, prob extensional		1\1	
1995	5	19	6:48	Kozani, Greece af C	M=5.1 (31)	Y	aftershock, prob extensional		1\1	
1995	6	11	18:51	Kozani, Greece af D	M=4.8 (31)	Y	aftershock, prob extensional		2\2	
1995	6	15		Greece	Ms=6.0? (31)	?	few small recs r>40km (31)			
1995	8	17		Ridgecrest, CA	ML=5.4 (32)	Y	normal mech (32)		?\5?	
1995	9	20		Ridgecrest, CA	ML=5.8 (32)	Y	str-slip, extensional (32)		?\5?	
1995	11	22	0416?	Gulf of Aqaba	Mw=7.1(33)	?	Probably extensional(29)		2\7	
1995	11	23	18:08	Gulf of Aqaba aft A	ML=5.4(33)	?	Probably extensional(29)		1\1	
1995	12	26	6:19	Gulf of Aqaba aft B	ML=5.0(33)	?	Probably extensional(29)		1\1	

Footnotes:

(1) too small: none of the magnitudes in Table 1 of WS89 equals or exceeds 5.0
(6) Erzincan is strike-slip but is in extensional zone.
(7) from Ritsema and Lay JGR, 1995
(8) Ritsema and Lay (1995) report rake = -14 for this event
(9) from Braunmiller et al (1995)
(10) 70 km deep, Nuttli (BSSA, 1952)
(11) see Maley and Etheredge (1981), also "Seismological Notes",. BSSA, v72,1982, also McJunkin and Kaliakin (1981)
(12) see Abercrombie et al (1995)
(13) CDMG OSMS 86-07 , 1986
(14) CDMG 0SMS 87-04, 1988
(15)NEIS
(16) this Imperial Valley event determined in extensional region
(17) Long Valley and nearby events are extensional
(18) Associated with range-front normal faults in extensional zone
(19) No extensional strains seen in geodetics or in stress indicators

76

Table 7 p6/7

TABLE 8; RECORDS OMITTED BECAUSE OF STRUCTURE, S TRIGGER, OR POOR DATA QUALITY

GRAY signifies irrelevant event

Earthquake Name	Date	Station No	Station Name	bad blgd?	S trig/ bad data?	Notes
Helena, Montana	1935 1031 1838	??	Helena Fed Bldg	y		bsmt, 4 story bldg
Helena, Montana	1935 1031 1918	2229	Helena Fed Bldg	y		bsmt, 4 story bldg
Helena, Montana	1935 1121 2028		Helena Fed Bldg	y		bsmt, 4 story bldg
Helena, Montana	1935 1128 0742		Helena Fed Bldg	y		bsmt, 4 story bldg
Imperial Valley	1938 0606 0242	USGS 117	El Centro Array #9		y	**S trigger**
Imperial Valley	1951 0124 0717	USGS 117	El Centro Array #9		y	**S trigger**
Imperial Valley	1955 1217 0607	USGS 117	El Centro Array #9		y	**S trigger**
Hebgen Lake, MT	1959 0818 0637	USGS	BOZ - Bozeman, MT	y		3 story bldg
Cache Valley, UT	1962 0830 1335	USGS	LOG - Logan, UT	y		3 story bldg
Oroville	1975 0801 2020	CDWR 1051	Oroville Dam Seismograph Station		y	**S trigger**
Oroville	1975 0802 2022	CDMG 1546	OR1 - Up & Down Cafe		y	**S trigger**
Thessaloniki, GR	1978 0620 2003		Thessaloniki, City Hotel	y		7 story bldg-Hotel
Thessaloniki, GR	1978 0407 0000		Thessaloniki, City Hotel	y		7 story bldg-Hotel
Valnerina (Norcia) Italy	1979 0919 2135	ENEA	NOU - Nocera Umbra		y	**S trigger**
Valnerina (Norcia) Italy	1979 0919 2135	ENEA	ADT - Arquata del Tronto		y	**S trigger**
Valnerina (Norcia) Italy	1979 0919 2135	ENEA	MAS - Mascioni		y	**S trigger**
Valnerina (Norcia) Italy	1979 0919 2135	ENEA	- San Vittorino		y	**S trigger**
Imperial Valley	1979 1015 2316	USGS 5052	Plaster City		y	bad data
Imperial Valley	1979 1015 2316	UNAM 6618	Agrarias		y	z comp bad, other ok
Imperial Valley	1979 1015 2316	UNAM 6619	SAHOP Casa Flores		y	bad data
Imperial Valley	1979 1015 2316	CDMG 5169	Westmorland Fire Sta		y	z comp bad, other ok
Mammoth Lakes	1980 0525 1634	CDMG 54214	Long Valley Dam (Upr L Abut)	y		upper left abutment records contaminated
Mammoth Lakes	1980 0525 1649	CDMG 54214	Long Valley Dam (Upr L Abut)	y		upper left abutment records contaminated
Mammoth Lakes	1980 0525 1944	CDMG 54214	Long Valley Dam (Upr L Abut)	y		upper left abutment records contaminated
Mammoth Lakes	1980 0525 2035	CDMG 54214	Long Valley Dam (Upr L Abut)	y		upper left abutment records contaminated
Mammoth Lakes	1980 0526 1858	CDMG 54214	Long Valley Dam (Upr L Abut)	y		upper left abutment records contaminated
Mammoth Lakes	1980 0527 1451	CDMG 54214	Long Valley Dam (Upr L Abut)	y		upper left abutment records contaminated
Mammoth Lakes	1980 0531 1516	USC 35	Long Valley Fire Sta		y	**S trigger**
Victoria, Mexico	**1980 0609 0328**	UNAM 6604	Cerro Prieto			bad data
Victoria, Mexico	1980 0609 0328		Mexicali Hosp Sot.		y	**S trigger**
Victoria, Mexico	1980 0609 0328		Victoria		y	glitchy digital data
Victoria, Mexico	1980 0609 0328	UNAM 6624	Victoria Hospital Sotano		y	**S trigger**
Mammoth Lakes	1980 0611 0441	USGS 45	MGE - McGee Creek		y	**S trigger**
Mammoth Lakes	1980 0611 0441	USC 40	USC Convict Lakes		y	**S trigger**
Campania (Irpinia)	**1980 1123 1834**	ENEA	AU3 - Auletta		y	**S trigger**
Campania (Irpinia)	1980 1123 1834	ENEA	BZ4 - Brienza		y	**S trigger**
Campania (Irpinia)	1980 1123 1834	ENEA	GA4 - Garigliano		y	**S trigger**
Campania (Irpinia)	1980 1123 1834	ENEA	SS4 - San Severo		y	**S trigger**
Campania (Irpinia)	1980 1123 1834	ENEA	VI4 - Vieste		y	**S trigger**

Table 8 p 1/2

Earthquake Name	Date	Station No	Station Name	bad blgd?	S trig/ bad data?	Notes
Campania (Irpinia)	1980 1123 1834	ENEA	TC4 - Tricarico		y	**S trigger**
Biga, Turkey	1983 0705 12:01	ERI	GON - Goenen		y	poor digitization
Biga, Turkey	1983 0705 1201	ERI	EDK - Edincik		y	poor digitization
Biga, Turkey	1983 0705 1201	ERI	BSR - Balikesir		y	poor digitization
Biga, Turkey	1983 0705 1201	ERI	EDR - Edremit		y	poor digitization
Borah Peak, ID	1983 1028 1406	INEL	ANL 767	y		basement, 6-story bldg
Borah Peak, ID	1983 1028 1406	INEL	ANL 768	y		basement, 4 story bldg
Borah Peak, ID	1983 1028 1406	INEL	CPP-601 basement	y		10 m deep embedment in soil
Borah Peak, ID	1983 1028 1406	INEL	PBF-620	y		second basement, reactor building
Borah Peak, ID	1983 1028 1406	INEL	TRA-642	y		basement, 4-story bldg
Borah Peak, ID	1983 1028 1406	INEL	TRA-670	y		4 story building
Lazio-Abruzzo, Italy	1984 0507 1749	ENEA	Bussi		y	**S trigger**
Lazio-Abruzzo, Italy	1984 0507 1749	ENEA	LDP - Lama dei Peligni		y	**S trigger**
Lazio-Abruzzo, Italy	1984 0507 1749	ENEA	MAN - Manoppello		y	**S trigger**
Lazio-Abruzzo, Italy	1984 0507 1749	ENEA	ORT - Ortucchio		y	**S trigger**
Granada, Spain	1984 0624	IGN	Beznar		y	Dam abutment, S trigger
Granada, Spain	1984 0624	IGN	Alhama		y	bad data
Granada, Spain	1984 0624	NARS	NE14		y	bad data
Edessa, Greece	1984 0709		Edessa	y		5-story bldg, basement
Edessa, Greece	1984 0709		Verola	y		3-story bldg, basement
Drama, Greece	1985 1109		Drama	y		4-story, basement
Chalfant Valley	1986 0721 1442	CDMG 54424	Bishop - Paradise Lodge		y	**S trigger**
Chalfant Valley	1986 0721 1442	CDMG 54214	Long Valley Dam (L Abut)	y		left abutment not used; downstream available
Kalamata, Greece	1986 0913 1724		Kalamata	y		7, 4-story, basement
Kalamata, Greece	1986 0915 1141		Kalamata	y		7, 4-story, basement
Kalamata, Greece	1986 0915 1141		Kalamata-2	y		7, 4-story, basement
San Salvador	1986 1010 1749		HCR Hotel El Camino Real	y		10-story, 2nd floor
San Salvador	1986 1010 1749		HSH Hotel Sheraton	y		10-story, 1st floor
San Salvador	1986 1010 1749		IVU Inst. Urban Construction	y		6-story, 1st floor
San Salvador	1986 1010 1749		UCA Centro Americana Un.	y		6-story, 1st floor
San Salvador	1986 1010 1749		MDE Minist de Educacion	y		4-story, 1st floor
Edgecomb, NZ	1987 0302 0151		Maraenui Primary School		y	**S trigger**
Superstitn Hills (A)	**1987 1124 0154**	USGS 5210	Wildlife Liquef. Array		y	**local liquefaction affected record**
Griva, Greece	1990 1221		Edessa	y		5-story, basement
Matata, New Zealand	1992 0622 1743	GNS	Kawerau Police St.		y	**S trigger**
Double Springs Flat	1994 0912 1223	CDMG 65430	Indian Creek Dam	y		earth dam crest

Table 8 p2/2

Figure 1. Magnitude-distance sampling for rock sites

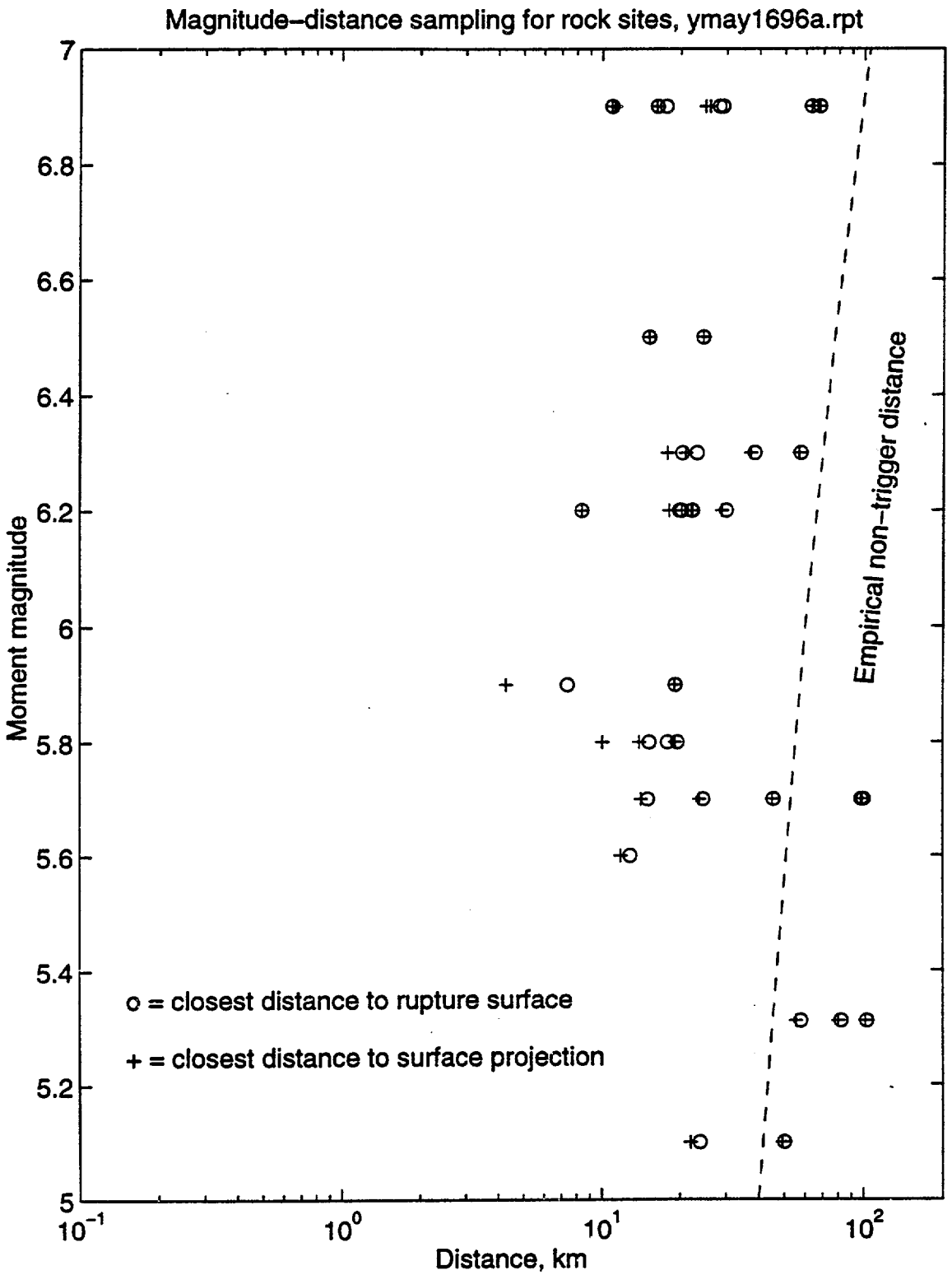

9a

Figure 2. Magnitude-distance sampling for soil sites

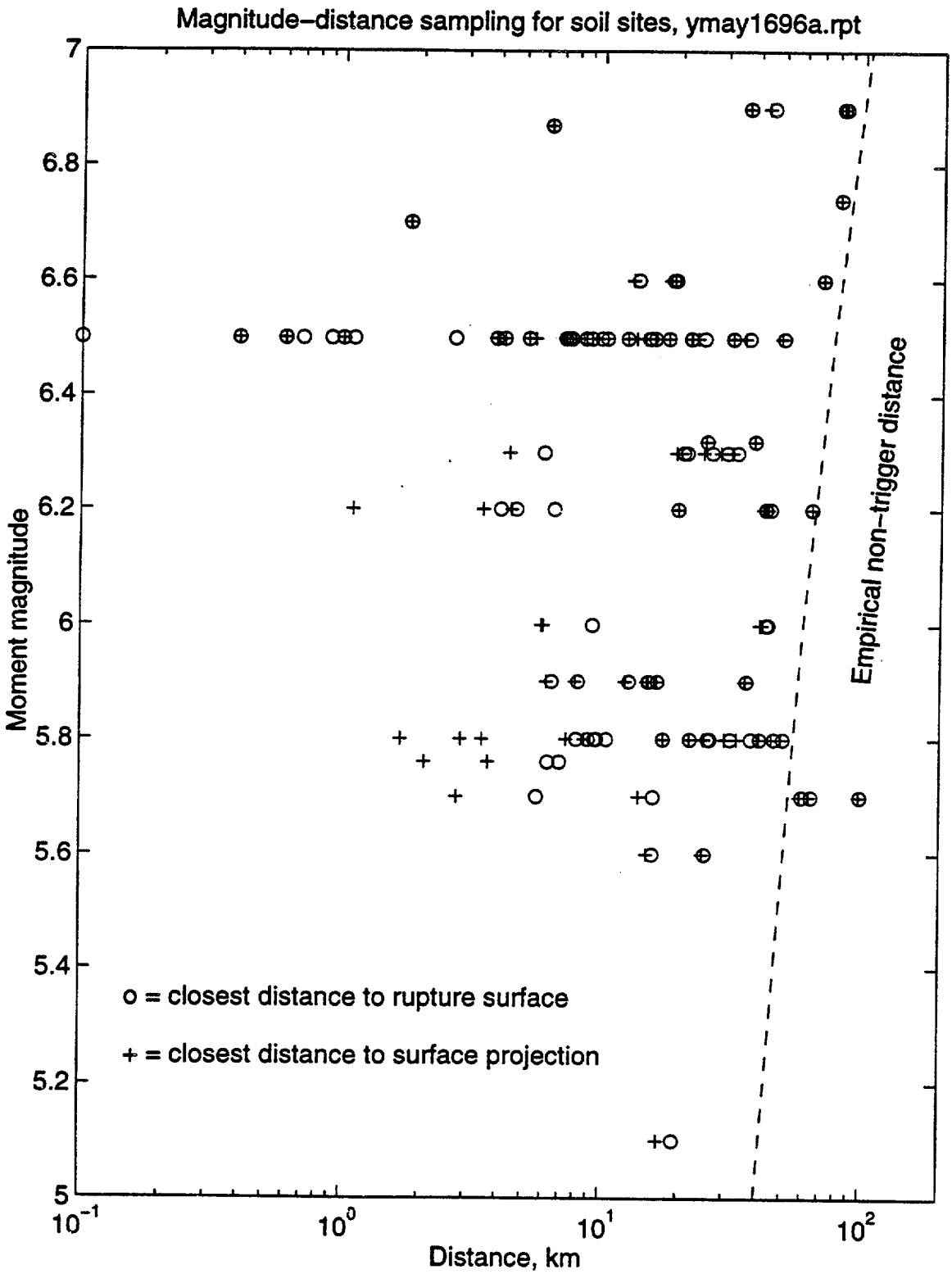

NOTE: throughout this work,

$$\log = \log_{10}$$

Illustration of bias correction and dispersion correction

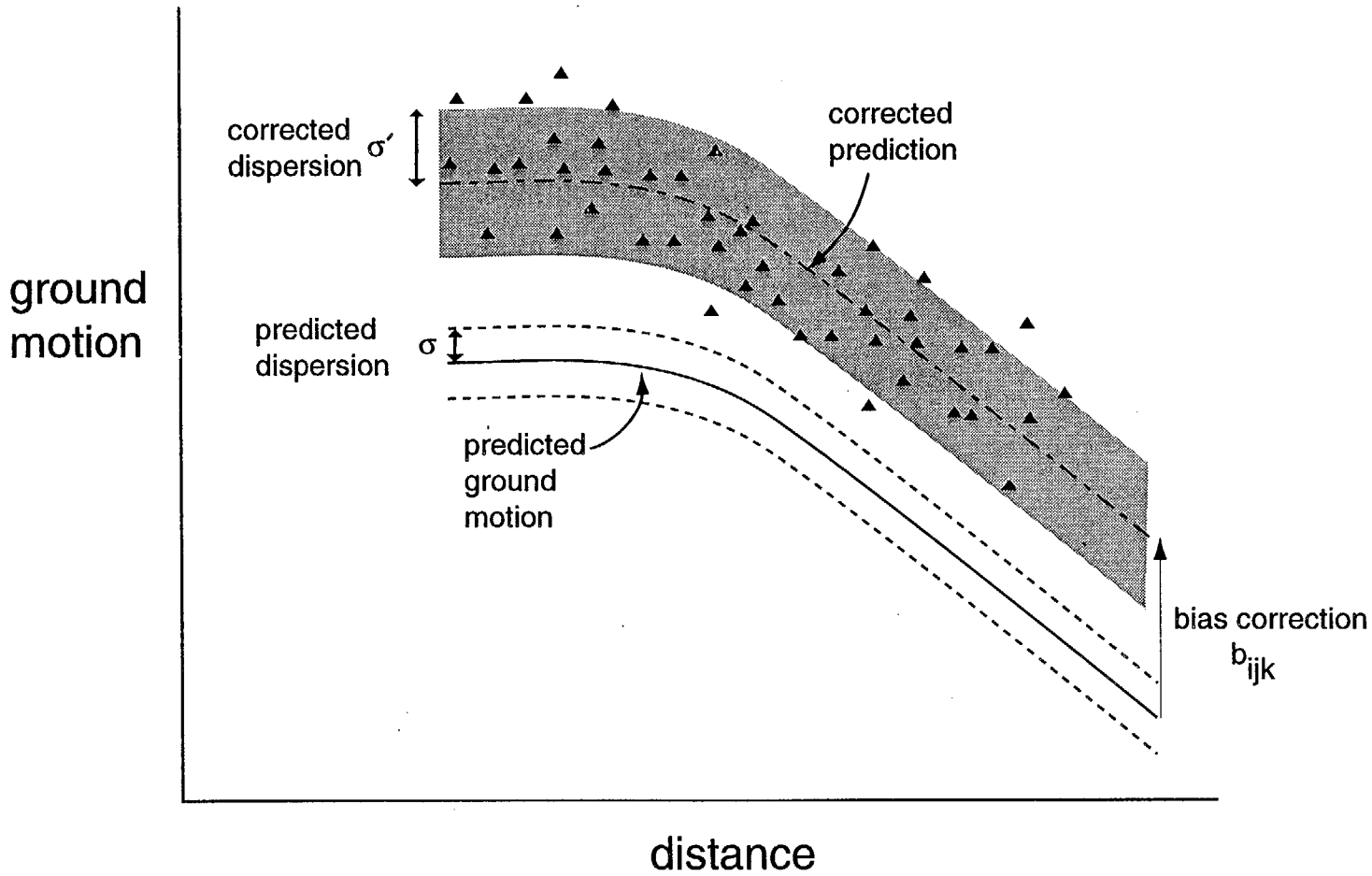

BIAS CORRECTIONS FOR ALL DISTANCES

bias bijk, sigma–b, and sigma–p for BJF94 h G=0,1,2 may1696b

mean = -0.18

1' = 67% y

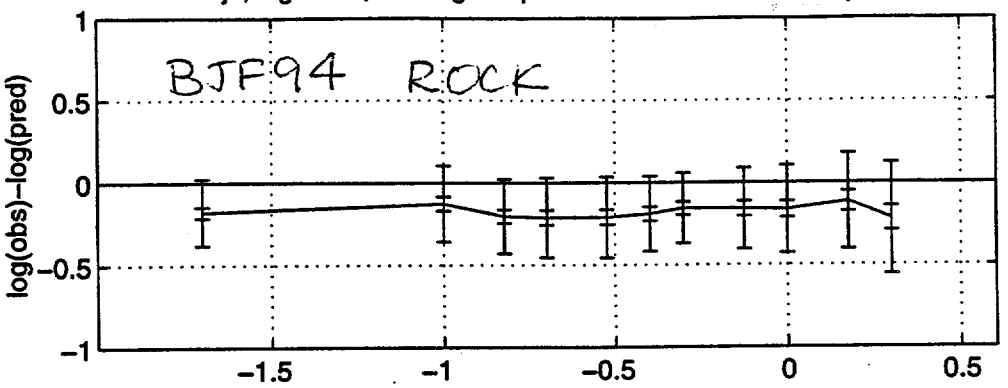

bias bijk, sigma–b, and sigma–p for BJF94 h G=5,6,7 may1696b

mean = -0.09

= 81% y

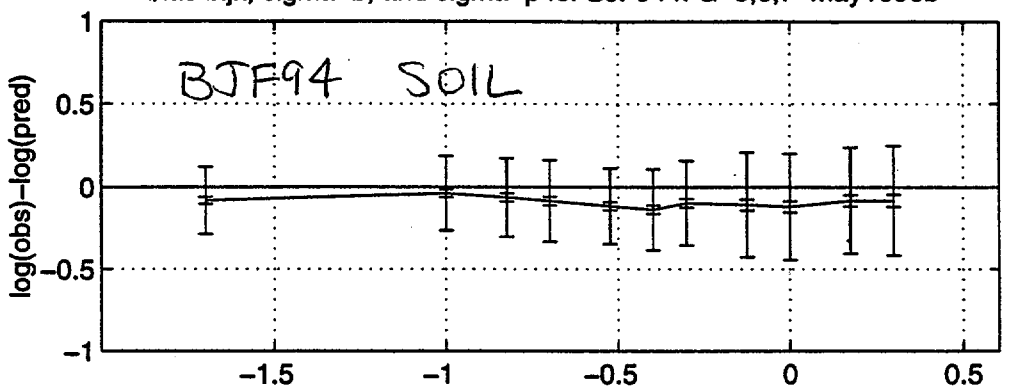

bias bijk, sigma–b, and sigma–p for C89/94 h G=5,6,7 may1696b

mean = -0.005

y' = 99% y

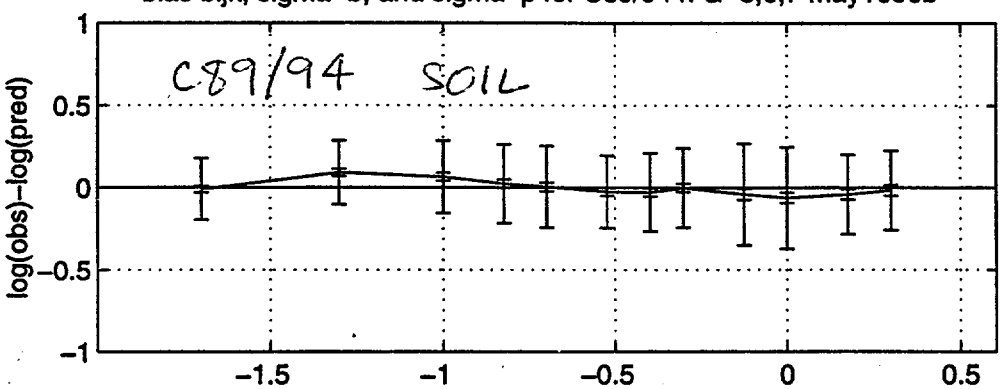

bias bijk, sigma–b, and sigma–p for S93 h G=0,1,2 may1696b

mean = 0.075

1' = 84% y

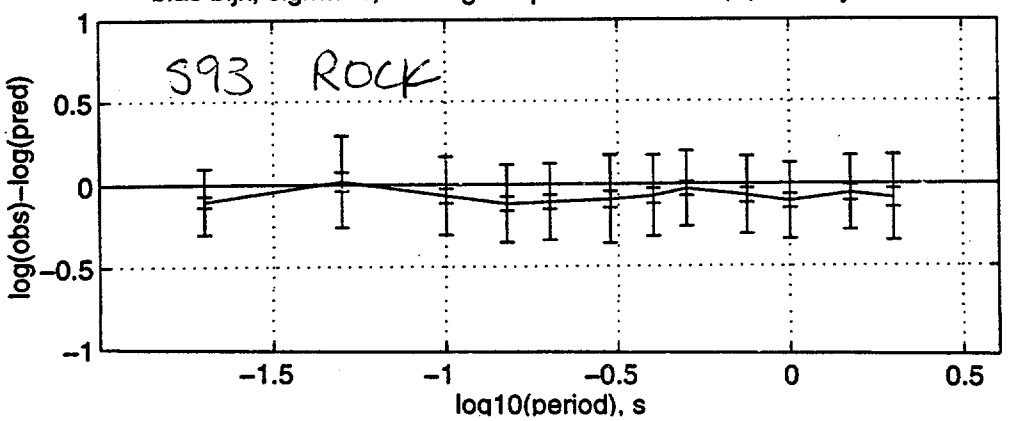

BIAS CORRECTIONS FOR DISTANCES ≤ 20 KM

mean = -0.059
y' = 87% y

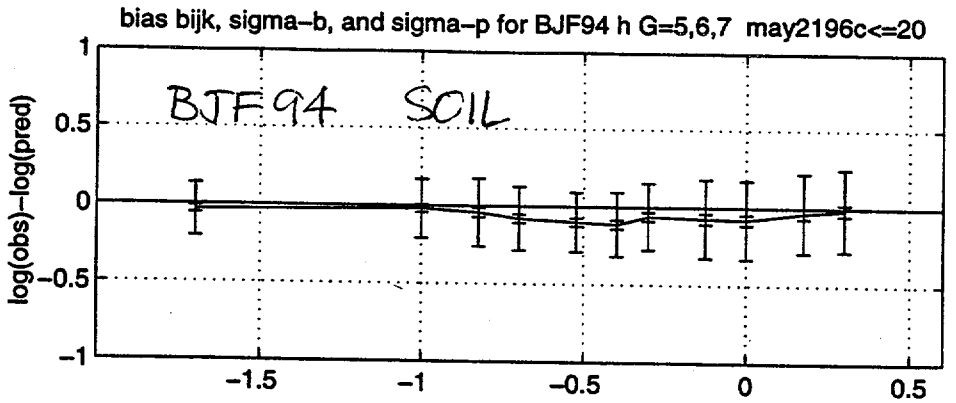

mean = -0.134
y' = 73% y

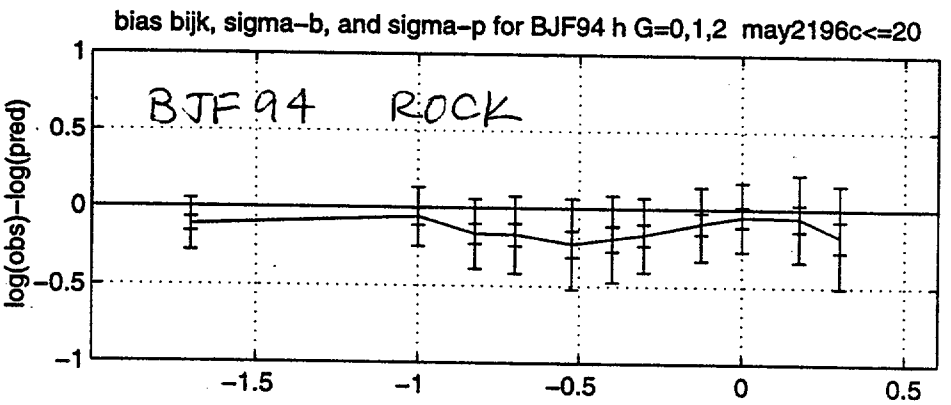

mean = -0.023
y' = 95% y

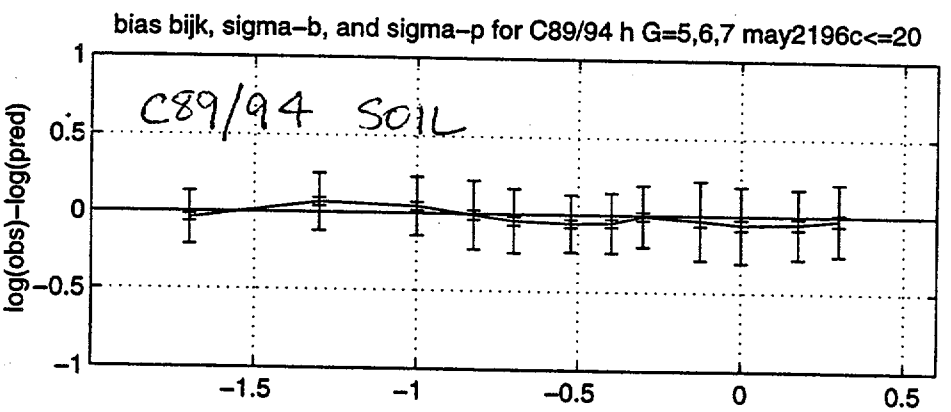

mean = -0.143
y' = 71% y

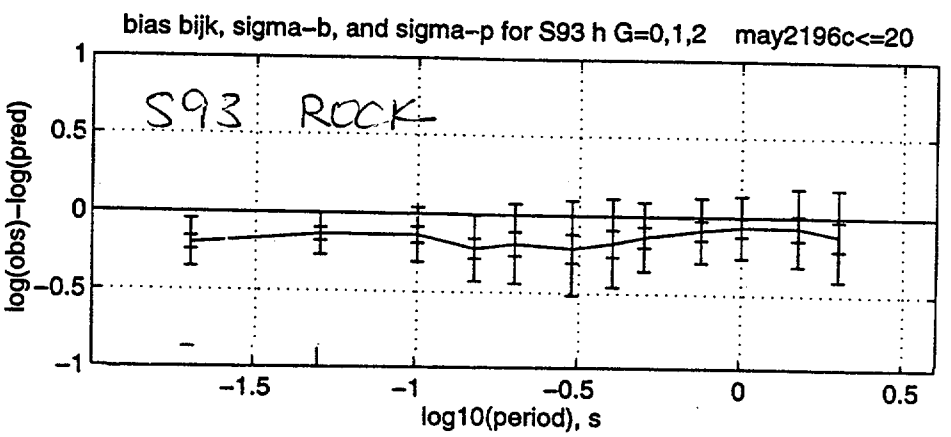

Figure 8. Comparison of predicted residuals showing strike slip events to have larger motions than normal faulting events (with caveats).

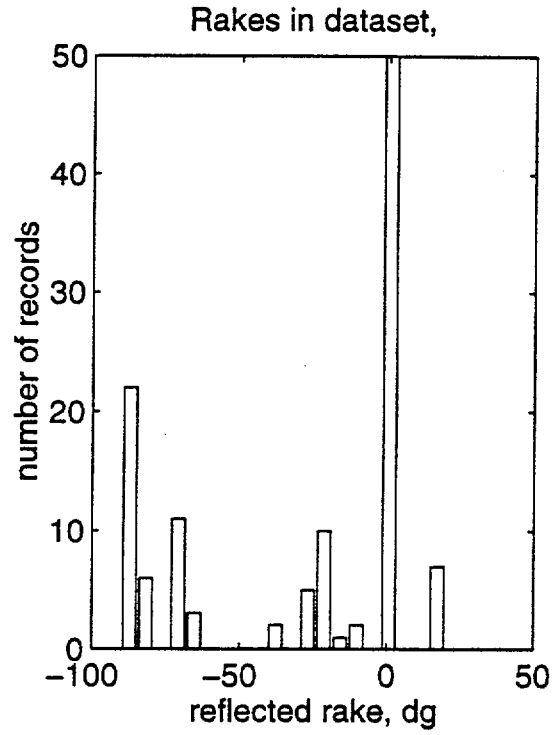

may2196b w/o TAN

mean normal residual = −0.01254

no. of normal residuals = 343

mean str−sl residual = 0.03015

no. of str−sl residuals = 837

Students t value =−2.77

Probability means differ = 0.9943

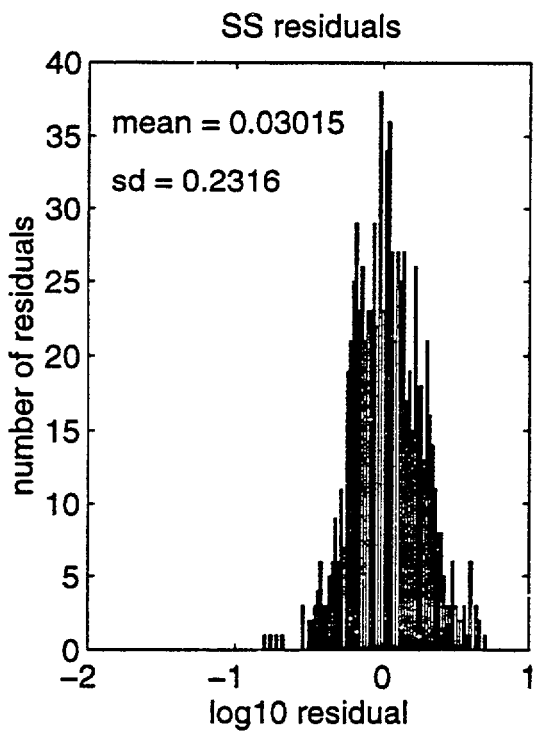

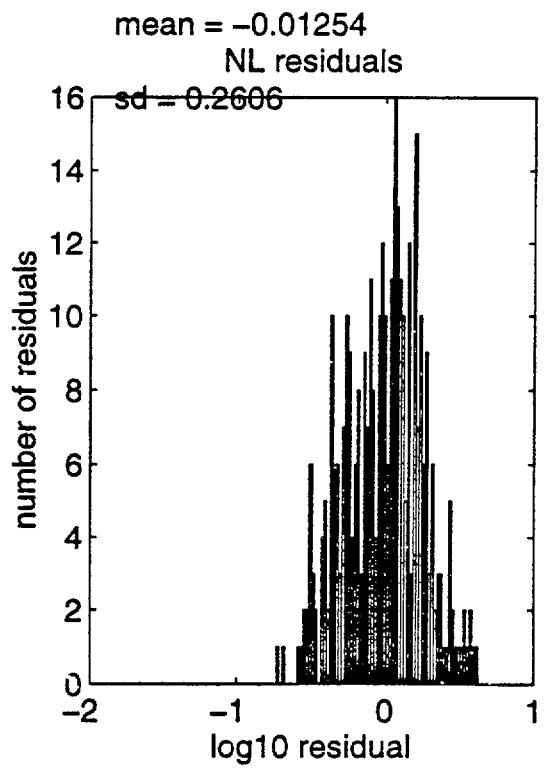

CAVEAT:

The difference in ground motions between strike-slip and normal faulting events depends on the selection of a reference curve used to calculate residuals. Use of Idriss(1993) or Sadigh et al. (1993) as reference curves leads to strike-slip ground motions *larger* than normal faulting ground motions. SEA96 is probably the more appropriate reference curve because it was derived from this data set using a two-step regression that reduces unwanted correlations. It suffers less distance-dependent residuals than the others, but its residuals are more magnitude-dependent.

Comparison of Little Skull Mountain ground motions with predictions of various authors

1 = BJF94
2 = C89/94 h or C89 z
3 = C90/94 h or C90 z
4 = C93/94 h
5 = I93
6 = SP96 h
7 = S93 h or S93 z
8 = C89 for velocity
9 = C90 for velocity
a = JB88
b = SP96 for velocity
c = Sea96

COMPARISON OF LITTLE SKULL MOUNTAIN HORIZONTAL PGA/PSV WITH VARIOUS PREDICTIVE RELATIONS

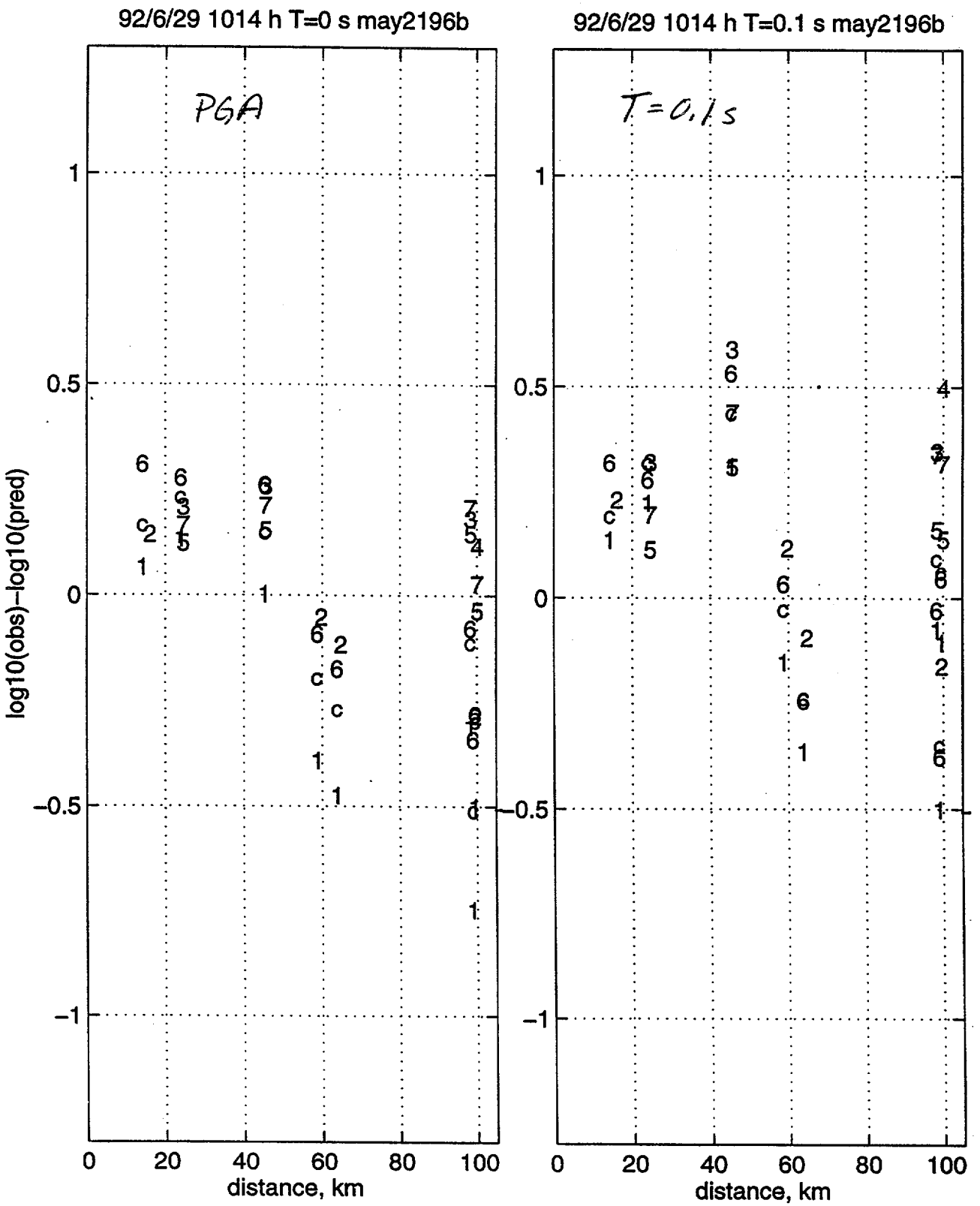

23a

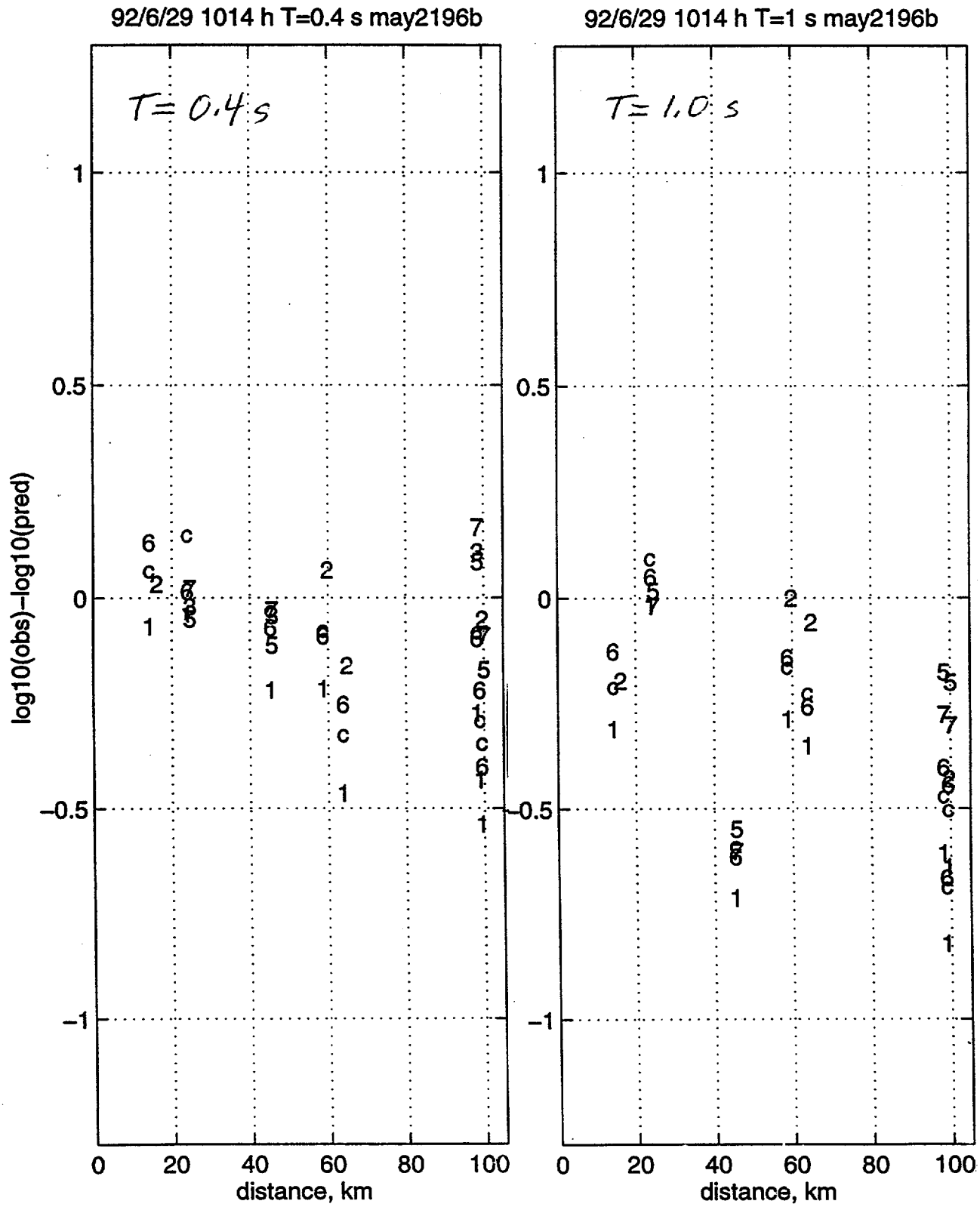
92/6/29 1014 h T=0.4 s may2196b
T= 0.4 s
92/6/29 1014 h T=1 s may2196b
T= 1.0 s
log10(obs)−log10(pred)
1
0.5
0
−0.5
−1
0
20
40
60
80
100
distance, km

23a

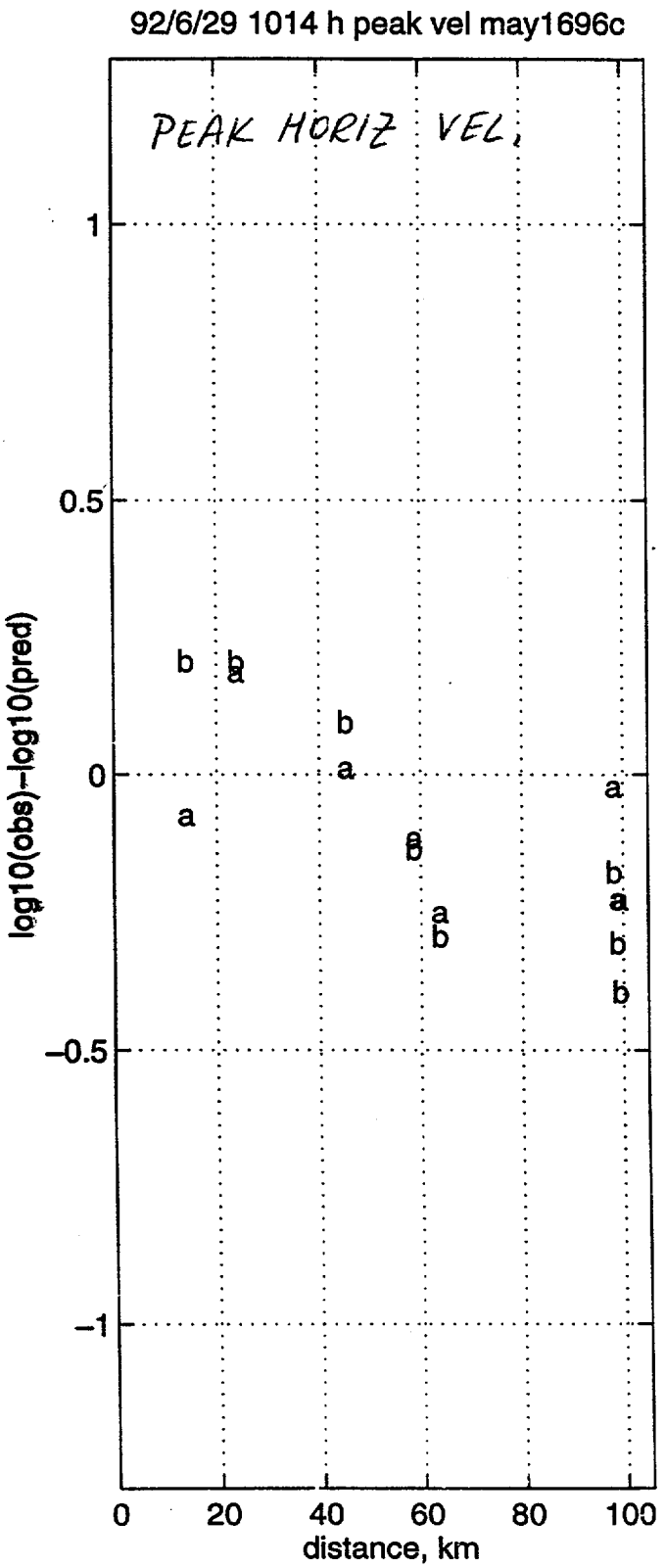
92/6/29 1014 h peak vel may1696c
PEAK HORIZ VEL.
log10(obs)-log10(pred)
distance, km

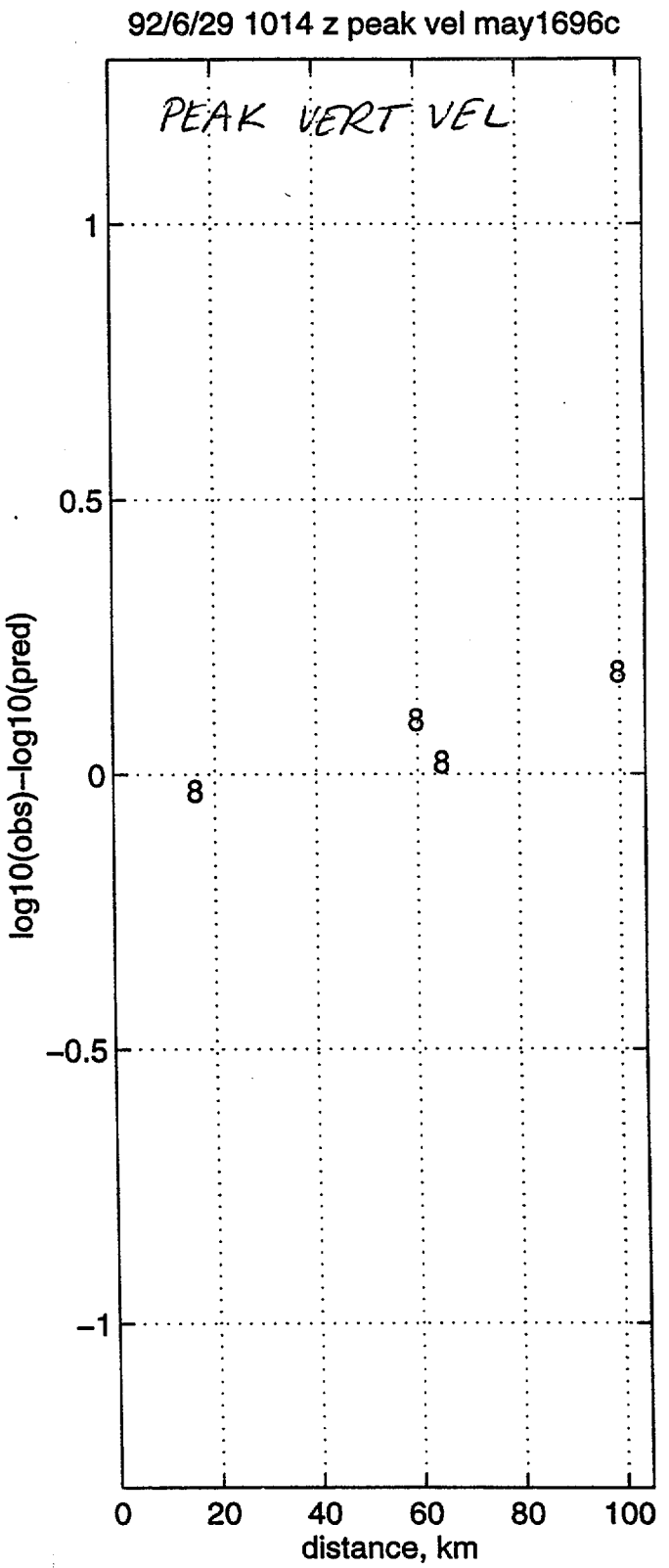
92/6/29 1014 z peak vel may1696c
PEAK VERT VEL
log10(obs)-log10(pred)
distance, km

22n

Develop attenuation curves as a function of frequency from weak motion data

Use data from the Little Skull Mountain aftershocks recorded on the Southern Great Basin Seismic Network

Ground motion spectra assumed proportional to

$$S(f)\, r^{-\gamma}\, e^{-\pi f(\kappa + T/Q)},$$

where T is travel time, r is distance, and S(f) is a site response spectrum.

Parameters to be determined:

S(f), site response spectra for groups of stations

γ, accounts for geometrical spreading

Q is a whole path anelastic attenuation

assumed either constant or frequency dependent:

$$Q(f) = Q_0 f^{\alpha}$$

κ is an average value for all stations and includes the effect of near-station attenuation. (Boatwright, Fletcher, and Fumal, BSSA, 1991; Boatwright, BSSA, 1994).

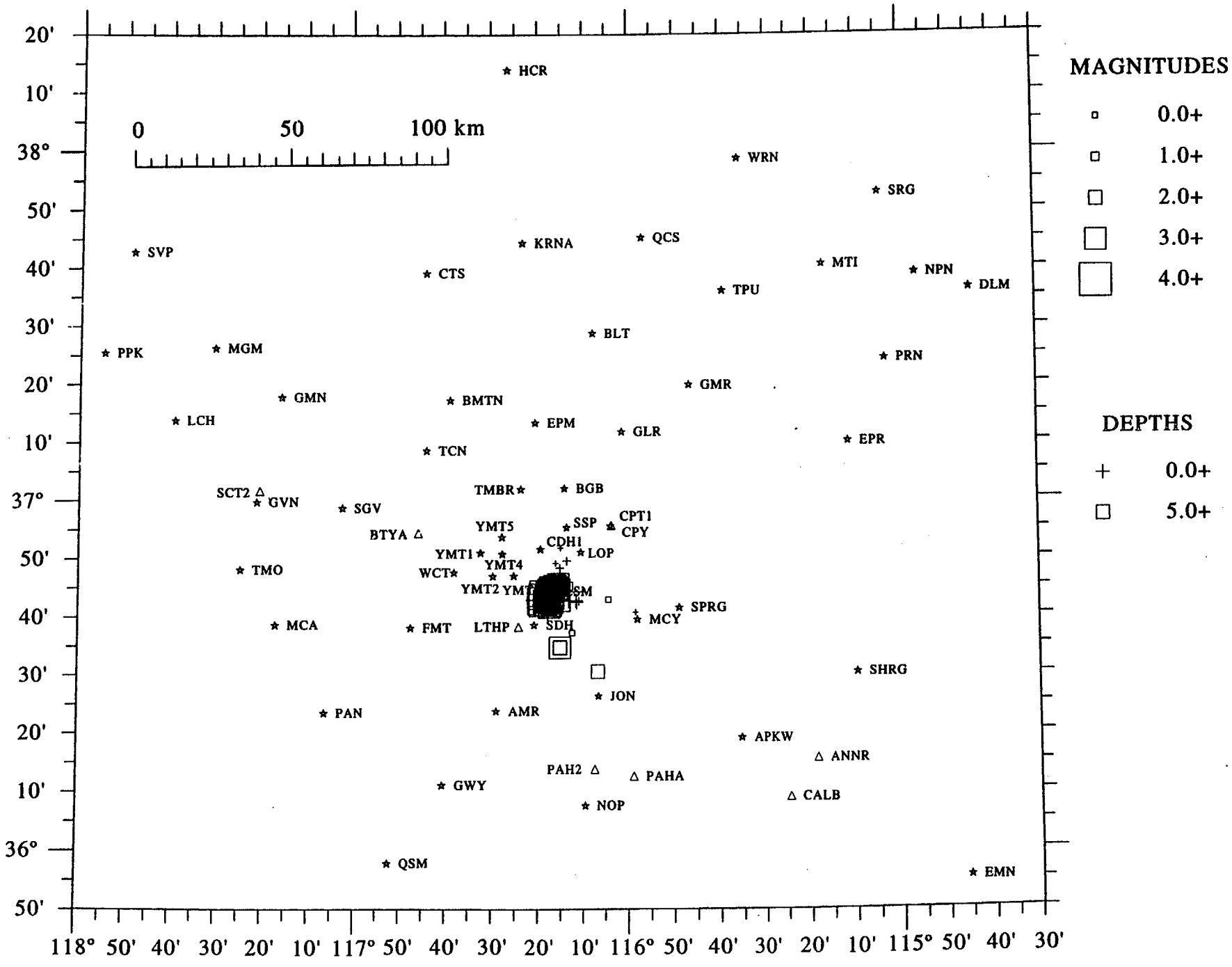
MAGNITUDES
0.0+
1.0+
2.0+
3.0+
4.0+
DEPTHS
0.0+
5.0+
0
50
100 km
HCR
WRN
SRG
SVP
KRNA
QCS
MTI
NPN
DLM
CTS
TPU
BLT
PPK
MGM
PRN
GMR
GMN
BMTN
LCH
EPM
GLR
EPR
TCN
SCT2
GVN
SGV
TMBR
BGB
BTYA
YMT5
SSP
CPT1
CPY
CDH1
YMT1
LOP
TMO
WCT
YMT4
YMT2
SM
SPRG
MCY
MCA
FMT
LTHP
SDH
SHRG
JON
PAN
AMR
APKW
ANNR
PAH2
PAHA
GWY
CALB
NOP
QSM
EMN
20'
10'
38°
50'
40'
30'
20'
10'
37°
50'
40'
30'
20'
10'
36°
50'
118° 50' 40' 30' 20' 10' 117° 50' 40' 30' 20' 10' 116° 50' 40' 30' 20' 10' 115° 50' 40' 30'

2

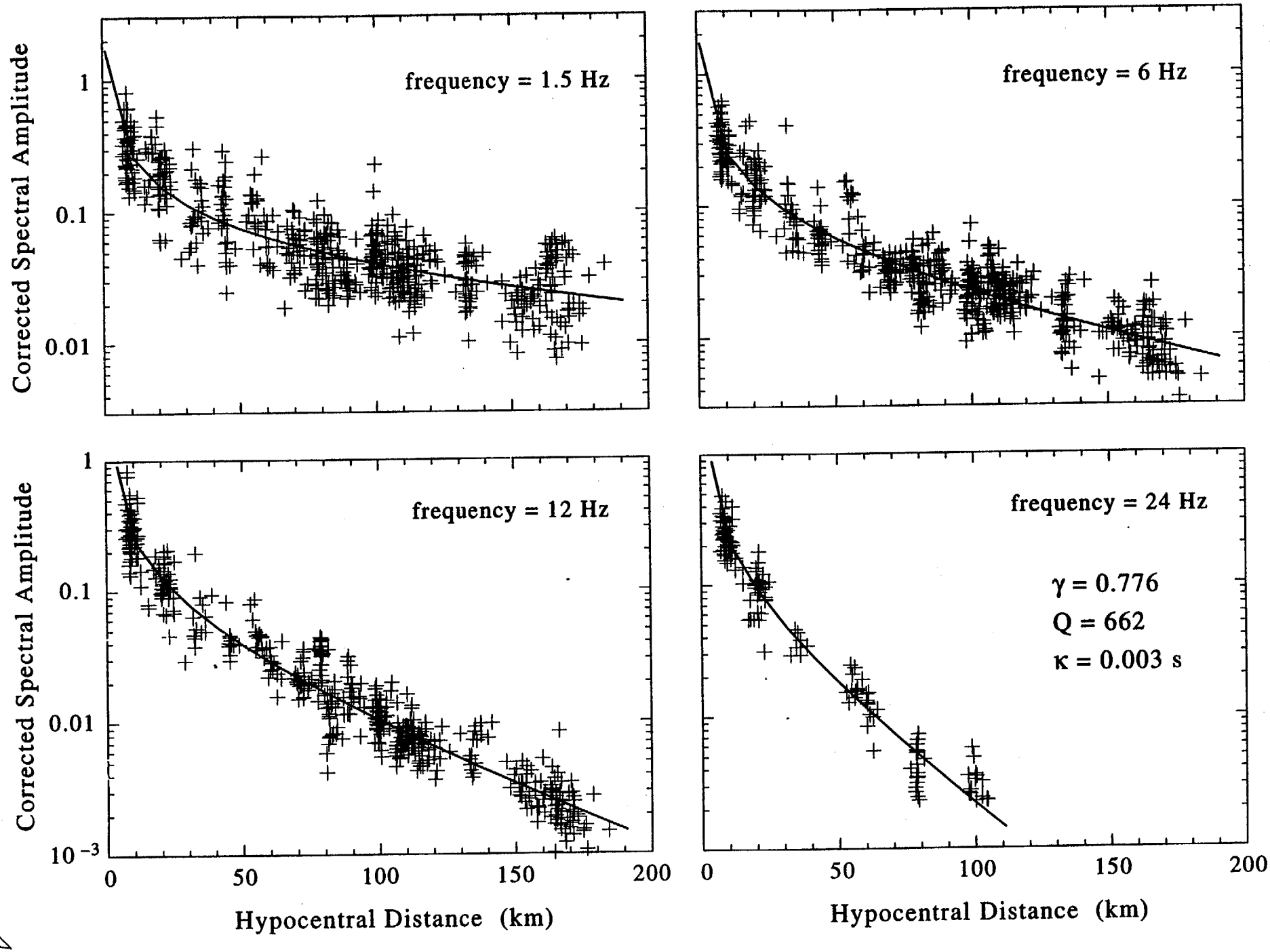
frequency = 1.5 Hz
frequency = 6 Hz
frequency = 12 Hz
frequency = 24 Hz
γ = 0.776
Q = 662
κ = 0.003 s
Corrected Spectral Amplitude
Corrected Spectral Amplitude
1
0.1
0.01
1
0.1
0.01
10 −3
0
50
100
150
200
0
50
100
150
200
Hypocentral Distance (km)
Hypocentral Distance (km)

4

Table 2. Propagation Parameters

grouping	#g	variance	γ	Q_o	Q(16)	α	κ	median f_c
G1	3	0.725%	0.526	623	623	0.0	-0.002 s	13.48 Hz
G1F	3	0.722%	0.450	401	608	0.15	-0.001 s	12.87 Hz
G2	8	0.508%	0.609	643	643	0.0	-0.007 s	11.12 Hz
G3	8	0.494%	0.684	706	706	0.0	-0.007 s	10.55 Hz
G4	8	0.394%	0.776	662	662	0.0	+0.003 s	12.41 Hz
G41	8	0.390%	0.722	489	642	0.1	+0.003 s	12.57 Hz
G43	8	0.385%	0.625	274	629	0.3	+0.004 s	12.61 Hz
G4F	8	0.385%	0.601	238	628	0.35	+0.002 s	12.31 Hz
G45	8	0.387%	0.539	159	637	0.5	+0.005 s	11.90 Hz
G47	8	0.399%	0.514	100	696	0.7	+0.007 s	10.59 Hz

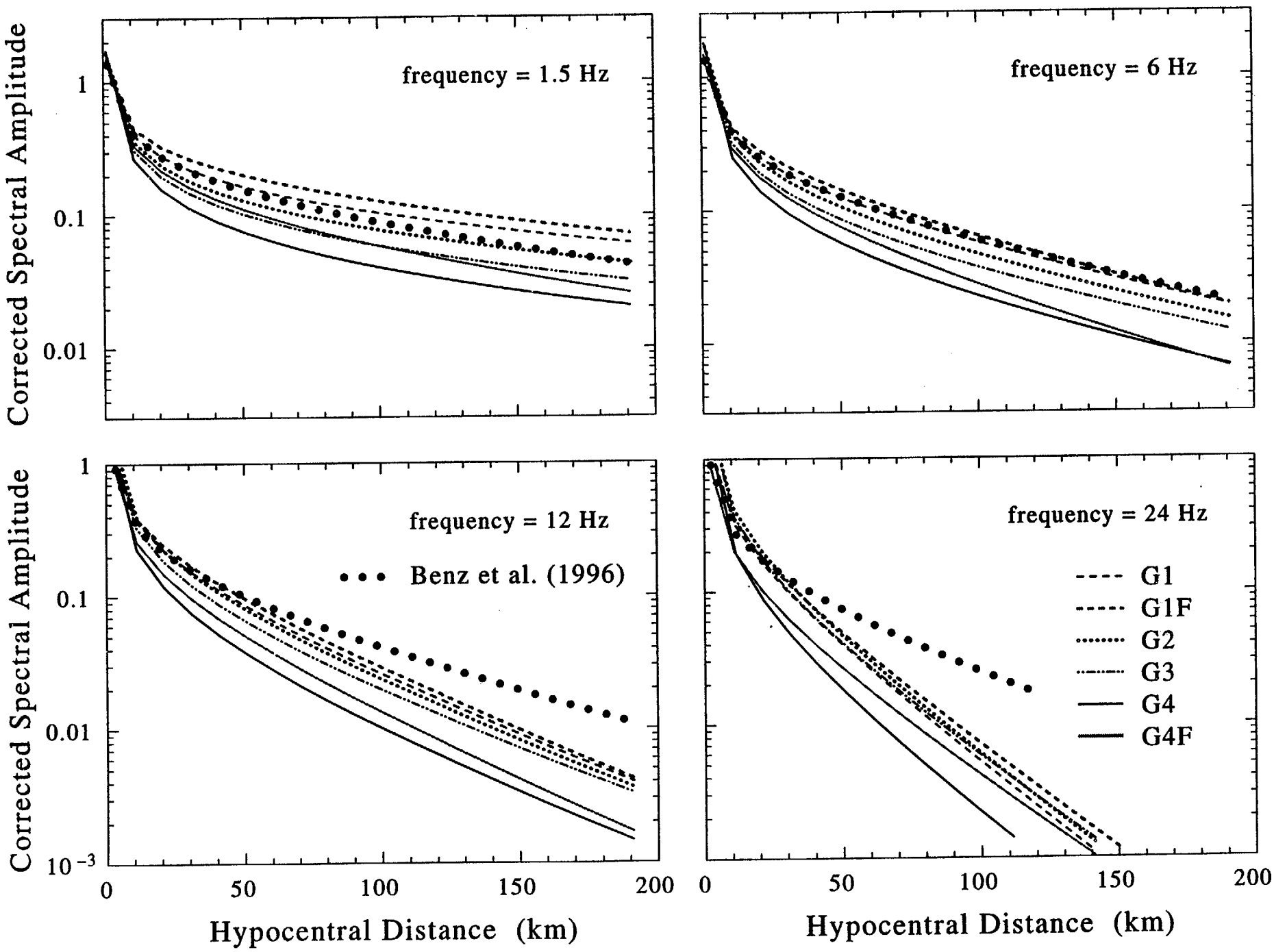
frequency = 1.5 Hz
frequency = 6 Hz
frequency = 12 Hz
frequency = 24 Hz
Benz et al. (1996)
G1
G1F
G2
G3
G4
G4F
Corrected Spectral Amplitude
Corrected Spectral Amplitude
1
0.1
0.01
1
0.1
0.01
10^{-3}
0
50
100
150
200
0
50
100
150
200
Hypocentral Distance (km)
Hypocentral Distance (km)

102

5

COMPARISON OF WEAK MOTION MODEL 64F
WITH LITTLE SKULL MOUNTAIN MOTIONS

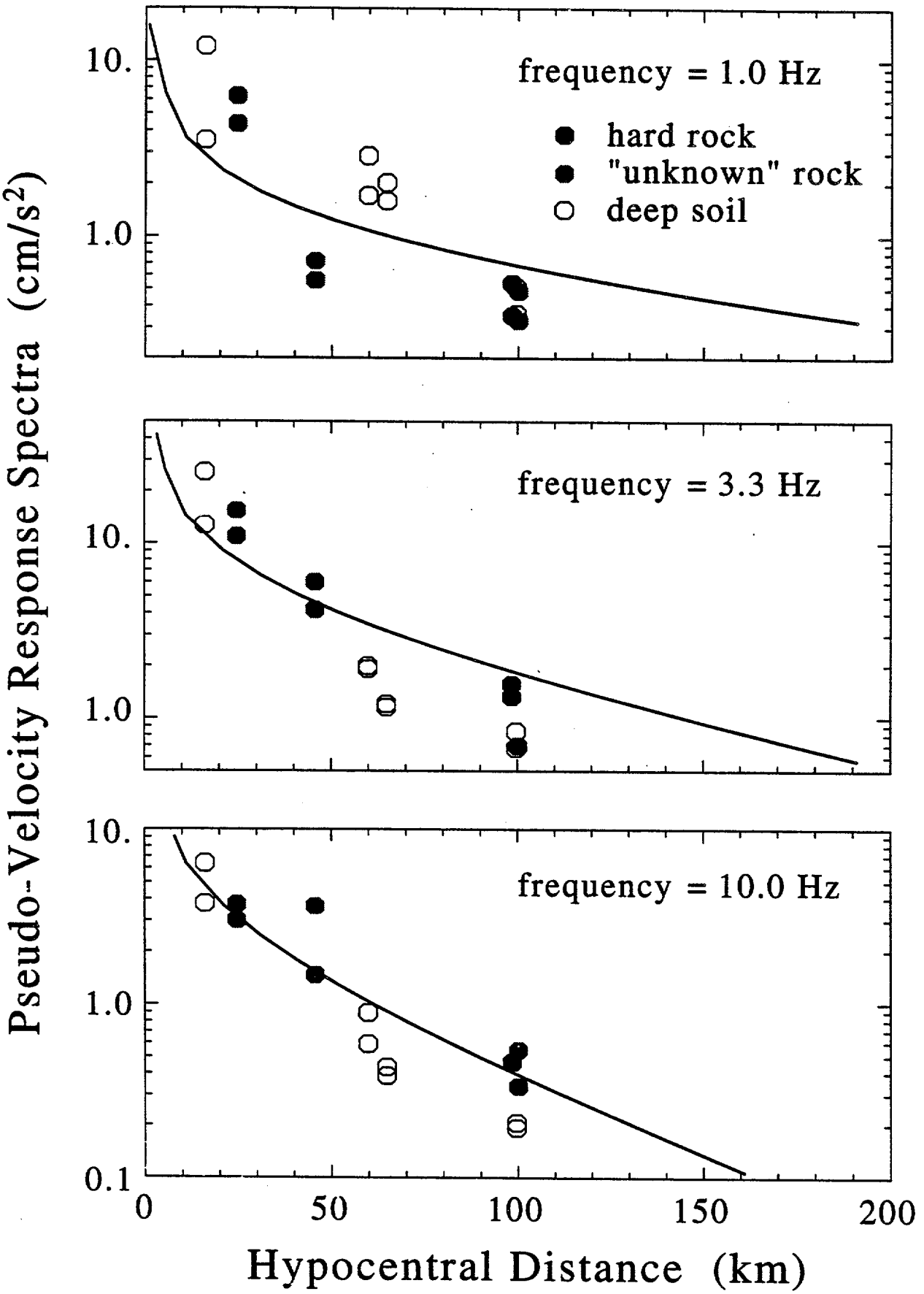

6

Results of weak motion study

Considerable tradeoff between geometric spreading exponent γ and α, exponent of f in frequency dependence of Q

Difficult to define frequency dependence of Q

Q at 16 Hz is 600 - 700 in all models, frequency dependent and independent

κ in the 0.002 - 0.007 range

LSM aftershock ground motions decay with distance a little faster than the result of Benz et al. (1996)

Weak motion decay of ground motion with distance roughly comparable to that observed for Little Skull Mountain strong motion data

STRESS DROPS IN NORMAL FAULTING EARTHQUAKES

GROUND MOTION CHARACTERIZATION WORKSHOP #2

Ann Becker

9 January 1997

EVENTS SELECTED FOR INVERSION[1]

	Date	M_W	Number of Rock[2] Sites	Number of Soil[3] Sites
Abruzzo	5/7/84 17:50	5.8	1 (19.2 km)	4 (30.2, 41.0, 45.6, 49.7)
Borah Peak (Aftershock)	10/29/83 23:29	5.1	2 (22.0, 49.3)	1 (16.9)
Borah Peak (Main Shock)	10/28/83 14:06	6.9	0	2 (83.1, 84.9)
Irpinia A	11/23/80 19:34:54	6.9	6 (10.9, 11.2, 16.2, 24.9, 25.9, 67.7)	2 (36.3, 43.1)
Irpinia B	11/23/80 19:35:04	6.2	6 (8.4, 18.2, 20.3, 22.1, 22.3, 28.9)	4 (41.9, 43.0, 43.9, 64.4)
Little Skull Mtn.	6/29/92 10:14	5.7	2 (23.8, 45.2)	3 (14.1, 58.6, 63.7)
Managua	12/23/72 6:29	6.2	0	1 (3.5)
New Zealand	3/2/87 1:42	6.6	0	2 (18.9, 70.1)
Roermond	4/13/92 1:20	5.3	3 (55.8, 80.7, 102.1)	0

[1] Selection criterion was a predominantly normal mechanism (rake between -45° and -135°)
[2] Hard or soft rock (Spudich et al. classes 0, 1, 2)
[3] Deep or shallow soil (Spudich et al. classes 5, 6, 7)

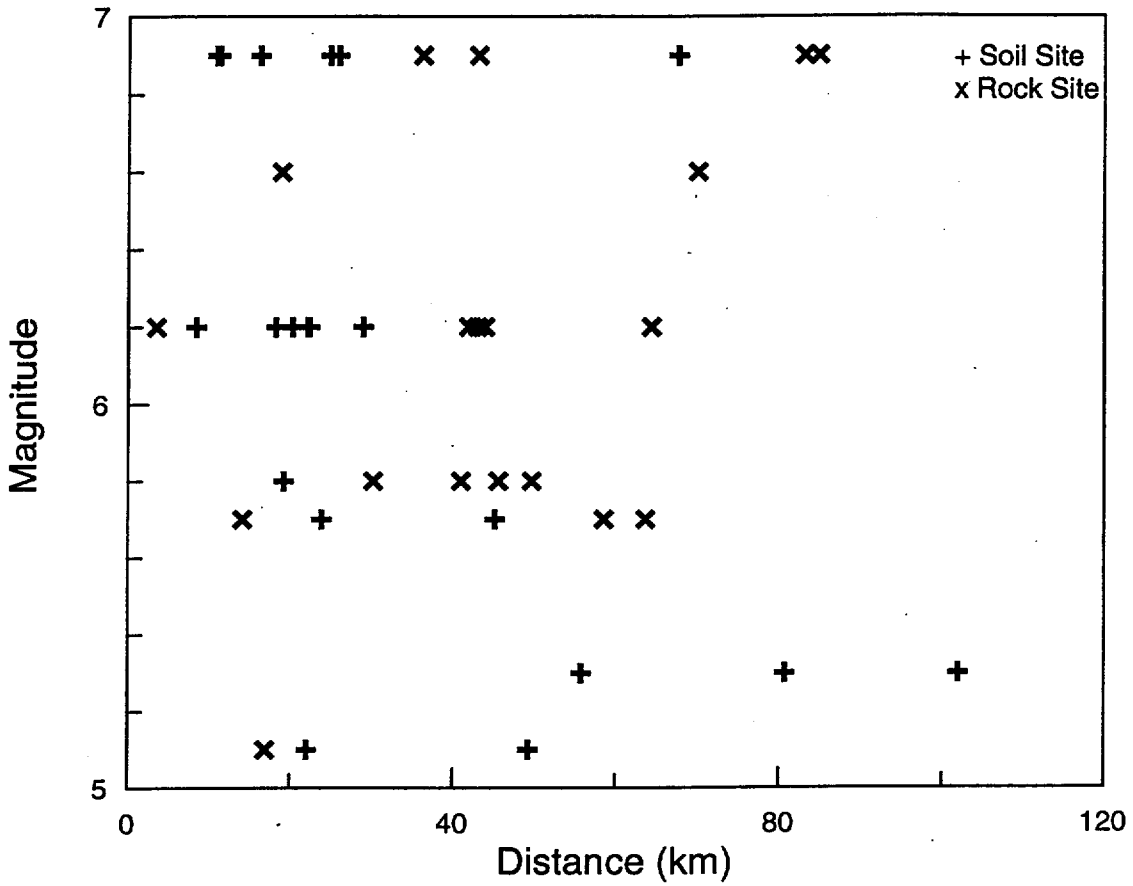

Magnitude and Distance Distribution
Events used in Q/kappa Inversion

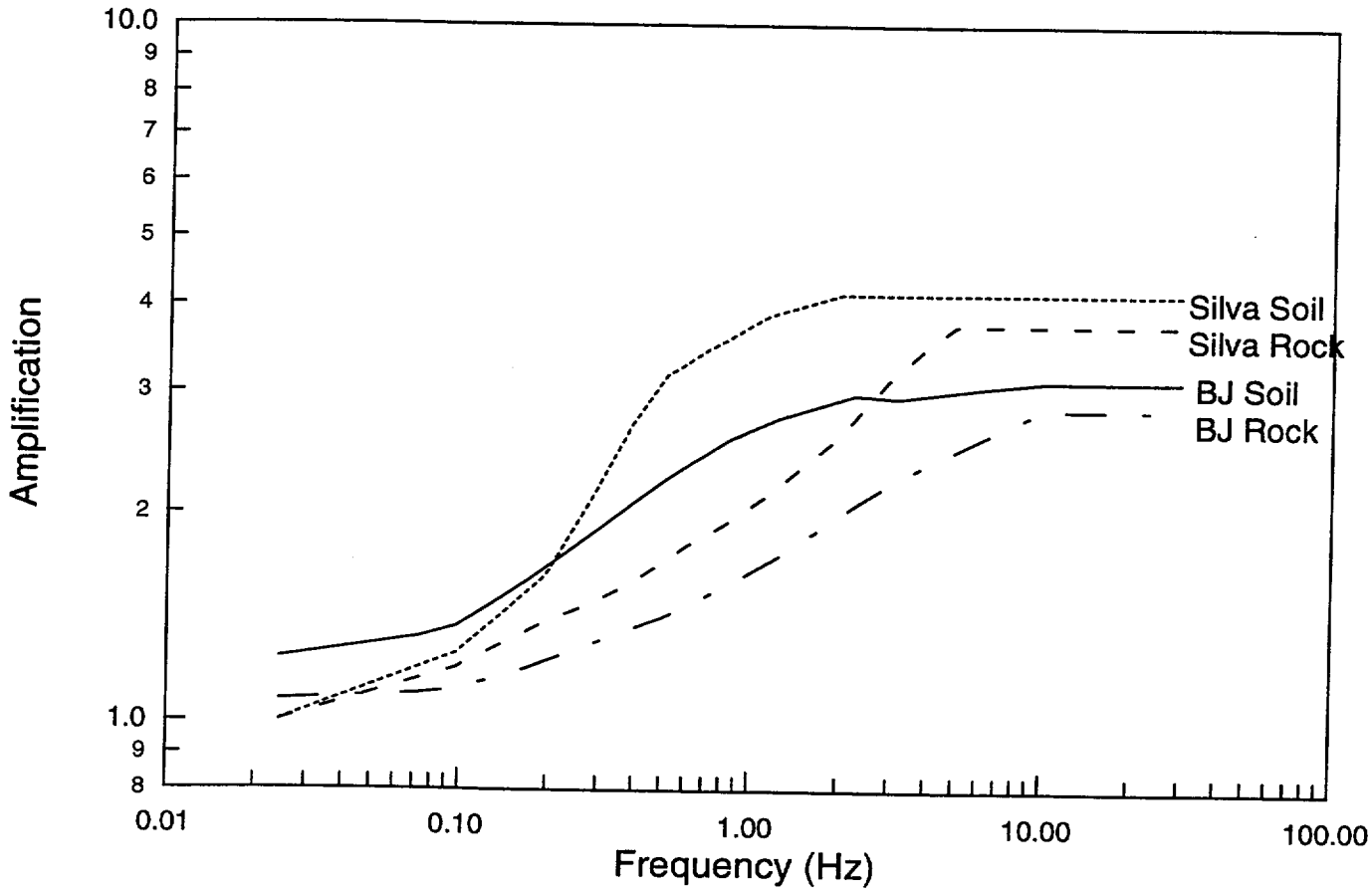

Transfer Functions used in Inversion

INVERSION RESULTS

Run #	1	2	3	4
Number of 'Sites'	32	12	32	32
Q	200[1]	200[1]	200[1]	346[1]
η	0.4[1]	0.4[1]	0.4[1]	0.53[1]
Transfer Function	Silva	Silva	Boore-Joyner	Silva
Stress Drop (bars)				
Abruzzo	95	95	165	82
Borah A/S	18	24	30	17
Borah M/S	42	42	69	32
Irpinia A	30	32	49	27
Irpinia B	28	27	47	25
LSM	45	33	74	29
Managua	16	16	27	16
NZ	31	31	51	26
Roermond	49	49	91	35
Median	32	34	58	29
Median κ, all sites	0.047	0.042	0.048	0.058
Mean κ, rock sites	0.057 ± 0.021		0.059 ± 0.021	0.066 ± 0.020
Mean κ, soil sites	0.047 ± 0.018		0.048 ± 0.018	0.057 ± 0.016
κ (sec)				
Abruzzo	0.061	0.058/0.062[2]	0.063	0.069
Borah A/S	0.033	0.048/0.043[2]	0.034	0.041
Borah M/S	0.013	--/0.013[2]	0.014	0.033
Italy	0.062	0.067/0.055[2]	0.063	0.070
LSM	0.036	0.016/0.031[2]	0.037	0.041
Managua	0.066	--/0.066[2]	0.067	0.067
NZ	0.045	--/0.045[2]	0.046	0.056
Roermond	0.062	0.062/--[2]	0.065	0.080

[1] Value fixed [2] Rock value/soil value

CONCLUSIONS

Silva:

6 California events
Mean magnitude 6.25
Strike-slip
Median $\Delta\sigma$ 37 bars
$\kappa \cong 0.05$

cf:

9 Normal earthquakes
Mean magnitude 6.1
Normal faulting
Median $\Delta\sigma$ 29 bars
κ 0.047 sec

Boore-Joyner:

WNA events
Magnitude 6.5
Mixed mechanisms
Median $\Delta\sigma$ 70 - 100 bars
κ 0.035

cf:

9 Normal earthquakes
Mean magnitude 6.1
Normal faulting
Median $\Delta\sigma$ 58 bars
κ 0.048

Dinar Earthquake Project

John Anderson

✓Where is Dinar?

✓Plot of the earthquake and station distribution?

✓Plot of accelerograms.

Map with aftershock locations (Suzi will do)

Source properties
- ✓- moment magnitude (Have Harvard CMT. Suzi will check USGS & Tokyo)
- static stress drop (JA will do)
- ✓ - rupture plane (dimensions and dip) (modify if data demand)

Strong Motion - basic analysis
- ✓ - Closest distances (Rupture and JB dist) for each station
- Plot of velocity (Yuehua will do)
- Plot of displacement (Yueha will do)
- Fourier spectra (Suzi will do. May allow educated guess of basin depth at Dinar.)
- response spectra at 5% damping (Yuehua will do)
- RMS stress drop (Suzi will do)

Path Properties:
- velocity structure and Q (Erzinincan, northern Nevada & Yucca Mtn models available. Suzi will look for others. Q an educated guess, test with synthetics.)

Site Properties:
- site classification (Dinar has good information. Suzi will look for geologic map of Turkey for the other sites.)
- kappa from weak motion (aftershocks) and strong motion (Suzi will do)

Source model
- Composite source model to match statistical properties (Yuehua will do)
- Specific composite source model (Yuehau will do)

Write report (All contribute, JA coordinate) Target date Feb 96.

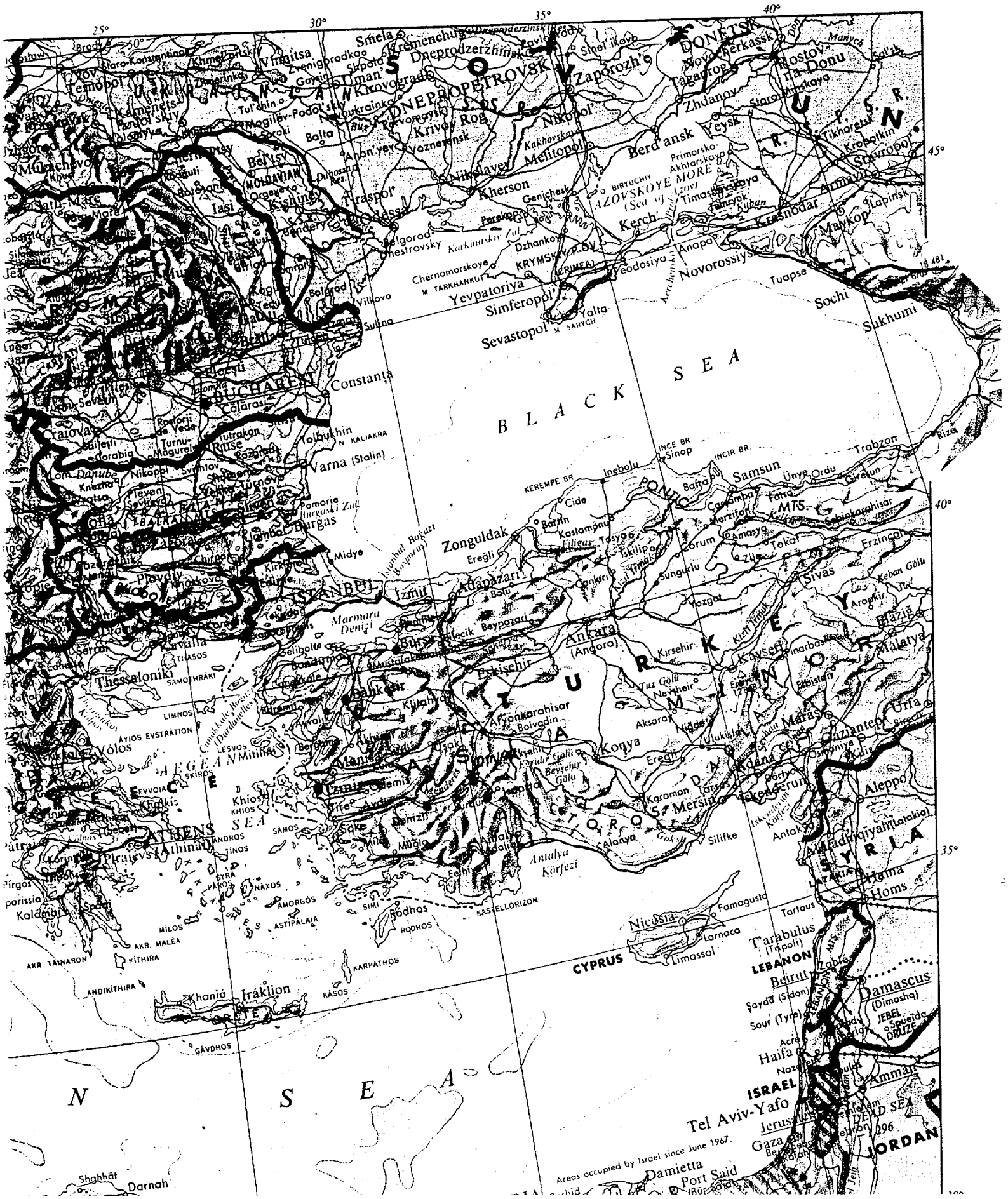
BLACK SEA
AZOVSKOYE MORE (Sea of Azov)
Sevastopol
Simferopol'
Yevpatoriya
Yalta
Kerch
Feodosiya
Novorossiysk
Sochi
Sukhumi
Tuapse
Krasnodar
Maykop
Rostov na Donu
Taganrog
Zhdanov
Yeysk
Berdyansk
Melitopol'
Nikopol'
Kherson
Nikolayev
Zaporozh'e
Dnepropetrovsk
Krivoy Rog
Dnepr
Donetsk
Odessa
Tiraspol'
Kishinev
Iasi
Constanța
Varna (Stalin)
Burgas
Zonguldak
Samsun
Sinop
Trabzon
Ordu
Giresun
Ankara (Angora)
Eskişehir
Konya
Adana
Mersin
Alanya
Antalya
Antakya
Aleppo
Latakia
Hama
Homs
Tartous
Tarabulus (Trípoli)
Beirut
Damascus (Dimashq)
Haifa
Tel Aviv-Yafo
Jerusalem
Amman
Gaza
Port Said
Damietta
Darnah
Shahhāt
Nicosia
Famagusta
Larnaca
Limassol
CYPRUS
LEBANON
ISRAEL
JORDAN
SYRIA
TURKEY
Istanbul
Izmir
Bursa
Thessaloniki
Athens
Piraeus
Khania
Iráklion
Rodhos
Khios
Samos
Lesvos
Mitilini
Kos
Karpathos
Kríti
Kithira
Milos
Naxos
Paros
Andros
Tinos
Syra
Amorgos
Astipalaia
Kastellorizon
Gavdhos
Akr. Tainaron
Akr. Malea
Andikithira
Skiros
Evvoia
Limnos
Samothráki
Thasos
Ayios Evstratios
Canakkale Boğazı (Dardanelles)
Marmara Denizi
Istanbul Boğazı (Bosporus)
Kerkenes Dağı
Erciyas Dağı
Van Gölü
Tuz Gölü
Keban Gölü
Kizil Irmak
Sakarya
Meriç
Vardar
Danube
Dnepr
Don
Volga
Kuban
Manych
Bug
Dniester
Prut
Siret
Olt
Mureş
Tisza
Sava
Drava
Vardar
Maritsa
Struma
Vistula
Oder
Elbe
Rhine
Po
Tiber
Arno
Ebro
Tagus
Guadiana
Guadalquivir
Areas occupied by Israel since June 1967.

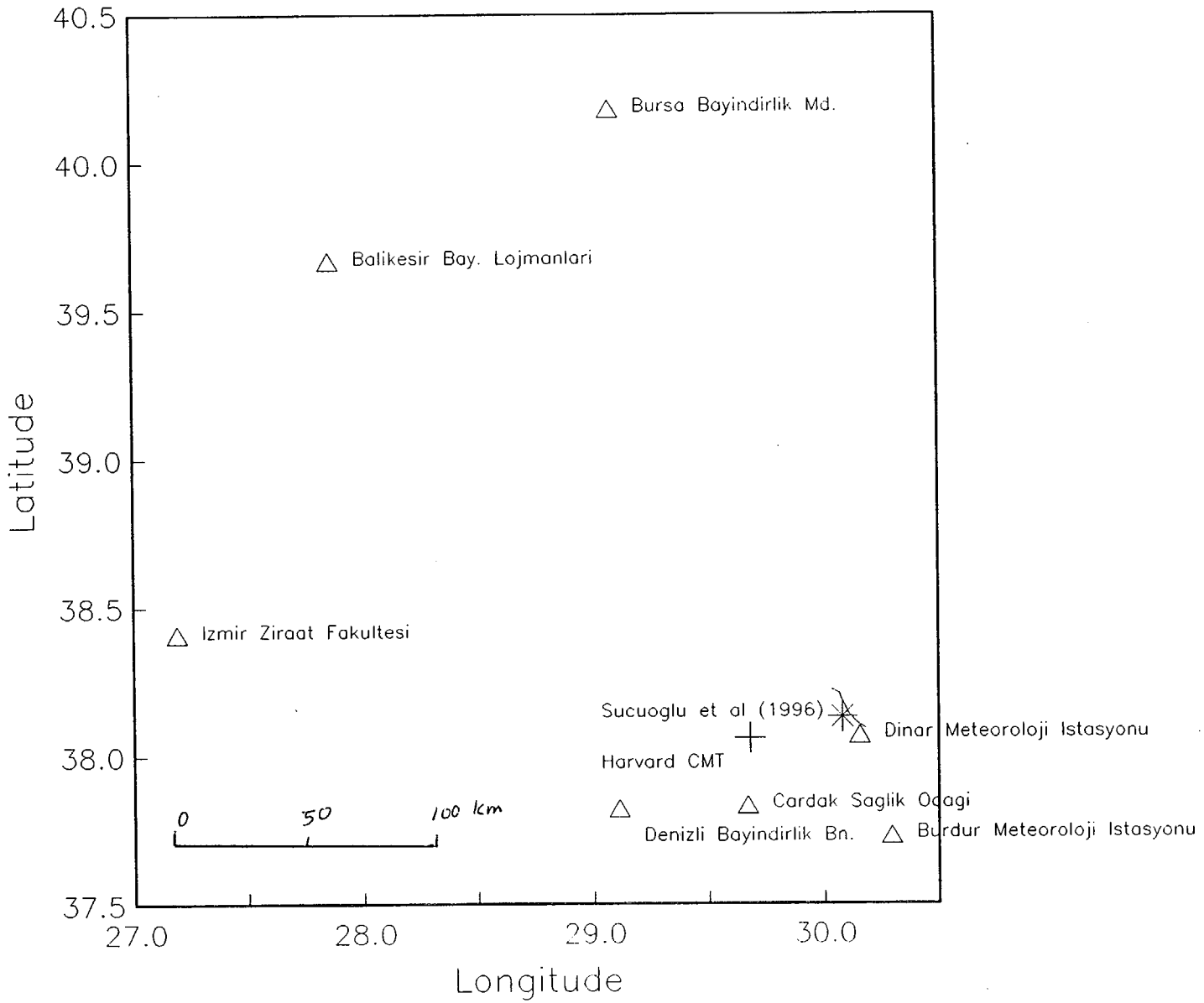
40.5
40.0
39.5
39.0
38.5
38.0
37.5
Latitude
27.0
28.0
29.0
30.0
Longitude
Bursa Bayindirlik Md.
Balikesir Bay. Lojmanlari
Izmir Ziraat Fakultesi
Sucuoglu et al (1996)
Dinar Meteoroloji Istasyonu
Harvard CMT
Cardak Saglik Ocagi
Denizli Bayindirlik Bn.
Burdur Meteoroloji Istasyonu
0
50
100 km

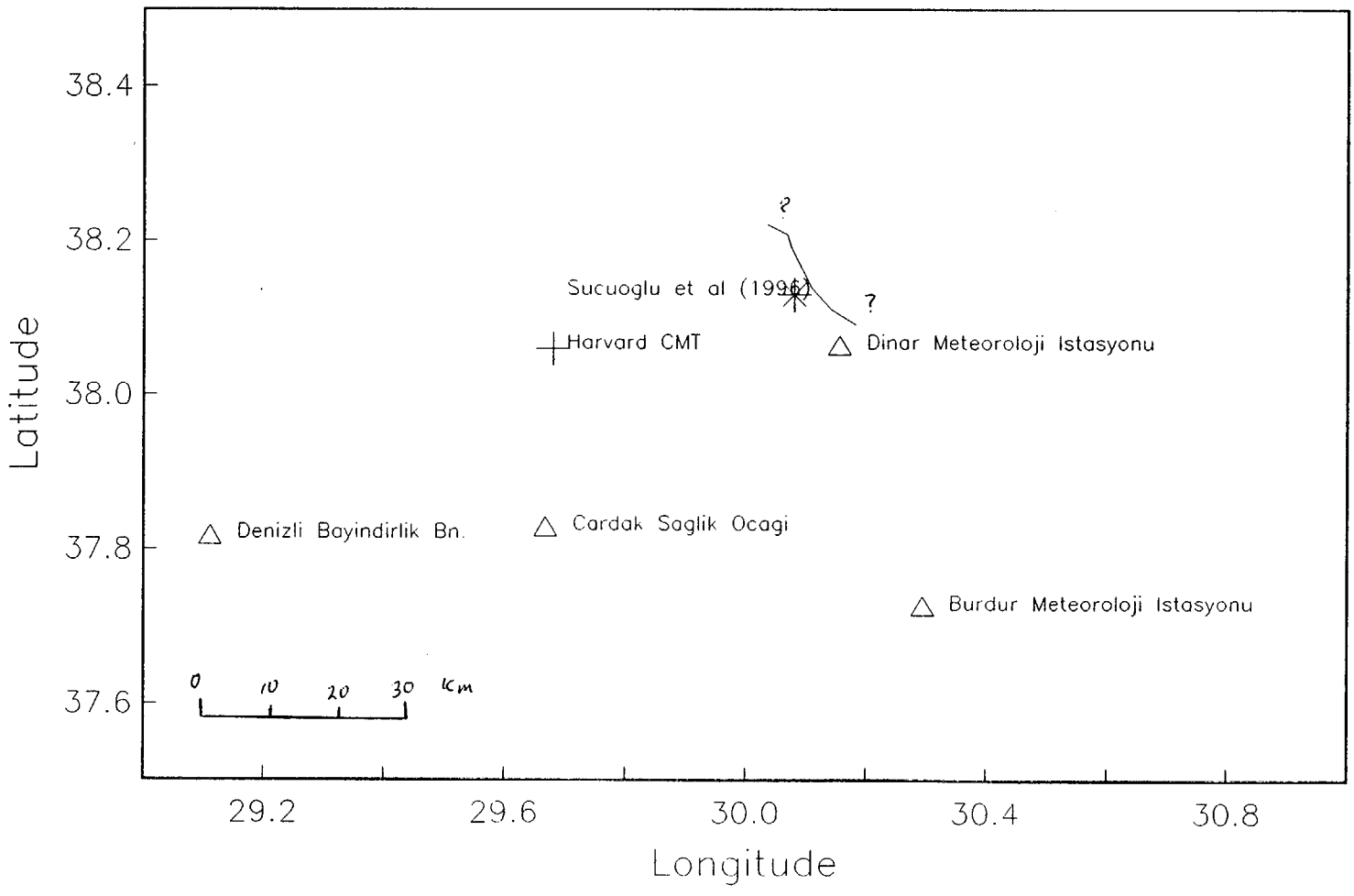
38.4
38.2
38.0
37.8
37.6
Latitude
29.2
29.6
30.0
30.4
30.8
Longitude
Sucuoglu et al (1996)
Harvard CMT
Dinar Meteoroloji Istasyonu
Denizli Bayindirlik Bn.
Cardak Saglik Ocagi
Burdur Meteoroloji Istasyonu
0 10 20 30 Km

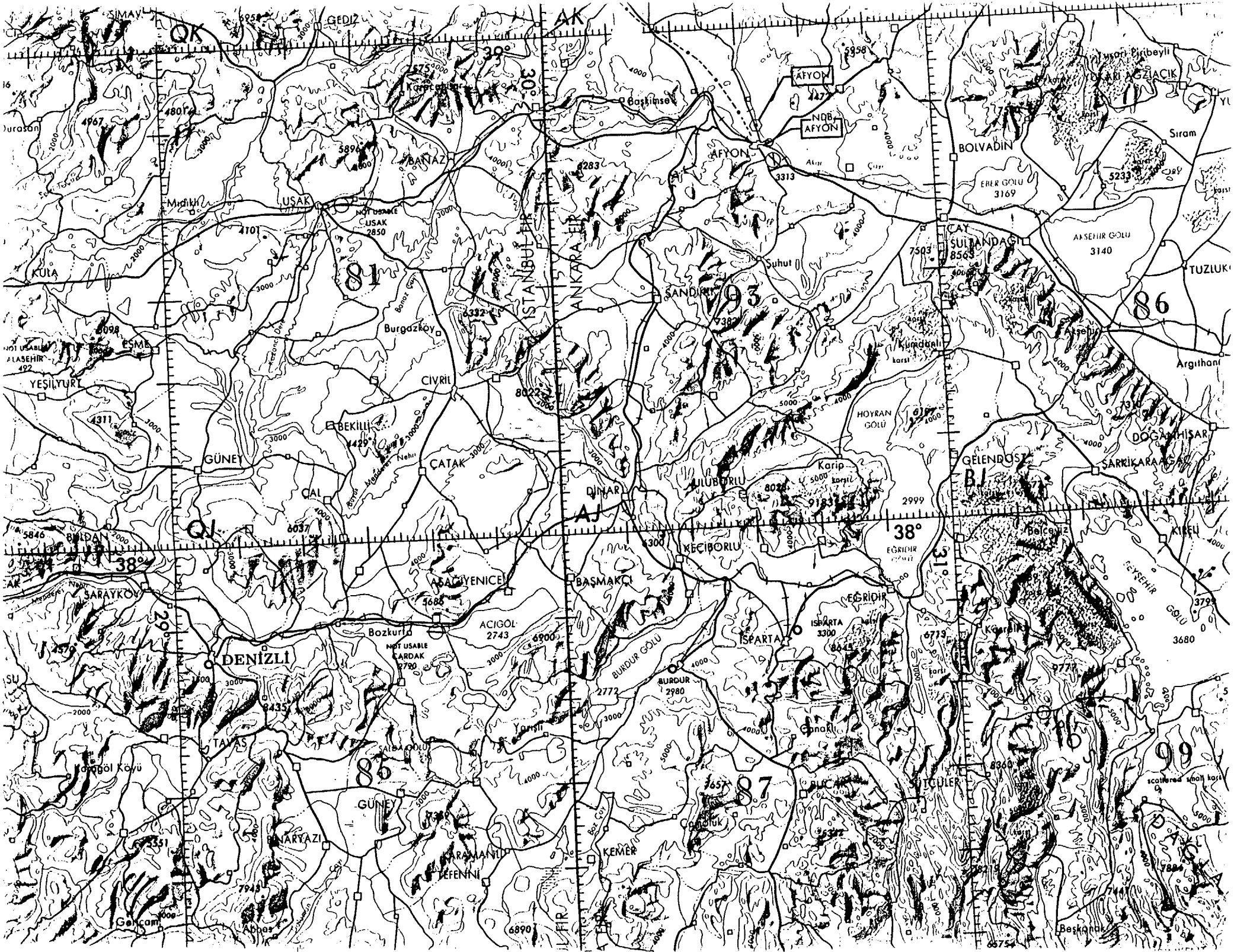
QK
AK
QJ
AJ
BJ
30°
31°
38°
29°
GEDIZ
SIMAV
Durasan
Kürecatur
Başkimse
AFYON
NDB AFYON
BOLVADİN
Yukarı Piribeyli
YUKARI AĞZIÇAK
Sıram
EBER GÖLÜ
3169
AKŞEHİR GÖLÜ
3140
TUZLUK
ÇAY
SULTANDAĞI
Suhut
SANDIKLI
BANAZ
UŞAK
NOT USABLE
UŞAK
2850
Midikli
KULA
ESME
YEŞİLYURT
Burgazköy
CİVRİL
BEKİLLİ
GÜNEY
CATAK
ÇAL
BOLDAN
SARAYKÖY
DİNAR
KEÇİBORLU
BAŞMAKÇI
AŞAĞIYENİCE
ACIGÖL
2743
Bozkurt
NOT USABLE
CARDAK
2780
DENİZLİ
TAVAS
Yenişi
SALDA GÖLÜ
BURDUR GÖLÜ
BURDUR
2980
ISPARTA
ISPARTA
3300
EĞRİDİR
HOYRAN GÖLÜ
Karıp
GELENDOST
DOĞANHİSAR
ŞARKIKARAAĞAÇ
Belceriz
KİREL
EĞİRDİR GÖLÜ
3680
Kürecik
Çanakli
BUCAK
SÜTÇÜLER
Gönüllük
KEMER
BİNARYAZI
KARAMANLI
DEFENNİ
Gelcan
Abbas
Beşkonak
Akşehir
Argıthanı
Kurudanlı
Bozkır
Çay
Çur
Alan
Bozkır Çayı
Menderes Nehri
Bonos Çayı
Kocaçay Dere
Kürecik Dere
Karıp Çayı
Yenişi Çayı
Çanakli Çayı
Kemer Çayı
Beşkonak Çayı
Abbas Çayı
Gelcan Çayı
Karamanlı Çayı
Defenni Çayı
Çay
Çur
Alan
karsi
scattered small karsi
ISTANBUL İL
ANKARA İL
İLÇE
DAĞ
81
93
86
85
87
99
4967
4801
5896
4600
6283
5958
4427
3313
7503
8505
5233
4101
6332
8022
9383
6098
4311
4429
6037
5846
6300
8028
9183
2999
6719
8445
9777
3799
5685
6900
2772
8435
7339
7943
6890
6754
8360
7657
6317
7821
7441
7884
4579
3351
3000
4000
5000
2000

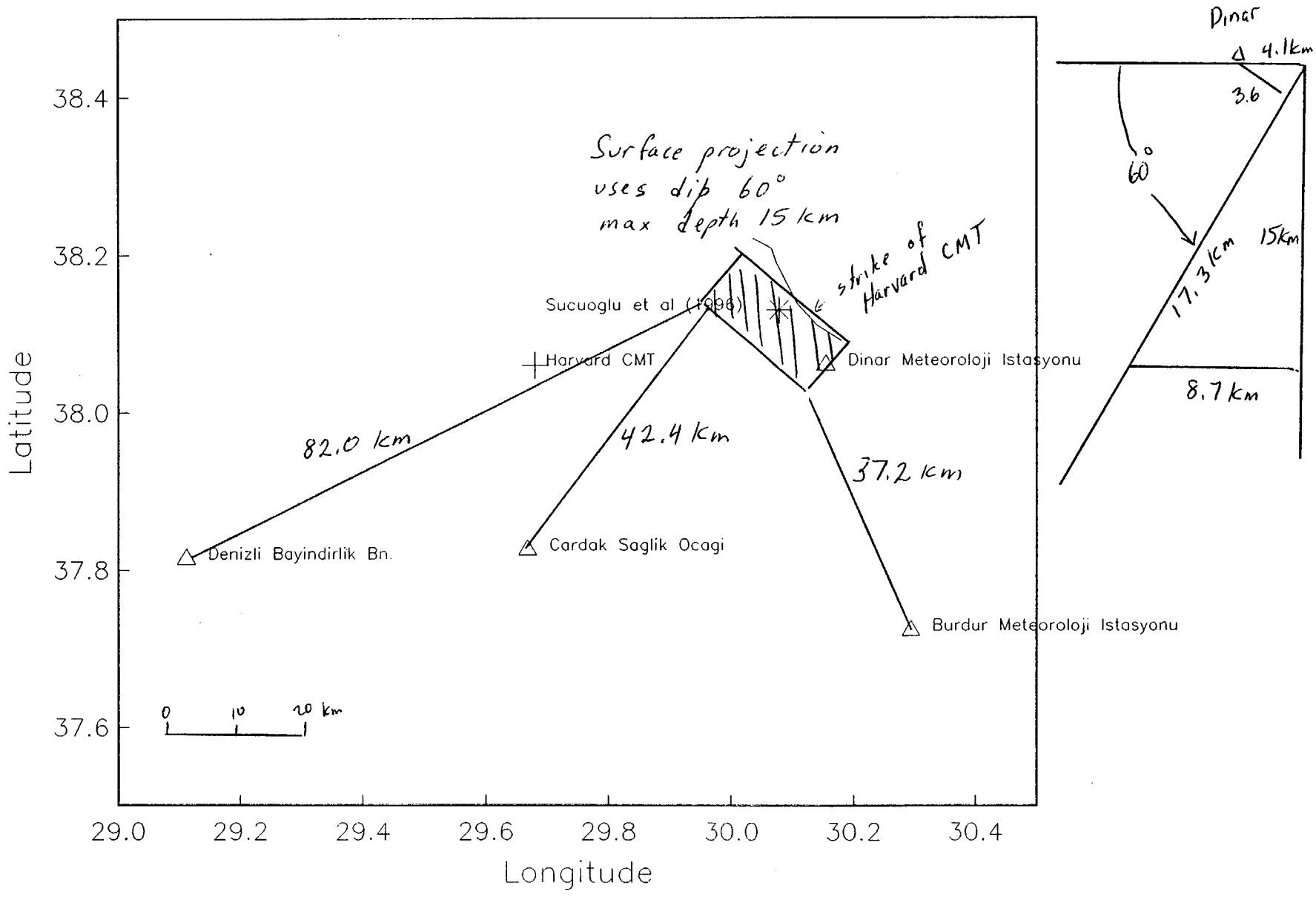
Surface projection
uses dip 60°
max depth 15 km
strike of Harvard CMT
Sucuoglu et al (1996)
Harvard CMT
Dinar Meteoroloji Istasyonu
82.0 km
42.4 km
37.2 km
Denizli Bayindirlik Bn.
Cardak Saglik Ocagi
Burdur Meteoroloji Istasyonu
0 10 20 km
Latitude
38.4
38.2
38.0
37.8
37.6
Longitude
29.0
29.2
29.4
29.6
29.8
30.0
30.2
30.4
Dinar
4.1km
3.6
60°
17.3km
15km
8.7km

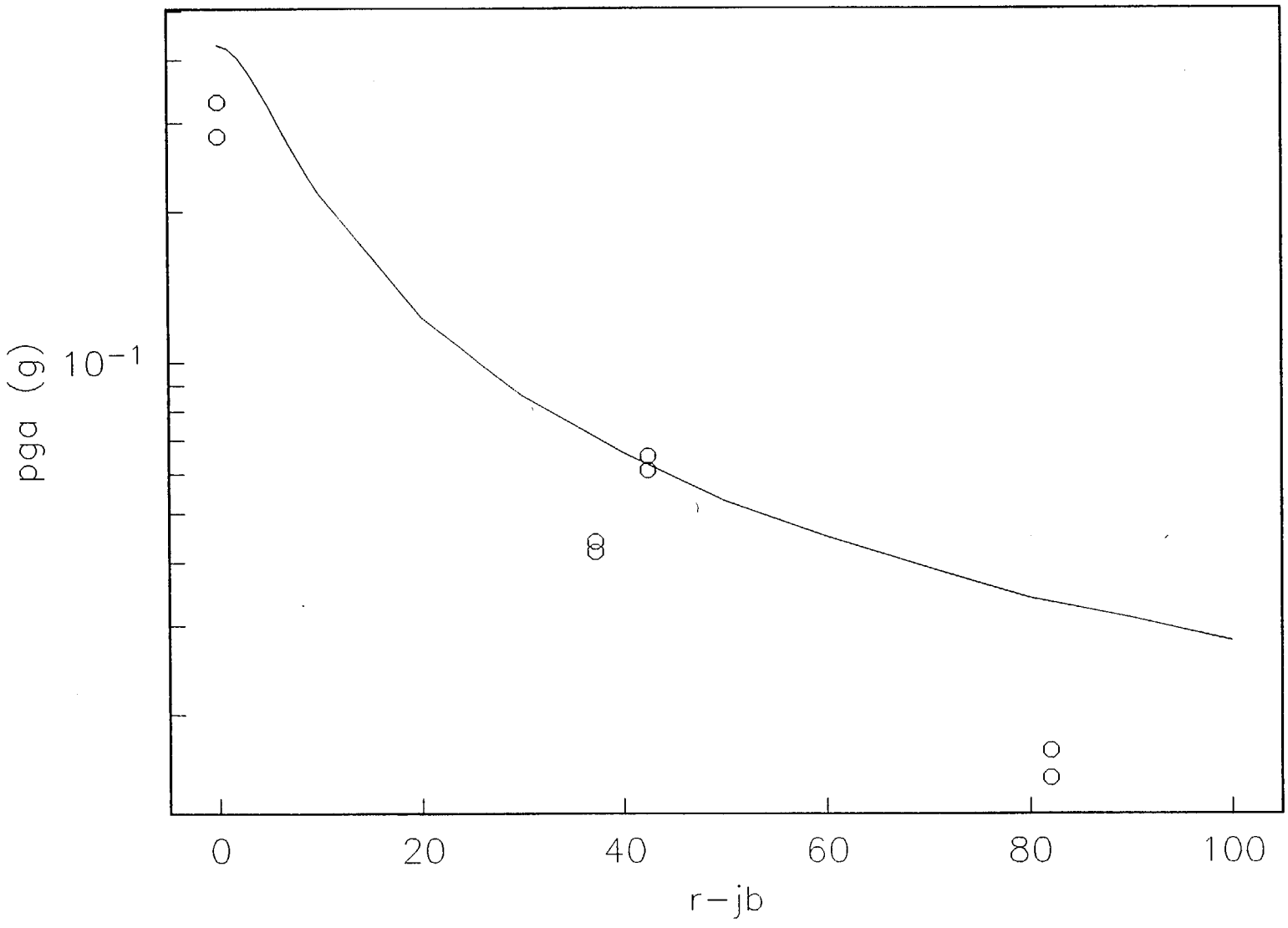
pga (g)
10^{-1}
0
20
40
60
80
100
r−jb

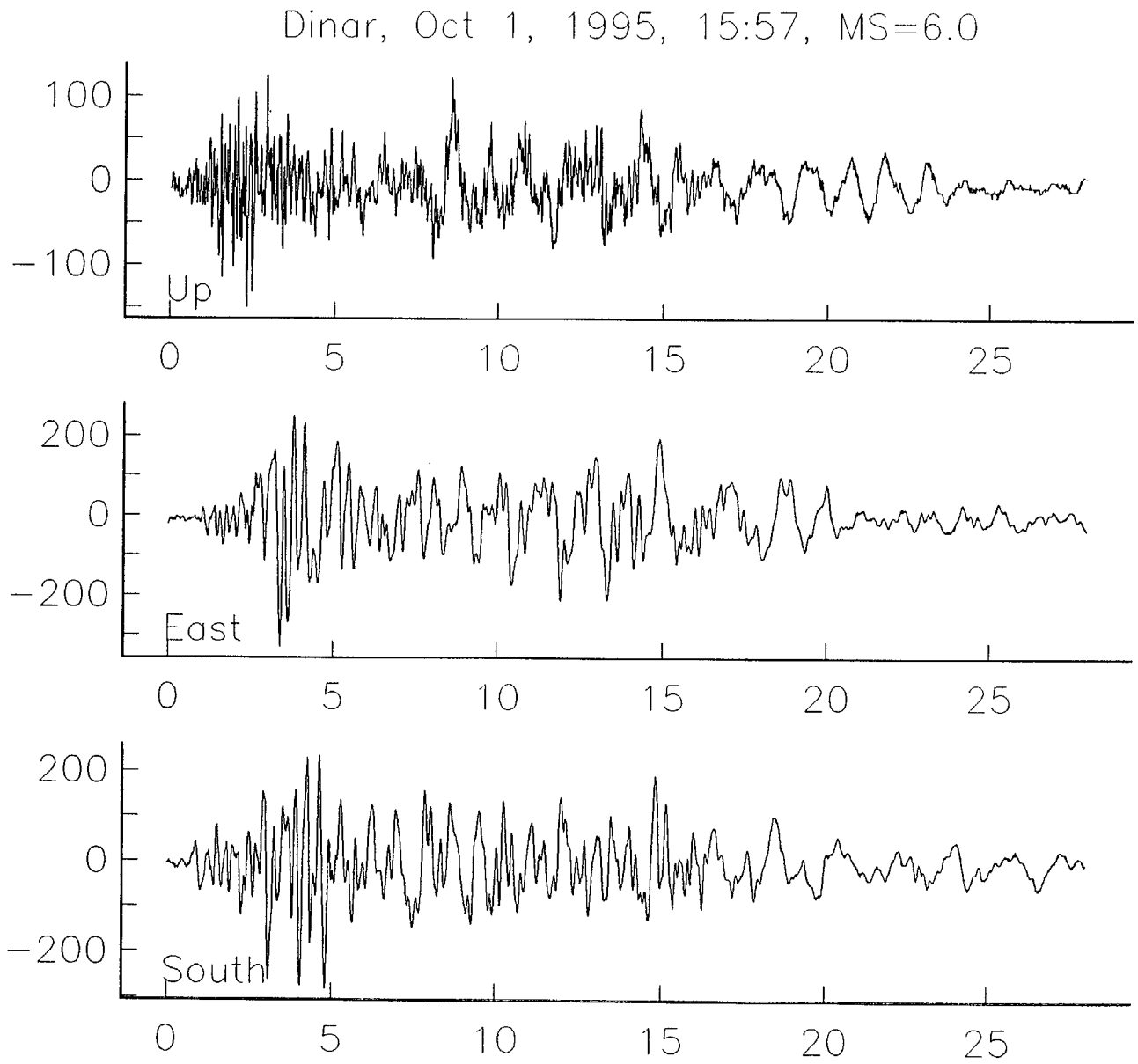
Dinar, Oct 1, 1995, 15:57, MS=6.0
100
0
−100
Up
0
5
10
15
20
25
200
0
−200
East
0
5
10
15
20
25
200
0
−200
South
0
5
10
15
20
25

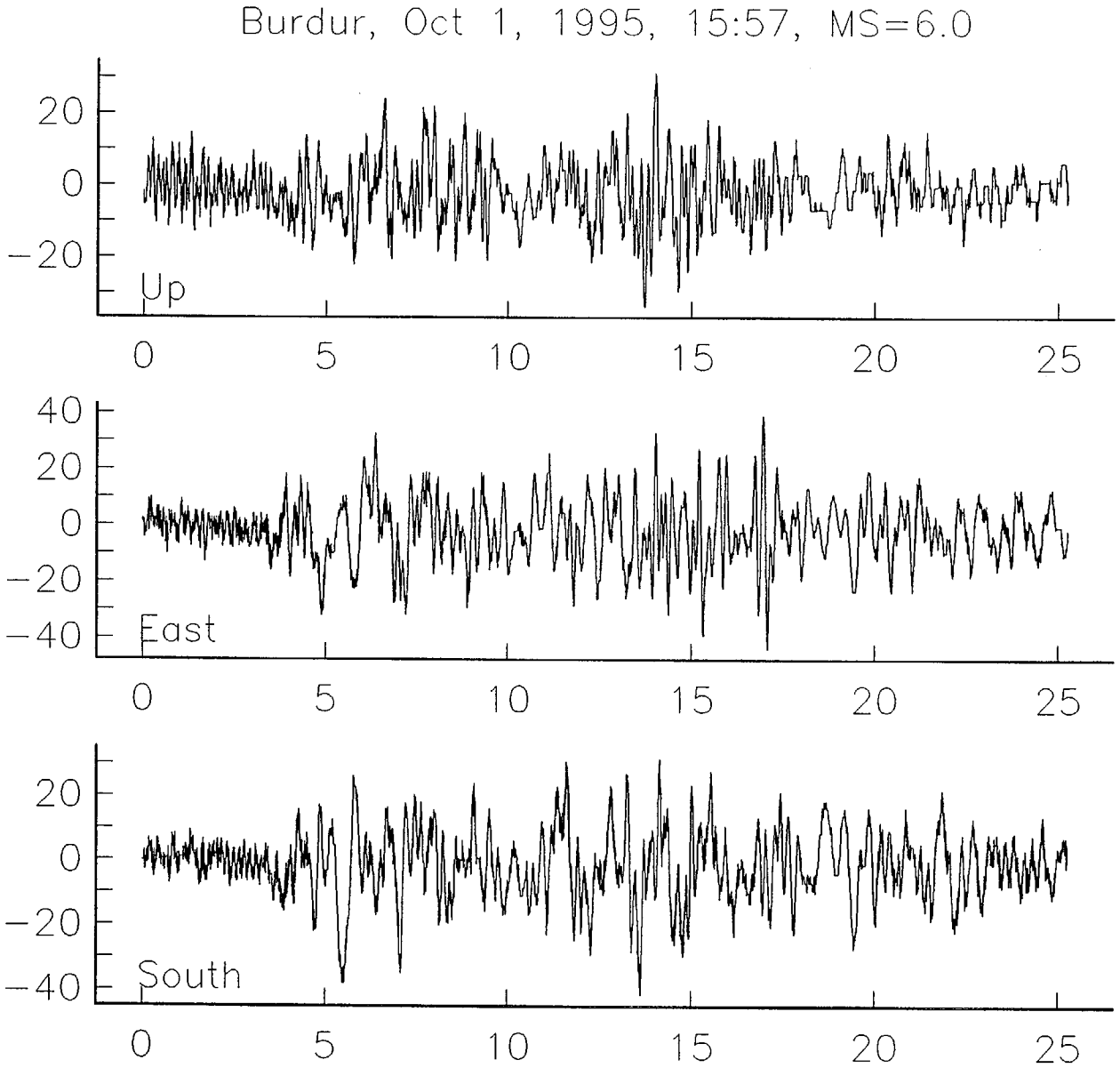
Burdur, Oct 1, 1995, 15:57, MS=6.0
20
0
−20
Up
0
5
10
15
20
25
40
20
0
−20
−40
East
0
5
10
15
20
25
20
0
−20
−40
South
0
5
10
15
20
25

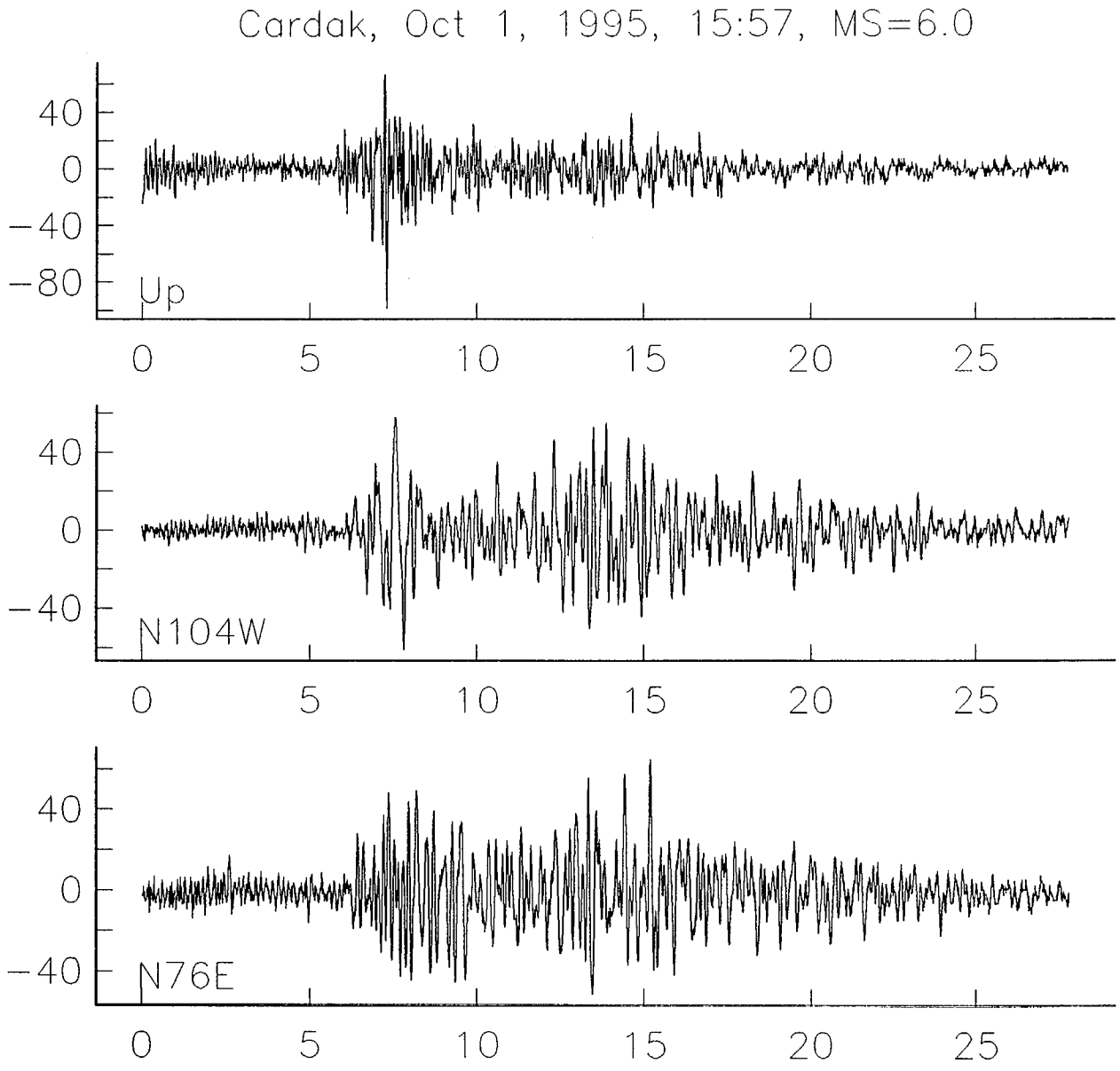
Cardak, Oct 1, 1995, 15:57, MS=6.0
40
0
−40
−80
Up
0
5
10
15
20
25
40
0
−40
N104W
0
5
10
15
20
25
40
0
−40
N76E
0
5
10
15
20
25

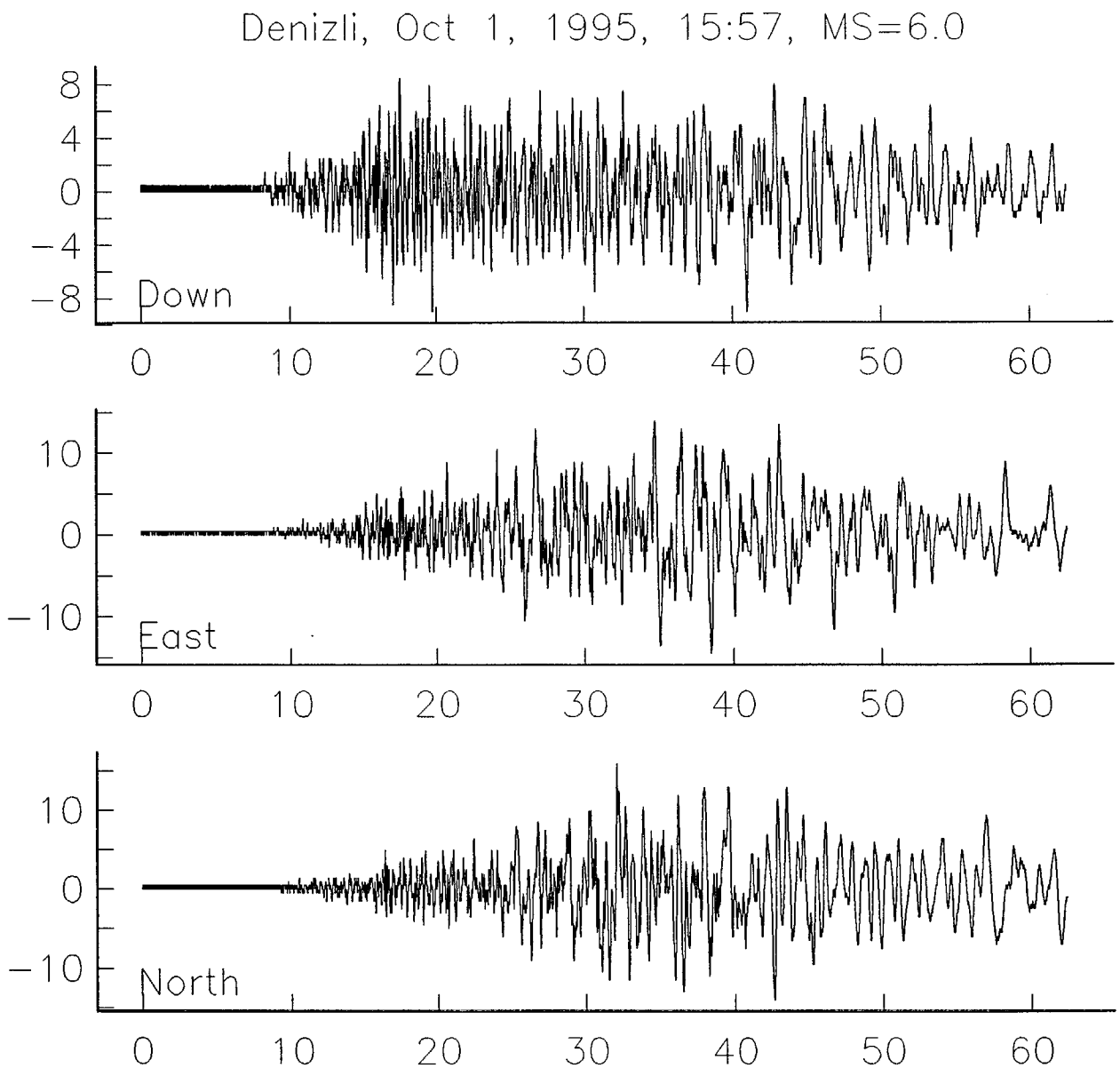
Denizli, Oct 1, 1995, 15:57, MS=6.0
8
4
0
−4
−8
Down
0
10
20
30
40
50
60
10
0
−10
East
0
10
20
30
40
50
60
10
0
−10
North
0
10
20
30
40
50
60

Bulletin of the Seismological Society of America, Vol. 87, No. 1, pp. 1–000, February 1997

Seismic Energy and Stress-Drop Parameters for a Composite Source Model

by John G. Anderson

Abstract This article examines relationships among radiated energy and several stress-drop parameters that are used to describe earthquake faulting. This is done in the context of a composite source model that has been quite successful in its ability to reproduce statistical characteristics of strong-motion accelerograms. The main feature of the composite source model is a superposition of subevents with a fractal distribution of sizes, but all with the same subevent stress drop ($\Delta\sigma_d$) that is independent of the static stress drop ($\Delta\sigma_s$). In the model, $\Delta\sigma_d$ is intended to represent the effective dynamic stress, and it does this well when $\Delta\sigma_d > 2\Delta\sigma_s$. The radiated energy in the S wave is $E_S^{CS} = \cancel{0.233}\, C_E\,(\Delta\sigma_d/\mu)\, M_0$, where M_0 is the seismic moment of the earthquake, μ is shear modulus, and C_E is a dimensionless parameter that equals unity when $\Delta\sigma_d > 2\Delta\sigma_s$. The apparent stress ($\sigma_a$) is $\sigma_a = \cancel{0.233}\, C_E\,\Delta\sigma_d$. The effective stress is $\sigma_e \approx 0.44 C_E\,\Delta\sigma_d$. The Orowan stress drop ($\Delta\sigma_o$) is $\Delta\sigma_o = \underline{0.48}\,\Delta\sigma_d$. The root-mean-square (rms) stress drop

OK

0.233 ~~0.243~~

0.243

0.486

$$(\Delta\sigma_{\rm rms}) \text{ is } \Delta\sigma_{\rm rms} = \Delta\sigma_d I_\theta^{1/2}\left(\frac{M_0}{M_{os}(R_{\max})}\right)^{1/2}\left(\frac{f_c}{f_o}\right)^{1/2},$$

where f_0 is corner frequency of the earthquake, M_{os} ($R_{\max}$) and f_c are the moment and corner frequency of the largest subevent, and $I_\theta^{1/2}$ is a dimensionless constant approximately equal to 1.7. Finally, the Savage–Wood ratio (SWR) is given by SWR $\approx C_E\,\Delta\sigma_d/2\,\Delta\sigma_s$. These results clarify the relationships among all of these stress parameters in the context of a complex fault, showing the critical role of the subevent stress drop. They also provide an additional tool for energy, stress, and Savage–Wood ratio estimation. Since the process of modeling strong motion with the composite source uses realistic Green's functions, estimates of energy and stress parameters using this model are expected to have a good correction for wave propagation.

ease make this part of the ragraph nstead of isplaying so ominently

Introduction

The use of strong-motion accelerograms to estimate the seismic energy release in earthquakes is somewhat problematical. One difficulty is geometrical since at this range the large extent of faulting cannot be ignored. Another difficulty is introduced by the complexities of wave propagation, since site effects, resonances, and a complex mixture of body and surface waves that are not easily separated all contribute to the accelerograms. Thus, methods that derive energy by integrating the observed velocity or its spectrum (e.g., Anderson *et al.*, 1986; Shoja-Taheri and Anderson, 1988) inevitably make some simplifying assumptions whose importance is difficult to assess. Another approach to computing energy is to calculate the energy leaving the source (e.g., Haskell, 1964; Vassiliou and Kanamori, 1982), but at strong-motion distances, typical source models are limited to modeling the low-frequency portion of the spectrum. On many accelerograms, the majority of the energy is carried in waves with frequencies below 1 to 3 Hz (e.g., Vassiliou and Kanamori, 1982; Shoja-Taheri and Anderson, 1988). Still, a method that more naturally incorporates the full frequency band is desirable.

Recently, Yu (1994) and Zeng *et al.* (1994) have proposed a composite source model for generating synthetic strong-motion accelerograms. Besides the composite source, which is discussed below, these synthetics utilize synthetic Green's functions generated for a layered medium. Several articles have demonstrated that the synthetics generated with this model are highly realistic, both in appearance in the time domain and in reproducing spectral amplitudes over the entire frequency band (Yu, 1994; Zeng *et al.*, 1994; Yu *et al.*, 1995; Su *et al.*, 1994a, 1994b; Anderson and Yu, 1996; Zeng and Anderson, 1996). Considering this realism, it seems natural to see if it is possible to estimate the energy that leaves the composite source. Thus, the initial motivation for this article is to derive an analytical expression for the seismic energy leaving a composite source as a function of the model parameters.

In the process, it became apparent that in addition to

energy, it is possible to derive analytical expressions for several of the commonly used stress parameters in the context of this model: apparent stress (Wyss, 1970), effective stress (Brune, 1970), Orowan stress drop (Kanamori, 1977; Vassiliou and Kanamori, 1982), and root-mean-square (rms) stress drop (Hanks, 1979; Hanks and McGuire, 1981). The results give some insight into the meaning of these parameters in the context of a source that is much more complex than the models that are the basis for their original definitions. Even though the composite source is a kinematic model, it is reasonable to expect that characteristics of these relationships will carry over to future models that more thoroughly incorporate the physics of complex faulting.

Theory

Composite Source Model

As described by Zeng *et al.* (1994), the composite source model consists of a superposition of radiation from a number of point sources on the fault. The point sources have a distribution of "sizes"

$$n(R) = pR^{-D-1} \tag{1}$$

in which $n(R)$ is the number density of sources with equivalent "radius" R, D is a fractal dimension (generally taken to be 2.0), and p is a constant defined by the constraint that the sum of the moments of the subevents is equal to the moment of the target event. The subevents all have a radius between R_{max} and R_{min}. In general, R_{min} can be chosen small enough that it has no numerical consequences. The subevents are placed at random, with a uniform probability distribution, on the fault plane, with the constraint that their edges do not overlap the edge of the fault; this places an upper limit on R_{max}. The source time function is generated by starting the rupture at a presumed hypocenter and allowing it to spread at a constant rupture velocity across the fault. Each subevent radiates a time function when the rupture front reaches its center.

Figure 1 shows a view of the slip for one realization of this source. To develop this, I treat each source as a crack with slip function:

$$s(a) = \frac{24}{7\pi}\frac{\Delta\sigma_d}{\mu}(R^2 - a^2)^{1/2}, \tag{2}$$

where μ is the shear modulus, R is the radius of the crack, a is the distance from its center, and $\Delta\sigma_d$ is the stress drop of the subevent. Figure 1 shows a relatively complex slip distribution resembling a fractal computer-generated topography and the self-similar slip distributions presented by Herrero and Bernard (1994).

Figures 2 through 4 investigate this source and its dependence on the subevent stress drop. Figure 2 shows realizations of the composite source time function for a rectangular fault (expressed as seismic moment rate) with three values of $\Delta\sigma_d$: 1, 10, and 100 bars. It is evident that lower values of $\Delta\sigma_d$ are associated with a smoother time function. Figure 3 shows average spectra associated with these three values of $\Delta\sigma_d$. Figure 4 is the equivalent of Figure 3, except that a square fault was used. These spectra are proportional to spectra of velocity seismograms. Thus, at the lowest frequencies, the spectra increase proportional to f, with the level determined by the moment. At the highest frequencies, the spectra decrease approximately as f^{-1}, as appropriate for an ω-square model (Hanks, 1979). The lowest corner frequency in Figures 3 and 4 is controlled by the fault dimension: $f_0 = (2T_d)^{-1}$, where T_d is fault length/rupture velocity. The spectra have multiple corners and variable behavior above f_0, with several showing an intermediate slope (between f and f^{-1}) before achieving the high-frequency behavior. Cor-

Figure 1. A perspective view of the "slip function" on a fault for the composite source model.

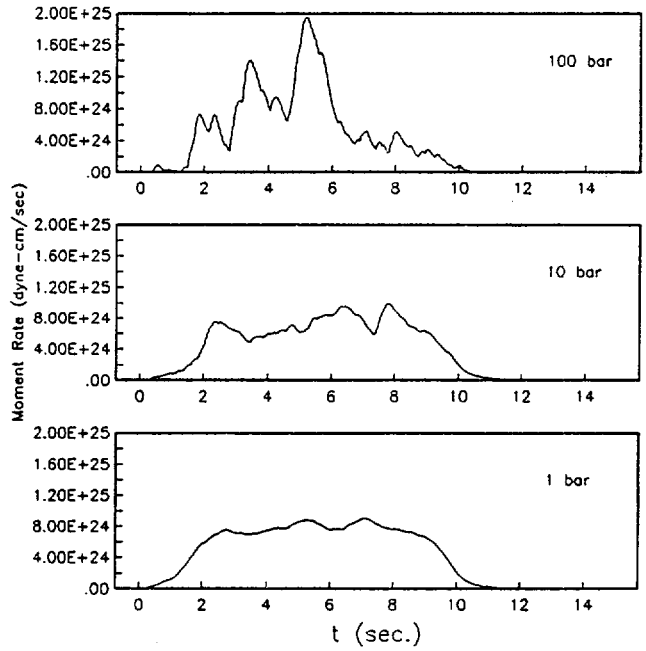

Figure 2. Realizations of the moment rate of a composite source for three values of the subevent stress drop. The fault has length $L = 30$ km and width $W = 10$ km. The three values of subevent stress drop are $\Delta\sigma_d = 1$, 10, and 100 bars, as shown. The fault has $M_0 = 6 \times 10^{25}$ dyne-cm, and according to equation (3), it has $\Delta\sigma_s = 12.7$ bars for all three cases.

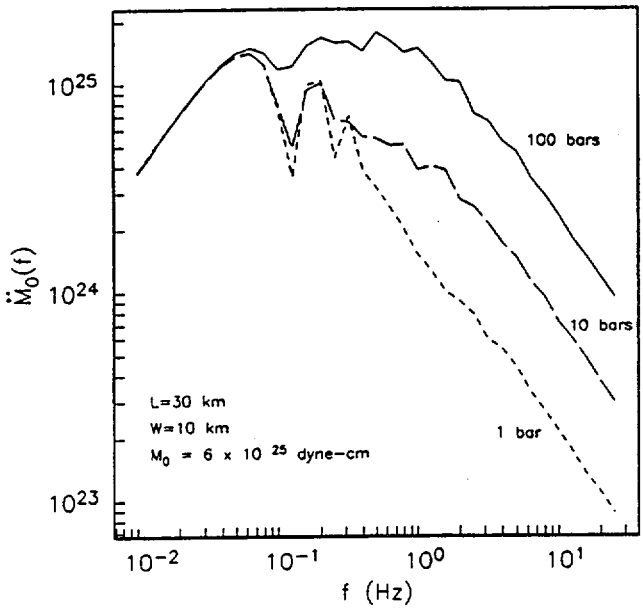

Figure 3. Average Fourier amplitude spectra generated from composite source models for the fault used in Figure 2. Each curve is the average of spectra from 25 realizations. Since energy is proportional to velocity, through equation (6) it is proportional to $\ddot{M}_0(t)$. Thus, to emphasize the contribution to the energy, these are averages of Fourier spectra of the first derivative of time series such as in Figure 2. The spectra are appropriate in the far field perpendicular to the fault, with no adjustment for, or averaging over, the azimuth from the fault to the station. Individual realizations show little variability at low (<0.05 Hz) or high (>5 Hz) frequencies.

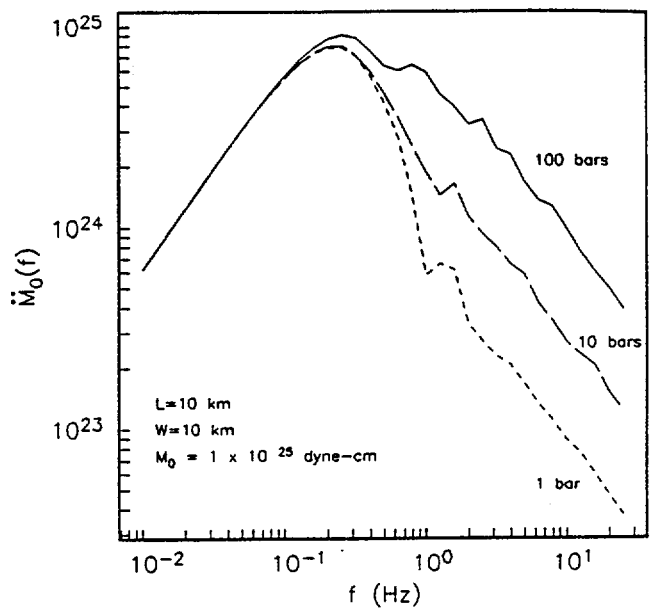

Figure 4. Equivalent of Figure 3, except that the fault has L = 10 km and W = 10 km, and M_0 = 1 × 10^{25} dyne-cm. According to equation (5), a circular fault with the same area and moment has $\Delta\sigma_s$ = 24 bars.

ner frequencies higher than f_0 can be controlled by fault width or rise time. The net result is that as $\Delta\sigma_d$ increases, f_0 remains constant, but the higher corner frequencies are increased, and the spectra are systematically enriched in high-frequency energy.

Static Stress Drop

For a composite event, with seismic moment M_0, the average static stress drop, $\Delta\sigma_s$, is determined by the usual formulas (e.g., Kanamori and Anderson, 1975). For a strike slip fault with length L greater than width W, it is

$$\Delta\sigma_s = \frac{2M_0}{\pi W^2 L}. \tag{3}$$

For a dip-slip fault with long, narrow proportions, it is

$$\Delta\sigma_s = \frac{4(\lambda + \mu)M_0}{\pi(\lambda + 2\mu)W^2 L}. \tag{4}$$

Equations (3) and (4) assume the fault ruptures the surface. In Equation (4), λ is the Lame constant. For a circular fault with radius R, it is

$$\Delta\sigma_s = \frac{7M_0}{16R^3}. \tag{5}$$

These relations use only the average slip, and thus complexity such as that seen in Figure 1 is not incorporated. Kanamori and Anderson (1975) suggest that a gross global average for $\Delta\sigma_s$ is about 60 bars. They suggest that $\Delta\sigma_s$ averages 30 bars for interplate earthquakes and 100 bars for intraplate earthquakes. Considering that the stress drop is proportional to the strain drop, it is evident from Figure 1 that locally on the fault, the composite source model allows for static stress drops that are larger or smaller than average.

In the composite source model, the subevent stress drop ($\Delta\sigma_d$) is independent of $\Delta\sigma_s$. The three source moment rates in Figure 2, and corresponding average spectra in Figure 3, are constrained to have the same value of $\Delta\sigma_s$, 13 bars. When $\Delta\sigma_d$ = 100 bars, then $\Delta\sigma_d > \Delta\sigma_s$, and the model is equivalent to the partial stress-drop model (Brune, 1970). As shown by Smith *et al.* (1991), it has a broad intermediate slope. Interpretation of the cases where $\Delta\sigma_d \leqq \Delta\sigma_s$ will be deferred.

Radiated Energy

The radiated energy is, in general, sensitive to the shape of the spectrum of the radiated waves, particularly near the corner frequency (e.g., Smith *et al.*, 1991). Thus, considering Figures 3 and 4, it is evident that the energy will depend on the subevent stress drop $\Delta\sigma_d$. Fortunately, it is possible to estimate the energy that is radiated from a composite source model without deriving an explicit expression for the shape

of the average spectrum. The derivation begins by determining the energy radiated from a subevent of radius R. The total energy is initially derived by integrating that result over the subevents. This initial approach assumes energy of the subevents is additive because they are randomly located and add incoherently. This point will be investigated further below.

The energy radiated by a point double-couple source may be derived starting with the equations in Aki and Richards (1980) for the far-field displacement $u(\mathbf{x}, t)$ at location $\mathbf{x}$ from a point source at the origin in an infinite homogeneous medium:

$$u(\mathbf{x}, t) = \frac{\mathbf{A}^{FP}}{4\pi\rho\alpha^3 r}\dot{M}_0\left(t - \frac{r}{\alpha}\right) + \frac{\mathbf{A}^{FS}}{4\pi\rho\beta^3 r}\dot{M}_0\left(t - \frac{r}{\beta}\right) \quad (6)$$

in which r is the source-to-station distance; $\dot{M}_0(t)$ is the moment rate at the source; ρ is density; α and β are the P and S velocities, respectively; and $\mathbf{A}^{FP}$ and $\mathbf{A}^{FS}$ are radiation patterns. Specifically, $\mathbf{A}^{FP} = \sin 2\theta \cos\phi\hat{r}$, and $\mathbf{A}^{FS} = \cos 2\theta \cos\phi\hat{\theta} - \cos\theta \sin\phi\hat{\phi}$ in which θ is the polar angle.

The kinetic energy in an elemental volume is $1/2\rho\dot{u}^2 dV$. The kinetic energy radiated into the far field is obtained by integrating this over all space. One may easily choose time late enough that all near-field and intermediate-field terms are zero. To carry out the integral, it is convenient to substitute $dr = \alpha dt$ or $dr = \beta dt$ for the P and S waves, respectively. Then, assuming that the potential energy is equal to the kinetic energy, the total radiated energy in the P wave from a point source is, as found by Vassiliou and Kanamori (1982),

$$E_P = \frac{I_{M_0}}{15\pi\rho\alpha^5}, \quad (7)$$

and the total radiated energy in the S wave from a point source is

$$E_S = \frac{I_{M_0}}{10\pi\rho\beta^5} \quad (8)$$

in which

$$I_{M_0} = \int_0^\infty \dot{M}_0^2(t)dt. \quad (9)$$

Based on these results, the total energy in the S wave is 23.4 times the energy in the P wave for a point source in a Poisson solid. Thus, for simplicity of expressions, it is sufficient to deal with the S waves alone and adjust the final result upward by 4%.

In their implementation of the composite source model, Zeng *et al.* (1994) assumed, following Brune (1970), that each subevent has the following moment rate:

$$\dot{M}_{os}(t) = (2\pi f_c)^2 M_{os} t e^{-2\pi f_c t} H(t) \quad (10)$$

in which case

$$I_{M_{os}} = \frac{1}{4}(2\pi f_c)^3 M_{os}^2. \quad (11)$$

It is important to note that both the subevent moment, M_{os}, and the subevent corner frequency, f_c, are functions of R. About 90% of the moment has been released at $t_{90} = 0.619/f_c$, f_c, and 99% of the moment has been released at $t_{99} = 1/f_c$. We will take t_{90} as a best estimate and t_{99} as an upper limit to the rise time of the pulse.

Zeng *et al.* (1994) used the same relationship as Brune (1970, 1971) between the source radius and corner frequency:

$$f_c(R) = \frac{2.34\beta}{2\pi R}. \quad (12)$$

In this model, the moment of a subevent is related to R by

$$M_{os}(R) = \frac{16}{7}\Delta\sigma_d R^3 \quad (13)$$

in which $\Delta\sigma_d$ is the subevent stress drop. Combining equations (8), (11), (12), and (13), the energy radiated in the S wave from a single Brune pulse for a source of radius R is

$$E_S^{\text{Brune}}(R) = 0.233\frac{\Delta\sigma}{\mu}M_{os}(R), \quad (14)$$

where μ is the shear modulus ($\mu = \rho\beta^2$). If all of the subevents add incoherently, the total energy in the S wave is

$$E_S^{CS} = \int_{R_{\min}}^{R_{\max}} n(R)E_S(R)dR. \quad (15)$$

To evaluate equation (15), using equations (1) and (14), it is also necessary to use the expression from Zeng *et al.* (1994):

$$p = \frac{7M_0}{16\Delta\sigma_d}\frac{3 - D}{(R_{\max}^{3-D} - R_{\min}^{3-D})} \quad (16)$$

in which M_0 is the seismic moment of the mainshock, equaling the sum of the moments of all the subevents. Carrying out the integration and combining and rearranging,

$$E_S^{CS} = 0.233\frac{\Delta\sigma_d}{\mu}M_0. \quad (17)$$

This can be adjusted upward by 4% to account for the *P*-wave energy.

Several numerical experiments have been used to investigate the importance of the assumption underlying equation (15) that the subevents add incoherently. The experiments consist of generating composite source time functions (as in Fig. 2), using equations (7), (8), and (9) to determine the radiated energy and comparing with the prediction in equation (17). The results are expressed as a correction factor (C_E), which is defined as

$$C_E = \frac{S\text{-wave energy from equation (8)}}{S\text{-wave energy from equation (17)}}. \quad (18)$$

The results are summarized in Figure 5, for several fault models, as a function of normalized subevent stress drop. The normalized subevent stress drop is defined as $\Delta\sigma_d/\Delta\sigma_s^*$, where $\Delta\sigma_s^* = M_0/W^2L$. The reason for using $\Delta\sigma_s^*$ instead of $\Delta\sigma_s$ from equations (3), (4), or (5) is to remove the ambiguity that arises from different mechanisms (i.e., strike-slip or dip-slip) or from arbitrary decisions on which equation to use when the aspect ratio is close to unity, and to make it possible to interpolate between curves for small aspect ratios. The mechanism does not affect the radiated energy estimates since it is derived using an infinite space model. This normalization is convenient for our usual procedure for generating composite source time functions, which is to define L and W even for nearly circular faults.

The main features of C_E are that it is larger than 1.0, a function of L/W, and a decreasing function of subevent stress drop. Thus, for small subevent stress drop, interference of subevent radiation is constructive, and equation (15) gives a stochastic lower bound on the radiated energy. For subevent stress drop greater than $\Delta\sigma_s$, it is asymptotic to approximately 1.0. For $\Delta\sigma_d > 2\Delta\sigma_s$, subevents are incoherent, and equation (17) can be used directly. At small values of $\Delta\sigma_d$, the value of C_E decreases approximately as $\Delta\sigma_d^{-1}$. Summarizing, a final estimate of the radiated seismic energy, incorporating subevent coherence, is

$$E_S^{CS} = 0.233\, C_E \frac{\Delta\sigma_d}{\mu} M_0. \quad (19)$$

It is necessary to consult Figure 5 to obtain the value of C_E to use in equation (19). As before, this can be adjusted upward by 4% to account for the *P*-wave energy.

The result in equation (19) is quite simple in its form. The seismic energy is linearly proportional to the stress drop of the subevents. The stress drop, in turn, through equations (10), (12), and (13), is inversely related to the rise times (τ) of the subevents ($\tau \sim \Delta\sigma_d^{-1/3}$) and, thus, the average rise time of the overall average displacement of the composite source. Thus, we obtain the expected result (e.g., Vassiliou and Kanamori, 1982) that for a fixed moment, the radiated energy is increased as the rise time decreases ($E_s \sim \tau^{-3}$).

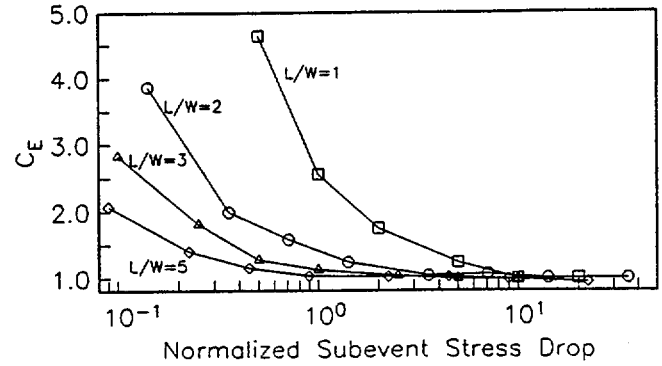

Figure 5. Energy ratio, C_E, as defined in equation (18). The normalized stress drop is $\Delta\sigma_d/\Delta\sigma_s^*$, where $\Delta\sigma_s^* = M_0/W^2L$, as discussed in the text. All of these computations use $R_{max} = L/2$, but the result is not very sensitive to smaller values.

In the development of the composite source model by Zeng *et al.* (1994) and Yu (1994), and other applications, estimation of the stress drop of the subevents has been unconstrained. Equation (19) suggests a simple method to constrain it, if the energy of the target event is known independently. An alternative approach, developed by Yu *et al.* (1996) for the composite source model used here, is to match an assumed (and empirically calibrated) spectral shape (e.g., Joyner, 1984; Tumarkin *et al.*, 1994).

Some insight is gained by a comparison between the energy radiated by a smooth Brune pulse and by a composite source of the same seismic moment. This can be obtained directly from equations (14) and (19). Setting the moments equal in (14) and (19), one obtains

$$\frac{E_S^{CS}}{E_S^{\text{Brune}}} = \frac{C_E\, \Delta\sigma_d}{\Delta\sigma_{\text{static}}}. \quad (20)$$

Thus, if the subevents have the same stress drop as the static stress drop of a single smooth mainshock, the energy that is radiated is increased by about 30%. To obtain this ratio, it is also necessary to adjust for the difference between $\Delta\sigma_s^*$ and $\Delta\sigma_s$ from equation (5) by finding the radius of the fault with the same area. Figure 4 shows spectra that approximately match this situation. When $\Delta\sigma_d$ = 100 bars and thus $\Delta\sigma_d > \Delta\sigma_s$, the spectrum has a relatively broad frequency band with an intermediate slope. Conversely, when $\Delta\sigma_d$ = 1 bar and thus $\Delta\sigma_d \ll \Delta\sigma_s$, the spectrum of the composite source falls off significantly faster than f^{-1} above the corner. However, the effect of subevent coherence is apparent in this case, causing the spectrum to match the spectrum for $\Delta\sigma_d$ = 10 bars to a frequency substantially above the corner frequency.

Strain Energy

Based on Kanamori and Anderson (1975), the change in strain energy is

$$\Delta W = \frac{M_0}{\mu}\bar{\sigma}, \tag{21}$$

and the radiated energy is related to this by

$$E_f = \eta \Delta W, \tag{22}$$

where η is the seismic efficiency. Comparing equations (19), (21), and (22), and adjusting to include P-wave energy, we find that

$$\eta\bar{\sigma} = \overset{0.243}{\cancel{0.273}}\, C_E\, \Delta\sigma_d. \tag{23}$$

Thus, the composite source model yields an estimate of the product of seismic efficiency and average stress but does not help determine either factor by itself.

Apparent Stress

Wyss (1970) defined the apparent stress of an earthquake as $\sigma_a = \eta\bar{\sigma} = \mu E_f/M_0$. Thus, for the composite source, one obtains

$$\sigma_a = \overset{0.243}{\cancel{0.233}}\, C_E\, \Delta\sigma_d. \tag{24}$$

Thus, in the context of the composite source model, the apparent stress is proportional to the subevent stress drop.

Effective Dynamic Stress

Effective dynamic stress (or effective stress) (σ_e) is defined as the difference between the initial shear stress at the beginning of faulting and the dynamic frictional stress. Its estimation is based on Brune's (1970) demonstration that the particle velocity at the fault is proportional to this stress parameter. Based on Brune (1970) and subsequent studies [reviewed by Kanamori and Anderson (1975) or Kanamori (1994)],

$$\dot{D} = C_{pv}\sigma_e\beta/\mu \tag{25}$$

in which $\dot{D}$ is the rate of sliding of opposite sides of the fault during the earthquake, and C_{pv} is a constant with a value between about 1 and 2, depending on the model. While recognizing that there is this factor of 2 uncertainty, this article follows Kanamori (1994) in using $C_{pv} = 1$.

Measurements of σ_e use equation (25) with inferred particle velocity on the fault (e.g., Kanamori, 1972b; Abe, 1974) or estimate $\Delta\sigma_d$ from the velocity pulse recorded nearby (e.g., McGarr *et al.*, 1981; Shoja-Taheri and Anderson, 1988). However, these two parameters are not the same. Combining the definition of the moment (equation 13) and the area (πR^2) to get the average slip, combining this with the best estimate of the rise time (t_{90} defined above), and using equation (12), one obtains that the Brune pulse has an estimated effective stress of $\sigma_e = (0.44/C_{pv})\,\Delta\sigma_d$. A rationale could be found for replacing the lead coefficient (0.44) with values between 0.27 (based on the upper limit on rise time) and 1.70 (based on the rise time that would result from the peak moment rate). Still, the mismatch in the best estimate introduces another factor of 2 uncertainty into estimates of σ_e.

Beyond this, as with the energy estimate, coherent subevents will combine to give an effective rate of sliding between the opposite sides of the fault that is greater than the rate in an individual subevent. For this reason, σ_e for a composite source model is greater than or equal to the effective stress that would characterize the largest subevents if they were isolated. In fact, the composite source model is incapable of describing earthquakes with σ_e significantly smaller than $\Delta\sigma_s$. Low values of σ_e should result in a slow earthquake or a tsunami earthquake. However, neither the duration at the source nor the rise time increases (Fig. 2) as $\Delta\sigma_d$ decreases below $\Delta\sigma_s$. This is because the durations of the subevents are fixed by their radius (equations 10 and 12) and are independent of $\Delta\sigma_d$. The maximum rise time is thus f_c^{-1} (R_{max}). The low slip in each subevent (e.g., equation 13) then becomes compensated with larger numbers of subevents (equation 16) that add coherently. Combining relations, $\sigma_e/\Delta\sigma_d$ cannot be less than ~1.17 for a strike-slip fault, ~0.88 for a dip-slip fault, or ~0.27 for a circular fault. Considering this, the relationship

$$\sigma_e = \frac{0.44 C_E}{C_{pv}}\,\Delta\sigma_d \tag{26}$$

is probably a reasonable approximation within all the uncertainties, since C_E is a measure of the net coherency of the subevents.

It may be possible to develop a modified composite source model without this limitation. One approach to try is to set the number of subevents so that their area is on the same order as the area of the fault being modeled. The subevent stress drop could be set to the effective stress and control the rate of sliding on the fault in the subevents. Equation (10) would have to be replaced with a function that is controlled by the rate of sliding and stops at the right time to match the seismic moment of the mainshock. The distribution of subevents in this approach might resemble the distribution in the composite source model for the normal earthquakes with high values of $\Delta\sigma_d$, where it has been proven successful.

Savage–Wood Inequality

Savage and Wood (1971) presented a model that introduces physics of faulting to develop a relationship between static and effective dynamic stress drops. In this model, if the final stress on the fault is less than or equal to the frictional stress, then $\sigma_a \leqq \Delta\sigma_s/2$. Considering equation (24), ~~adjusted to include P-wave energy~~, this will be true if $\Delta\sigma_d \leqq 2.06\, C_E^{-1}\,\Delta\sigma_s$. In this model, equality occurs when the final and frictional stresses are equal. Following Savage and

Wood (1971) and Smith *et al.* (1991), the Savage–Wood ratio (SWR) is defined as

$$\mathrm{SWR} = \frac{2\sigma_a}{\Delta\sigma_s}. \tag{27}$$

Smith *et al.* (1991) argue that a partial stress-drop earthquake (e.g., Brune, 1970) with an intermediate slope above the first corner frequency proportional to f^{-1} gives SWR > 1. In the context of the composite source model, equation (27) gives

$$\mathrm{SWR} = \frac{\overset{0.486}{\cancel{0.47}}\, C_E\, \Delta\sigma_d}{\Delta\sigma_s}. \tag{28}$$

As noted above, these two stress drops are independent parameters input into the composite source model. These considerations suggest that they are linked through the physics of the earthquake-generating process. It is evident that an understanding of the Savage–Wood ratio has direct applications to prediction of strong ground motions.

Savage and Wood (1971) suggested that typically SWR $\approx$ 0.3, thus implying that the Savage–Wood inequality is valid, but they show a considerable amount of scatter with some earthquakes showing SWR > 1. Kanamori and Anderson (1975) suggested that typically, $\sigma_a \approx \Delta\sigma_s/2$, implying that SWR $\approx$ 1. Data given by Kanamori (1994) would imply that SWR < 1, but he emphasizes that there are large uncertainties, and thus probably for that data, SWR is not distinguishable from unity. Smith *et al.* (1991) suggest that for several earthquakes with well-determined energy estimates, SWR > 1, meaning that the Savage–Wood inequality is violated. Earthquake models using the composite source model could eventually provide a large set of estimates of SWR that will help to clarify this situation.

Savage–Wood ratios in Figure 3 drop from 5 to ~0.4 as $\Delta\sigma_d$ decreases from 100 bars to 1 bar. As noted above, the composite source model is not capable of producing a source time function with a long rise time, so significantly smaller values of SWR cannot be synthesized here. The case where $\Delta\sigma_d$ = 100 bars has a broad spectral shape as expected for a case with SWR > 1 (Smith *et al.*, 1991). Equation (28) and Figures 3 and 4 invite a discussion of the case where $\Delta\sigma_d \ll \Delta\sigma_s$. Considering Savage and Wood (1971), one interpretation of this is that it corresponds to a source model with "overshoot," in which the inertia of the moving blocks carries the opposite sides to a final equilibrium position with final stress that is less than the dynamic frictional forces. However, in the modified composite source model proposed earlier, the low SWR would be achieved using subevents with a low effective stress and thus a very long rise time. This is a very different mechanism, more akin to tsunami earthquakes or slow earthquakes (e.g., Kanamori, 1972a; Kanamori and Hauksson, 1992; Kanamori and Kikuchi, 1993).

Orowan Stress Drop

Vassiliou and Kanamori (1982) show that when the final and dynamic frictional stresses are equal, i.e., the Orowan (1960) conditions are met, then the radiated seismic energy is

$$E_I = \frac{M_0 \Delta\sigma_0}{2\mu} \tag{29}$$

in which $\Delta\sigma_0$, the "Orowan stress drop," is the difference between the initial and final stresses on the fault. Comparing equation (29) with equation (19), we find

$$\Delta\sigma_0 = 0.48\overset{6}{\cancel{3}}\, C_E\, \Delta\sigma_d \tag{30}$$

in which the coefficient includes *P*-wave radiation. Equation (30) demonstrates that $\Delta\sigma_0$ is about half of the subevent stress drop that is used in the composite source model and, considering equation (26), that $\sigma_e \approx \Delta\sigma_0$, as also noted by Kanamori (1994).

Kanamori (1977) used the result, similar to equation (29), that $E_I = M_0\Delta\sigma_s/2\mu$, together with an average range of $\Delta\sigma_s$ between 20 and 60 bars, to establish the M_W magnitude scale. Considering equation (29), it appears that the additional assumption that the static stress drop approximately equals the effective dynamic stress or the Orowan stress drop is embedded in his equations.

RMS Stress Drop

Hanks (1979) recognized that the rms acceleration is proportional to a stress-drop parameter, and McGuire and Hanks (1980) and Hanks and McGuire (1981) demonstrated that this stress-drop parameter ($\Delta\sigma_{\mathrm{rms}}$) shows much less variation than the variation typically seen in estimates of static stress drop (equations 2 through 4). This section relates $\Delta\sigma_{\mathrm{rms}}$ to parameters in the composite source model.

It is useful to quickly review the derivation of rms acceleration as a function of the Fourier spectrum. Here, the derivation is for a site in the infinite, homogeneous medium instead of for a site on the free surface, as used by Hanks (1979). Defining the duration of faulting at the source as T_d, the rms acceleration is

$$a^2_{\mathrm{rms}} = \frac{1}{T_d}\int_0^\infty a^2(t)dt \tag{31}$$

in which $a(t)$ is the acceleration time series. By Parseval's theorem, it is easily shown that

$$a^2_{\mathrm{rms}} = f_0 \int_0^\infty |\, a^2(f)\,|\, df, \tag{32}$$

where $a(f)$ is the Fourier transform of $a(t)$. Equation (32)

differs from Hanks (1979), who used the approximation that $f_0 = T_d^{-1}$, while I used $f_0 = (2T_d)^{-1}$. This is a better approximation for the corner frequencies in Figures 3 and 4, as noted above, and is also consistent with the theoretical corner of one-sided pulses of duration T_d. The Fourier transform of the far-field S-wave acceleration (from equation 6) with the moment rate given by equation (10) is, as noted by Brune (1970),

$$| a_s(f) | = \frac{\mathbf{A}^{FS}}{4\pi\rho\beta^3 r} \frac{(2\pi f)^2 M_{os}}{\left(1 + \left(\frac{f}{f_c}\right)^2\right)}. \tag{33}$$

This function is essentially flat for $f > f_c$. In reality, there is also an upper limit to the flat part of the spectrum, given the generic label $f_{\max}$ (Hanks, 1982). Changing the lower and upper limits of the integral in equation (32) to f_c and $f_{\max}$, respectively, substituting equation (33), and integrating, one obtains

$$a_{\rm rms} = \mathbf{A}^{FS} \frac{\pi}{\sqrt{2}} \frac{M_{os} f_c^3}{\beta^3} \frac{1}{\rho r} \left(\frac{f_0}{f_c}\right)^{1/2} \left(\frac{f_{\max}}{f_c} - 1\right)^{1/2}. \tag{34}$$

Using equations (12) and (13), one finds that

$$\frac{M_{os} f_c^3}{\beta^3} = 0.118 \Delta\sigma. \tag{35}$$

If this substitution is made in equation (34), and if $f_{\max} \gg f_c$, one obtains

$$a_{\rm rms} = 0.158 \frac{\Delta\sigma_{\rm rms}}{\rho r} \left(\frac{f_0}{f_c}\right)^{1/2} \left(\frac{f_{\max}}{f_c}\right)^{1/2}, \tag{36}$$

where $\mathbf{A}^{FS}$ has been replaced by the rms value used by Hanks ($\overline{\mathbf{A}^{FS}} = 0.6$). Hanks (1979) assumed a model with total stress drop on a circular fault and thus equated f_c with f_0. The ratio of these two frequencies in equation (36) adjusts for the difference in duration of the direct S wave from the actual fault and the circular fault assumption. If these durations (or frequencies) are equal, equation (36) becomes

$$a_{\rm rms} = 0.158 \frac{\Delta\sigma_{\rm rms}}{\rho r} \left(\frac{f_{\max}}{f_c}\right)^{1/2}. \tag{37}$$

Equation (37) differs from Hanks (1979) only by the leading constant. To obtain his coefficient of 0.445, one multiplies equation (37) by 2 to account for the different relationship between corner frequency and fault duration, multiplies by 2 to account for the free surface, and divides by $\sqrt{2}$ to account for partitioning of energy between two horizontal components.

As an aside, there should also be a correction for difference in velocity at the surface and at the depth of faulting. Day (1996) has shown theoretically that in a layered half-space with infinite Q, the rms response over a sufficiently broad spectral bandwidth depends only on the average velocity near the surface and is independent of the properties of the intervening layers. Anderson *et al.* (1996) extended this to an attenuating medium in numerical experiments and found that the average Q is a second critical factor. These results apply directly to the rms acceleration, since it depends on a broadband spectral property.

Equations (31) to (37) demonstrate the steps that need to be followed to determine the rms acceleration from the composite source model. The acceleration spectrum of radiation from the composite source is the superposition of numerous spectra, each having the shape of equation (33), but with the moment and corner frequency functions of R. We make the simplifying assumption that these spectra add incoherently, and thus obtain

$$| a^2(f) | = \int_{R_{\min}}^{R_{\max}} n(R) \left| \frac{\mathbf{A}^{FS}}{4\pi\rho\beta^3 r} \frac{(2\pi f)^2 M_{os}(R)}{1 + \left(\frac{f}{f_c(R)}\right)} \right|^2 dR. \tag{38}$$

With a change of variables, and the assumption that $R_{\max} \gg R_{\min}$, this is transformed to

$$| a^2(f) | = 1.165(\mathbf{A}^{FS})^2 (3 - D) \left(\frac{2.34\beta}{2\pi R_{\max}}\right)^{3-D} \frac{M_0 \Delta\sigma\beta}{(\mu r)^2} f^{D-1} I_\theta(f) \tag{39}$$

in which

$$I_\theta(f) = \int_{\theta_{\min}}^{\theta_{\max}} \frac{\tan^{5-D}\theta}{\sec^2\theta} d\theta. \tag{40}$$

The frequency dependence enters through the limits of the integral:

$$\theta_{\min} = \tan^{-1}\left(\frac{2\pi f R_{\min}}{2.34\beta}\right), \tag{41a}$$

$$\theta_{\max} = \tan^{-1}\left(\frac{2\pi f R_{\max}}{2.34\beta}\right). \tag{41b}$$

The integrand for equation (40) is shown in Figure 6. The rapid monatonic increase of the integrand indicates that the greatest contribution comes from the upper limit of integration. Thus, the result is most sensitive to $R_{\max}$.

Numerical experiments for a range of $R_{\min}$ confirm that I_θ is not sensitive to this parameter for typical values. These same experiments show that I_θ takes values between about 1.0 and 5.0 for nearly the entire range of f and $R_{\max}$ encountered in applications of the composite source model. The

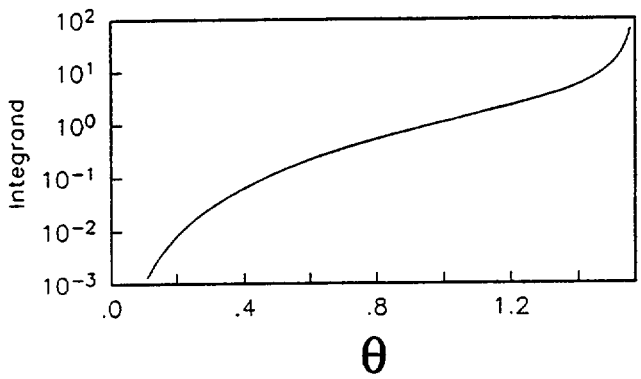

Figure 6. Integrand for I_θ, as in equation (40).

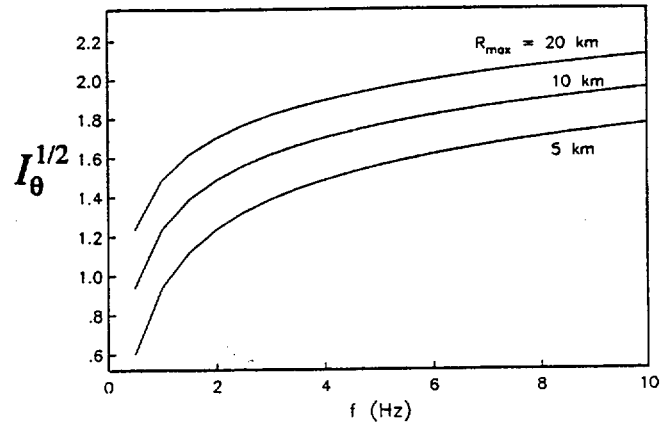

Figure 7. Numerical values of $I_\theta^{1/2}$ for the case where $D = 2$ and $R_{min} = 0.1$ km. The results are shown for three values of R_{max}.

functional dependence can be roughly approximated as $\sim f^{0.25}$ in some of these experiments. This dependence makes it impractical to obtain a closed-form expression for a_{rms} when $a(f)$ is substituted into equation (32). As an approximation, we treat I_θ as a constant. Then, substituting equation (39) into equation (32), integrating, simplifying, and assuming as before that $A^{FS} = 0.6$, leads to the following result:

$$a_{rms} = 0.158 \sqrt{\frac{3-D}{D-1}} I_\theta^{1/2} \left(\frac{M_0}{M_{os}(R_{max})}\right)^{1/2} \frac{\Delta\sigma_d}{\rho r} \left[\left(\frac{f_{max}}{f_c}\right)^{D-1} - 1\right]^{1/2}. \quad (42)$$

In this approximation, $I_\theta^{1/2}$ takes numerical values between about 1.0 and 2.0, as shown in Figure 7. Choosing an intermediate value, say 1.7, would not be particularly misleading, but one could take an average of the appropriate curve for frequencies $f \leqq f_{max}$.

In equation (42), the rms acceleration for the composite source model is proportional to the subevent stress drop. The ratio of moments in this equation can be correlated to the total number of subevents. The rms acceleration is thus logically increased as the square root of this ratio since the subevent contributions are incoherent at high frequencies.

When equation (42) is equated with equation (36), we obtain the following relationship between $\Delta\sigma_{rms}$ and $\Delta\sigma_d$:

$$\Delta\sigma_{rms} = \Delta\sigma_d \sqrt{\frac{3-D}{D-1}} I_\theta^{1/2} \left(\frac{M_0 f_c}{M_{os}(R_{max}) f_0}\right)^{1/2} \left(\frac{f_{max}}{f_c}\right)^{(D/2)-1}. \quad (43)$$

For the typical case where $D = 2$, this simplifies to

$$\Delta\sigma_{rms} = \Delta\sigma_d I_\theta^{1/2} \left(\frac{M_0}{M_{os}(R_{max})}\right)^{1/2} \left(\frac{f_c}{f_0}\right)^{1/2}. \quad (44)$$

Thus, the rms stress drop will be larger than the subevent stress drop, since all of the multipliers for $\Delta\sigma_d$ are greater than one.

Applications

Many of the parameters discussed in this article have been evaluated for the 1985 Michoacan, Mexico, earthquake. Testing the model on these parameters is actually a relatively demanding application since the earthquake was somewhat unusual. Anderson *et al.* (1986) show that peak accelerations were far below expectations, and the computed energy based on near-field records was much smaller than predicted by regressions. Table 1 presents first the parameters for the composite source model, as developed by Yu (1994), that provide a reasonable fit to statistical properties of accelerograms for the Michoacan earthquake. In developing this model, Yu (1994) used Green's functions for a layered medium to more fully represent the effects of wave propagation on the ground motions. The seismic moment, rupture velocity, and fault dimensions were constrained from other studies, so only the subevent stress drop was a free parameter. The value of $\Delta\sigma_d = 10$ bars was determined to provide a good match between the statistical properties of the synthetics and the data.

The second part of Table 1 compares predictions from the composite source model with stress and energy parameters for this earthquake derived from earlier studies. The energy based on equation (19) is 10% larger than the energy estimated by Anderson *et al.* (1986) from near-field records. Anderson *et al.* point out that the Gutenberg–Richter energy formula predicts that the energy for this event would be 9×10^{23} ergs, which is a factor of 9 times larger than their estimate. Equation (19) has done a very good job of predicting the energy. The apparent stress estimates based on equation (24) and obtained from the Anderson *et al.* (1986) estimate for the energy are in proportion to the energy estimates.

Table 1

Stress and Energy Parameters Michoacan, Mexico, Earthquake, 19 September, 1985 (M_W = 8.1)

Composite source model*			
Seismic moment (dyne-cm)	1.1×10^{28}		
Fault dimension (km)	178 × 80 km		
Subevent stress drop (bars)	10 bars		
Maximum radius of subevent (km)	20 km		
Rupture velocity (km/sec)	2.8 km/sec		
Fractal dimension D	2.0		
Applications of this article	**Predictions from above parameters†**	**Observations****	**Ratio (observation/CSM prediction)**
C_E (from Fig. 5, validated by independent calculation)	1.3		
Radiated energy (equation 19) (ergs)	1.1×10^{23}	1.0×10^{23}	0.9
Static stress drop (equation 4) (bars)	8	19	2.4
Apparent stress (equation 24) (bars)	~~[illegible]~~ 3	3.0††	~~1.0~~ 1.0
Effective dynamic stress (equation 26) (bars)	6	6–12‡	1.0–2.0
Savage–Wood ratio (equation 28)	0.8	0.3‡‡	0.4
rms stress drop (equation 44) (bars)	~~200~~ 210	50–325§	0.2~~4~~–1.~~0~~5 0.24–1.5

*These parameters are those used by Yu (1994).

**Anderson *et al.* (1986), except as noted otherwise.

†This uses $\mu = 3.3 \times 10^{11}$ dyne/cm^2.

††This estimate is from the definition and the estimates of seismic moment and energy. Anderson *et al.* (1986) merely state "under 6 bars."

‡Anderson *et al.* (1986) give this range for effective dynamic stress. The value of 6 bars is internally consistent with parameter choices in this article, as discussed in the text.

‡‡Presented here from the definition (equation 27).

§Based on horizontal components of accelerogram from the closest station, Caleta de Campos, which give a_{rms} or 39 and 45 cm/sec^2, or an average of 42 cm/sec^2. These were substituted into equations (36) or (37), except with the Hanks (1979) coefficient of 0.445 since this is a free-surface observation. The factor of 2 associated with the difference in relation between duration and corner frequency was kept, but for the purpose of compensating for the soft material at the surface. Other parameters are ρ = 2.8 gm/cm^3, r = 24 km, f_{max} = 4.5 Hz. The uncertainties are associated with a range of values of f_c from 0.025 to 0.5 Hz, as discussed in the text.

Anderson *et al.* (1986) derived the effective dynamic stress very directly from the near-field velocity of a station that recorded a static offset. The estimate of 6 bars is consistent with the decisions in this article on how uncertainties in coefficients are handled, and the same as the prediction using equation (26) using the parameters of Yu's (1994) composite source model also.

The SWR (equation 28) is 0.8 for the parameters of the composite source model used by Yu (1994). In considering this, it may be important to note that Yu used a fault width (80 km) that is greater than the width of the aftershock zone (50 km, Anderson *et al.*, 1986), and when the narrower fault width is used, the estimated static stress drop is increased to 19 bars. A smaller fault might also be compensated by a smaller subevent stress drop. Both of these effects would decrease SWR, and thus it seems that by this method, SWR is smaller than unity for this earthquake. On the other hand, based on a combination of teleseismic and local spectra, Smith *et al.* (1991) estimated SWR ≈ 4 to 8 for the event, about an order of magnitude larger. The discrepancy is part of a larger problem of reconciling local and teleseismic estimates of the seismic energy (e.g., Winslow and Ruff, 1995).

Equation (44) predicts an rms stress drop for the Michoacan earthquake of ~~205~~ 210 bars. The moment of the largest subevent is, from equation (13), 1.8×10^{26} dyne-cm, so the square root of the moment ratios in equation (44) gives a factor of 7.8. From the accelerograms in Anderson *et al.* (1986), the duration of the strongest shaking is about 20 sec, implying that it is appropriate to use f_0 = 0.025 Hz. For R_{max} = 20 km, equation (12) gives f_c = 0.06~~0~~4 Hz. Thus, the term in the ratio of corner frequencies contributes a multiplicative factor of 1.~~5~~6 in equation (44). Finally, using the factor of 1.7 for I_θ leads to the prediction that in this case, $\Delta\sigma_{rms}$ will be 2~~0~~1 times greater than $\Delta\sigma_d$.

Anderson *et al.* (1986) did not compute the rms acceleration, but horizontal components of accelerograms from one of the stations (Caleta de Campos) give an average of about 42 cm/sec^2. The range of rms stress drops in Table 1 (50 to 210 bars) is based on this value. There are two problems associated with determining $\Delta\sigma_{rms}$ from a_{rms}. The first is with the definition of the lower corner frequency. Hanks (1979) defined $\Delta\sigma_{rms}$ to explain the level of the flat portion of the acceleration spectrum. For the Michoacan earthquake, the spectrum is approximately flat from 0.5 to 4.5 Hz. The problem is that the lower frequency of this flat part is larger than either f_0 (= 0.025 Hz) or $f_c(R_{max})$ (= 0.060 Hz). The second problem is that the ratio f_0/f_c is quite different from unity, but a ratio of 1 is assumed in going from equation (36) to (37). The uncertainty range on observed values of $\Delta\sigma_{rms}$, from 50 to 325 bars, was determined using the range of f_c from 0.025 to 0.5 Hz in equation (37), and the range of f_c from 0.06 to 0.5 Hz in ratio of f_{max}/f_c in equation (36). The ratio of the observed value of $\Delta\sigma_{rms}$, from equation (36),

to the predicted value, from equation (44), ranges from 0.55 to 1.6 for f_c from 0.06 to 0.5 Hz. Considering the approximations made in the derivation of equation (44), this agreement is satisfactory.

Yu (1994) did not discuss, in detail, her choice of model parameters. While by trial and error they do an excellent job of fitting the seismograms, there was no attempt to optimize them in any formal sense. Considering this, the agreement, within uncertainties, of all of the predicted parameters with independent estimates is quite encouraging. Thus, it seems reasonable to suggest that the relationships among the various stress-drop parameters considered here are predicted by the composite source model, using the equations given in this article.

Discussion

This article introduces the opportunity to evaluate methods that estimate the energy radiated from earthquakes. Methods to estimate this energy tend to make simplifying assumptions that do not fully take into account the complexities of wave propagation, including the mix of body and surface waves and resonances near the surface, and the complexity of the earthquake source. However, for the composite source model, it is possible to determine the amount of energy leaving the source in the form of far-field radiation. The synthetic seismograms, generated with theoretical Green's functions for a layered medium and modified to accommodate random scattering into the seismic coda, incorporate most of the major factors in wave propagation with the notable exception of basin resonances. Therefore, a test of energy equations is possible.

In the context of the composite source model, the roles of static stress drop and subevent stress drop are very clear and independent. The static stress drop is, as usual, proportional to the average slip divided by a characteristic dimension (Kanamori and Anderson, 1975; Brune, 1976). The subevent stress drop is independent of the static stress drop and determines the rise time of the displacement on the fault. In reality, though, they could be linked through the physics of earthquake generation. This article shows that the apparent stress, the effective stress, the Orowan stress drop, and the RMS stress drop are all proportional to the subevent stress drop. The relationships derived in this article have been confirmed, within uncertainties, for the case of the Michoacan, Mexico, earthquake, and application to other earthquakes is underway.

Acknowledgments

In preparation of this manuscript, I benefitted from discussions with James Brune, Kenneth Smith, Steven Wesnousky, Guang Yu, and Yuehua Zeng. Kenneth Smith, Steven Wesnousky and Yuehua Zeng also critically reviewed the manuscript. I also appreciate reviews by D. J. Andrews, M. C. Chapman, and an anonymous reviewer. This research was supported by the Southern California Earthquake Center and by the National Science Foundation Grant Numbers EAR 9418922 and CMS 9506675.

References

Abe, K. (1974). Seismic displacement and ground motion near a fault: the Saitama earthquake of September 21, 1931, *J. Geophys. Res.* **79**, 4393–4399.

Aki, K. and P. G. Richards (1980). *Quantitative Seismology: Theory and Methods*, Vol. I, W. H. Freeman and Co., New York, 557 pp.

Anderson, J. G., P. Bodin, J. N. Brune, J. Prince, S. K. Singh, R. Quaas, and M. Onate (1986). Strong ground motion from the Michoacan, Mexico, earthquake, *Science* **233**, 1043–1049.

Anderson, J. G., Y. Lee, Y. Zeng, and S. Day (1996). Control of strong motion by the upper 30 meters ~~(submitted for publication)~~. Bull. Seism. Soc. Am (in press Dec 199.

Anderson, J. G. and G. Yu (1996). Composite source model predictions for the Northridge earthquake, *Bull. Seism. Soc. Am.* **86**, 000–000.

Brune, J. N. (1970). Tectonic stress and spectra of seismic shear waves from earthquakes, *J. Geophys. Res.* **75**, 4997–5009.

Brune, J. N. (1971). Correction. Tectonic stress and spectra of seismic shear waves from earthquakes, *J. Geophys. Res.* **76**, 5002.

Brune, J. N. (1976). The physics of earthquake strong motion, in *Seismic Risk and Engineering Decisions*, C. Lomnitz and E. Rosenblueth (Editors), Elsevier Scientific Publishing Company, Amsterdam, 141–177.

Day, S. M. (1996). RMS response of a one-dimensional halfspace to SH ~~(submitted for publication)~~. Bull. Seism. Soc. Am. 86, 363-370.

Hanks, T. C. (1979). b values and $\omega^{-\gamma}$ seismic source models: implications for tectonic stress variations along active crustal fault zones and the estimation of high-frequency strong ground motion, *J. Geophys. Res.* **84**, 2235–2242.

Hanks, T. C. (1982). f_{max}, *Bull. Seism. Soc. Am.* **72**, 1867–1879.

Hanks, T. C. and R. K. McGuire (1981). The character of high-frequency strong ground motion, *Bull. Seism. Soc. Am.* **71**, 2071–2095.

Haskell, N. A. (1964). Total-energy and energy spectral density of elastic wave propagation from propagating faults, *Bull. Seism. Soc. Am.* **54**, 1811–1841.

Herrero, A. and P. Bernard (1994). A kinematic self-similar rupture process for earthquakes, *Bull. Seism. Soc. Am.* **84**, 1216–1228.

Joyner, W. B. (1984). A scaling law for the spectra of large earthquakes, *Bull. Seism. Soc. Am.* **74**, 1167–1188.

Kanamori, H. (1972a). Mechanism of tsunami earthquakes, *Phys. Earth Planet. Interiors* **6**, 346–359.

Kanamori, H. (1972b). Determination of effective tectonic stress associated with earthquake faulting: the Tottori earthquake of 1943, *Phys. Earth Planet. Interiors* **5**, 426–434.

Kanamori, H. (1977). The energy release in great earthquakes, *J. Geophys. Res.* **82**, 2971–2987.

Kanamori, H. (1994). Mechanics of earthquakes, *Ann. Rev. Earth Planet. Sci.* **22**, 207–237.

Kanamori, H. and D. L. Anderson (1975). Theoretical basis of some empirical relations in seismology, *Bull. Seism. Soc. Am.* **65**, 1073–1095.

Kanamori, H. and E. Hauksson (1992). A slow earthquake in the Santa Maria basin, California, *Bull. Seism. Soc. Am.* **82**, 2087–2096.

Kanamori, H. and M. Kikuchi (1993). The 1992 Nicaragua earthquake: a slow tsunami earthquake associated with subducted sediments, *Nature* **361**, 714–716.

McGarr, A., R. E. Green, and S. M. Spottiswood (1981). Strong ground motion of mine tremors: some implications for near-source ground motion parameters, *Bull. Seism. Soc. Am.* **71**, 295–319.

McGuire, R. K. and T. C. Hanks (1980). RMS accelerations and spectral amplitudes of strong ground motion during the San Fernando, California, earthquake, *Bull. Seism. Soc. Am.* **70**, 1907–1919.

Orowan, E. (1960). Mechanism of seismic faulting, *Geol. Soc. Am. Mem.* **79**, 323–345.

Savage, J. C. and M. D. Wood (1971). The relation between apparent stress and stress drop, *Bull. Seism. Soc. Am.* **61**, 1381–1388.

Shoja-Taheri, J. and J. G. Anderson (1988). The 1978 Tabas, Iran, earthquake: an interpretation of the strong motion records, *Bull. Seism. Soc. Am.* **78**, 142–171.

Smith, K. D., J. N. Brune, and K. F. Priestley (1991). The seismic spectrum,

radiated energy, and the Savage and Wood inequality for complex earthquakes, *Tectonophysics* **188**, 303–320.

Su, F., Y. Zeng, and J. G. Anderson (1994a). Simulation of Landers earthquake strong motion using a composite source model, 89th Annual Meeting of the Seismological Society of America, Pasadena, California, *Seism. Res. Lett.* **65**, 52.

Su, F., Y. Zeng, and J. G. Anderson (1994b). Simulation of the Loma Prieta earthquake strong ground motion using a composite source model, Abstract, 1994 Fall Meeting, American Geophysical Union, San Francisco, California, 448.

Tumarkin, A. G., R. J. Archuleta, and R. Madariaga (1994). Scaling relations for composite earthquake models, *Bull. Seism. Soc. Am.* **84**, 1279–1283.

Vassiliou, M. S. and H. Kanamori (1982). The energy release in earthquakes, *Bull. Seism. Soc. Am.* **72**, 371–387.

Winslow, N. W. and L. J. Ruff (1995). "Direct" teleseismic estimates of radiated energy (abstract), *EOS* **76**, 1995 Fall Meeting Supplement, F381.

Wyss, M. (1970). Stress estimates for South American shallow and deep earthquakes, *J. Geophys. Res.* **75**, 1529–1544.

Yu, G. (1994). Some aspects of earthquake seismology: slip partitioning along major convergent plate boundaries; composite source model for estimation of strong motion; and nonlinear soil response modeling, *Ph.D. Thesis*, University of Nevada, Reno, 144 pp.

Yu, G., K. N. Khattri, J. G. Anderson, J. N. Brune, and Y. Zeng (1995). Strong ground motion from the Uttarkashi, Himalaya, India, Earthquake: comparison of observations with synthetics using the composite source model, *Bull. Seism. Soc. Am.* **85**, 31–50.

Yu, G., S. M. Day, and J. G. Anderson (1996). Composite earthquake model: a promising method for predicting ground motions (submitted for publication).

Zeng, Y. and J. G. Anderson (1996). A composite source model of the 1994 Northridge earthquake using genetic algorithms, *Bull. Seism. Soc. Am.* **86**, S71–S83.

Zeng, Y., J. G. Anderson, and G. Yu (1994). A composite source model for computing realistic synthetic strong ground motions, *Geophys. Res. Lett.* **21**, 725–728.

Seismological Laboratory and Department of Geological Sciences
University of Nevada
Reno, Nevada 89557

Manuscript received 13 February 1996.

Seismic Energy and Stress Drop Parameters for a Composite Source Model

John G. Anderson[1]

1 Seismological Laboratory and Department of Geological Sciences, University of Nevada, Reno, Nevada 89557.
Phone: (702)784-4265; email: jga@seismo.unr.edu

Introduction

This paper presents a technique to estimate seismic energy release in earthquakes from strong motion accelerograms. The methods which derive energy from strong motion by integrating the observed velocity seismogram or its spectrum (e.g. Anderson et al, 1986; Shoja-Taheri and Anderson, 1988) inevitably make some simplifying assumptions about the wave propagation whose importance is difficult to assess. This paper takes the alternative approach of computing energy leaving the source (e.g. Haskell, 1964; Vassiliou and Kanamori, 1982).

Yu (1994) and Zeng et al (1994) have proposed a composite source model for generating synthetic strong motion accelerograms. These synthetics utilize synthetic Green's functions generated for a layered medium. Thus many of the complexities of wave propagation are incorporated. Several papers have demonstrated that the synthetics generated with this model are highly realistic, both in appearance in the time domain and in reproducing spectral amplitudes over the entire frequency band (Yu, 1994; Zeng et al, 1994; Yu et al, 1995; Su et al, 1995a,b; Anderson and Yu, 1996; Zeng and Anderson, 1996). Considering this realism, it seems natural to derive an analytical expression for the seismic energy leaving a composite source.

In addition to energy, it is possible to derive analytical expressions for several of the commonly used stress parameters in the context of this model: apparent stress (Wyss, 1970), effective stress (Brune, 1970), Orowan stress drop (Kanamori, 1977; Vassiliou and Kanamori, 1982), and RMS stress drop (Hanks, 1979; Hanks and McGuire, 1981).

Composite source model

Credits: Zeng et al (1994), Yu (1994)

The composite source model superimposes radiation from a number of point sources on the fault. The point sources have a distribution of "sizes":

$$n(R) = pR^{-D-1}$$

$n(R)$ = the number of sources with equivalent "radius" R

D = a fractal dimension (generally taken to be 2.0)

$$p = \frac{7M_o^T}{16\Delta\sigma_d} \frac{3-D}{(R_{\max}^{3-D} - R_{\min}^{3-D})}$$

M_o^T = moment of target event

$\Delta\sigma_d$ = subevent stress drop

Subevent spatial distribution: random, uniform on the fault plane.

Subevent radiates when the rupture front reaches its center.

Subevent time function: $\dot{M}_o(t) = (2\pi f_c)^2 M_o t e^{-2\pi f_c t} H(t)$

Rupture starts at epicenter, grows with rupture velocity v.

View of the composite source, assuming

$$s(r) = \frac{24}{7\pi}\frac{\Delta\sigma_d}{\mu}(R^2 - a^2)^{1/2}$$

for each subevent:

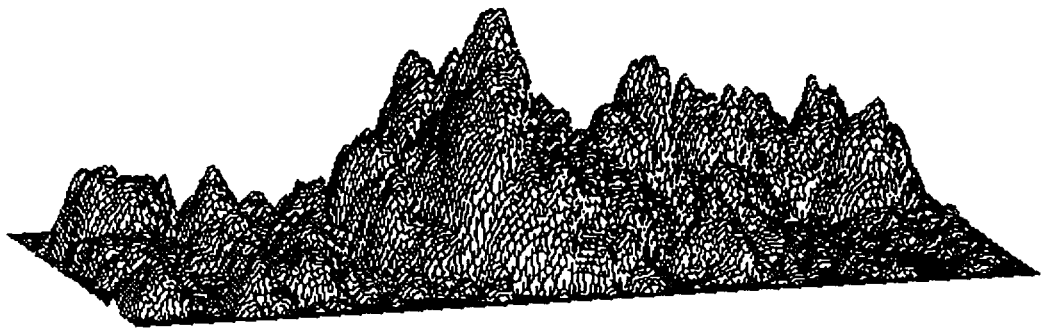

The following figures shows realizations of the composite source time function for a rectangular fault (expressed as seismic moment rate) with three values of $\Delta\sigma_d$: 1, 10, and 100 bars, and associated Fourier spectra.

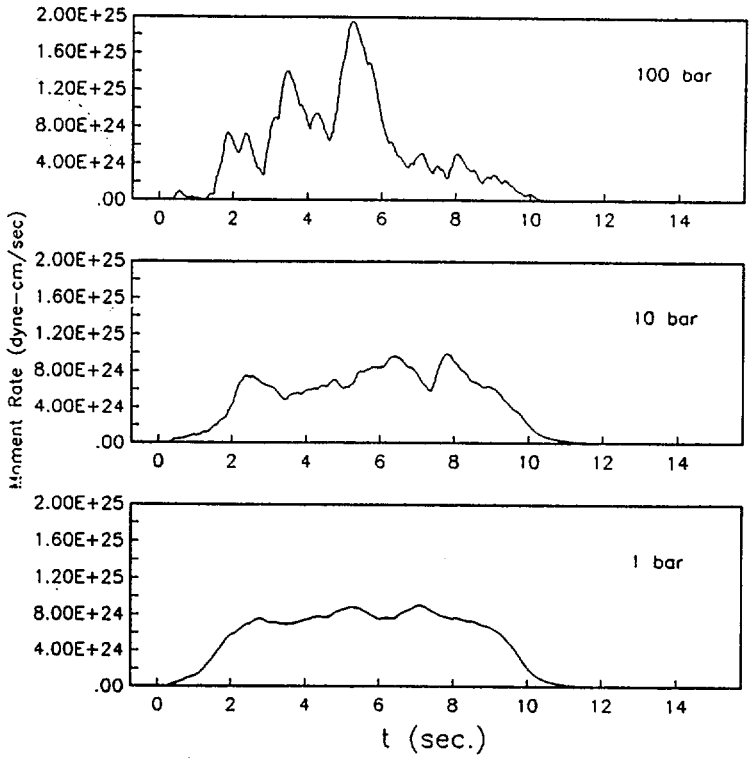

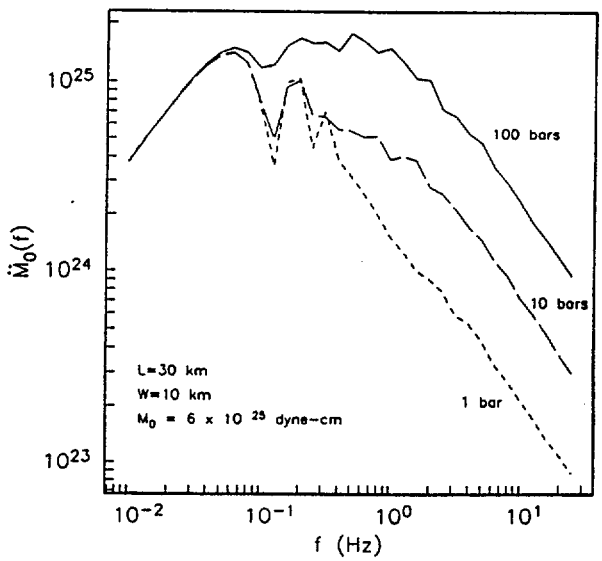

Static stress drop, $\Delta\sigma_s$

Usual formulas (e.g. Kanamori and Anderson, 1975).

Strike slip, length L greater than width W, surface rupture:

$$\Delta\sigma_s = \frac{2M_o}{\pi W^2 L}$$

Dip slip fault, length L greater than width W, surface rupture:

$$\Delta\sigma_s = \frac{4(\lambda + \mu)M_o}{\pi(\lambda + 2\mu)W^2 L}$$

Circular fault, radius R:

$$\Delta\sigma_s = \frac{7M_o}{16R^3}$$

Note: In the composite source model, the subevent stress drop ($\Delta\sigma_d$) is independent of $\Delta\sigma_s$.

Radiated energy

Energy radiated to far field from a point source (e.g. Vassiliou and Kanamori, 1982):

$$E_P(R) = \frac{I_{M_o}}{15\pi\rho\alpha^5}$$

$$E_S(R) = \frac{I_{M_o}}{10\pi\rho\beta^5}$$

$$I_{M_o} = \int_0^\infty \dot{M}_o^2(t)dt$$

Note: $E_S = 23.4\ E_P$

For a subevent in the composite source model:

$$E_S^{Brune}(R) = 0.233\frac{\Delta\sigma_d}{\mu}M_o(R)$$

Total energy in a composite source S wave:

$$E_S^{CS} = 0.233C_E\frac{\Delta\sigma_d}{\mu}M_o^T$$

Adjust upwards by 4% to account for the P wave energy.

Explanation of factor C_E

This factor is estimated in numerical experiments, to correct for coherence of the radiation from subevents. When there are few subevents and the radiation is totally incoherent, $C_E = 1.0$.

The figure below shows $C_E = 1.0$ several fault models, as a function of normalized subevent stress drop. The normalized subevent stress drop is defined as

$\Delta\sigma_d/\Delta\sigma_s^*$

where

$$\Delta\sigma_s^* = \frac{M_o}{W^2 L}.$$

I used $\Delta\sigma_s^*$ instead of $\Delta\sigma_s$ to remove the ambiguity that arises from different mechanisms (i.e. strike-slip or dip-slip) or aspect ratios. With the composite source the mechanism does not affect the radiated energy estimates since it is derived using an infinite space model.

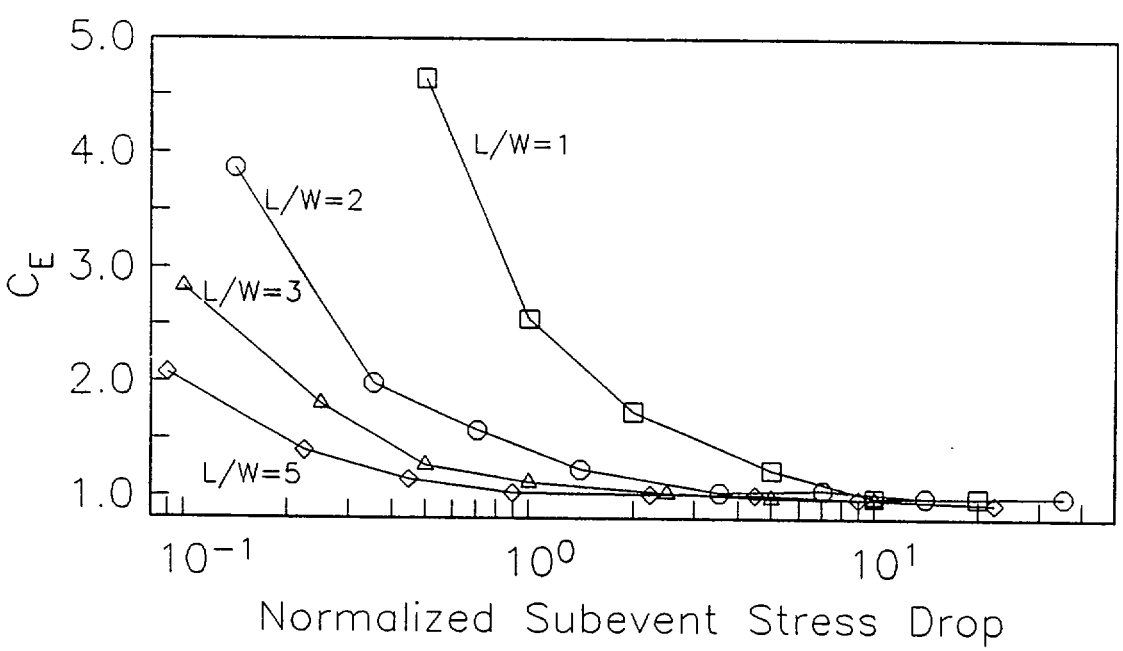

Strain Energy

Change in strain energy (Kanamori and Anderson, 1975):

$$\Delta W = \frac{M_o}{\mu}\bar{\sigma}$$

Radiated energy:

$$E_S = \eta \Delta W$$

where η = seismic efficiency

So:

$$\eta\bar{\sigma} = 0.243 C_E \Delta\sigma_d$$

Apparent stress σ_a

Definition (Wyss, 1970):

$$\sigma_a = \eta\bar{\sigma} = \mu E_s / M_o$$

So:

$$\sigma_a = 0.243 C_E \Delta\sigma_d$$

Effective Dynamic Stress, σ_e

Definition (Brune, 1970): Difference between the initial shear stress at the beginning of faulting and the dynamic frictional stress. From Brune (1970), the particle velocity at the fault, $\dot{D}$, is proportional to σ_e.

Kanamori and Anderson (1975), or Kanamori (1994) give:

$$\dot{D} = C_{pv}\sigma_e\beta/\mu$$

C_{pv} ~ 1 - 2, depending on the model[2].

For a Brune pulse: $\sigma_e = \frac{0.44}{C_{pv}}\Delta\sigma_d$.

This is based on the average slip and the rise time to release 90% of the total seismic moment. The lead coefficient (0.44) is uncertain between 0.27 and 1.70.

For the composite source,

$$\sigma_e = \frac{0.44C_E}{C_{pv}}\Delta\sigma_d$$

is probably a reasonable approximation within all the uncertainties, since C_E is a measure of the net coherency of the subevents.

2 While recognizing that there is this factor of two uncertainty, this paper follows Kanamori (1994) in using $C_{pv} = 1$.

Orowan stress drop, $\Delta\sigma_o$

Definition: the difference between the initial and final stresses on the fault.

Assuming the final and dynamic frictional stresses are equal, i.e. the Orowan (1960) conditions are met, then the radiated seismic energy is (Vassiliou and Kanamori, 1982):

$$E_s = \frac{M_o \Delta\sigma_o}{2\mu}$$

Composite source model estimation:

$$\Delta\sigma_o = 0.486\ C_E\ \Delta\sigma_d$$

RMS Stress Drop, $\Delta\sigma_{rms}$

Hanks (1979) defines $\Delta\sigma_{rms}$ from RMS acceleration:

$$a_{rms}^2 = \frac{1}{T_d}\int_0^\infty a^2(t)dt$$

T_d = duration of faulting at source.

After some work, in an infinite medium:

$$a_{rms} = 0.158\frac{\Delta\sigma_{rms}}{\rho r}\left(\frac{f_{\max}}{f_c}\right)^{1/2}$$

For the composite source model, with some approximations, and taking the typical case where $D = 2$:

$$\Delta\sigma_{rms} = \Delta\sigma_d I_\theta^{1/2}\left(\frac{M_o}{M_{os}(R_{\max})}\right)^{1/2}\left(\frac{f_c}{f_o}\right)^{1/2}$$

The RMS stress drop will be larger than the subevent stress drop, since all of the multipliers for $\Delta\sigma_d$ are greater than one.

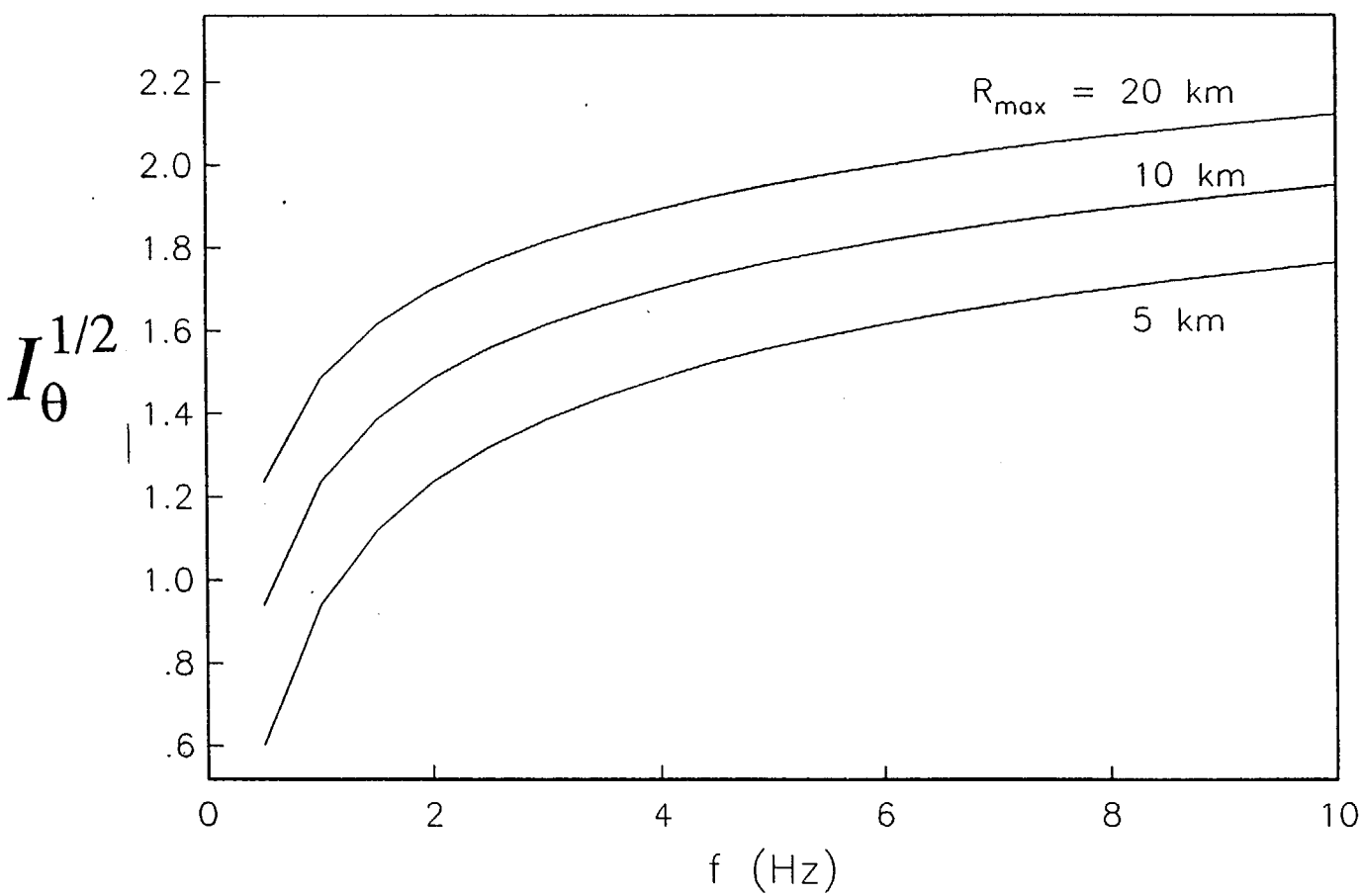
$I_\theta^{1/2}$
2.2
2.0
1.8
1.6
1.4
1.2
1.0
.8
.6
0
2
4
6
8
10
f (Hz)
R_{max} = 20 km
10 km
5 km

Savage-Wood Inequality, (*SWR*)

Definition (Savage and Wood, 1971):

$$SWR = \frac{2\sigma_a}{\Delta\sigma_s}$$

Composite source model:

$$SWR = \frac{0.486\, C_E\, \Delta\sigma_d}{\Delta\sigma_s}$$

Savage and Wood (1971) model: static and effective dynamic stress drops are linked through the physics of the earthquake generating process.

$SWR < 1$ --> overshoot

$SWR > 1$ --> partial stress drop (sense of Brune, 1970)

Observations show considerable scatter:

Savage and Wood (1971): $SWR \approx 0.3$
considerable scatter (some earthquakes have $SWR > 1$).

Kanamori and Anderson (1975): $SWR \approx 1$.

Smith et al. (1991): $SWR > 1$

Applications

Yu (1994) developed a composite source model for the 1985 Michoacan, Mexico, earthquake (M8.1). Many of the other parameters discussed in this paper have been estimated independently. Table 1 first describes the composite source model, then compares predictions using these parameters with the independent estimates.

Yu (1994) did not discuss, in detail, her choice of model parameters. While by trial and error they do an excellent job of fitting the seismograms, there was no attempt to optimize them in any formal sense. Considering this, the agreement, within uncertainties, of all of the predicted parameters with independent estimates is quite encouraging.

Table 1
Composite Source Model Parameters Michoacan, Mexico Earthquake, September 19, 1985 (M_W=8.1).

Composite Source Model[3]

Seismic Moment *(dyne-cm)*	1.1×10^{28}
Fault dimension *(km)*	178×80 km
Subevent stress drop *(bars)*	10 bars
Maximum radius of subevent *(km)*	20 km
Rupture velocity *(km/sec)*	2.8 km/sec
Fractal dimension D	2.0

3 These parameters are those used by Yu (1994).

Table 1 (continued)
Stress and Energy Parameters
Michoacan, Mexico Earthquake, September 19, 1985 (M_W=8.1).

	Predictions from csm parameters[5]	Observed[4]	Ratio (observed / CSM prediction)
C_E	1.3		
Radiated Energy *(ergs)*	1.1×10^{23}	1.0×10^{23}	0.9
Static stress drop *(bars)*	8	19	2.4
Apparent stress *(bars)*	3.0	3.0[6]	1.0
Effective dynamic stress *(bars)*	6	6-12[7]	1.0-2.0
Savage-Wood Ratio	0.8	0.3[8]	0.4
RMS stress drop *(bars)*	200	50-325[9]	0.25-1.6

4 Anderson et al. (1986), except as noted otherwise.

5 This uses $\mu = 3.3 \times 10^{11} dyne/cm^2$.

6 This estimate is from the definition and the estimates of seismic moment and energy. Anderson et al (1986) merely state "under 6 bars".

7 Anderson et al (1986) give this range for effective dynamic stress. The value of 6 bars is internally consistent with parameter choices in this paper, as discussed in the text.

8 Presented here from the defintion (Equation 27).

9 Based on horizontal components of accelerogram from the closest station, Caleta de Campos, which give a_{rms} of 39 and 45 cm/sec^2, or an average of 42 cm/sec^2. These were substituted into Equations (36) or (37), except with the Hanks (1979) coefficient of 0.445 since this is a free surface observation. The factor of 2 associated with the difference in relation between duration and corner frequency was kept, but for the purpose of compensating for the soft material at the surface. Other parameters are $\rho = 2.8$ gm/cm^3, $r = 24$ km, $f_{max} = 4.5$ Hz. The uncertainties are associated with a range of values of f_c from 0.025 Hz to 0.5 Hz, as discussed in the text.

Summary

In the context of the composite source model, the static stress drop and subevent stress drop are independent. In reality, they could be linked through the physics of earthquake generation. This paper shows that the apparent stress, the effective stress, the Orowan stress drop, and the RMS stress drop are all proportional to the subevent stress drop. From parameters of the composite source model, it is easy to estimate energy and all of these stress parameters.

The results give some insight into the meaning of several stress parameters in the context of a source that is much more complex than the models that are the basis for their original definitions. Even though the composite source is a kinematic model, it is reasonable to expect that characteristics of these relationships will carry over to future models that more thoroughly incorporate the physics of complex faulting.

In the development of the composite source model by Zeng et al (1994) and Yu (1994), and other applications, estimation of the stress drop of the subevents has been unconstrained. These results suggest a simple method to constrain it, if the energy, or any of the related stress parameters, of the target event is known independently.

Earthquake Size as a Function of Fault Slip Rate

John G. Anderson[1]

This presentation is based on the following publication:

John G. Anderson, Steven G. Wesnousky[2], and Mark W. Stirling[3] (1996). Earthquake Size as a Function of Fault Slip Rate, Bulletin of the Seismological Society of America 86, 683-690.

Presentation to Seismic Source Characterization
Workshop on Hazard Methodologies
October 16-18, 1996
Doubletree Hotel
Salt Lake City, Utah

[1] Seismological Laboratory and Department of Geological Sciences
University of Nevada, Reno, Nevada 89557
Tel: (702) 784-4265 FAX: (702) 784-1833 email: jga@seismo.unr.edu
[2] Center for Neotectonic Studies, Department of Geological Sciences
University of Nevada, Reno, Nevada 89557
Tel: (702) 784-6067 FAX: (702) 784-1382 email: stevew@seismo.unr.edu
[3] Center for Neotectonic Studies, Department of Geological Sciences
University of Nevada, Reno, Nevada 89557
Tel: (702) 784-1764 FAX: (702) 784-1382 email: stirling@seismo.unr.edu

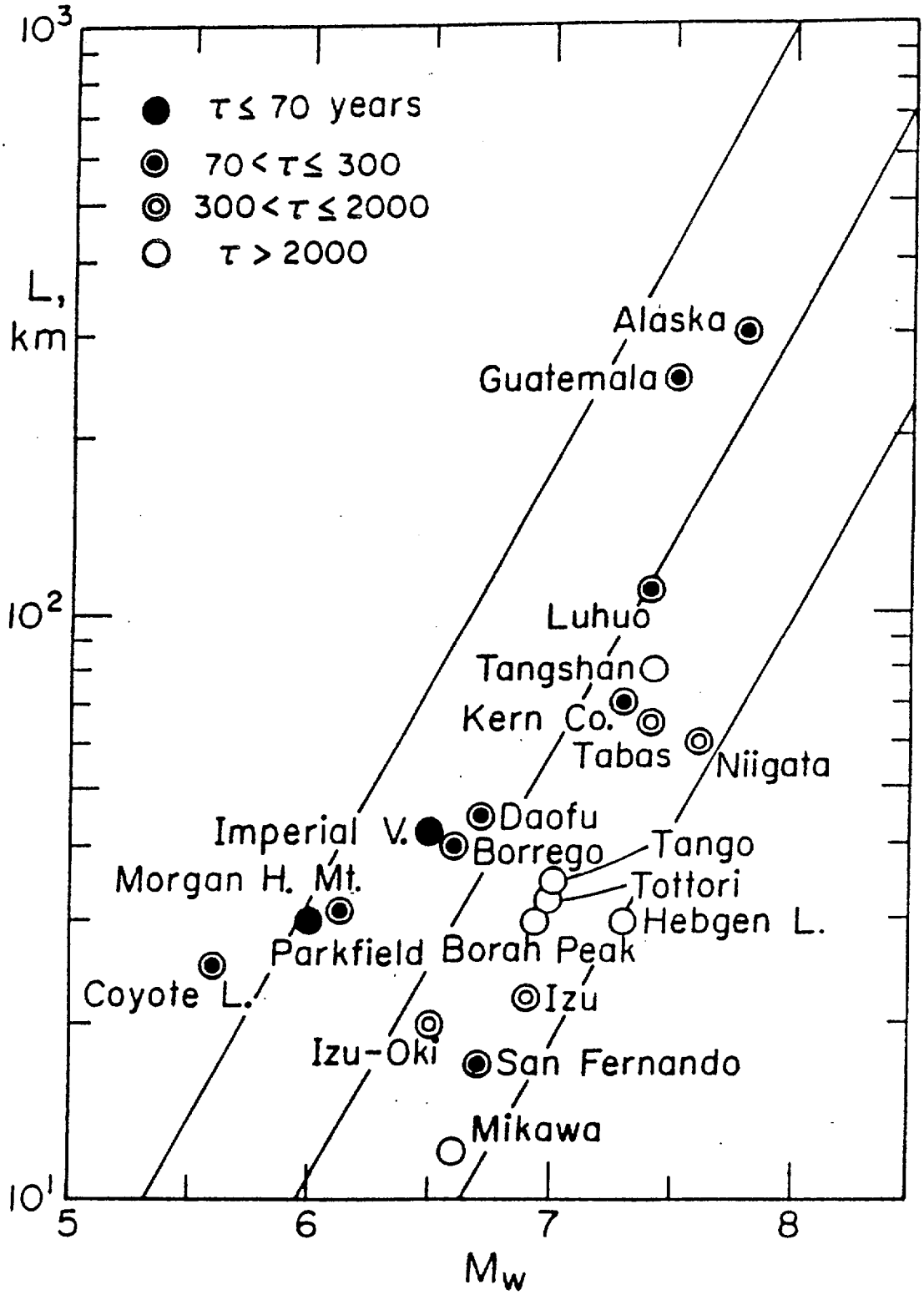

Fig. 2. The relations between the moment magnitude, M_W, and the fault length, L. The solid lines indicate the trend for a constant stress drop.

Kanamori and Allen, 1986

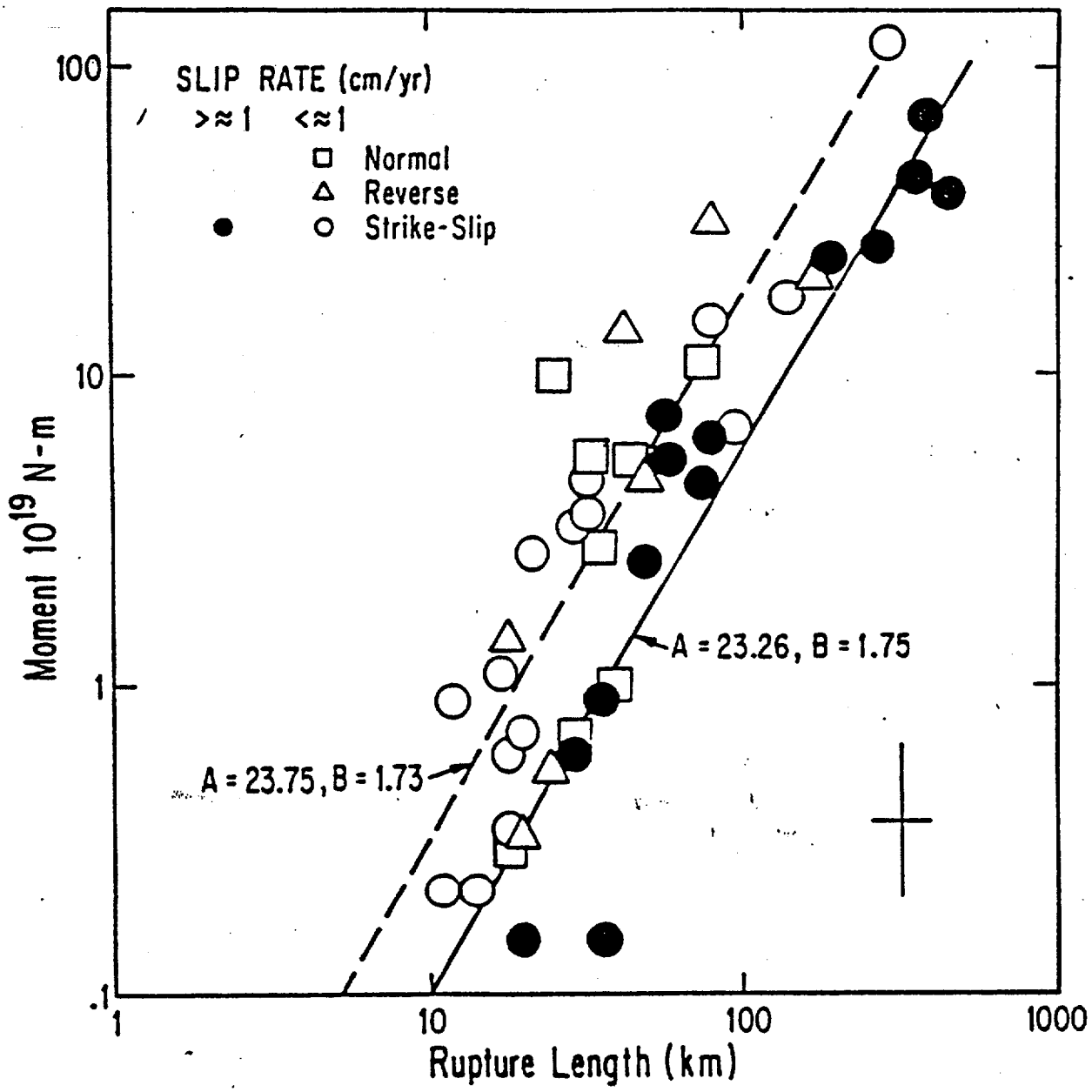

Fig 14. Earthquake rupture length versus earthquake moment, this figure distinguishes faults with slip rates above and below 1 cm/yr, and indicates the sense of displacement for the data points (from Wesnouski, 1986)

Table 1
Historical Earthquake Data

No.	Year	Location	M_0 ($\times 10^{26}$ dyne-cm)	M_w	Refs*	Length (km)	Refs*	Slip Rate (mm/yr)	Refs*
1	1811	New Madrid, Missouri	—	8.2[f]	86	60–250[h]	93, 70	0.01–2[l,m]	70, 93
2	1848	Marlborough, New Zealand	—	7.1[f]	88	95[g]	83	4–10[l]	5, 105
3	1857	Fort Tejon, California	53–87[a]	7.7–7.9[e]	1	360–400[g]	1, 16	16–43[l]	12
4	1868	Hayward, California	1.56[a]	6.8[e]	78	48[g]–52[i]	78, 108	8–10[l,n]	4
5	1872	Owens Valley, California	18–44[a]	7.4–7.7[e]	92	108[g]	92	1–3[l]	92
6	1888	Canterbury, New Zealand	—	7.0–7.3[f]	94	25–35[g]	87, 94	11–25[l]	18, 19, 87
7	1891	Nobi, Japan	~15[a]	7.4[e]	37	80[g]	39	1–10[l]	21
8	1896	Rikuu, Japan	14[a,b]	7.4[e]	39	36–50[h,i]	38, 39	0.1–1[l]	21
9	1906	San Francisco, California	35–43[a]	7.6–7.7[e]	1	420–470[g]	1, 62	15–28[l]	23, 24, 25, 26
10	1915	Pleasant Valley, Nevada	3–8[a]	6.9–7.2[e]	17, 78	34[g]	17	0.3–1[l]	27, 28
11	1927	Tango, Japan	4.6[a]	7.1[e]	40	33[h,i]	40	0.01–1[l]	21
12	1930	N. Izu, Japan	2.7[a,b]	6.9[e]	42	22[g,i]	36, 42	1–10[l]	21, 29
13	1933	Long Beach, California	0.41[c,d]	6.4[e]	78	23[h]	78	0.1–6[l]	12
14	1934	Parkfield, California	0.15[d]	6.1[e]	6	20[h]	7	29–39[l]	61
15	1939	Erzincan, Turkey	45[a]	7.7[e]	59	350[g]	30	5[l]–25[n]	31, 84, 107
16	1940	Imperial Valley, California	2.7[c,d]	6.9[e]	78	60[g]	8, 9	18–23[l]	32
17	1942	Erbaa Niksar, Turkey	2.5[a]	6.9[e]	59	50[g]	30	5[l]–25[n]	31, 84, 107
18	1944	Gerede-Bolu, Turkey	24[a]	7.6[e]	59	190[g]	30	5[l]–25[n]	31, 84, 107
19	1952	Kern County, California	11[a]	7.3[e]	10	75[i]	10	3–8.5[l]	10
20	1953	Golen-Yenice, Turkey	7.3[a]	7.2[e]	59	58[g]	30	5[l]–25[n]	31, 84, 107
21	1954	Fairview Peak, Nevada	6.4[c,d]	7.2[e]	78	46–64[g]	64	0.01–1[l]	103
22	1954	Dixie Valley, Nevada	2.9[c,d]	6.9[e]	78	46[g]	64	0.3–1[l]	27, 28
23	1956	San Miguel, Mexico	1.0[c,d]	6.6[e]	78	22[h]	78	0.1–0.5[l]	33
24	1959	Hebgen Lake, Montana	10.3[c]	7.3[e]	58	26[g]	20	0.8–2.5[l]	34
25	1964	Niigata, Japan	32[d]	7.6[e]	48	80[h]	48	0.01–1[l]	21
26	1966	Parkfield, California	0.15[d]	6.1[e]	2	37[g]	3	29–39[l]	6, 61
27	1967	Mudurnu Valley, Turkey	8.8[c]	7.3[e]	96	80[g]	30	5[l]–25[n]	31, 84, 107
28	1968	Borrego Mtn, California	1.2[c]	6.7[e]	11	30–45[g,h]	13, 14	1.4–5[l]	12, 106
29	1971	San Fernando, California	1.0[c,d]	6.6[e]	78	16[g]–17[h]	78	2–7.5[l]	35, 41
30	1973	Luhuo, China	19[c]	7.5[e]	72	89[g]–110[h]	78	5–10[l]	43
31	1979	Coyote Lake, California	0.051[c,d]	5.8[e]	78	14[h,j]	95, 73	15–19[l]	44
32	1979	Imperial Valley, California	0.6[d]	6.5[e]	52	30.5[g]	15	18–23[l]	32
33	1981	Daofu, China	1.3[c]	6.7[e]	75	46[h]	75	5–10[l]	43

(continued)

Table 1 (Continued)
Historical Earthquake Data

No.	Year	Location	M_0 ($\times 10^{26}$ dyne-cm)	M_w	Refs*	Length (km)	Refs*	Slip Rate (mm/yr)	Refs*
34	1983	Coalinga, California	0.54^d	6.5^a	60	25^h	46	$1–7^o$	45, 91
35	1983	Borah Peak, Idaho	$2.1^c–3.5^d$	$6.8–7.0^e$	56, 57	$30^h–39.5^g$	90, 74	$0.07–0.3^l$	34
36	1984	Morgan Hill, California	$0.2^{c,d}$	6.2^e	78	30^h	67	$3–6.4^l$	47, 49
37	1986	N. Palm Springs, California	$0.16^{c,d}$	6.1^e	78	$9^g–16^h$	78	$14–25^l$	50
38	1987	Edgecumbe, New Zealand	$0.63^{c,d}$	6.5^e	78	$18^g–32^h$	78	$1.3–2.8^l$	51
39	1987	Superstition Hills, California	1.1^c	6.7^e	68	27^g	69	$2–6^l$	12
40	1989	Loma Prieta, California	3.0^c	7.0^e	76	34^i	77	$12–28^{l,o}$	53, 24, 91
41	1990	Luzon, Philippines	39^c	7.7^e	65	$110^g–120^h$	66	$10–20^l$	104
42	1992	Landers, California	$6–11.5^{c,d}$	$7.1–7.3^e$	97–101	$70^{g,h}$	71, 82	$0.08–2^l$	12, 54
43	1994	Northridge, California	$0.76–2.6^{c,d}$	$6.5–6.9^e$	22, 63, 79, 85, 89, 102	$8–16^{h,i,k}$	80, 81, 22	$1.4–1.7^l$	55

Explanation of Data

The superscripts beside each of the estimates of M_o, M_w, L, and slip rate represent the following:

M_o estimated from (a) geological observations, (b) intensity data, (c) body waves, and (d) surface waves.

M_w estimated from (e) M_o, using the equation $\log M_o = 16.1 + 1.5M$ (Hanks and Kanamori, 1979). If a range of M_o is given, then the equivalent range of M_w is shown; (f) intensity data.

Length estimated from (g) geological observations, (h) aftershock distribution, (i) geodetic data, (j) broadband data, and (k) borehole-dilatational strainmeter data.

Slip rate estimated from (l) geological observations; (m) the equation $U^g = \dot{M}_0^g/\mu LW$, in which U^g is the slip rate, $\dot{M}_0^g$ is the seismic moment rate [New Madrid $\dot{M}_0^g$ is calculated by estimating the M_0 of the 1811 event from $\log M_0 = 16.1 + 1.5M$ (Hanks and Kanamori, 1979), and then dividing M_0 by return times estimated from paleoliquefaction studies], μ is the rigidity modulus, and L and W are the fault length and width; (n) geodetic data; and (o) slip partitioning studies.

*The references for the data sources are as follows:

1. Sieh (1978). 2. Tsai and Aki (1969). 3. Brown and Vedder (1967). 4. Lienkaemper *et al.* (1991). 5. Knuepfer (1992). 6. Bakun and McEvilly (1984). 7. Wilson (1936). 8. Brune and Allen (1967). 9. Trifunac (1972). 10. Stein and Thatcher (1981). 11. Petersen *et al.* (1991). 12. Petersen and Wesnousky (1994). 13. Clark (1972). 14. Hamilton (1972). 15. Sharp *et al.* (1982). 16. Hanks and Kanamori (1979). 17. Page (1935). 18. Van Dissen and Yeats (1991). Cowan and McGlone (1991). 20. Witkind (1964). 21. Research Group for Active Faults of Japan (1992). 22. Hudnut *et al.* (1994). 23. Prentice (1989). 24. Sims (1991). 25. Niemi and Hall (1992). 26. Clahan *et al.* (1994). 27. Wallace and Whitney (1984). 28. Bell and Katzer (1990). 29. Okada and Ikeda (1991). 30. Ambraseys (1970). 31. Straub and Kahle (1994). 32. Thomas and Rockwell (1996). 33. Hirabayashi *et al.* (1995). 34. Doser (1985a). 35. Sharp (1981). 36. Matsuda (1974). 37. Mikumo and Ando (1976). 38. Matsuda *et al.* (1980). 39. Thatcher *et al.* (1980). 40. Kanamori (1973). 42. Abe (1978). 43. Teng *et al.* (1983). 44. Savage *et al.* (1979). 45. Trumm *et al.* (1986). 46. Urhammer *et al.* (1983). 47. Galehouse (1991). 48. Abe (1975). 49. Bird and Kong (1994). 50. Hardin and Matti (1989). 51. Nairn and Beanland (1989). 52. Kanamori and Regan (1982). 53. Weber and Anderson (1990). 54. Jennings (1975). 55. Yeats and Huftile (1995). 56. Doser and Smith (1985). 57. Tanimoto and Kanamori (1986). 58. Doser (1985b). 59. Sykes and Quittmeyer (1981). 60. Kanamori (1983). 61. Sieh and Jahns (1984). 62. Thatcher (1975). 63. Thio and Kanamori (1994a). 64. Caskey *et al.* (1995). 65. Romanowicz (1992). 66. Yoshida and Abe (1992). 67. Bakun *et al.* (1984). 68. Bent *et al.* (1989). 69. Sharp *et al.* (1989). 70. Nuttli (1983). 71. Ad Hoc Working Group on the Probabilities of Future Large Earthquakes in Southern California (1992). 72. Zhou *et al.* (1983b). 73. Reasenberg and Ellsworth (1982). 74. Crone *et al.* (1987). 75. Zhou *et al.* (1983a). 76. Hanks and Krawinkler (1991). 77. Marshall *et al.* (1991). 78. Wells and Coppersmith (1994). 79. Zhao (1994). 80. Dreger *et al.* (1994). 81. Johnston and Linde (1994). 82. Sieh *et al.* (1993). 83. Lensen (1978). 84. Oral *et al.* (1995). 85. Wald and Heaton (1994b). 86. Johnston and Kanter (1990). 87. Cowan (1990). 88. Eiby (1973). 89. Thio and Kanamori (1994b). 90. Kanamori and Allen (1986). 91. Jones and Wesnousky (1992). 92. Beanland and Clark (1995). 93. Wesnousky and Leffler (1992). 94. Cowan (1991). 95. Bouchon (1982). 96. Hanks and Wyss (1972). 97. Freymueller (1994). 98. Johnson *et al.* (1994). 99. Wald and Heaton (1994a). 100. Cohee and Beroza (1994). 101. Dreger (1994). 102. Song *et al.* (1994). 103. J. Caskey, personal comm. 104. T. Nakata, personal comm. 105. Berryman (1979). 106. Gurrolo and Rockwell (1996). 107. Barka and Gulen (1988). 108. Yu and Segall (1995).

Proposed Regression Equation

$$M_W = A + B \log L + C \log S$$

Monte Carlo Method

10,000 Runs

M_W, L, S choosen at random within their bounds

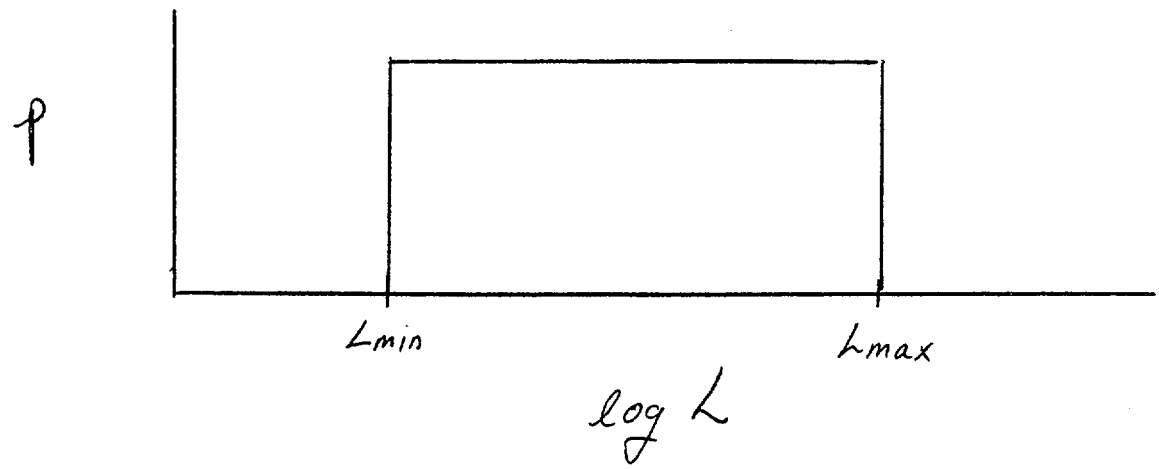

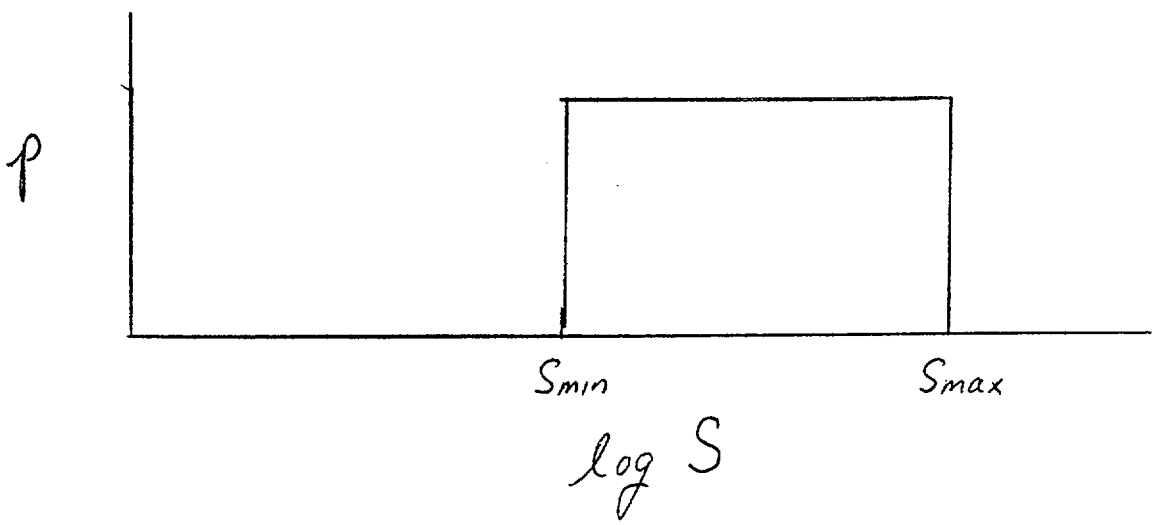

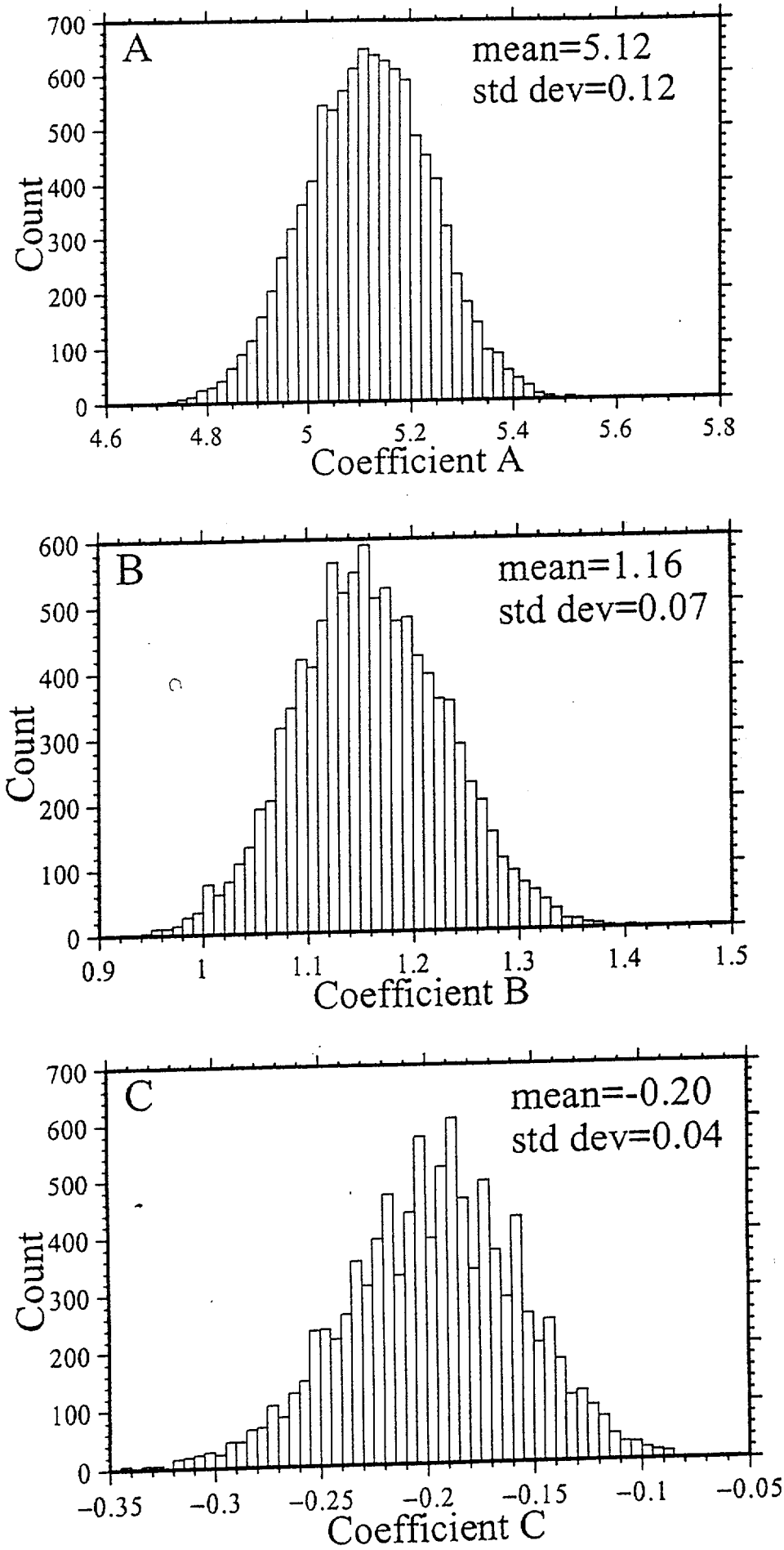
A
mean=5.12
std dev=0.12
Count
Coefficient A
B
mean=1.16
std dev=0.07
Count
Coefficient B
C
mean=-0.20
std dev=0.04
Count
Coefficient C

Fig 2

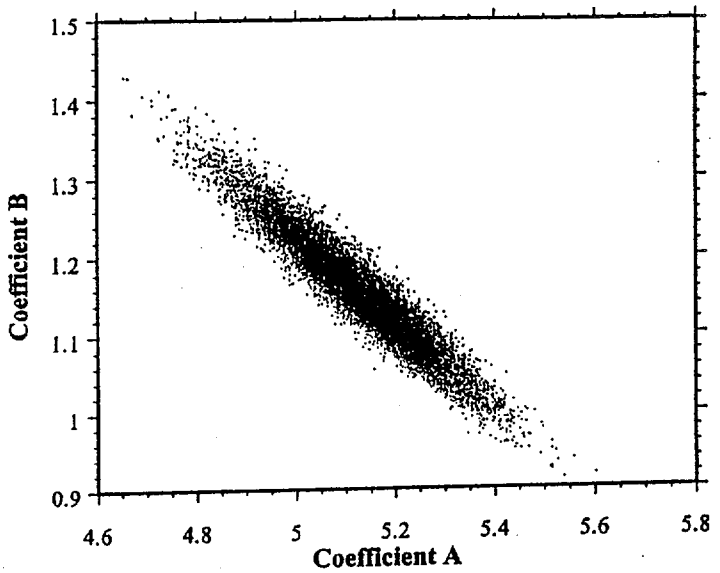
Coefficient B
1.5
1.4
1.3
1.2
1.1
1
0.9
4.6
4.8
5
5.2
5.4
5.6
5.8
Coefficient A

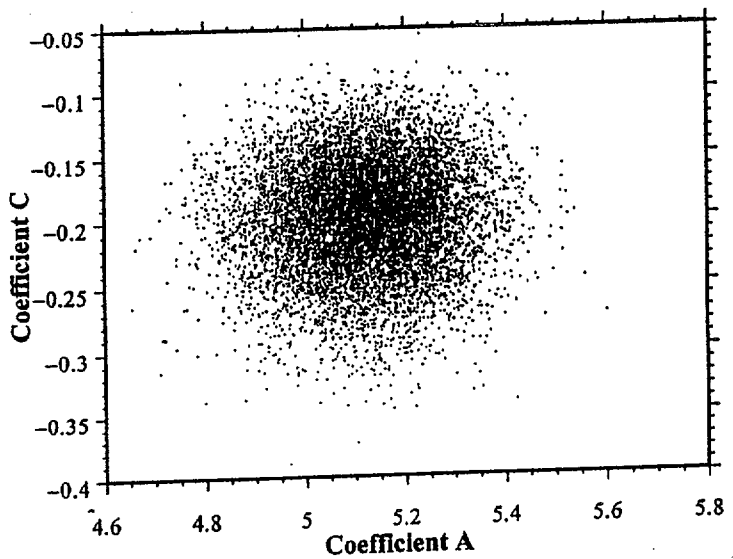
Coefficient C
−0.05
−0.1
−0.15
−0.2
−0.25
−0.3
−0.35
−0.4
4.6
4.8
5
5.2
5.4
5.6
5.8
Coefficient A

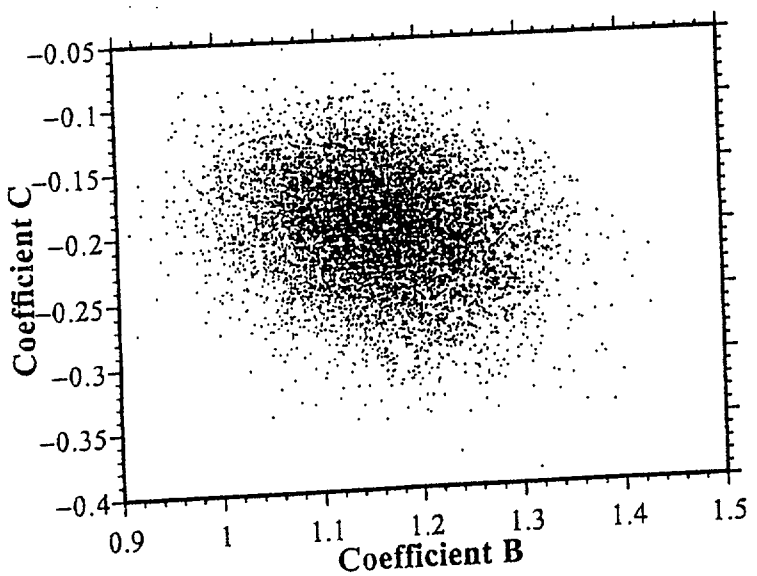
Coefficient C
−0.05
−0.1
−0.15
−0.2
−0.25
−0.3
−0.35
−0.4
0.9
1
1.1
1.2
1.3
1.4
1.5
Coefficient B

ALL EVENTS

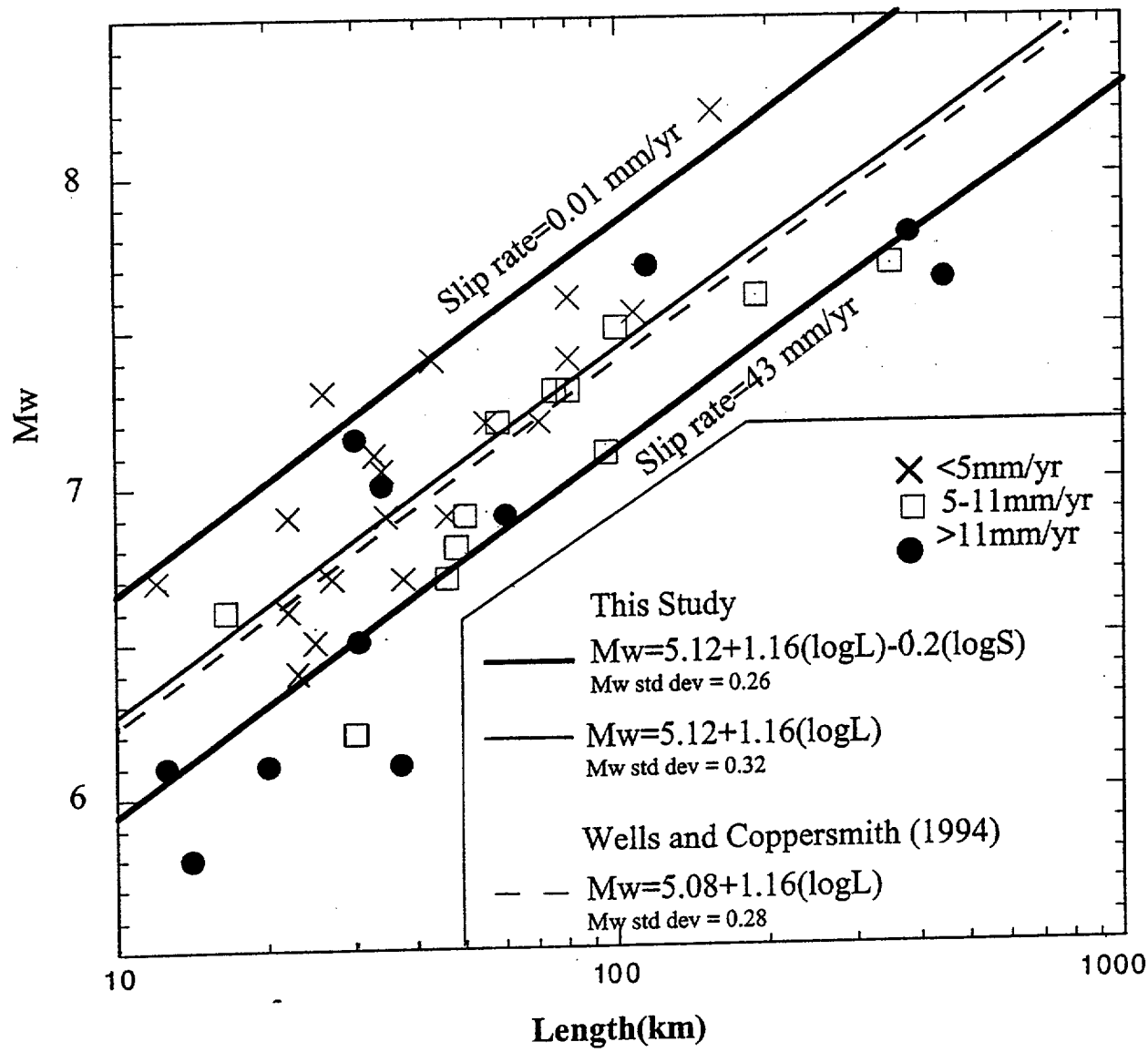
Slip rate=0.01 mm/yr
Slip rate=43 mm/yr
<5mm/yr
5-11mm/yr
>11mm/yr
This Study
Mw=5.12+1.16(logL)-0.2(logS)
Mw std dev = 0.26
Mw=5.12+1.16(logL)
Mw std dev = 0.32
Wells and Coppersmith (1994)
Mw=5.08+1.16(logL)
Mw std dev = 0.28
Mw
8
7
6
10
100
1000
Length(km)

Variance Reduction

L2 Norm (Standard Deviation)

$$\sigma = \left\{ \frac{1}{N} \sum_{i=1}^{N} (M_i - \hat{M}_i)^2 \right\}^{1/2}$$

Excluding slip rate:

$$\sigma = 0.32$$

Including slip rate:

$$\sigma = 0.26$$

This variance reduction is significant with 75% confidence.

L1 norm: variance reduction is significant with 95% confidence.

C is never closer to zero than -0.05, indicating less than one chance in 10^4 of finding a set of parameters, within the specified ranges of the data, for which the coefficient on slip rate is zero.

Seismic moment

$$M_o = \mu L W D$$

Moment magnitude

$$M_W = 2/3(\log M_o - 16)$$

Combining relations:

$$M_W = 2/3 \log L + 2/3 \log D + 2/3(\log \mu + \log W - 16)$$

For our data, W has a narrow range so the last term is nearly constant.

If $D \propto W$, B should be 0.67. (W model)

If $D \propto L$, B should be 1.33. (L model)

In our regression, $B = 1.16 \pm 0.07$. This is closer to the L model, but it differs from the L model prediction by over twice its standard deviation.

ALL EVENTS

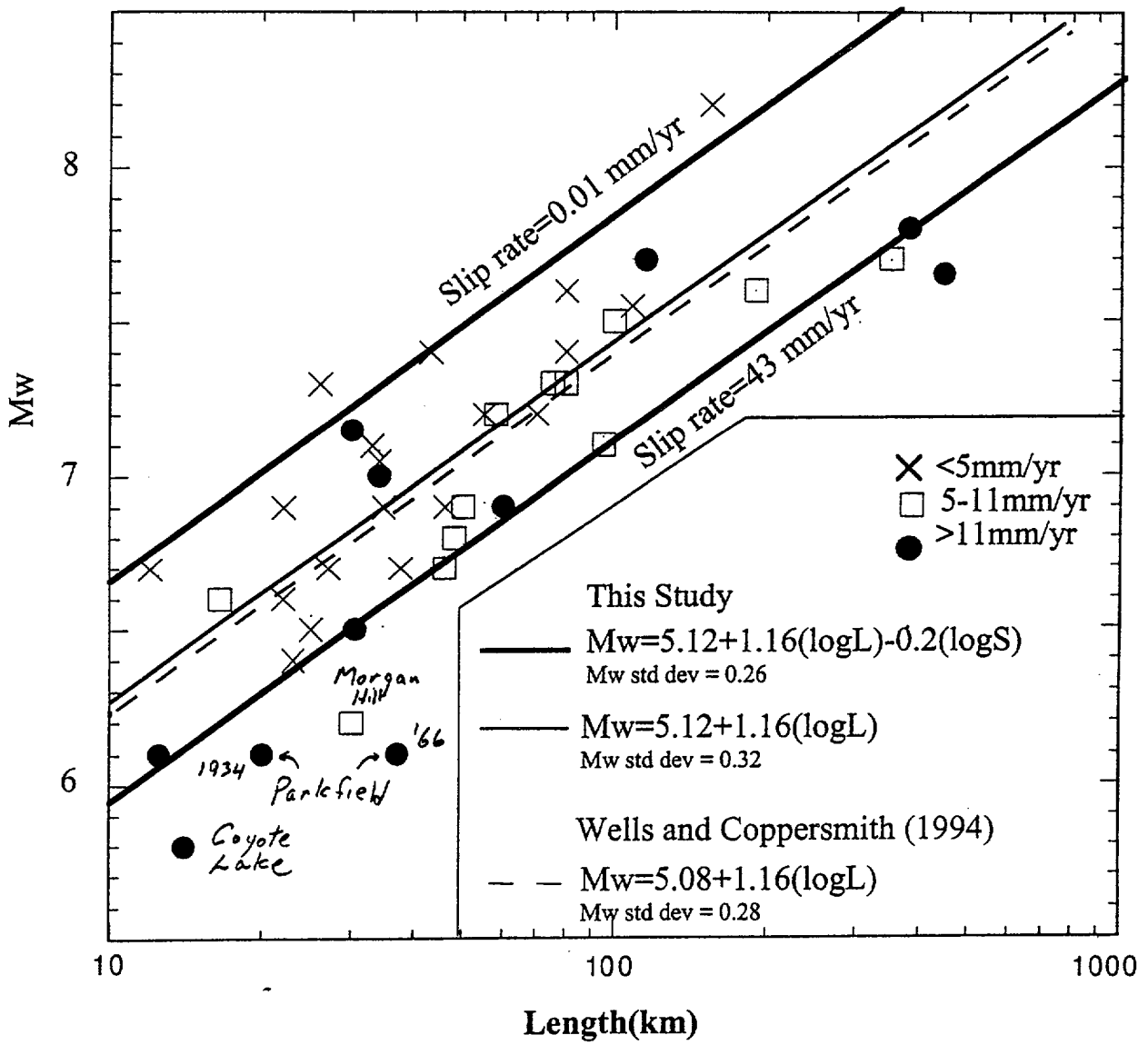

Events that adjoin creeping sections are marked

MLS Table for Normal Faults									
		Range	Used	Range		Used		Pred.	
			M	L	S	L	S	Magnitude	Residual
10	Pleasant Valley, Neva	6.9-7.2	7.05	34	.3-1	34	0.6	6.95	0.10
21	Fairview Peak	7.2	7.2	46-64	.01-1	55	0.1	7.36	-0.16
22	Dixie Valley	6.9	6.9	46	.3-1	46	0.6	7.10	-0.20
24	Hebgen Lake	7.3	7.3	26	.8-2.5	26	1.4	6.73	0.57
35	Borah Peak	6.8-7.0	6.9	30-39.5	.07-.3	35	0.14	7.10	-0.20
38	Edgecumbe, NZ	6.5	6.5	18-32	1.3-2.8	25	1.9	6.68	-0.18
							Average Residual		-0.01
							Standard deviation		0.31
MLS for extensional environments									
5	Owens Valley	7.4-7.7	7.55	108	3-Jan	108	2	7.41	0.14
10	Pleasant Valley, Neva	6.9-7.2	7.05	34	.3-1	34	0.6	6.95	0.10
16	Imperial Valley 1940	6.9	6.9	60	18-23	60	21.5	6.89	0.01
21	Fairview Peak	7.2	7.2	46-64	.01-1	55	0.1	7.36	-0.16
22	Dixie Valley	6.9	6.9	46	.3-1	46	0.6	7.10	-0.20
24	Hebgen Lake	7.3	7.3	26	.8-2.5	26	1.4	6.73	0.57
32	Imperial Valley 1979	6.5	6.5	30.5	18-23	30.5	21.5	6.55	-0.05
35	Borah Peak	6.8-7.0	6.9	30-39.5	.07-.3	35	0.14	7.10	-0.20
38	Edgecumbe, NZ	6.5	6.5	18-32	1.3-2.8	25	1.9	6.68	-0.18
							Average Residual		0.00
							Standard deviation		0.25

Conclusions

The distribution of coefficient C shows that a regression that does not include slip rate as a parameter will systematically overestimate the expected magnitudes on the fastest slipping faults, and will systematically underestimate the expected magnitudes on the slowest slipping faults.

Faults with slower slip rates tend to fail in earthquakes with higher static stress drop.

Bulletin of the Seismological Society of America, Vol. 86, No. 3, pp. 683–690, June 1996

Earthquake Size as a Function of Fault Slip Rate

by John G. Anderson, Steven G. Wesnousky, and Mark W. Stirling

Abstract Estimates of the potential size of earthquakes on mapped active faults are generally based on regressions of earthquake magnitude (M_w) versus length (L) of fault rupture for historical earthquakes. The fault slip rate (S) has been ignored in formal prediction equations, but more accurate predictions of future earthquake magnitudes on mapped faults may be obtained when it is included. A least-squares regression for a data set of 43 earthquakes occurring on faults for which slip rates are reported shows $M_w = 5.12 + 1.16 \log L - 0.20 \log S$, where L is in units of Km and S is in units of mm/yr. The result indicates that the largest earthquakes will occur on the slowest slipping faults if the rupture length is held constant.

Introduction

The estimate of earthquake size on mapped faults is fundamental to seismic hazard analysis. As a result, there is a long history of efforts to use historical data to develop regressions between earthquake size (magnitude or seismic moment) and earthquake rupture length, area, or fault displacement. A thorough review of past efforts, a synthesis of new observations, and the development of new regressions has recently been put forth by Wells and Coppersmith (1994). The slip rate of the fault on which an earthquake occurs has been generally ignored in such regressions when applied to seismic hazard analysis, except by Wesnousky (1986) who sorted the faults into high and low slip rate categories. However, within the community of seismologists concerned with the mechanics of faulting, it has been previously established that there also exists a dependency of earthquake size on earthquake return time and the tectonic environment in which earthquakes occur (e.g., Kanamori and Allen, 1986; Scholz *et al.*, 1986). Here, we use observations from 43 earthquakes that occurred on faults for which slip rates are reported and develop a regression for moment magnitude (M_w; Hanks and Kanamori, 1979) as a function of surface rupture length (L) and fault slip rate (S). Our result shows that the inclusion of fault slip rate in such regressions reduces the misfit between predicted and observed values of M_w as compared with regressions based solely on L and, hence, can yield more accurate predictions of future earthquake magnitudes on active faults.

Data and Analysis

We start with a list of 43 historical earthquakes for which there exist estimates of the moment magnitude M_w, the fault rupture length L, and the slip rate S of the respective fault on which the earthquake occurred (Table 1). The data are the result of a global search of observations, limited to earthquakes that occur in regions where the seismogenic depth is 15 to 20 km. The distribution of the data is shown in Figure 1.

The regression we develop has the form

$$M_w = A + B \log L + C \log S, \qquad (1)$$

where A, B, and C are constants to be determined by the regression. We avoid assuming a preferred slip rate or rupture length for each fault in our study by using a Monte Carlo approach. Values of S for each fault were chosen at random, assuming the probability density of $\log S$ is constant between the minimum and maximum estimates. Likewise, in setting up each regression, we chose L at random, assuming the probability density of $\log L$ is constant between its minimum and maximum values or between a range of $\pm 20\%$ of the rupture length if minimum and maximum values are absent in Table 1. This range is the average of rupture length ranges shown in Table 1. M_w is similarly chosen at random between the minimum and maximum values, or between the range of $M_w - 0.3$ and $M_w + 0.3$ if the minimum and maximum values are absent in Table 1. The width of the interval on the magnitude (± 0.3) is chosen to represent an uncertainty on the moment of plus or minus a factor of 3, which we believe to be conservative in most cases.

We generated 10,000 Monte Carlo realizations consistent with the above ranges of data, and for each we used a standard least-squares technique (e.g., Menke, 1989) to find A, B, and C. The distribution of values for A, B, and C is shown in Figure 2. There is almost no correlation between B and C in the Monte Carlo simulations (Fig. 3), indicating that the rupture length and slip rate act independently. The mean values and standard deviations of these distributions may be taken for regression coefficients:

$$M_w = (5.12 \pm 0.12) + (1.16 \pm 0.07)\log L - (0.20 \pm 0.04)\log S. \qquad (2)$$

Table 1
Historical Earthquake Data

No.	Year	Location	M_0 ($\times 10^{26}$ dyne-cm)	M_w	Refs*	Length (km)	Refs*	Slip Rate (mm/yr)	Refs*
1	1811	New Madrid, Missouri	—	8.2[f]	86	60–250[h]	93, 70	0.01–2[l,m]	70, 93
2	1848	Marlborough, New Zealand	—	7.1[f]	88	95[g]	83	4–10[l]	5, 105
3	1857	Fort Tejon, California	53–87[a]	7.7–7.9[e]	1	360–400[g]	1, 16	16–43[l]	12
4	1868	Hayward, California	1.56[a]	6.8[e]	78	48[g]–52[i]	78, 108	8–10[l,n]	4
5	1872	Owens Valley, California	18–44[a]	7.4–7.7[e]	92	108[g]	92	1–3[l]	92
6	1888	Canterbury, New Zealand	—	7.0–7.3[f]	94	25–35[g]	87, 94	11–25[l]	18, 19, 87
7	1891	Nobi, Japan	~15[a]	7.4[e]	37	80[g]	39	1–10[l]	21
8	1896	Rikuu, Japan	14[a,b]	7.4[e]	39	36–50[h,i]	38, 39	0.1–1[l]	21
9	1906	San Francisco, California	35–43[a]	7.6–7.7[e]	1	420–470[g]	1, 62	15–28[l]	23, 24, 25, 26
10	1915	Pleasant Valley, Nevada	3–8[a]	6.9–7.2[e]	17, 78	34[g]	17	0.3–1[l]	27, 28
11	1927	Tango, Japan	4.6[a]	7.1[e]	40	33[h,i]	40	0.01–1[l]	21
12	1930	N. Izu, Japan	2.7[a,b]	6.9[e]	42	22[g,i]	36, 42	1–10[l]	21, 29
13	1933	Long Beach, California	0.41[c,d]	6.4[e]	78	23[h]	78	0.1–6[l]	12
14	1934	Parkfield, California	0.15[d]	6.1[e]	6	20[h]	7	29–39[l]	61
15	1939	Erzincan, Turkey	45[a]	7.7[e]	59	350[g]	30	5[l]–25[n]	31, 84, 107
16	1940	Imperial Valley, California	2.7[c,d]	6.9[e]	78	60[g]	8, 9	18–23[l]	32
17	1942	Erbaa Niksar, Turkey	2.5[a]	6.9[e]	59	50[g]	30	5[l]–25[n]	31, 84, 107
18	1944	Gerede-Bolu, Turkey	24[a]	7.6[e]	59	190[g]	30	5[l]–25[n]	31, 84, 107
19	1952	Kern County, California	11[a]	7.3[e]	10	75[i]	10	3–8.5[l]	10
20	1953	Golen-Yenice, Turkey	7.3[a]	7.2[e]	59	58[g]	30	5[l]–25[n]	31, 84, 107
21	1954	Fairview Peak, Nevada	6.4[c,d]	7.2[e]	78	46–64[g]	64	0.01–1[l]	103
22	1954	Dixie Valley, Nevada	2.9[c,d]	6.9[e]	78	46[g]	64	0.3–1[l]	27, 28
23	1956	San Miguel, Mexico	1.0[c,d]	6.6[e]	78	22[h]	78	0.1–0.5[l]	33
24	1959	Hebgen Lake, Montana	10.3[c]	7.3[e]	58	26[g]	20	0.8–2.5[l]	34
25	1964	Niigata, Japan	32[d]	7.6[e]	48	80[h]	48	0.01–1[l]	21
26	1966	Parkfield, California	0.15[d]	6.1[e]	2	37[g]	3	29–39[l]	6, 61
27	1967	Mudurnu Valley, Turkey	8.8[c]	7.3[e]	96	80[g]	30	5[l]–25[n]	31, 84, 107
28	1968	Borrego Mtn, California	1.2[c]	6.7[e]	11	30–45[g,h]	13, 14	1.4–5[l]	12, 106
29	1971	San Fernando, California	1.0[c,d]	6.6[e]	78	16[g]–17[h]	78	2–7.5[l]	35, 41
30	1973	Luhuo, China	19[c]	7.5[e]	72	89[g]–110[h]	78	5–10[l]	43
31	1979	Coyote Lake, California	0.051[c,d]	5.8[e]	78	14[h,j]	95, 73	15–19[l]	44
32	1979	Imperial Valley, California	0.6[d]	6.5[e]	52	30.5[g]	15	18–23[l]	32
33	1981	Daofu, China	1.3[c]	6.7[e]	75	46[h]	75	5–10[l]	43

(*continued*)

Table 1 (Continued)
Historical Earthquake Data

No.	Year	Location	M_0 ($\times 10^{26}$ dyne-cm)	M_w	Refs*	Length (km)	Refs*	Slip Rate (mm/yr)	Refs*
34	1983	Coalinga, California	0.54^d	6.5^a	60	25^h	46	$1–7^o$	45, 91
35	1983	Borah Peak, Idaho	$2.1^c–3.5^d$	$6.8–7.0^e$	56, 57	$30^h–39.5^g$	90, 74	$0.07–0.3^l$	34
36	1984	Morgan Hill, California	$0.2^{c,d}$	6.2^e	78	30^h	67	$3–6.4^l$	47, 49
37	1986	N. Palm Springs, California	$0.16^{c,d}$	6.1^e	78	$9^g–16^h$	78	$14–25^l$	50
38	1987	Edgecumbe, New Zealand	$0.63^{c,d}$	6.5^e	78	$18^g–32^h$	78	$1.3–2.8^l$	51
39	1987	Superstition Hills, California	1.1^c	6.7^e	68	27^g	69	$2–6^l$	12
40	1989	Loma Prieta, California	3.0^c	7.0^e	76	34^i	77	$12–28^{l,o}$	53, 24, 91
41	1990	Luzon, Philippines	39^c	7.7^e	65	$110^g–120^h$	66	$10–20^l$	104
42	1992	Landers, California	$6–11.5^{c,d}$	$7.1–7.3^e$	97–101	$70^{g,h}$	71, 82	$0.08–2^l$	12, 54
43	1994	Northridge, California	$0.76–2.6^{c,d}$	$6.5–6.9^e$	22, 63, 79, 85, 89, 102	$8–16^{h,i,k}$	80, 81, 22	$1.4–1.7^l$	55

Explanation of Data

The superscripts beside each of the estimates of M_o, M_w, L, and slip rate represent the following:

M_o estimated from (a) geological observations, (b) intensity data, (c) body waves, and (d) surface waves.

M_w estimated from (e) M_o, using the equation $\log M_o = 16.1 + 1.5M$ (Hanks and Kanamori, 1979). If a range of M_o is given, then the equivalent range of M_w is shown; (f) intensity data.

Length estimated from (g) geological observations, (h) aftershock distribution, (i) geodetic data, (j) broadband data, and (k) borehole-dilatational strainmeter data.

Slip rate estimated from (l) geological observations; (m) the equation $U^g = \dot{M}_0^g/\mu LW$, in which U^g is the slip rate, $\dot{M}_0^g$ is the seismic moment rate [New Madrid $\dot{M}_0^g$ is calculated by estimating the M_0 of the 1811 event from $\log M_0 = 16.1 + 1.5M$ (Hanks and Kanamori, 1979), and then dividing M_0 by return times estimated from paleoliquefaction studies], μ is the rigidity modulus, and L and W are the fault length and width; (n) geodetic data; and (o) slip partitioning studies.

*The references for the data sources are as follows:

1. Sieh (1978). 2. Tsai and Aki (1969). 3. Brown and Vedder (1967). 4. Lienkaemper *et al.* (1991). 5. Knuepfer (1992). 6. Bakun and McEvilly (1984). 7. Wilson (1936). 8. Brune and Allen (1967). 9. Trifunac (1972). 10. Stein and Thatcher (1981). 11. Petersen *et al.* (1991). 12. Petersen and Wesnousky (1994), 13. Clark (1972). 14. Hamilton (1972). 15. Sharp *et al.* (1982). 16. Hanks and Kanamori (1979). 17. Page (1935). 18. Van Dissen and Yeats (1991). Cowan and McGlone (1991). 20. Witkind (1964). 21. Research Group for Active Faults of Japan (1992). 22. Hudnut *et al.* (1994). 23. Prentice (1989). 24. Sims (1991). 25. Niemi and Hall (1992). 26. Clahan *et al.* (1994). 27. Wallace and Whitney (1984). 28. Bell and Katzer (1990). 29. Okada and Ikeda (1991). 30. Ambraseys (1970). 31. Straub and Kahle (1994). 32. Thomas and Rockwell (1996). 33. Hirabayashi *et al.* (1995). 34. Doser (1985a). 35. Sharp (1981). 36. Matsuda (1974). 37. Mikumo and Ando (1976). 38. Matsuda *et al.* (1980). 39. Thatcher *et al.* (1980). 40. Kanamori (1973). 42. Abe (1978). 43. Teng *et al.* (1983). 44. Savage *et al.* (1979). 45. Trumm *et al.* (1986). 46. Urhammer *et al.* (1983). 47. Galehouse (1991). 48. Abe (1975). 49. Bird and Kong (1994). 50. Hardin and Matti (1989). 51. Nairn and Beanland (1989). 52. Kanamori and Regan (1982). 53. Weber and Anderson (1990). 54. Jennings (1975). 55. Yeats and Huftile (1995). 56. Doser and Smith (1985). 57. Tanimoto and Kanamori (1986). 58. Doser (1985b). 59. Sykes and Quittmeyer (1981). 60. Kanamori (1983). 61. Sieh and Jahns (1984). 62. Thatcher (1975). 63. Thio and Kanamori (1994a). 64. Caskey *et al.* (1995). 65. Romanowicz (1992). 66. Yoshida and Abe (1992). 67. Bakun *et al.* (1984). 68. Bent *et al.* (1989). 69. Sharp *et al.* (1989). 70. Nuttli (1983). 71. Ad Hoc Working Group on the Probabilities of Future Large Earthquakes in Southern California (1992). 72. Zhou *et al.* (1983b). 73. Reasenberg and Ellsworth (1982). 74. Crone *et al.* (1987). 75. Zhou *et al.* (1983a). 76. Hanks and Krawinkler (1991). 77. Marshall *et al.* (1991). 78. Wells and Coppersmith (1994). 79. Zhao (1994). 80. Dreger *et al.* (1994). 81. Johnston and Linde (1994). 82. Sieh *et al.* (1993). 83. Lensen (1978). 84. Oral *et al.* (1995). 85. Wald and Heaton (1994b). 86. Johnston and Kanter (1990). 87. Cowan (1990). 88. Eiby (1973). 89. Thio and Kanamori (1994b). 90. Kanamori and Allen (1986). 91. Jones and Wesnousky (1992). 92. Beanland and Clark (1995). 93. Wesnousky and Leffler (1992). 94. Cowan (1991). 95. Bouchon (1982). 96. Hanks and Wyss (1972). 97. Freymueller (1994). 98. Johnson *et al.* (1994). 99. Wald and Heaton (1994a). 100. Cohee and Beroza (1994). 101. Dreger (1994). 102. Song *et al.* (1994). 103. J. Caskey, personal comm. 104. T. Nakata, personal comm. 105. Berryman (1979). 106. Gurrolo and Rockwell (1996). 107. Barka and Gulen (1988). 108. Yu and Segall (1995).

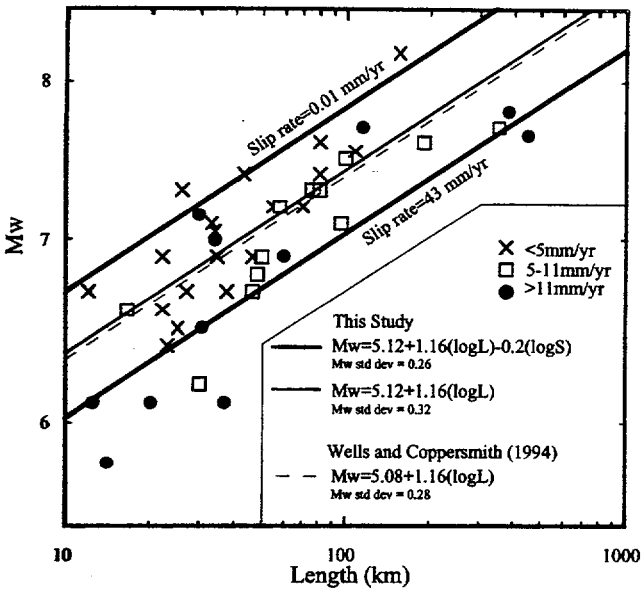

Figure 1. Relationship between magnitude, rupture length, and slip rate. Data are shown as points (mean values of length and M_w), with different symbols depending on the range of fault slip rate. The heavy lines are from equation (2), which includes slip rate, and are shown for slip rates of 0.01 mm/yr and 43 mm/yr, as labeled on the graph. The light solid line is the prediction from equation (3) in which slip rate is not included as a parameter. The dashed line shows regression results of Wells and Coppersmith (1994) for magnitude as a function of surface rupture length.

Predicted magnitudes using equation (2) are shown in Figure 1. For comparison, we also determined the regression relationship between only magnitude and fault rupture length to equal

$$M_w = (5.12 \pm 0.12) + (1.16 \pm 0.07)\log L \qquad (3)$$

Equation (3) is shown by the thin line on Figure 1.

The sample standard deviation is defined by

$$\sigma = \left\{\frac{1}{N}\sum(M_i - \hat{M}_i)^2\right\}^{1/2},$$

where M_i is the observation and $\hat{M}_i$ is the predicted magnitude, and the sum is over all observations. For equation (2), we found $\sigma = 0.26$ magnitude units. For the predictions of equation (3), $\sigma = 0.32$ magnitude units. Although the F-test (e.g., Mason *et al.*, 1989) indicates that this error reduction is significant at only 75% confidence, equation (2) is better than equation (3) with 95% confidence when an $L1$ norm (e.g., Menke, 1989) is used to measure the misfit. More importantly, the coefficient, C, on slip rate, in distribution on Figure 2, is never closer to zero than -0.05, indicating much less than 1 chance in 10,000 of finding a set of parameters, within the specified ranges, for which the coefficient on slip rate is zero. That is to say, the distribution on coefficient C shows that a regression that does not include slip rate as a parameter will systematically overestimate the expected magnitude of earthquakes on the fastest slipping faults and, conversely, will systematically underestimate the expected magnitude of earthquakes on the slowest slipping faults. It is on these bases that we assert that inclusion of slip rate leads to meaningful improvement in the fit to the data.

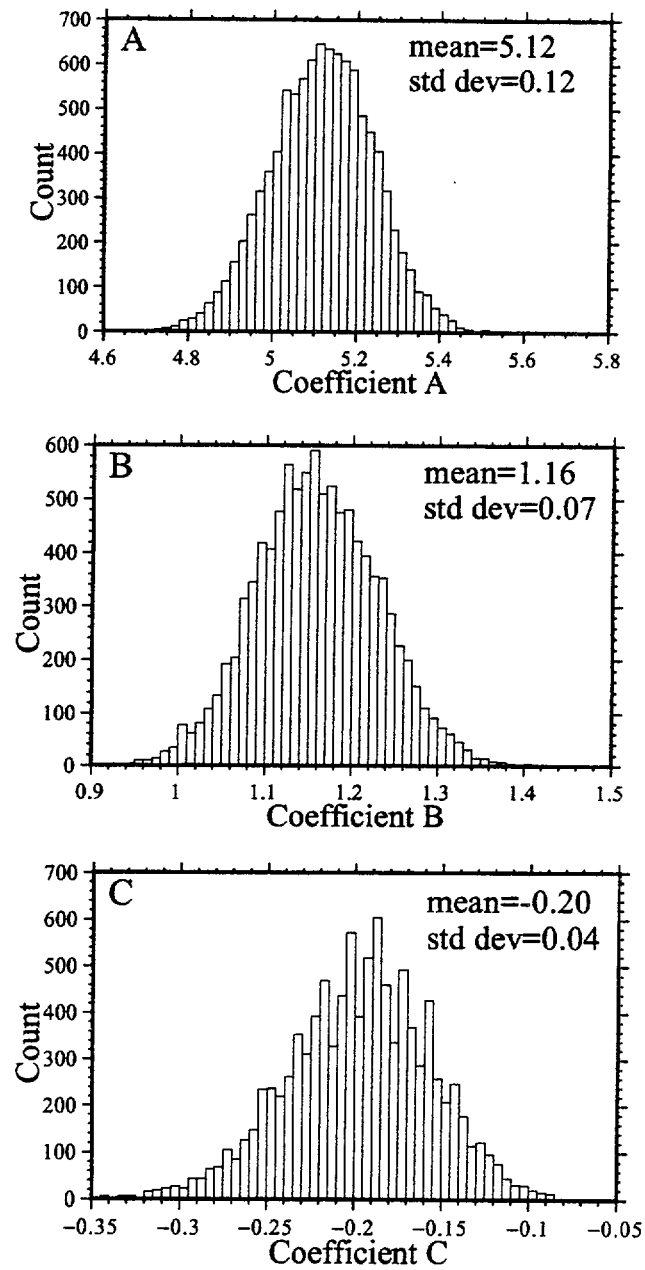

Figure 2. Distribution of coefficients A, B, and C (equation 1) in 10,000 runs in which the slip rate and rupture length on each fault and M_w are chosen at random from a uniform distribution within a range of allowed values, as discussed in the text. Specifically, log S and log L are given uniform distributions between their minimum and maximum values.

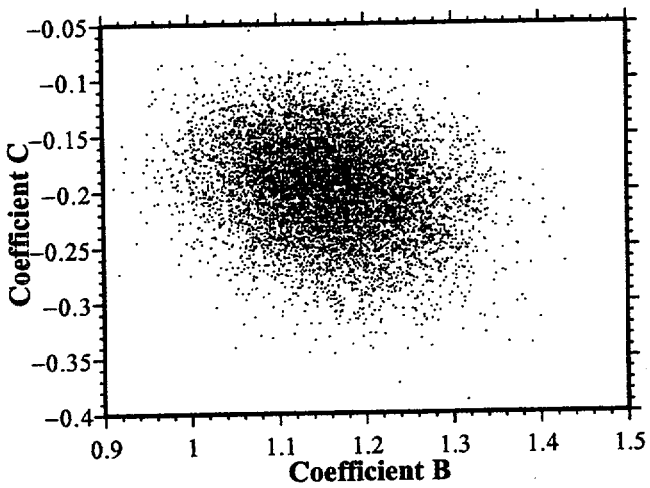

Figure 3. Scatter plot of coefficients B and C for 10,000 individual runs in the Monte Carlo calculations.

Discussion

Because we have considered only faults for which slip rate estimates exist, our data set is much smaller than used in the recent summary and regression analyses of Wells and Coppersmith (1994). Nonetheless, Figure 1 shows that equation (3) is virtually identical to the Wells and Coppersmith regression. It thus appears that our data are not obviously biased in any significant manner relative to the data used by Wells and Coppersmith.

For any given fault length, the curve for the slowest slip rate in Table 1 (S = 0.01 mm/yr) yields estimates of magnitude about 0.7 magnitude units greater than the curve for the fastest slip rate in Table 1 (S = 43 mm/yr curve), a difference twice the standard deviation of the curve fit. The regression of M_w on L that ignores slip rate (equation 3) would agree with the regression in equation (2) for S = 1 mm/yr. The comparison of curves illustrates that simple regressions of M_w on L that ignore fault slip rate appear to underestimate the magnitude of earthquakes on the relatively slow slipping faults. That is to say, information useful to making accurate estimates of future earthquake size is being ignored when fault slip rate is not considered in estimating potential earthquake size on active faults.

It is also useful to briefly consider our results in the context of the definition of seismic moment. The seismic moment is defined as $M_0 = \mu LWD$, in which L is fault length, W is fault width, D is average slip, and μ is the shear modulus, which is about 3×10^{11} dyne/cm^2. The relationship between seismic moment and magnitude is $M_w = (2/3)(\log M_0 - 16)$, where M_0 is in units of dyne-cm (Hanks and Kanamori, 1979). Combining the two relationships yields

$$M_w = \frac{2}{3}\log L + \frac{2}{3}\log D + \frac{2}{3}(\log \mu + \log W - 16).$$

We may consider W approximately constant because our data set is limited to earthquakes with moderate to high dip and in regions where the seismogenic depth is limited to the upper 15 to 20 km. Thus, M_w will be primarily dependent on L and D. If $D \propto W$ (the W model), B should equal 2/3. If $D \propto L$ (the L model), as suggested by Scholz (1982) and approximately confirmed by the data set of Wells and Coppersmith (1994), then M_w = 4/3 Log L + const. The value we obtain for B (equation 2) is between these two values. If only faults with $L > 30$ km are included in the regression to assure that L is greater than the fault width, the coefficient B is 1.18, which is about the same as the result with the full data set. Thus, B is much closer to the prediction of the L model than it is to the prediction of the W model, but it is significantly different from either one.

The reduction of magnitude with a higher slip rate is consistent with a physical model in which, as the time from the last earthquake increases, geological processes strengthen the fault (Kanamori and Allen, 1986; Scholz *et al.*, 1986). Stated another way, a fault with a slow slip rate tends to have earthquakes with a greater static stress drop and greater average slip than a fault with a faster slip rate. The compilation of Wells and Coppersmith (1994) suggested that dip-slip faults tend to have a larger average slip per event (magnitude held constant) than strike-slip faults. To test this, the data were divided into faults with strike-slip mechanisms and faults with dip-slip mechanisms. The regression on strike-slip data gave similar coefficients to those in equation (2). The dip-slip data cover only a small range of slip rates, and consequently, the coefficient on slip rate is smaller. Nonetheless, the regression on dip-slip faults alone predicts similar magnitudes as equation (2) for the slip rates spanned by the data. Hence, fault mechanism does not appear to be as important a factor as the slip rate on the fault on which the earthquake occurs when trying to estimate the earthquake size or stress drop as a function of fault length.

In the context of the physical model, it is interesting to consider some of the events that are conspicuously below the prediction curves in Figure 1. Four events with $L < 50$ km fall between 0.2 and 0.5 magnitude units below the curve for 43 mm/yr. All are from central or northern California: 1934 Parkfield; 1966 Parkfield; 1984 Morgan Hill; 1979 Coyote Lake. An interesting feature of all of these events is that they occurred adjacent to creeping sections of the San Andreas system. Considering that fault strength is probably significantly below average on the creeping sections, it is plausible that strength for all of these segments is somewhat lower than average, contributing to the anomalies.

It is plausible that amplitudes of dynamic strong ground motions correlate with static stress drop. If so, our observations predict that strong ground motion amplitudes are inversely related to fault slip rate. Recently, Boore *et al.* (1995) observed that reverse faults have larger ground motions than strike-slip faults. The result is probably consistent with our result because most of the reverse faults in their data set are characterized by low slip rate. In other words, it is reasonable

that fault slip rate has more influence on dynamic strong ground motion than does fault mechanism and that estimation techniques for the dynamic ground motions from earthquakes might be improved by incorporating slip rate.

Conclusions

We conclude that a regression for moment magnitude (M_w) as a function of surface rupture length (L) and fault slip rate (S) reduces the uncertainty in estimating the potential size of future earthquakes on mapped faults as compared to the standard regressions of M_w on L that are commonly used in seismic hazard analysis. The results of the regression indicate that faults with slower slip rates tend to fail in earthquakes with higher static stress drop.

Acknowledgments

Takashi Nakata and John Caskey supplied unpublished slip-rate data for the Philippines and Dixie Valley faults, respectively. Michael P. Sleeman and Takashi Kumamoto helped with some initial data gathering and analysis. We thank Donald Wells and an anonymous reviewer for their helpful comments. This research was supported by the U.S. Geological Survey (Grants 1434-94-G-2460 and 1434-94-G-2479) and the Southern California Earthquake Center. Center for Neotectonic Studies Contribution No. 14.

References

Abe, K. (1975). Reexamination of the fault model for the Niigata earthquake of 1964. *J. Phys. Earth* **23,** 394–366.

Abe, K. (1978). Dislocations, source dimensions and stresses associated with earthquakes in the Izu Peninsula, Japan, *J. Phys. Earth* **26,** 253–274.

Ad Hoc Working Group on the Probabilities of Future Large Earthquakes in Southern California (1992). *Future Seismic Hazards in Southern California; Phase I: Implications of the 1992 Landers Earthquake Sequence,* National Earthquake Prediction Evaluation council, California Earthquake Prediction Evaluation council, and Southern California Earthquake Center technical report, 42 pp.

Ambraseys, N. (1970). Some characteristic features of the Anatolian fault zone, *Tectonophysics* **9,** 143–165.

Bakun, W. H., M. M. Clark, R. S. Cockerham, W. L. Ellsworth, A. G. Lindh, W. H. Prescott, A. F. Shakal, and P. Spudich (1984). The 1984 Morgan Hill, California, earthquake, *Science* **225,** 288–291.

Bakun, W. H. and T. V. McEvilly (1984). Recurrence models and Parkfield earthquakes, *J. Geophys. Res.* **89,** 3051–3058.

Barka, A. A. and L. Gulen (1988). New constraints on age and total offset of North Anatolian fault zone: implications for tectonics of the eastern Mediterranean region, in *Special Publication of the Middle East Technological University 1987. Meloh Tokay Geology Symposium,* Ankara, Turkey.

Beanland, S. and M. M. Clark (1995). The Owens Valley fault zone, eastern California, and surface faulting associated with the 1872 earthquake, *U.S. Geol. Soc. Bull.* **1982,** 29 pp.

Bell, J. W. and T. Katzer (1990). Timing of late Quaternary faulting in the 1954 Dixie Valley earthquake area, central Nevada, *Geology* **18,** 622–625.

Bent, A. L., D. V. Helmberger, R. J. Stead, and P. Ho-Liu (1989). Waveform modeling of the November 1987 Superstition Hills earthquakes, *Bull. Seism. Soc. Am.* **79,** 500–514.

Berryman, K. R. (1979). Active faulting and derived PHS directions in the South Island, New Zealand, *Roy. Soc. New Zealand Bull.* **18,** 29–34.

Bird, P. and X. Kong (1994). Computer simulations of California tectonics confirm very low strength of major faults, *Geol. Soc. Am. Bull.* **106,** no. 2, 159–174.

Bonilla, M. G. (1973). Trench exposures across surface fault ruptures associated with San Fernando earthquake, in San Fernando, California, earthquake of February 9, 1971, 3, pp. 173–182, United States Department of Commerce, Washington, D.C.

Boore, D. M., W. B. Joyner, and T. E. Fumal (1995). Ground motion estimates for strike- and reverse-slip faults (preprint).

Bouchon, M. (1982). The rupture mechanism of the Coyote Lake earthquake of August 6, 1979 inferred from near field data, *Bull. Seism. Soc. Am.* **72,** 745–757.

Brown, R. D., Jr. and J. G. Vedder (1967). The Parkfield-Cholame, California, earthquakes of June–August 1966: surface tectonic fractures along the San Andreas Fault, *U.S. Geol. Surv. Profess. Paper 579.*

Brune, J. N. and C. R. Allen (1967). A low stress-drop, low-magnitude earthquake with surface faulting: the Imperial, California, earthquake of March 4, 1966, *Bull. Seism. Soc. Am.* **57,** 501–514.

Canitez, N. and M. N. Toksoz (1972). Static and dynamic study of earthquake source mechanism: San Fernando Earthquake, *J. Geophys. Res.* **77,** 2583–2594.

Caskey, S. J., S. G. Wesnousky, P. Zhang, and D. B. Slemmons (1995). Surface faulting of the 1954 Fairview Peak (Ms = 7.2) and Dixie Valley (Ms = 6.9) earthquakes, Central Nevada, *Bull. Seism. Soc. Am.* **85,** 000–000.

Clahan, K. B., N. T. Hall, and R. H. Wright (1994). Preliminary late Holocene slip rate for the San Francisco Peninsula segment of the San Andreas fault (abstracts with programs), *Geol. Surv. Am.* **26,** no. 2.

Clark, M. M. (1972). Surface rupture along the Coyote Creek fault, the Borrego Mountain Earthquake of April 9, 1968, *U.S. Geol. Surv. Profess. Paper 787,* 55–57.

Cohee, B. P. and G. C. Beroza (1994). Slip distribution of the 1992 Landers earthquake and its implications for earthquake source mechanics, *Bull. Seism. Soc. Am.* **84,** 692–712.

Cowan, H. A. (1990). Late Quaternary displacements on the Hope fault at Glynn Wye, North Canterbury, *New Zealand J. Geol. Geophys.* **33,** 285–294.

Cowan, H. A. (1991). The North Canterbury earthquake of September 1, 1888, *J. Roy. Soc. New Zealand* **21,** 1–12.

Cowan, H. A. and M. S. McGlone (1991). Late Holocene displacements and characteristic earthquakes on the Hope River segment of the Hope fault, New Zealand, *J. Roy. Soc. New Zealand* **21,** 373–384.

Crone, A. J., M. N. Machette, M. G. Bonilla, J. J. Lienkaemper, K. L. Pierce, W. E. Scott and R. C. Bucknam (1987). Surface faulting accompanying the Borah Peak earthquake and segmentation of the Lost River fault, central Idaho, *Bull. Seism. Soc. Am.* **77,** 739–770.

Doser, D. I. (1985a). The 1983 Borah Peak, Idaho and 1959 Hebgen Lake, Montana earthquakes: models for normal fault earthquakes in the Intermountain Seismic Belt, in *Proceedings of Workshop XXVIII, on the Borah Peak, Idaho earthquake, U.S. Geol. Surv. Open-File Rept.* **85–290.**

Doser, D. I. (1985b). Source parameters and faulting processes of the 1959 Hebgen Lake, Montana earthquake sequence, *J. Geophys. Res.* **90,** 4537–4555.

Doser, D. I. and R. B. Smith (1985). Source parameters of the 28 October 1983 Borah Peak, Idaho, earthquake from body wave analysis, *Bull. Seism. Soc. Am.* **90,** 1041–1051.

Dreger, D. S. (1994). Investigation of the rupture process of the 28 June 1994 Landers Earthquake Utilizing TERRAscope, *Bull. Seism. Soc. Am.* **84,** 713–714.

Dreger, D., M. Pasyanos, S. Loper, R. McKenzie, N. Gregor and B. Romanowicz (1994). The January 17, 1994 Northridge earthquake: a regional perspective, *Program for Northridge Abstracts, 89th Seismological Society of America Meeting.*

Eiby, G. A. (1973). A descriptive catalog of New Zealand earthquakes, *New Zealand J. Geol. Geophys.* **16,** 857–907.

Freymueller, J. (1994). The co-seismic slip distribution of the Landers earthquake, *Bull. Seism. Soc. Am.* **84,** 646–659.

Galehouse, J. S. (1991). Creep rates on the Bay Area faults during the past decade, *Seism. Res. Lett.* **62,** 12.

Gurrola, L. D. and T. K. Rockwell (1996). Timing and slip for prehistoric

earthquakes on the Superstition Mountain fault, Imperial Valley, southern California, *J. Geophys. Res.* (in press).

Hamilton, R. M. (1972). Aftershocks of the Borrego Mountain earthquake from April 12 to June 12, 1968, The Borrego Mountain Earthquake of April 9, 1968, *U.S. Geol. Surv. Profess. Paper 787.*

Hanks, T. and H. Kanamori (1979). A moment magnitude scale, *J. Geophys. Res.* **84,** 2348–2350.

Hanks, T. C. and H. Krawinkler (1991). The 1989 Loma Prieta earthquake and its effects: introduction to the special issue, *Bull. Seism. Soc. Am.* **81,** 1415–1423.

Hanks, T. C. and M. Wyss (1972). The use of body-wave spectra in the determination of seismic-source parameters, *Bull. Seism. Soc. Am.* **62,** 561–589.

Harden, J. W. and J. C. Matti (1989). Holocene and late Pleistocene slip rates on the San Andreas Fault in Yucaipa, California, using displaced alluvial-fan deposits and soil chronology, *Geol. Soc. Am. Bull.* **101,** 1107–1117.

Hirabayashi, K. C. and T. K. Rockwell (1996). A neotectonic study of the San Miguel-Vallecitos fault, Baja California, Mexico, *Bull. Seism. Soc. Am.* **86,** 000–000.

Hudnut, K. W., M. H. Murray, A. Donnellan, Y. Bock, P. Fang, M. Cline, Y. Feng, Z. Shen, B. Hager, T. Herring, and R. King (1994). Coseismic displacements of the 1994 Northridge, California, earthquake, *The 89th Annual Meeting of the Seismological Society of America.*

Hudnut, K. W. and K. E. Sieh (1989). Behavior of the Superstition Hills Fault during the past 330 years, *Bull. Seism. Soc. Am.* **79,** 304–329.

Hudnut, K. W., M. H. Murray, A. Donnellan, Y. Bock, P. Fang, M. Cline, Y. Feng, Z. Shen, B. Hager, T. Herring, and R. King (1994). Coseismic displacements of the 1994 Northridge, California, earthquake, Program for Northridge abstracts, *89th Seismological Society of America Meeting.*

Jennings, C. W. (1975). Fault map of California, California geologic data map series, Department of Conservation, San Francisco, California.

Johnson, H. O., D. C. Agnew, and K. Hudnut (1994). Bounds on earthquake movement from geodetic data: application to the Landers earthquake, *Bull. Seism. Soc. Am.* **84,** 660–667.

Johnston, A. C. and L. R. Kanter (1990). Earthquakes in stable continental crust, *Scientific Am.* **262,** 68–75.

Johnston, M. J. S. and A. T. Linde (1994). Continuous borehole strain before, during and after the Jan 17, 1994, M6.7 Northridge, California, earthquake, Program for Northridge abstracts. *89th Seismological Society of America Meeting.*

Jones, C. H. and S. G. Wesnousky (1992). Variations in strength and slip rate along the San Andreas Fault System, *Science* **256,** 83–86.

Kanamori, H. (1973). Mode of strain release associated with major earthquakes, in Japan, *Annu. Rev. Earth Planet Sci.* **1,** 213–239.

Kanamori, H. (1983). Mechanism of the 1983 Coalinga earthquake determined from long-period surface waves, *Calif. Div. Mines Geol. Spec. Publ.* **66,** 233–240.

Kanamori, H. and C. R. Allen (1986). Earthquake repeat time and average stress drop, *Earthquake Source Mechanics* S. Das, J. Boatwright, and C. H. Scholz (Editors), *Geophysical Monograph* **37,** 227–235.

Kanamori, H. and J. Regan (1982). Long-period surface waves, *U.S. Geol. Surv. Profess. Pap. 1254,* 55–58.

Knuepfer, P. L. (1992). Temporal variations in latest Quaternary slip across the Australian-Pacific plate boundary, northeastern South Island, New Zealand, *Tectonics* **11,** no. 3, 449–464.

Lensen, G. J. (1960). A 12 mile lateral drag along the Awatere fault, Abstract for the 9th Science Congress, Royal Society of New Zealand, 47.

Lensen, G. J. (1978). Historic tectonic earth deformation, in *The Geology of New Zealand,* R. P. Suggate, G. R. Stevens, and M. T. TePunga (Editors), Government Printer. Wellington, 33–37.

Lienkaemper, J. J., G. Borchardt, and M. Lisowski (1991). Historic creep rate and potential for seismic slip along the Hayward fault, California, *J. Geophys. Res.* **96,** 18261–18283.

Marshall, G. A., R. S. Stein, and W. Thatcher (1991). Faulting Geometry and slip from co-seismic elevation changes: the 18 October 1989, Loma Prieta, California, earthquake, *Bull. Seism. Soc. Am.* **81,** 1660–1693.

Mason, R. L., R. F. Gunst, and J. L. Hess (1989). *Statistical Design and Analysis of Experiments,* John Wiley & Sons, New York, 692 pp.

Matsuda, T. (1974). Surface faults associated with Novi (mino-Owari) earthquake of 1891, Japan, *Bull. Seism. Soc. Am.* **13,** 85–126.

Matsuda, T. (1975). Magnitude and recurrence interval of earthquakes from a fault, *J. Seism. Soc. Japan, Series 2,* **28,** 269–283.

Matsuda, T., H. Yamazaki, T. Nakata, and T. Imaizumi (1980). The surface faults associated with the Rikuu earthquake of 1896, *Bull. Earthquake Res. Inst. Univ. Tokyo* **55,** 795–855.

Menke, W. (1989). *Geophysical Data Analysis: Discrete Inverse Theory,* Academic Press, San Diego, 289 pp.

Mikumo, T. and M. Ando (1976). A search into the faulting mechanism of the 1891 great Nobi earthquake, *J. Phys. Earth* **24,** 63–87.

Nairn, I. A. and S. Beanland (1989). Geological setting of the 1987 Edgecumbe earthquake, New Zealand, *New Zealand J. Geol. Geophys.* **32,** 1–13.

Niemi, T. M. and N. T. Hall (1992). Late Holocene slip rate and recurrence of great earthquakes on the San Andreas fault in northern California, *Geology* **20,** no. 3, 195–198.

Nuttli, O. W. (1983). Average seismic source parameter relations for mid-plate earthquakes, *Bull. Seism. Soc. Am.* **73,** 519–535.

Okada, A. and Y. Ikeda (1991). Active faults and neotectonics in Japan, *Quaternary Res.* **30,** 161–174.

Oral, M. B., M. Reilinger, T. Nafi, R. W. King, A. A. Barka, K. Ibrahim, and O. Lenk (1995). Global positioning system offers evidence of plate motions in eastern Mediterranean, *EOS* **76,** no. 2, 9–11.

Page, B. M. (1935). Basin-Range faulting in Pleasant Valley, Nevada, *J. Geol.* **43,** 690–707.

Petersen, M. D., L. Seeber, L. R. Sykes, J. F. Nabelek, J. Armbruster, J. Pacheco, and K. W. Hudnut (1991). Seismicity and fault interaction, southern San Jacinto fault, southern California: implications for seismic hazard, *Tectonics* **10,** 1187–1203.

Petersen, M. D. and S. G. Wesnousky (1994). Fault slip rates and earthquake histories for active faults in southern California, *Bull. Seism. Soc. Am.* **84,** no. 5, 1608–1649.

Prentice, C. S. (1989). Earthquake geology of the northern San Andreas fault near Point Arena, California, *Ph.D. Thesis.* California Institute of Technology, Pasadena, California.

Reasenberg, P. and W. L. Ellsworth (1982). Aftershocks of the Coyote Lake, California, earthquake of August 6, 1979, *J. Geophys. Res.* **87,** 10637–10655.

Research Group for Active Faults of Japan (1992). Map of Active Faults in Japan with an Explanatory Text, University of Tokyo Press.

Romanowicz, B. (1992). Strike-slip earthquakes on quasi-vertical transcurrent faults: inferences for general scaling relations, *Geophys. Res. Lett.* **19,** 481–484.

Savage, J. C., W. H. Prescott, M. Lisowski and N. King (1979). Geodetic measurements of deformation near Hollister, California, 1971–1978, *J. Geophys. Res.* **84,** 7599–7615.

Scholz, C. H. (1982). Scaling laws for large earthquakes: consequences for physical models, *Bull. Seism. Soc. Am.* **72,** 1–14.

Scholz, C. H., C. A. Aviles, and S. G. Wesnousky (1986). Scaling differences between large intraplate and interplate earthquakes, *Bull. Seism. Soc. Am.* **76,** 65–70.

Sharp, R. V. (1981). Displacements on tectonic ruptures in the San Fernando earthquake of February 9, 1971: discussion and some implications. *U.S. Geol. Surv. Open-File Rept. 81-668.*

Sharp, R. V., K. E. Budding, J. Boatright, M. J. Ader, M. G. Bonilla, M. M. Clark, T. E. Fumal, K. K. Harms, J. J. Lienkaemper, D. M. Morton, B. J. O"Niel, C. L. Ostergren, D. J. Ponti, M. J. Rymer, J. L. Saxton, and J. D. Sims (1989). Surface faulting along the Superstition Hills fault zone and nearby faults associated with the earthquakes of 24 November 1987, *Bull. Seism. Soc. Am.* **79,** 252–281.

Sharp, R. V., J. J. Lienkaemper, M. G. Bonilla, D. B. Burke, B. F. Cox, D. G. Herd, D. M. Miller, D. M. Morton, D. J. Ponti, M. J. Rymer, J. C. Tinsley, J. C. Yount, J. F. Kahle, E. W. Hart, and K. E. Sieh (1982).

Surface faulting in central Imperial Valley, California, earthquake of October 15, 1979, in the Imperial Valley, California, earthquake of October 15, 1979, *U.S. Geol. Surv. Profess. Pap.* **1254,** 119–143.

Sieh, K., L. Jones, E. Hauksson, K. Hudnut, D. Eberhart-Phillips, T. Heaton, S. Hough, K. Hutton, H. Kanamori, A. Lilje, S. Lindvall, S. F. McGill, J. Mori, C. Rubin, J. A. Spotila, J. Stock, H. Thio, J. Treiman, B. Wernicke, and J. Zachariasen (1993). Near-field investigations of the Landers earthquake sequence, April to July 1992, *Science* **260,** 171–176.

Sieh, K. E. (1978). Slip along the San Andreas fault associated with the great 1857 earthquake, *Bull. Seism. Soc. Am.* **68,** 1421–1448.

Sieh, K. E. and R. H. Jahns (1984). Holocene activity of the San Andreas Fault at Wallace Creek, California, *Geol. Soc. Am. Bull.* **95,** 883–896.

Sieh, K., L. Jones, E. Hauksson, and K. Hudnut (1993). Near-field investigations of the Landers earthquake sequence, April to July, 1992, *Science* **260,** 171–176.

Sims, J. D. (1991). Distribution and rate of slip across the San Andreas transform boundary, Hollister area, central California, *Geol. Soc. Am.* (abstracts with programs), **23,** no. 2, 98.

Song, X., L. E. Jones, and D. Helmberger (1994). Source characteristics of the January 17, 1994 Northridge California earthquake from regional broadband modeling, Program for Northridge abstracts. *89th Seismological Society of America Meeting.*

Stein, R. S. and W. Thatcher (1981). Seismic and aseismic deformation associated with the 1952 Kern County, California, earthquake and relationship to Quaternary history of the White Wolf fault, *J. Geophys. Res.* **86,** 4913–4928.

Straub, C. and H. Kahle (1994). Global Positioning System (GPS) estimates of crustal deformation in the Marmara Sea region, northwestern Anatolia, *Earth Planet. Sci. Lett.* **121,** 495–502.

Sykes, L. R. and R. C. Quittmeyer (1981). Repeat times of great earthquakes along simple plate boundaries, in *Earthquake Prediction: An International Review, Maurice Ewing Series 4,* D. W. Simpson and P. G. Richards (Editors), American Geophysical Union, Washington, D.C., 217–247.

Tanimoto, T. and H. Kanamori (1986). Linear programming approach to moment tensor inversion of earthquake sources and some tests on the three-dimensional structure of the upper mantle, *Geophys. J. R. Astr. Soc.* **84,** 413–430.

Teng, R., Z. Huang, H. Qian, T. Deng, L. Jiang, P. Ge, S. Liu, Y. Cao, and C. Zhang (1983). On the recent tectonic activity and earthquakes of the Xianshuihe fault zone in *A Collection of Papers of International Symposium on Continental Seismicity and Earthquake Prediction,* Seismological Press, Beijing.

Thatcher, W. (1975). Strain accumulation and release mechanism of the 1906 San Francisco earthquake, *J. Geophys. Res.* **80,** 4862–4872.

Thatcher, W., T. Matsuda, and J. B. Rundle (1980). Lithospheric loading by the 1896 Rikuu earthquake in northern Japan: implications for plate flexure and asthenospheric rheology, *J. Geophys. Res.* **85,** 6429–6435.

Thio, H. K. and H. Kanamori (1994a). Source complexity of the 1994 Northridge earthquake, Program for Northridge Abstracts, *89th Seismological Society of America Meeting.*

Thio, H. K. and H. Kanamori (1994b). Moment tensor solutions for the Northridge earthquake sequence, Program for Northridge Abstracts, *89th Seismological Society of America Meeting.*

Thomas, A. P. and T. K. Rockwell (1996). Slip on the Imperial fault in the past 300 years at the U.S.-Mexico international border based on trenching, *Bull. Seism. Soc. Am.* **86,** (in press).

Trifunac, M. D. (1972). Tectonic stress and the source mechanism of the Imperial Valley, California, earthquake of 1940, *Bull. Seism. Soc. Am.* **62,** 1283–1302.

Trumm, D. A., J. C. Tinsley, and R. S. Stein (1986). Holocene fold deformation and earthquake recurrence at Coalinga anticline, California: fluvial stratigraphic analysis, *EOS* **67,** 1222.

Tsai, Y. B. and K. Aki (1969). Simultaneous determination of the seismic moment and attenuation of seismic surface waves, *Bull. Seism. Soc. Am.* **59,** 275–287.

Urhammer, R. A., Darragh, R. D. and B. Bolt (1983). The 1983 Coalinga earthquake sequence: May 2 through Aug. 1, *Spec. Rept. Calif. Div. Mines Geol.* **66,** 221–232.

Van Dissen, R. J. and R. S. Yeats (1991). Hope fault, Jorden thrust, and uplift of the Seaward Kaikoura Range, New Zealand, *Geology* **19,** 393–396.

Wald, D. J. and T. H. Heaton (1994a). A multidisciplinary source analysis of the 1994 (Mw6.7) Northridge earthquake using strong motion, teleseismic, and geodetic data, Program for Northridge Abstracts, *89th Seismological Society of America Meeting.*

Wald, D. J. and T. H. Heaton (1994b). Spatial and temporal distribution of slip for the 1992 Landers, California, earthquake, *Bull. Seism. Soc. New Zealand* **84,** 668–692.

Wallace, R. E. and R. A. Whitney (1984). Late Quaternary history of the Stillwater seismic gap, Nevada, *Bull. Seism. Soc. Am.* **74,** 301–314.

Weber, G. E. and R. S. Anderson (1990). Marine terrace deformation pattern: its implications for repeat times of Loma Prieta earthquakes and for the long term evolution of the Santa Cruz mountains, *U.S. Geol. Surv. Open-File Rept. 90–274.*

Wells, D. G. and K. J. Coppersmith (1994). New empirical relationships among magnitude, rupture length, rupture width, rupture area, and surface displacement, *Bull. Seism. Soc. Am.* **84,** 974–1002.

Wesnousky, S. G. (1986). Earthquakes, Quaternary faults, and seismic hazard in California, *J. Geophys. Res.* **91,** 12587–12631.

Wesnousky, S. G. and L. M. Leffler (1992). The repeat time of the 1811 and 1812 New Madrid earthquakes: a geological perspective, *Bull. Seism. Soc. Am.* **82,** 1756–1785.

Wilson, J. T. (1936). Foreshocks and aftershocks of the Nevada earthquake of December 20, 1932, and the Parkfield earthquake of June 7, 1934, *Bull. Seism. Soc. Am.* **26,** 189–194.

Witkind, I. J. (1964). Reactivated faults north of Hebgen Lake, *U.S. Geol. Surv. Profess. Pap.* **435,** 37–50.

Yeats, R. S. and G. J. Huftile (1995). The Oak Ridge fault system and the 1994 Northridge earthquake, *Nature* **373,** 418–420.

Yoshida, Y. and K. Abe (1992). Source Mechanism of the Luzon, Philippines Earthquake of July 16, 1990, *Geophys. Res. Lett.* **19,** 545–548.

Yu, E. and P. Segall (1995). Slip in the 1868 Hayward earthquake from the analysis of historical triangulation data, *EOS* **76,** no. 46, 406.

Zhao, L. (1994). Regional waveform modeling of the main shock of 17 January 1994 Northridge, California earthquakes, Program for Northridge Abstracts. *89th Seismological Society of America Meeting.*

Zhou, H., Liu, H. L. and H. Kanamori (1983a). Source processes of large earthquakes along the Xianshuihe fault in Southwestern China, *Bull. Seism. Soc. Am.* **73,** 537–551.

Zhou, H. L., C. R. Allen and H. Kanamori (1983b). Rupture complexity of the 1970 Tonghai and the 1973 Luhuo earthquakes, China, from P-wave inversion and relationship to surface faulting, *Bull. Seism. Soc. Am.* **73,** 1585–1597.

Seismological Laboratory and Department of Geological Sciences
Mackay School of Mines
University of Nevada
Reno, Nevada 89557
E-mail: jga@seismo.unr.edu
(J.G.A.)

Center for Neotectonic Studies and Department of Geological Sciences
Mackay School of Mines
Reno, Nevada 89557
(S.G.W., M.W.S.)

Manuscript received 29 June 1995.

Expected Shape of Regressions for Ground Motion Parameters on Rock

John Anderson

Seismological Laboratory and

Department of Geological Sciences

University of Nevada

Reno, Nevada 89557

Office: (702) 784-4265

FAX: (702) 784-1833

email: jga@seismo.unr.edu

Introduction

This note discusses the expected shape of regressions for ground motion parameters on rock as a function of magnitude and distance. Most current regressions use an assumed magnitude and distance dependence that is dominantly ad hoc. Figure 1 illustrates two extremes. The regression by Boore et al (1993) assumes the distance dependence is independent of magnitude, while the regression by Idriss (1991) assumes the distance dependence varies with magnitude. The problem arises because of the scarcity of records from large earthquakes at short distances that are needed to difinitively resolve the problem. This paper compares predictions using synthetic seismograms to the models in Figure 1. It uses both empirical and theoretical Green's functions.

This examination of the physical processes that are present at ideal rock sites gives an unambiguous answer to the question of whether the distance dependence of attenuation curves should be affected by the magnitude.

Method 1. A simple approach using synthetic Green's functions

Figure 2 illustrates the geometry used in a simple approach which illustrates the processes that are involved. For each of 4 sites, I generated synthetic Green's functions from a linear array of eleven sources. Figure 3 shows the transverse component of the synthetic contributions from the eleven points along the fault (Fig 2) for each of the four stations. Each contribution is convolved with a synthetic source time function, derived from the composite source model of Zeng et al (1994), appropriate for a square source with 5 km on a side, and thus has about a two second duration. Figure 3 also shows the effect of adding these contributions with proper time delays to allow for rupture propagation at 2.5 km/sec.

At the short distances (5 and 25 km), the synthetic Green's functions in Figure 3 have a short duration, consisting essentially of a single spike. However, at larger distances, the complexity of the crustal model becomes more important, causing the synthetics to have multiple impulses spread out over increasingly long durations. At 5 km and 25 km distances, because the Green's functions are brief, the separate sources on the fault cause motions at separated times, and there is little constructive interference. Consequently, the sum of the subevents has a peak amplitude that is about the same as the largest of the subevents. However at 50 km and 100 km distances, because of the multiple arrivals, energy from adjacent parts of the fault arrives simultaneously at the station. The first phases from a part of the fault that ruptures later arrive at the same time as

the later phases from a part of the fault that ruptures earler, and there is the opportunity for constructive interference. The peak acceleration on the sum of the subevents is 14% larger than the largest subevent at 50 km, and 48% larger than the largest subevent at 100 km in this example. This constructive interference can be regarded as random, so that the increase in the amplitudes is related to the square root of the number of contributing Green's functions. Another way to describe the effect is that the multiple arrivals at large distances allow the distant station to "see" more of the fault rupturing at any one time. The net effect, shown in Figure 3, is that the peak amplitude of the sum of several subevent contributions decreases less rapidly with distance than the peak amplitude from any one of the subevents.

Method 2: Empirical Green's Functions

The tendencies observed in Figure 3 are repeated in a simple example of summation of empirical Green's functions. I selected empirical Green's functions from an earthquake in Mexico recorded on the Guerrero accelerograph network (Anderson et al, 1995). An earthquake on May 2, 1989 was recorded at 13 stations with epicentral distances from 17 to 220 km (Anderson et al, 1991). According to Humphrey and Anderson (1994), this event has seismic moment $M_o = 8.9 \times 10^{23}$ dyne-cm (M_W=5.3) and a source radius of 1.4 km. To generate a larger event, the accelerograms were assumed to represent empirical Green's functions for a line of eleven sources with the geometry in Figure 2. Seismograms were delayed according to the assumed rupture velocity and distance from the source to the station.

Figure 4 illustrates results using the seismograms from stations at 17, 33, 68, and 220 km distance. It shows some of the individual contributions, and the total sum which is taken to represent a synthetic seismogram for a larger earthquake with a nearest fault distance equal to the

distance of the station from the original event. Subevent amplitudes from source locations larger than the original event distance could be adjusted before summing, but this was not done. Figure 4 shows that the ratios of pga for the composite seismogram to the contributing empirical Green's functions tends to increase with distance, although the percentage increase is scattered because of characteristics of the input data. For the 16 km station, because of the relatively short duration of the strongest part of the shaking from the small event, the synthetic main event has an amplitude that is only 18% larger than the empirical Green's function. At the station 33 km from the May 2 event, the peak acceleration on the synthetic seismogram is 50% larger than on the empirical Green's function, and at the station at 68 km, it is 97% larger. The station at 220 km does not continue the trend, as the sum is only 62% larger than the contributing traces. Considering other records, though, it seems that the 68 km record is more of the anomaly, perhaps because its seismogram has a longer duration due to a site effect, or perhaps because by chance several phases happened to interfere constructively. Considering these and the results of the same experiment using other seismograms recorded from the May 2 event, it is evident that even though the trend is more scattered in the presence of real data, the tendency persists for the peak acceleration of synthetic seismograms generated from these empirical Green's functions to decrease less rapidly than the peak values from the small event.

The anomaly at 68 km (Ocotito) calls attention to the point that at any distance, there will be some stations with local site effects that tend to increase the duration of that seismogram. When that occurs, regardless of distance, the ratio of the peak amplitudes of synthetics of large earthquakes to the amplitude of the empirical Green's function will be enhanced, compared to behavior at ideal rock sites.

Example 3: Complete synthetic seismograms

The previous examples have been selected to illustrate the physical principles affecting the distance dependence of attenuation curves for large and small earthquakes. However, it is also appropriate to illustrate the results using full synthetic seismograms. For this, I used the composite source model approach (Zeng et al, 1994; Yu, 1994) to generate a profile of synthetics from four seismic sources. Figure 5 illustrates the extent of assumed faulting and the station locations for this example. The fault in this case is a thrust fault with a dip of about 60°. The assumed events have moment magnitudes of 5.0, 6.0, 7.0, and 7.5. Figure 6 shows representative profiles of synthetic accelerations, and Figure 7 shows the corresponding peak values.

In this synthetic model, the peak accelerations decrease more rapidly for the small earthquake than for the large earthquake. For instance, on the sets of traces on the lower half of these figures, the peak motions for the M=5 earthquake at site S025 are barely visible, on the scale of motions at site S010, while for the M=7.5 event they have about 50% the amplitude of the nearer site. Put another way, the attenuation of peak values for the synthetics between sites S010 and S025 for the M=5 earthquake is about the same as the attenuation between sites S010 and S100 for the M=7.5 earthquake.

Discussion

The results shown above give a clear indication of what should be expected from empirical regressions. The attenuation of ground motions on rock should have a shape that depends on the fault dimension. Earthquakes on large faults should have an attenuation function that decreases less rapidly with distance than earthquakes on small faults. Since there is a strong correlation

between fault dimension and magnitude (e.g. Wells and Coppersmith, 1993), this conclusion supports the shape characterized in Figure 1b, rather than in Figure 1a. The result is consistent with the attenuation in Mexico found by Anderson and Lei (1993) using a non-parametric curve fitting procedure.

The predicted shape is the result of an interaction of two effects. First, the Green's function becomes more complex, with multiple arrivals spread out over a longer time window, at larger distances. Second, the fault is larger with larger magnitude earthquakes. Consequently, more distant stations can receive signals from a larger area of fault rupture at any one time. This happens during large earthquakes, when the fault is large, explaining the less rapid attenuation in this circumstance.

This paper has concentrated on peak acceleration, but the synthetics in Figure 6 show similar behavior for peak velocity, peak displacement, and response spectral values. Obviously, the results will depend on the relationship between the size of the fault and the wavelength of the waves that are involved. When the wavelength is long compared to the fault dimension, the attenuation will resemble the attenuation of the Green's function. As the wavelength becomes shorter, the interactions illustrated in Figures 3 and 5 will become effective. Knowing the rupture duration, easily estimated from fault dimension, and characterizing the duration of the Green's function, it should be possible to develop a model which realistically describes the magnitude dependence of the shape of attenuation curves.

Acknowledgements

Yuehua Zeng critically reviewed the manuscript. This research was supported by the Southern California Earthquake Center and by the National Science Foundation through Grants CMS 9506675 and CMS 9528517.

References

Anderson, J. G., J. N. Brune, J. Prince, R. Quaas, S. K. Singh, D. Almora, P. Bodin, M. Onate, R. Vazquez and J. M. Velasco (1994). The Guerrero accelerograph network, Geofisica Internacional 33, No. 3, 341-371.

Anderson, J. G., R. Quaas, R. Vasquez, D. Almora, J. R. Humphrey, J. M. Velasco, R. Castro, and C. Perez(1991a). Guerrero, Mexico Accelerograph Array: Summary of data collected in 1989, Report GAA-11, Seismological Laboratory, Mackay School of Mines, University of Nevada, Reno, Nevada.

Anderson J. G. and Y. Lei (1994). Nonparametric description of peak acceleration as a function of magnitude, distance, and site in Guerrero, Mexico, Bulletin of the Seismological Society of America 84, 1003-1017.

Boore, D. M., W. B. Joyner and T. E. Fumal (1993). Estimation of response spectra and peak accelerations from western North American earthquakes: an interim report, Open File Report 93-509, U. S. Geological Survey, Menlo Park, CA 94025.

Humphrey, J. R. Jr. and J. G. Anderson (1994). Seismic source parameters from the Guerrero subduction zone, Bulletin of the Seismological Society of America 84, 1754-1769.

Idriss, I. M. (1991). Empirical procedures for estimating earthquake ground motions, Attachment 1 to final progress report ...

Wells, D. L. and K. J. Coppersmith (1994). New empirical relationships among magnitude, rupture length, rupture width, rupture area, and surface displacement, Bull. Seism. Soc. Am. 84, 974-1002.

Yu, G. (1994). Some aspects of earthquake seismology: slip partitioning along major convergent plate boundaries; composite source model for estimation of strong motion; and nonlinear soil response modeling, Ph. D. Thesis, University of Nevada, Reno, 144 pages.

Zeng, Y., J. G. Anderson and G. Yu (1994). A composite source model for computing realistic synthetic strong ground motions, Geophysical Research Letters 21, 725-728.

Tables

Table 1

Velocity model used for synthetic seismograms

Layer	Thickness (km)	P-wave velocity (km/sec)	Q_P	S-wave velocity (km/sec)	Q_S	Density (gm/cm^3)
1	2.0	2.90	200	1.60	100	2.28
2	2.3	4.90	200	2.85	100	2.68
3	4.7	5.82	400	3.38	200	2.86
4	36.0	6.55	400	3.81	200	3.03
5	1000.0	8.10	800	4.70	400	3.32

Table 2

Characteristics of seismograms used as empirical Green's functions (from Anderson et al, 1991)

Earthquake parameters:

Date: May 2, 1989

Origin Time: 09:30:16.72 GMT

Latitude: 16.637°N

Longitude: 99.513°W

Hypocentral Depth: 13.4 km

Magnitudes: m_b=5.4, M_S=4.9, M_{coda}=5.1

Station parameters

Station	Epicentral Distance (km)
San Marcos	16.9
Las Vigas	33.0
Ocotito	67.7
Teacalco	219.7

Figure Captions

Figure 1. Predicted values of peak accelerations on as a function of distance, from the regressions of a) Boore et al (1993) and b) Idriss (1991).

Figure 2. Geometry used to consider expected attenuation. The goal is to examine distance effects on a profile perpendicular to a 50 km long fault. Sources used to compute Green's functions are placed at 5 km intervals along the fault (circles). The receivers are at a distances of 5, 25, 50, and 100 km along the perpendicular bisector.

Figure 3. Synthetic seismograms from eleven point sources, located as in Figure 2, and the sum of these synthetics (shown at the top). Green's functions are all convolved with the same composite source time function with duration of about 2 seconds. To illustrate the concepts with maximum clarity, the SH component of the synthetic seismograms has been used for each point source. Numerical values give peak acceleration of the composite seismograms and the largest subevent.

Figure 4. Empirical Green's functions and resulting synthetic seismogram. The empirical seismograms are from a magnitude MW=5.3 earthquake recorded in Guerrero, Mexico. The sum of eleven of the seismograms, shifted as explained in the text, is shown at the top. (Only four of the eleven seismograms are shown in this figure.) Notice how at the two closer stations the main contributions to the composite seismogram come from only one or two of the contributing subevents, while for the two farther stations three or four are contributing at once.

Figure 5. Geometry for profiles of synthetic seismograms.

Figure 6. Profiles of synthetic seismograms for the magnitude 5 and 6 (6A) and 7 and 7.5 (6B) earthquakes described in Figure 5. In the upper half of this figure, the profiles are normalized by the peak value of each trace. In the lower half, the profiles are all on a common scale determined by the peak value of station S010. Note that for the magnitude 5 and 6 earthquake, the peak values at station S010 are near the largest anyplace in the model, but for the magnitude 7 and 7.5 earthquakes, stations nearer the fault outcrop would give much larger peak values.

Figure 7. Peak accelerations corresponding to Figure 6, as a function of fault distance.

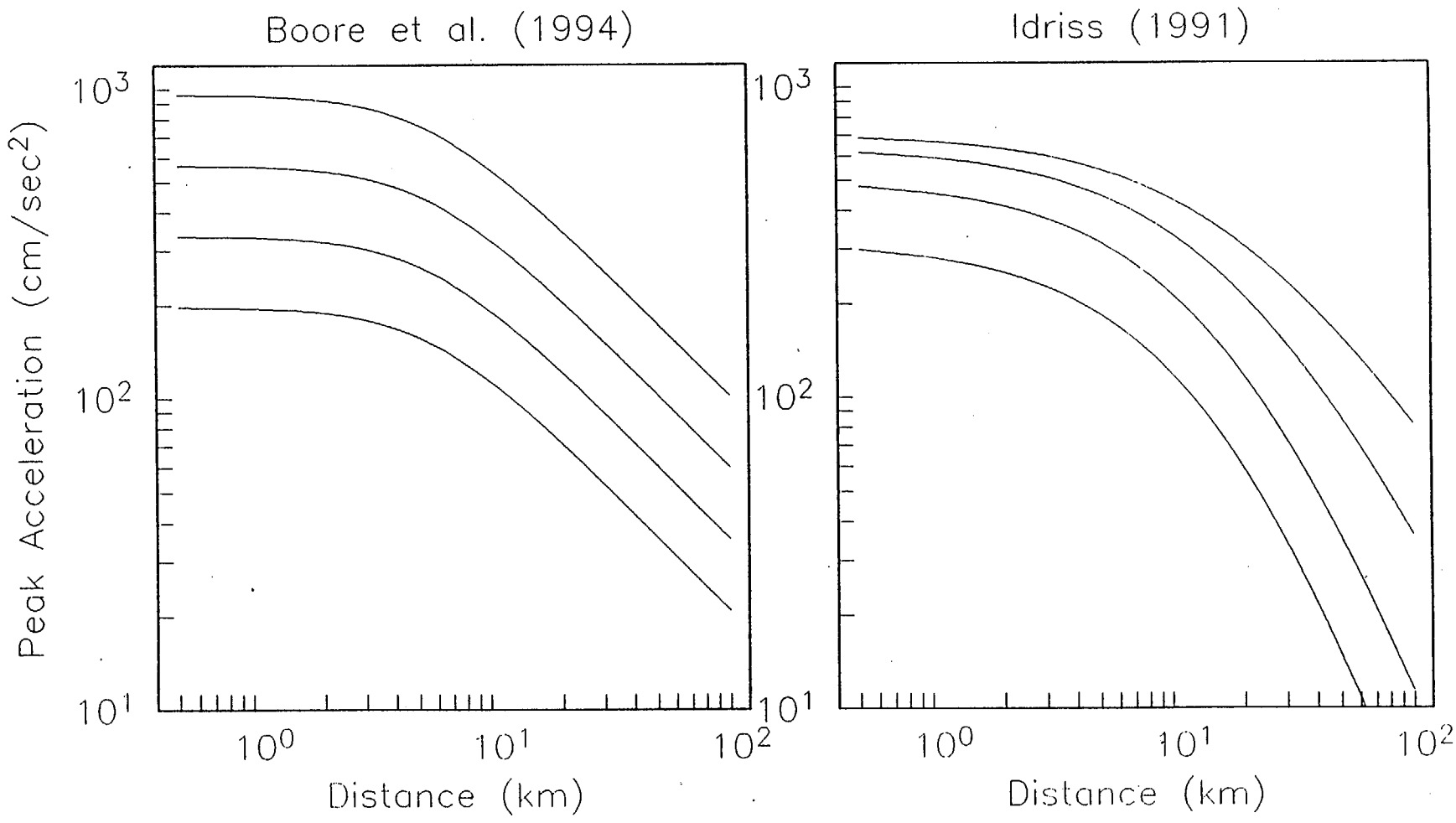
Boore et al. (1994)
Idriss (1991)
Peak Acceleration (cm/sec^2)
10^3
10^2
10^1
10^0
10^1
10^2
Distance (km)
Distance (km)

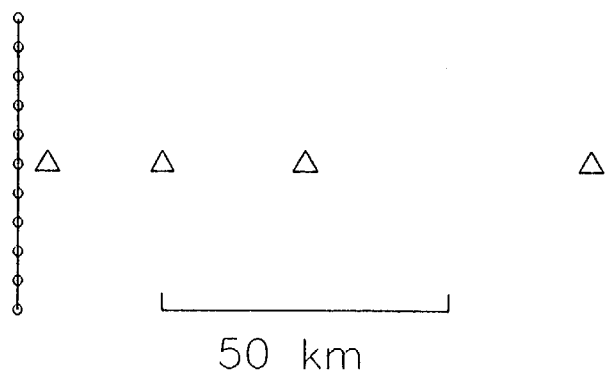
50 km

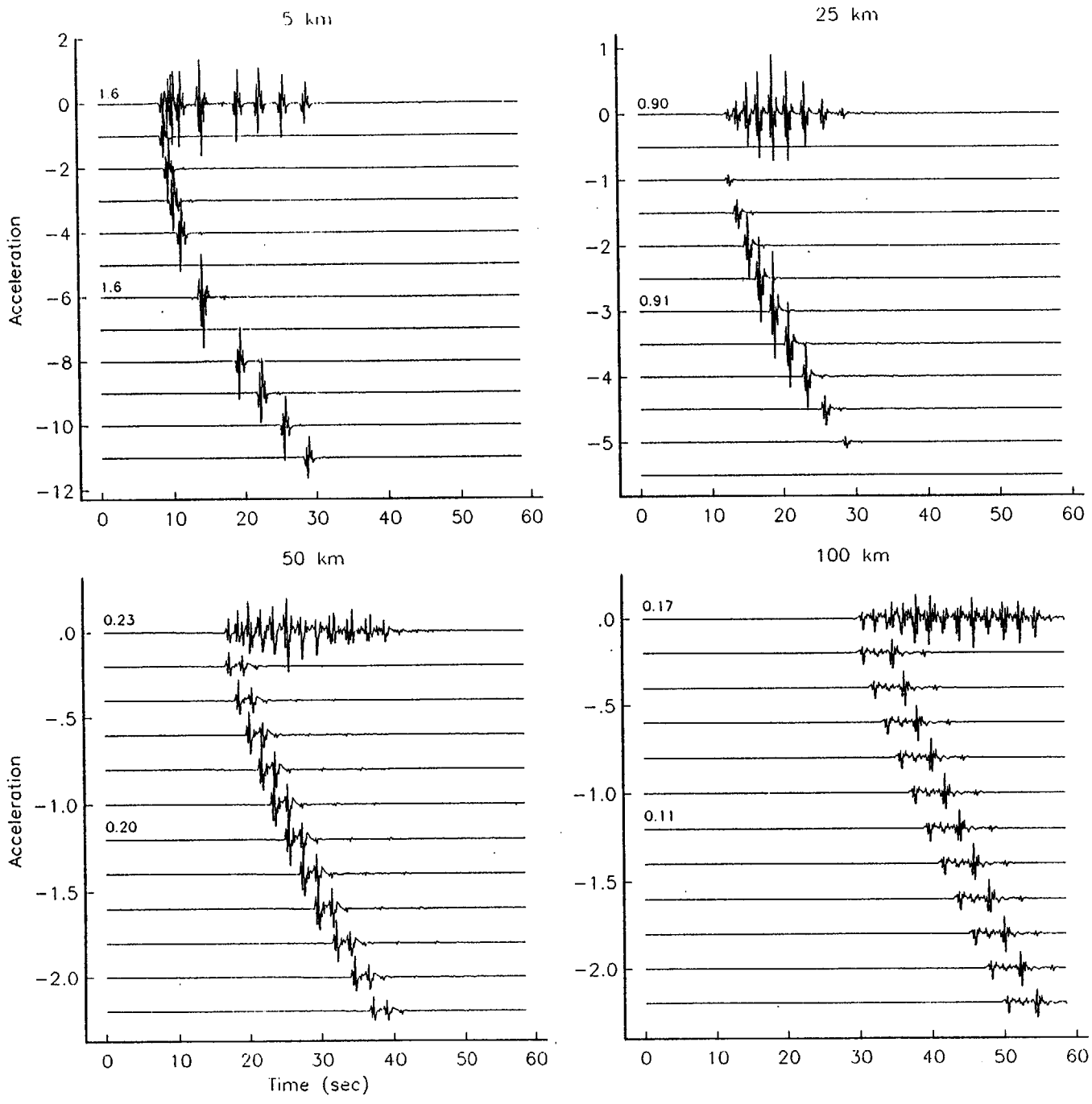
5 km
25 km
50 km
100 km
Acceleration
Time (sec)
1.6
1.6
0.90
0.91
0.23
0.20
0.17
0.11

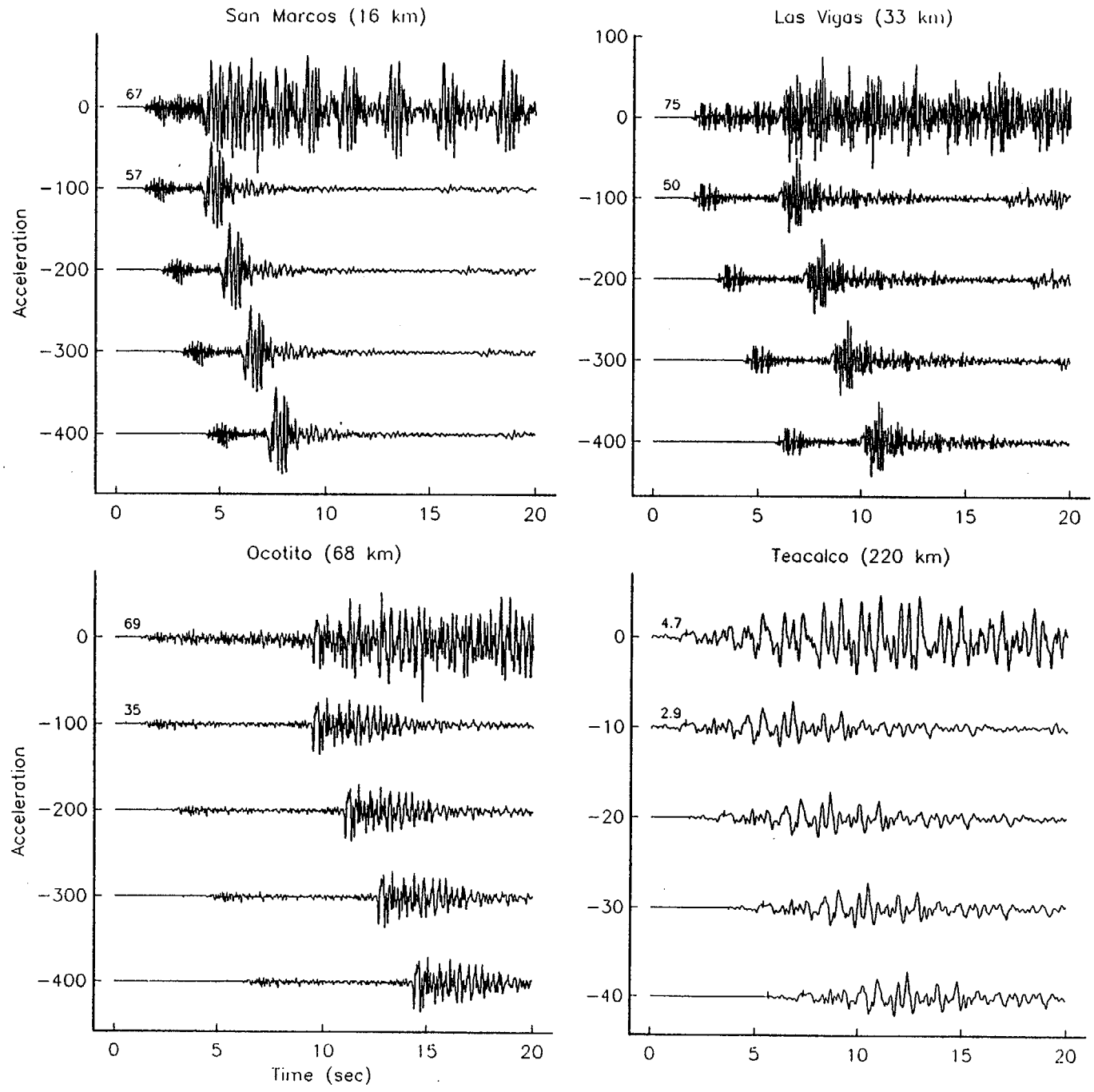
San Marcos (16 km)
Las Vigas (33 km)
Ocotito (68 km)
Teacalco (220 km)
Acceleration
Time (sec)
67
57
75
50
69
35
4.7
2.9
0
-100
-200
-300
-400
100
-10
-20
-30
-40
0
5
10
15
20

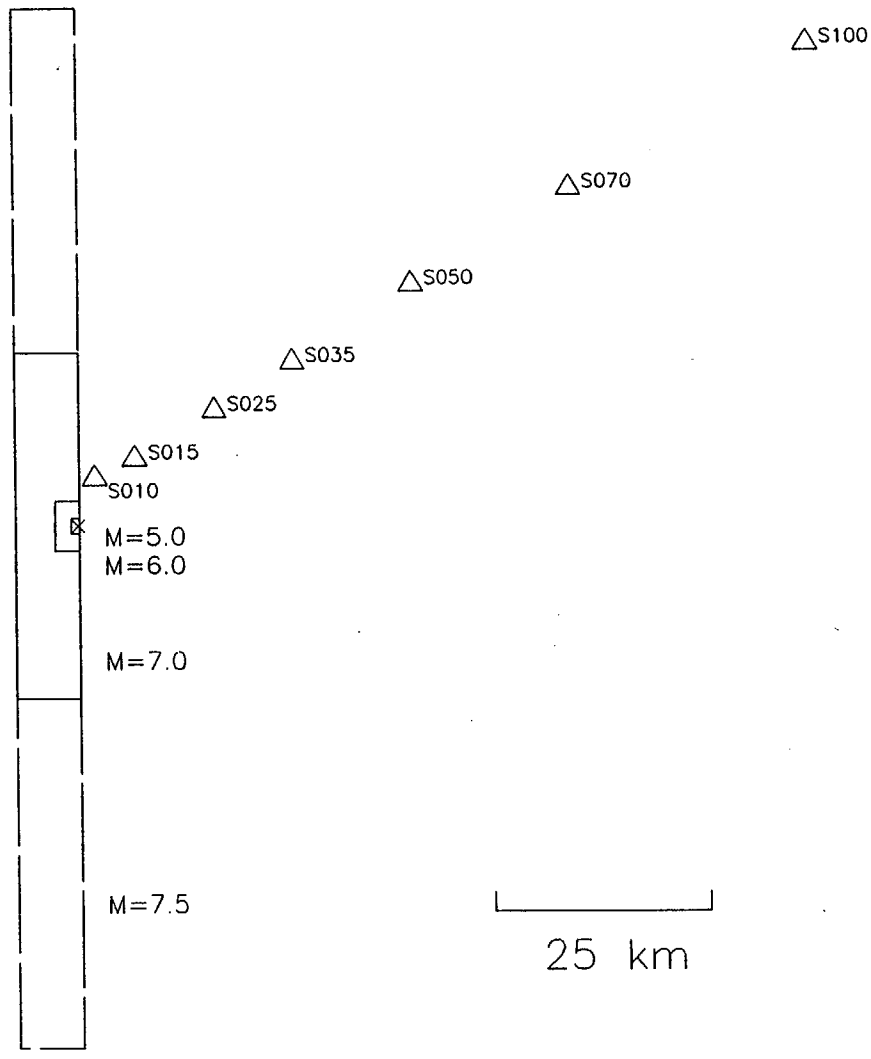
S100
S070
S050
S035
S025
S015
S010
M=5.0
M=6.0
M=7.0
M=7.5
25 km

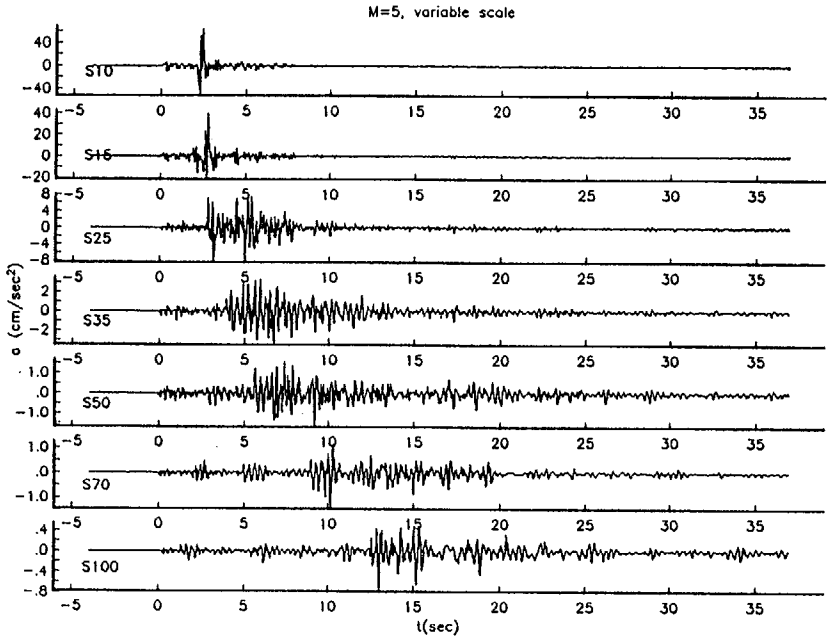
M=5, variable scale
S10
S15
S25
S35
S50
S70
S100
a (cm/sec²)
t(sec)

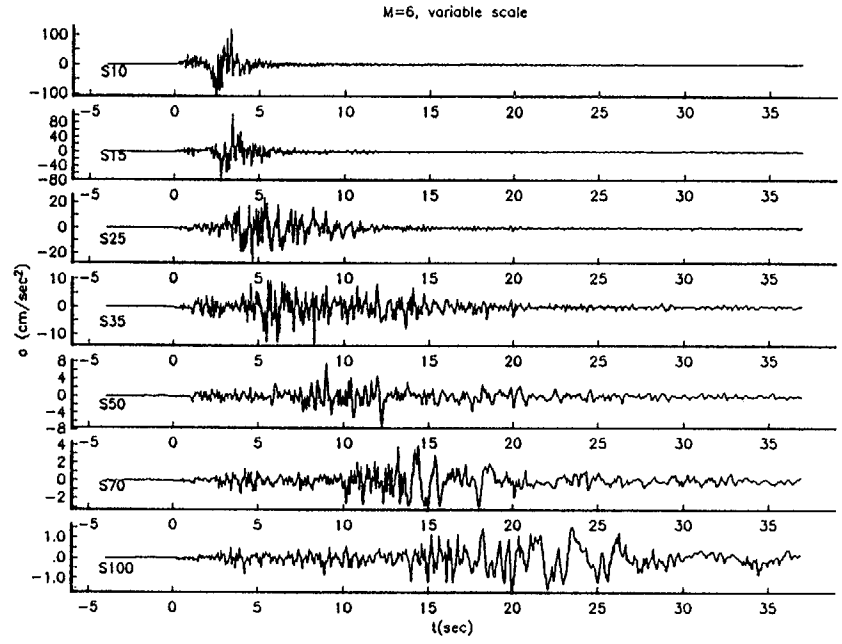
M=6, variable scale
S10
S15
S25
S35
S50
S70
S100
a (cm/sec²)
t(sec)

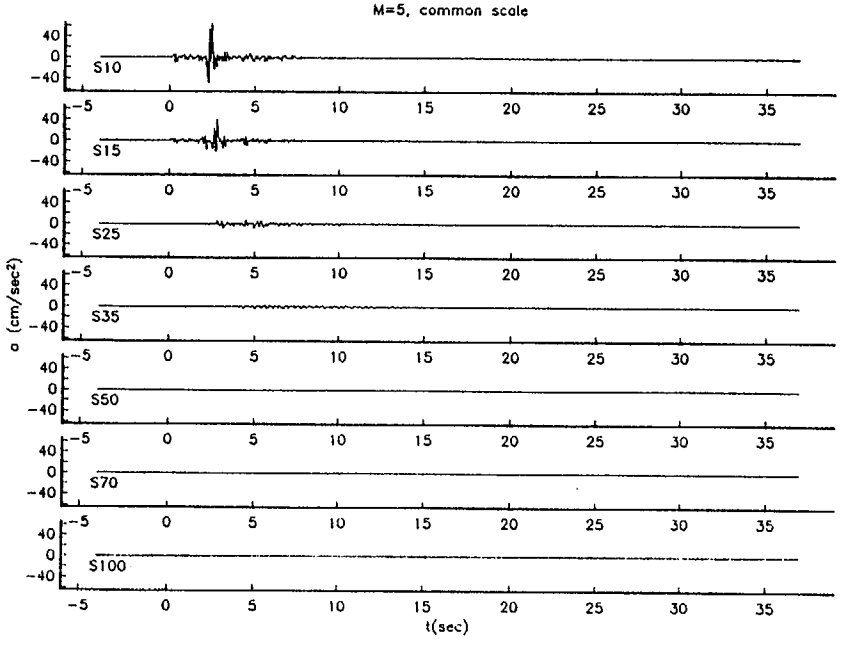
M=5, common scale
S10
S15
S25
S35
S50
S70
S100
a (cm/sec²)
t(sec)

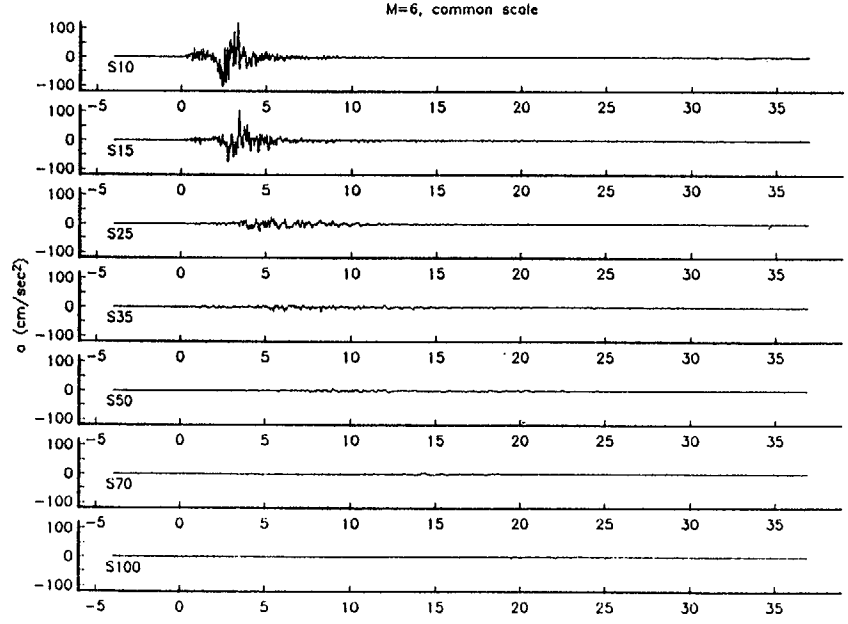
M=6, common scale
S10
S15
S25
S35
S50
S70
S100
a (cm/sec²)

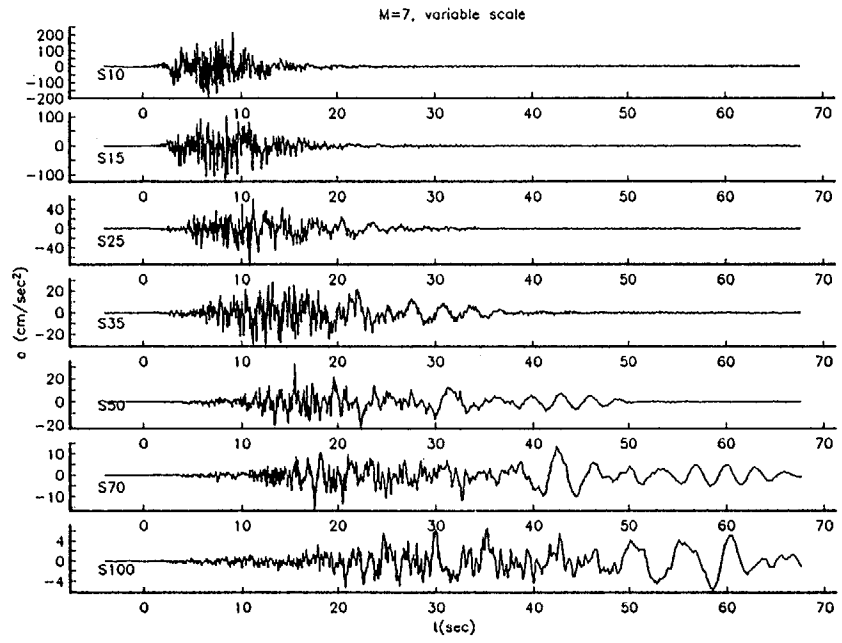
M=7, variable scale
S10
S15
S25
S35
S50
S70
S100
a (cm/sec²)
t(sec)

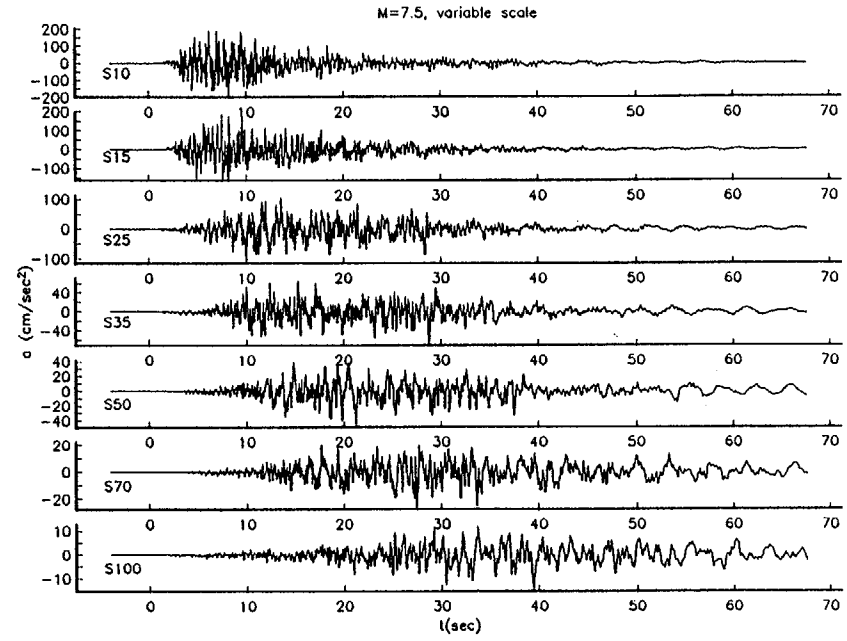
M=7.5, variable scale
S10
S15
S25
S35
S50
S70
S100
a (cm/sec²)
t(sec)

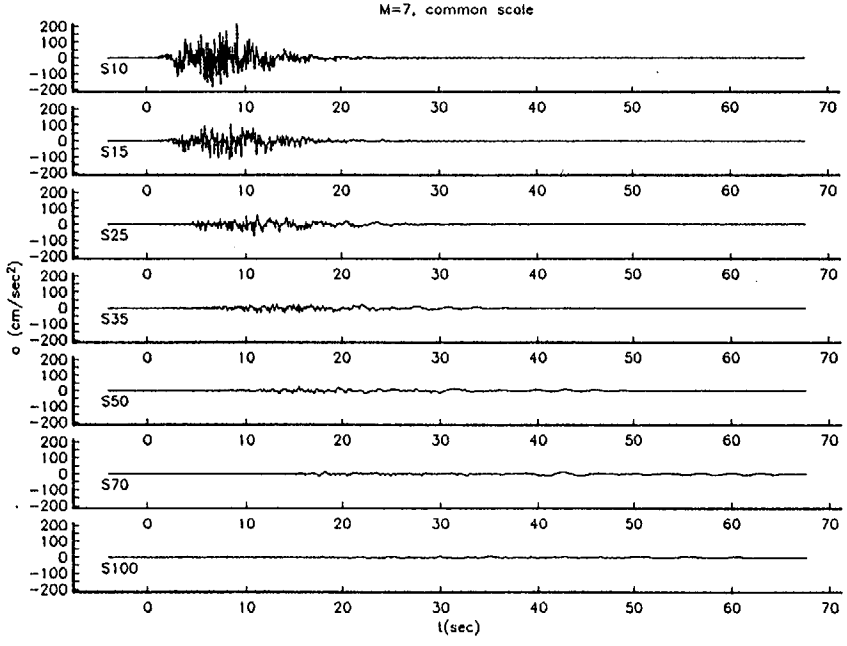
M=7, common scale
S10
S15
S25
S35
S50
S70
S100
a (cm/sec²)
t(sec)

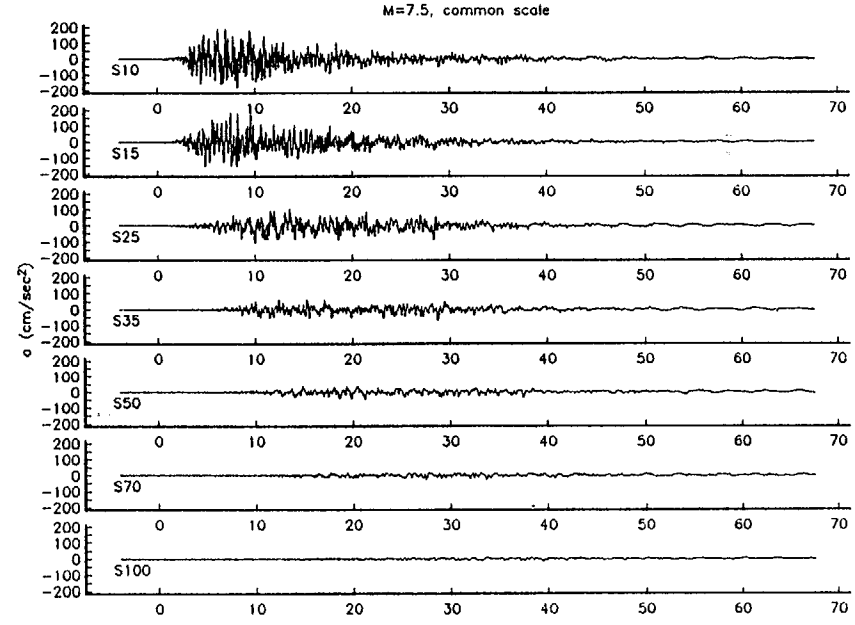
M=7.5, common scale
S10
S15
S25
S35
S50
S70
S100
a (cm/sec²)

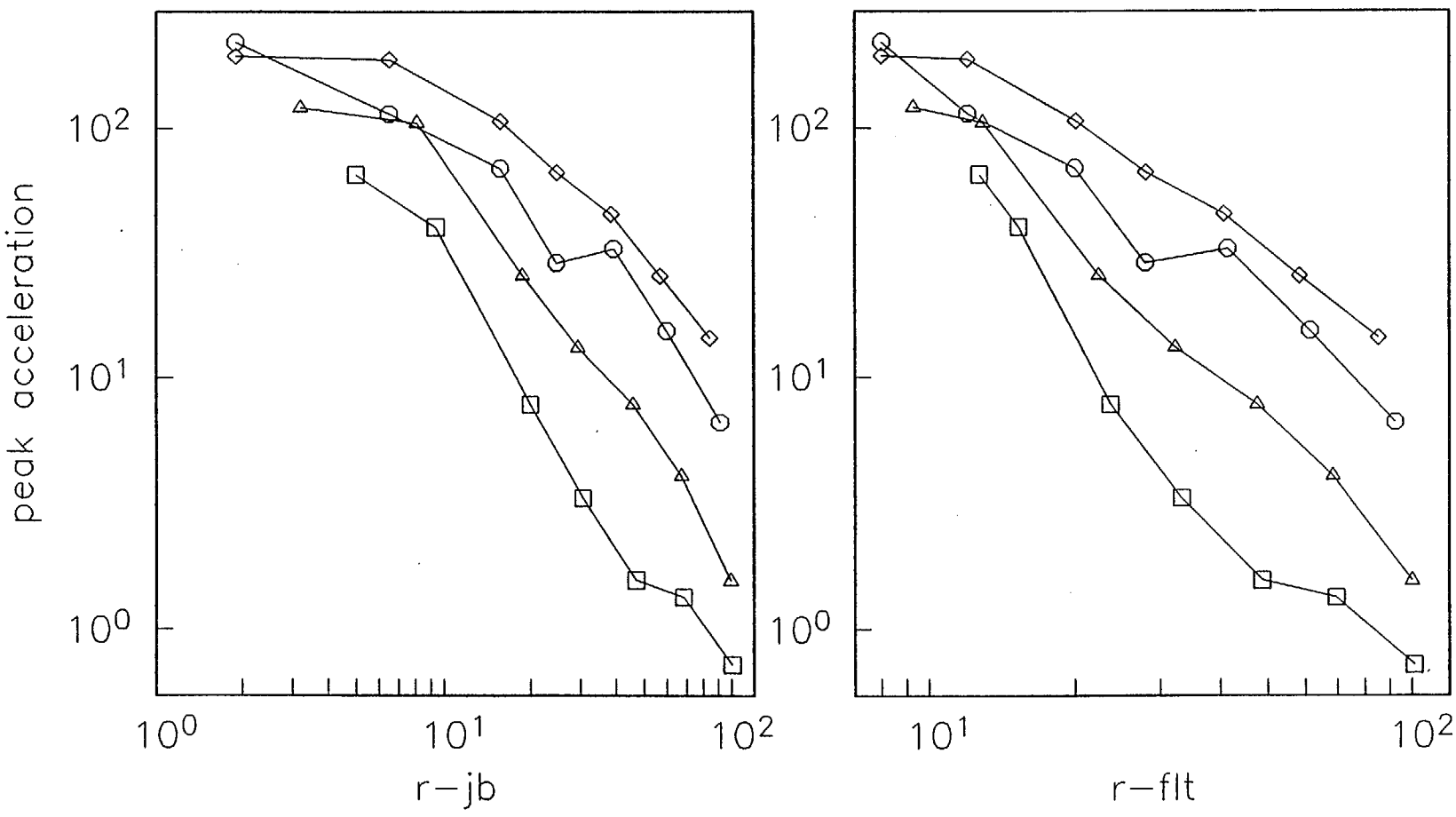
peak acceleration
10^2
10^1
10^0
10^0
10^1
10^2
r−jb
10^2
10^1
10^0
10^1
10^2
r−flt

Journal of Earthquake Engineering
© Imperial College Press

ENGINEERING EVALUATION OF THE 1 OCTOBER 1995 DİNAR EARTHQUAKE (M_L=5.9)

HALUK SUCUOĞLU AND ALPHAN NURTUĞ
Earthquake Engineering Research Center
Department of Civil Engineering, Middle East Technical University
Ankara 06531, Turkey

OKTAY ERGÜNAY AND SİNAN GENÇOĞLU
General Directorate of Disaster Affairs
Ankara 06530, Turkey

In 1995, a swarm of earthquakes affected the city of Dinar, Turkey, which is located in Southwest Anatolia and has a population of 35 000. The mainshock having a local magnitude of 5.9 occurred on 1 October 1995. It was preceded by foreshocks for four days, the largest one having a magnitude of 4.7. These foreshocks initiated structural damage in many buildings, which was then severely aggravated by the mainshock and a strong aftershock two hours later, with a magnitude of 5.0. Numerous aftershocks were recorded in the following three months. Strong ground motions were recorded within the city where the mainshock produced horizontal peak accelerations of 0.28*g* and 0.29*g*. The Dinar earthquake caused a death toll of 90, and more than 200 injuries. The economic losses due to structural damage alone are estimated at 250 million USD.

Keywords: Dinar earthquake, Anatolian block, Dinar-Çivril fault, foreshock, earthquake damage.

1. Introduction

Following a quiescent period of seventy years, a damaging earthquake of magnitude M_L=5.9 occurred in Dinar, Turkey on 1 October 1995 at 17.57 local time (3:57 PM, GMT). An intriguing aspect of this earthquake was the arrival of a series of foreshocks of varying magnitudes between M_L=3.5 and 4.7 within the preceding four days. More than 70 aftershocks with magnitudes between 3.5 and 5.0 were recorded in the following days. Aftershocks were still continuing after three months with decreasing magnitudes.

The earthquake caused 90 deaths and injured more than 200. Eventually, the essential life-lines were affected by the earthquake particularly at their connections to the collapsed buildings: the electricity was cut, the water supply and sewerage systems were seriously influenced. The communication system failed for a short period. The structural damage perspective of the earthquake was also drastic. Out of 24 000 households in the affected region, sheltering a population of 100 000, 4340 were heavily damaged, 3712 experienced moderate damage and 6140 experienced light damage. The Dinar earthquake caused the collapse of about 200 buildings. The replacement and repair costs of the collapsed and damaged buildings totals 250 million US Dollars. Indirect losses due to interruption of business and temporary resettlement expenses are not accounted for in this cost. Since the earthquake occurred in early winter which is severe in Dinar, reconstruction and rehabilitation works could not have been initiated until March 1996. This inevitable delay led to a sudden drop in the city population in the days following the earthquake. Citizens of Dinar who left the city started moving back in summer 1996 with resumption of the construction activity.

The ground motion events were recorded by a digital SMA-1 Kinemetrics accelerograph which is installed in the Dinar Meteorolgical Station. A brief engineering assessment of the nature and consequences of the Dinar earthquake is presented in this paper.

2. Seismotectonics of the Region

The region where Dinar is located has been troubled by earthquakes for centuries. In the Phrygian period (1200-600 BC), the region was called Celainai. In the 8th century BC, Celainai was destroyed by a major earthquake. It is stated in the ancient Anhoros myths that, during the earthquake, water sprang out from the ground. The Hellenistic town Apameia, which was settled in the same region, was devastated by a strong earthquake in 84 BC. During the Roman period (72 BC-395 AD), Apameia was resettled. However, a major earthquake occurred around 225-235 AD and the town was again destroyed. During this last event, some lakes were formed in the region. Apameia was given the name of Geyikler during the Ottoman period. In 1853 and 1875 two major earthquakes struck Geyikler again, the latter caused 1300 deaths. The last major earthquake that Dinar -the name the town bears in the Turkish Republic period- experienced was of magnitude 6.0 in 1925. The epicentral coordinates[1] of this earthquake indicate a location 60 km west of Dinar and the damage it caused was scattered in the rural areas. No one in Dinar today bears the memories of this earthquake.

Anatolia lies at the junction of three major converging plates: the Eurasian, African and Arabian plates as shown in Fig.1. The Arabian plate converges to the Eurasian plate which results in compression along the Bitlis-Zagros thrust and fold belt. This compression is compensated by the westward escape of the Anatolian block along the right-lateral North Anatolian fault and the left-lateral East Anatolian fault, also with the Eastward movement of the North-East Anatolian block. On the other hand, with the hindrance of this movement by the Hellenic arc on the West, the Anatolian block is redirected towards Southwest. Besides, the African plate subducts under the Anatolian block at the Northeast side of the Rhodes Island via the Hellenic arc. Under-these complex effects, Dinar and its surrounding region experience extensional faulting in the Northeast-Southwest and compressional faulting in the Northwest-Southeast directions. Accordingly, this region covering the Aegean graben system and Hellenic arc produces very high seismic activity with respect to the surrounding

regions. Detailed information on the seismotectonics and seismicity of West Anatolia and the Aegean system can be found in References 1-4.

The earthquakes which occurred in this century in the Aegean region exhibited a spatial migration Northward, from the Hellenic arc to the Aegean graben system. A remarkable increase in seismic activity had been observed in two time cycles[2], first from 1900 to 1920 and the second from 1920 to 1960. Seismic activity has decreased from 1960 to the present day. The epicenters of the earthquakes that occurred in the period 1900-1994 are plotted in Fig.2. There are four major identified active faults in the vicinity of Dinar. On the East there are Tatarlı and Kumdanlı faults. The Burdur and the Acıgöl faults are to the South and Southwest of Dinar, respectively. All of these faults have left lateral slip. However, the causative fault of the October 1 Dinar earthquake was the previously unrecognized 50 km long Dinar-Çivril fault. This is a normal fault with a slight right lateral strike slip. During the last 70 years, there were no moderate to major earthquakes which affected the Dinar region. Hence, this resulted in significant accumulation of strain energy in the active fault system over the ensuing years. A spot panchromatic satellite view of Dinar and vicinity pictured after the last earthquake is shown in Fig.3. Local faults have been traced on the picture after an extensive field survey in the region, by matching the pictorial information with the field observations. The fault scarp is indicated with the light line on the figure. Dinar is in the lower middle part of the picture, to the South of the ruptured faults end. A close-up picture of the fault scarp is shown in Fig.4.

The first fault rupture occurred on September 26 which resulted in minor earthquakes (M_L <4.7). The mainshock took place at 17:57 local time on October 1 (M_L=5.9, M_w=6.1), which was followed by a strong aftershock (M_L=5.0) two hours later. The mainshock was produced by the 25 seconds rupture of the Dinar-Çivril fault at a focal depth of 24 km. Epicenters of the recorded earthquakes after the first rupture are depicted in Fig.5. The epicentral coordinates of the mainshock are 38.13 N-30.08 E. The distribution of the magnitudes of earthquakes during 21 days are presented in Fig.6.

The surface rupturing and fault plane solutions have indicated normal faulting with a slight right-lateral component. The vertical displacements along the fault scarp ranged from 20 cm to 50 cm whereas the horizontal displacements were between 5 and 10 cm.

The Dinar earthquake has been assigned a local magnitude M_L=5.9, a moment magnitude M_w=6.1 and a seismic moment of 1.68×10^{25} dyne.cm by the Earthquake Research Department of the General Directorate of Disaster Affairs. The faulting surface area is estimated as 15 x16 km^2 and the first nodal plane has a Strike=144°, Dip=48° and Slip=-125°.

3. Ground Motion Intensity and Strong Motion Characteristics

The isoseismal contours constructed to reveal the intensity distribution of the Dinar earthquake exhibit circular shapes where the inner circle for an MKS[6] intensity of VIII has an approximate diameter of 20 km, and the next circle with intensity VII has a diameter of 30 km. Dinar town is divided into two by the intensity VIII contour along the slope border indicated in Fig.7. The Western part of the town located on alluvial deposits is in the intensity zone VIII whereas the eastern part settled along the hillside remains in the intensity zone VII. According to MKS intensity scale, VIII corresponds to 5% heavy and 75% medium damage in reinforced concrete structures.

The strong ground motions of the Dinar earthquakes were recorded by an analog Kinemetrics SMA-1 accelerograph installed in the Dinar Meteorological Station (Fig.7). The station is located in the Southwest end of the city which is underlain by alluvial deposits. Hence, there is considerable damage in the vicinity. The location of concentrated building damage within the city is given in Fig.7.

During a time span of ten days, the number of earthquakes which occurred in Dinar with magnitudes $M_L \geq 4.5$ is seven, as indicated in Fig.6. Three of them are foreshocks,

one is the mainshock and three are aftershocks. The strong ground motions induced by these earthquakes are all recorded by the Dinar SMA-1 station. Their basic properties are listed in Table 1, and the time variations of the respective horizontal ground acceleration components are presented in Fig.8.

Table 1. Strong Motion Data for Dinar Shocks with $M_L \geq 4.5$

Date	Time (GMT)	Depth (km)	Distance (km)	M_L	Peak Acceleration (g)			Peak Velocity (cm/s)		
					NS	EW	V	NS	EW	V
26.09.1995	14:58	20	6	4.7	0.106	0.174	0.056	4.9	8.6	2.5
27.09.1995	14:16	30	8	4.7	0.077	0.163	0.040	5.6	13.1	2.5
01.10.1995	15:57	24	13	5.9	0.294	0.275	0.111	17.7	21.1	5.7
01..10.1995	18:03	20	18	5.0	0.208	0.118	0.038	16.4	10.6	2.1
05.10.1995	16:15	20	2	4.6	0.089	0.151	0.057			
06.10.1995	16:16	24	24	4.5	0.093	0.152	0.042	2.9	8.9	1.7

The Dinar earthquake mainshock is also recorded by three distant strong motion accelerograph stations. These station locations, their epicentral distances and larger horizontal peak accelerations are as follows: Çardak, 54 km, 0.070*g*; Burdur, 70 km, 0.0519*g*; and Denizli, 87 km, 0.013*g*. Burdur and Denizli are indicated on Fig.5, whereas Çardak is on the midway between Dinar and Denizli.

Dinar is located in earthquake Zone-1 (most severe) of the Turkish Seismic Zones Map which was substantially revised in 1996 in view of an extensive study[7], summarized in Reference 8. Dinar was always in Zone-1 in the previous versions of the seismic zones maps as well. According to Reference 7, the peak ground acceleration expected in Dinar with a 10% probability of exceedance in 50 years, i.e. with a return period of 475 years, is 0.486*g*. The effective peak acceleration assigned to Zone-1 in the Turkish Seismic Design Code[9] is 0.40*g*. This value appears rational for Dinar concerning the difference between the effective and actual peak ground accelerations. In the same study[7], peak ground acceleration with 40% probability of exceedance in 50 years (return period of 100 years) is calculated as 0.336*g*. Since the

recorded peak ground acceleration in Dinar is 0.294g (Table 1), the 1 October 1996 earthquake falls into an event category with a return period close to, but less than 100 years. This is in conformance with the seismicity of the region discussed above.

The elastic acceleration response spectra for Dinar earthquakes calculated for 5% damping are shown in Fig.9. It is observed from the figure that the effective period range of the lateral forces resulting from the earthquakes is not broad. The main shock is observed to have no significant effect on very short period structures. Although the forces acting on intermediate period structures are higher, these forces decay quickly beyond the period of 1 second.

The smaller earthquakes recorded in Dinar have no appreciable horizontal force contribution on the existing buildings. However, these forces may increase the damage that a structure experienced earlier. A softened, and consequently increased period structure may undergo large displacements under the effect of the mainshock and aftershocks.

The correlation between the intensity of the earthquake ground motions and the damage experienced by structures can be expressed by the dissipated energy spectrum. This is because the energy which is dissipated by the structural system during the ground motion duration is directly related to the structural damage. Dissipated energy spectrum is sensitive to the peak acceleration, effective duration and the frequency content of the earthquake excitation, which are the dominant characteristics of the intensity of shaking. The accumulated and the mainshock's individual dissipated energy spectra are presented in Fig.10. Although it is not possible to supply a cumulative elastic acceleration response spectrum for sequential shocks, a cumulative energy spectrum can be provided. It can be observed from Fig.10 that foreshocks and aftershocks have contributed significantly to the probable damage of medium period structures.

4. Influence of Soil Properties on the Observed Damage

It is evident in Fig.7 that the slope border defines a sharp boundary to the section of the city where damage is concentrated. Most of the damaged buildings are located on loose alluvial deposits. Surprisingly however, the foundations of the damaged buildings did not exhibit any signs of failure or settlement. This decision is based on the observations of footings from 35 damaged buildings unearthed randomly by digging pits around them. There were no failures also to underground service mains due to any soil deformation. Although water was cut after the earthquake for several days, this had resulted from broken pipe connections at the service entrances of collapsed buildings.

A general distribution of damage density in Dinar is shown in Fig.11, where the city center is mapped on to the satellite view indicating close faults, global topography and soil conditions. Alluvial deposits are marked with light plain color along the valleys. It can be observed that the districts which sustained damage are located on the alluvial plain deposits. It is difficult however to propose a significant correlation between the intensity of damage and the thickness or bearing capacity of alluvial soil. Damage distribution on the alluvial region is fairly irregular although the construction quality is uniformly poor throughout the entire city.

Five shallow borehole logs of 30 m depth have been taken from the heavily damaged part of the city, circled in Fig.7. The boring data indicate that the water table depth varies between 3-5 m. Similar soil composition is observed from all five boring logs, which is mainly constituted of sand and gravel with small amounts of clay and silt. A loose filler material covers the surface with a thickness varying between 0.2-4.2 m. Standard penetration (SPT) blow counts are between 4-20 in the first fifteen meters, and between 20-50 in the second fifteen meters. Accordingly, sand and gravel series can be classified as loose and medium dense in the two consecutive surface layers.

Saturated sand and gravel layers with low SPT blow counts increase liquefaction potential substantially during an earthquake. However there was no evidence of liquefaction during the Dinar earthquake, except for isolated sand mounds along an irrigation canal. Grain size and the duration of strong motion did not perhaps provide necessary conditions for liquefaction.

Since Dinar is still vulnerable to future earthquakes, the seismic response characteristics of the alluvial basin should be determined through detailed studies. A number of research studies have already been initiated; however, the insufficiency of strong motion data handicaps the accuracy of these studies.

5. Evaluation of Structural Damage

The total population affected from the earthquake in the region is 100,000 and the number of households is about 24,000. The damage survey conducted in the affected region after the earthquake revealed that, out of 24,000 households 4340 (18%) were heavily damaged, 3712 (15%) were moderately damaged, 6104 (25%) were lightly damaged and the remaining 9844 (41%) were undamaged. In the city center (Fig.7), heavy damage in residential units increases to 31%. Two hundred buildings were completely collapsed. According to these figures, a death toll of 90 might be considered less than expected. The foreshocks in the preceding four days of the mainshock considerably reduced the death toll because many residents had already left the city before October 1 by fear and expectation of a big quake.

The building stock in the city mainly consists of 3-6 story reinforced concrete and 2-4 story masonry buildings at the city center where damage was concentrated, and 1-2 story adobe, stone and brick masonry buildings on the slopes and outskirts of the city. Considering that seismic energy is intensified within the period range of 0.3-1 seconds (Fig.10), buildings having three or more stories which were already damaged

to some extent and softened due to foreshocks possibly received high seismic forces during the mainshock.

An independent survey had been conducted by the Chamber of Civil Engineers on 103 public buildings in Dinar after the earthquake. According to their quick expert evaluation, 20 of these buildings were heavily damaged or collapsed, 10 were medium damaged, 20 were lightly damaged and the remaining 53 were undamaged. Fourteen of the twenty heavily damaged buildings were 3-5 story reinforced concrete framed buildings, which constitute the most vulnerable building class in Turkey.

Damage evaluation is presented in two parts here, seperately for heavily damaged or collapsed buildings and moderately damaged buildings. The reasons leading to building collapses are usually very obvious and not informative other than repeating the well known mistakes. Moderately damaged buildings on the other hand manifest relatively less obvious facts on structural weaknesses, hence their evaluation may contribute to improving our current knowledge.

5.1. Heavily Damaged and Collapsed Buildings

A structural classification of collapsed buildings is given in Table 2. Single story buildings did not experience partial or total collapse, including adobe dwellings. There were no steel or precast concrete structures in Dinar during the earthquake.

Table 2. Classification of 200 Collapsed Buildings in Dinar

Structural System	Number of Stories	Number of Collapsed Buildings	
		Single Story Collapse	Total Collapse
R/C Frame	≥4	33	28
R/C Frame	3	29	18
Brick Masonry	4	32	41
Brick Masonry	3	10	4
Composite Masonry	2	6	-

It is revealed in Table 2 that soft story formation is responsible for many reinforced concrete building collapses. A weak ground story is usually created with the intention of reserving open space for commercial use. Since this story does not benefit from the presence of infill masonry walls, as shown in Fig.12, damage accumulates in this story and eventually leads to failure. It should be noted that the entire framing systems of such buildings are weak, as the three story building in Fig.12, but the contribution of infills to overstrength masks these weaknesses in the other stories. Another example of weak concrete frame is shown in Fig.13, in which one of the three identical buildings under construction had collapsed before receiving its full vertical load. None of the joints satisfied strong column-weak beam criteria, no shearwalls were employed, and orientation of strong column axes had led to an even weaker frame in one direction.

An extraordinary failure is shown in Fig.14, where the standing building was constructed with four stories originally. The collapsed building on the left had later been constructed as five storied by the same owner and contractor, during which a fifth story was added to the building on the right, and a common roof was shared. The hanging roof fell down due to an aftershock a few days later. The standing building was heavily damaged due to several reasons, soft story, weak frame, and pounding by the short adjacent building. It was demolished later.

A middle story failure is presented in Fig.15 due to pounding. The brick masonry building on the right served as a lateral support in one direction, resulting in accumulation of shear forces at the intermediate story. Seismic joints are never taken into consideration in Turkey, although it is mandatory due to the seismic code[9].

Low concrete quality also plays an important role in the failure of buildings discussed above. A material quality survey conducted in Dinar on 35 buildings by performing both destructive and non-destructive testing revealed an average concrete compressive strength of 10 MPa. The concrete in these buildings were prepared at the site by ordinary workers, which is a common practice in many small towns as Dinar. It is

very difficult to obtain a 28 day concrete strength of 15 MPa under these conditions, which is a minimum requirement in the seismic Zone 1 according to Turkish code.

The number of stories in brick masonry buildings is limited to two in Zone 1 by the Turkish seismic code. The masonry buildings shown in Figs.16 and 17 were constructed originally as single storied by using solid bricks. Several years later, with a permission from the municipality, two more stories were added despite violating the code. Hollow, non-load bearing bricks were used to construct these additional stories in order to reduce both the weight and the cost. No damage occured in the original stories while the poor performance of added stories have severely punished code violation. Unfortunately non-load bearing hole bricks with hollow ratios exceeding 50%, actually produced for infill wall construction, are being widely used in bearing wall construction in the recent years. Future earthquakes will definitely be brutal against this practice.

5.2. *Medium damaged buildings*

Structural irregularities are the main cause of medium damage in buildings which otherwise possess code specified lateral resistance. The building shown in Fig.18 has both plan and elevation irregularity which is not accounted for in its seismic design. A sudden change in story plan and height above the ground story (Figs.19, 20) has again resulted in soft story formation, displayed by broken storefront windows.

Many buildings with poor lateral resistance remained in the medium damage level due to the overstrength provided by masonry infill walls (Figs.21, 22). The extent of damage would be more dramatic without the presence of infill walls in most of the concrete framed buildings. They had acted as passive energy dissipation devices as long as they maintained their integrity within the enlosing frame. However such a positive performance should not be expected during a longer ground excitation.

Reinforced concrete connections which do not satisfy strong colum-weak beam requirement experienced damage at the column ends (Fig.23). If this condition prevails in all connections, heavy damage becomes inevitable. Another case of joint failure was due to the formation of cold joints at the top of columns (Fig.24). This is a result of casting slab and girder concrete several days after casting the column concrete below. Hence, the associated joint behaves as a semi-rigid connection.

Inadequate frame configurations may lead to premature failure of certain elements under seismic effects. The columns in a small industry complex in Dinar, shown in Fig.25, received systematic damage in all frames although they support a very light roof. However total frame action could not have been developed since the individual frames were not connected to each other transversally. Accordingly, these columns were forced to restrain the transverse drift of longitudinal frames, similar to the fixed support of a lever arm.

It can be concluded finally that the predominant reason for structural damage in Dinar was the violation of the basic seismic code requirements. Those buildings which satisfy the 1975 seismic code[9] (which was valid in 1995 and updated in 1996) did not sustain any serious damage during the 1995 Dinar earthquake.

6. References

1. N.N. Ambraseys, "Engineering seismology", *Earthquake Eng. Structural Dynamics* **17** (1988) 1-105.

2. R. Demirtaş and R. Yılmaz, *Seismotectonics of Turkey* (Ministry of Public Works and Settlement, Ankara, 1996).

3. T. Taymaz, J.A. Jackson and D. McKenzie, "Active tectonics of the north and central Aegean Sea", *Geophysical Journal Int.* **106** (1991) 433-490.

4. S. Price and B. Scott, "Fault-block rotations at the edge of a zone of contiental extension: Southwest Turkey", *J. of Str. Geology* **16** (1994) 381-392.

5. R. Demirtaş *et.al., The mechanism of the Dinar earthquake of 1 October 1995, SW Turkey* (General Directorate of Disaster Affairs, Ankara, 1995).

6. S.V. Medvedev, W. Sponheuer and V. Karnik, "Seismic Intensity Scale, Version 1964", *Soviet Geophys. Com.* (1965).

7. P. Gülkan *et.al.,* "Turkish Seismic Zones Map", Report No.93-01, Earthquake Eng. Research Center, Middle East Technical University, 1993.

8. P. Gülkan, N. Başöz, M.S. Yücemen and O. Ergünay, "A proposed seismic zones map of Turkey incorporating source zone boundary uncertainty", *Proc. 5th U.S. National Conference on Earthquake Eng.,* Chicago, 1994, pp. 661-670.

9. *Requirements for Buildings in Disaster Regions* (Ministry of Public Works and Settlement, Ankara, 1975).

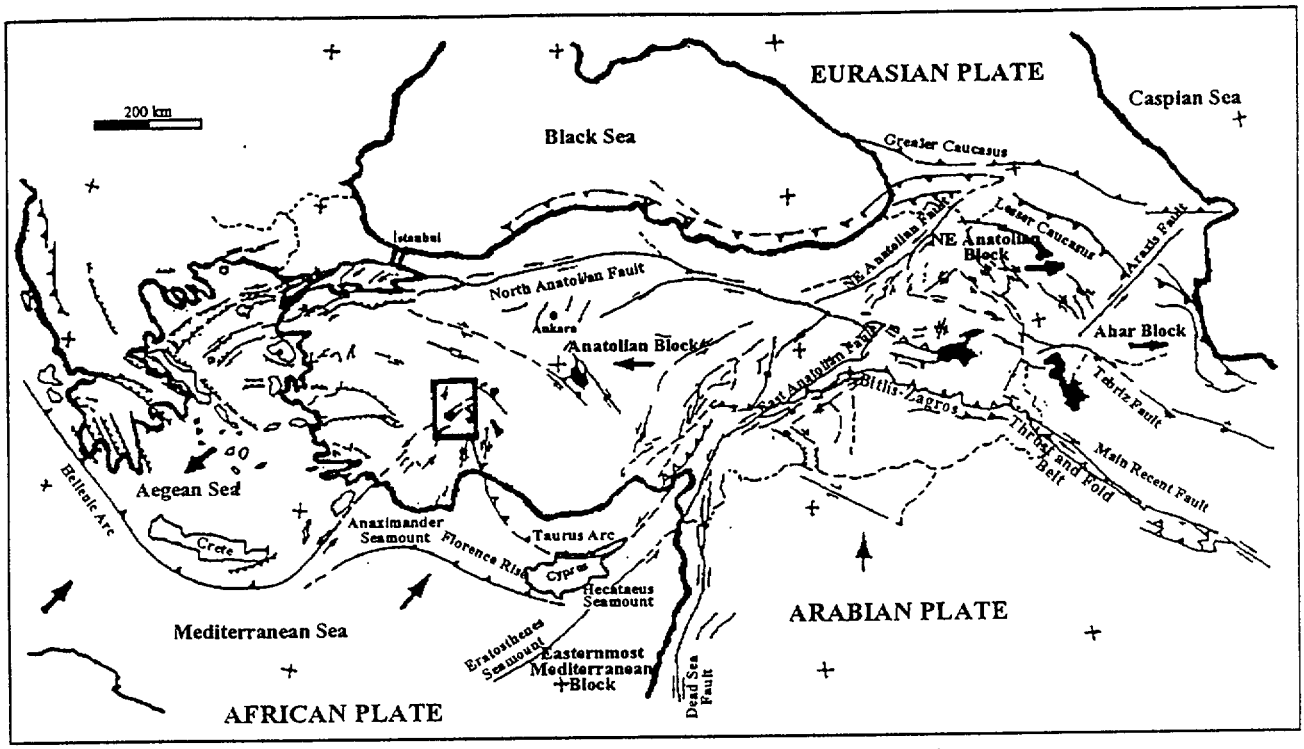

Fig.1. A general neo-tectonic map of Turkey. The rectangle to the Southwest of the map circumscribes the region affected by the 1 October 1995 earthquake and is enlarged in Figs.2 and 5.

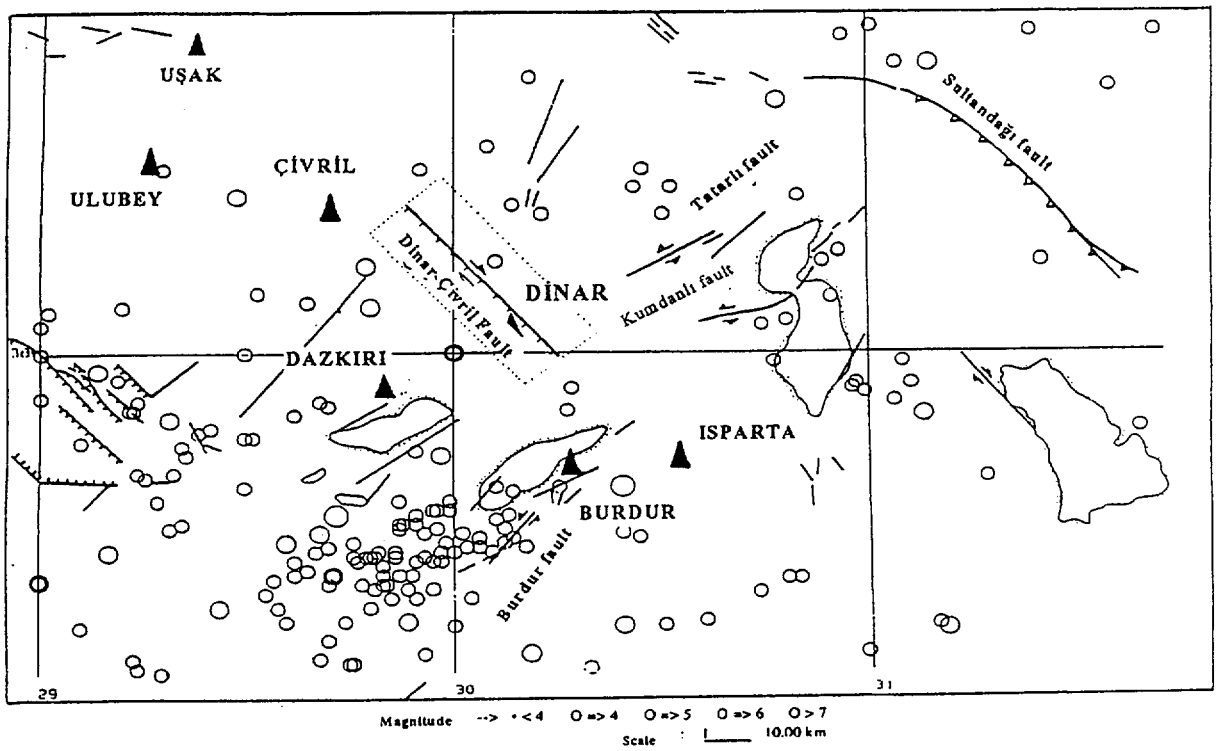

Fig. 2. Major faults around Dinar and epicenters of the earthquakes between 1900-1994.

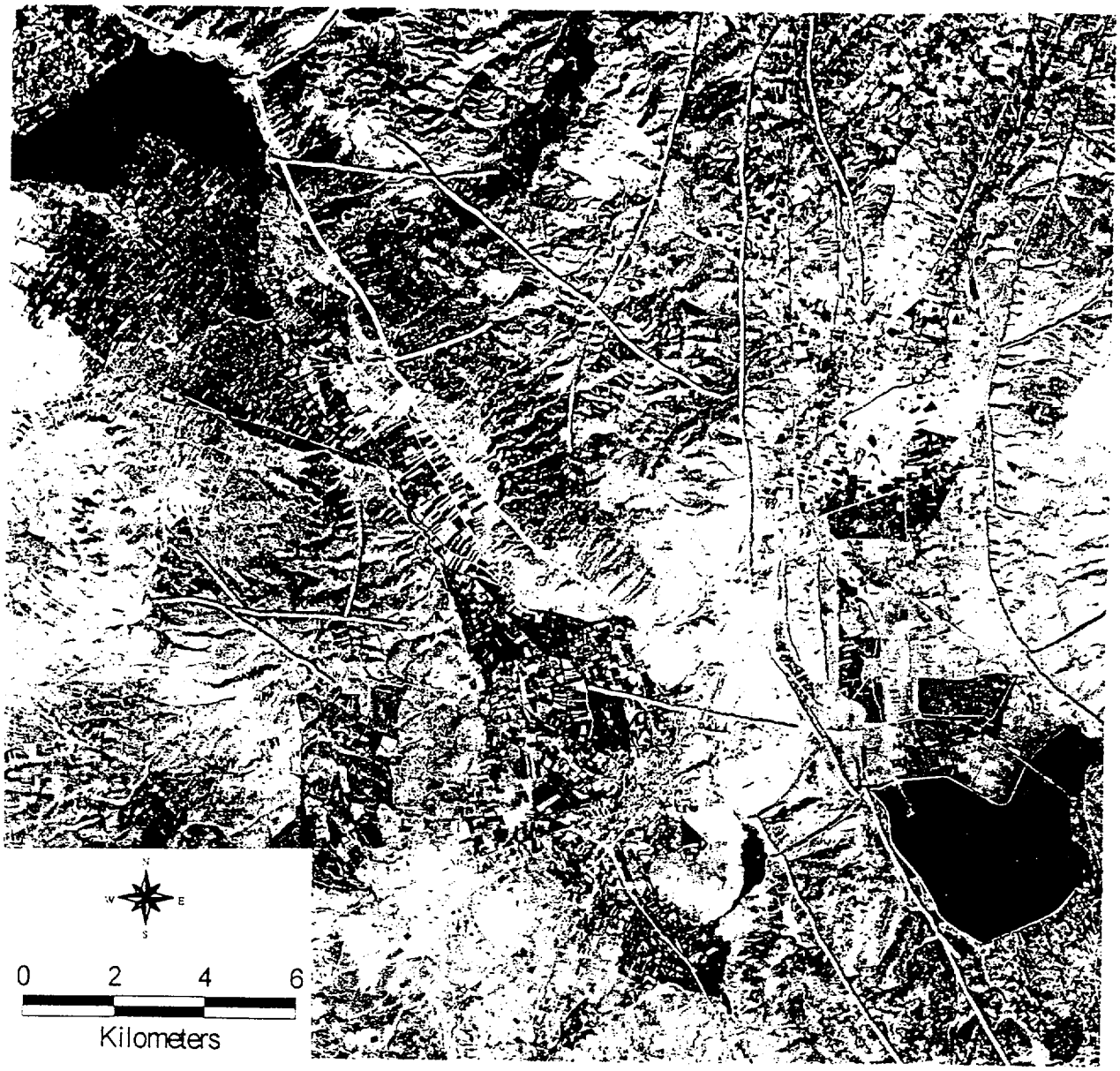

Fig.3. Satellite view of Dinar and vicinity. Local faults are marked with dark lines and the ruptured fault is marked with a light line.

Fig.4. Fault rupture during the Dinar earthquake.

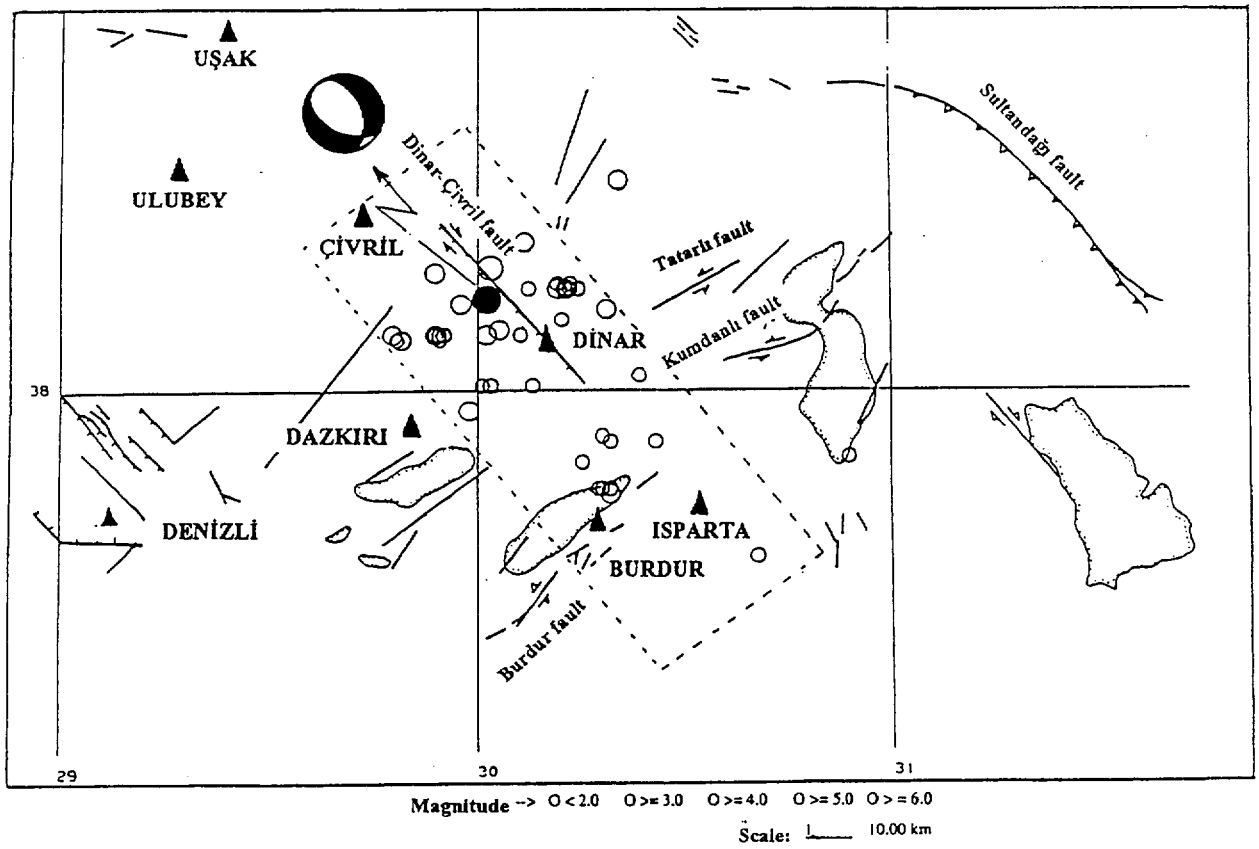

Fig.5. The epicenters of the mainshock and aftershocks of the October 1, 1995 earthquake

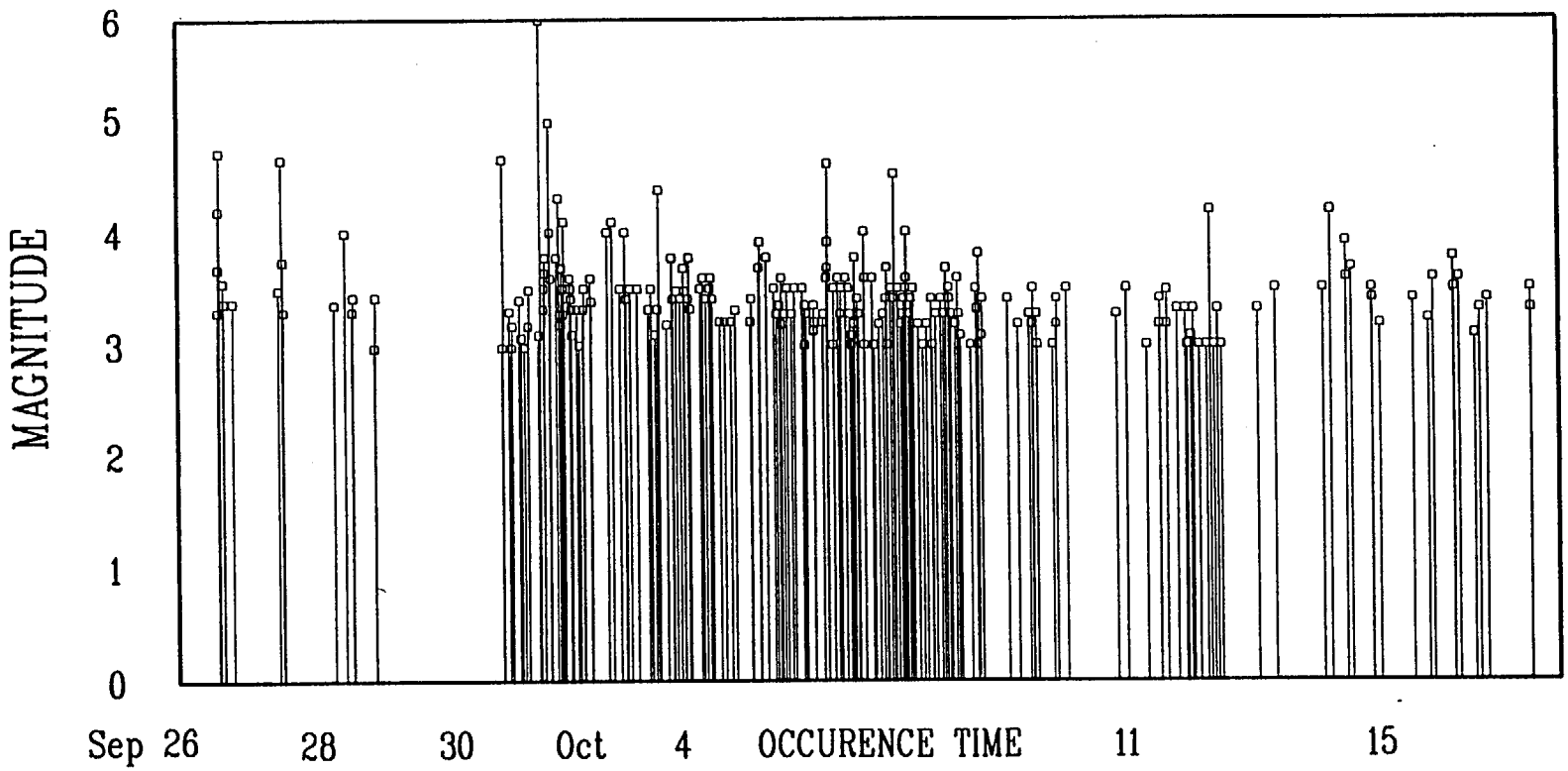

Fig.6. The magnitude distribution of earthquakes which occurred between September 26 and October 16, in Dinar.

Fig.7. Dinar settlement plan.

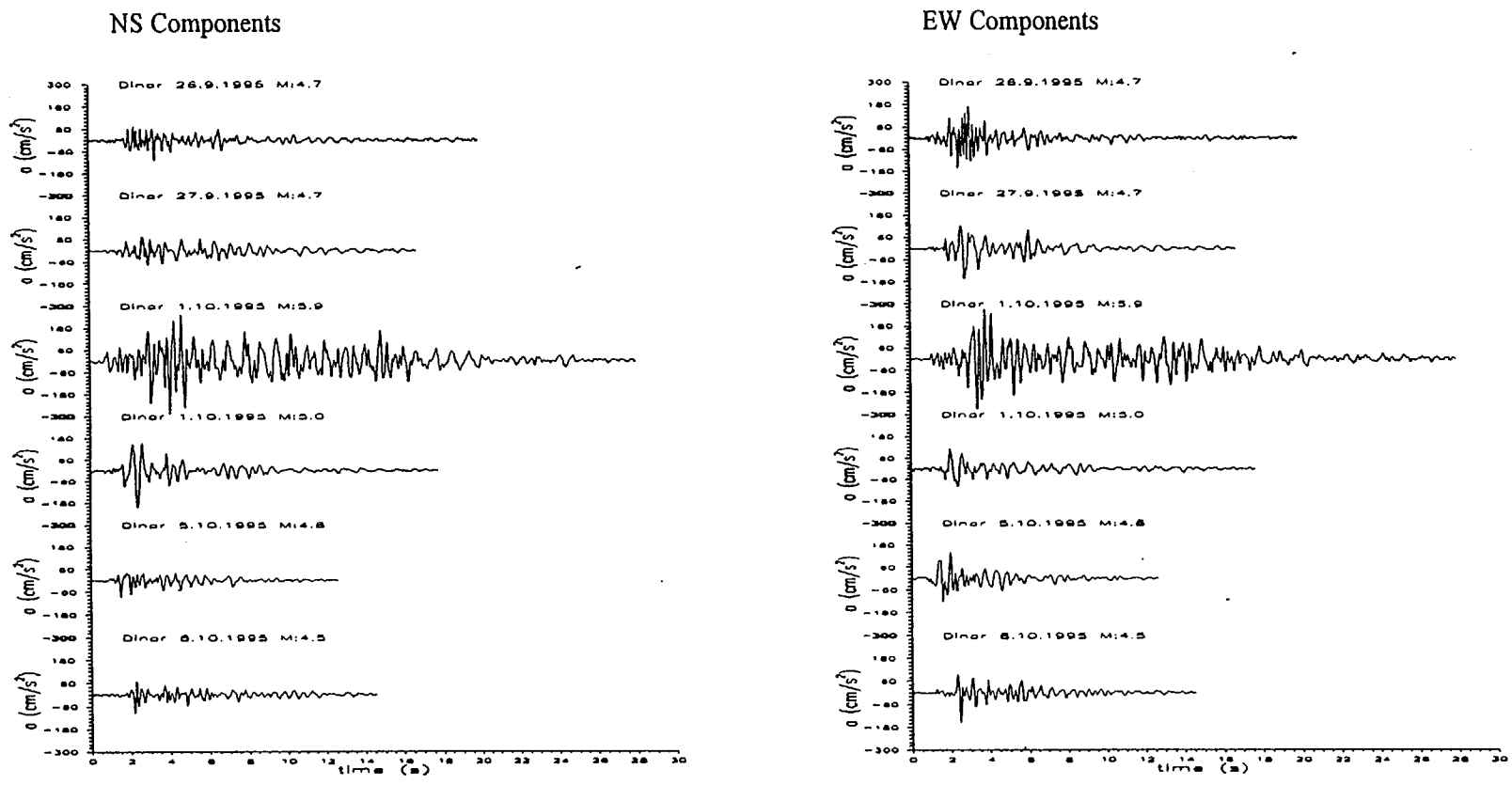

Fig.8. Time variations of the horizontal ground motion acceleration components which have magnitudes greater than 4.5.

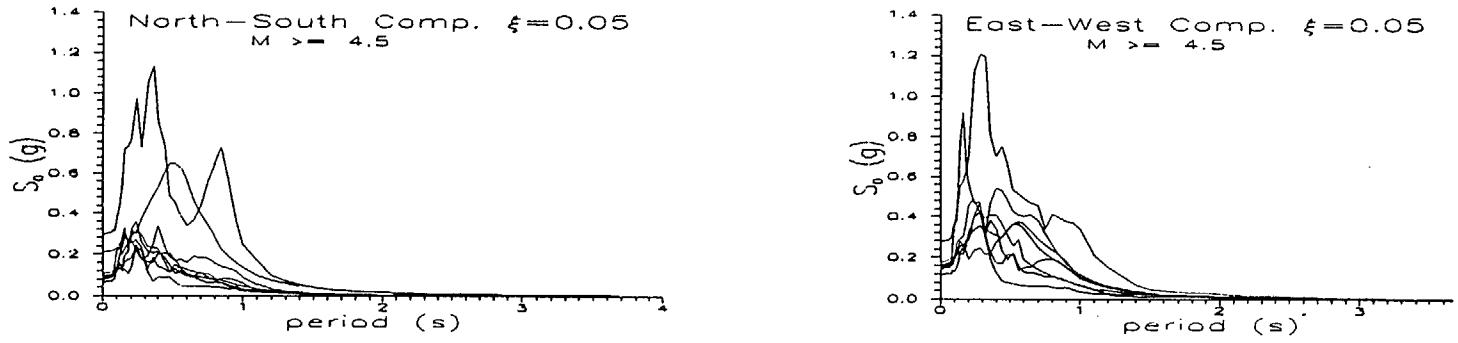

Fig.9. The elastic acceleration response spectra.

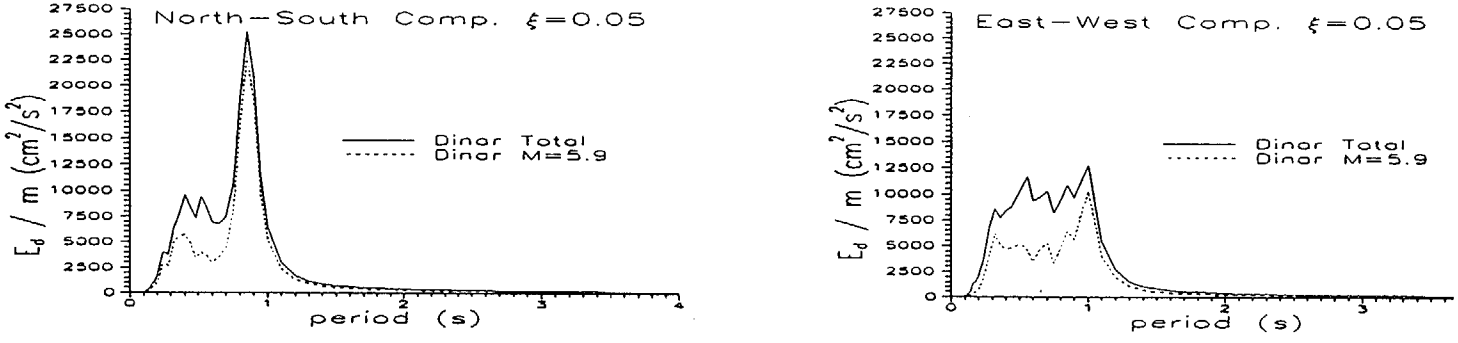

Fig.10. The elastic dissipated energy spectra.

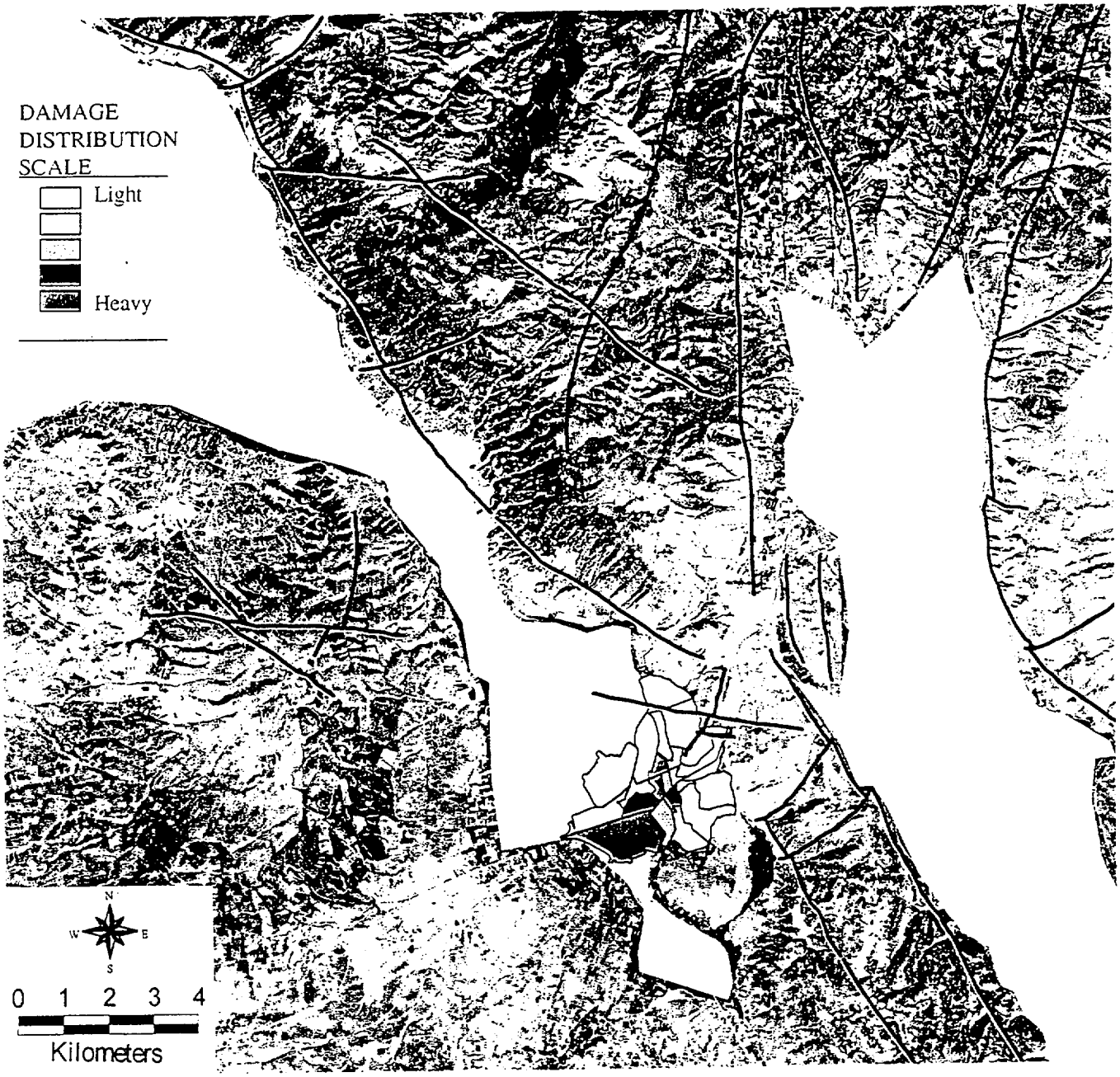

Fig.11. A general distribution of damage density in Dinar, mapped onto the satellite view. Alluvial deposits along the valleys are indicated with light plain color.

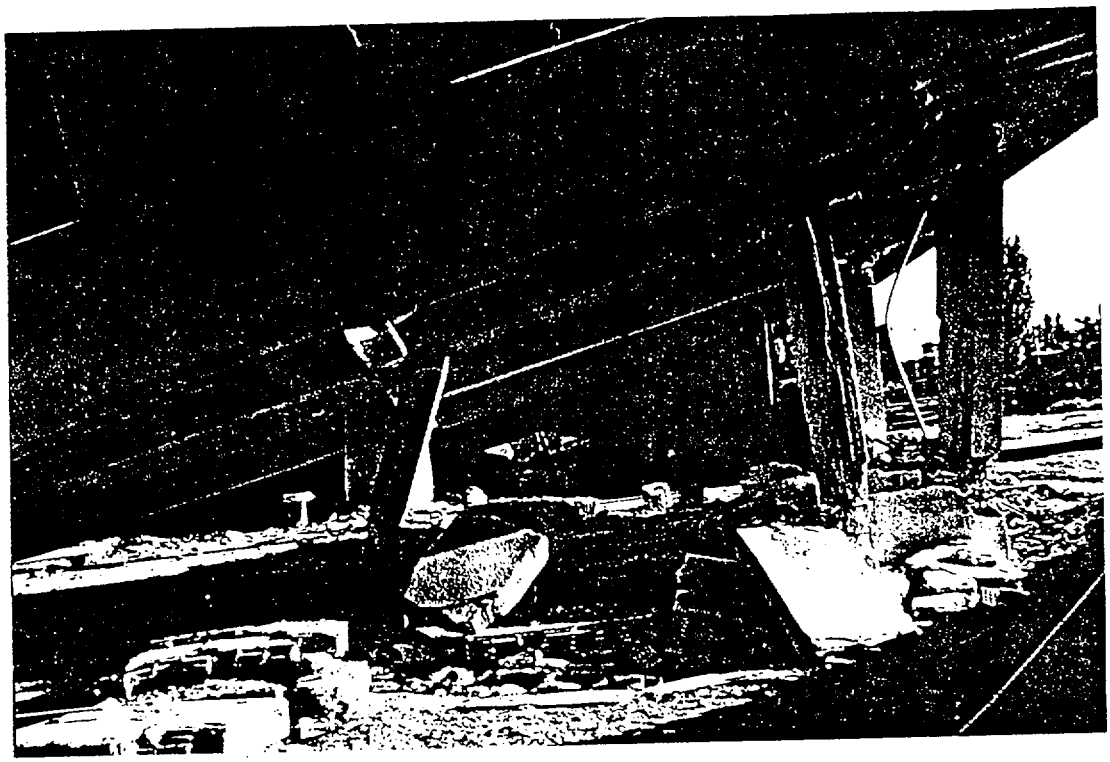

Fig.12. Soft story failure in a three story building

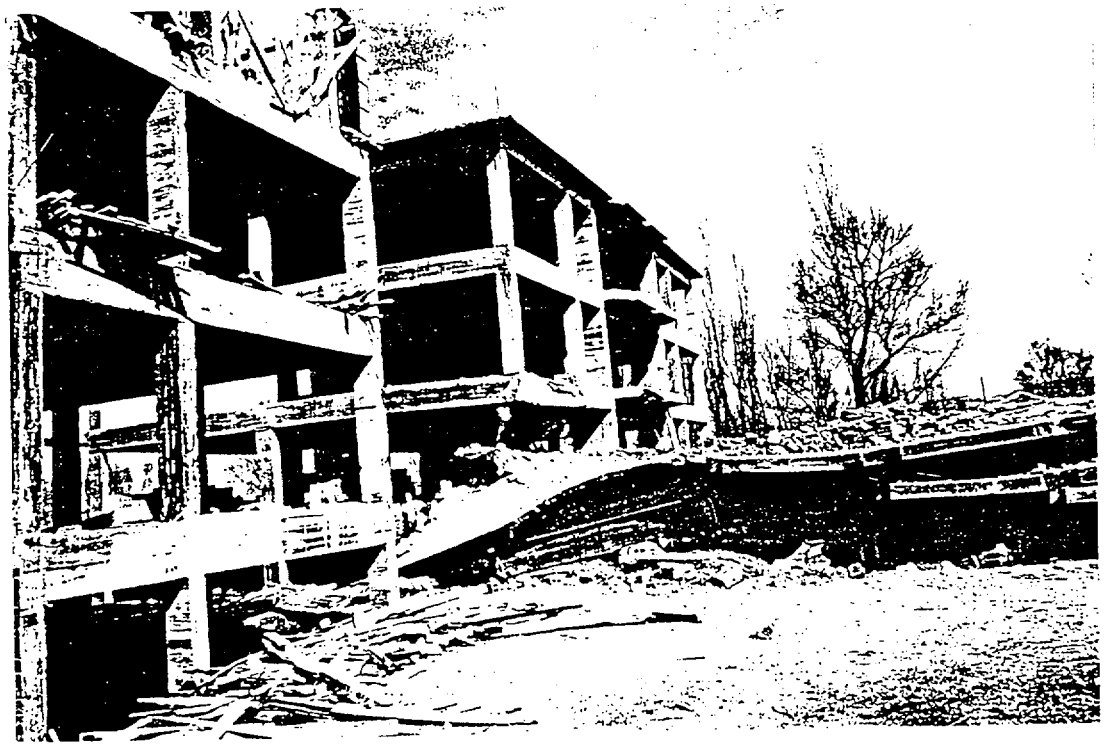

Fig.13. Three identical reinforced concrete building frames under construction.
Notice that the strong column axes oriented in the same direction.

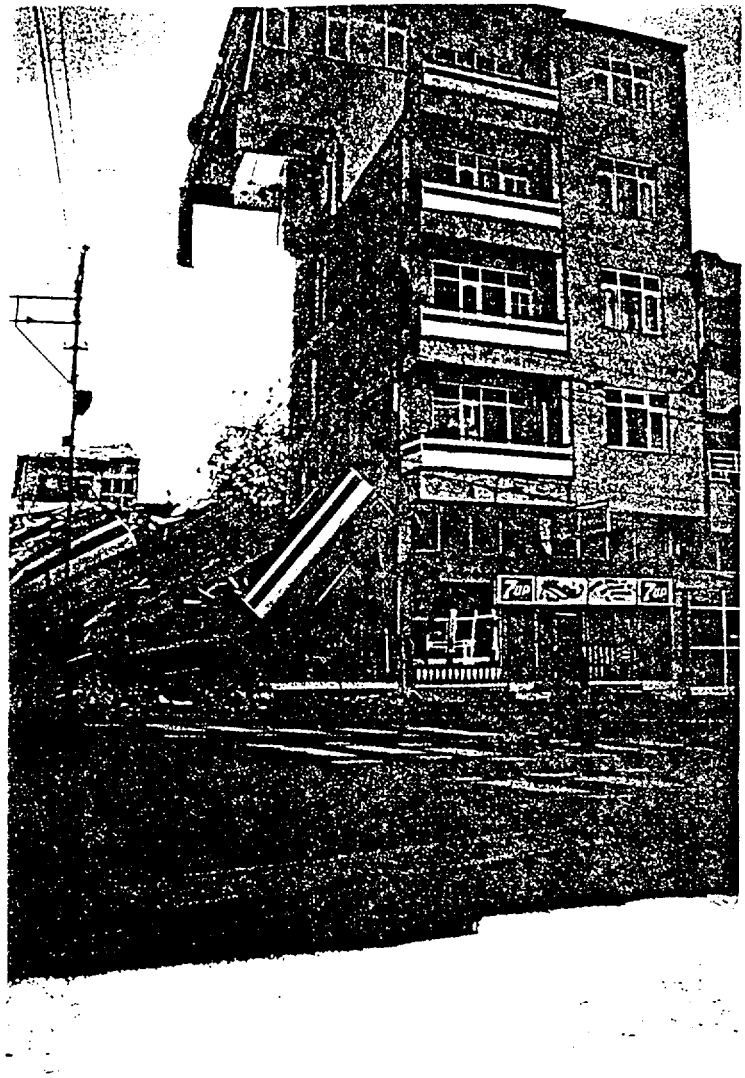

Fig.14. Adjacent collapsed and heavily damaged buildings sharing the same roof.

Fig.15. Middle story failure due to pounding.

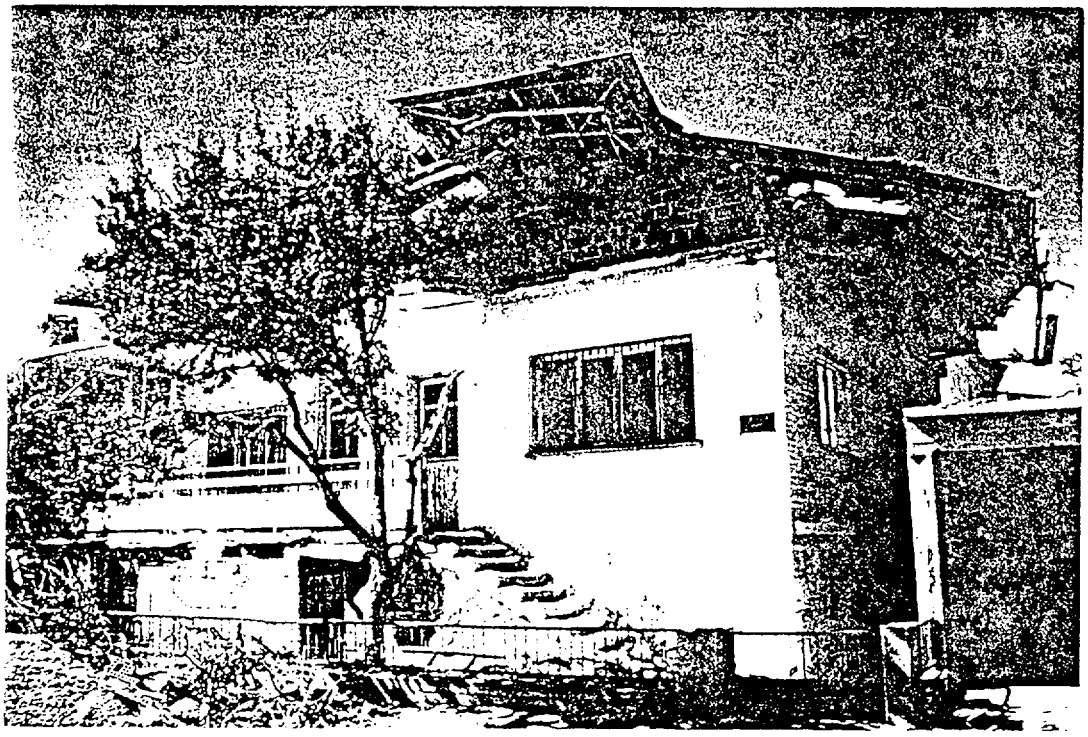

Fig.16. Three story masonry building. Top two stories constructed with hollow bricks collapsed onto the first story with solid brick walls.

Fig.17. Three story masonry building having identical failure pattern with the building in Fig.16. The original first stories sustained light damage in both buildings.

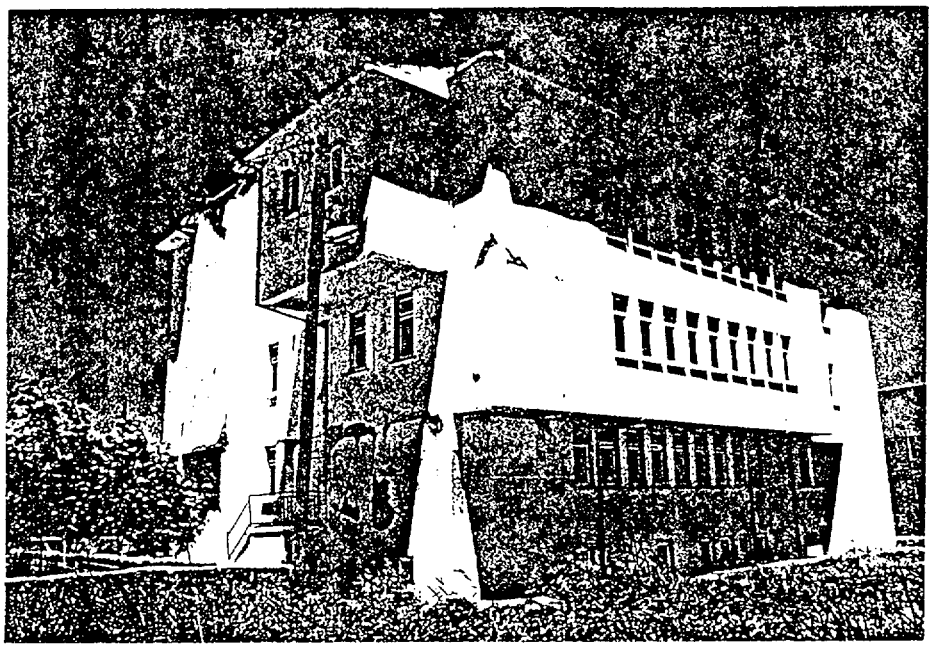

Fig.18. Irregular building with medium damage.

Fig.19. Medium damage in a five story reinforced concrete frame due to soft ground story.

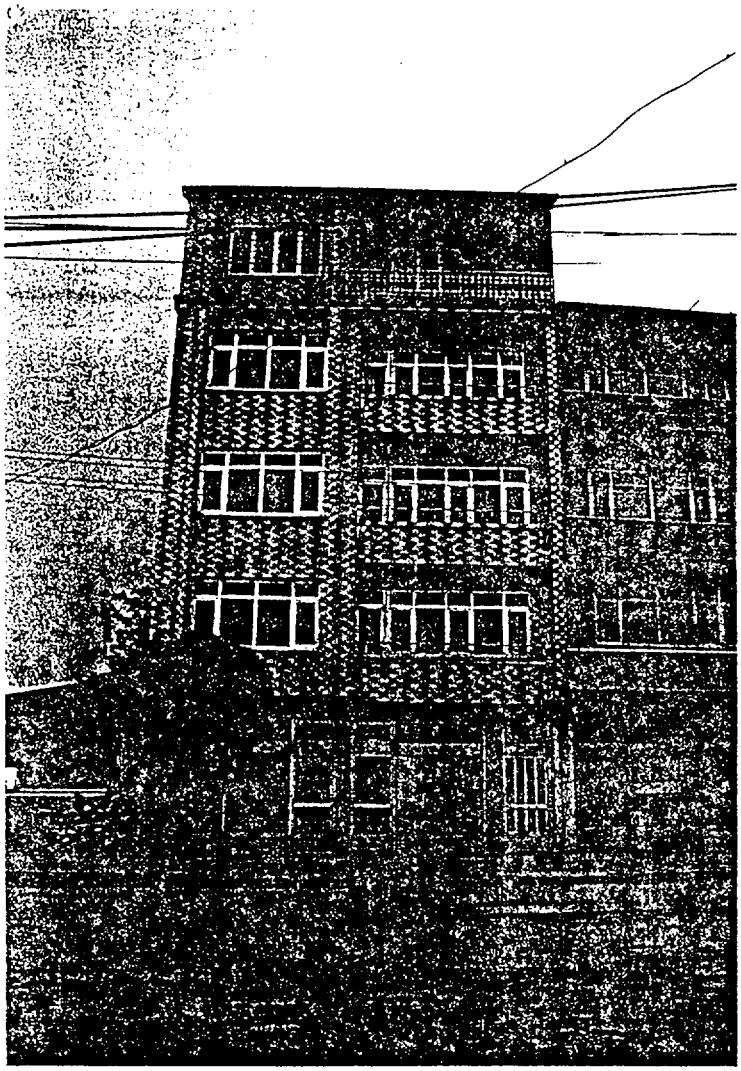

Fig.20. Medium damage in a five story reinforced concrete frame. Structural configuration and story plan changes above the ground story.

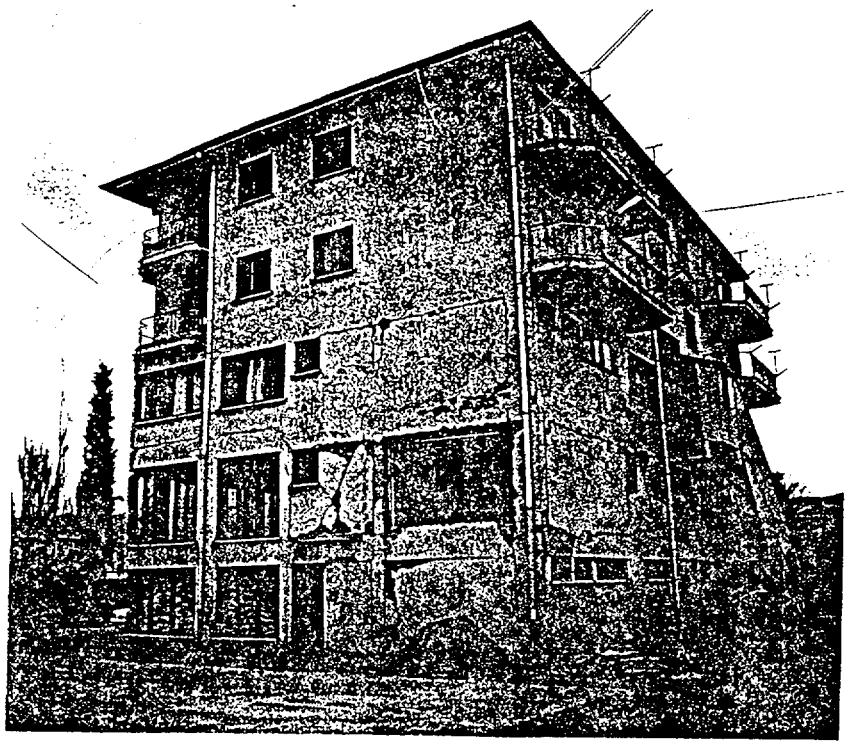

Fig.21. Five story reinforced concrete building where lateral stiffness increases with height. Infill walls resist excessive drift demands at the lower stories.

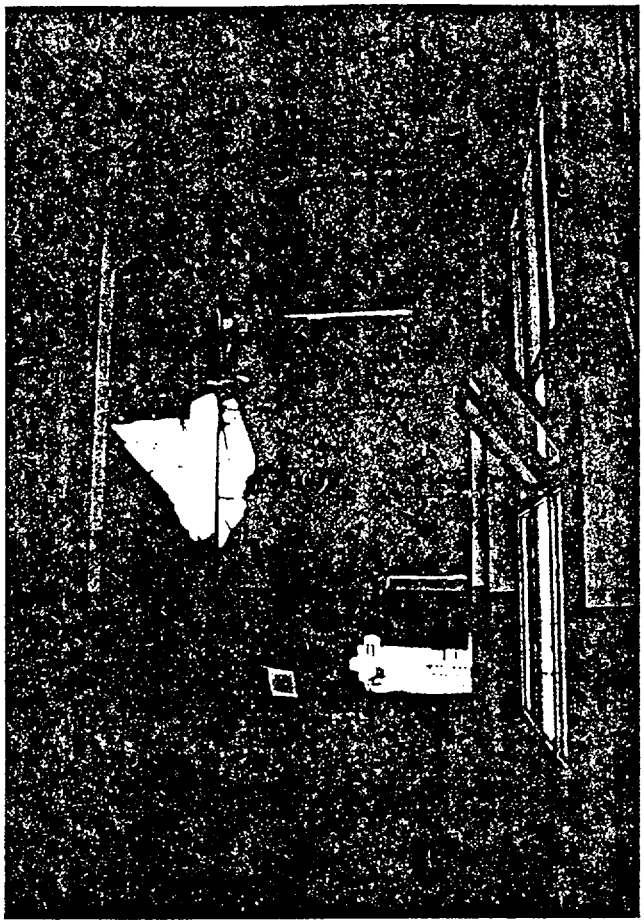

Fig.22. Infills walls providing lateral resistance in a weak frame.

Fig.23. Shear-flexure failure in a weak column connecting to stronger beams. Notice inadequate spacing of stirrups.

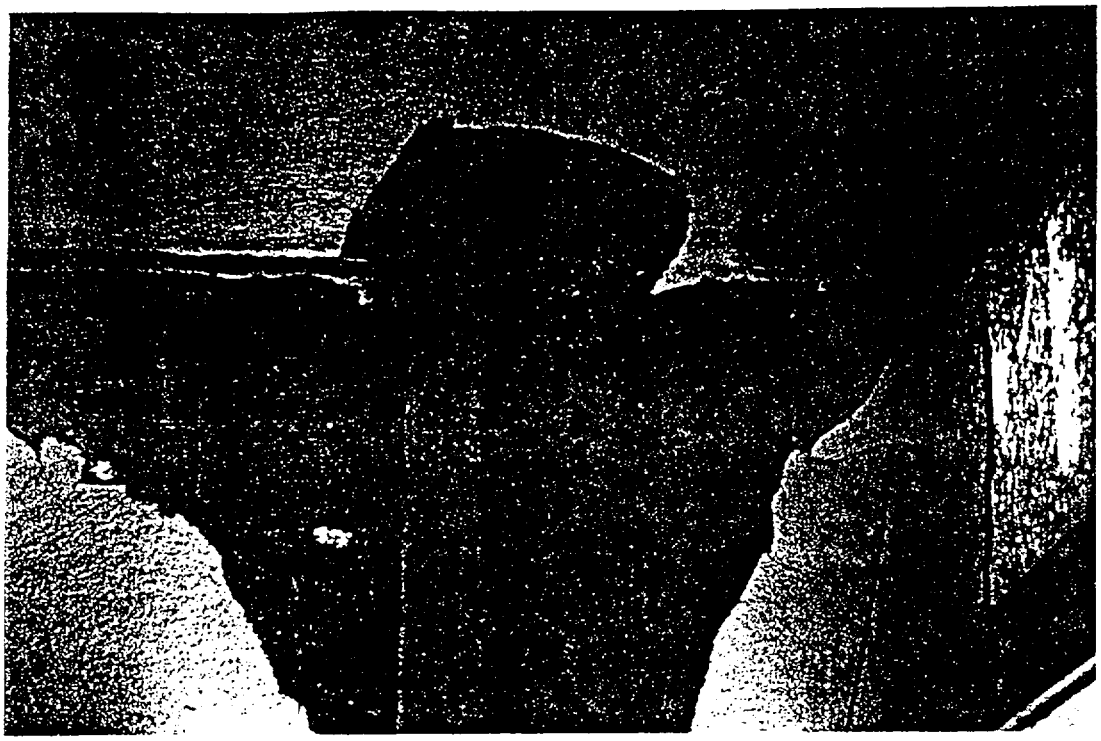

Fig.24. Cold joint at the top of a column.

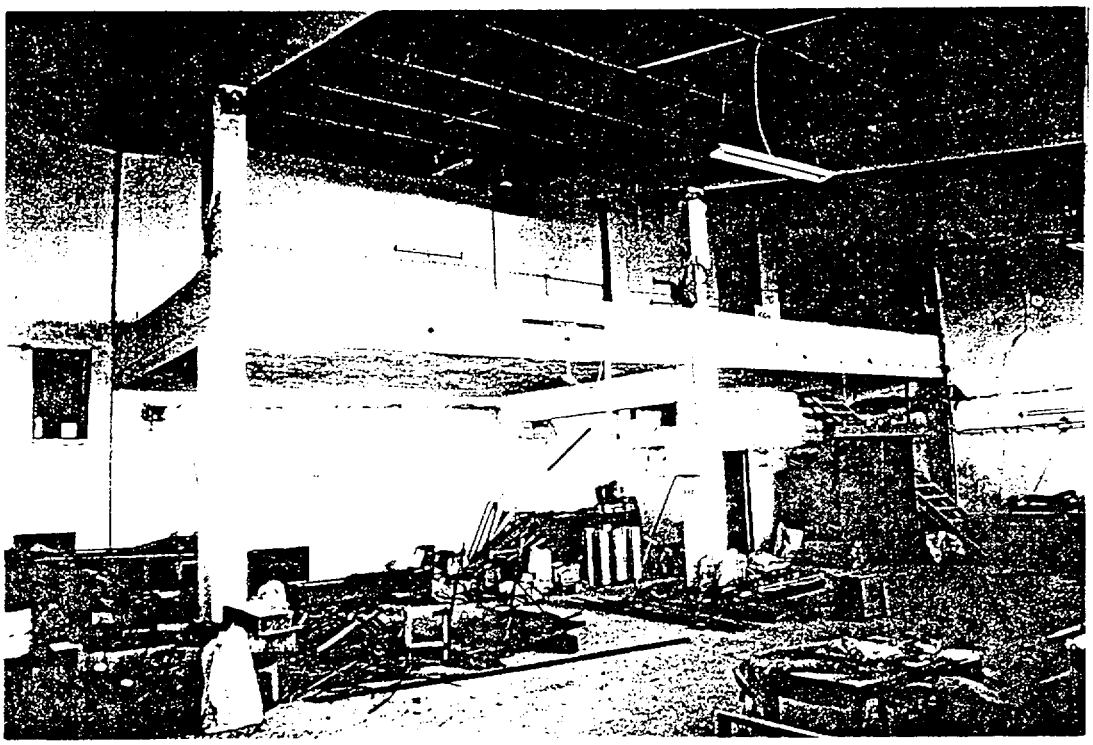

Fig. 25. Transversally unconnected frames in a small industry complex.

Evaluation of Linear and Nonlinear Dynamic Rock Properties: Yucca Mountain Samples

by
Kenneth H. Stokoe, II
Mehmet Darendeli
Seon-Keun Hwang

The University of Texas at Austin
Department of Civil Engineering
Austin, Texas 78712

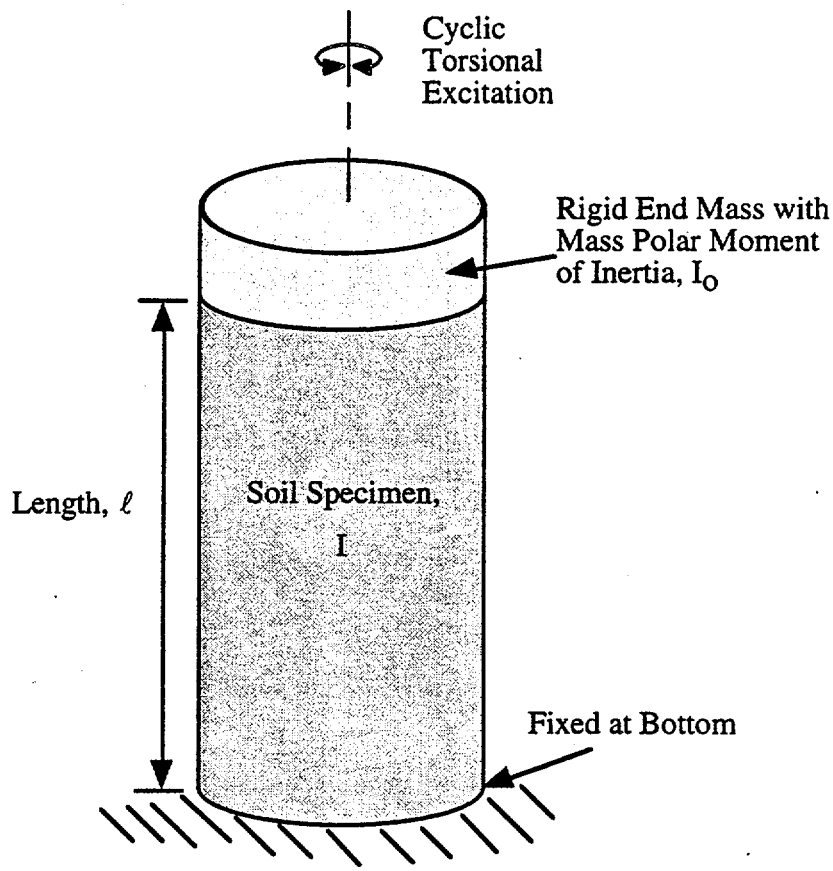

Fig. 1 Idealized Test Configuration of the Fixed-Free Resonant Column/Torsional Shear (RCTS) Device

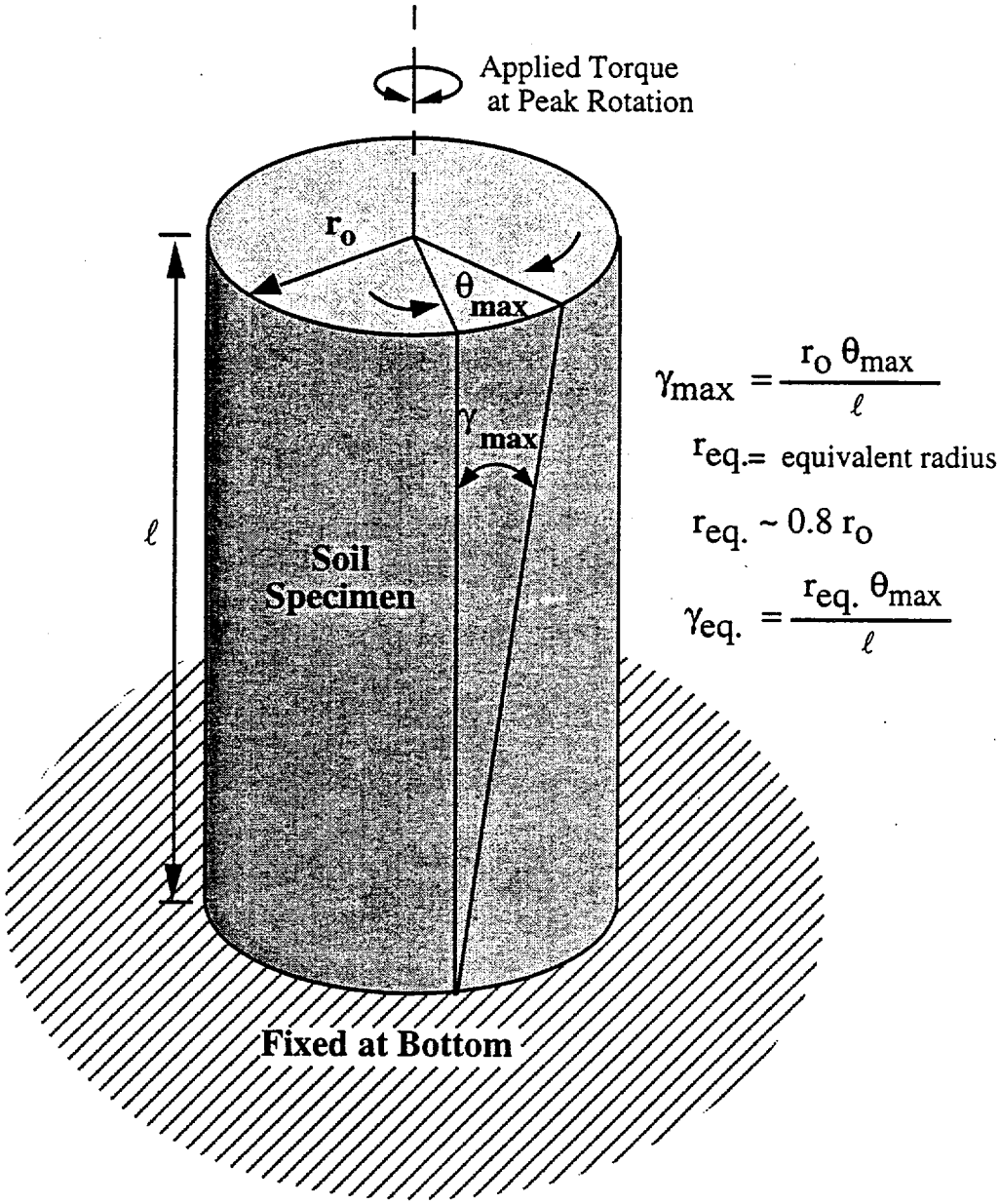

Fig. 2 Illustration of "Equivalent" Shearing Strain in a RCTS Specimen

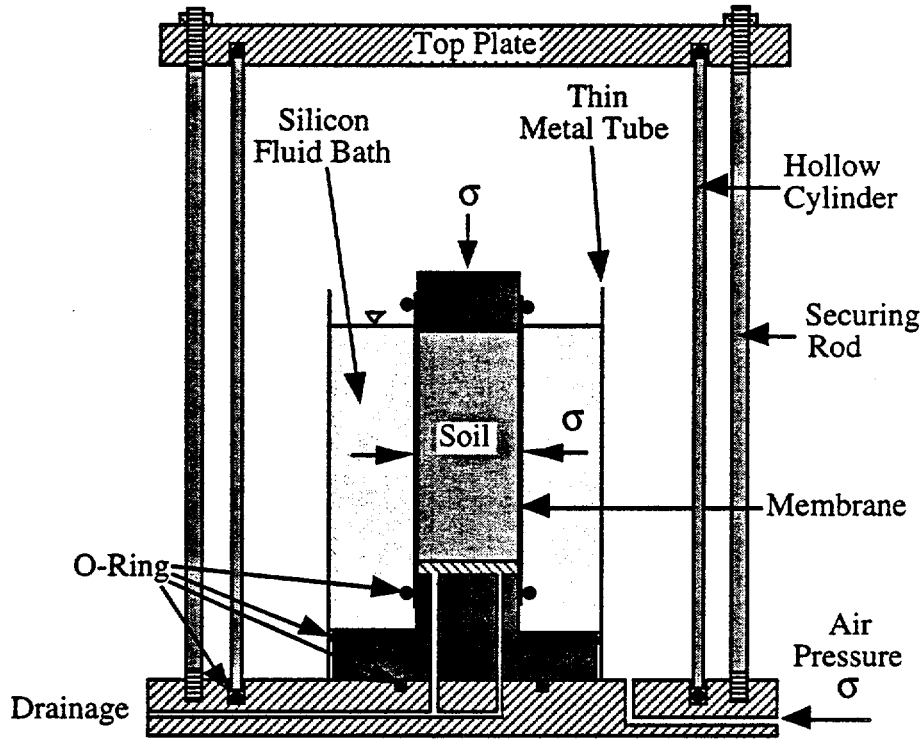

Fig. 3 Simplified Cross-Sectional View of RCTS Confinement System

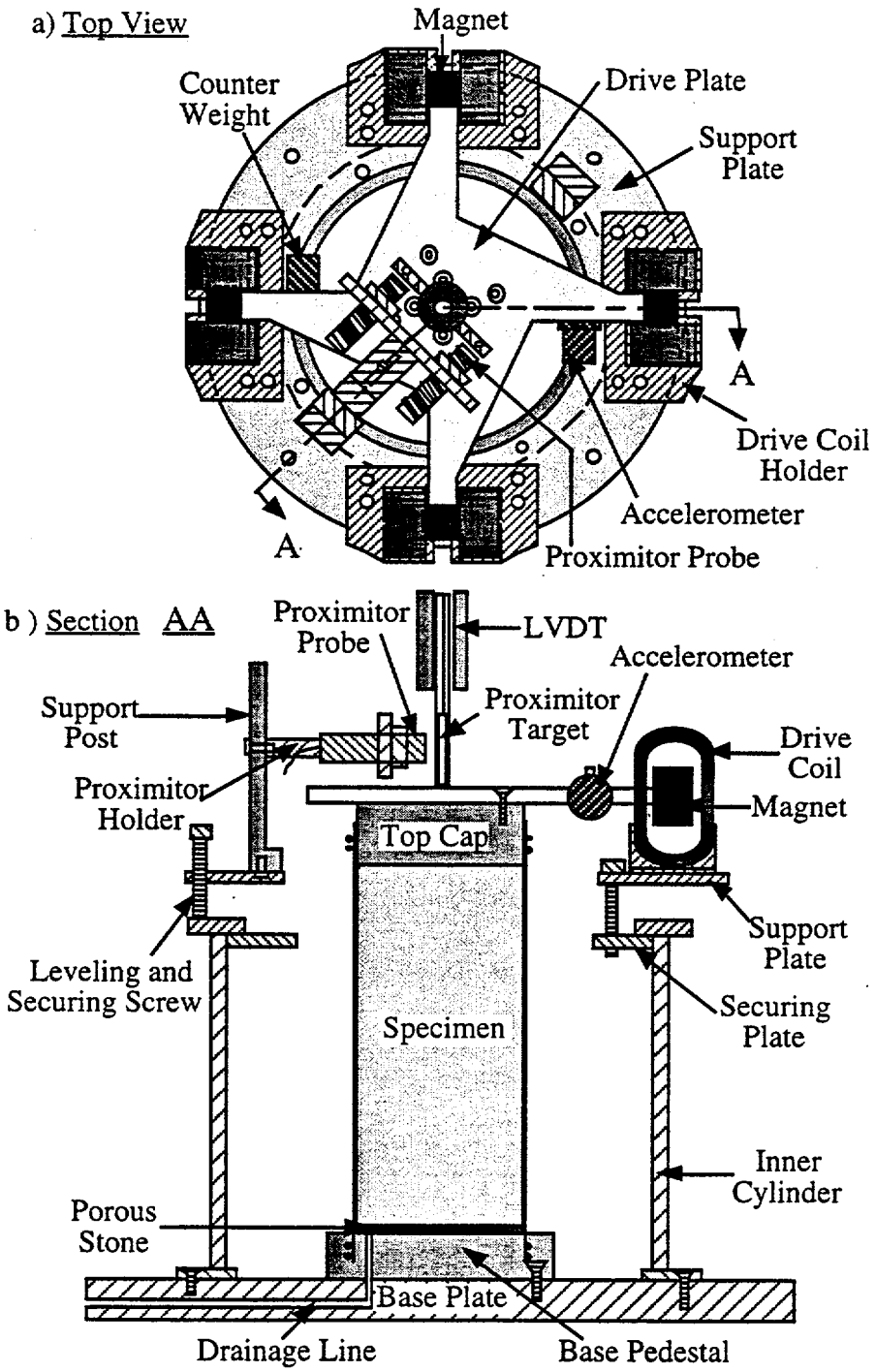

Fig. 4 General Configuration of RCTS Equipment

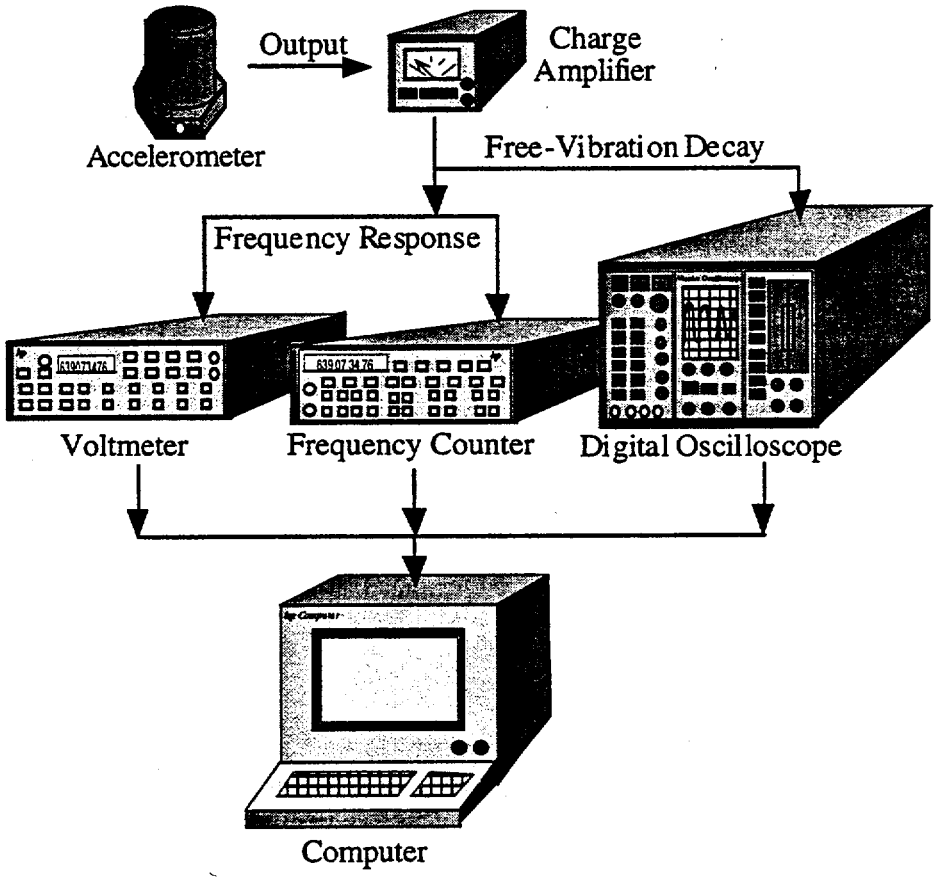

Fig. 5 Schematic Diagram of The Motion Monitoring System in The Resonant Column Test

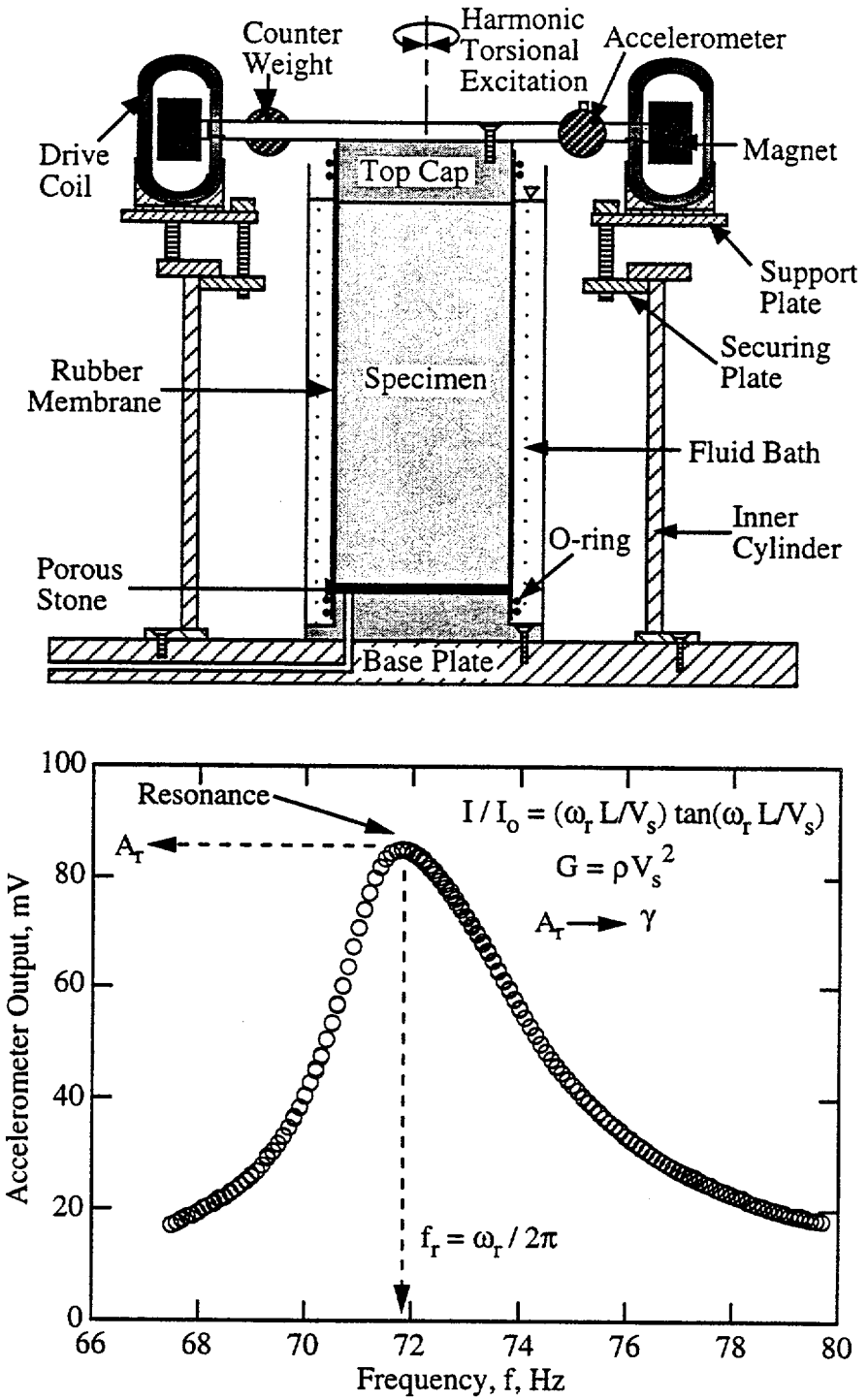

Fig. 6 Side View of a Fixed-Free Resonant Column Test Set-up and a Typical Frequency Response Curve

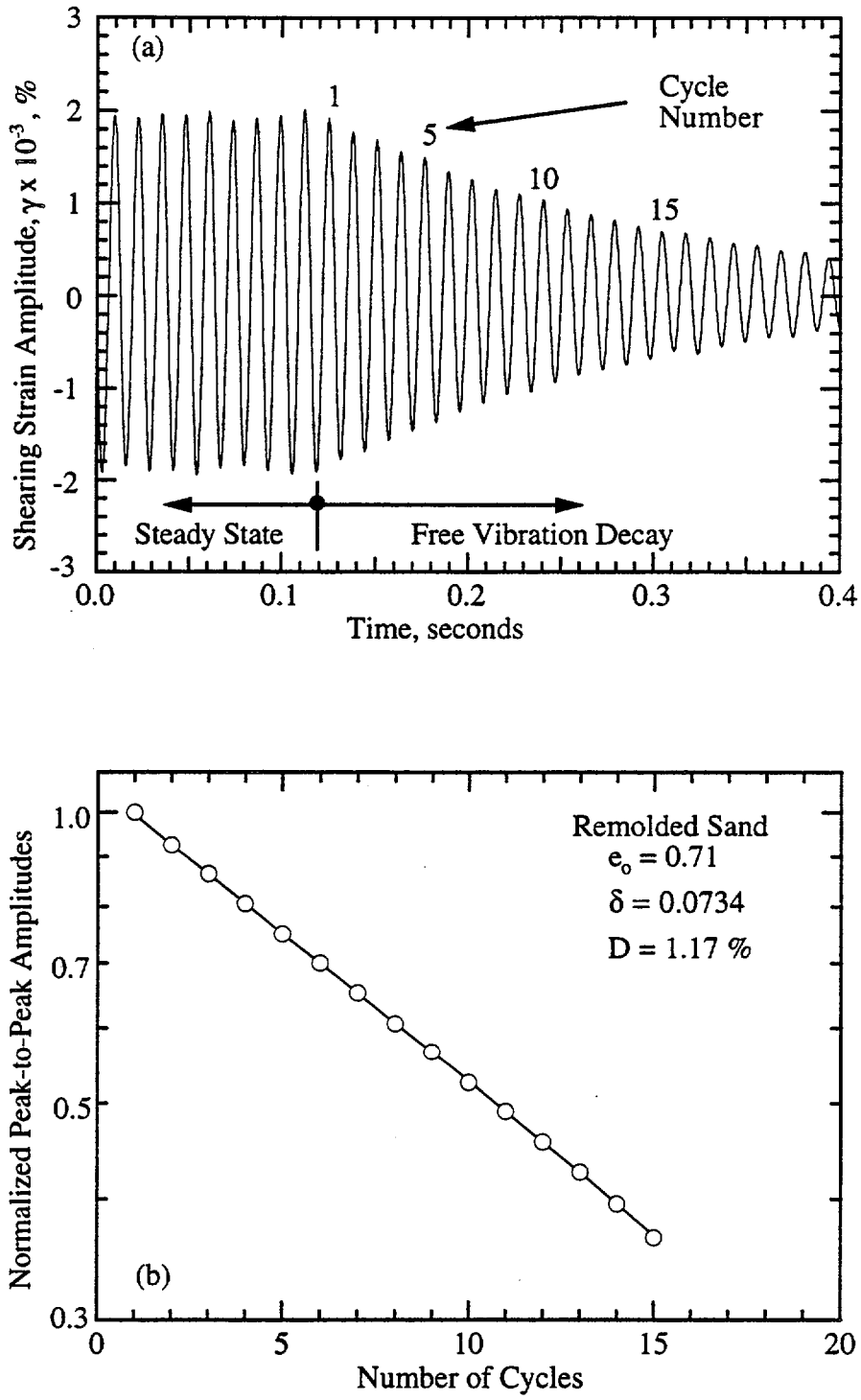

Fig. 7 Typical Free-Vibration Decay Curve (a) and Material Damping Measurement (b) in the Resonant Column Test Using Remolded Sand

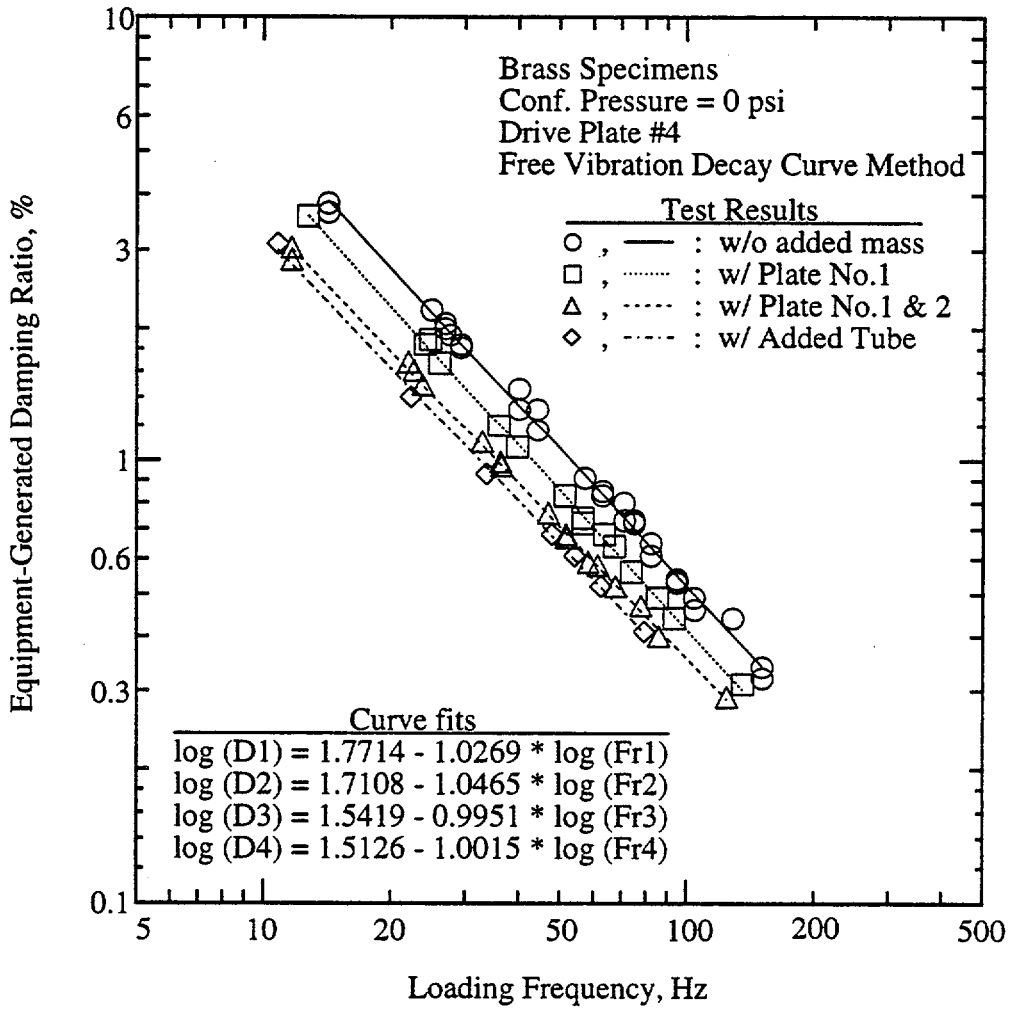

Fig. 8 Variation of the Equipment-Generated Damping Ratio Measured by Free-Vibration Decay Curve Method with Three Different Masses Added on Top of the Drive Plate No. 4

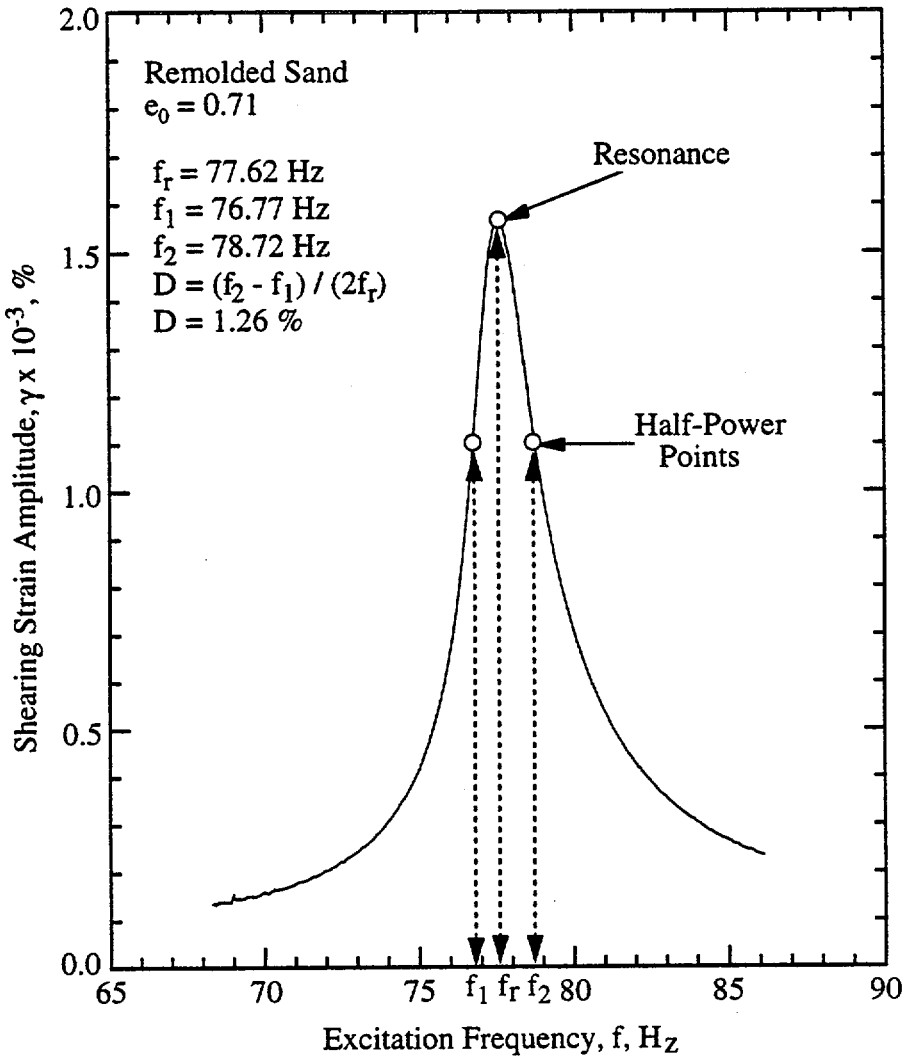

Fig. 9 Typical Material Damping Measurement from the Frequency Response Curve in the Resonant Column Test Using the Half-Power Bandwidth Method Using Remolded Sand

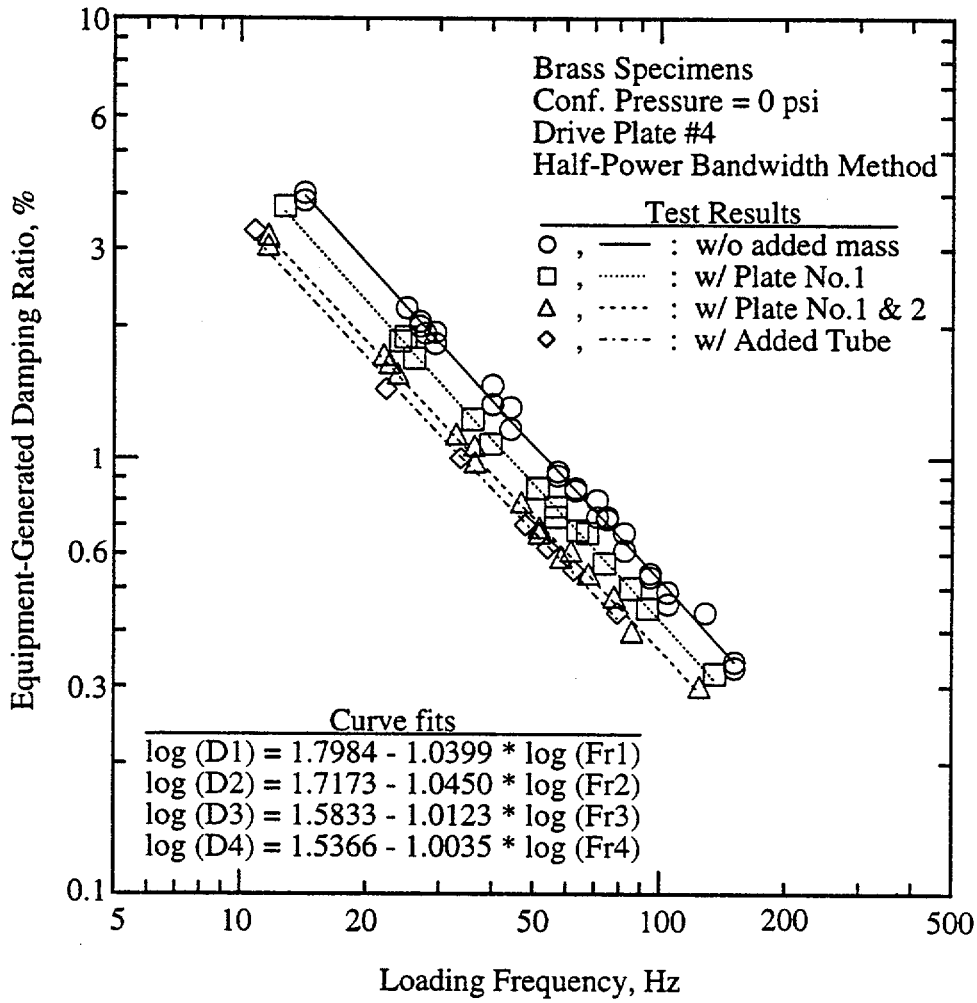

Fig. 10 Variation of the Equipment-Generated Damping Ratio Measured by Half-Power Bandwidth Method with Three Different Masses Added on top of the Drive Plate No. 4

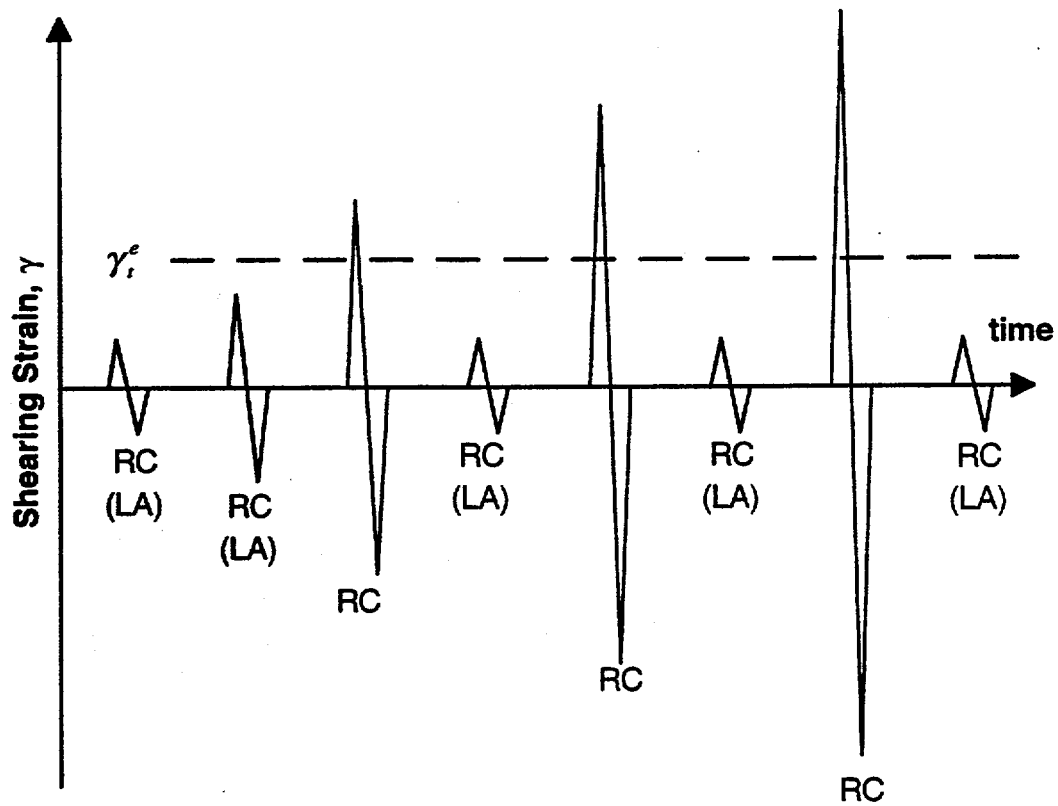

γ_t^e = elastic threshold strain; below γ_t^e, G is constant and equal to G_{max}

RC (LA) = resonant column test at low-amplitude strain

RC = resonant column test in which 500 to 1000 cycles of loading is applied during each measurement

Fig. 11 Testing Procedure Used in the Resonant Column Test to Investigate the Effects of Strain Amplitude on Shear Modulus (G) and Material Damping Ratio (D)

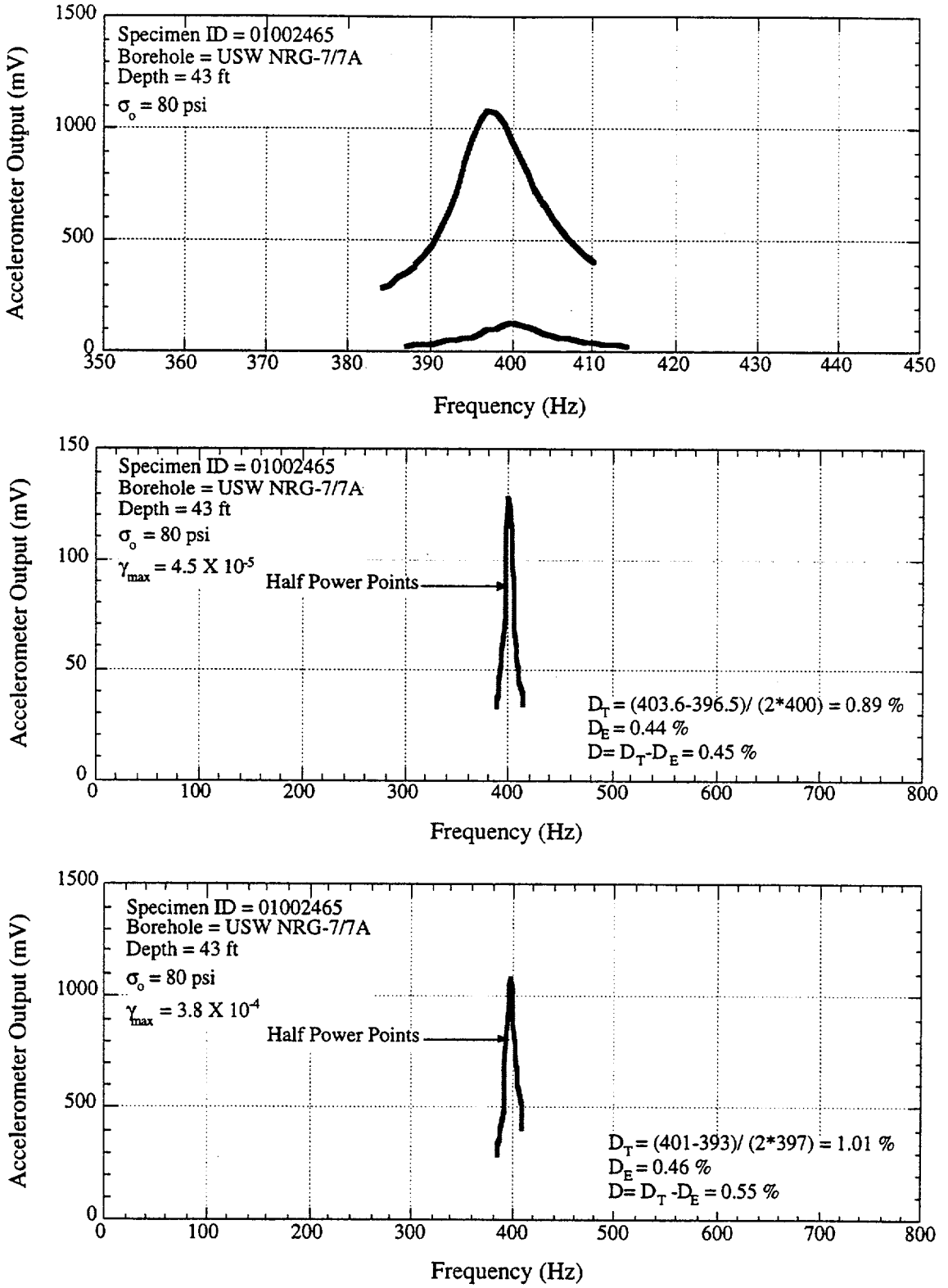

Fig. 12 Determination of Material Damping Ratio from the Half-Power Bandwidth Method

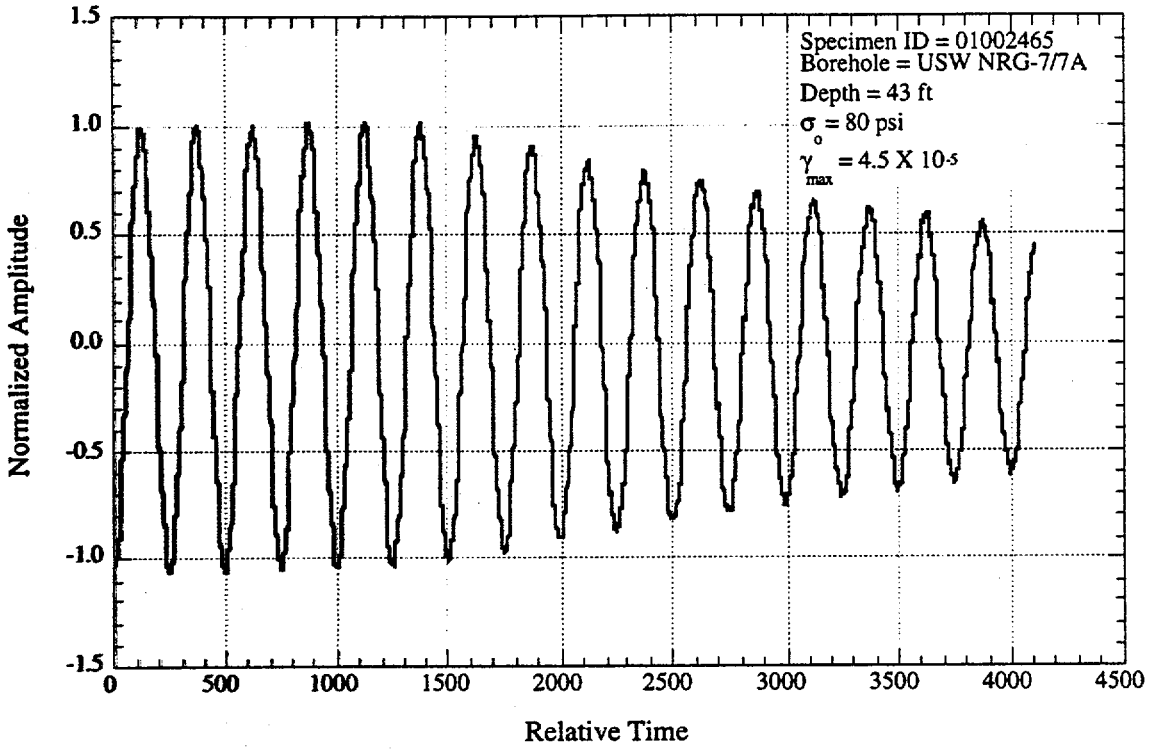

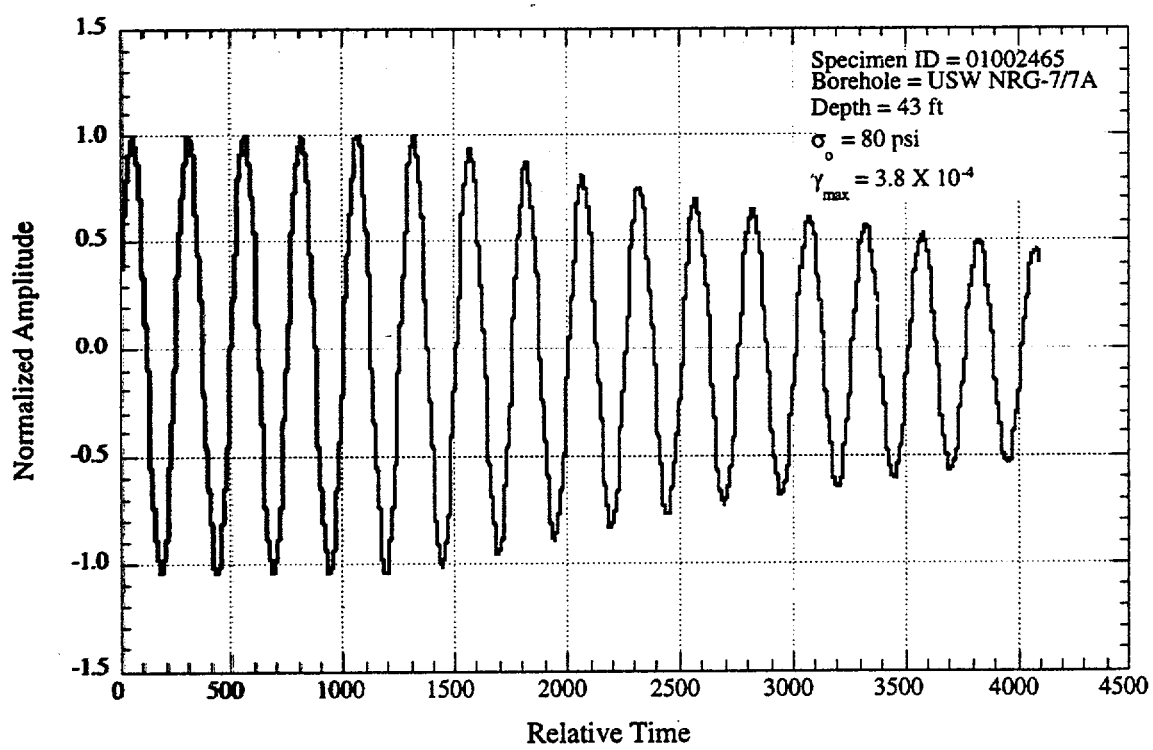

Fig. 13 Typical Free-Vibration Decay Curves at Two Strain Amplitudes

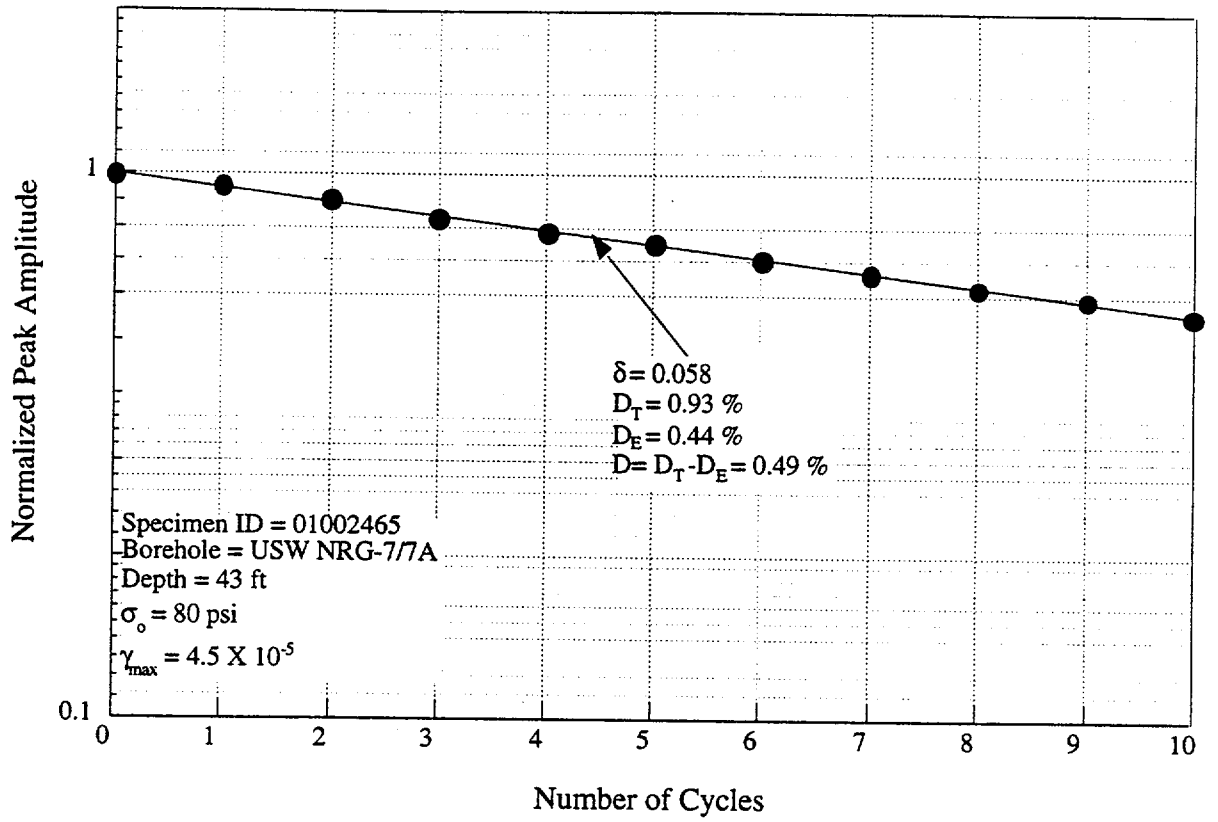

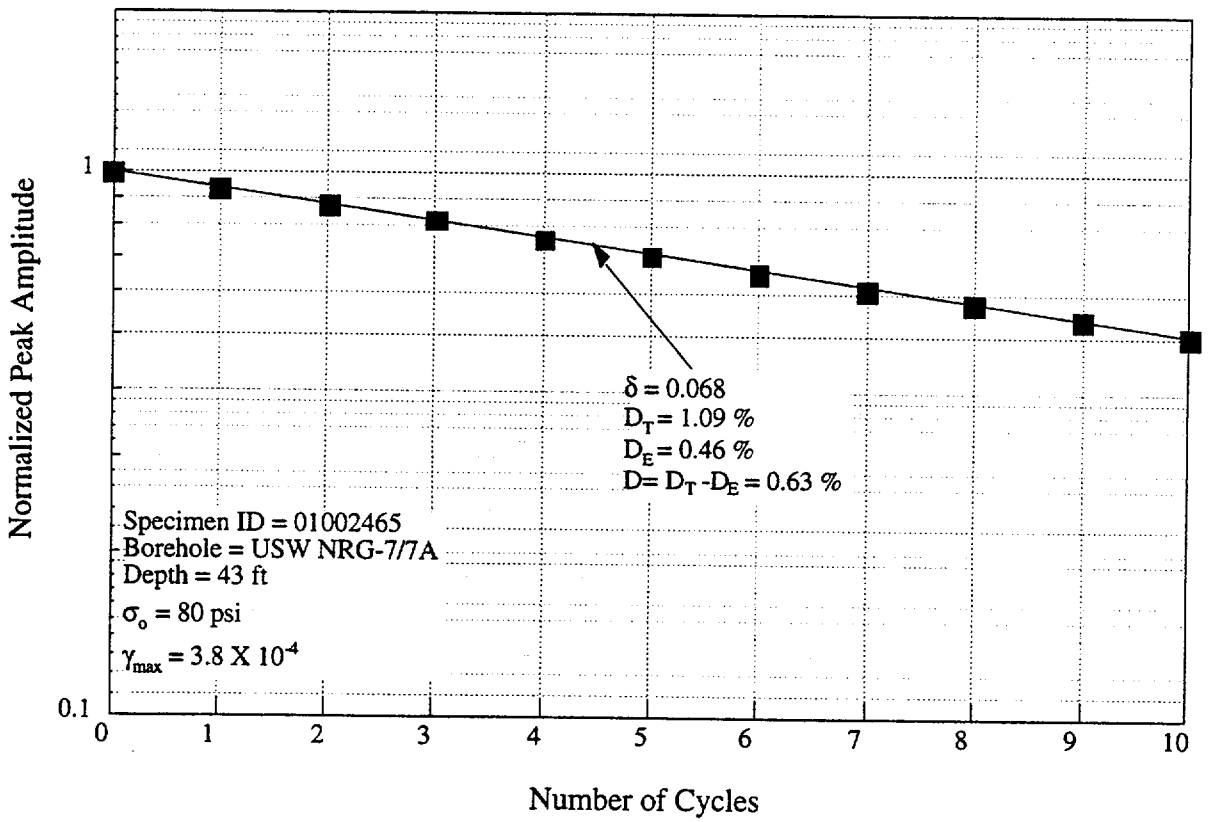

Fig. 14 Determination of Material Damping Ratio from Free-Vibration Decay Curves

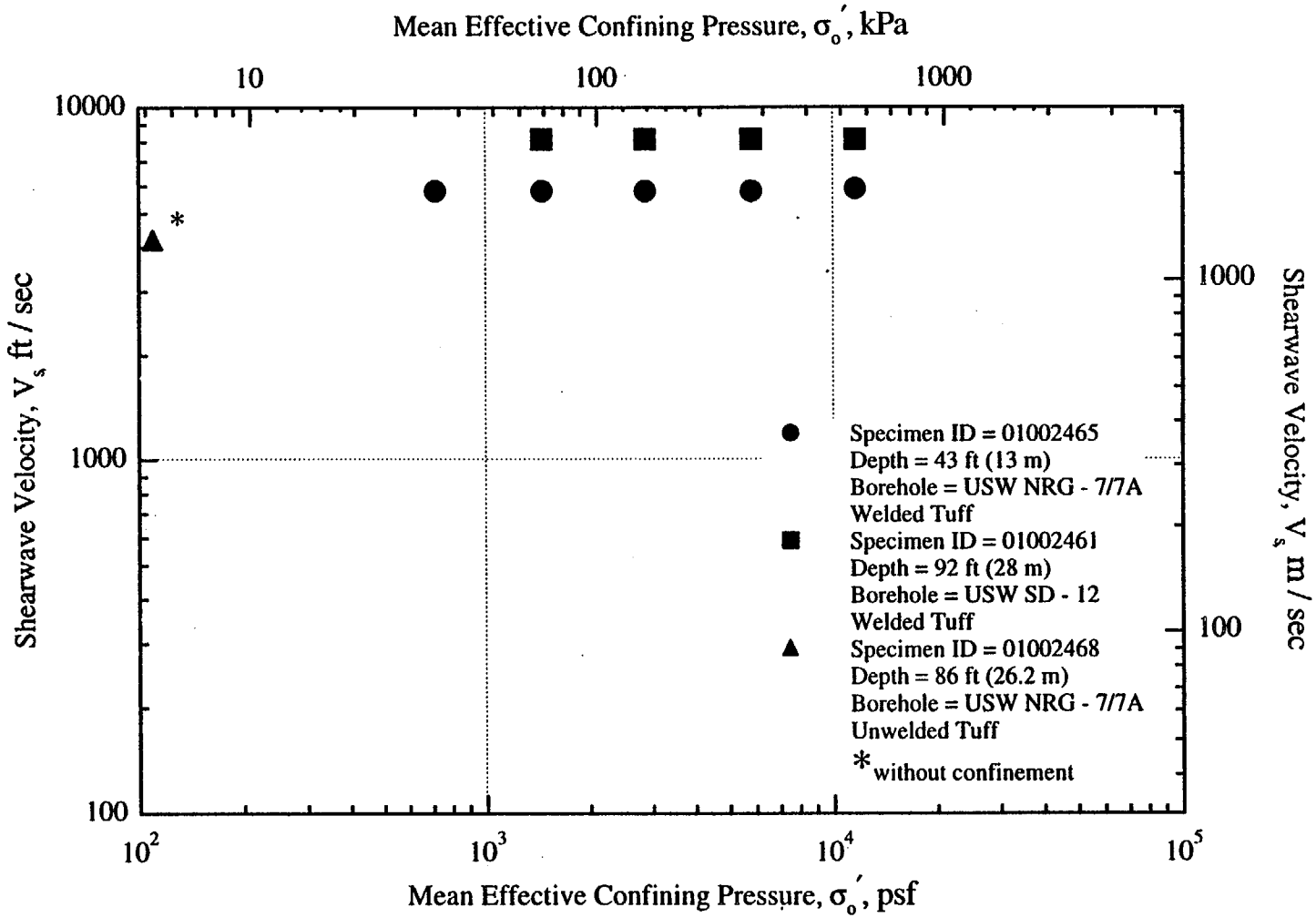

Fig. 19 Variation in Shearwave Velocity with Effective Confining Pressure from Resonant Column Tests of Intact Specimens from Yucca Mountain

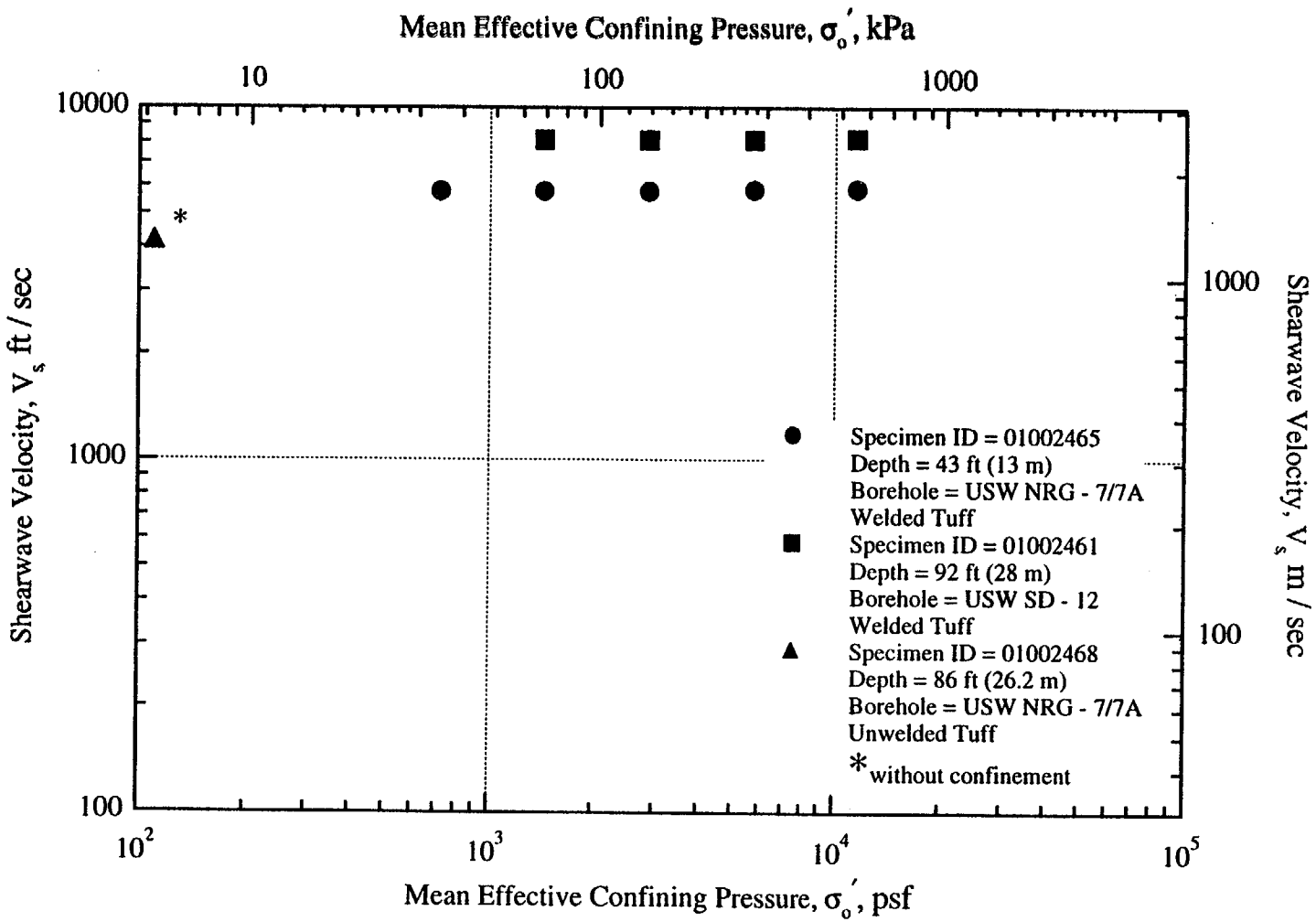

Fig. 20 Variation in Low-Amplitude Material Damping Ratio with Effective Confining Pressure from Resonant Column Tests of Intact Specimens from Yucca Mountain

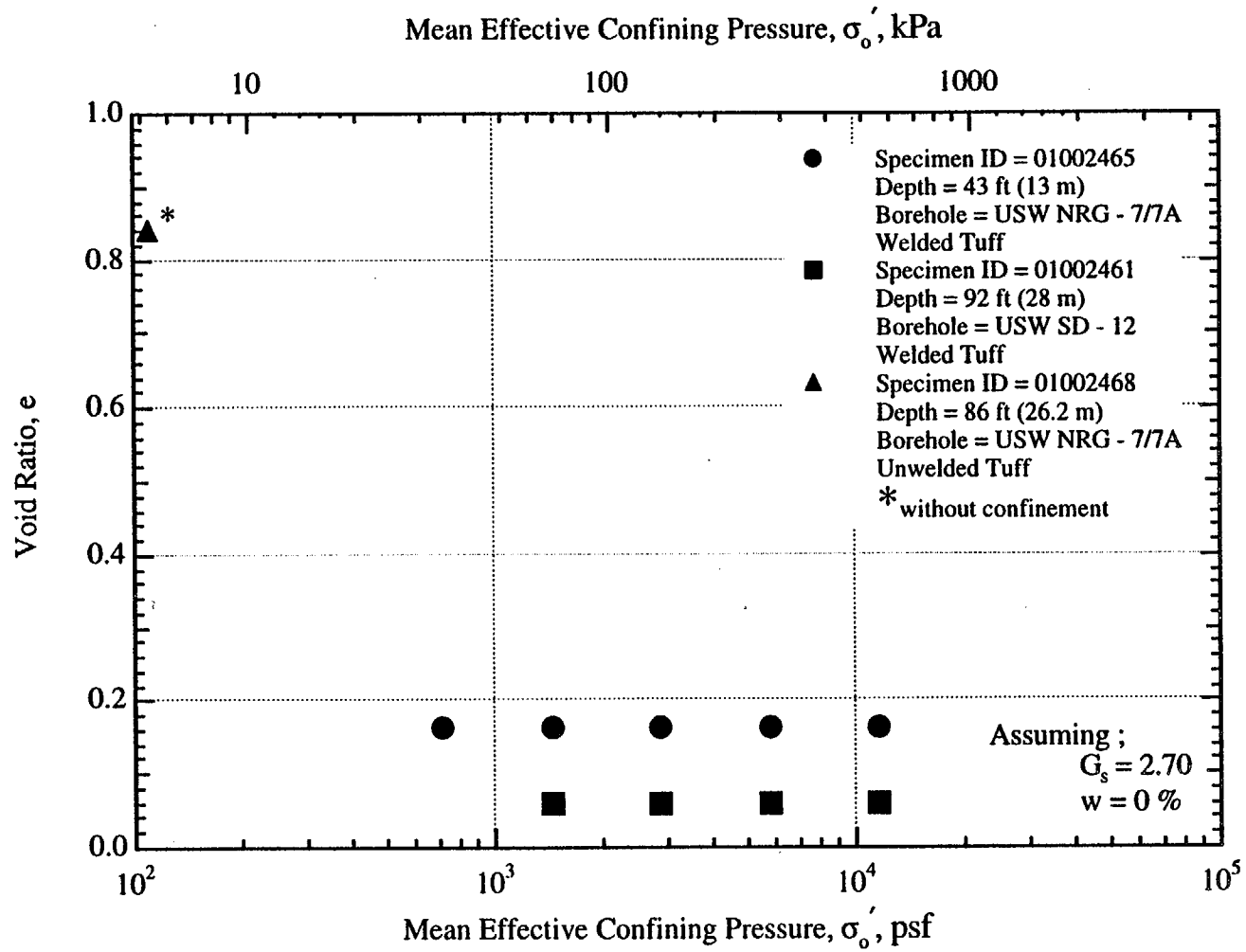

Fig. 21 Variation in Void Ratio with Effective Confining Pressure from Resonant Column Tests of Intact Specimens from Yucca Mountain

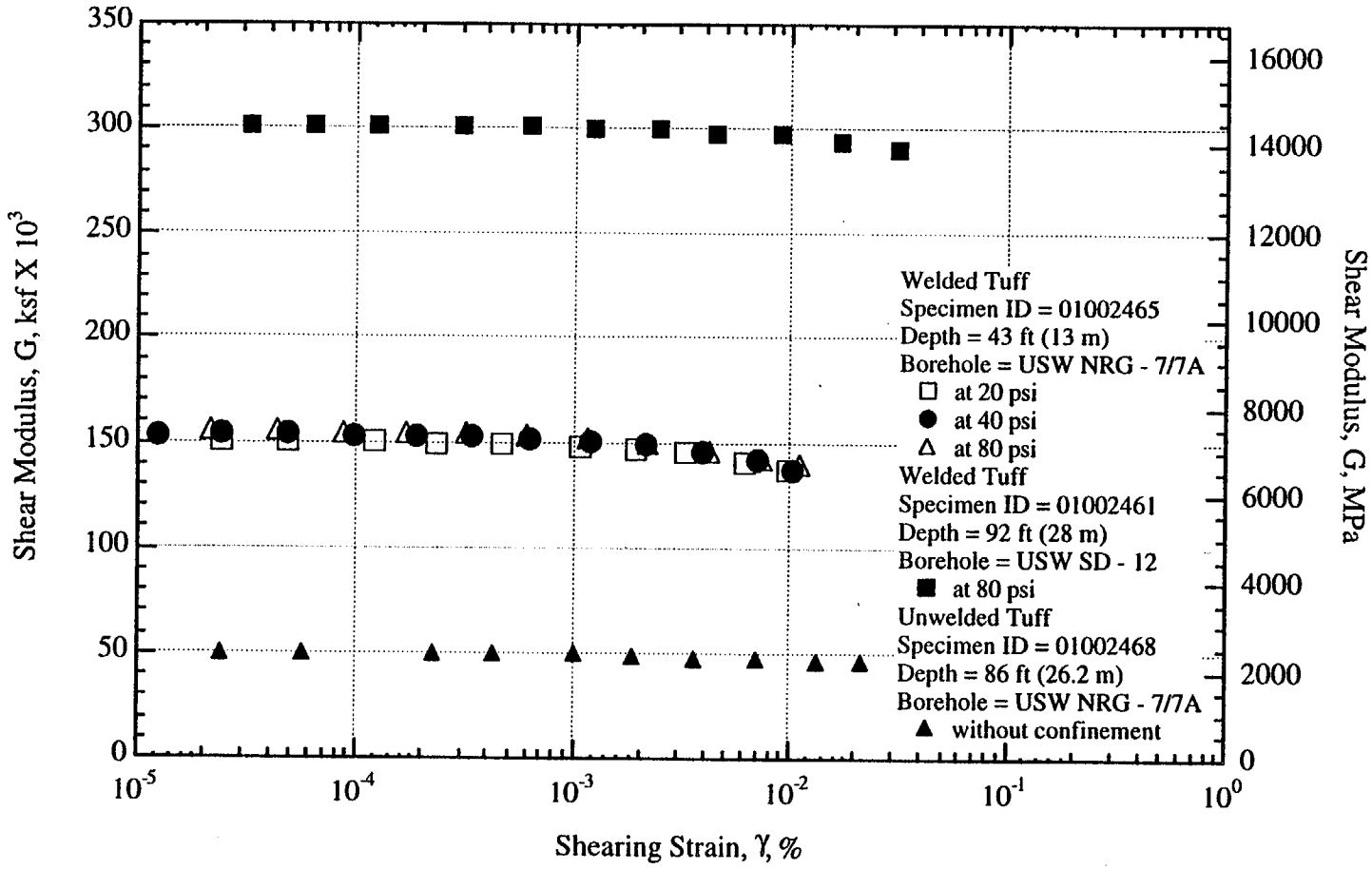

Fig. 22 Variation in Shear Modulus with Shearing Strain from Resonant Column and Torsional Shear Tests of Intact Specimens from Yucca Mountain

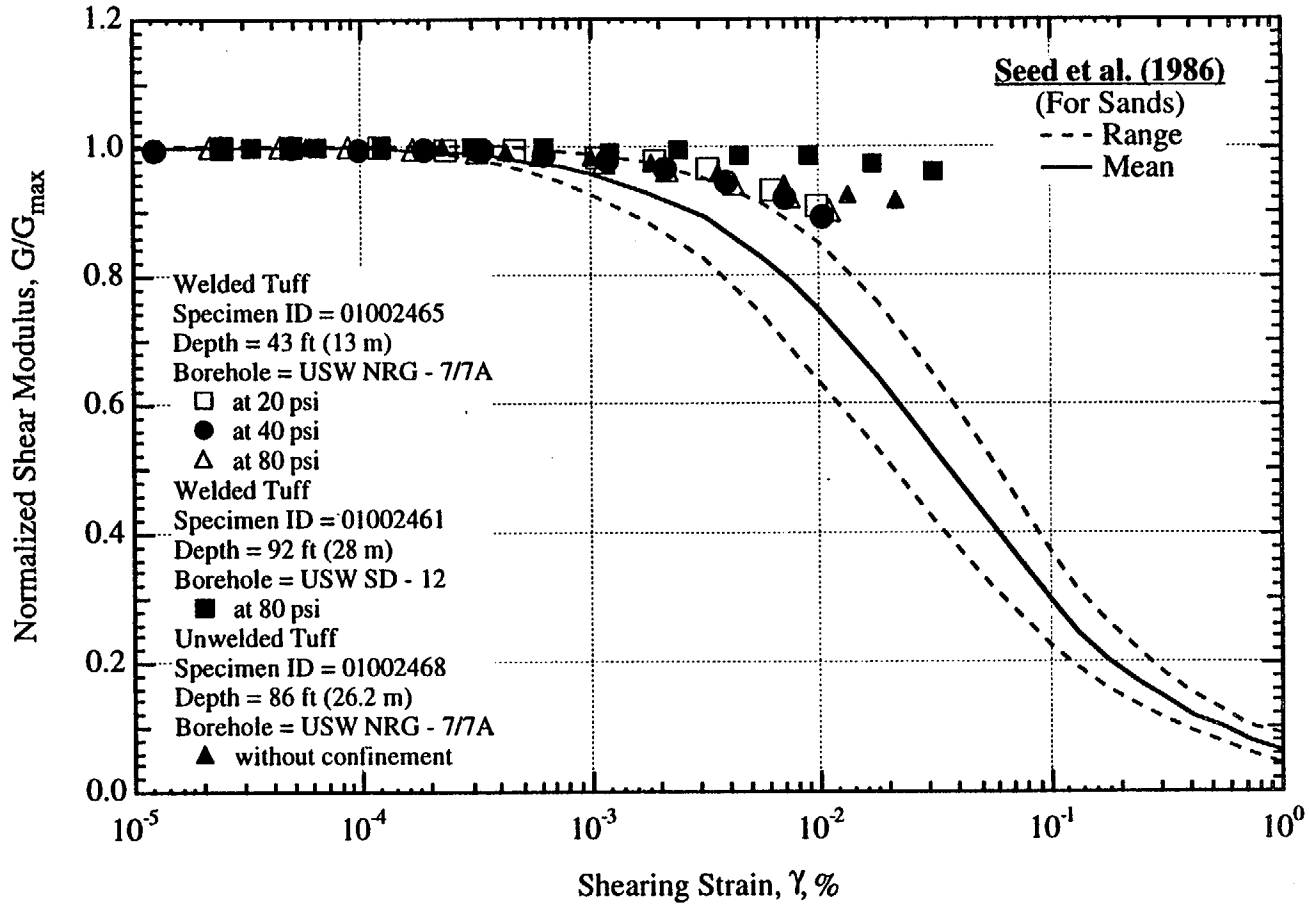

Fig. 23 Variation in Normalized Shear Modulus with Shearing Strain from Resonant Column Tests of Intact Specimens from Yucca Mountain

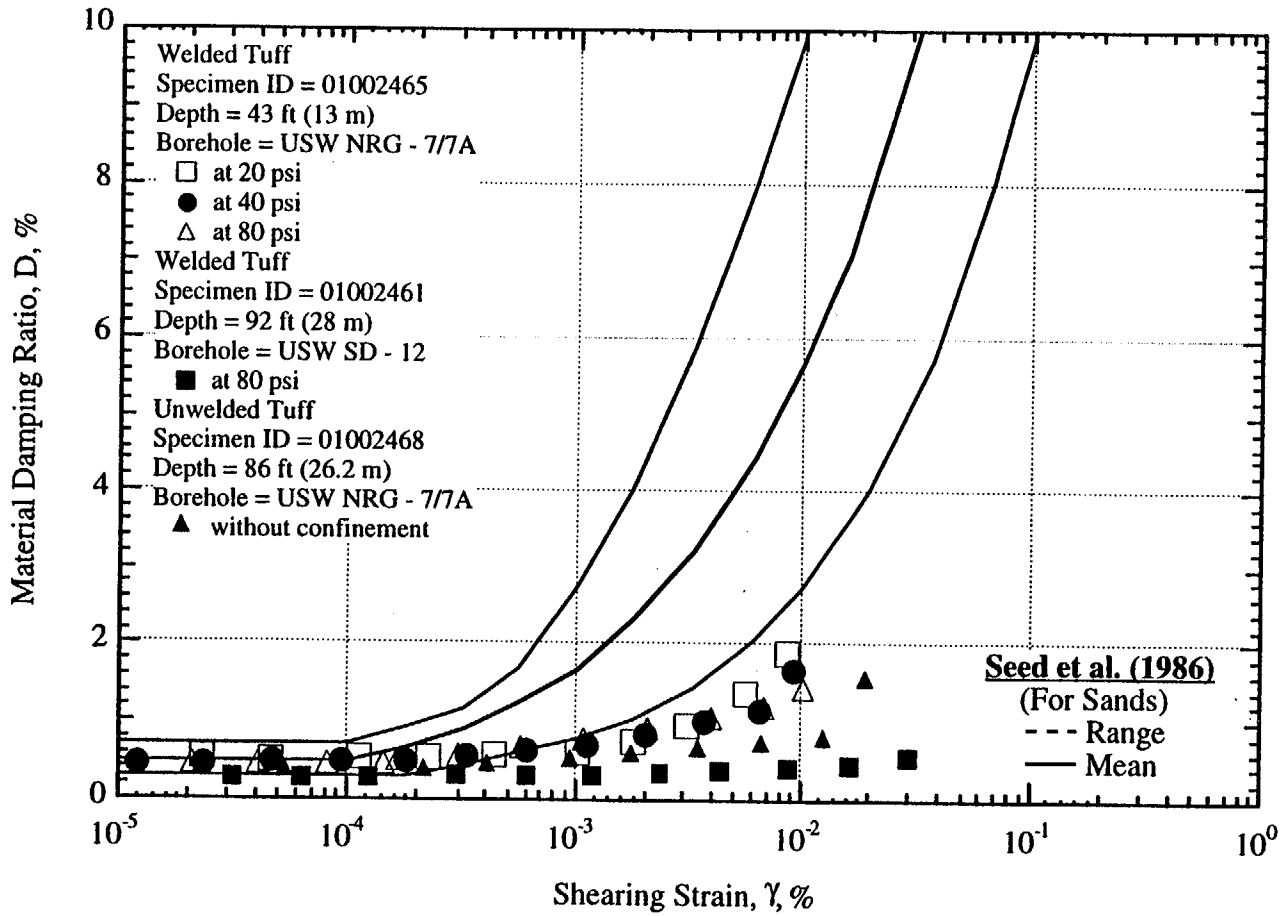

Fig. 24 Variation in Material Damping Ratio with Shearing Strain from Resonant Column Tests of Intact Specimens from Yucca Mountain

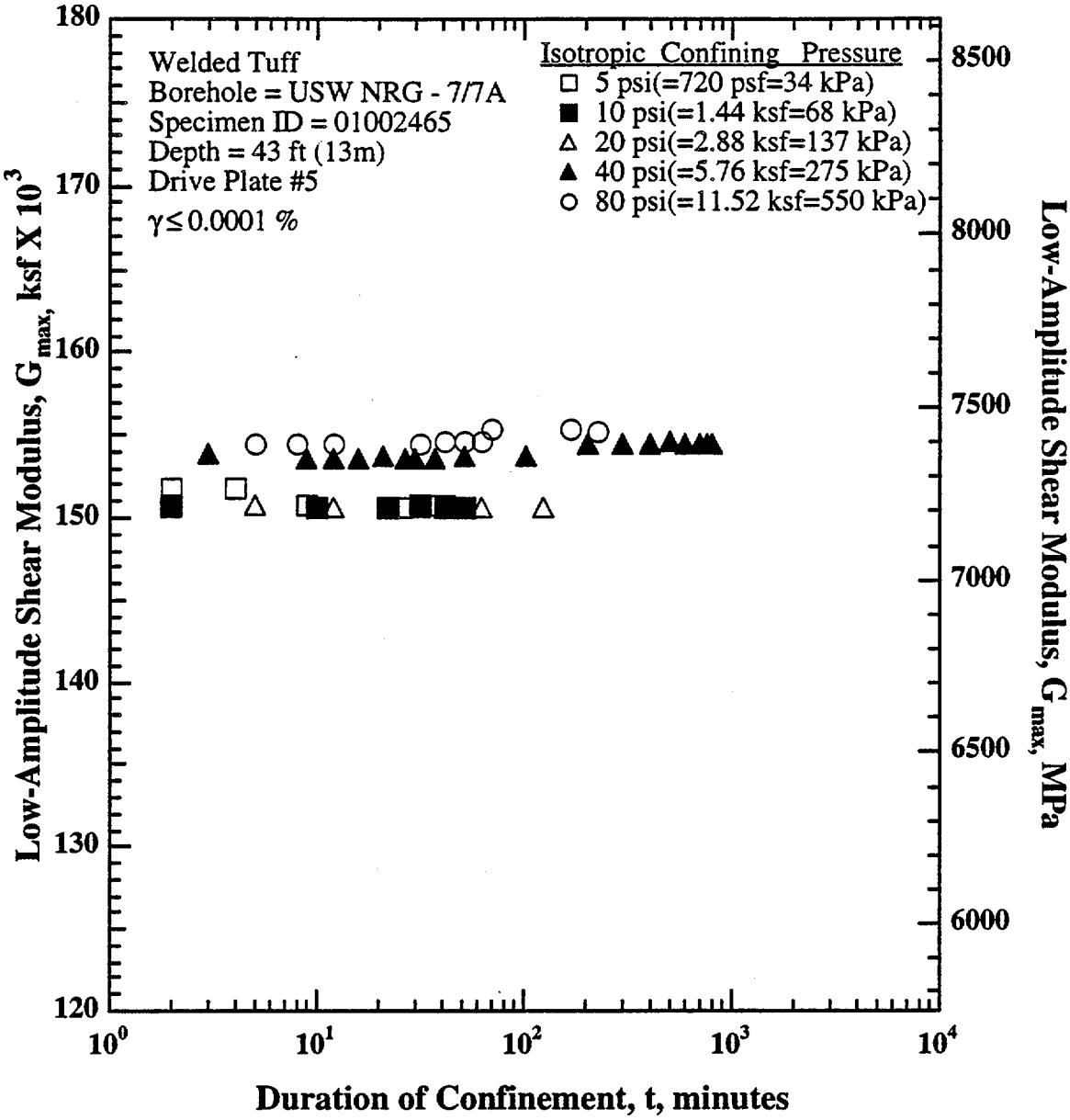

Fig. A.1 Variation in Low-Amplitude Shear Modulus with Magnitude and Duration of Isotropic Confining Pressure from Resonant Column Testing of Specimen 01002465 from Borehole USW NRG - 7/7A; Depth = 43 ft (13 m)

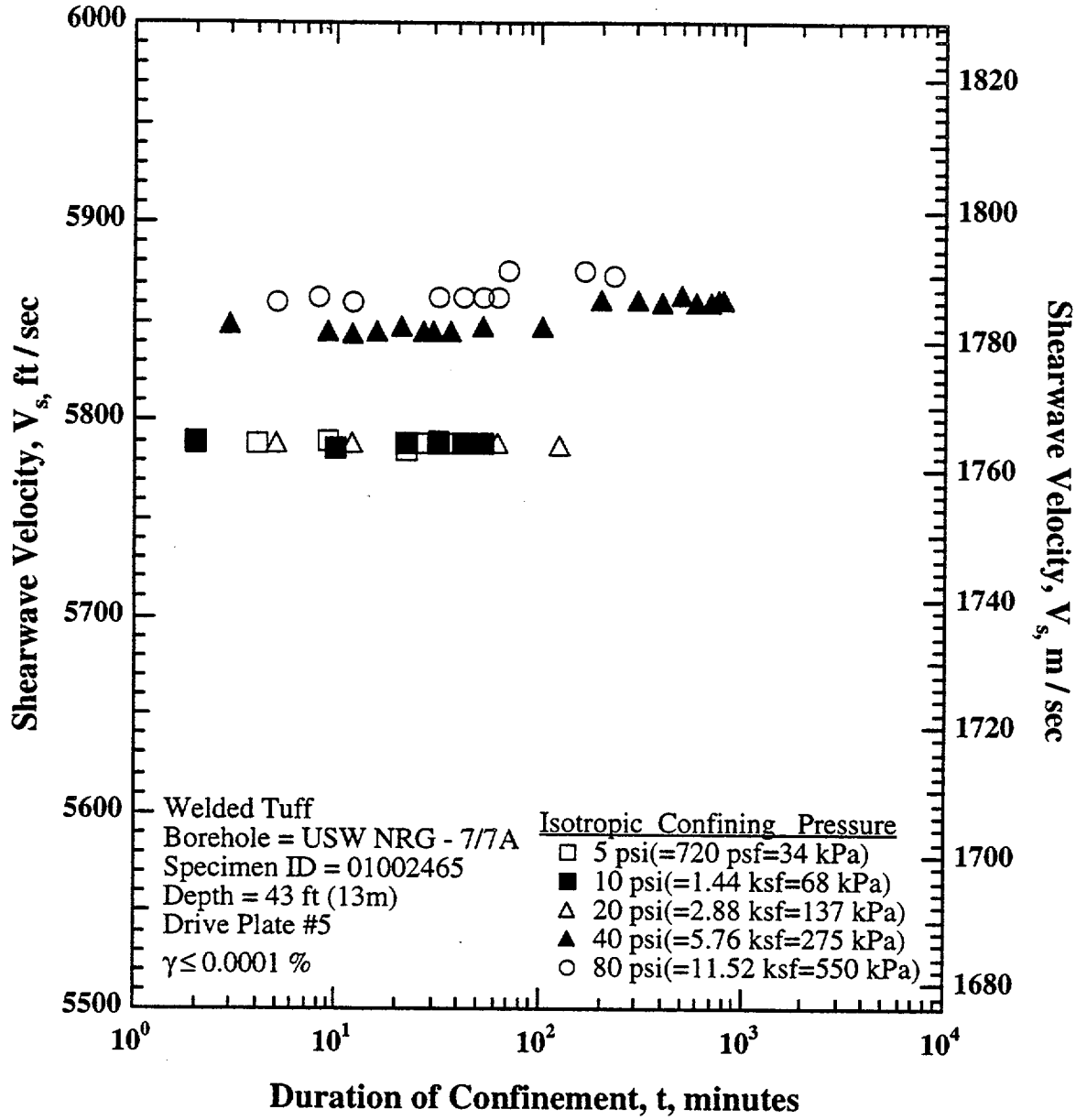

Fig. A.2 Variation in Shear Wave Velocity with Magnitude and Duration of Isotropic Confining Pressure from Resonant Column Testing of Specimen 01002465 from Borehole USW NRG - 7/7A; Depth = 43 ft (13 m)

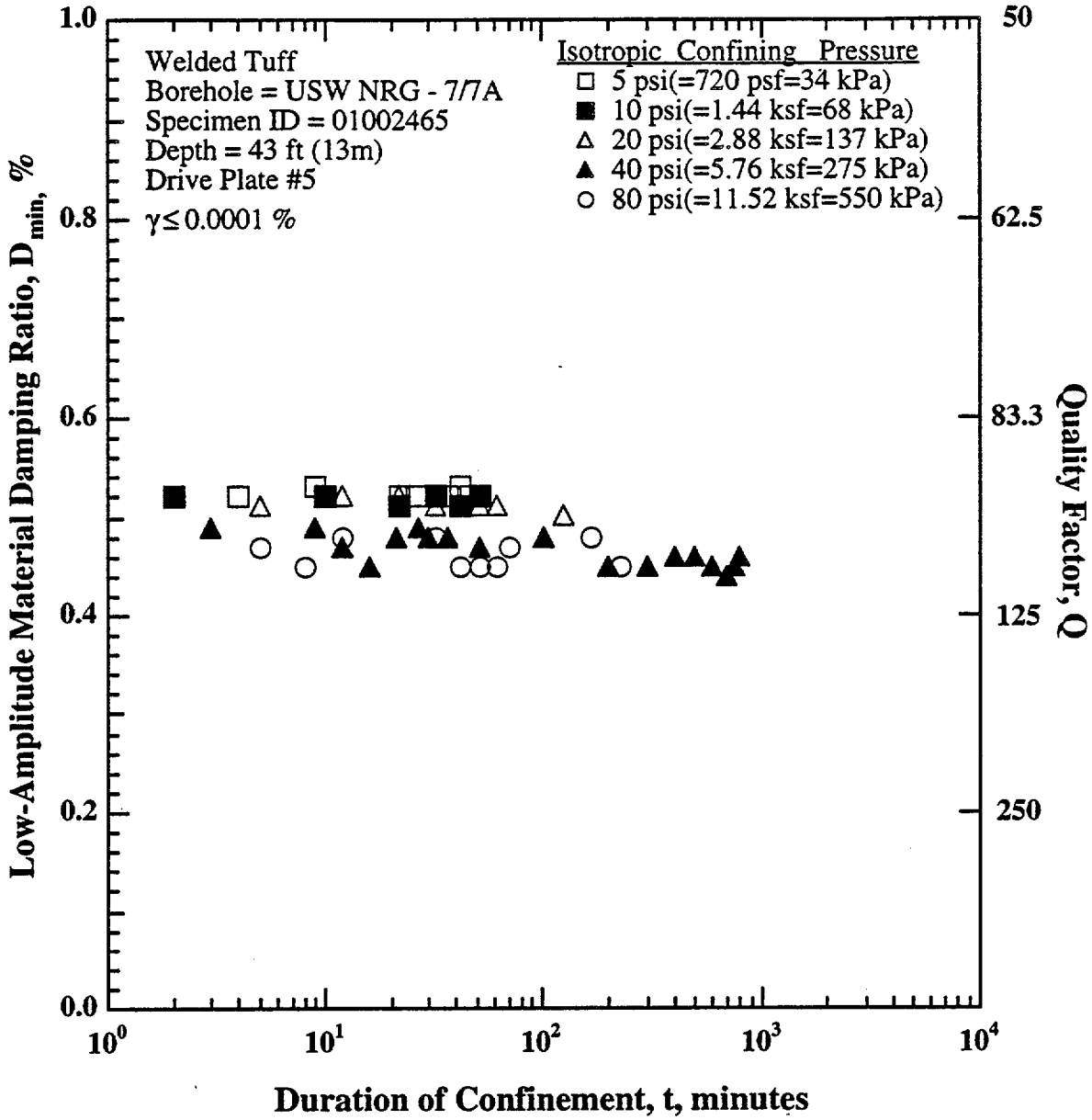

Fig. A.3 Variation in Low-Amplitude Material Damping Ratio with Magnitude and Duration of Isotropic Confining Pressure from Resonant Column Testing of Specimen 01002465 from Borehole USW NRG - 7/7A; Depth = 43 ft (13 m)

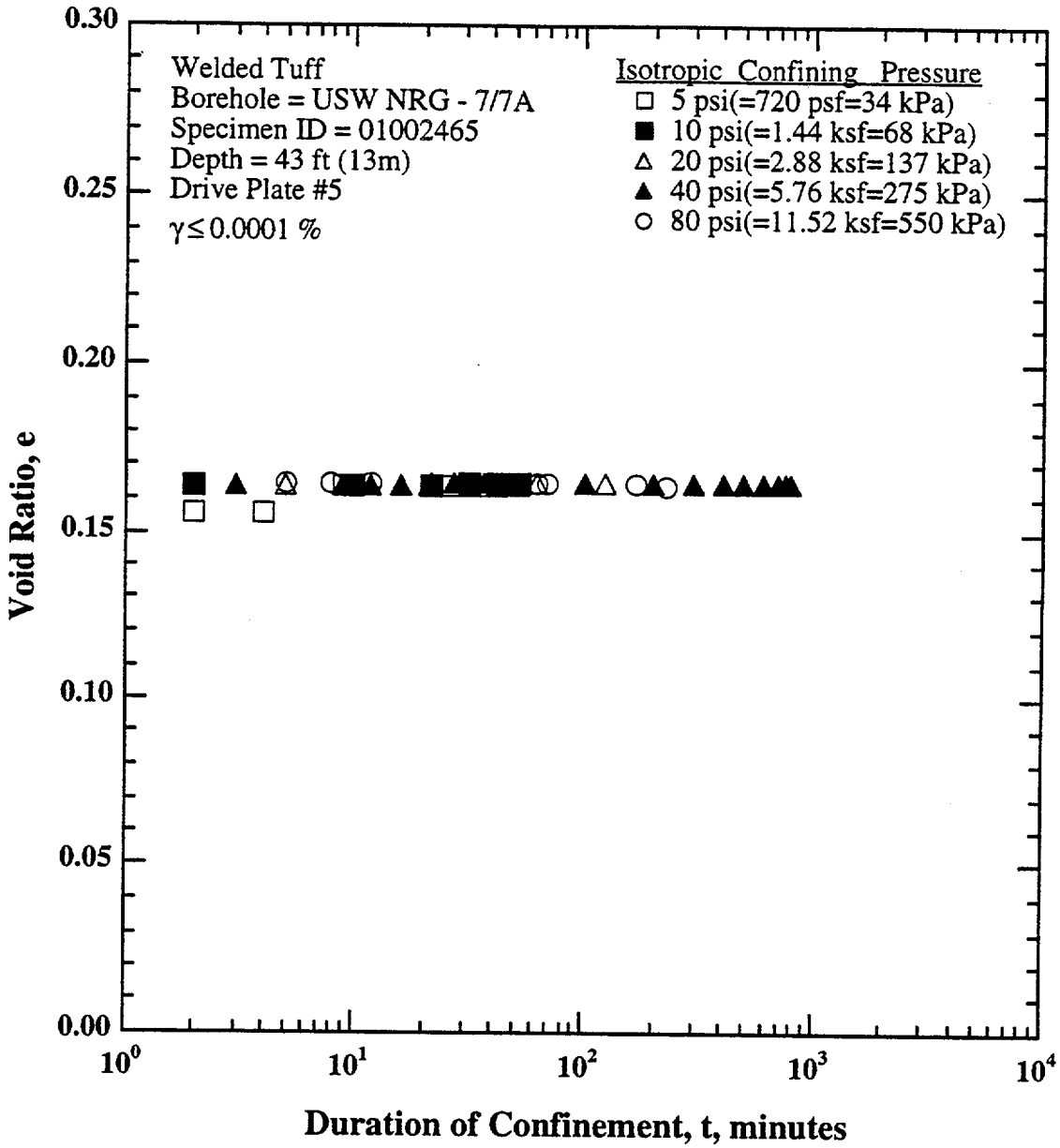

Fig. A.4 Variation in Void Ratio with Magnitude and Duration of Isotropic Confining Pressure from Resonant Column Testing of Specimen 01002465 from Borehole USW NRG - 7/7A; Depth = 43 ft (13 m)

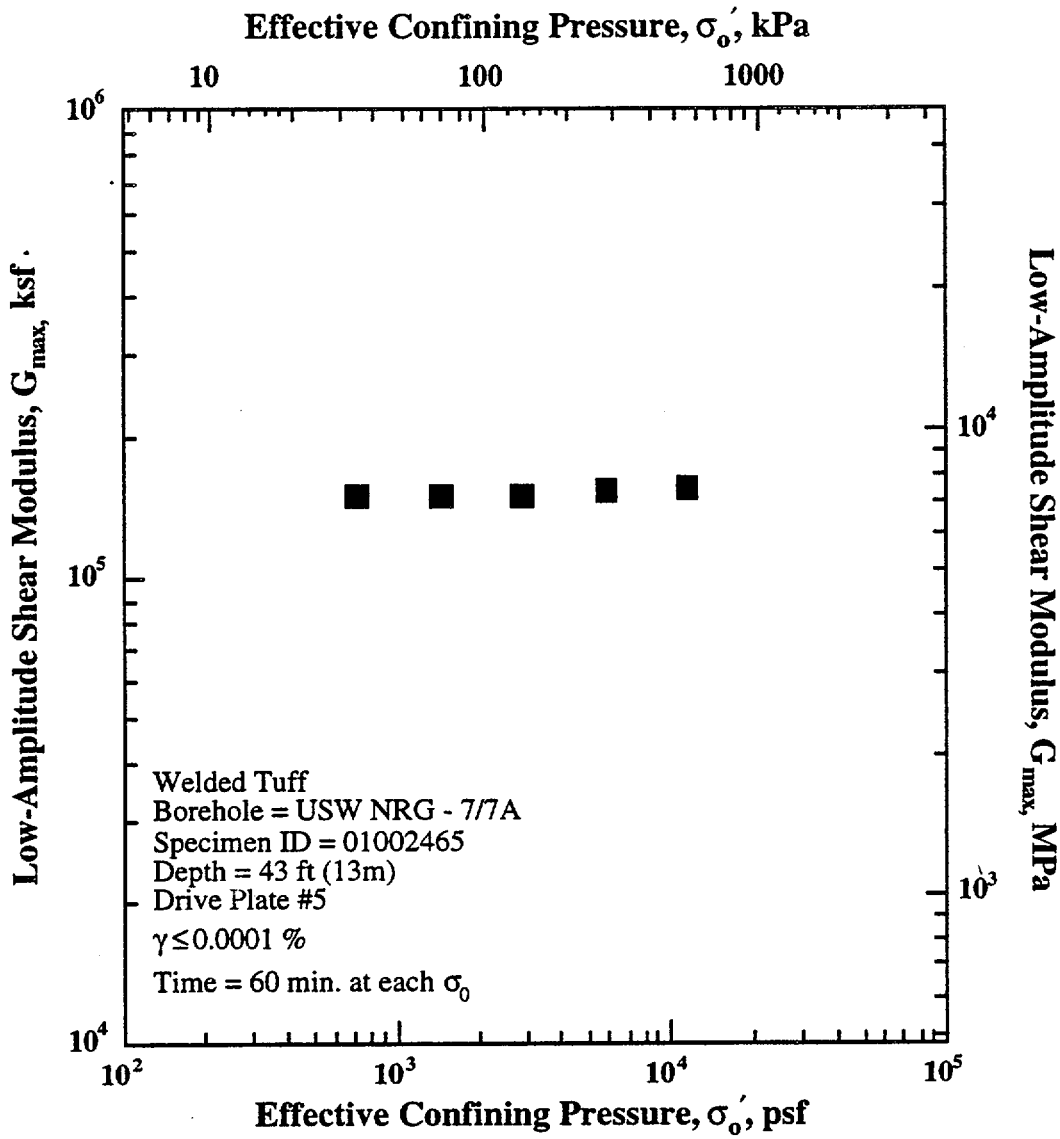

Fig. A.5 Variation in Low-Amplitude Shear Modulus with Effective Confining Pressure from Resonant Column Testing of Specimen 01002465 from Borehole USW NRG - 7/7A; Depth = 43 ft (13 m)

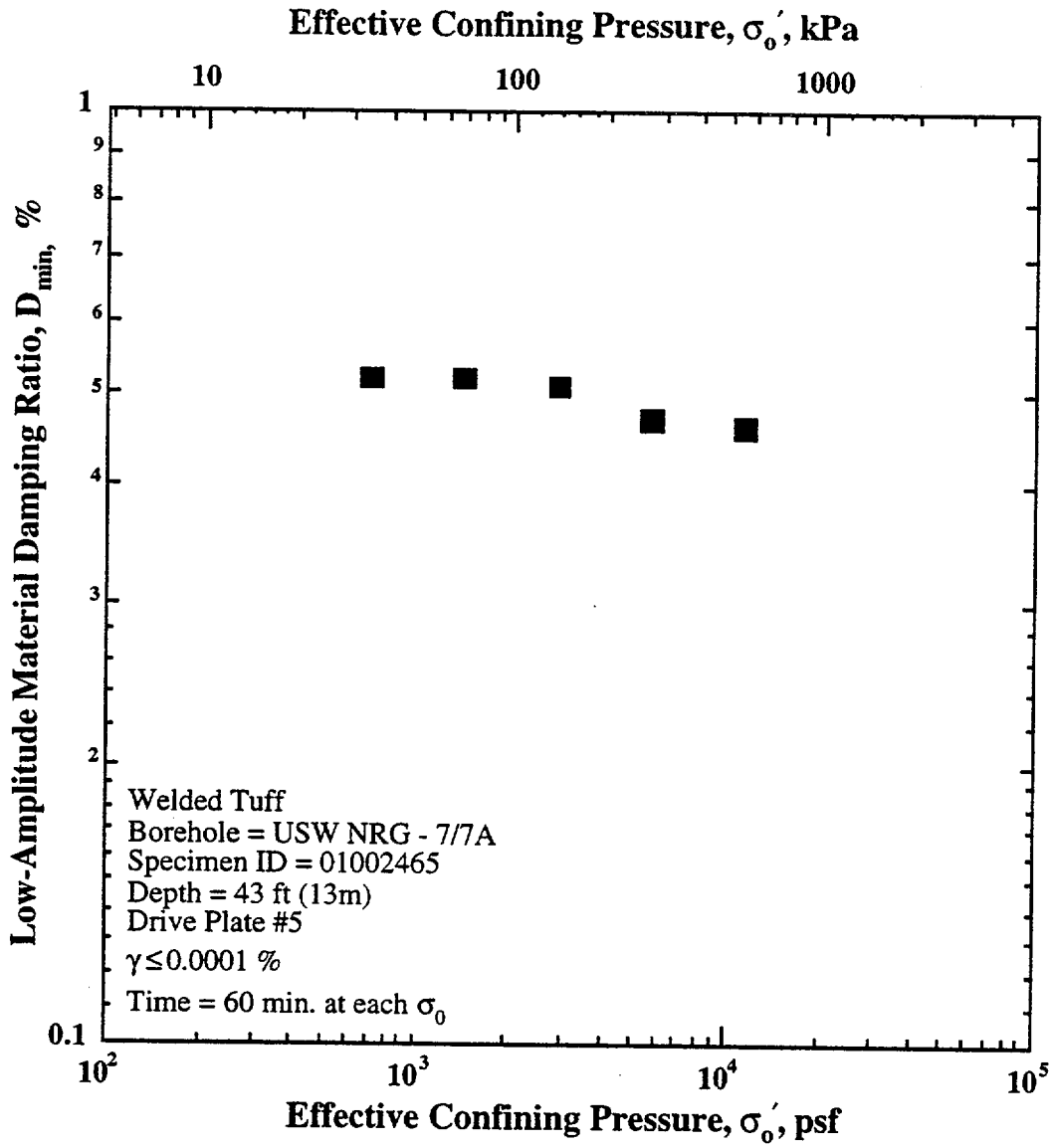

Fig. A.6 Variation in Low-Amplitude Material Damping Ratio with Effective Confining Pressure from Resonant Column Testing of Specimen 01002465 from Borehole USW NRG - 7/7A; Depth = 43 ft (13 m)

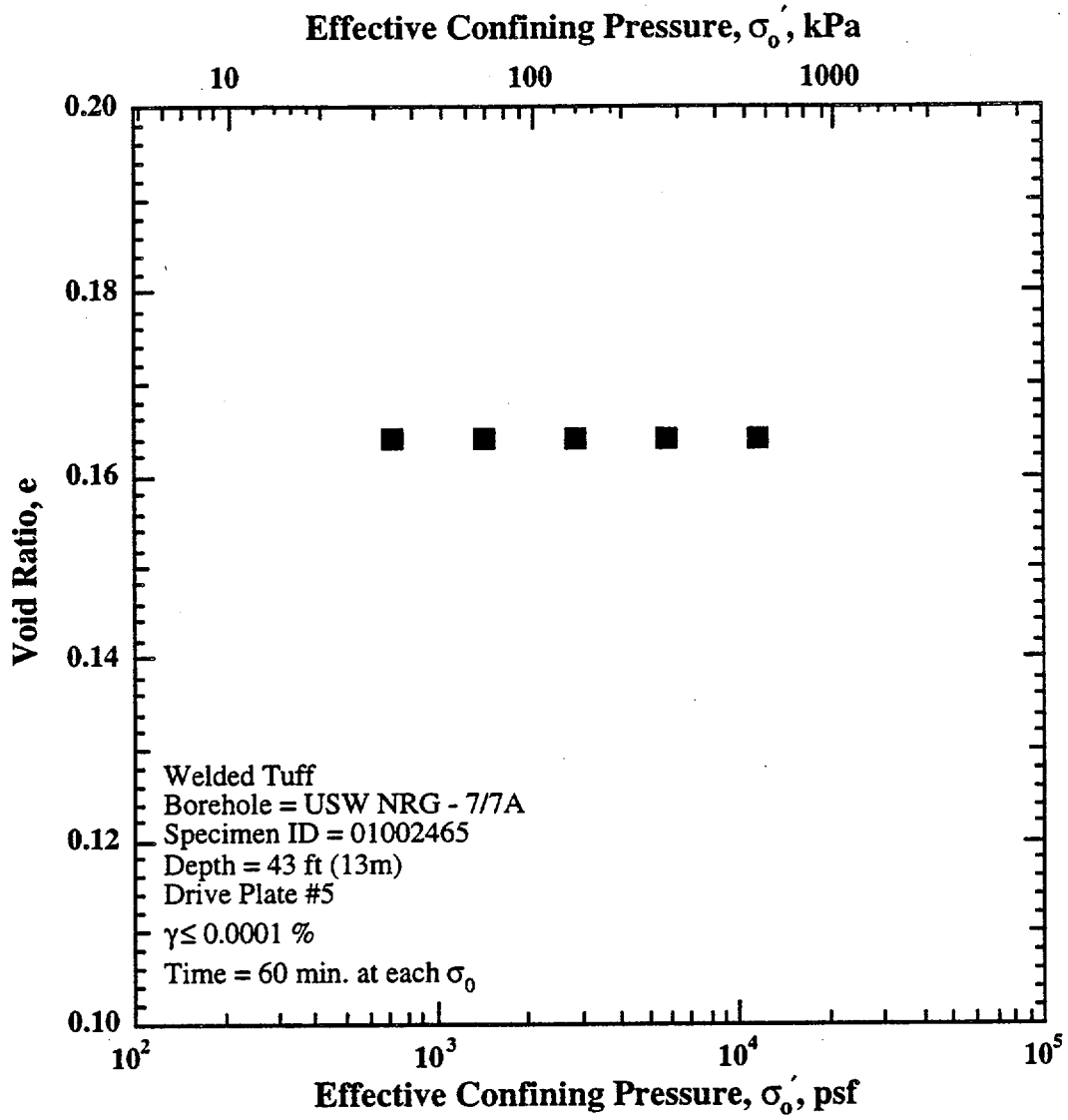

Fig. A.7 Variation in Void Ratio with Effective Confining Pressure from Resonant Column Testing of Specimen 01002465 from Borehole USW NRG - 7/7A; Depth = 43 ft (13 m)

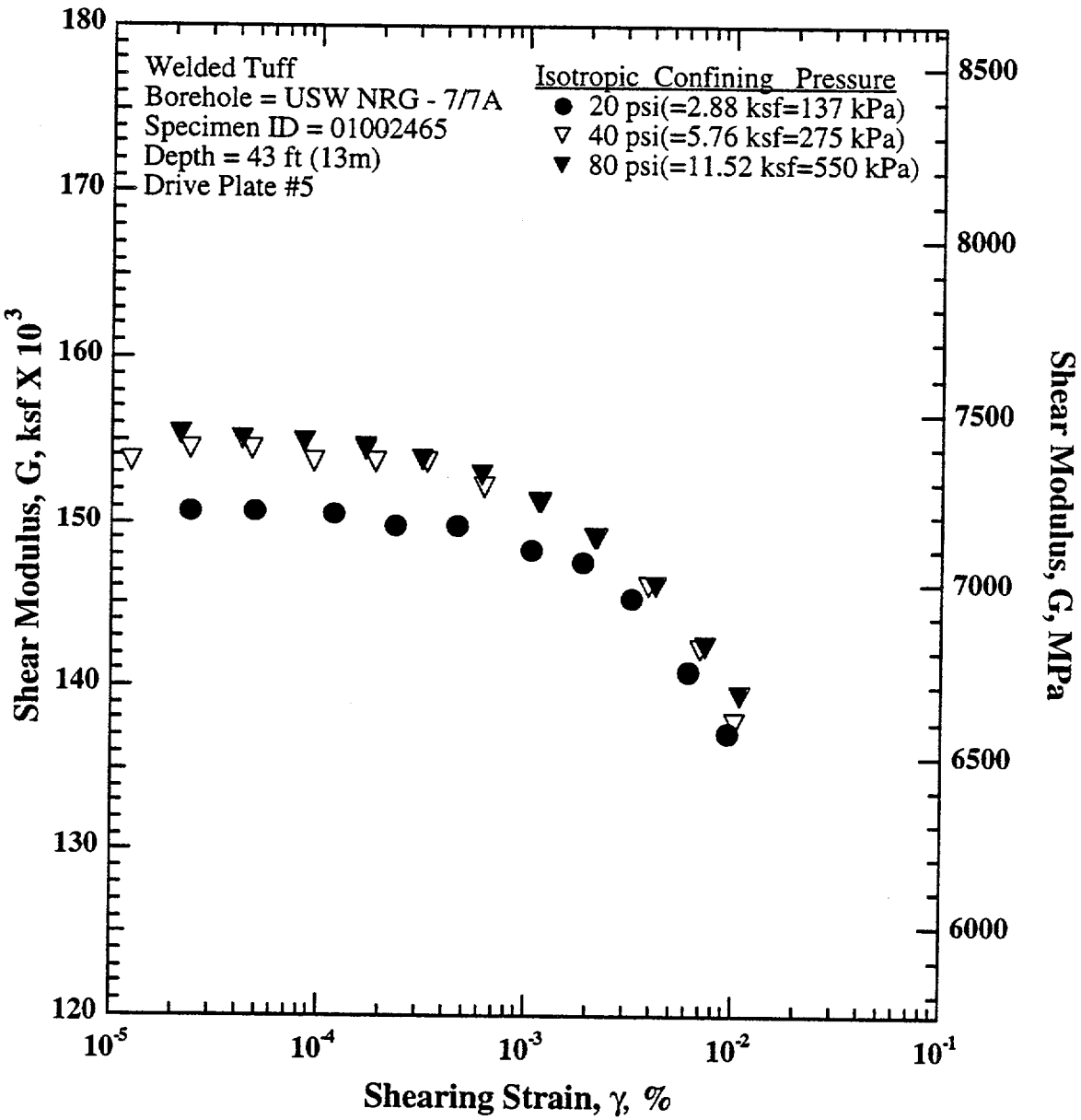

Fig. A.8 Variation in Shear Modulus with Shearing Strain and Effective Confining Pressure from Resonant Column Testing of Specimen 01002465 from Borehole USW NRG - 7/7A; Depth = 43 ft (13 m)

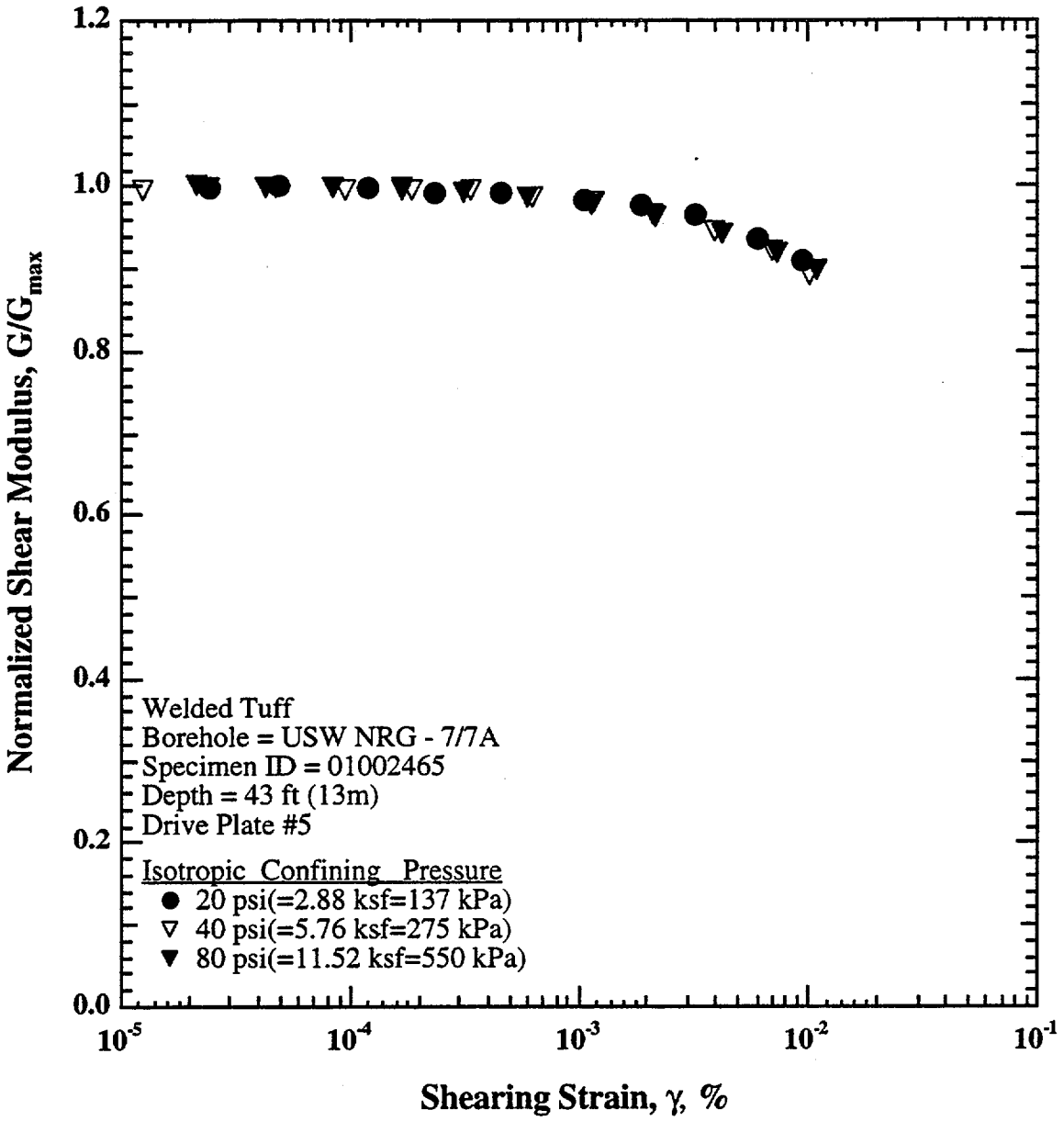

Fig. A.9 Variation in Normalized Shear Modulus with Shearing Strain and Effective Confining Pressure from Resonant Column Testing of Specimen 01002465 from Borehole USW NRG - 7/7A; Depth = 43 ft (13 m)

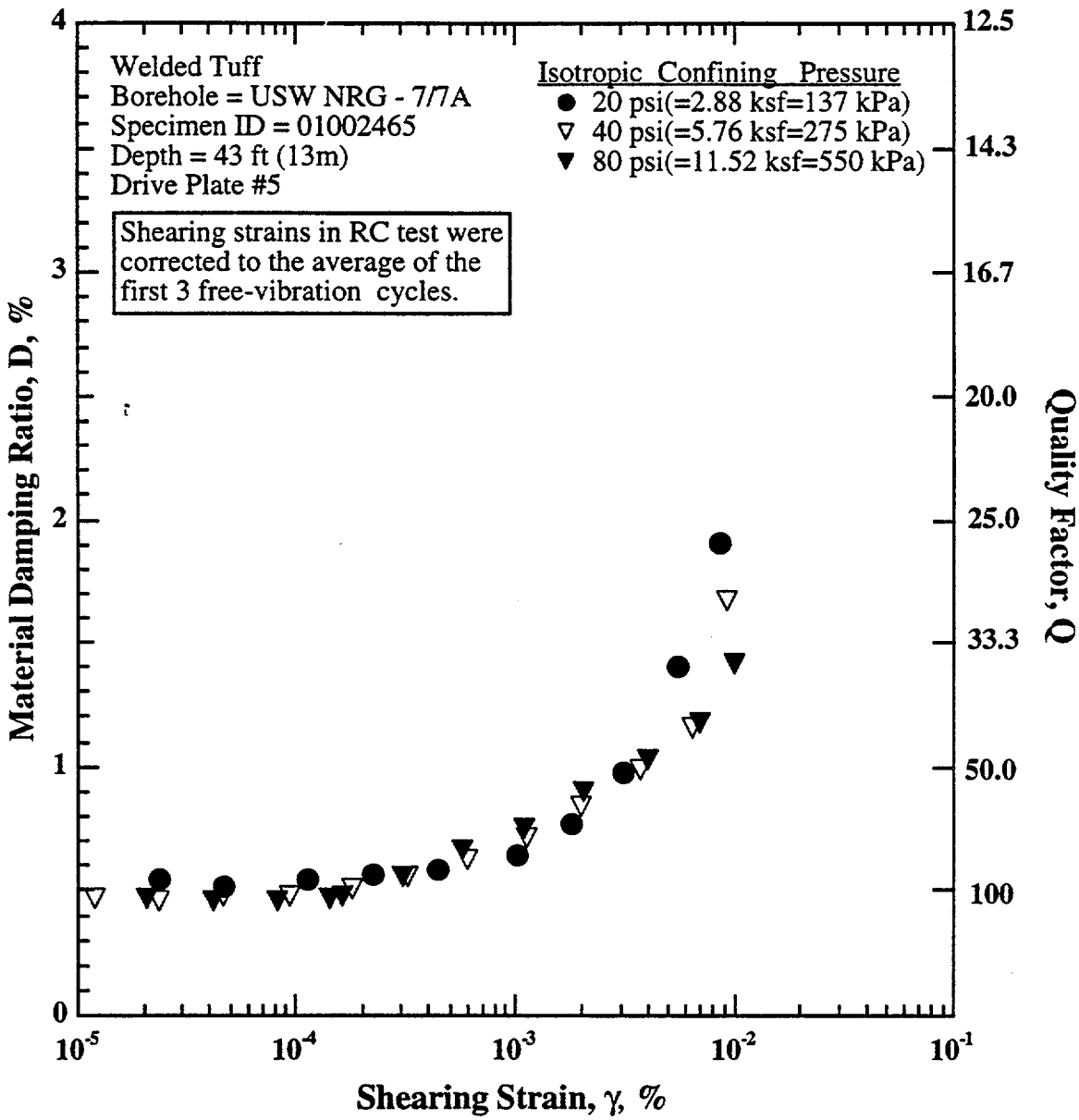

Fig. A.10 Variation in Material Damping Ratio with Shearing Strain and Effective Confining Pressure from Resonant Column Testing of Specimen 01002465 from Borehole USW NRG - 7/7A; Depth = 43 ft (13 m)

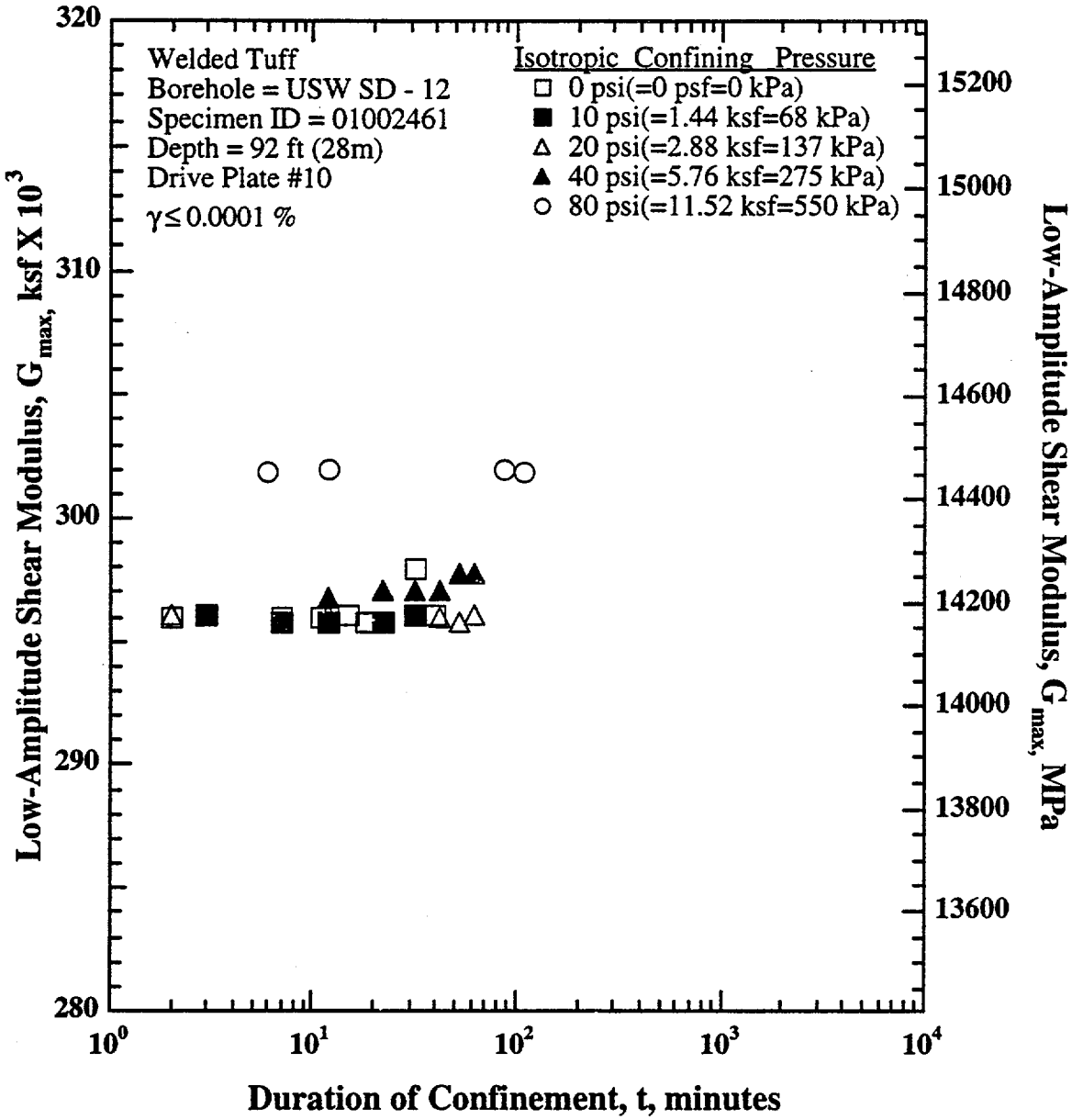

Fig. B.1 Variation in Low-Amplitude Shear Modulus with Magnitude and Duration of Isotropic Confining Pressure from Resonant Column Testing of Specimen 01002461 from Borehole USW SD - 12; Depth = 92 ft (28 m)

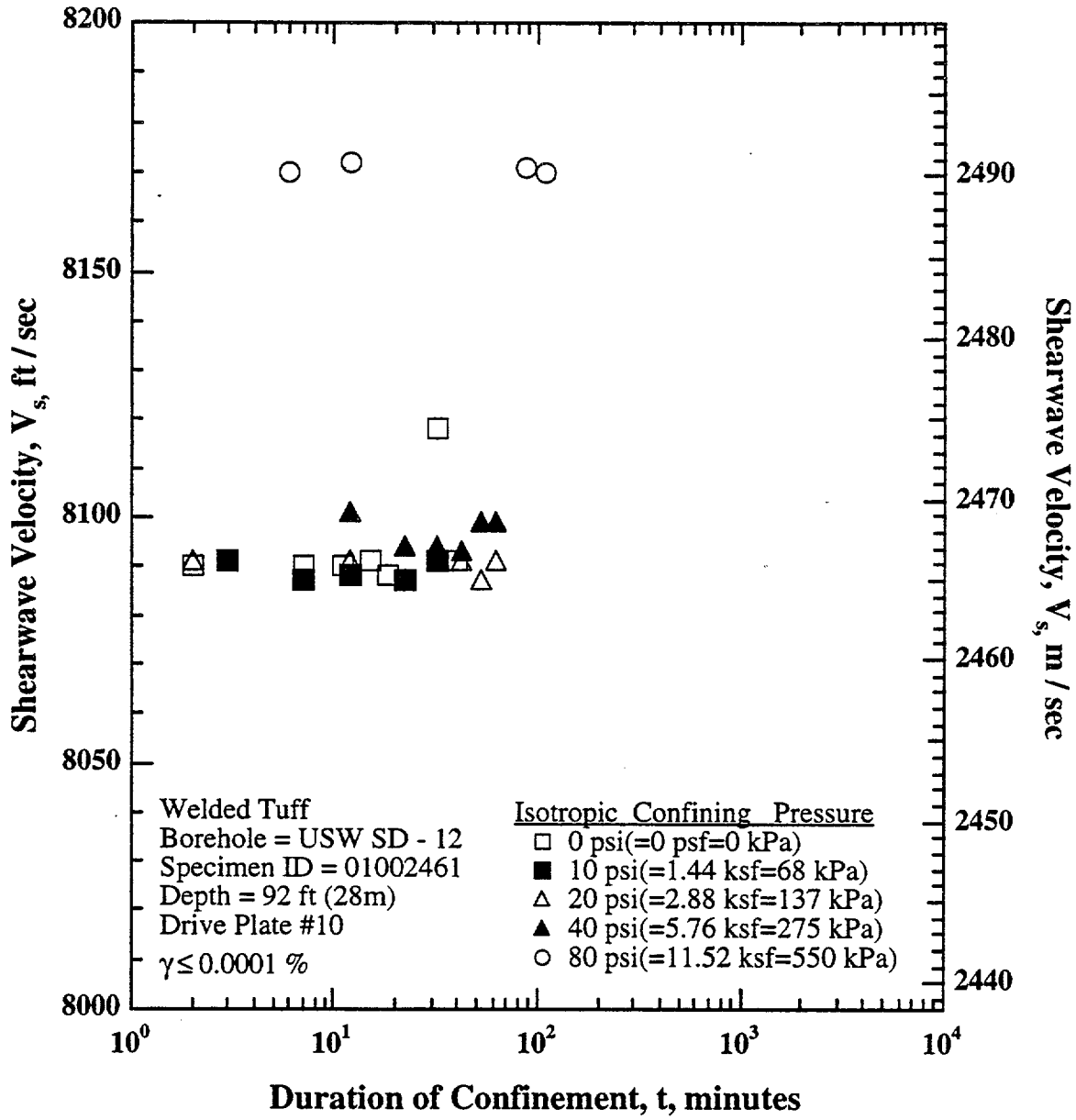

Fig. B.2 Variation in Shear Wave Velocity with Magnitude and Duration of Isotropic Confining Pressure from Resonant Column Testing of Specimen 01002461 from Borehole USW SD - 12; Depth = 92 ft (28 m)

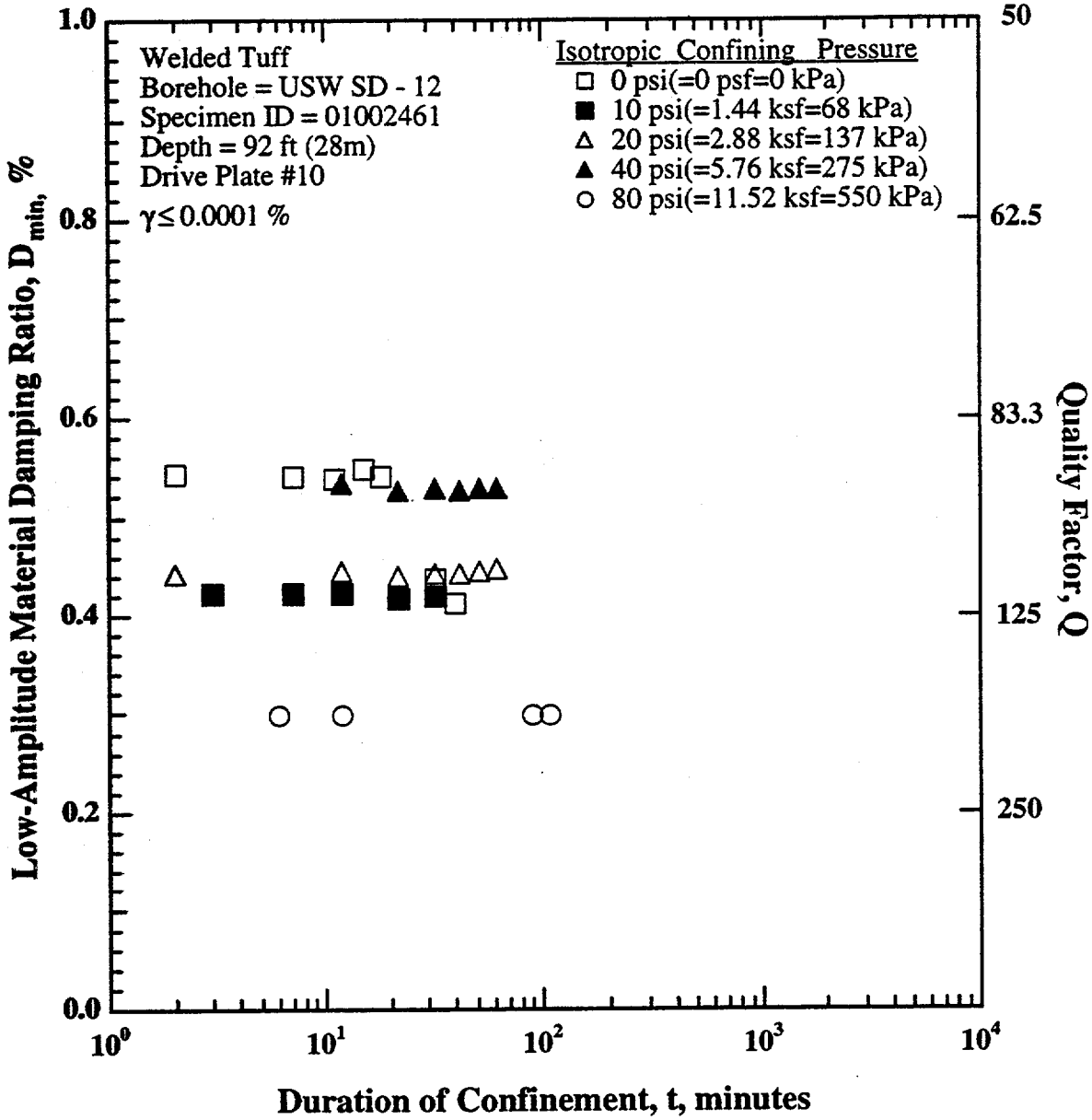

Fig. B.3 Variation in Low-Amplitude Material Damping Ratio with Magnitude and Duration of Isotropic Confining Pressure from Resonant Column Testing of Specimen 01002461 from Borehole USW SD - 12; Depth = 92 ft (28 m)

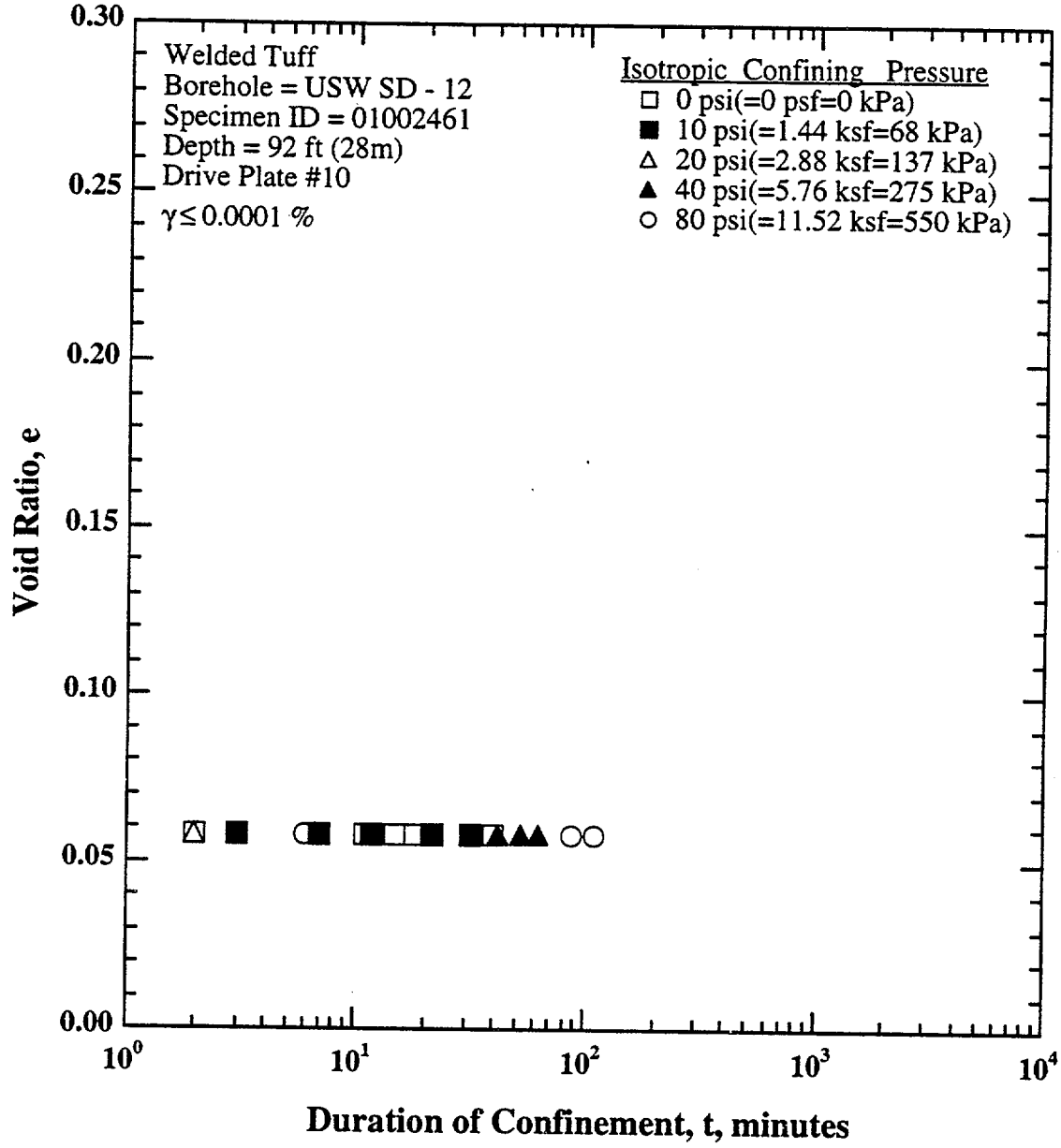

Fig. B.4 Variation in Void Ratio with Magnitude and Duration of Isotropic Confining Pressure from Resonant Column Testing of Specimen 01002461 from Borehole USW SD - 12; Depth = 92 ft (28 m)

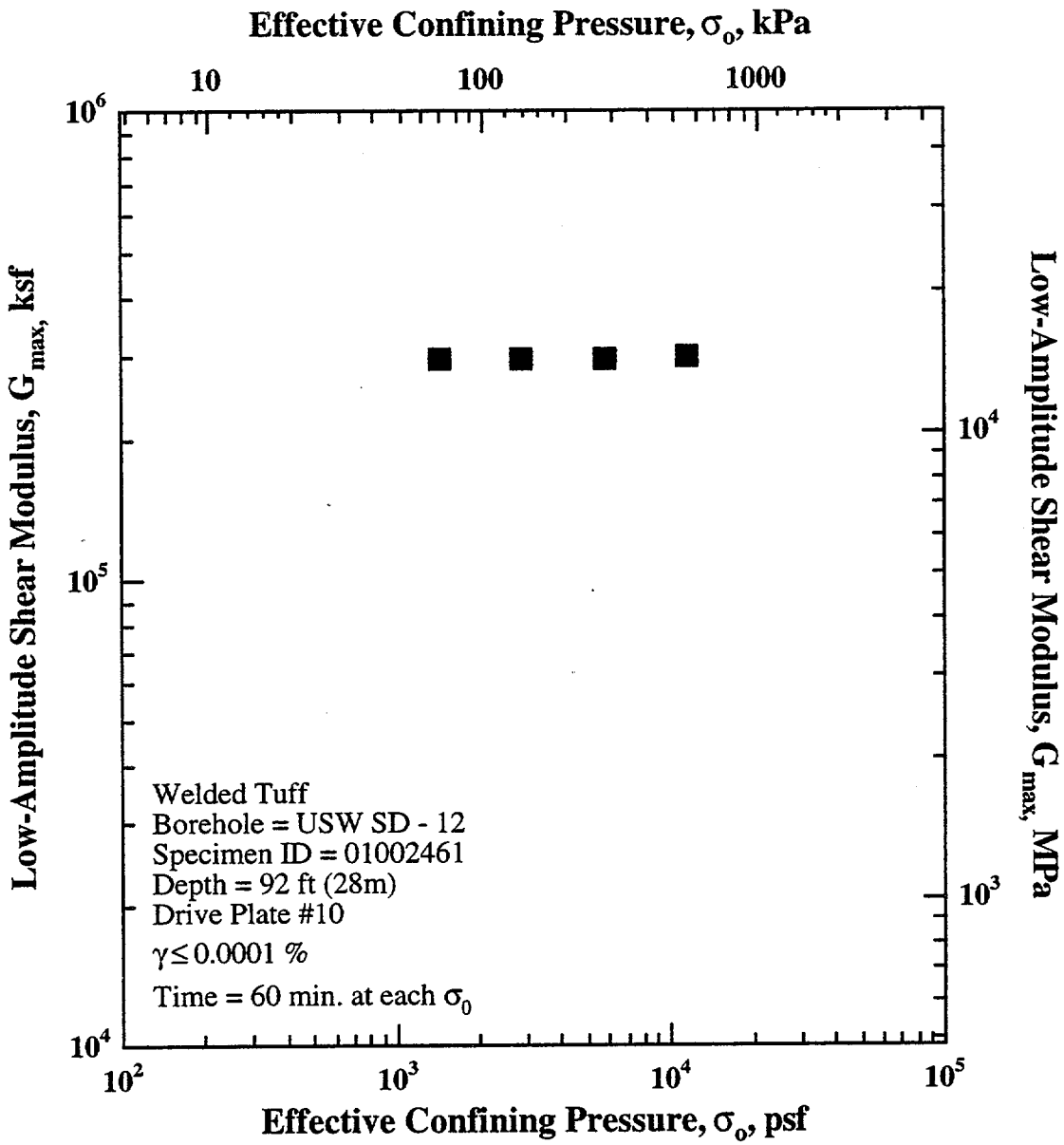

Fig. B.5 Variation in Low-Amplitude Shear Modulus with Effective Confining Pressure from Resonant Column Testing of Specimen 01002461 from Borehole USW SD - 12; Depth = 92 ft (28 m)

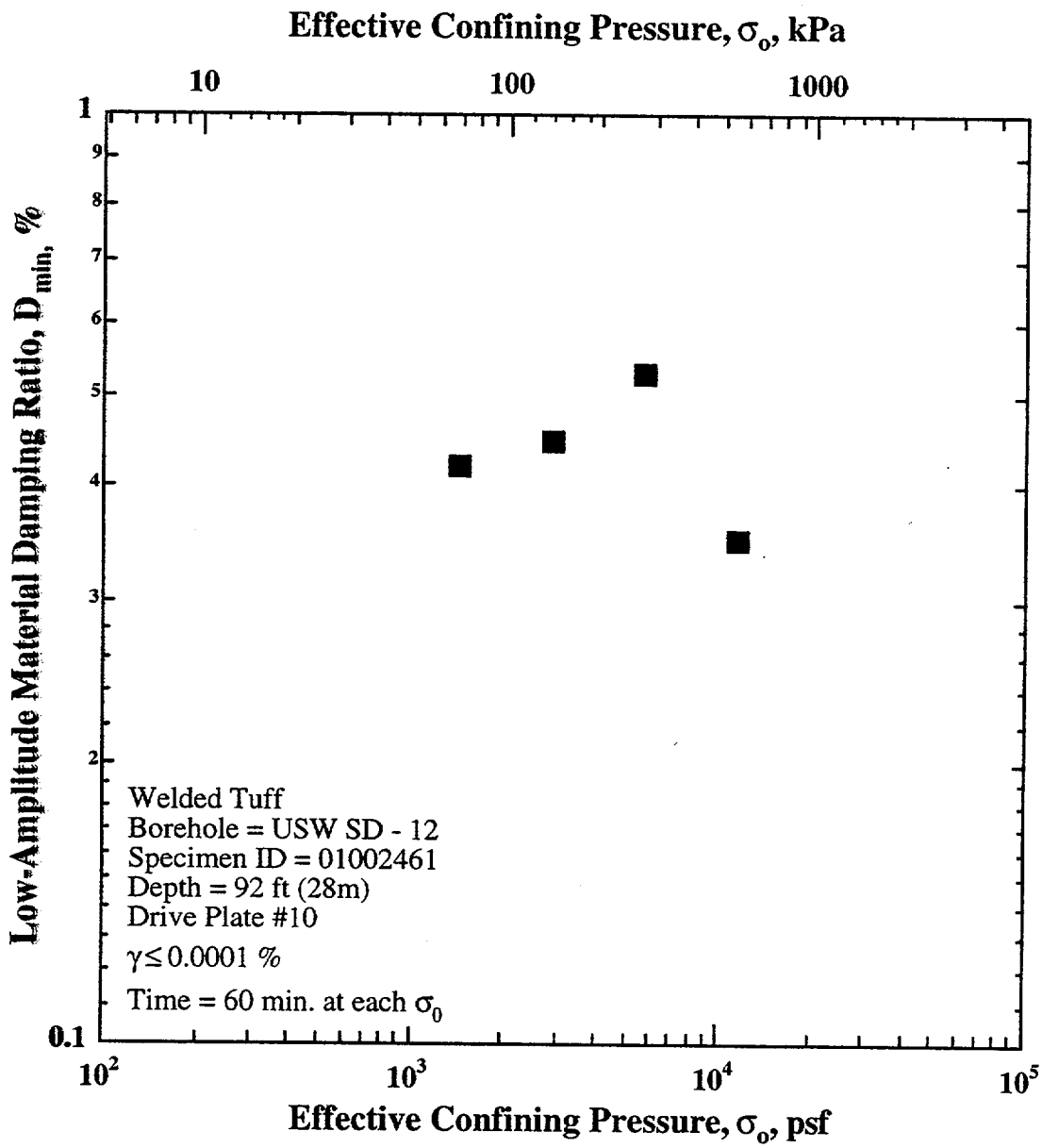

Fig. B.6 Variation in Low-Amplitude Material Damping Ratio with Effective Confining Pressure from Resonant Column Testing of Specimen 01002461 from Borehole USW SD - 12; Depth = 92 ft (28 m)

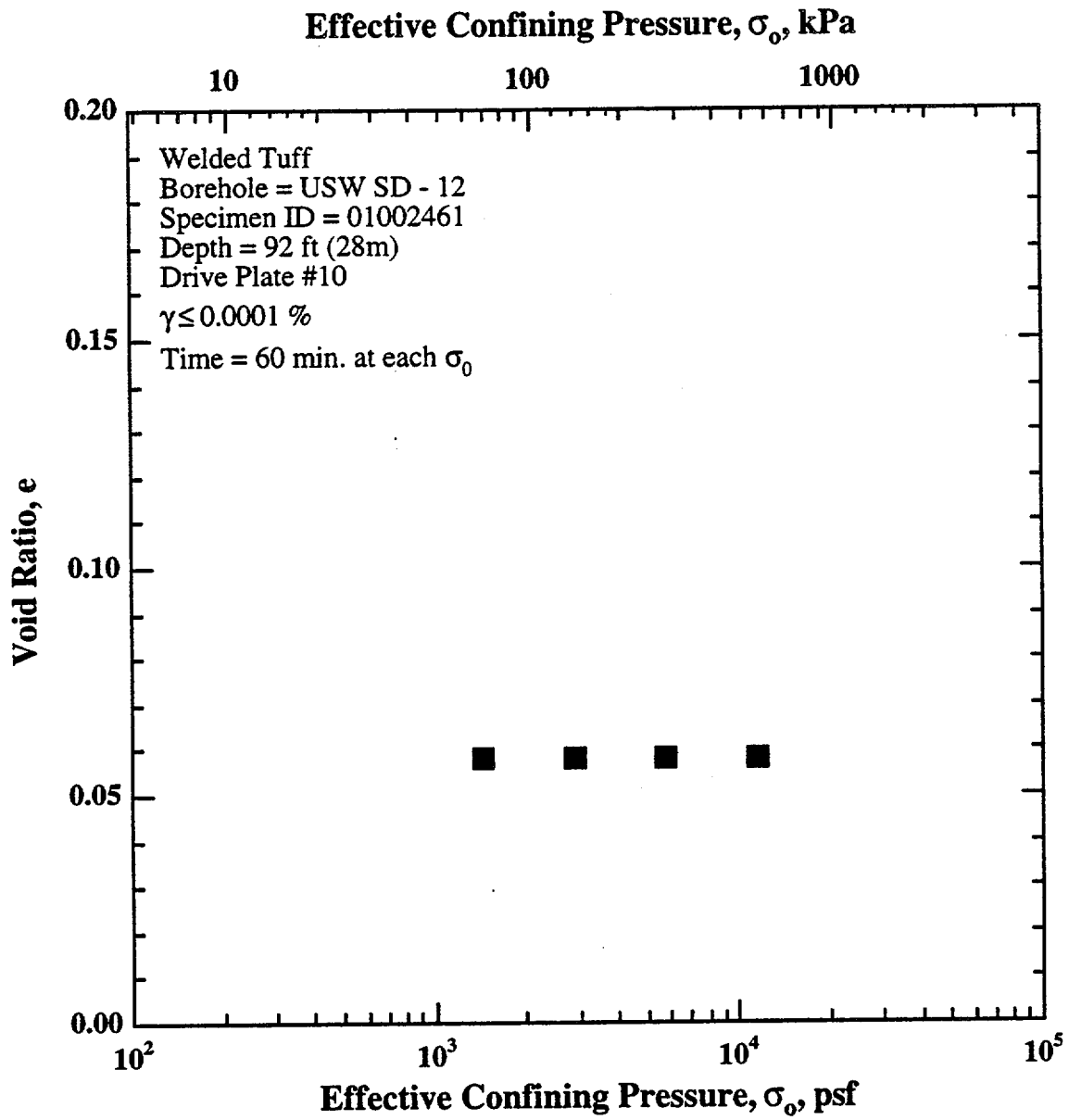

Fig. B.7 Variation in Void Ratio with Effective Confining Pressure from Resonant Column Testing of Specimen 01002461 from Borehole USW SD - 12; Depth = 92 ft (28 m)

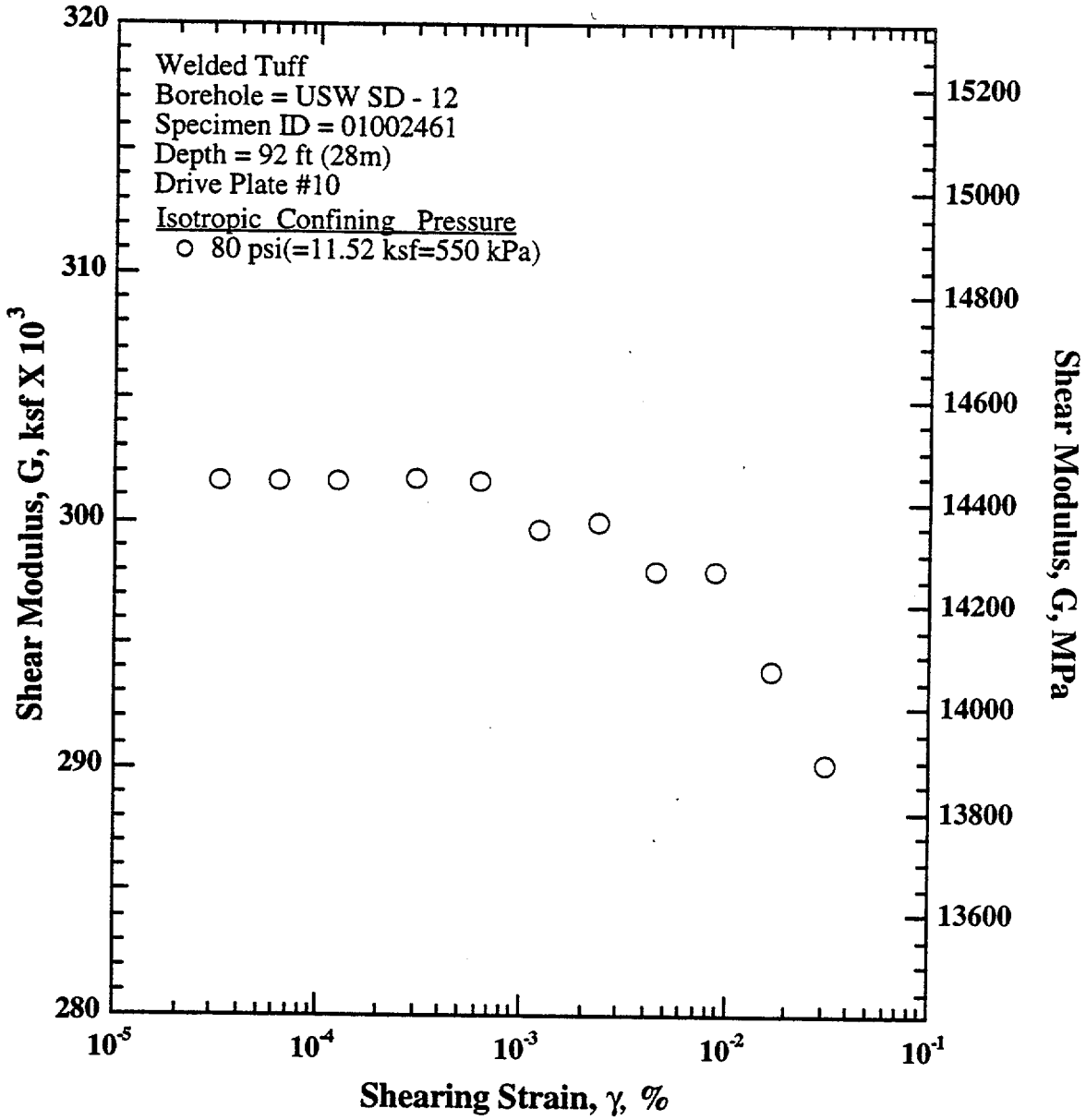

Fig. B.8 Variation in Shear Modulus with Shearing Strain at an Effective Confining Pressure of 80 psi (= 11.52 ksf = 550 kPa) from Resonant Column Testing of Specimen 01002461 from Borehole USW SD - 12; Depth = 92 ft (28 m)

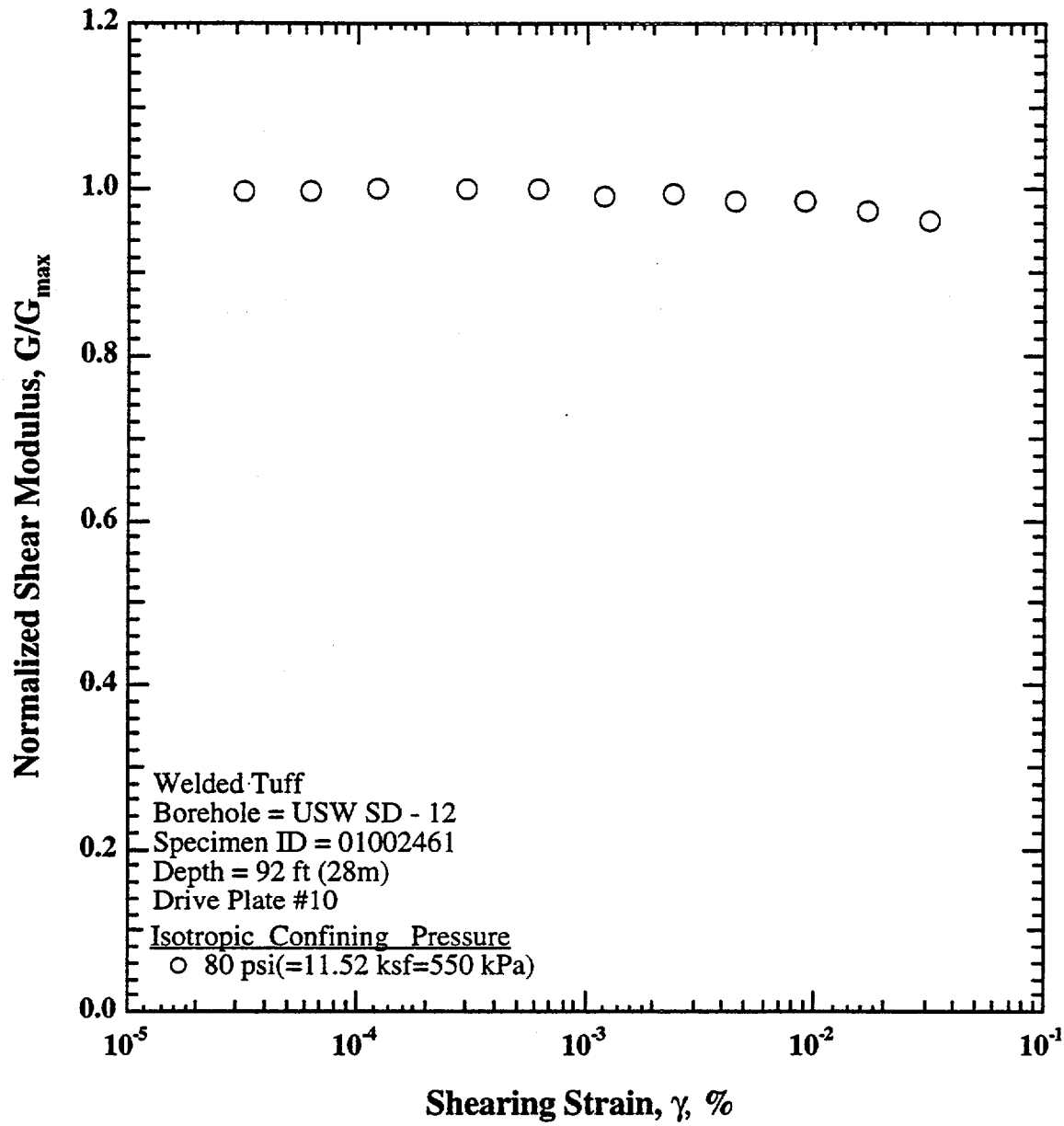

Fig. B.9 Variation in Normalized Shear Modulus with Shearing Strain at an Effective Confining Pressure of 80 psi (= 11.52 ksf = 550 kPa) from Resonant Column Testing of Specimen 01002461 from Borehole USW SD - 12; Depth = 92 ft (28 m)

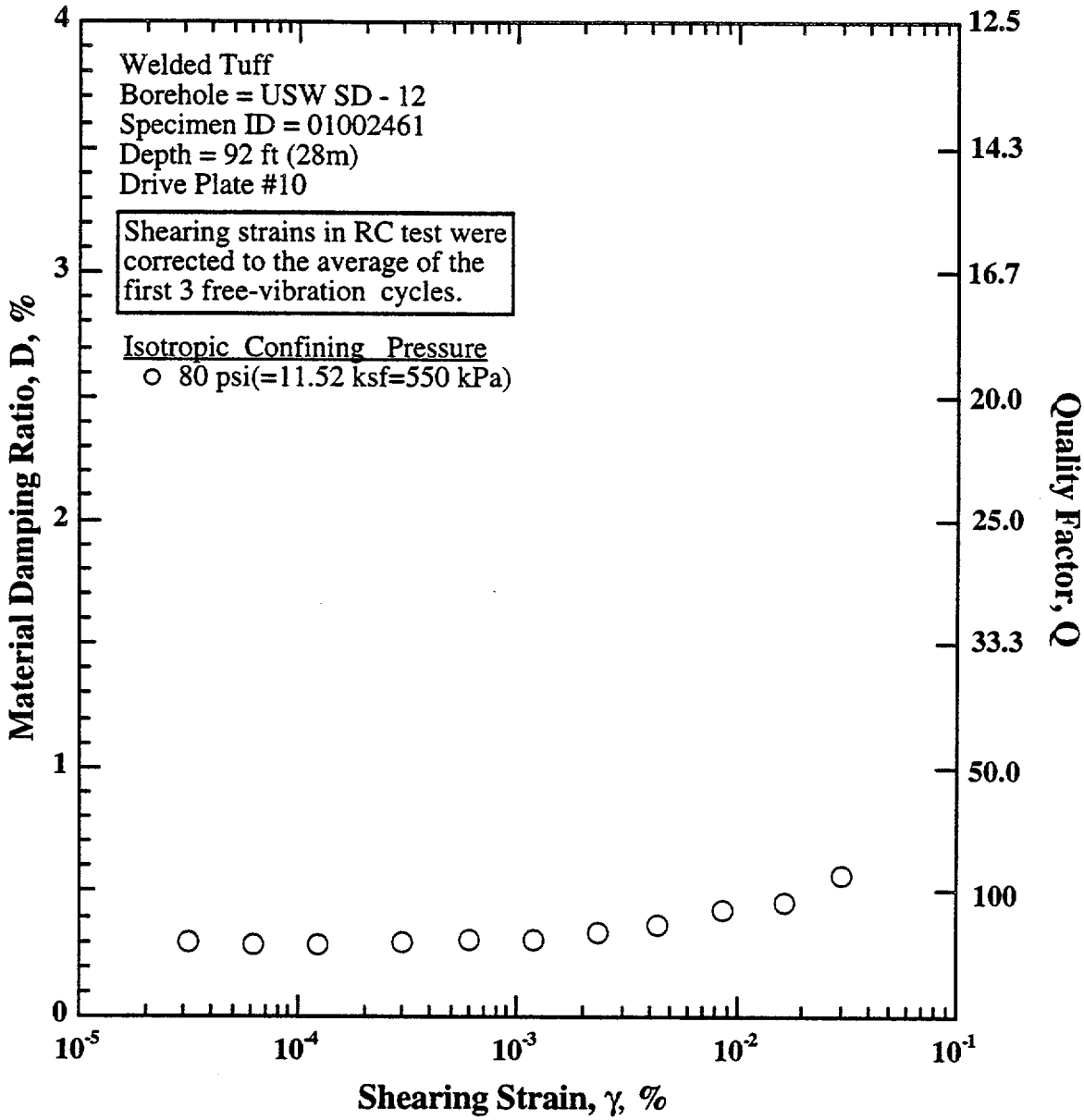

Fig. B.10 Variation in Material Damping Ratio with Shearing Strain at an Effective Confining Pressure of 80 psi (= 11.52 ksf = 550 kPa) from Resonant Column Testing of Specimen 01002461 from Borehole USW SD - 12; Depth = 43 ft (28 m)

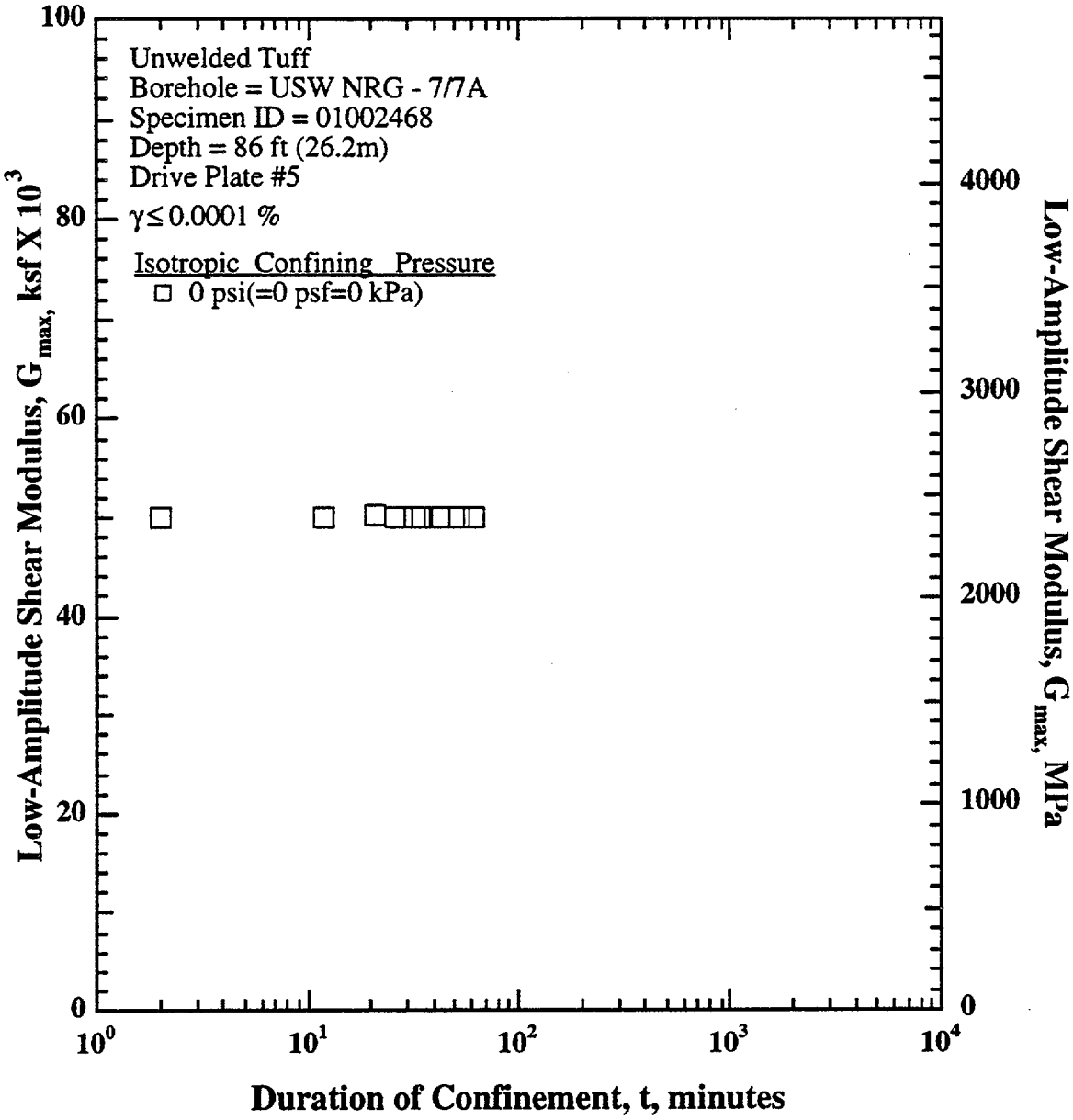

Fig. C.1 Variation in Low-Amplitude Shear Modulus with Magnitude and Duration of Isotropic Confining Pressure from Resonant Column Testing of Specimen 01002468 from Borehole USW NRG - 7/7A; Depth = 86 ft (26.2 m)

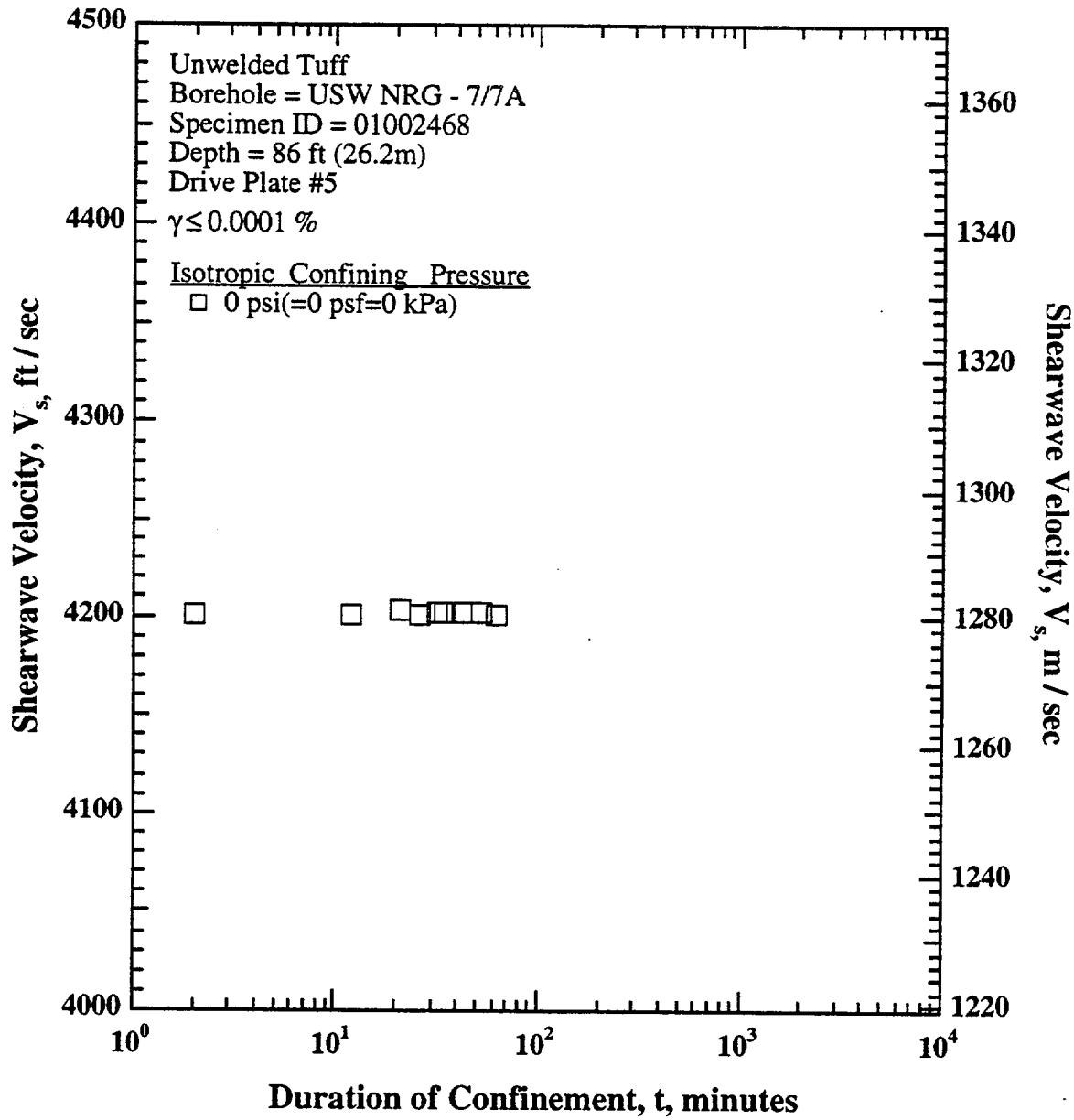

Fig. C.2 Variation in Shear Wave Velocity with Magnitude and Duration of Isotropic Confining Pressure from Resonant Column Testing of Specimen 01002468 from Borehole USW NRG - 7/7A; Depth = 86 ft (26.2 m)

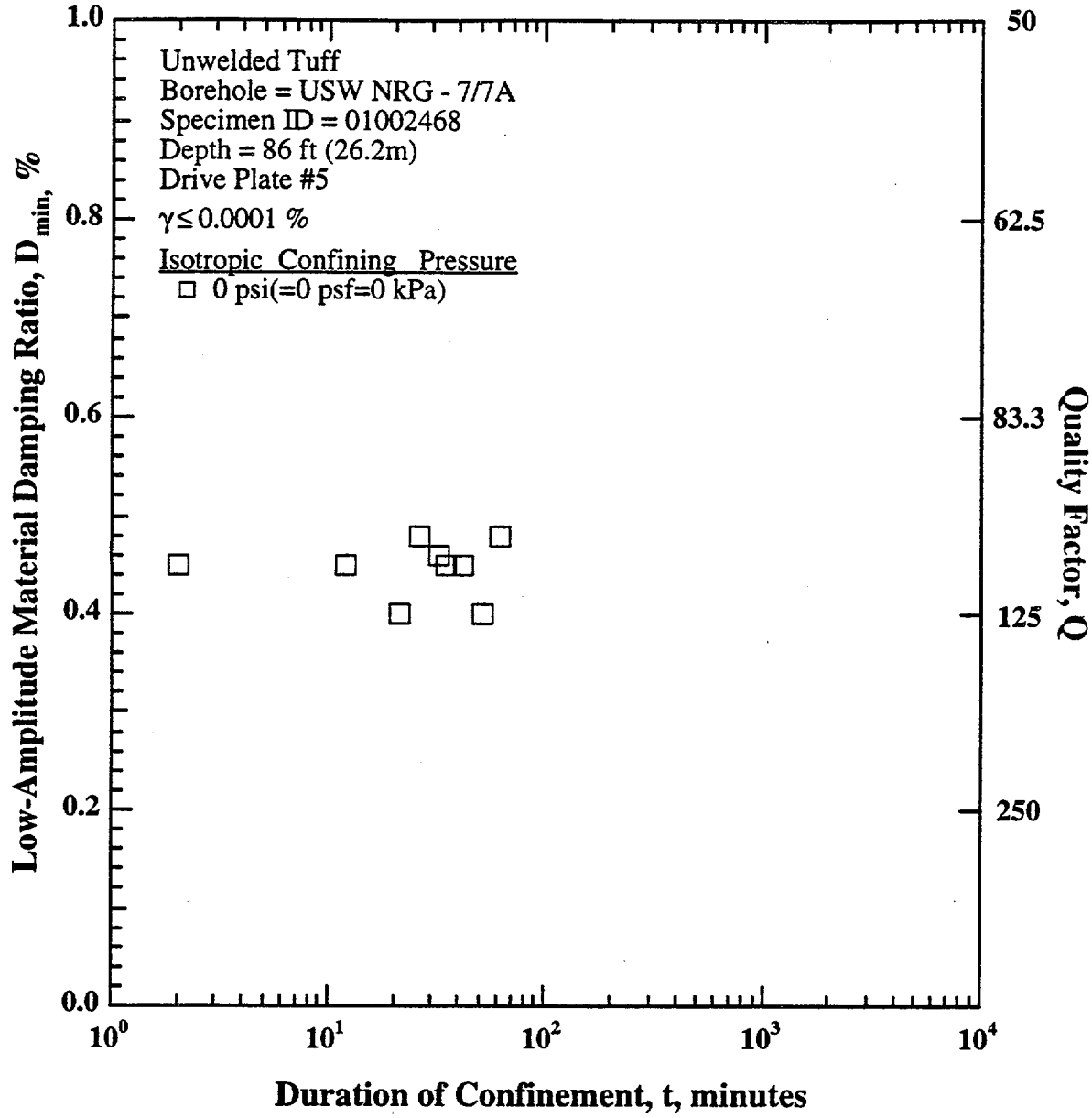

Fig. C.3 Variation in Low-Amplitude Material Damping Ratio with Magnitude and Duration of Isotropic Confining Pressure from Resonant Column Testing of Specimen 01002468 from Borehole USW NRG - 7/7A; Depth = 86 ft (26.2 m)

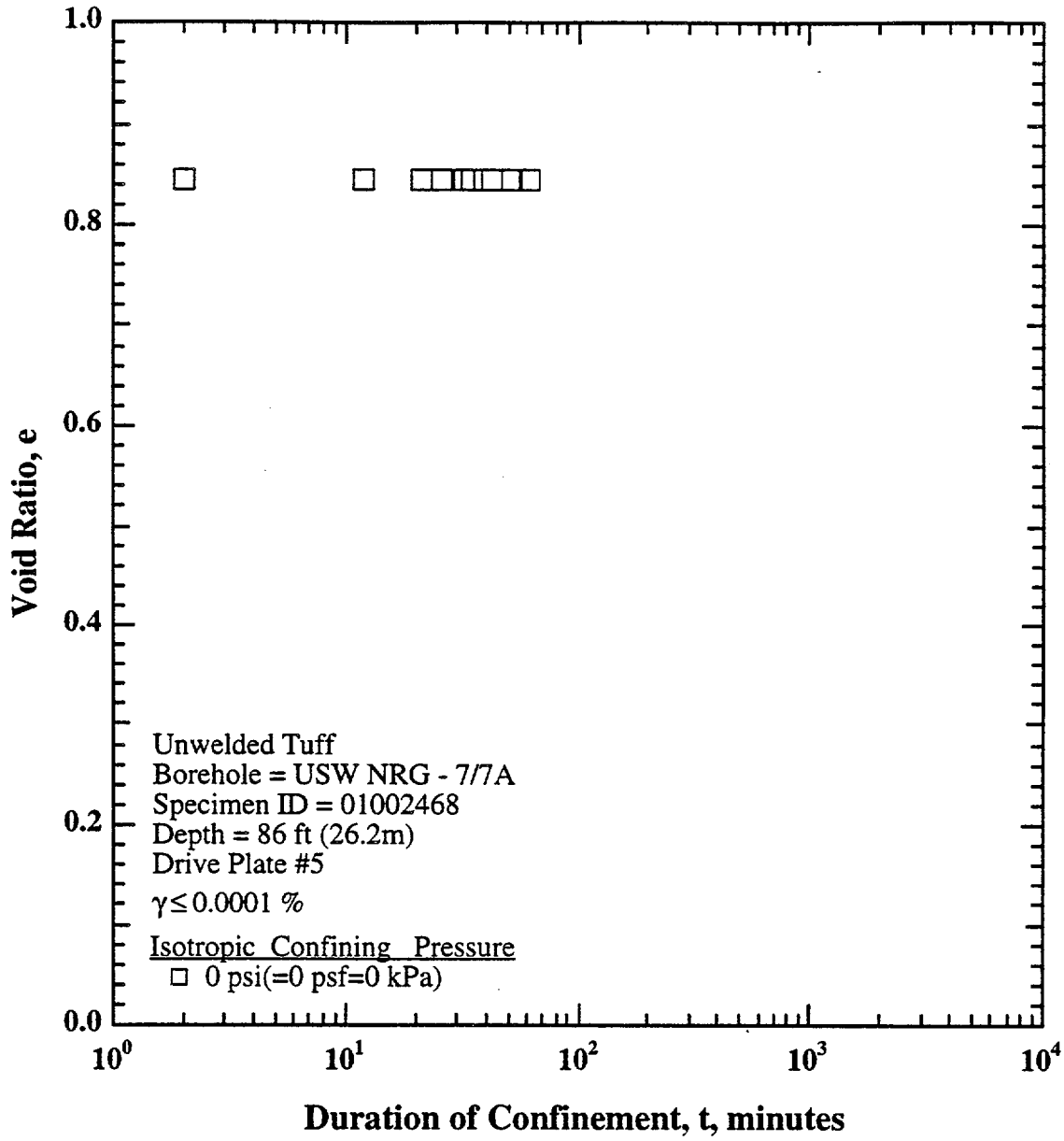

Fig. C.4 Variation in Void Ratio with Magnitude and Duration of Isotropic Confining Pressure from Resonant Column Testing of Specimen 01002468 from Borehole USW NRG - 7/7A; Depth = 86 ft (26.2 m)

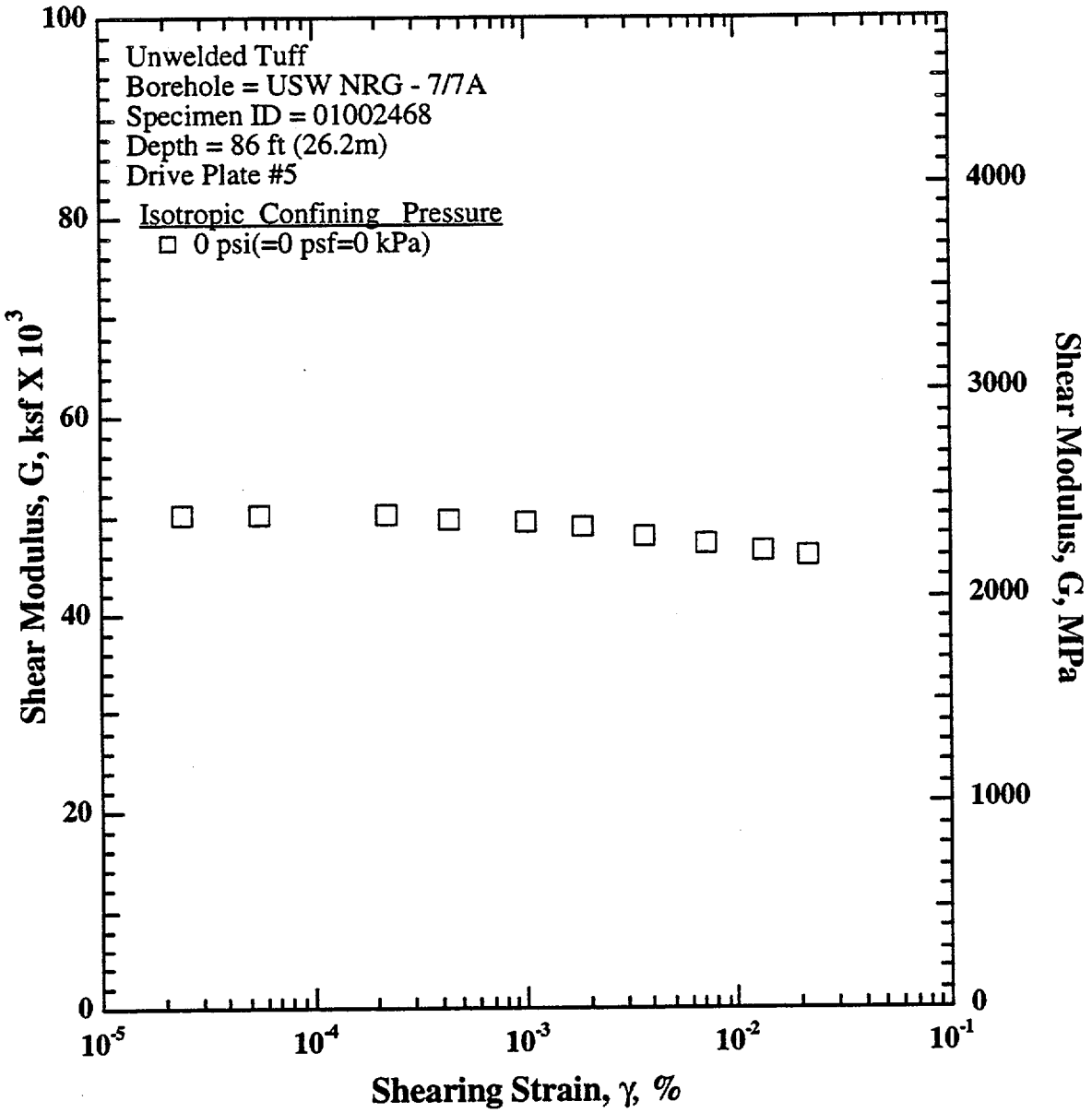

Fig. C.5 Variation in Shear Modulus with Shearing Strain at Zero Confining Pressure from Resonant Column Testing of Specimen 01002468 from Borehole USW NRG - 7/7A; Depth = 86 ft (26.2 m)

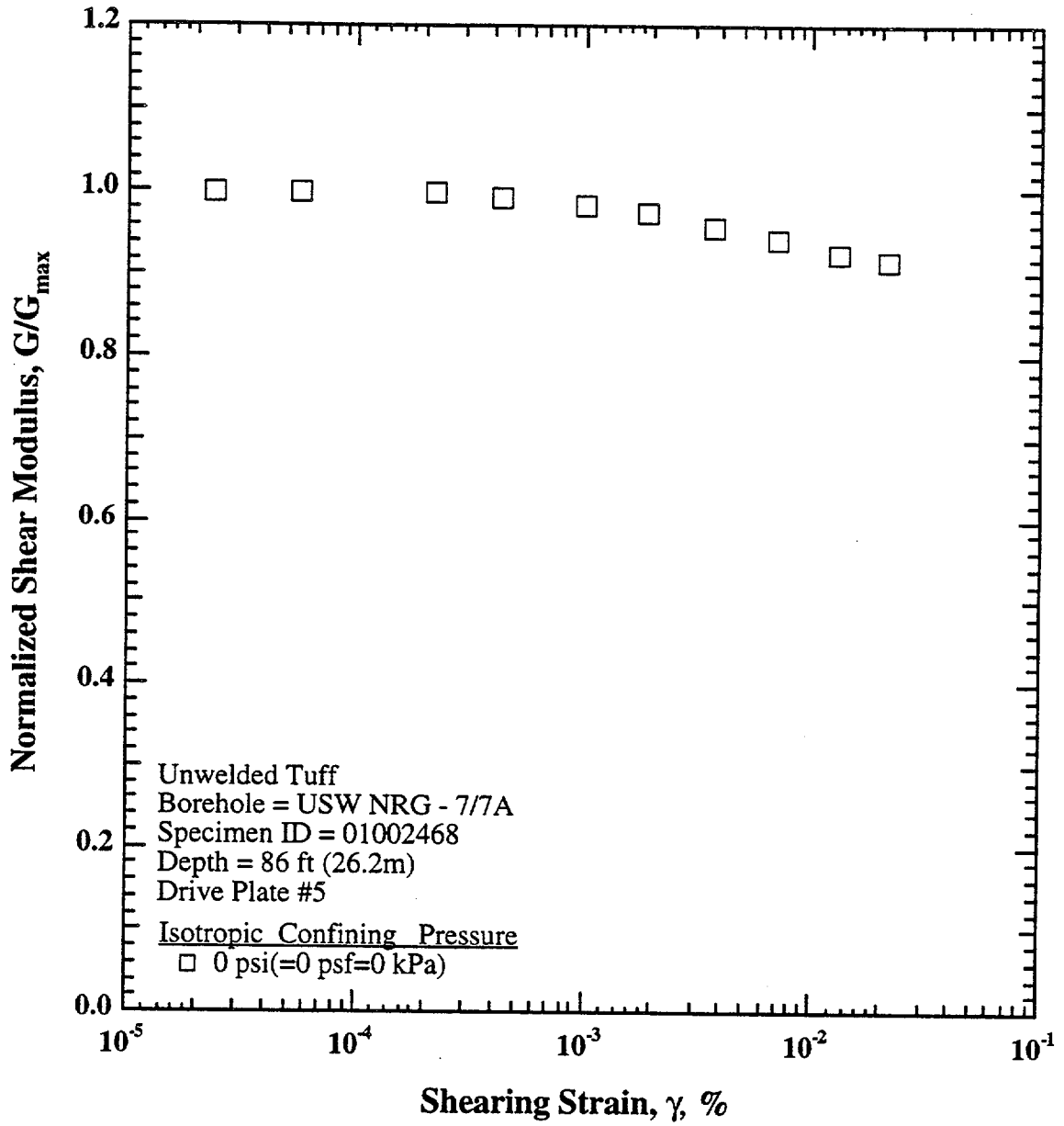

Fig. C.6 Variation in Normalized Shear Modulus with Shearing Strain at Zero Confining Pressure from Resonant Column Testing of Specimen 01002468 from Borehole USW NRG - 7/7A; Depth = 86 ft (26.2 m)

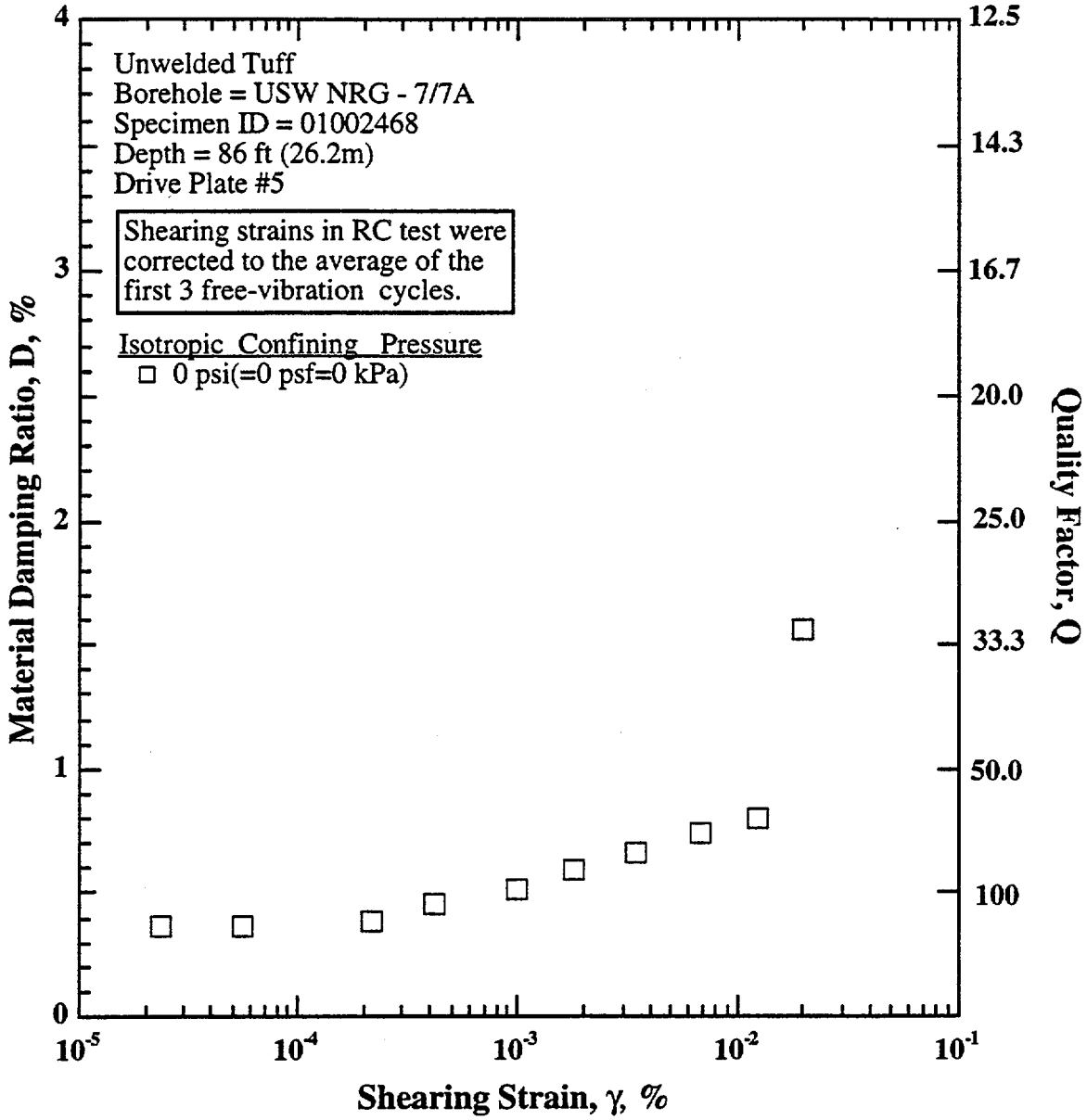

Fig. C.7 Variation in Material Damping Ratio with Shearing Strain at Zero Confining Pressure of from Resonant Column Testing of Specimen 01002468 from Borehole USW NRG - 7/7A; Depth = 86 ft (26.2 m)

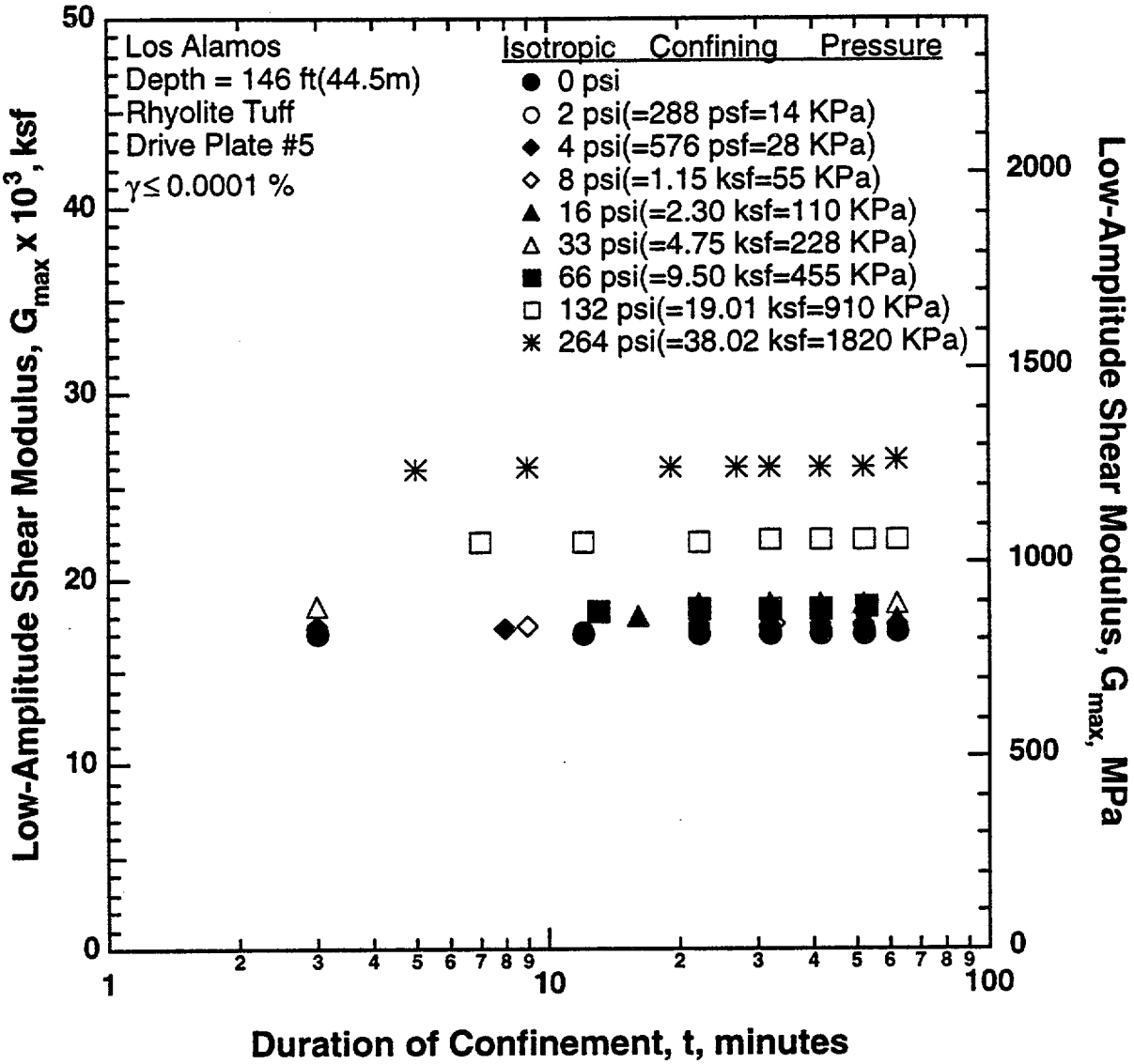

Fig. D.1 Variation in Low-Amplitude Shear Modulus with Magnitude and Duration of Isotropic Confining Pressure from Resonant Column Testing of Sample HQ30 from Borehole TA55

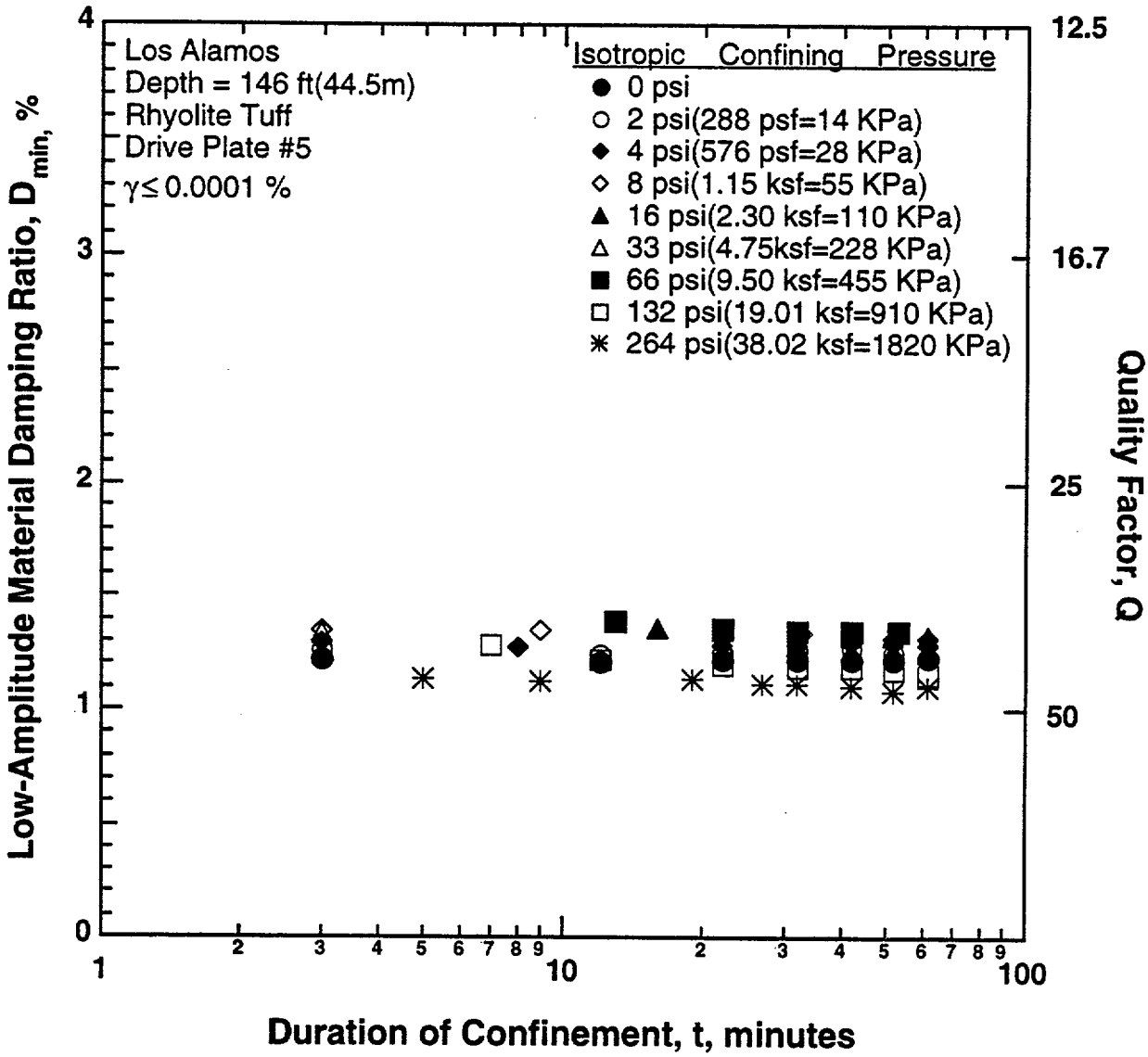

Fig. D.2 Variation in Low-Amplitude Material Damping Ratio with Magnitude and Duration of Isotropic Confining Pressure from Resonant Column Testing of Sample HQ30 from Borehole TA55

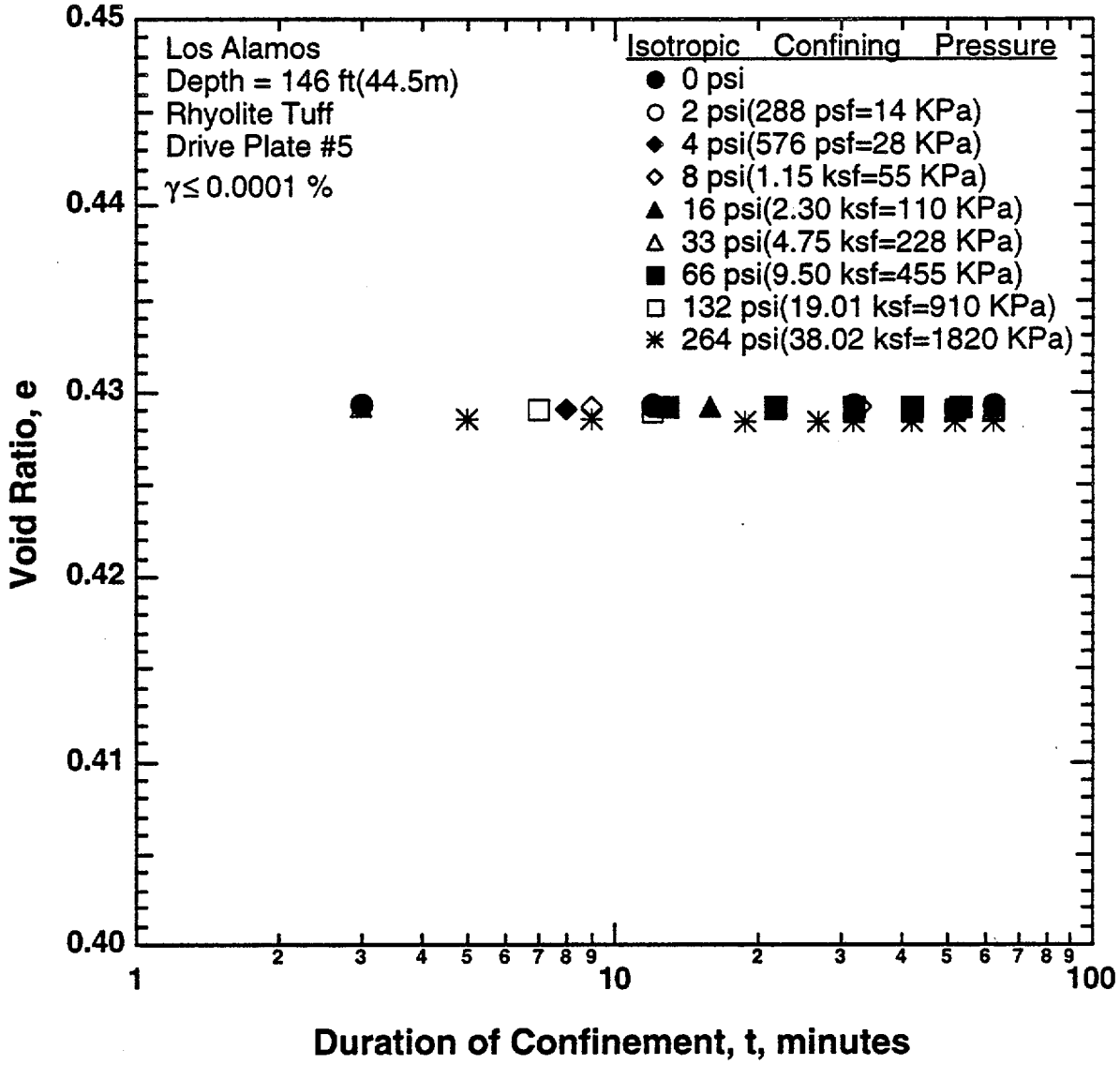

Fig. D.3 Variation in Void Ratio with Magnitude and Duration of Isotropic Confining Pressure from Resonant Column Testing of Sample HQ30 from Borehole TA55

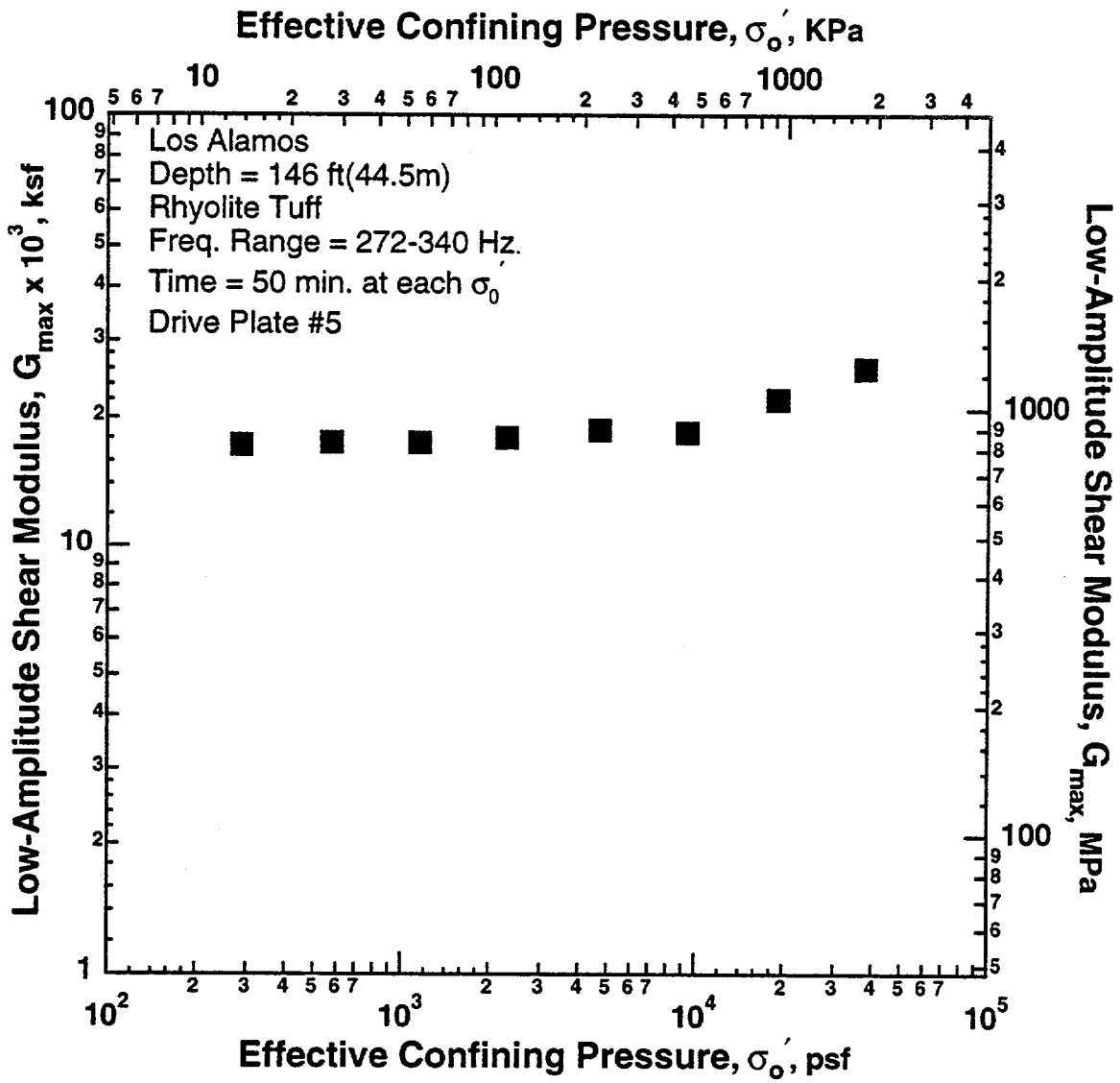

Fig. D.4 Variation in Low-Amplitude Shear Modulus with Effective Confining Pressure from Resonant Column Testing of Sample HQ30 from Borehole TA55

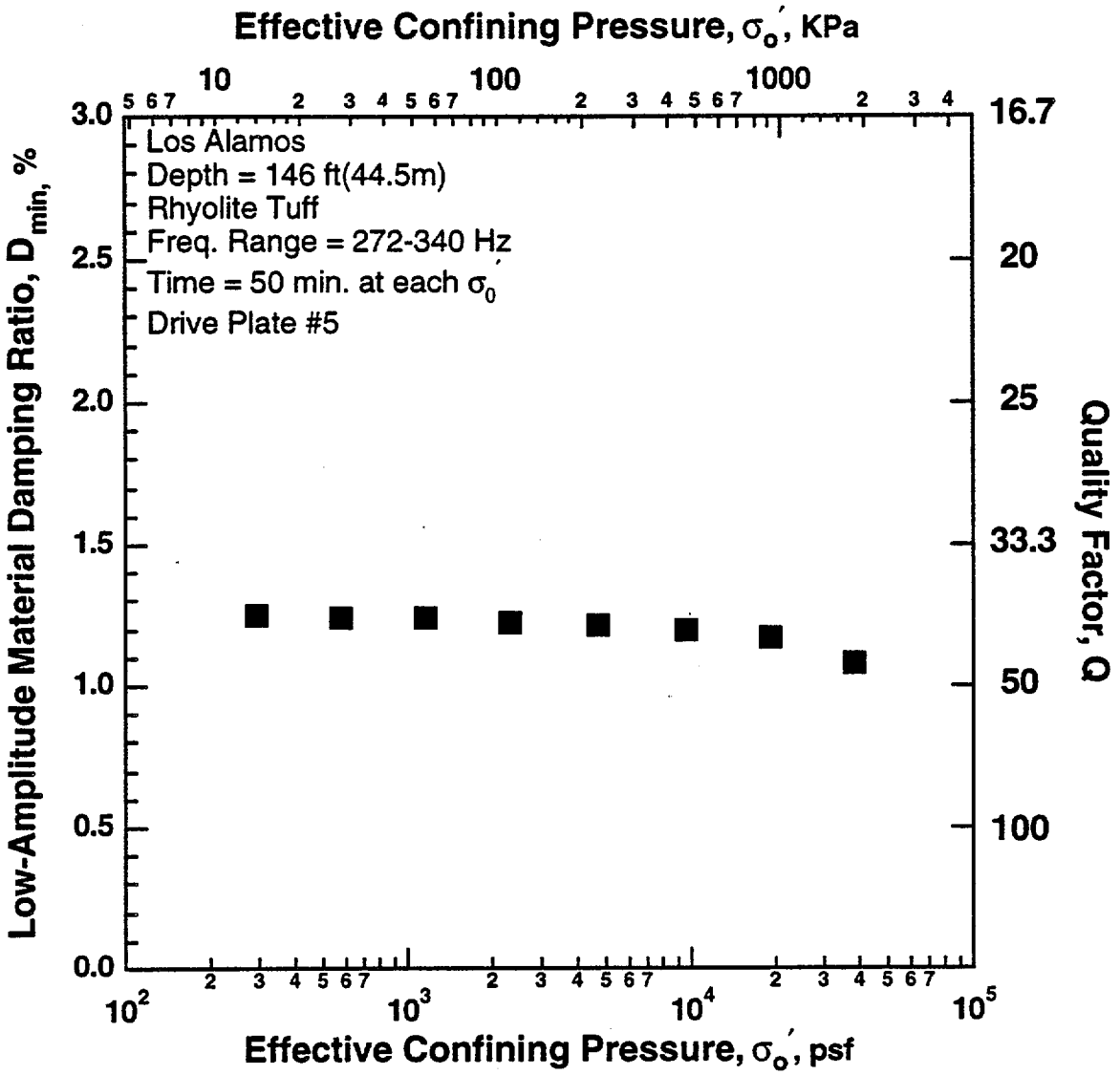

Fig. D.5 Variation in Low-Amplitude Material Damping Ratio with Effective Confining Pressure from Resonant Column Testing of Sample HQ30 from Borehole TA55

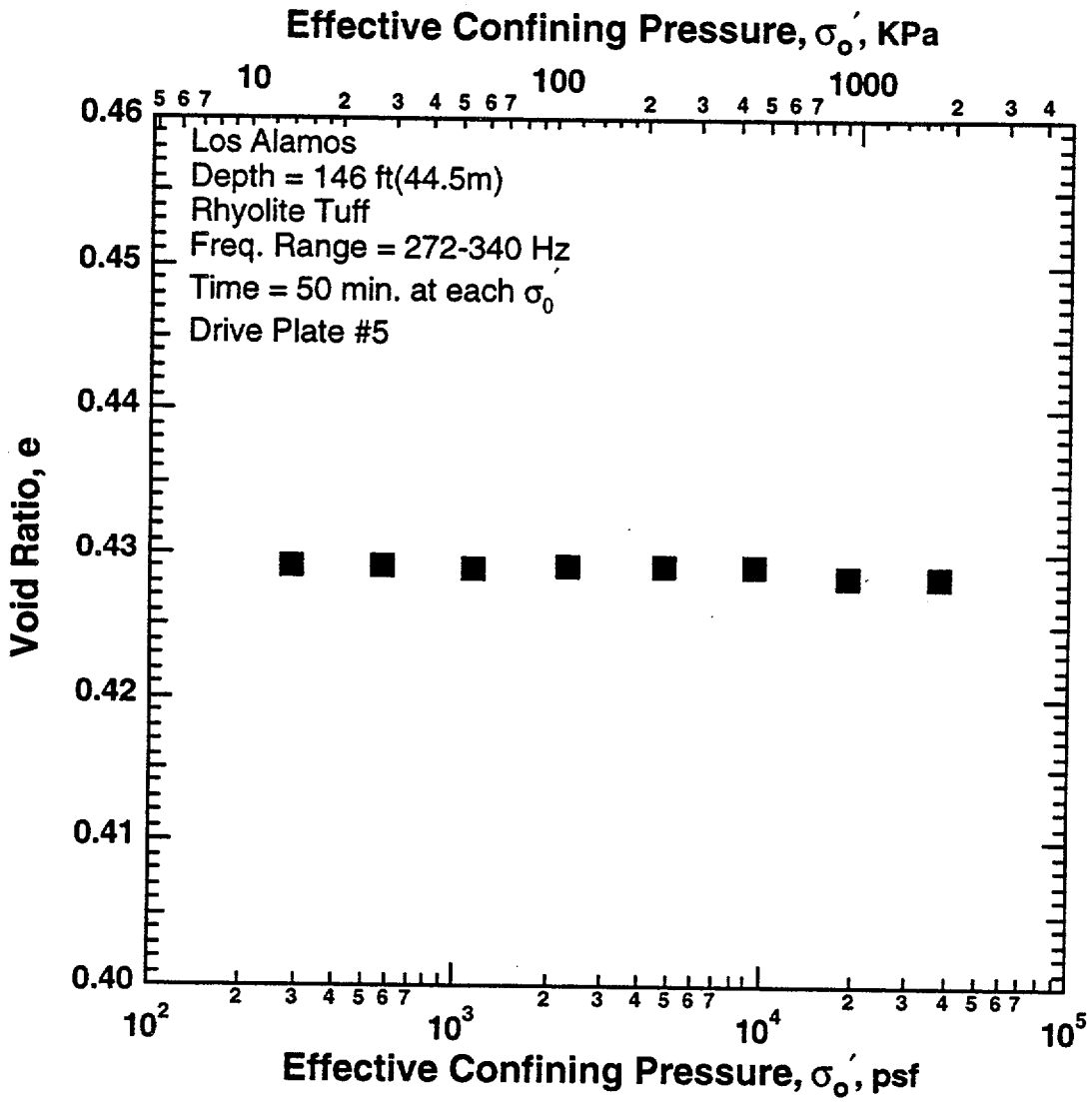

Fig. D.6 Variation in Void Ratio with Effective Confining Pressure from Resonant Column Testing of Sample HQ30 from Borehole TA55

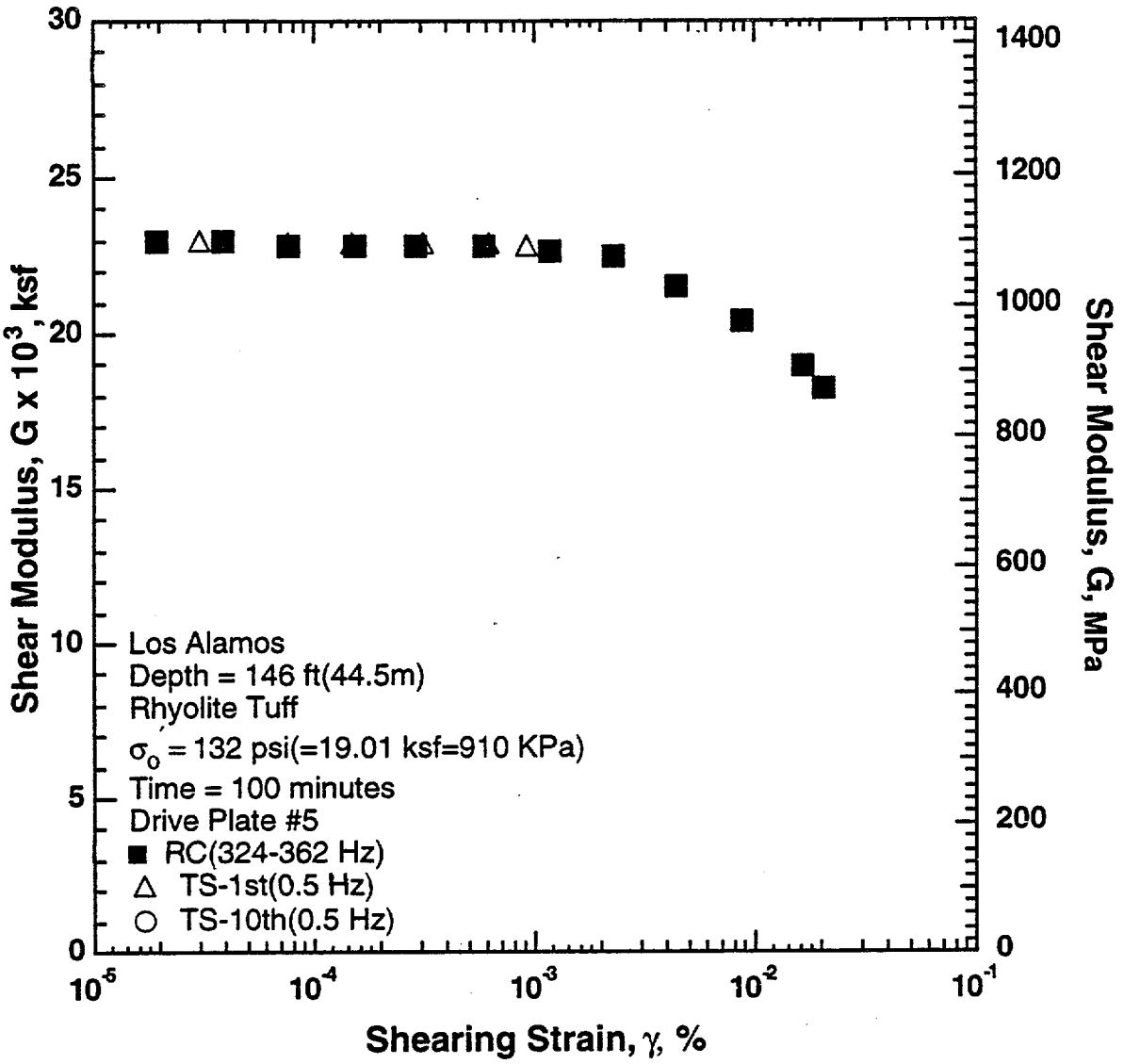

Fig. D.7 Variation in Shear Modulus with Shearing Strain at an Effective Confining Pressure of 132 psi (=19.01 ksf=910 KPa) from RCTS Tests of Sample HQ30 from Borehole TA55

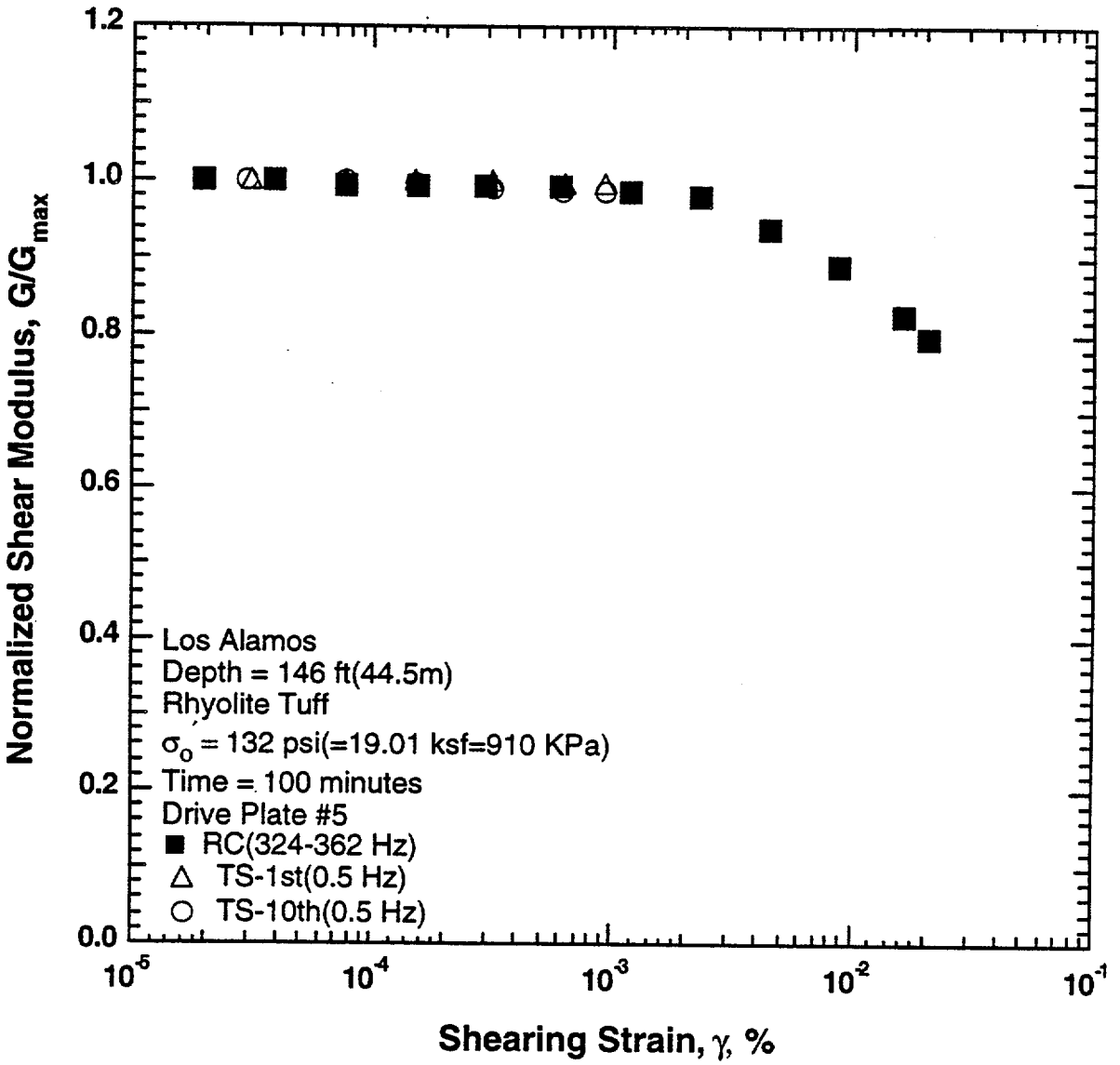

Fig. D.8 Variation in Normalized Shear Modulus with Shearing Strain at an Effective Confining Pressure of 132 psi (=19.01 ksf=910 KPa) from RCTS Tests of Sample HQ30 from Borehole TA55

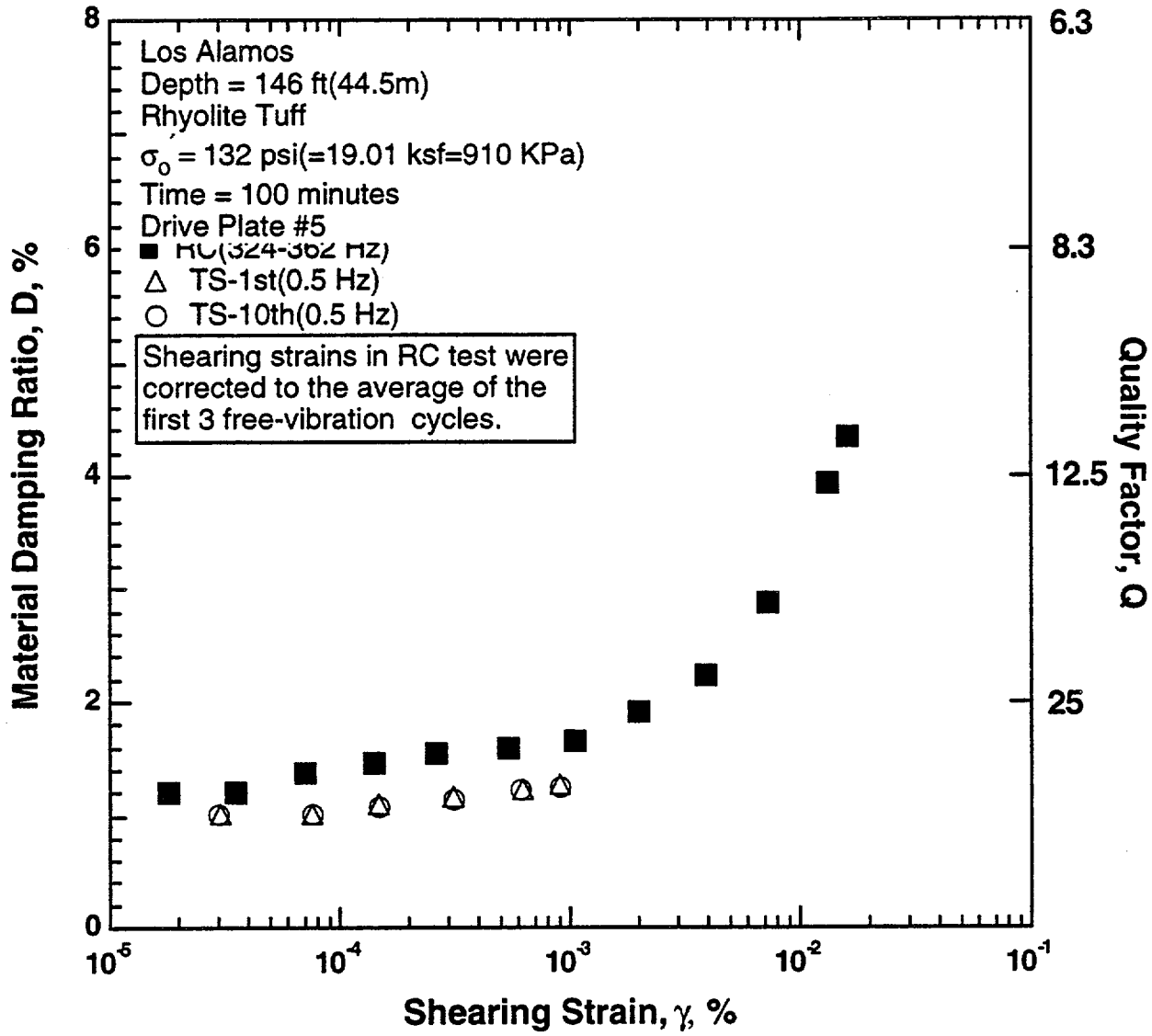

Fig. D.9 Variation in Material Damping Ratio with Shearing Strain at an Effective Confining Pressure of 132 psi (=19.01 ksf=910 KPa) from RCTS Tests of Sample HQ30 from Borehole TA55

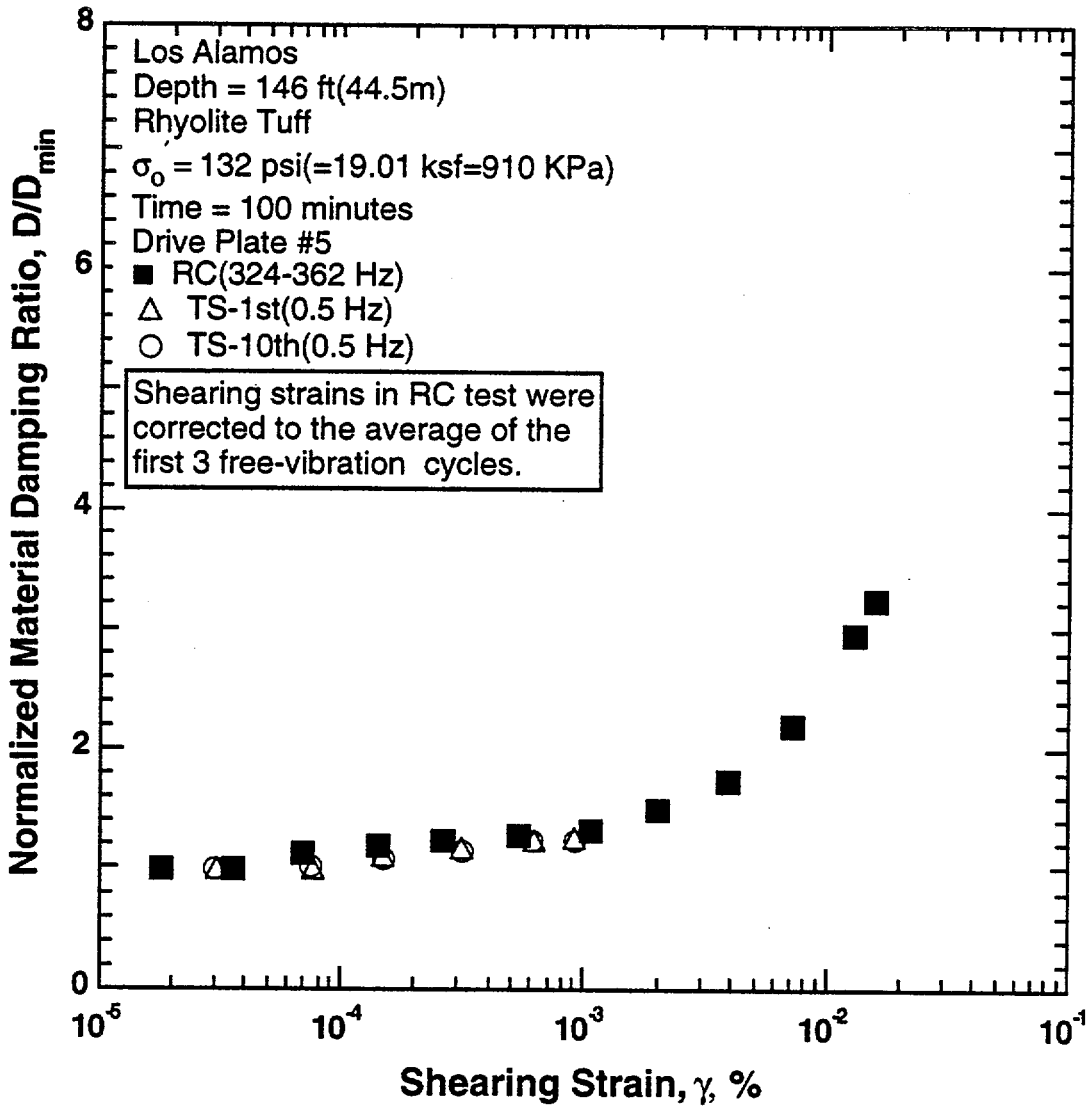

Fig. D.10 Variation in Normalized Material Damping Ratio with Shearing Strain at an Effective Confining Pressure of 132 psi(=19.01 ksf=910 KPa) from RCTS Tests of Sample HQ30 from Borehole TA55

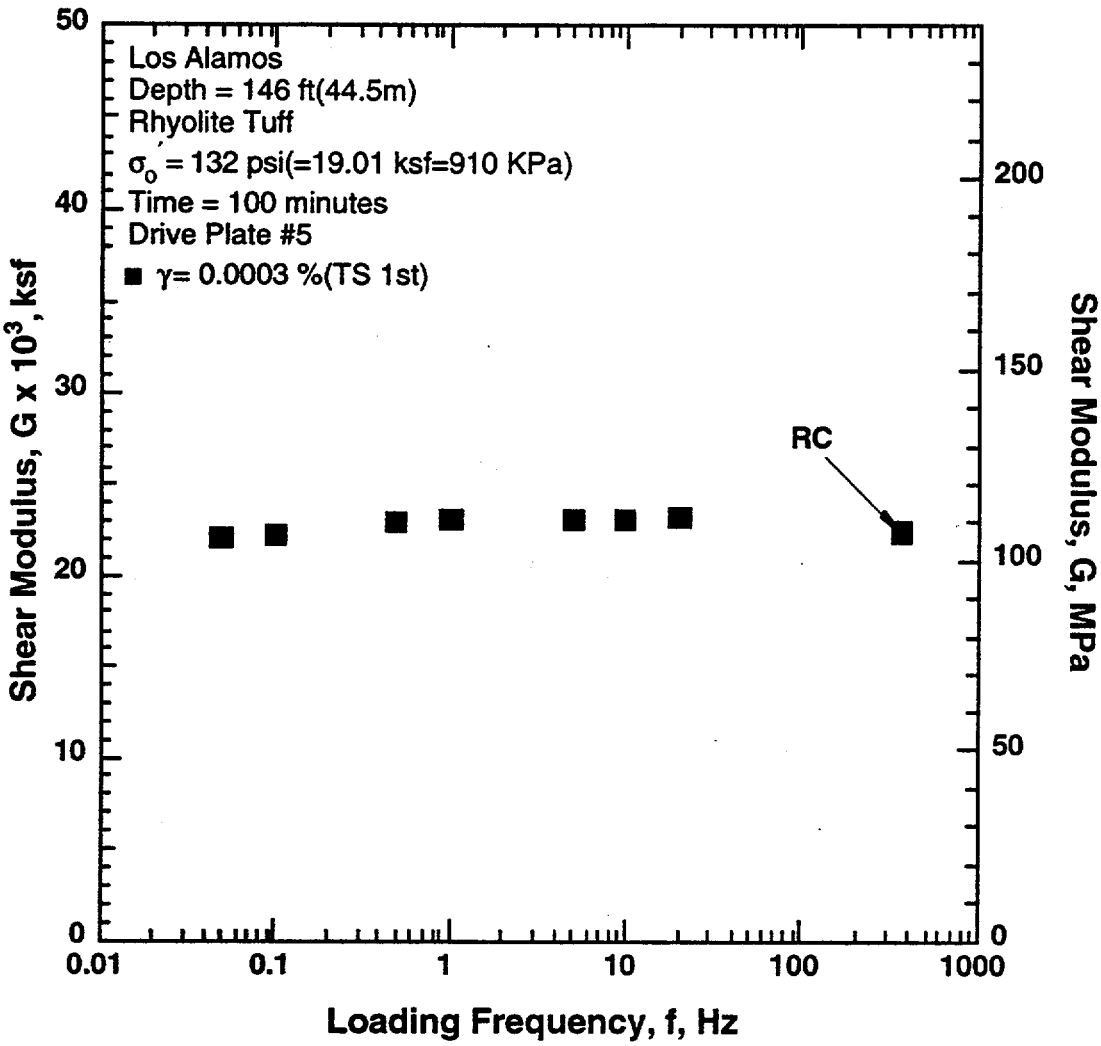

Fig. D.11 Variation in Shear Modulus with Loading Frequency and Shearing Strain at an Effective Confining Pressure of 132 psi(=19.01 ksf=910 KPa) from RCTS Tests of Sample HQ30 from Borehole TA55

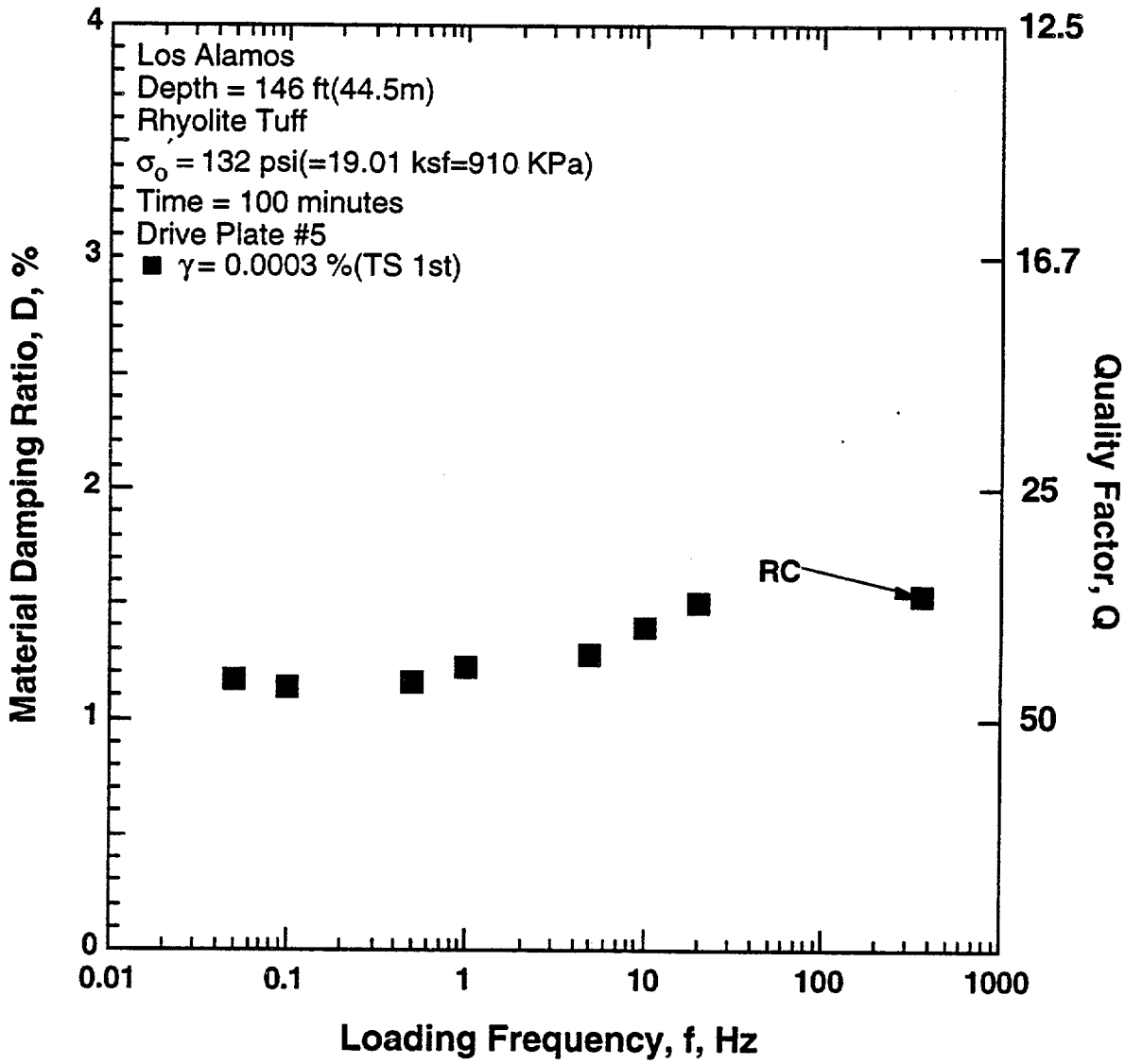

Fig. D.12 Variation in Material Damping Ratio with Loading Frequency and Shearing Strain at an Effective Confining Pressure of 132 psi(=19.01 ksf=910 Kpa) from RCTS Tests of Sample HQ30 from Borehole TA55

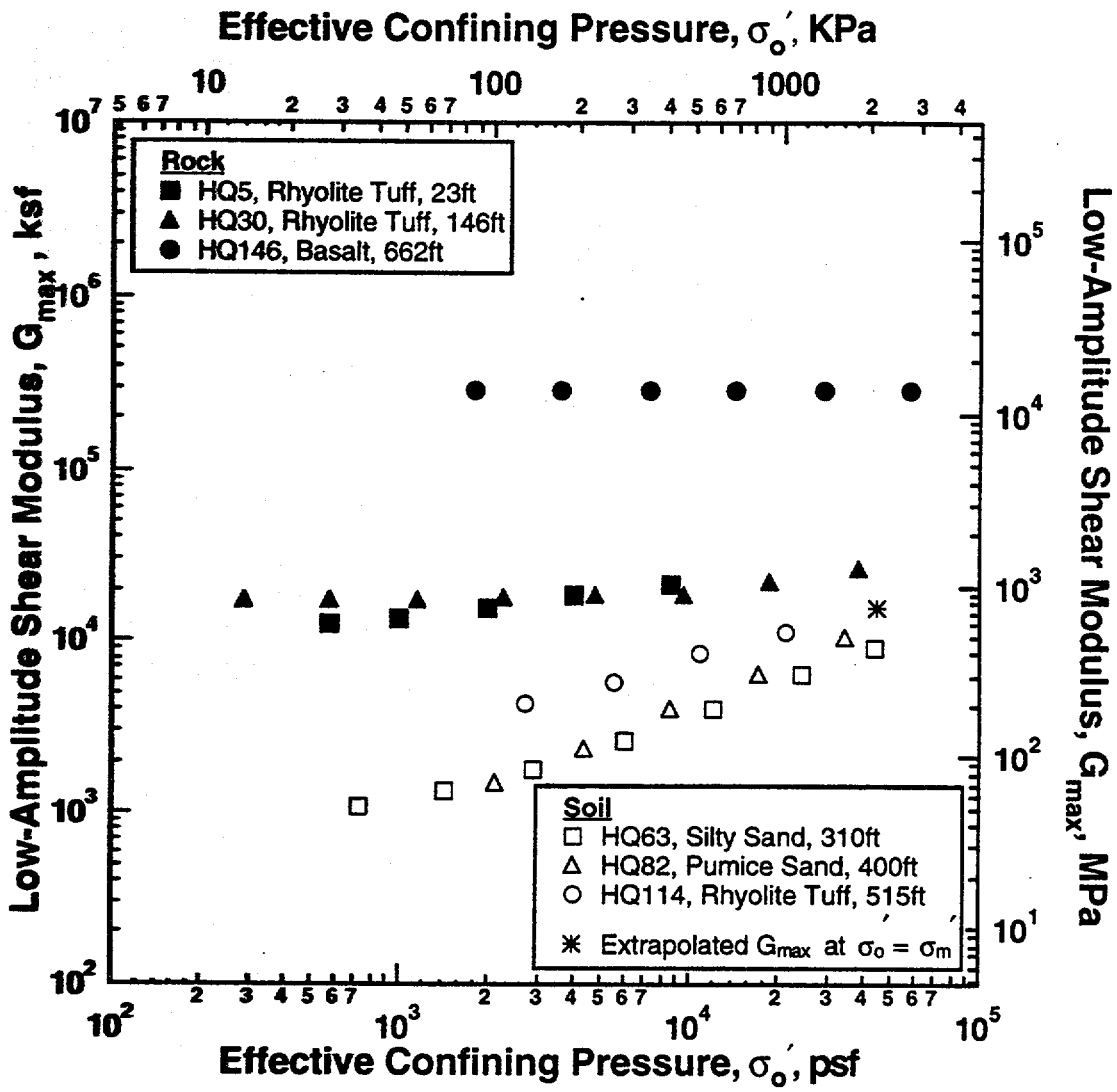

Notes:

1. G_{max} measured at t = 1000 min. at each σ_o' for each soil specimen (HQ63, HQ82 and HQ114) and at 50 min. for rock specimens HQ5 and HQ30 and at 20 min. for rock specimen HQ146.

Fig. E.1 Variation in Low-Amplitude Shear Modulus with Effective Confining Pressure from Resonant Column Tests of Undisturbed Soil and Rock Samples from Los Alamos

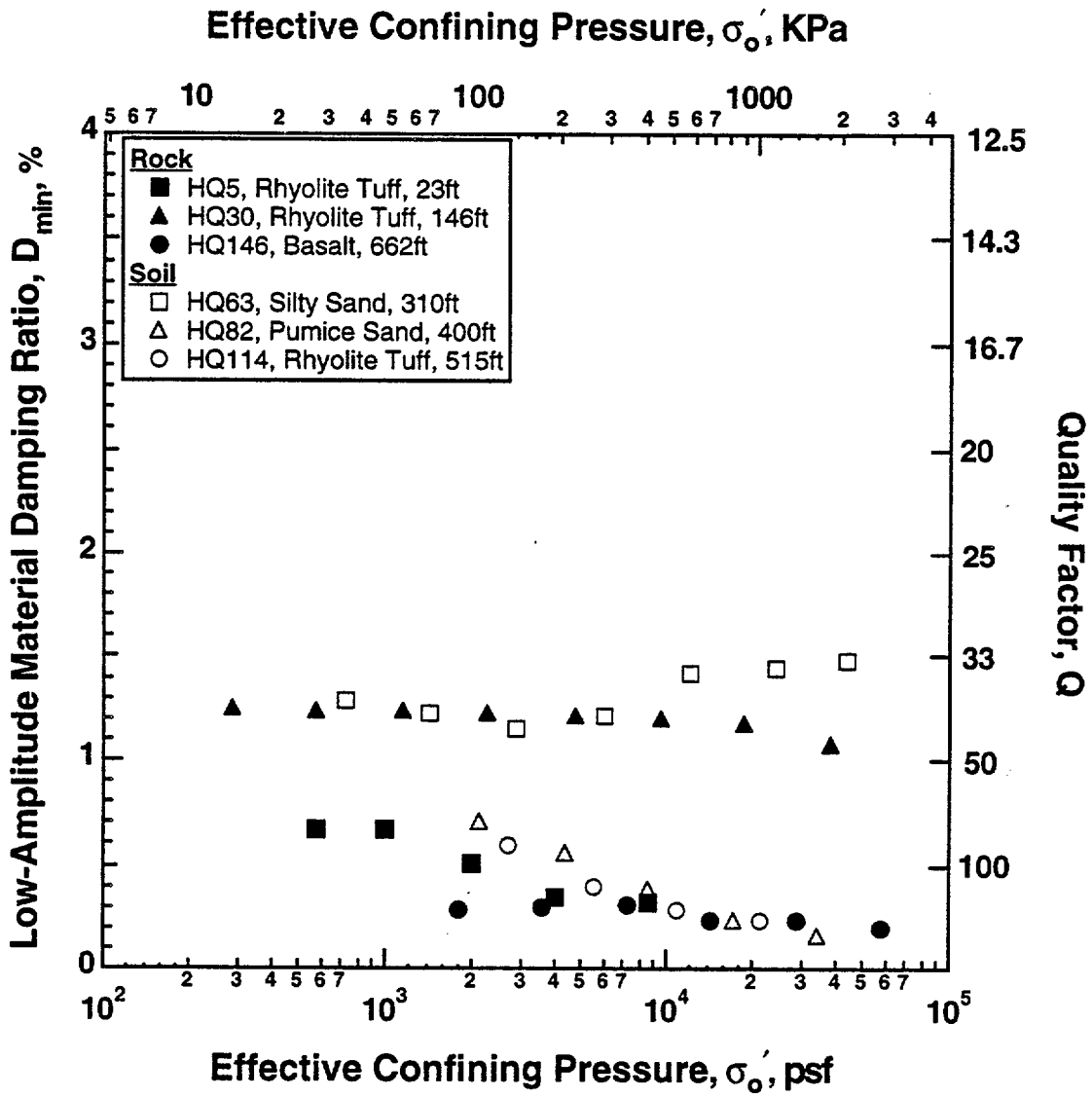

Notes:

1. D_{min} measured at t = 1000 min. at each σ_o' for each soil specimen (HQ63, HQ82 and HQ114) and at 50 min. for rock specimens HQ5 and HQ30 and at 20 min. for rock specimen HQ146.

Fig. E.2 Variation in Low-Amplitude Material Damping Ratio with Effective Confining Pressure from Resonant Column Tests of Undisturbed Soil and Rock Samples from Los Alamos

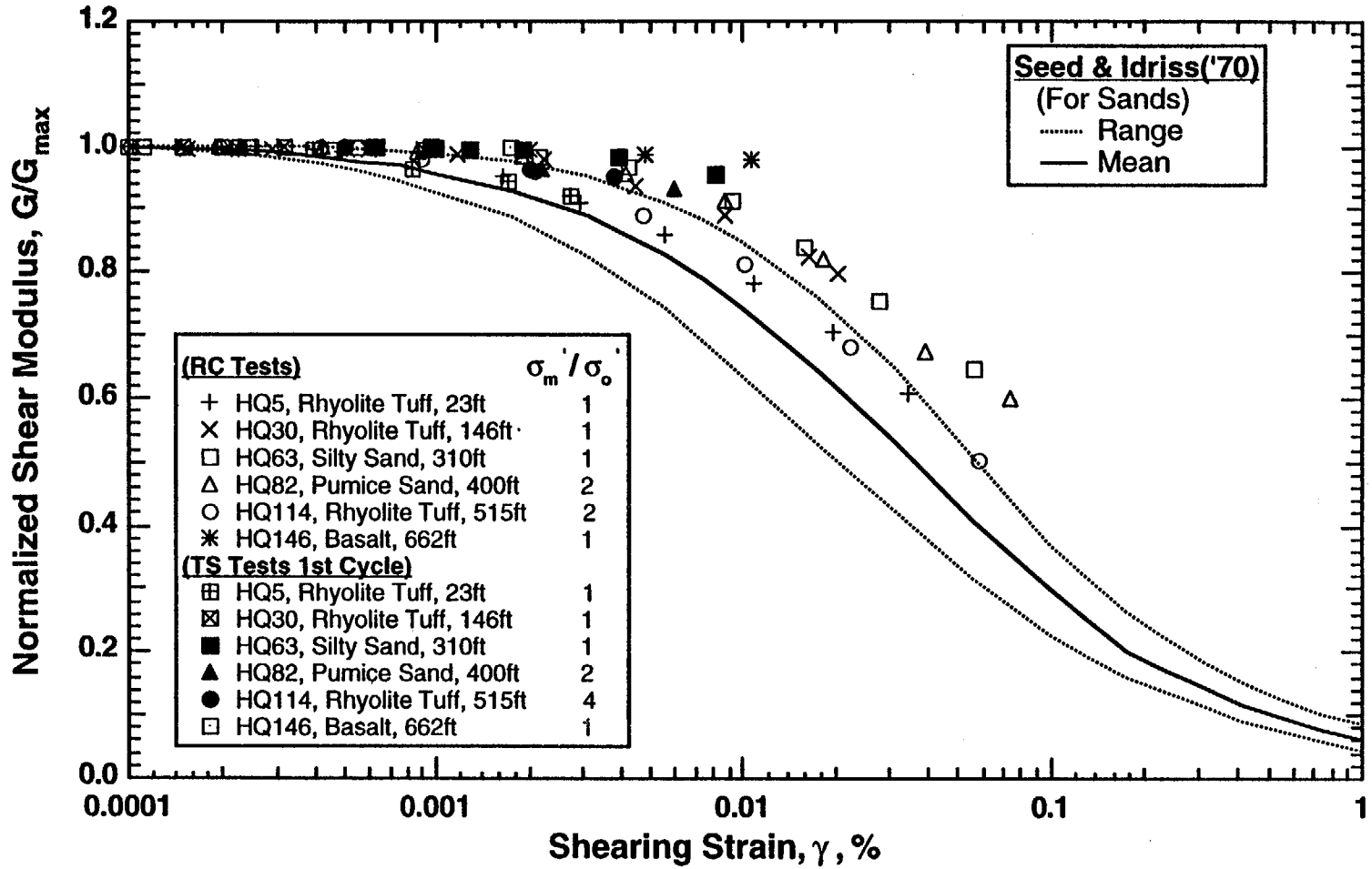

Notes:

1. Only results at a confining pressure within a factor of four of the estimate in situ mean effective stress are plotted.
2. σ_m' = estimated in situ mean effective stress using $K_o' = 0.5$.
3. σ_o' = effective confining pressure of the tests.

Fig. E.3 Variation in Normalized Shear Modulus with Shearing Strain from Resonant Column and Torsional Shear Tests of Undisturbed Samples from Los Alamos

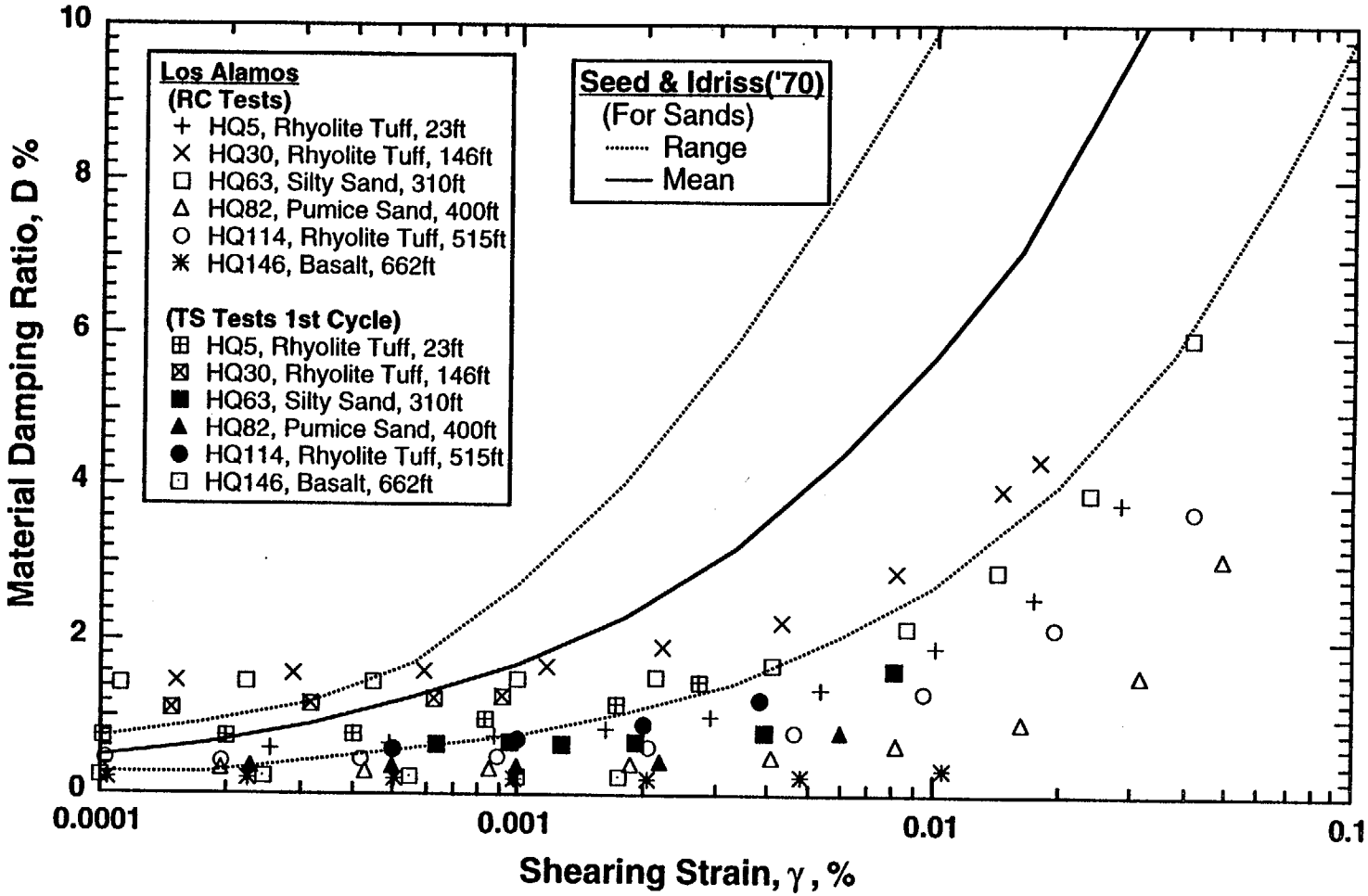

Notes:

1. Only results at a confining pressure within a factor of four of the estimate in situ mean effective stress are plotted.
2. σ'_m = estimated in situ mean effective stress using $K'_o = 0.5$.
3. σ'_o = effective confining pressure of the tests.
4. Shearing strains were corrected to the average of the first 3 free-vibration cycles.

Fig. E.4 Variation in Material Damping Ratio with Shearing Strain for g , 0.1 % from Resonant Column and Torsional Shear Tests of Undisturbed Soil and Rock Samples from Los Alamos

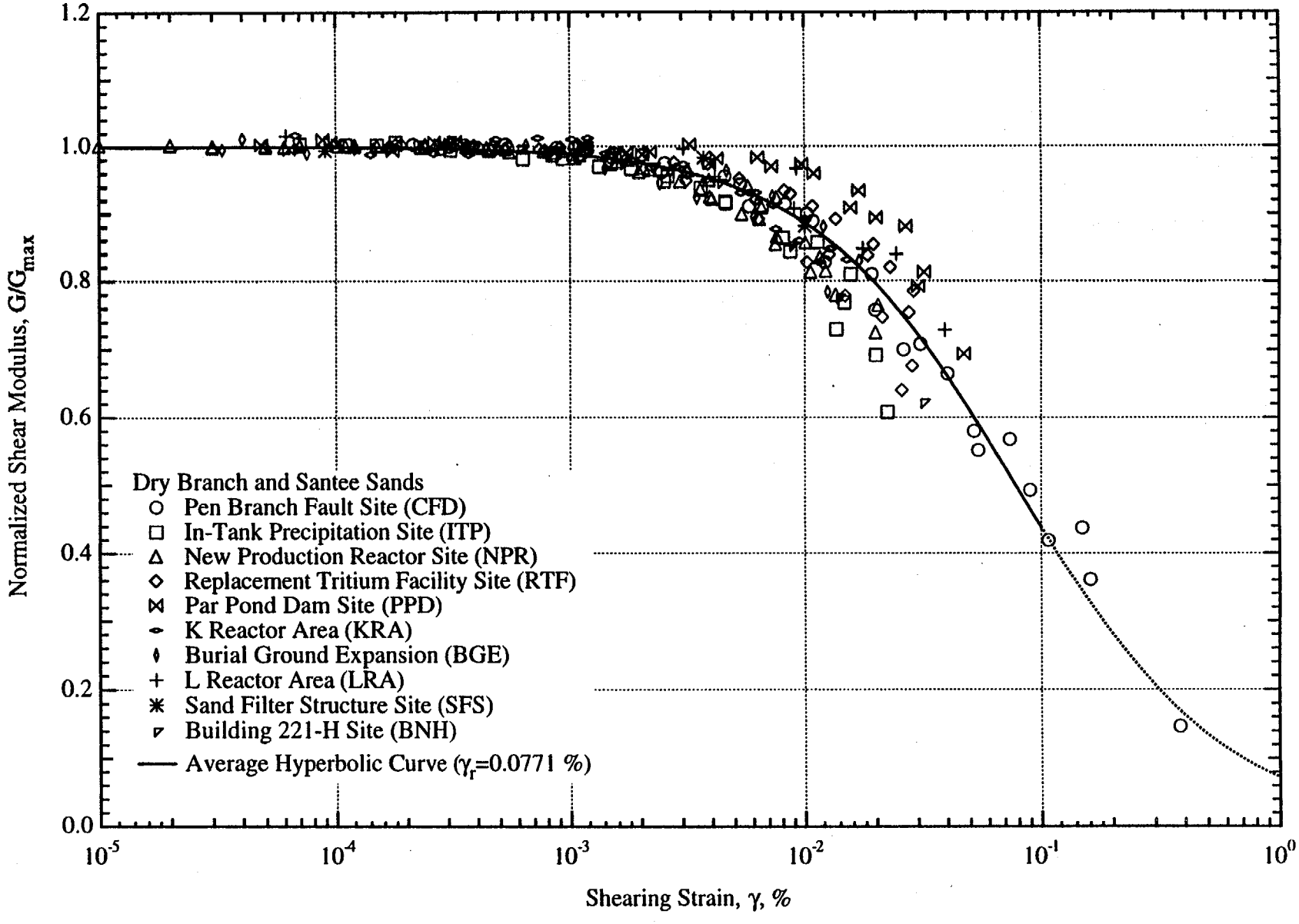

Fig. F.1 Summary Plot of All G/G_{max} - log γ Relationships Determined by Resonant Column Testing with the Specimens Confined At or Near the In-Situ Mean Effective Stress for the Dry Branch and Santee Sands

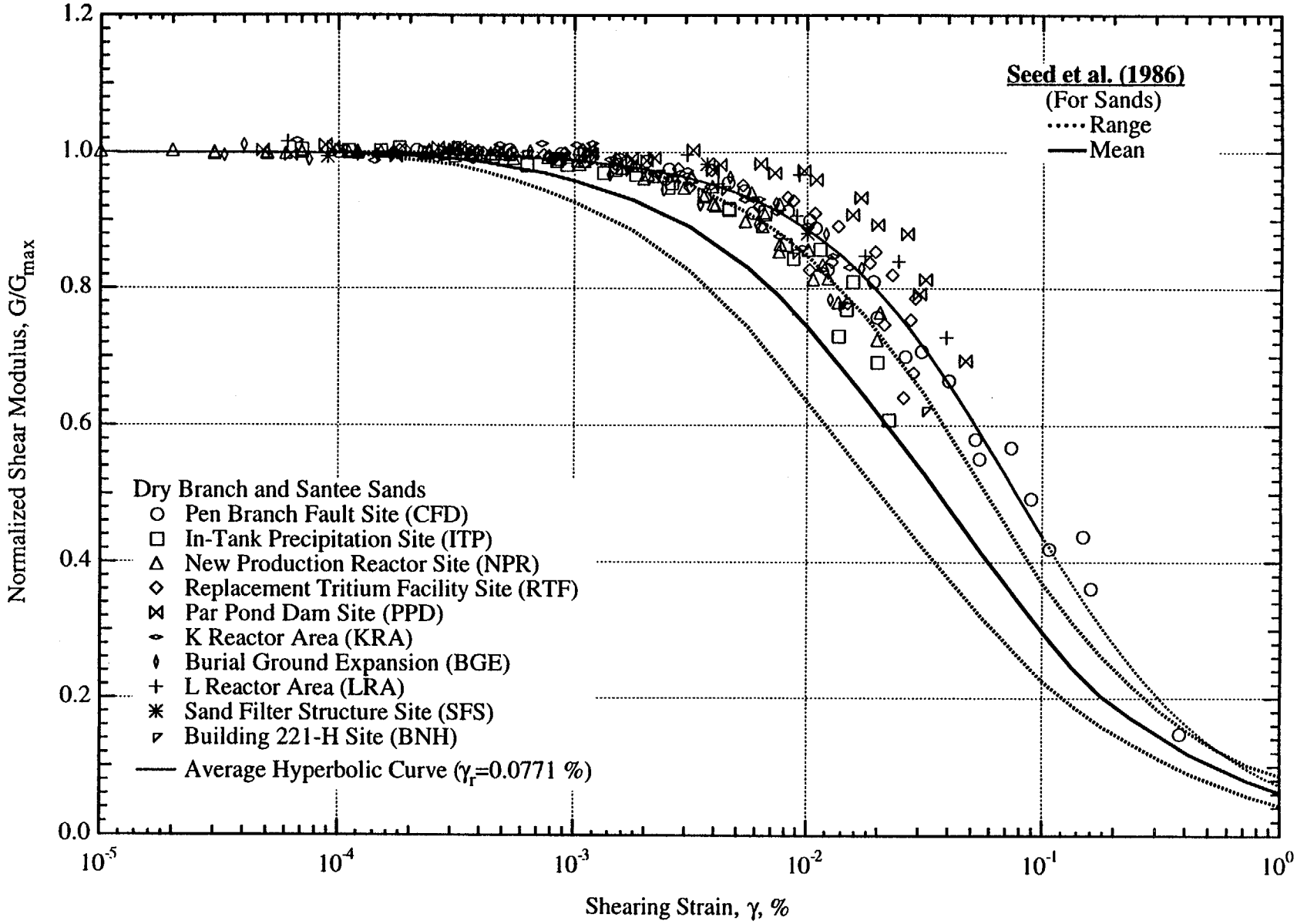

Fig. F.2 Comparison of the G/G_{max} - log γ Relationships Determined by Resonant Column Testing of Sands from the Dry Branch and Santee Formations with the Relationship Recommended by Seed et al. (1986) for Sands

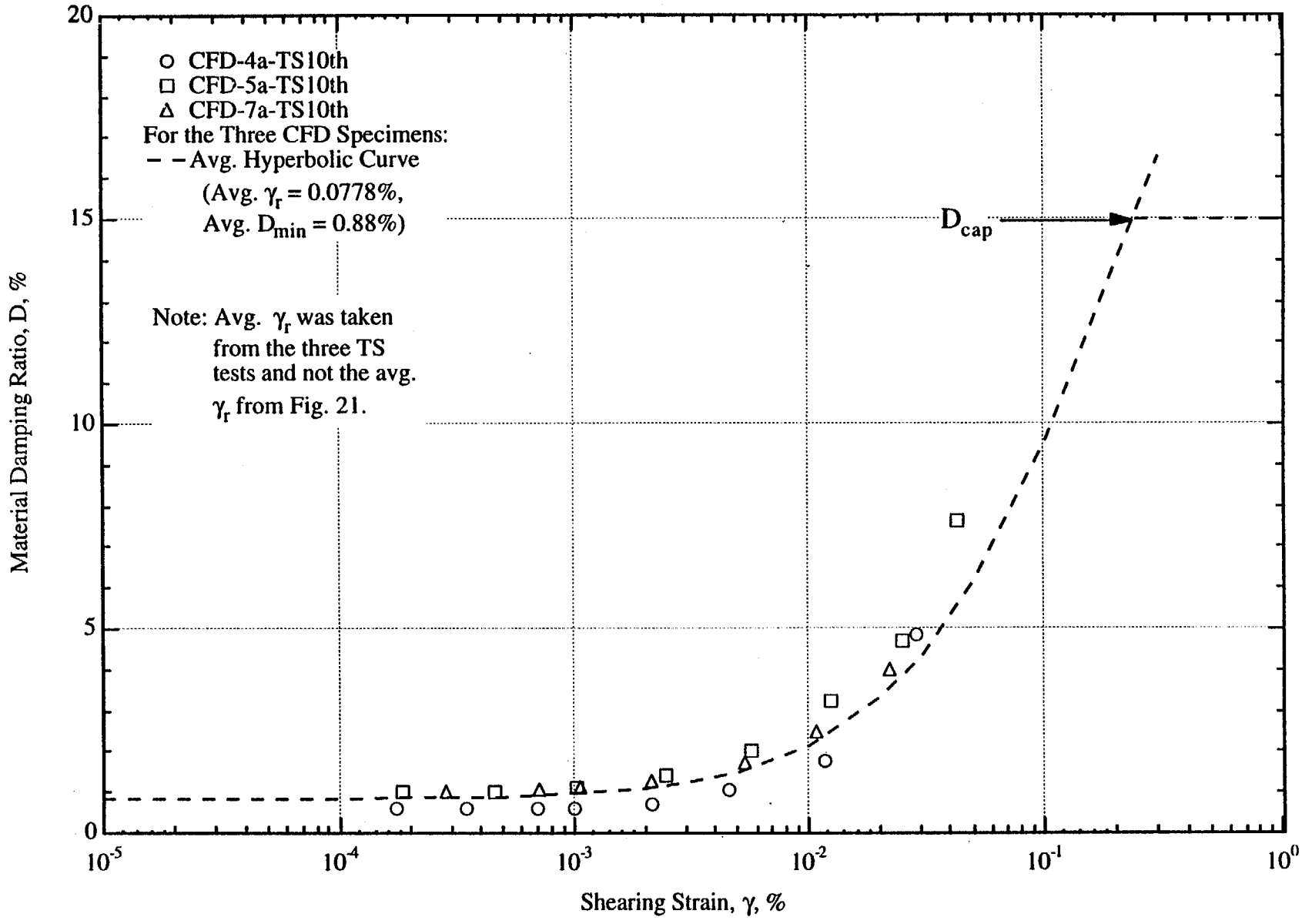

Fig. F.3 Comparison of the D - log γ Relationships Measured in the Tenth Cycle of TS Testing with an Average Hyperbolic Relationship and Material Damping Cap for the Dry Branch and Santee Sands

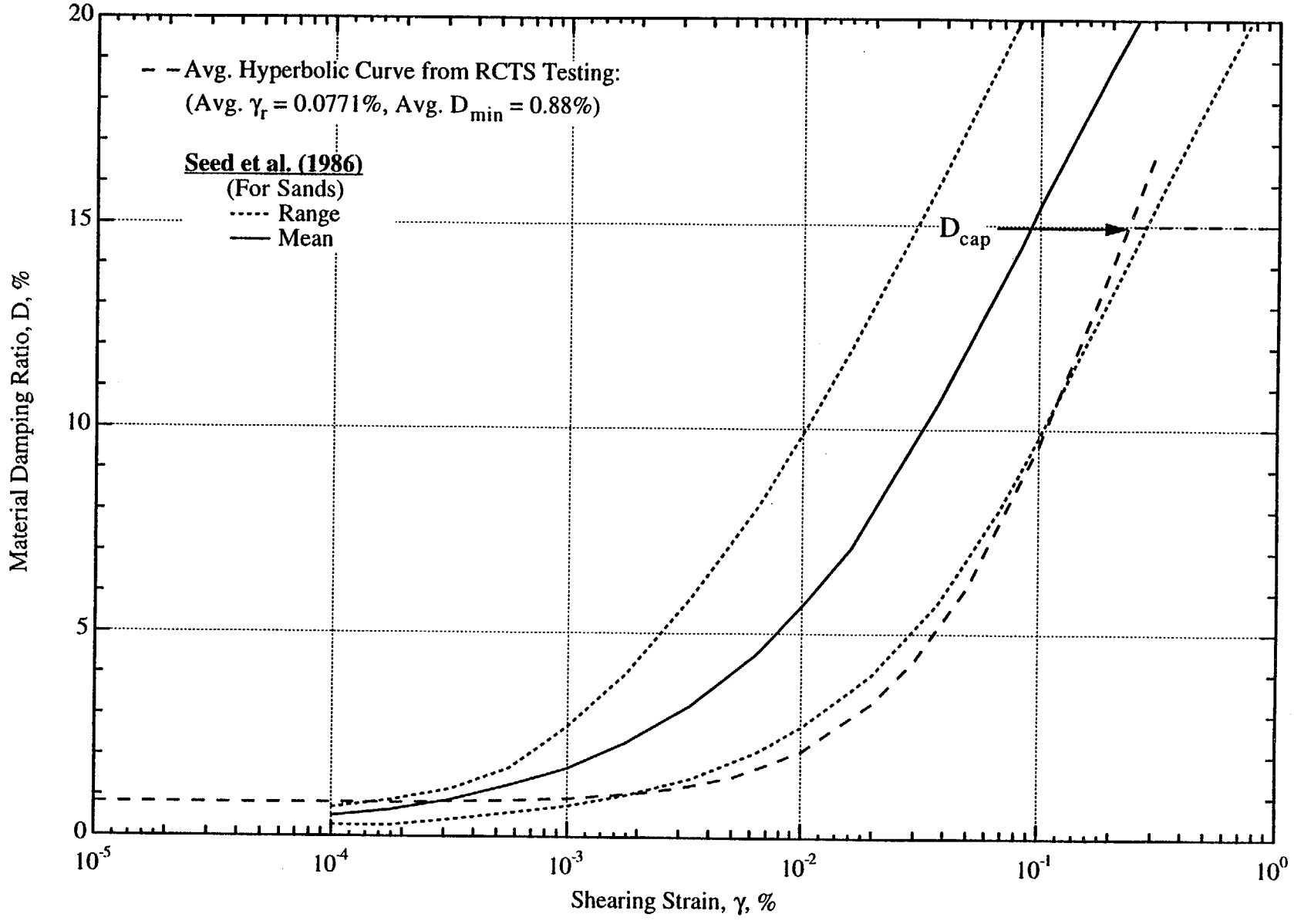

Fig. F.4 Comparison of the Recommended Average Hyperbolic D - log γ Relationship for the Dry Branch and Santee Sands with the D-log γ Relationship Recommended by Seed et al. (1986) for Sands

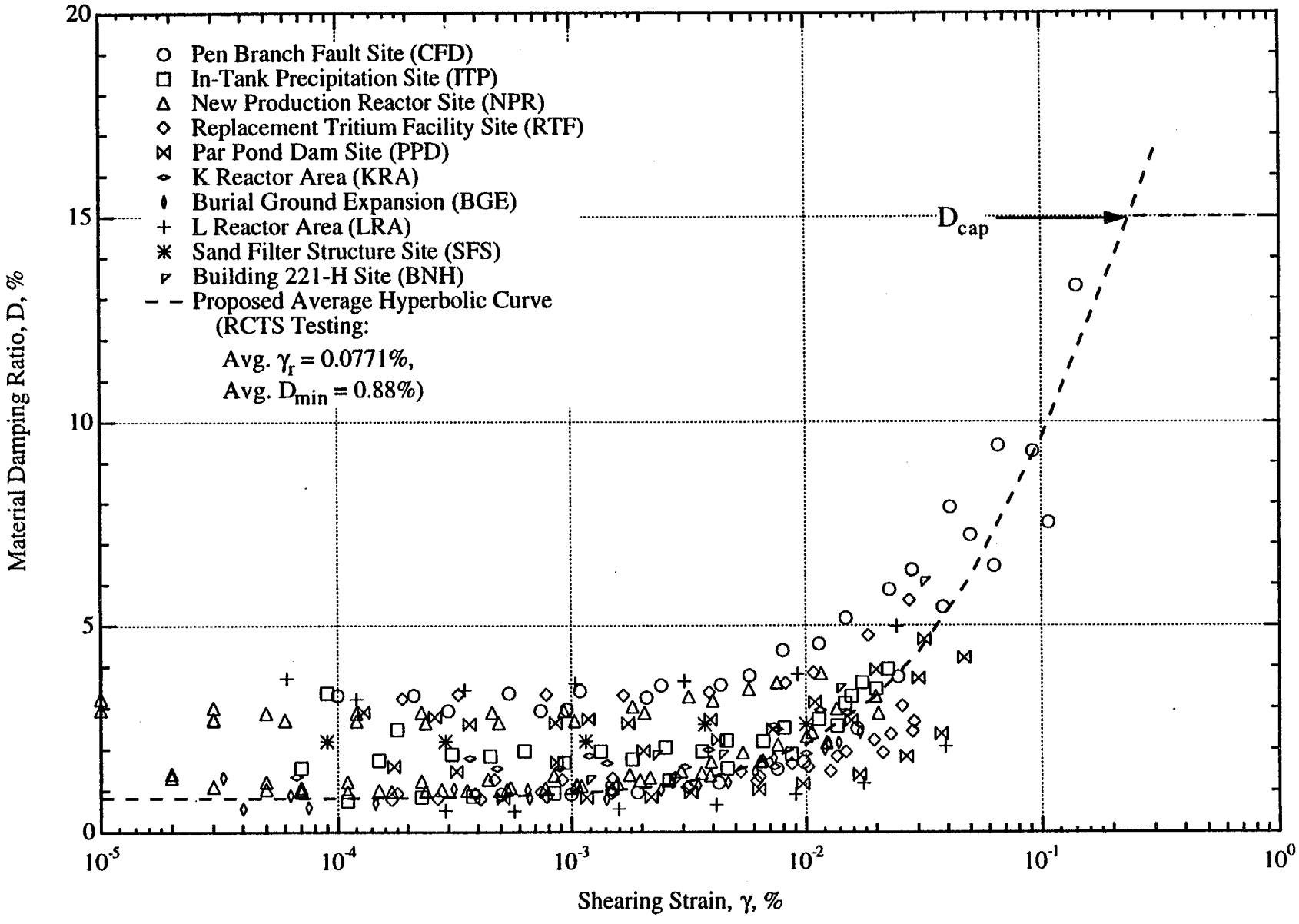

Fig. F.5 Comparison of the Recommended Average Hyperbolic D - log γ Relationship Determined from RCTS Testing with the Resonant Column Results for the Dry Branch and Santee Sands

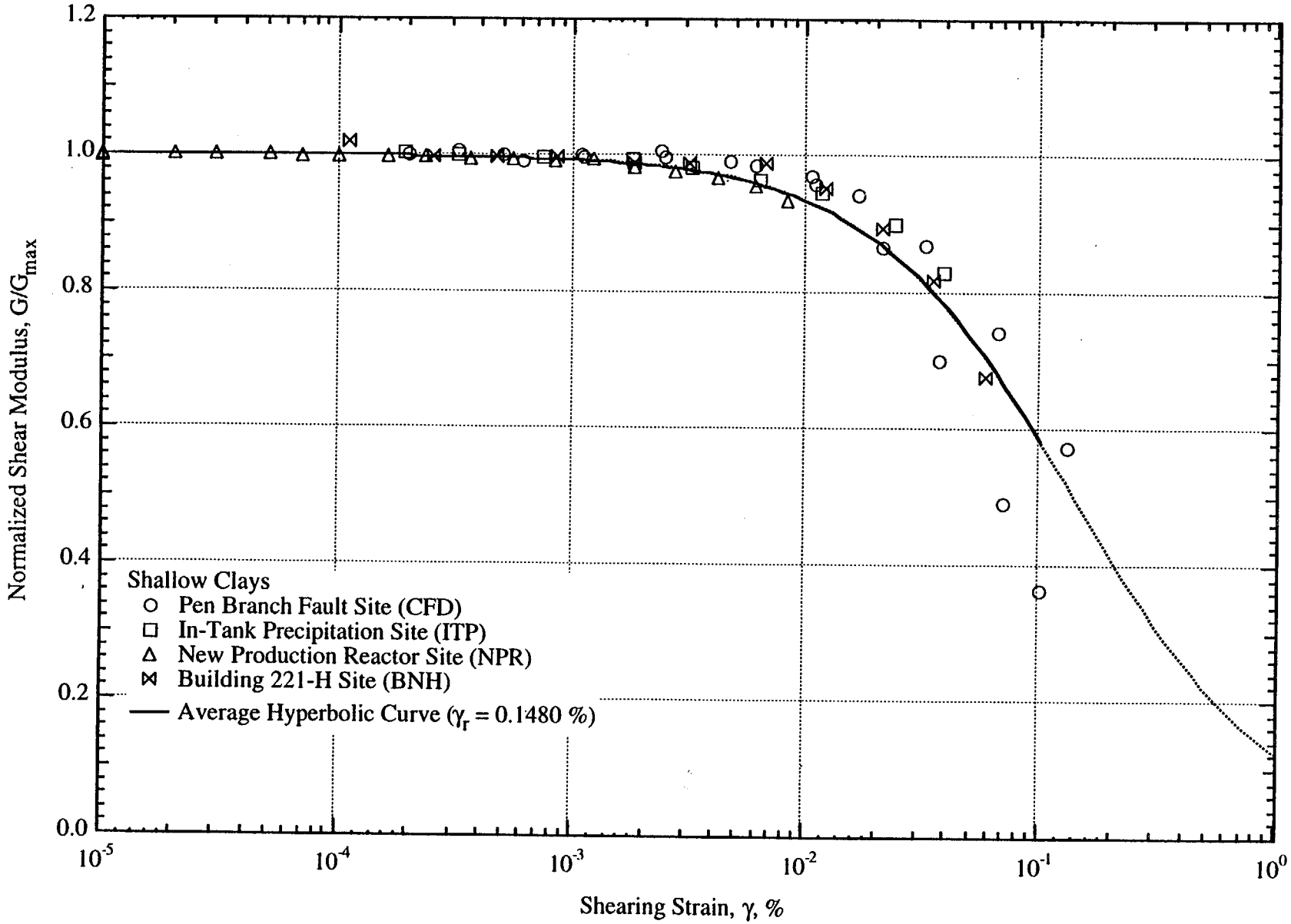

Fig. F.6 Summary Plot of All G/G_{max} - log γ Relationships Determined by Resonant Column Testing with the Specimens Confined At or Near the In-Situ Mean Effective Stress for the Shallow Clays

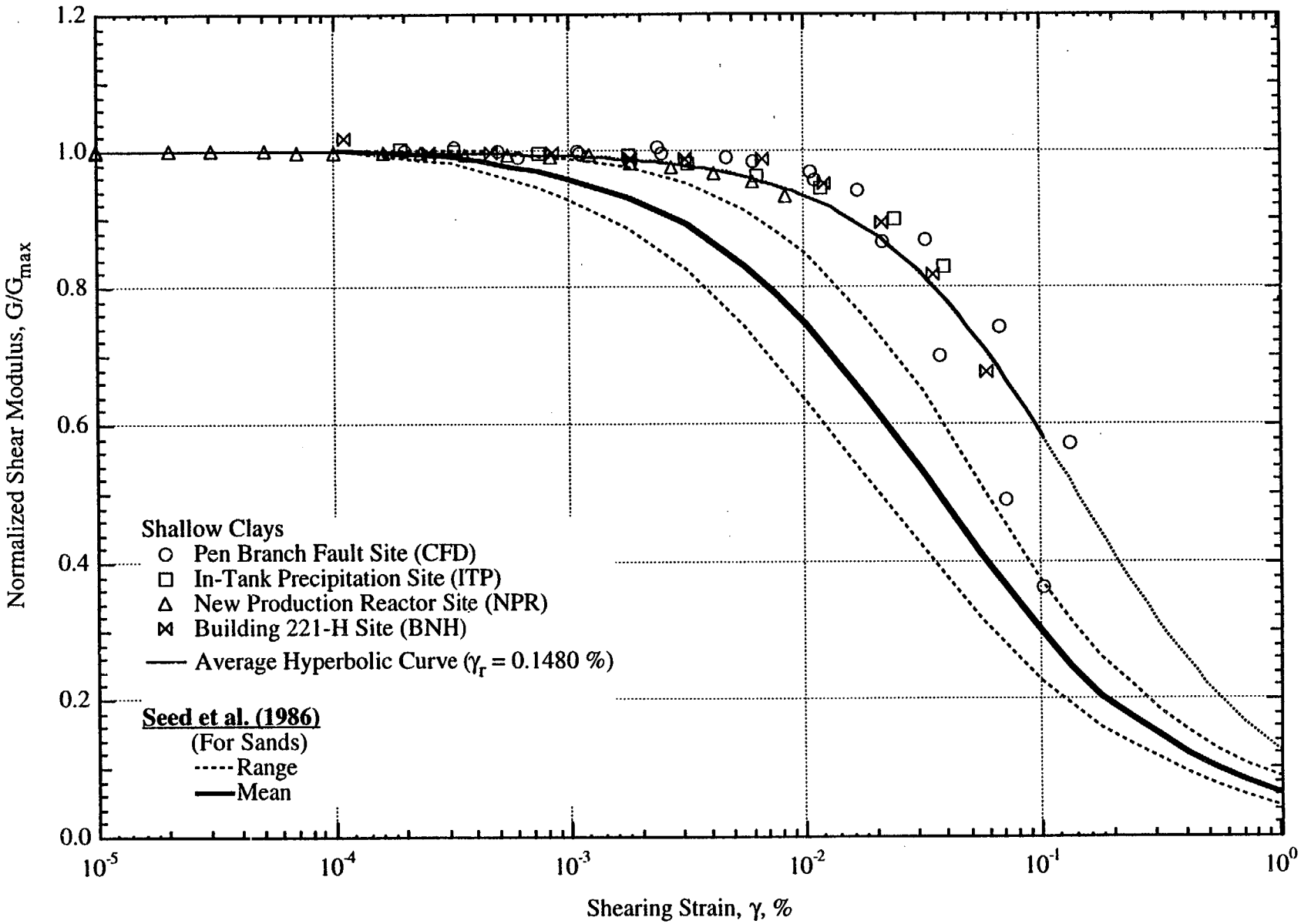

Fig. F.7 Comparison of the G/G_{max} - log γ Relationships Determined by Resonant Column Testing of the Shallow Clays with the Relationship Recommended by Seed et al. (1986) for Sands

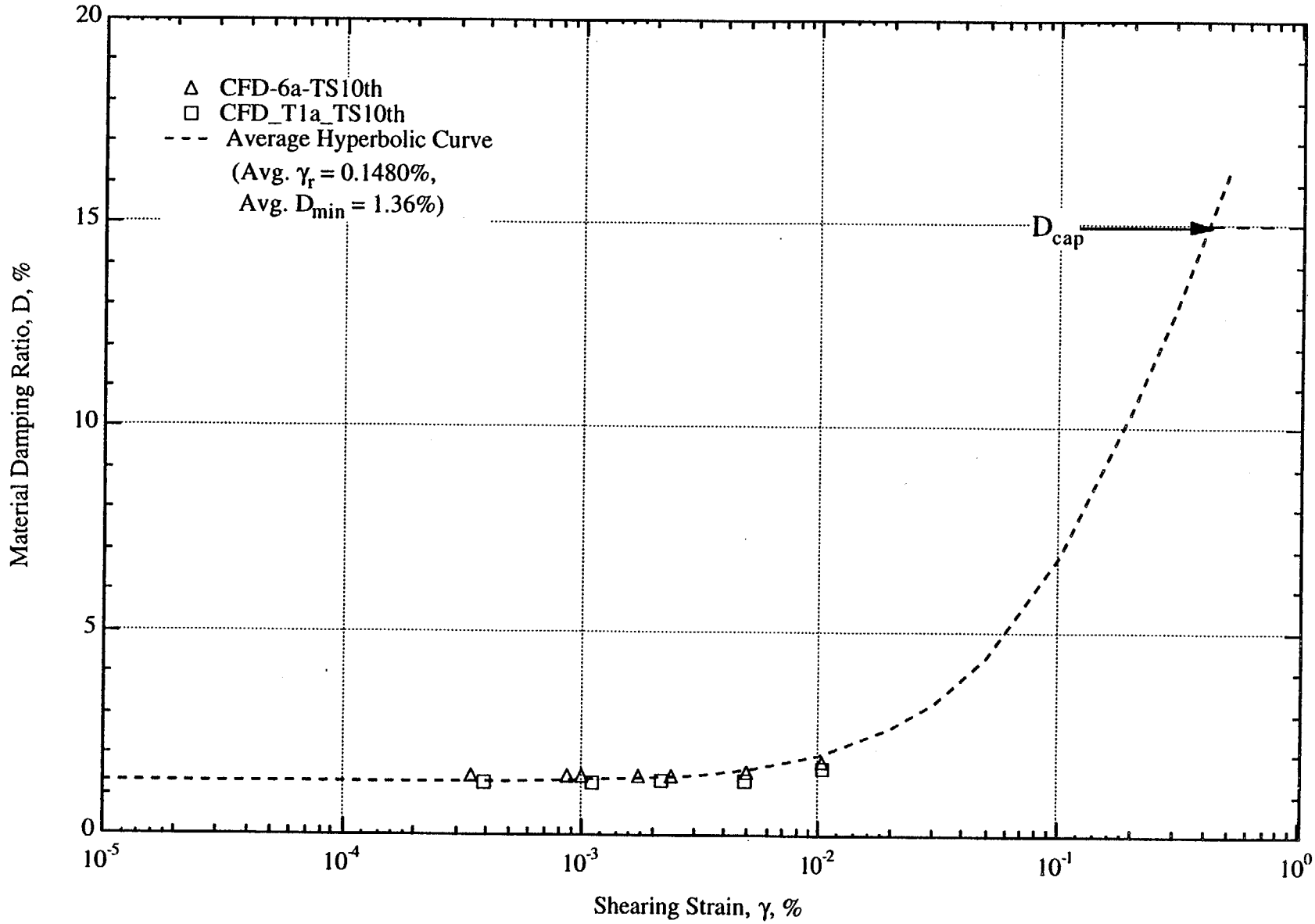

Fig. F.8 Comparison of the D - log γ Relationships Measured in the Tenth Cycle of TS Testing with the Recommended Average Hyperbolic Relationship and Material Damping Cap for the Shallow Clays

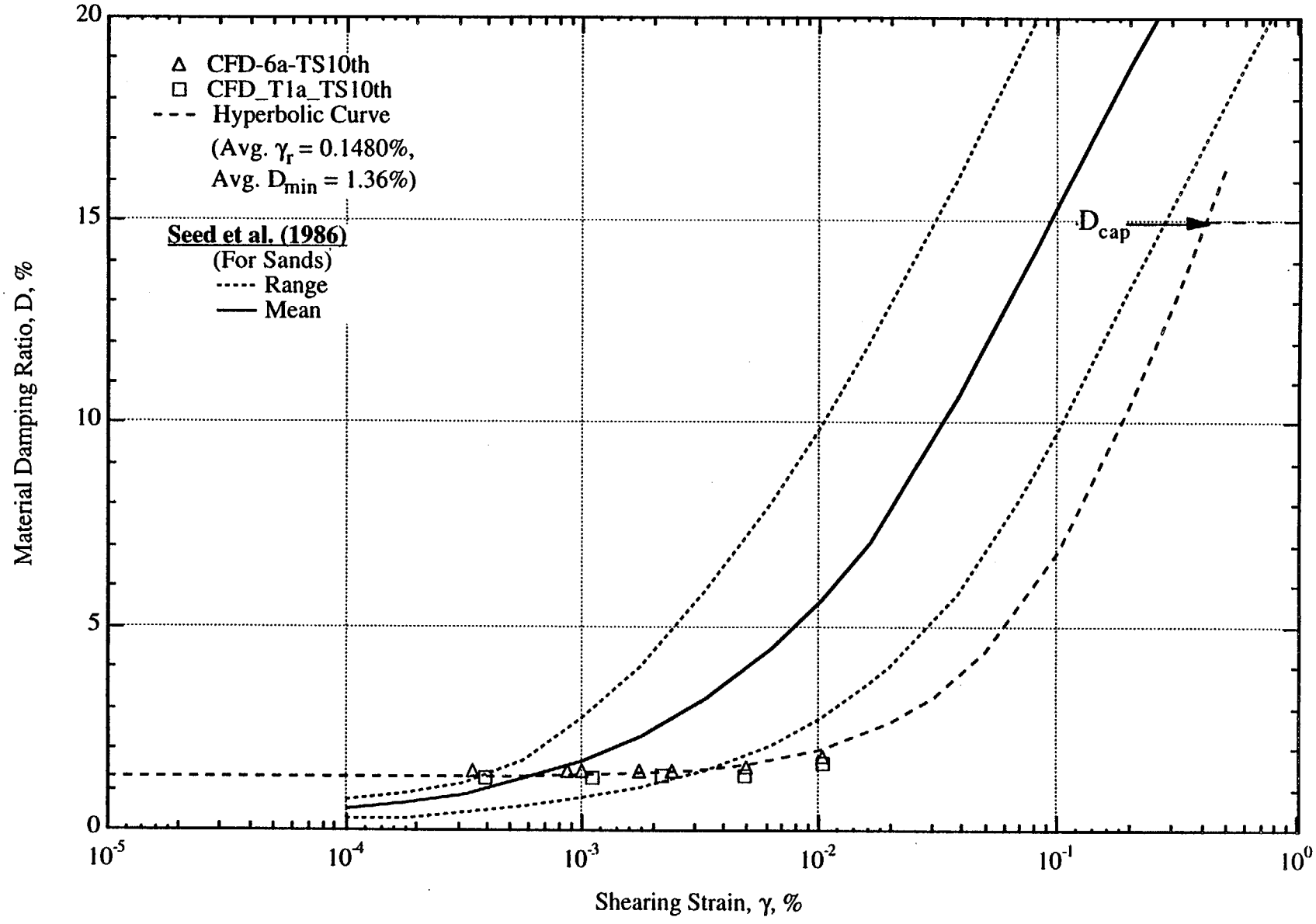

Fig. F.9 Comparison of the Recommended Average Hyperbolic D - log γ Relationship for the Shallow Clays with the Relationship Recommended by Seed et al. (1986) for Sands

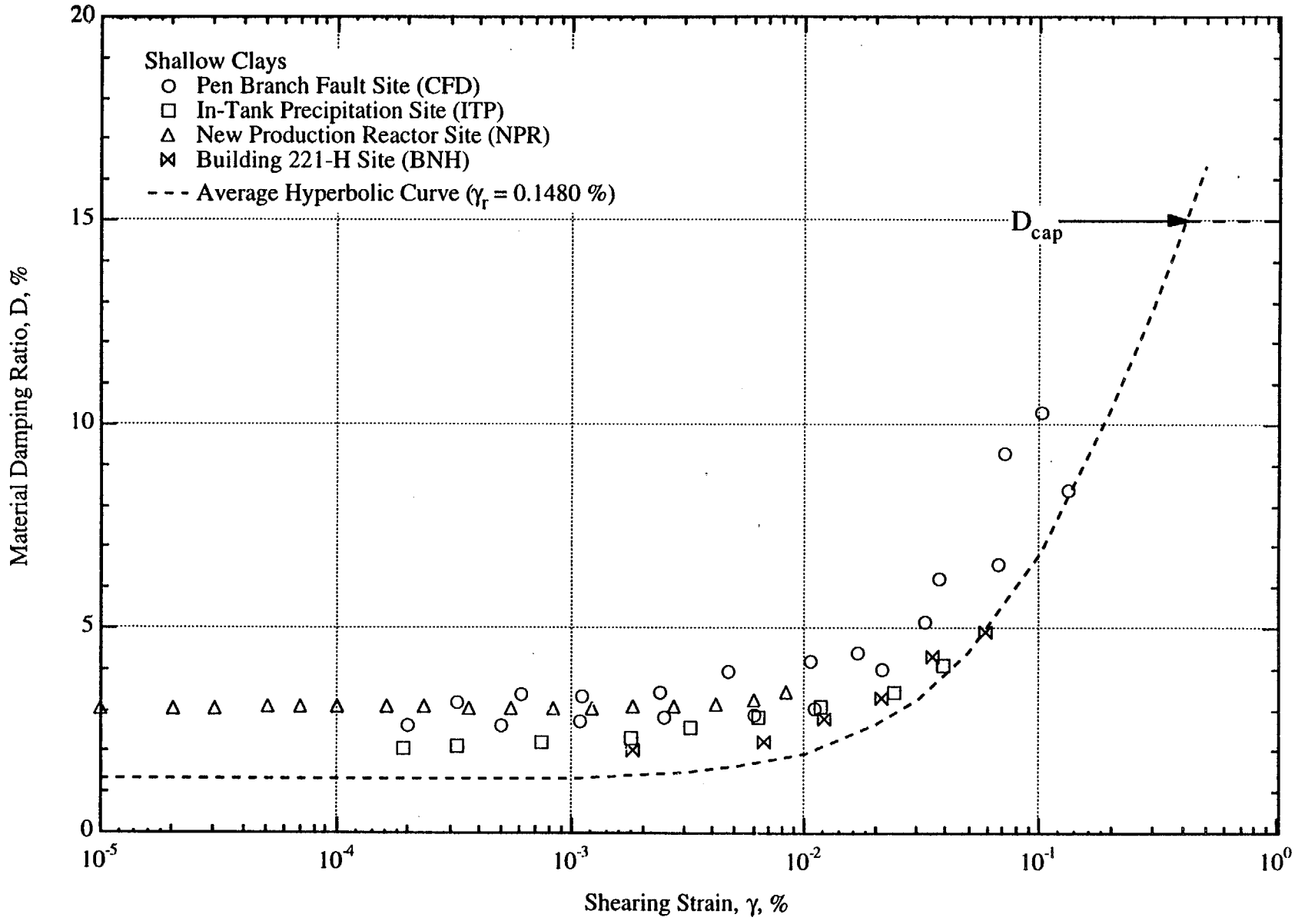

Fig. F.10 Comparison of the Recommended Average Hyperbolic D - log γ Relationship Determined from RCTS Testing with the Resonant Column Results for the Shallow Clays

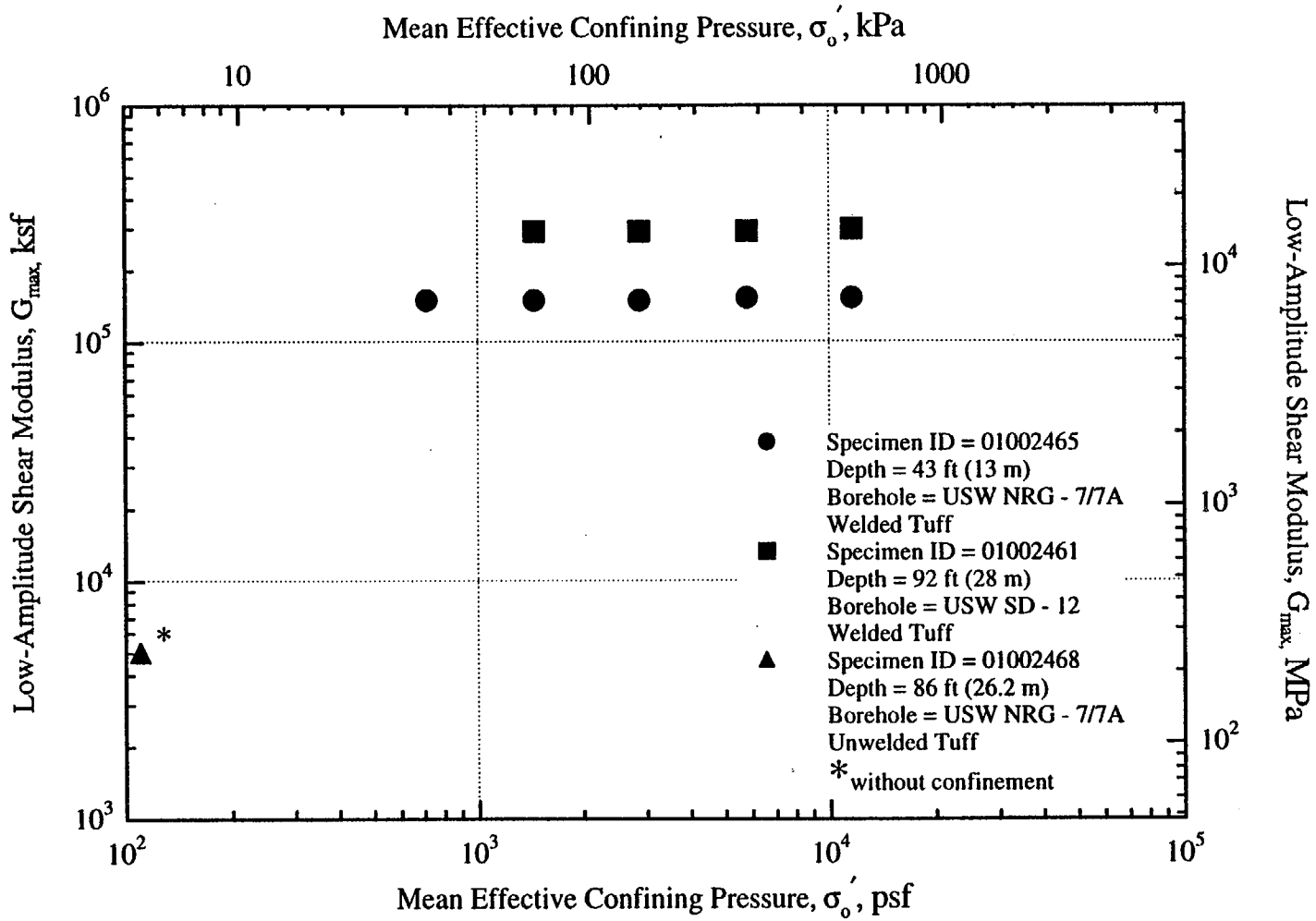

Fig. 18 Variation in Low-Amplitude Shear Modulus with Effective Confining Pressure from Resonant Column Tests of Intact Specimens from Yucca Mountain

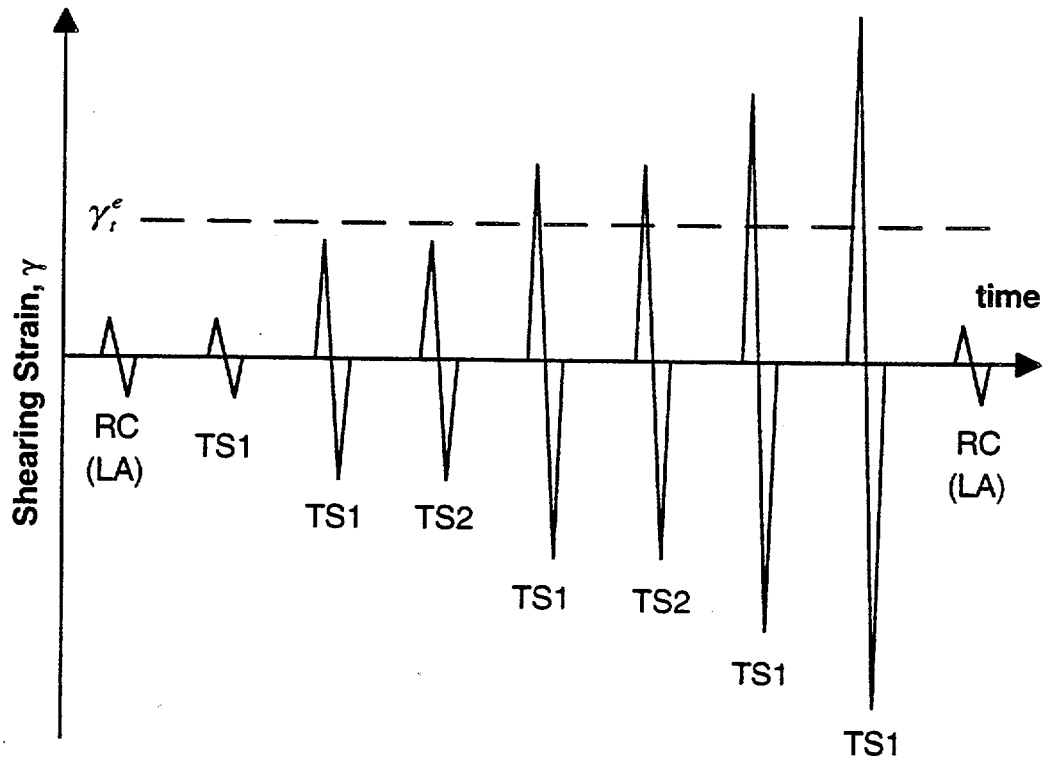

γ_t^e = elastic threshold strain; below γ_t^e, G is constant and equal to G_{max}

RC (LA) = resonant column test at low-amplitude strain

TS1 = torsional shear test in which 1 to 10 cycles are applied at 0.5 Hz

TS2 = torsional shear test in which 4 cycles are applied at each of approximately 5 frequencies between 0.1 and 10 Hz

Fig. 17 Testing Procedure Used in the Torsional Shear Test to Investigate the Effects of Strain Amplitude, Number of Loading Cycles and Excitation Frequency on Shear Modulus (G) and Material Damping Ratio (D)

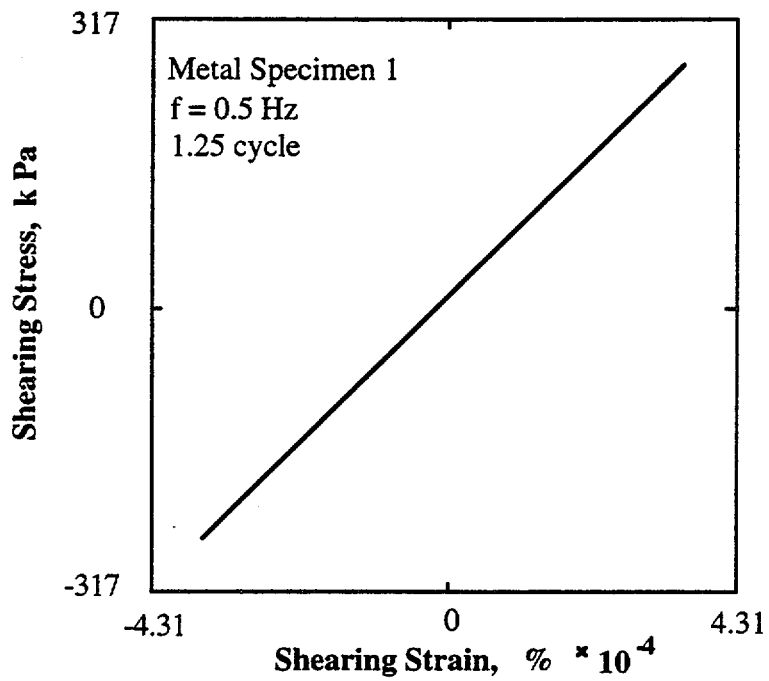

Fig. 16 Hysteresis Loops of Metal Specimen Determined by Torsional Shear Testing at a Frequency of 0.5 Hz

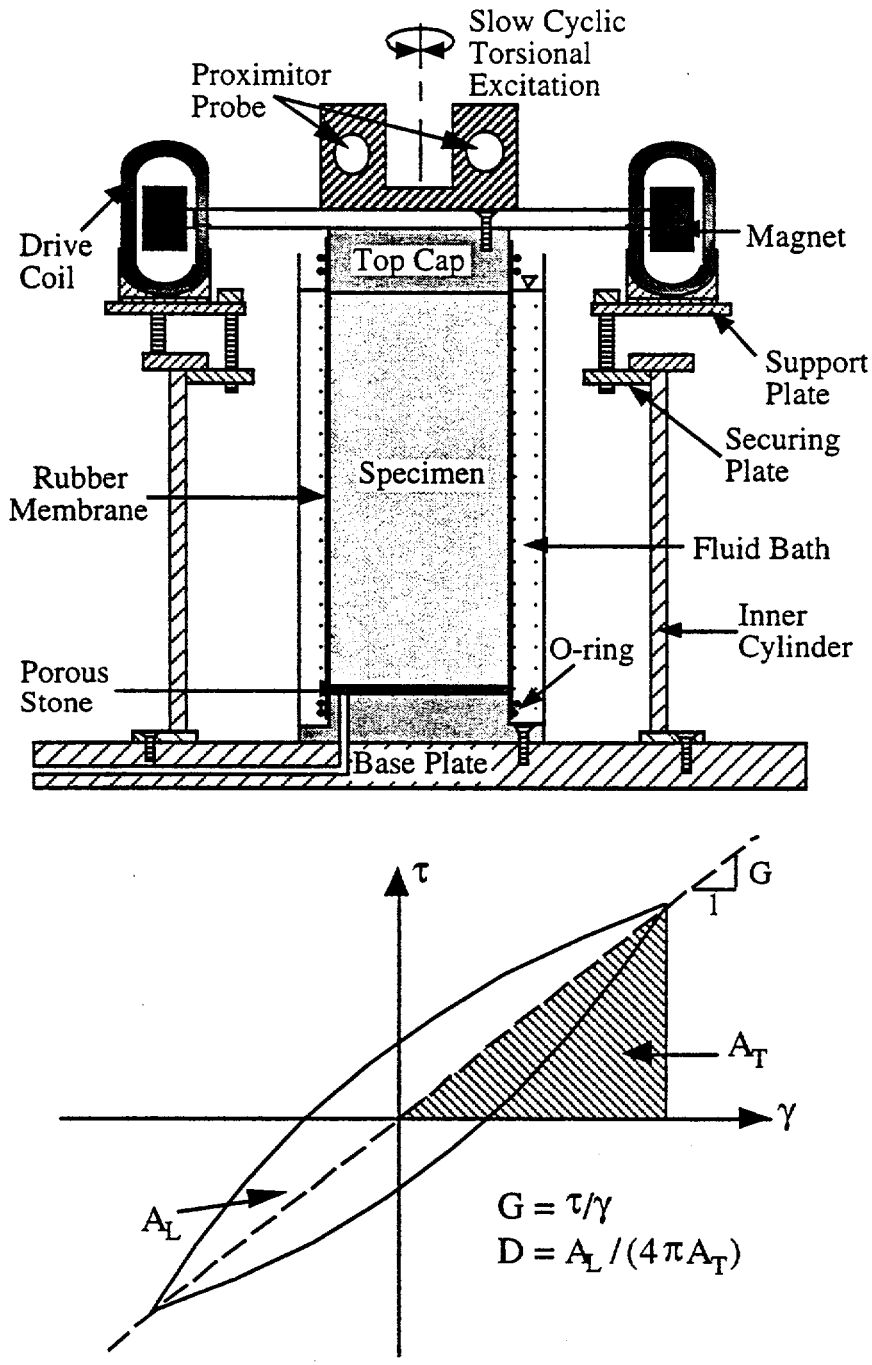

Fig. 15 Side View of a Fixed-Free Torsional Shear Test Set-Up and a Typical Hysteretic Loop for Shear Modulus and Material Damping Measurements

YUCCA MOUNTAIN/CALIFORNIA SCALING RELATIONS

Kenneth W. Campbell

Yucca Mountain Ground Motion Workshop #2

Salt Lake City, Utah

January 9-10, 1997

EQE

Regional Scaling Characteristics

- Regional differences included in this study:
  - Crustal structure (β, ρ)
  - Crustal attenuation (Q)
  - Site attenuation (κ_0)
  - Stress drop ($\Delta\sigma$)
- Regional differences excluded in this study:
  - Source scaling relation
  - Magnitude measure
  - Distance measure

EQE

Methodology

- Point-source BLWN model
- Regional Earthquake, Crustal, and Site Characteristics
- RVT Estimate of Ground Motion Parameters
- Ratio of Ground Motions - California/Yucca Mountain

EQE

Regional Characteristics

- California:
  - Crustal structure (Boore & Joyner, 1996)
  - Crustal attenuation ($Q = 150\ f^{0.6}$)
  - Site attenuation ($\kappa_0 = 0.04$ sec)
  - Stress drop ($\Delta\sigma = 100$ bars)
- Yucca Mountain:
  - Crustal structure (Yucca Mtn. Scenario Report)
  - Crustal attenuation ($Q = 250\ f^{0.4}$)
  - Site attenuation ($\kappa_0 = 0.02$ sec)
  - Stress drop ($\Delta\sigma = 50, 75, 100$ bars)

EQE

Conclusions

- Greatest sensitivity to regional characteristics between California and Yucca Mountain result from:
  - Site attenuation (κ_0) at high frequencies
  - Stress drop ($\Delta\sigma$) at all frequencies

EQE

CRUSTAL AMPLIFICATION
Quarter-Wavelength Approximation

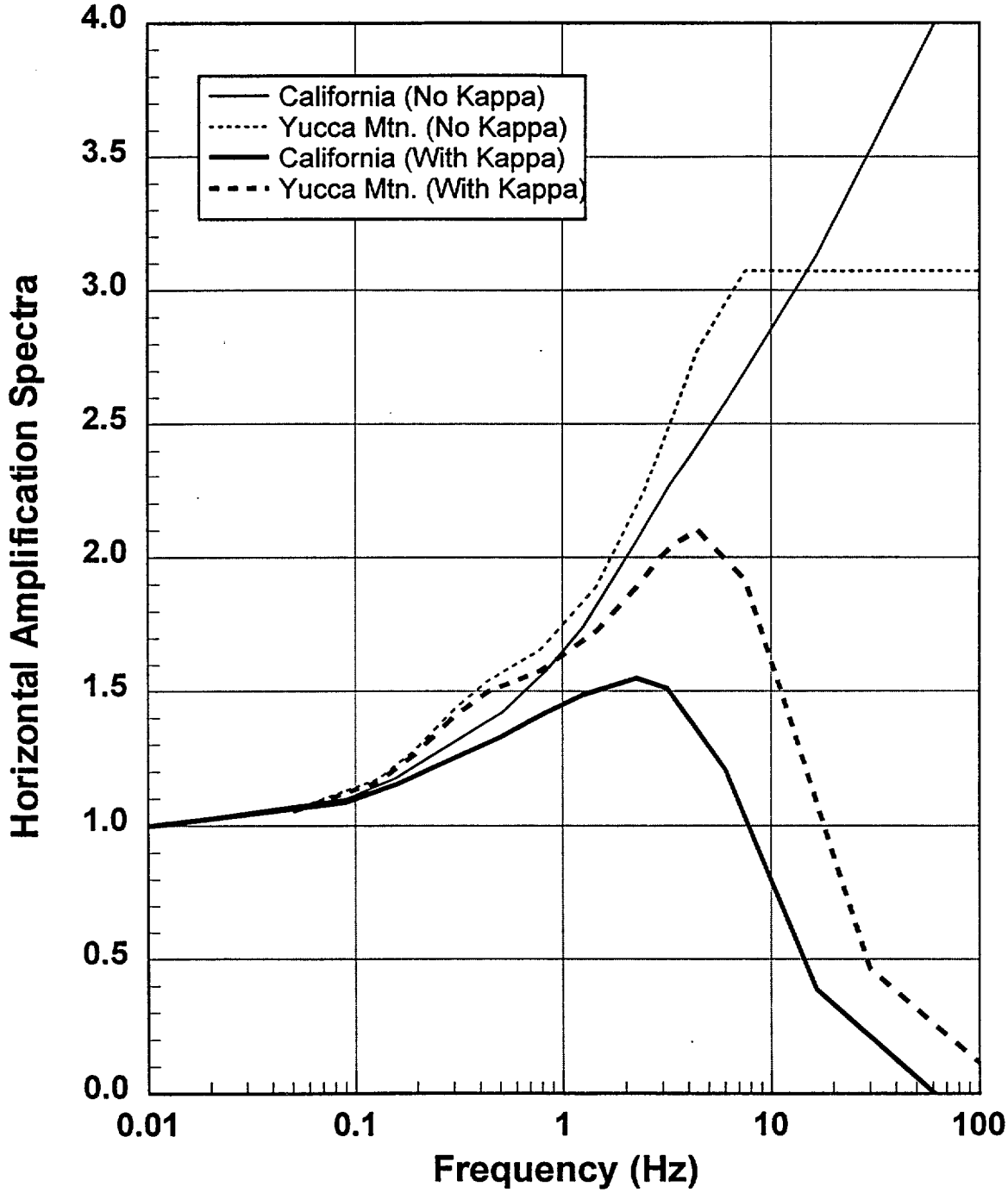

REGIONAL PARAMETRIC EFFECTS
5%-Damped Spectral Acceleration

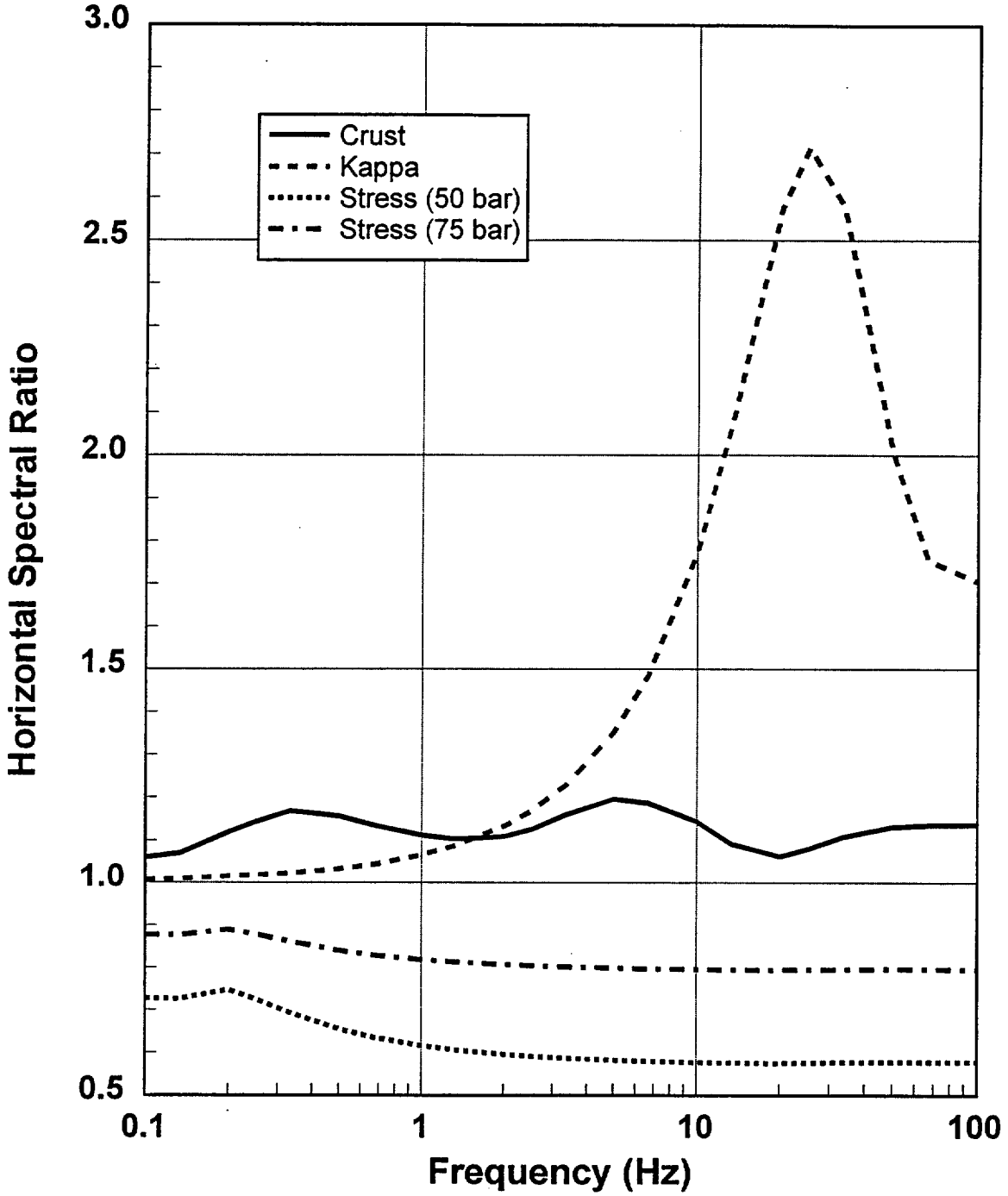

TOTAL REGIONAL EFFECTS
5%-Damped Spectral Acceleration

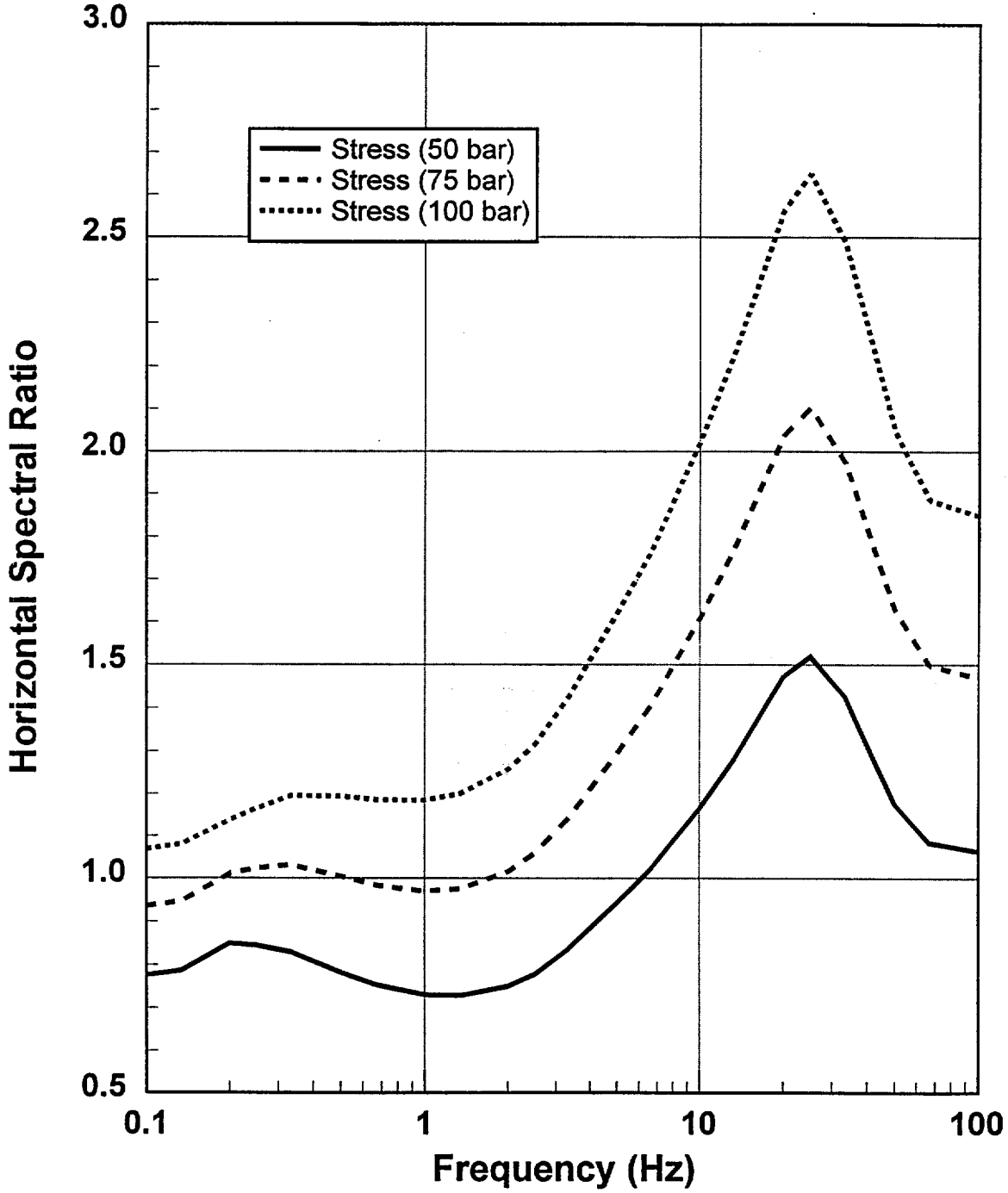

YUCCA MOUNTAIN GROUND MOTION WORKSHOP #2 - METHODS, MODELS AND PRELIMINARY INTERPRETATIONS

Salt Lake City
January 9-10, 1997

GROUND MOTIONS AT YUCCA MOUNTAIN FROM SHALLOW EVENTS

Paul Somerville
Woodward-Clyde, Pasadena

ISSUE 1: PATH EFFECTS AND SITE AMPLIFICATION AT YUCCA MOUNTAIN

Analysis of strong motion recordings of NTS explosions at Yucca Mountain sites indicates that they have larger motions than those of other NTS stations by a factor of two on average over the period range of 0.5 to 5 Hz (Phillips, SAND88-3032, 1991). Phillips concluded that this was due to site response at Yucca Mountain, and tentatively attributed it to topographic amplification effects.

A preliminary analysis of explosion and earthquake recordings was described in Appendix B.2 of Seismic Design Inputs for the Exploratory Studies Facility at Yucca Mountain, which is attached. This preliminary analysis indicates that the large motions are due to surface waves which are generated by both NTS explosions and very shallow earthquakes such as those of the Rock Valley sequence of 1993. It is shown that the amplification does not occur in the body wave parts of these seismograms, and so would not affect the ground motions of earthquakes, which are dominated by body waves. It is demonstrated that these surface waves are not present in recordings of two deeper events of the 1993 Eureka Valley sequence that occurred at depths of 2 and 6 km.

At present, the argument in Appendix B.2 is anecdotal, and needs more systematic and rigorous development in order to effectively refute the hypothesis of Phillips (1991). This work should include data analyses of the kind already begun in Appendix B.2, but using a much more comprehensive set of seismograms. It should also include wave propagation modeling studies to investigate whether the crustal structure between NTS and the Yucca Mountain site, as delineated by Walck and Phillips (SAND88-3033; 1990), can give rise to the large surface waves that are observed at Yucca Mountain. The ability to explain these surface waves by modeling would provide a strong demonstration that the amplification effects can be accounted for by path effects, and that no site amplification effect is required to explain them. Since the path model of Walck and Phillips (1990) is a 2-D model, it may be necessary to use 2-D finite difference modeling of the type described by Graves (1993; 1995) to model the wave propagation effects along this path.

ISSUE 2: SHALLOW FAULTING NEAR YUCCA MOUNTAIN

It was noted in the discussion of Issue 1 that the 1993 Rock Valley earthquakes, which had very shallow depths, generated large surface waves at Yucca Mountain. This raises the question of whether very shallow earthquakes could occur closer to Yucca Mountain (a source characterization issue), and if so, how large their surface waves would be (a ground motion characterization issue). This gives rise to uncertainty in the median value and dispersion of ground motion attenuation relations for use at the site.

GROUND MOTION SIMULATIONS USING A BROADBAND GREEN'S FUNCTION METHOD

A ground motion modeling exercise will be discussed as part of this meeting. This is an extension of Activity 8.3.1.17.3.3, ground modeling of scenario earthquakes at Yucca Mountain, performed by six ground motion modelers. They generated strong ground motion time histories for specific scenario earthquakes having discrete magnitudes and distances. One of these was a broadband Green's function method used by Somerville and Saikia (Somerville, 1992; Saikia, 1994). In the following, we briefly summarize how the broadband Green's function method was used. We also point out extensions of this method that could incorporate the effects of laterally varying velocity structure described under Issue 1. The results of these modeling activities could also be extended to produce ground motion attenuation relations for use in the probabilistic seismic hazard analysis program to complement the empirical models. This could be done using a comprehensive set of ground motion calculations for the full range of magnitudes and distances relevant to the site.

For source characterization, we considered seismic moment, fault length, fault width, strike, dip, rake, depth of top of fault, hypocenter, rupture velocity, slip distribution, and rise time, using models developed by Somerville and Abrahamson (1991). The most sensitive parameters are source depth, and fault length and width for a given seismic moment. Some constraints on these parameters were obtained from the source parameters of past Basin and Range earthquakes. We modeled the near-fault recordings of the 1992 Little Skull Mountain earthquake, and estimated the modeling and parametric uncertainty in the calculated ground motions using the procedure of Abrahamson et al. (1990).

The path is characterized by seismic velocities, density, and Q of a crustal model. The most sensitive parameters are velocity gradients in the shallow and deep parts of the crust, which should be well controlled by data at Yucca Mountain. Our wave propagation model could be further calibrated by modeling the recorded waveforms of earthquakes (such as the 1971 Massachusetts Mountain earthquake and the 1992 Little Skull Mountain earthquake sequence) and NTS explosions, to test whether flat layered models are adequate given the strong lateral variations in crustal structure noted by Walck and Phillips (1991). As discussed under Issue 1, the large surface waves generated at Yucca Mountain by shallow earthquakes such as the 1993 Rock Valley sequence (CRWMS, 1994, Appendix B2) need to be addressed. Similar large surface waves are recorded routinely at Yucca Mountain from NTS explosions and gave rise to the "site effects" (actually path effects according to our analysis) at Yucca Mountain noted by

Phillips (1991).

The site response is characterized using surface seismic velocities, density, and Q (kappa). The most sensitive parameter is kappa, which should be well controlled by data from Yucca Mountain. Abundant downhole recordings at Yucca Mountain and other NTS sites from NTS explosions, in addition to sparse underground recordings of the 1992 Little Skull Mountain earthquake sequence, could be used to further calibrate site response models.

The ground motion attenuation function is determined by the crustal structure and the source depth, and thus has predictive power in locations such as Yucca Mountain where crustal structure and source depth are available but few strong motion recordings exist. Our method can include Green's functions calculated using 2-D or 3-D models of crust structure, which may be quite relevant in view of the evidence for significant lateral changes in crustal structure around Yucca Mountain, especially at shallow crustal depths (Walck and Phillips, 1991).

We use empirical source functions to represent several stochastic aspects of high frequency ground motions that are difficult to model using deterministic methods. These include the incoherence that develops in the source radiation pattern at high frequencies, and scattering along the path and in the site region. Ideally, we would like to use recordings from the region to generate empirical source functions for use the site. To date we have not used empirical source functions from the Yucca Mountain region, but it may be possible to use strong motion recordings of the Little Skull Mountain earthquake and its aftershocks.

An important source of uncertainty is in knowing whether earthquake sources near the site radiate significantly at shallow depths, as occurred during the 1993 Rock Valley earthquake sequence (CRWMS, 1993). If so, then large surface waves are expected at Yucca Mountain, and it may be necessary to use 2-D or 3-D models to adequately model the propagation of these surface waves.

REFERENCES

Abrahamson, N.A., P.G. Somerville, and C.A. Cornell (1990). Uncertainty in numerical strong motion predictions. Proc. *Fourth U.S. Nat. Conf. Earthq. Eng., Palm Springs, CA,* 1, 407-416.

CRWMS (1994). Seismic Design Inputs for the Exploratory Studies Facility at Yucca Mountain. Technical Report BAB000000-01717-5705-00001 REV01.

Graves, R.W. (1993). Modeling three-dimensional site response effects in the Marina District basin, San Francisco, California.

Graves, R.W. (1995). Preliminary analysis of long-period basin response in the Los Angeles region from the 1994 Northridge earthquake, *Geophys. Res. Lett.,* 22, 101-104.

Phillips, J.S. (1991). Prediction of pseudo relative velocity response spectra at Yucca Mountain for underground nuclear explosions conducted in the Pahute Mesa testing area at the Nevada Test Site, SAND88-3032 UC-814.

Saikia, C.K. (1994). Modified frequency-wavenumber algorithm for regional seismograms using Filon's quadrature: modeling of Lg waves in eastern North America. *Geophys. J. Int.* 118, 142-158.

Somerville, P.G. and N.A. Abrahamson (1991). Characterizing earthquake slip models for the prediction of strong ground motions, EOS 72, 341. (abstract).

Somerville, P.G. (1992). Engineering applications of strong motion simulation, *Tectonophysics*, 218, 195-219.

Walck, M.C. and J.S. Phillips (1991). Two-dimensional velocity models for paths from Pahute Mesa and Yucca Flat to Yucca Mountain, SAND88-3033, Sandia Laboratories, Albuquerque, N.M.

WBS: 1.2.3
QA: QA

Civilian Radioactive Waste Management System
Management & Operating Contractor

Seismic Design Inputs for the Exploratory Studies Facility at Yucca Mountain

-Technical Report-

BAB000000-01717-5705-00001 REV00

April 29, 1994

Prepared for:

U.S. Department of Energy
Yucca Mountain Site Characterization Project Office
P.O. Box 98608
Las Vegas, NV 89193-8608

Prepared by:

Civilian Radioactive Waste Management System
Management & Operating Contractor
101 Convention Center Drive
Suite P-110
MS 423
Las Vegas, NV 89109

Under Contract Number
DE-AC01-91RW00134

APPENDIX B SITE-SPECIFIC EFFECTS ON GROUND MOTION

B.2 PATH EFFECTS: EFFECT OF SHALLOW SOURCE DEPTH ON GROUND MOTIONS AT YUCCA MOUNTAIN

Phillips (1991) analyzed recordings of underground nuclear explosions (UNEs)at four stations near Yucca Mountain and identified an amplification of ground motion by about a factor of 2 relative to other stations recording the events. An understanding of the cause of this amplification is important to assessing ground motion hazard for the ESF from earthquakes. Whether the amplification results from path effects or represents a site response at Yucca Mountain will determine if the probabilistically derived ground motion values need to be modified.

Figure B-1, modified from Walck and Phillips (1990), shows the locations of UNE sources and strong motion recording stations at Yucca Mountain and Jackass Flats. The four sites shown in Figure B-2 (Sites 14, 21, 22 and 23) have significantly larger ground motions than at other stations at comparable distances within the Nevada Test Site (NTS) (Figures B-3 through B-6). Amplifications of horizontal PSRV in the frequency range of 0.5 to 5 Hz are about a factor of 2 on average. Specifically, the amplification factors for horizontal motions are approximately 2.1, 2.4, 2.0 and 1.8 for frequencies of 0.5, 1, 2 and 5 Hz; the corresponding amplification factors for vertical motions are 2.4, 2.4, 2.3, and 1.8.

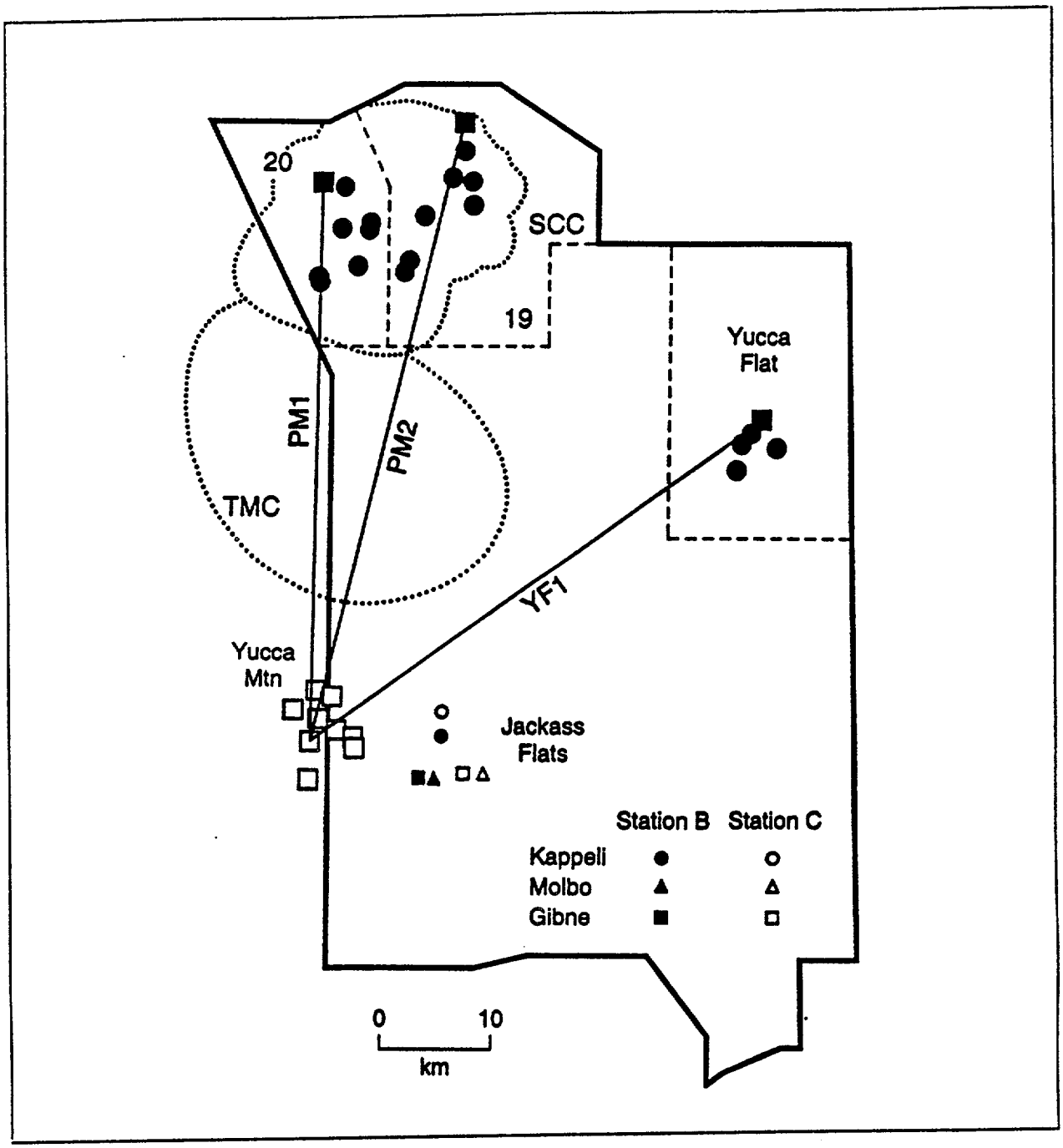

Figure B-1. Map showing locations of seismic stations, explosions, and velocity profiles PM1, PM2, and YF1. Large open squares represent stations at Yucca Mountain. The small circle, square, and triangle west of Jackass Flats indicate the location of station B (solid) and C (open). The larger, solid squares and circles indicate explosion locations. Area 19 and 20 encompass the Pahute Mesa area. Also shown are the Timber Mountain Caldera (TMC) and the Silent Caldera (SCC). (From Walck and Phillips, 1990)

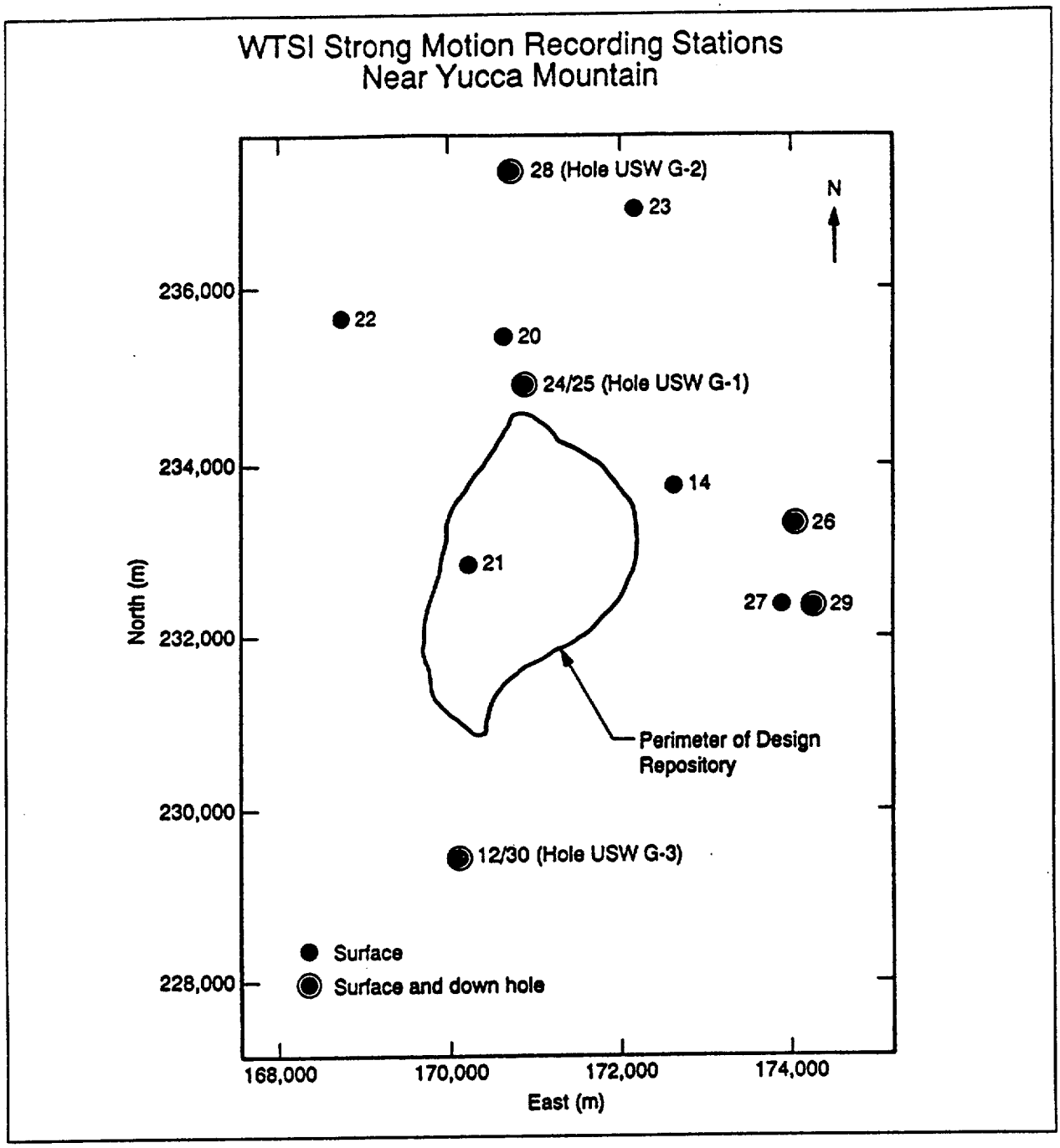

Figure B-2. Location of strong motion recording stations near Yucca Mountain operated as part of WTSI. Solid circles indicate surface recording stations; solid circles enclosed within an open circle represent sites with both surface and down-hole stations. (From Phillips, 1991)

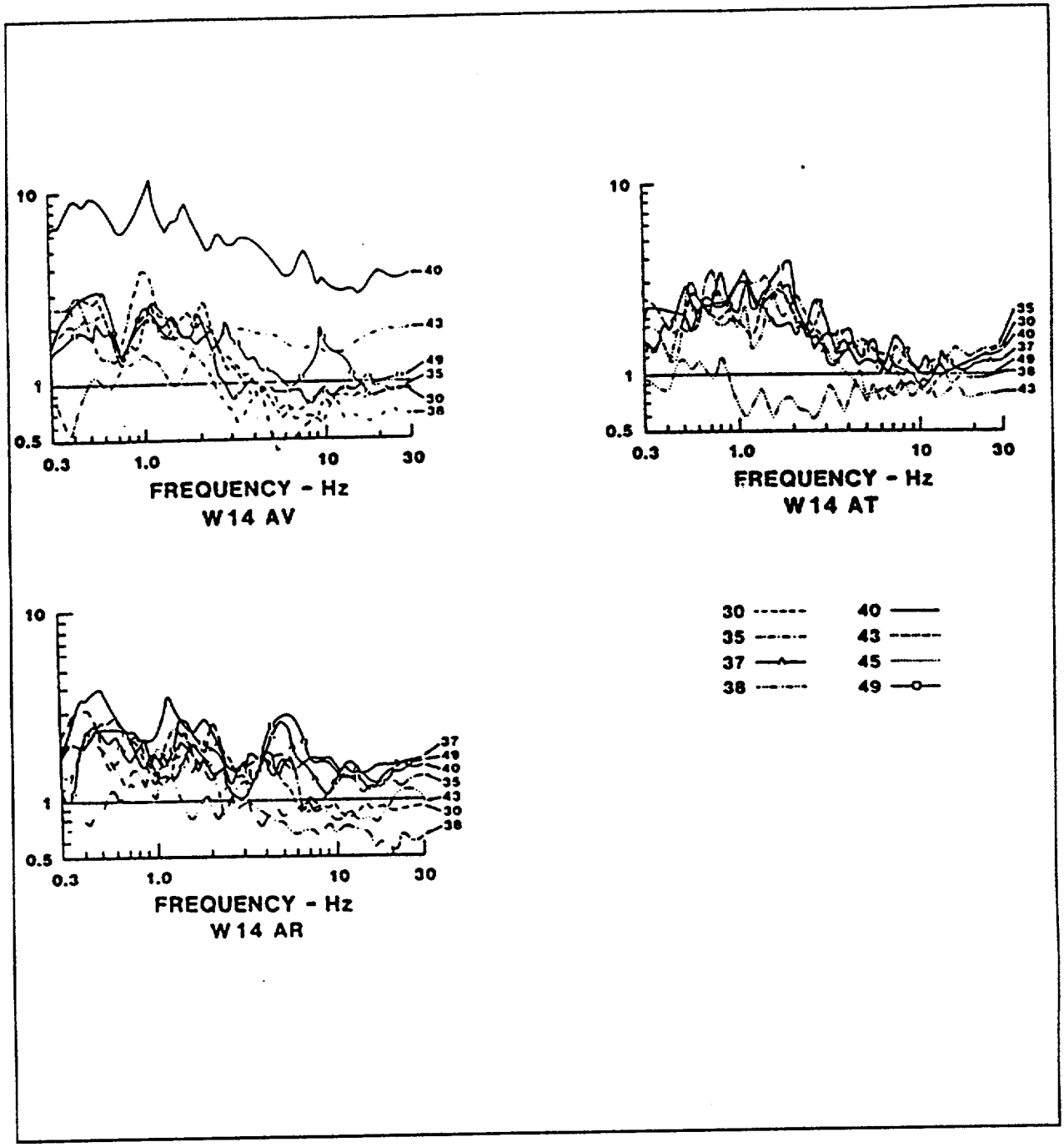

Figure B-3. Ratios of recorded to average response spectral velocities for individual events recorded at Stations W-14. (From Phillips, 1991).

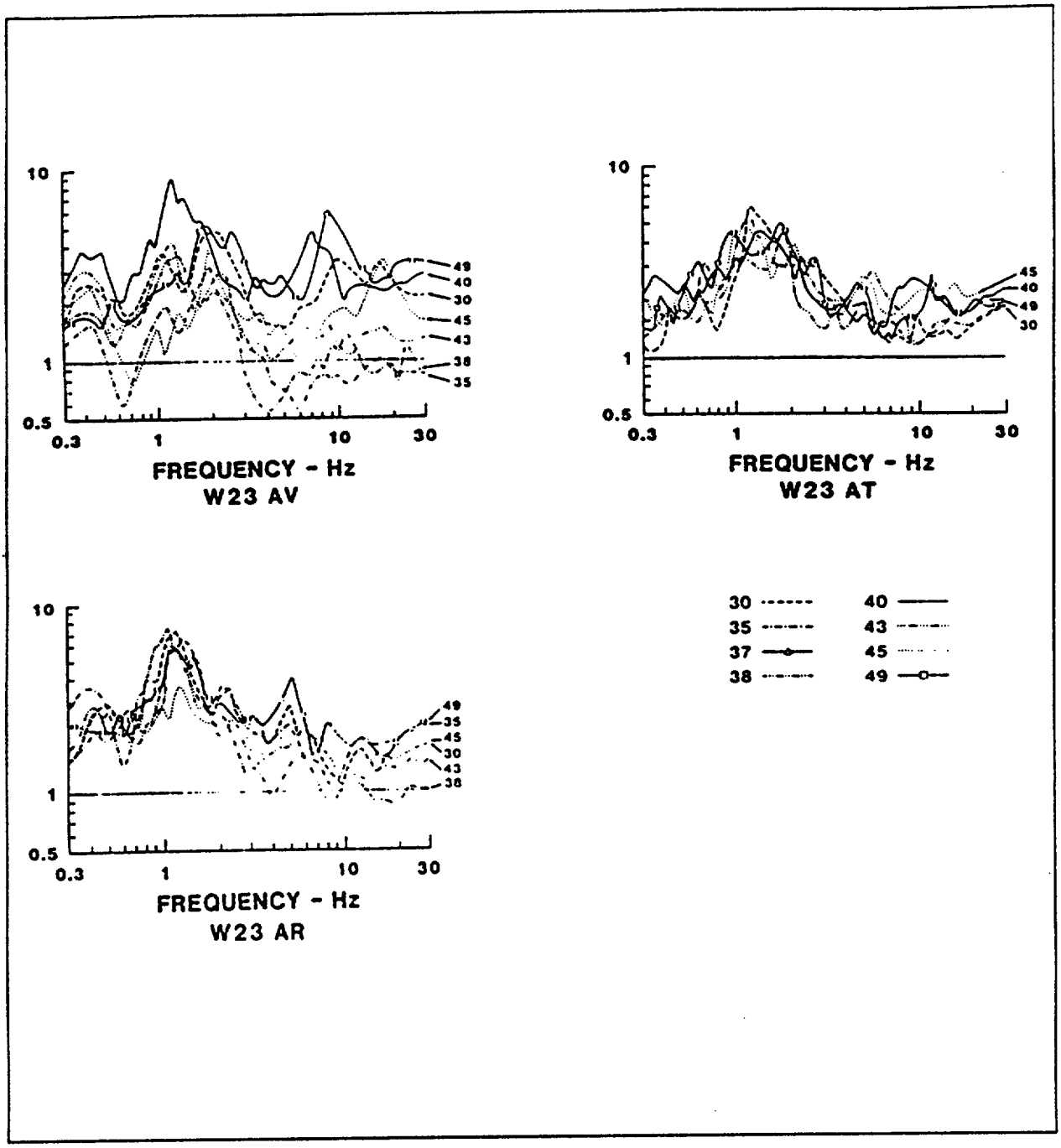

Figure B-4. Ratios of recorded to average response spectral velocities for individual events recorded at Stations W-23. (From Phillips, 1991).

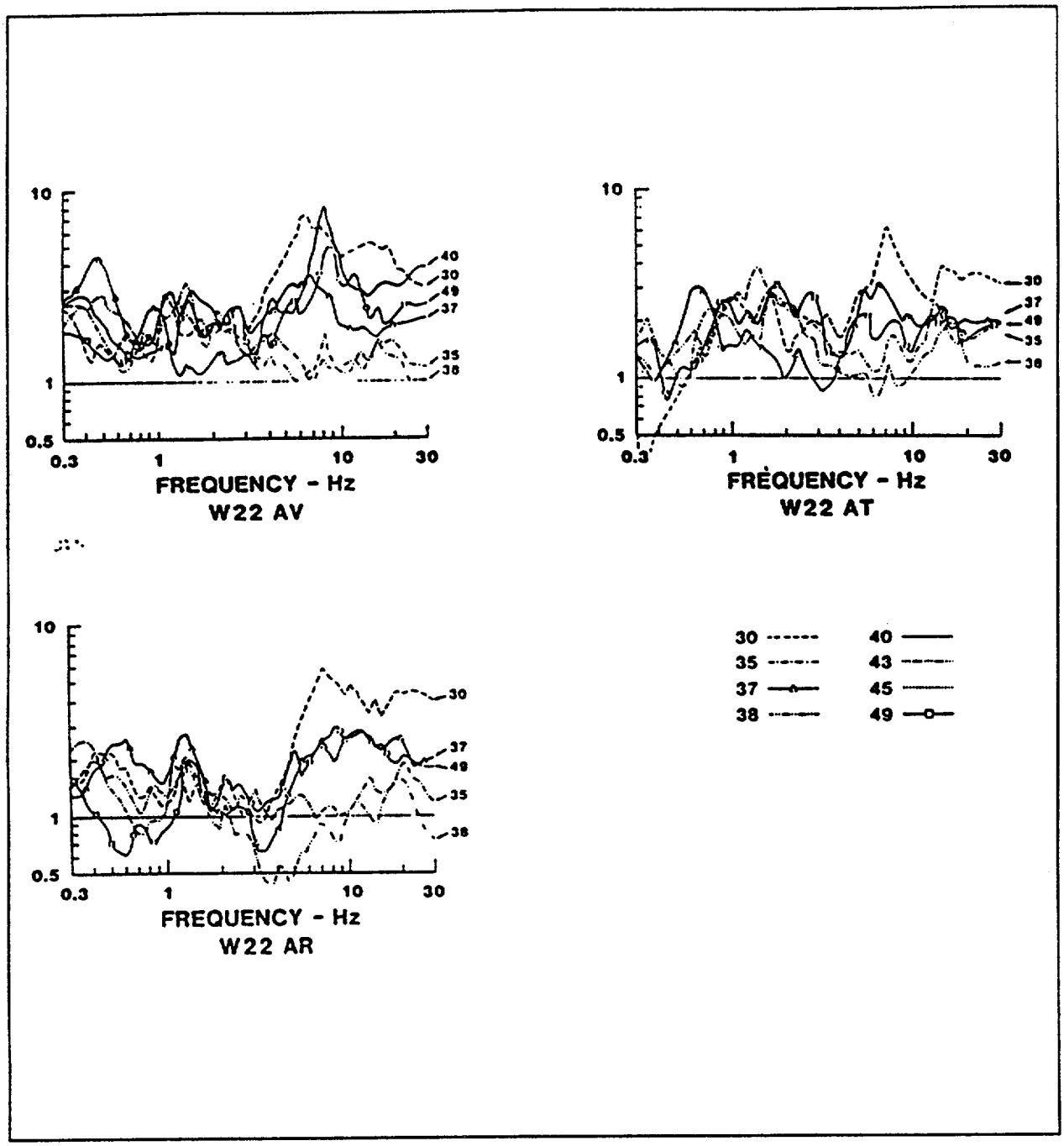

Figure B-5. Ratios of recorded to average response spectral velocities for individual events recorded at Stations W-22. (From Phillips, 1991).

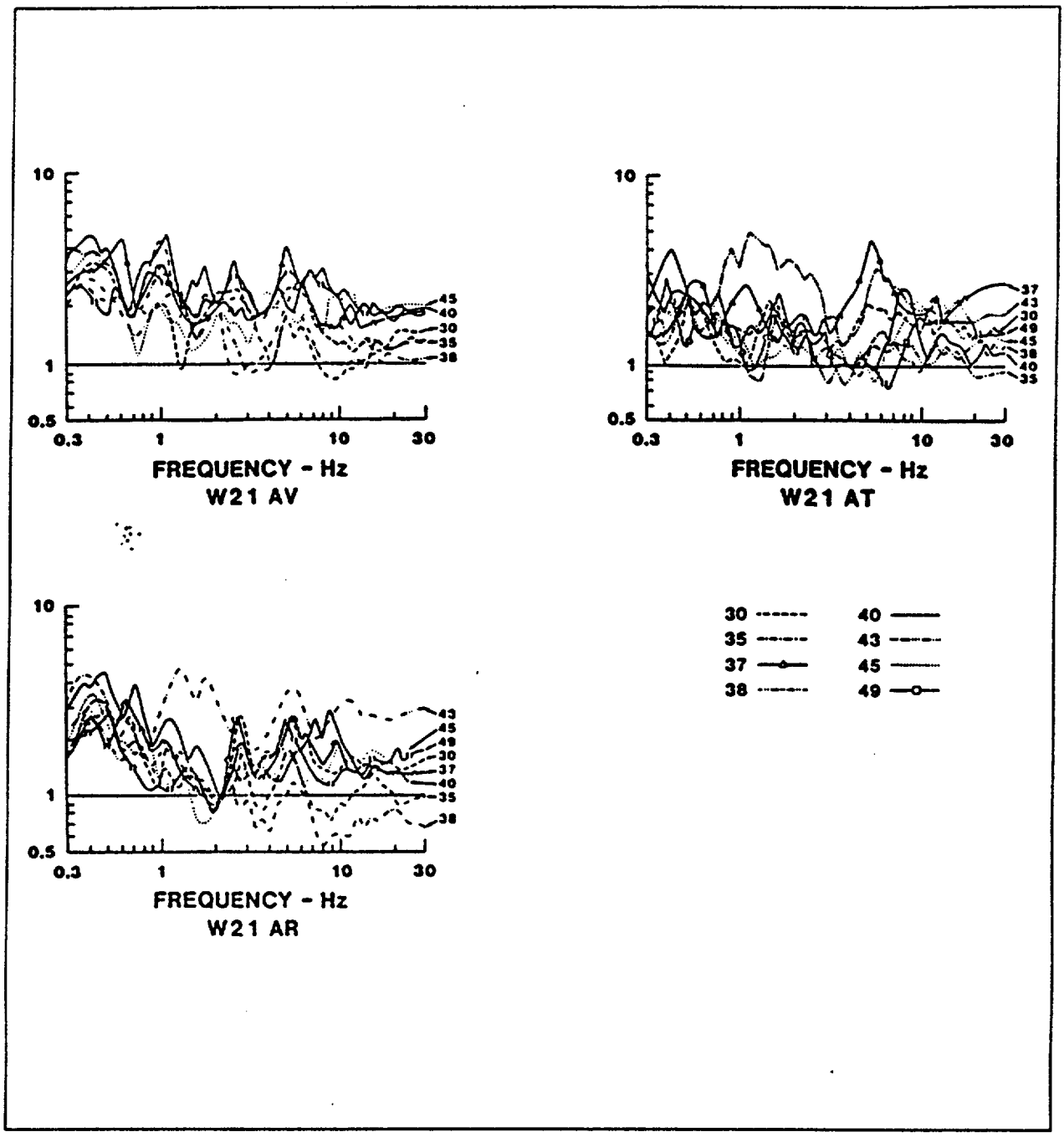

Figure B-6. Ratios of recorded to average response spectral velocities for individual events recorded at Stations W-21. (From Phillips, 1991).

Based on the analysis that follows, it is demonstrated that the amplification effects observed in the Yucca Mountain recordings are due to the shallow path between NTS and Yucca Mountain, and not to site effects. It is shown that the amplification effects occur only in the surface waves and not in the shear waves. Surface waves are insignificant in Yucca Mountain recordings of earthquakes occurring at normal depths. Therefore, it is not expected that the amplification effects observed in the explosion data at Yucca Mountain will be present in the strong ground motions of earthquakes that occur at normal crustal depths.

B.2.1 SEPARATION OF PATH AND SITE EFFECTS

Figures B-7 shows the locations of strong motion stations that recorded NTS explosions Gibne and Molbo. The radial component velocity recordings of Gibne along this profile are shown in Figure B-8. This profile shows the presence of surface waves not only at the Yucca Mountain stations W14, W21, W22 and W23, but also at stations both to the north and south of the repository. The surface waves propagate from near Pahute Mesa to Yucca Mountain along this profile. The profile for event Molbo shows similar features indicating that they are characteristic of this path.

The shallow structure for this path to Yucca Mountain (path PM2 in Figure B-1) is shown in the center panel of Figure B-9 (Walck and Phillips, 1990). This structure has been approximated using a 1-D velocity model shown in Table B-1, and the travel times for direct and reflected phases shown in Figure B-8 were calculated. The P wave onset is generally no larger than the immediately following coda, and there is no distinct change in the character of the motions at the expected S wave arrival time. The large surface waves, which may be described as Rg, arrive at a time that corresponds to the time of the direct S wave in the top layer. This direct S wave is not expected to have any significant energy, and its arrival time is shown only as a guideline for interpreting the surface wave.

Although the stations due south of Pahute Mesa all contain surface waves, they are absent from stations in Jackass Flats, which include stations W6, W7, and W10; this absence is particularly notable in station W6. For event Kappeli, Jackass Flats stations B and C (Figure B-1) were located on tuff like that at the Yucca Mountain stations W14 and W21. The tangential component velocity seismograms for the Kappeli event at stations B and C are compared with those at stations W21 and W14 in Figures B-10 and B-11, respectively. The plots all have different vertical axes scaled to the maximum velocity. The presence of much larger surface waves at the two Yucca Mountain stations W14 and W21 is evident in these recordings. The very heterogeneous nature of the shallow structure shown in Figure B-9 may explain why the path from Pahute Mesa to Yucca Mountain can produce such different seismograms compared with the path from Pahute Mesa to Jackass Flats.

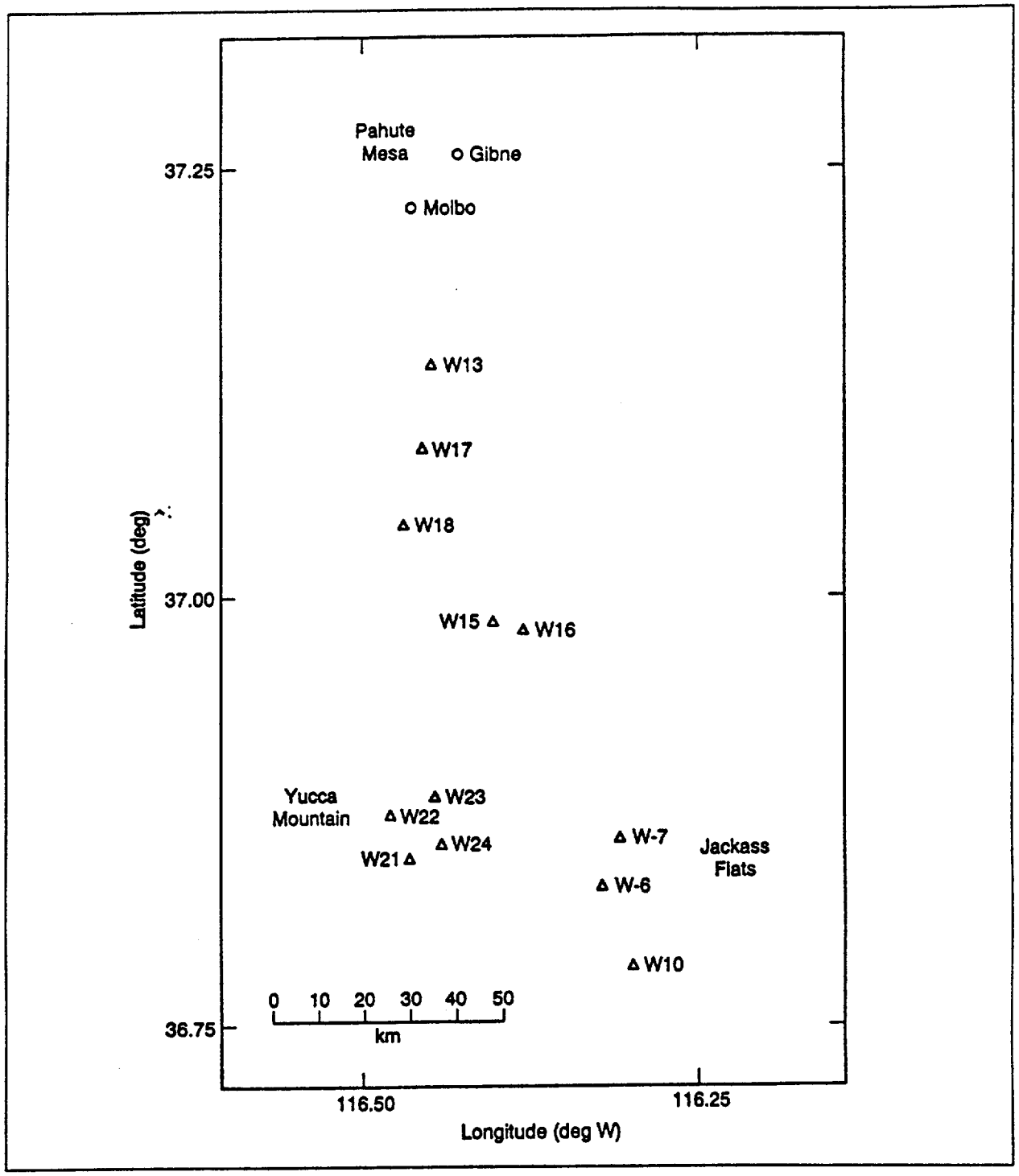

Figure B-7. Locations of stations that recorded UNE's Gibne and Molbo. Stations are shown by triangles; the two events by open circles.

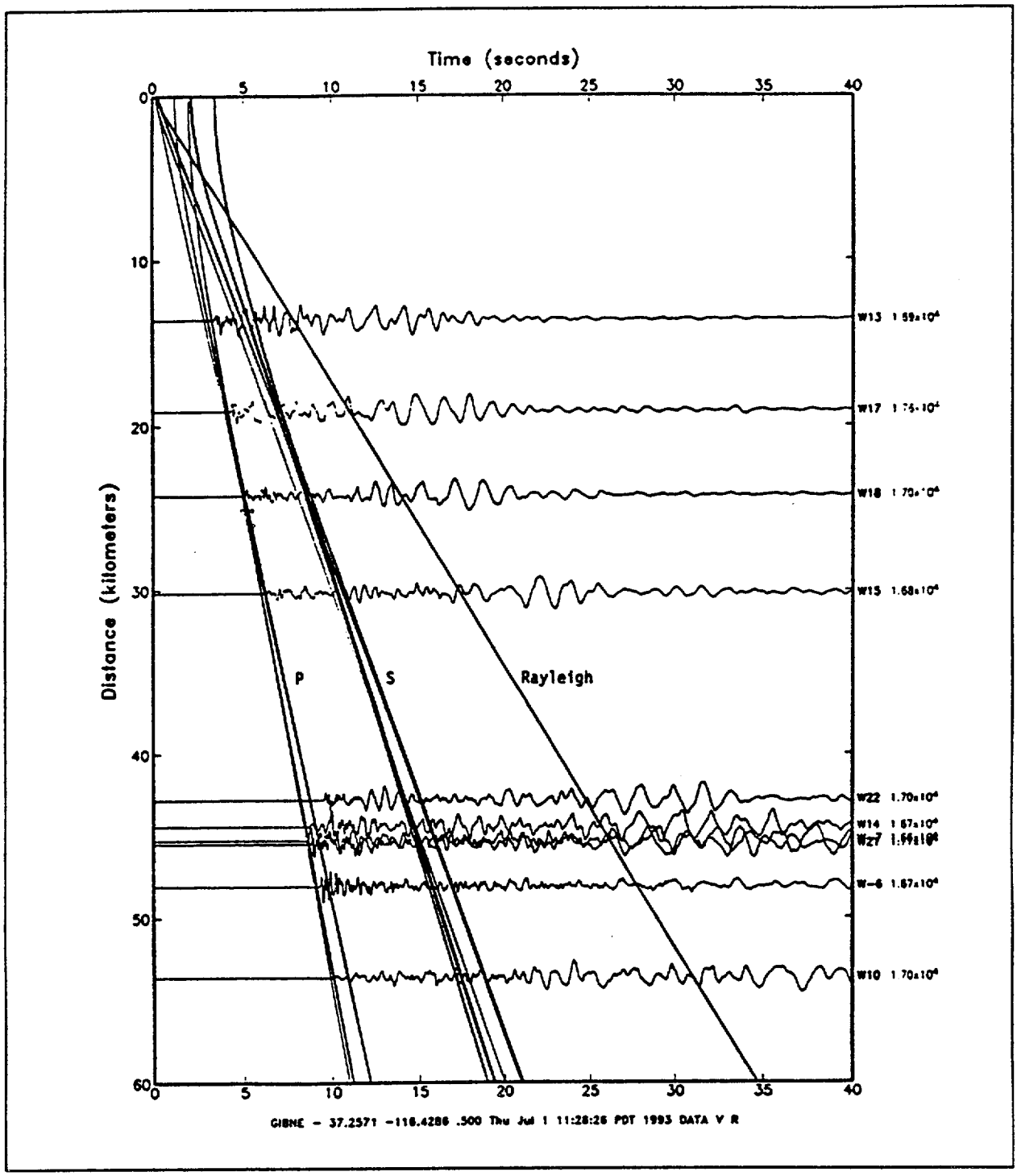

Figure B-8. Profile of velocity seismograms recorded from UNE Gibne at stations shown in Figure B-7..

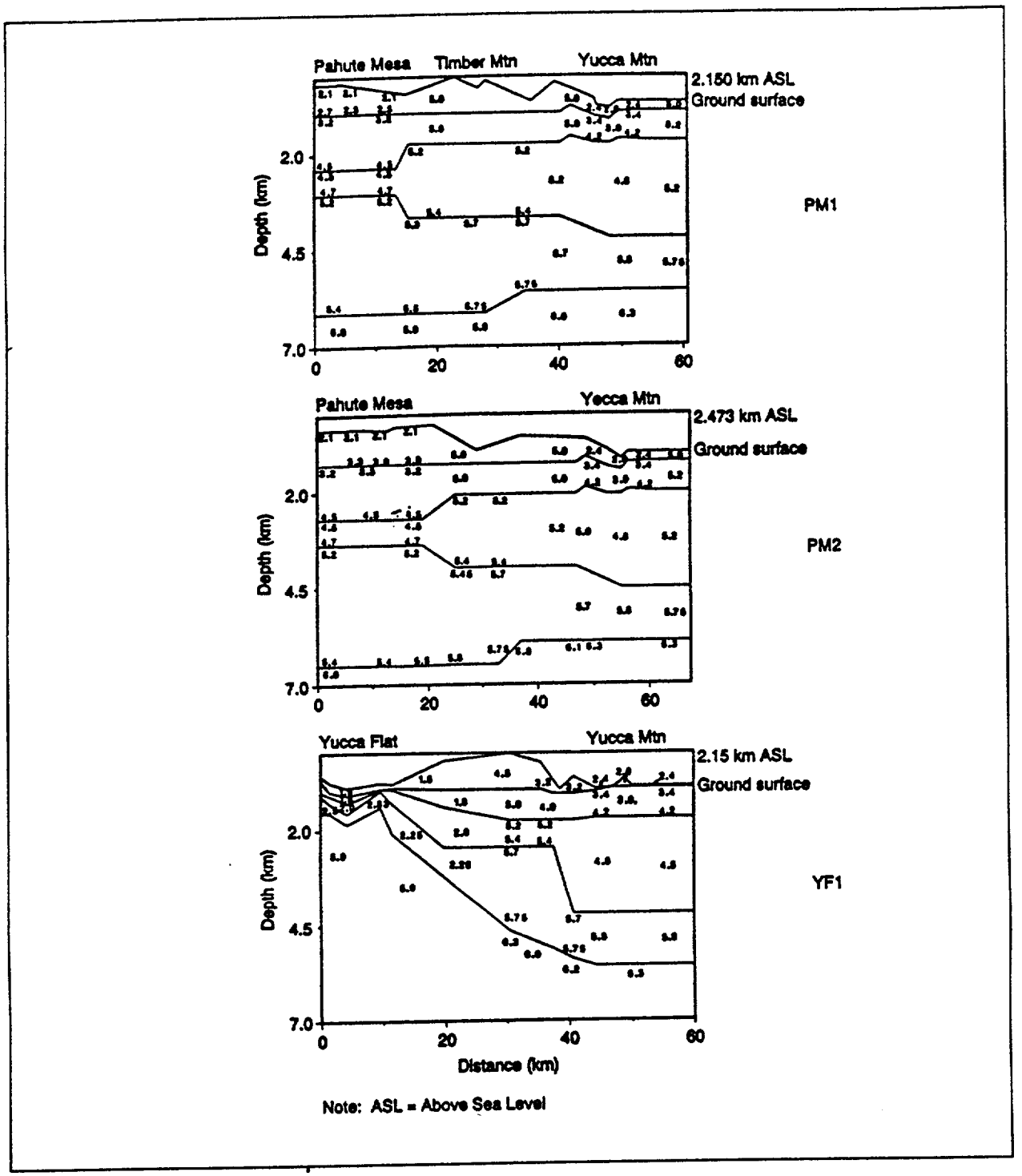

Figure B-9. Crustal seismic velocity cross sections to Yucca Mountain from the three UNE source areas shown in Figure B-1. (From: Walck and Phillips, 1990.)

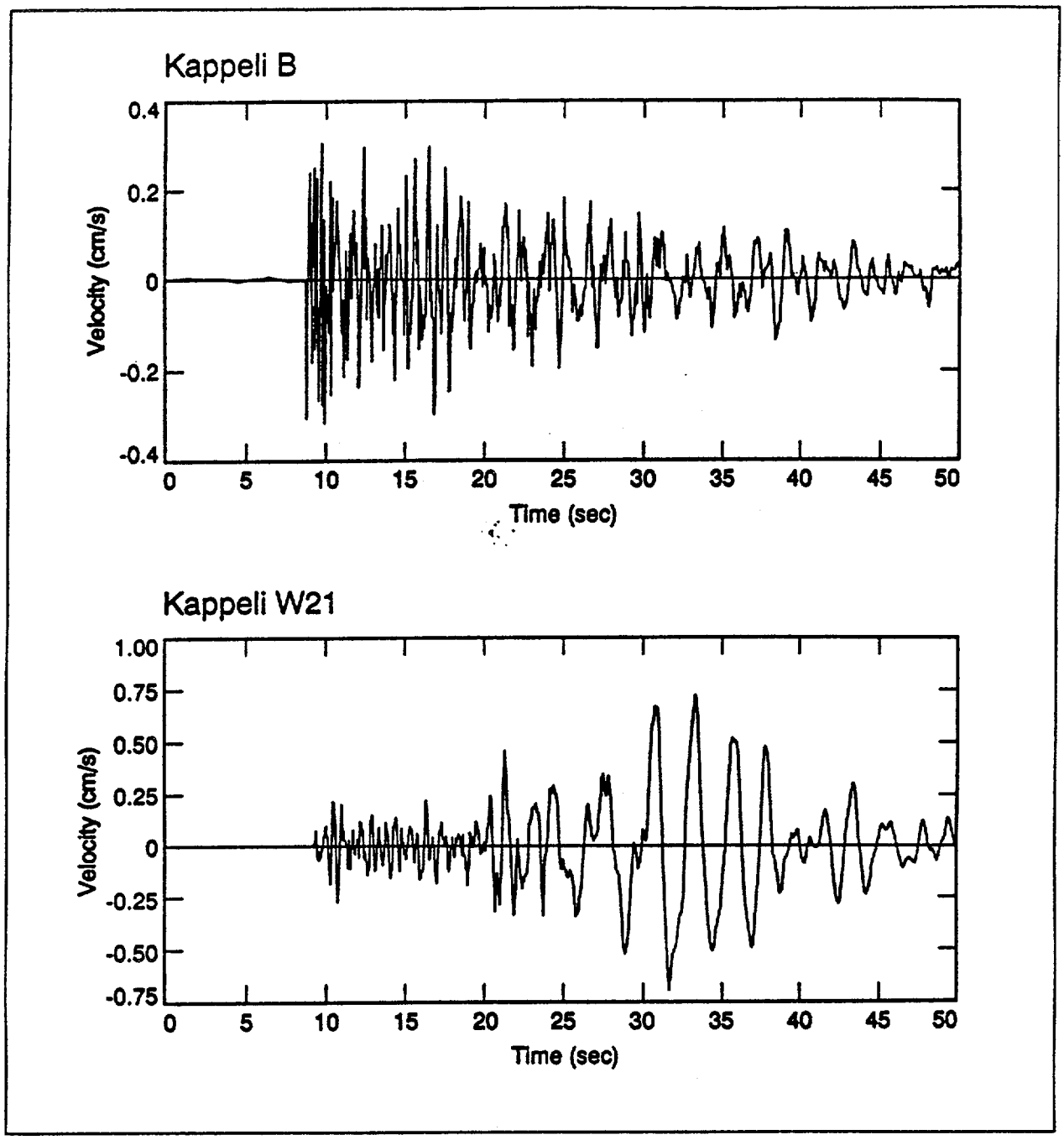

Figure B-10. Velocity seismograms of UNE Kappeli recorded at Stations B and W21.

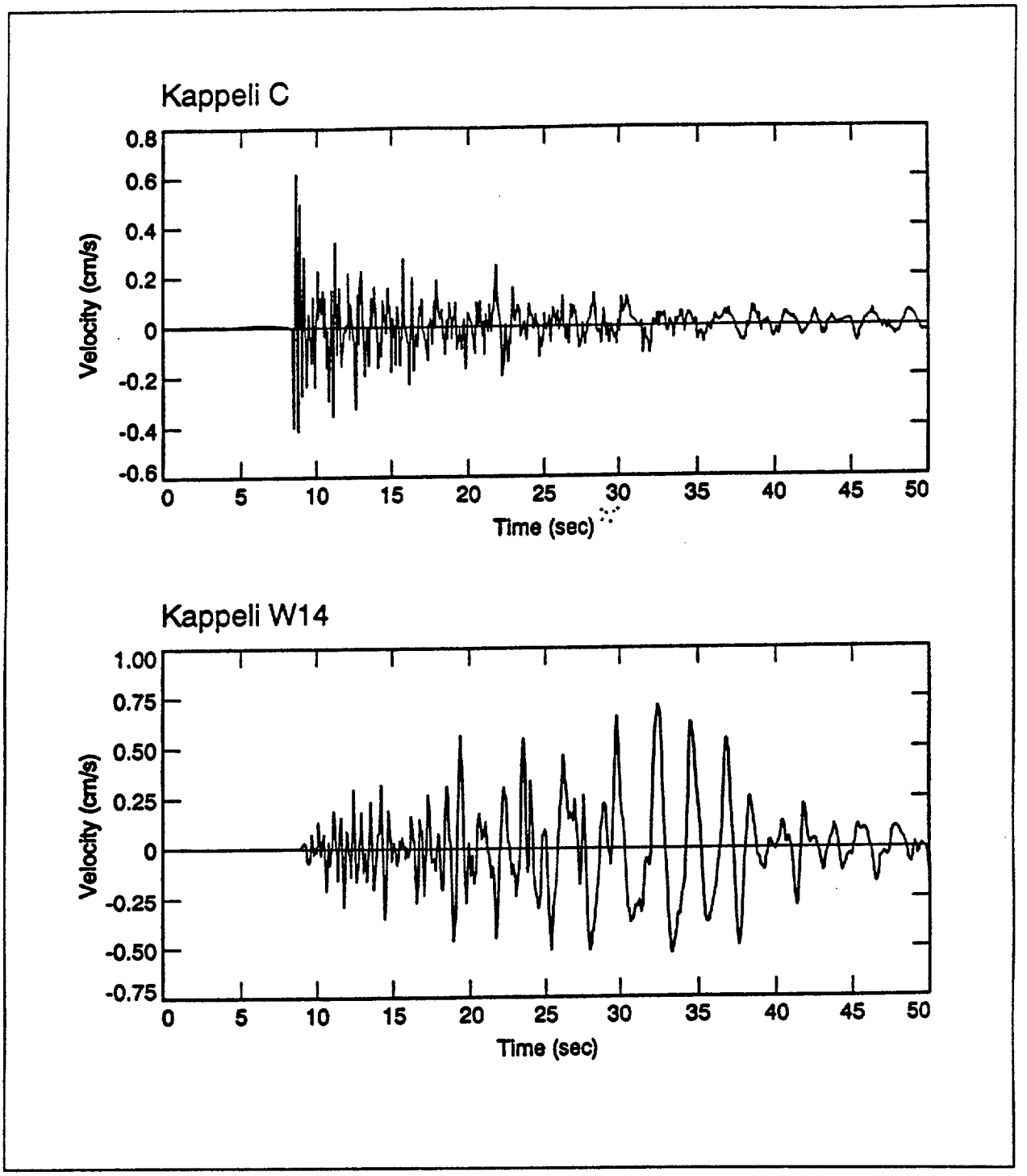

Figure B-11. Velocity seismograms of UNE Kappeli recorded at Stations C and W14.

Table B-1. Yucca Mountain Crustal Structure

P Wave Velocity (km/sec)	S Wave Velocity (km/sec)	Density (gm/cc)	Depth to Top (km)
3.0	1.73	2.21	0.0
5.0	2.89	2.53	0.5
5.7	3.29	2.65	3.2
6.0	3.47	2.70	5.3

B.2.2 DEMONSTRATION THAT THE SHALLOW PATH EFFECT DOES NOT AFFECT BODY WAVES

The next step of the analysis is to show that surface waves, not body waves, cause the amplification effects observed in the Yucca Mountain recordings of explosions. The amplification is therefore not expected to be present in the recordings of earthquakes except those that have significant energy release at shallow depths, generating higher mode surface waves. The approach is to compare amplitudes between Yucca Mountain and Jackass Flats for both the surface wave and the shear wave. It is found that the surface wave amplitudes at Yucca Mountain are larger than those at Jackass Flats, but the shear wave amplitudes are approximately equal.

The separation of seismic phases is difficult in seismograms of nuclear explosions recorded at this distance range. While the first motion is certainly the P wave, the S wave does not have a clear onset. It is assumed that the first 5 seconds of motion are P waves, the second five seconds are predominantly S waves, and the subsequent waves are predominantly surface waves. These assumptions are consistent with the sense of particle motion inferred from superposition of the vertical and radial components.

The recordings of the three explosions used in this study are listed in Table B-2. Measurements of the peak velocity and peak acceleration of each component of each record were made in each of these three time windows. For peak velocity, the predominant period of the wave having the peak velocity was also measured. The results are given in Table B-3 for peak velocity, Table B-4 for period of peak velocity, and Table B-5 for peak acceleration. Neglecting the differences in magnitude between the three events, and the differences in site conditions, the ground motions of the three events at each pair of stations are averaged to derive an overall comparison of ground motion characteristics between the Yucca Mountain stations and those on Jackass Flats.

It is observed that the S wave peak horizontal velocity amplitudes between the two pairs of stations are comparable, but the surface wave peak velocities are about twice as large at Yucca Mountain as at Jackass Flats. Also, the period of the peak S wave horizontal velocity is comparable (about 0.7 sec. in each case), but the period of the peak surface wave velocity is about twice as long (about 2.0 sec) for Yucca Mountain as it is on Jackass Flats (about 1.0 sec). The peak horizontal accelerations are similar between Yucca Mountain and Jackass Flats for both the S wave and the surface wave. These results support the hypothesis that the amplification of peak velocity observed in Yucca Mountain recordings of explosions is due to surface waves.

Table B-2. Recordings Used to Evaluate the Ground Motion Amplification at Yucca Mountain

Event	Station	Range (km)
Kappeli	14	45.6
Kappeli	21	46.7
Kappeli	B	45.9
Kappeli	C	44.0
Molbo	14	40.8
Molbo	21	41.7
Molbo	B	45.6
Molbo	C	45.6
Gibne	14	44.2
Gibne	21	45.3
Gibne	B	48.1
Gibne	C	48.1

Table B-3. Peak Particle Velocity (m/sec) by Recording Station for Three Distinct Time Windows

Event	Com-ponent	Station 14			Station 21			Station B			Station C		
		0<t≤5 (P)	5<t≤10 (S)	t>10 (Surf)	0<t≤5 (P)	5<t≤10 (S)	t>10 (Surf)	0<t≤5 (P)	5<t≤10 (S)	t>10 (Surf)	0<t≤5 (P)	5<t≤10 (S)	t>10 (Surf)
Kappeli	V	0.0049	0.0030	0.0038	0.0039	0.0027	0.0027	0.0044	0.0018	0.0014	0.0029	0.0014	0.0013
	R	0.0032	0.0032	0.0051	0.0025	0.0025	0.0041	0.0043	0.0037	0.0030	0.0029	0.0029	0.0014
	T	0.0030	0.0047	0.0072	0.0026	0.0022	0.0073	0.0032	0.0030	0.0020	0.0062	0.0028	0.0024
Molbo	V	0.0053	0.0026	0.0040	0.0061	0.0032	0.0049	0.0085	0.0030	0.0010	0.0088	0.0021	0.0025
	R	0.0040	0.0044	0.0065	0.0032	0.0046	0.0059	0.0095	0.0038	0.0035	0.0029	0.0035	0.0036
	T	0.0039	0.0053	0.0064	0.0036	0.0035	0.0053	0.0047	0.0024	0.0029	0.0035	0.0044	0.0045
Gibne	V	0.0041	0.0022	0.0036	0.0056	0.0030	0.0044	0.0041	0.0016	0.0016	0.0034	0.0019	0.0025
	R	0.0043	0.0037	0.0044	0.0040	0.0027	0.0053	0.0035	0.0022	0.0024	0.0033	0.0024	0.0025
	T	0.0022	0.0044	0.0063	0.0057	0.0031	0.0045	0.0030	0.0035	0.0040	0.0026	0.0026	0.0027
Average Horizontal			0.0043	0.0060		0.0031	0.0056		0.0030	0.0029		0.0031	0.029

Table B-4. Period of Peak Particle Velocity by Recording Station for Three Distinct Time Windows

Event	Com-ponent	Station 14			Station 21			Station B			Station C		
		0<t≤5 (P)	5<t≤10 (S)	t>10 (Surf)	0<t≤5 (P)	5<t≤10 (S)	t>10 (Surf)	0<t≤5 (P)	5<t≤10 (S)	t>10 (Surf)	0<t≤5 (P)	5<t≤10 (S)	t>10 (Surf)
(Surf) Kappeli	V		0.4	1.0		0.9	1.8		0.7	1.1		0.9	1.1
	R		0.5	2.0		0.5	2.0		0.7	0.9		0.4	0.7
	T		0.7	2.2		0.7	3.0		0.9	0.8		0.5	0.7
Molbo	V		1.0	1.8		0.8	2.1		0.3	0.8		1.0	0.9
	R		0.5	1.8		1.0	2.3		0.7	2.1		0.9	0.9
	T		0.4	0.9		0.6	2.5		0.4	1.3		0.4	1.2
Gibne	V		0.7	1.8		0.8	1.9		0.9	0.8		1.0	0.9
	R		1.1	2.1		0.8	2.2		0.6	0.3		1.0	0.5
	T		1.0	1.0		0.9	1.8		0.6	2.0		0.5	1.1
Average Horizontal			0.7	1.7		0.8	2.3		0.7	1.2		0.6	0.8

Table B-5. Peak Particle Acceleration (m/sec/sec) by Recording Station for Three Distinct Time Windows

Event	Com-ponent	Station 14			Station 21			Station B			Station C		
		0<t≤5 (P)	5<t≤10 (S)	t>10 (Surf)	0<t≤5 (P)	5<t≤10 (S)	t>10 (Surf)	0<t≤5 (P)	5<t≤10 (S)	t>10 (Surf)	0<t≤5 (P)	5<t≤10 (S)	t>10 (Surf)
Kappeli	V												
	R	0.059	0.052	0.037	0.043	0.039	0.031	0.145	0.055	0.050	0.083	0.048	0.043
	T	0.044	0.047	0.047	0.042	0.036	0.043	0.107	0.057	0.048	0.147	0.054	0.034
Molbo	V												
	R	0.063	0.055	0.042	0.060	0.051	0.031	0.314	0.070	0.040	0.088	0.050	0.047
	T	0.059	0.071	0.057	0.083	0.064	0.036	0.146	0.062	0.038	0.088	0.060	0.038
Gibne	V												
	R	0.085	0.037	0.032	0.063	0.031	0.024	0.135	0.022	0.018	0.065	0.038	0.040
	T	0.047	0.043	0.054	0.104	0.030	0.027	0.096	0.054	0.032	0.050	0.040	0.027
Average Horizontal			0.051	0.045		0.042	0.032		0.053	0.038		0.048	0.038

B.2.3 ABSENCE OF SHALLOW PATH EFFECT ON GROUND MOTIONS FROM NORMAL DEPTH EARTHQUAKES

The next step of our analysis is to evaluate whether surface waves like those recorded from explosions could be present in the ground motions of the earthquakes that dominate the seismic hazard at the site. The analyses that follow indicate that the large surface waves evident in the explosion data recorded at Yucca Mountain are not present in the recordings of earthquakes that occur at depths greater than a few km.

A list of some of the larger earthquakes that have been recorded recently at the Yucca Mountain site is given in Table B-6. In the following, velocity seismograms of four earthquakes recorded on rock in Midway Valley are described. The first is a magnitude 3.2 aftershock of the June 29, 1992 Little Skull Mountain earthquake, which occurred at a depth of about 9.5 km at a distance of about 16 km from the recording station on 9 May 1993. The second is a magnitude 4.0 earthquake in Rock Valley that occurred on 30 May 1993 at a very shallow depth (1.5 km). The third and fourth are magnitude 4 aftershocks of the May 17, 1993 Eureka Valley earthquake at depths of 6 and 2 km respectively. The parameters of the earthquakes are listed at the bottom of Table B-6, and the locations of the first two epicenters and the recording station are shown in Figure B-12.

The three component velocity seismograms of the first two earthquakes are shown in Figure B-13. The seismograms of the deeper event have S waves that are much larger in amplitude than the surface waves. In contrast, the seismograms of the shallow event have surface waves that are larger than the S waves. The three component velocity seismograms of the two Eureka Valley aftershocks are shown in Figures B-14 and B-15. The peak velocities of both seismograms are dominated by body waves. However, surface waves are present in both seismograms, and are more pronounced for the shallower event. For the Massachusetts Mountain earthquake of August 5, 1971, which occurred at a depth of about 4 km and had a magnitude of 4.3, displacement seismograms exhibit large shear waves and small surface waves (Vortmann, 1982).

While the general question of site response at Yucca Mountain has not been addressed by this analysis, it has been shown that the amplification effects evident in explosion data recorded at Yucca Mountain are related to the shallow nature of the source. Further, such effects are not observed for earthquakes occurring at more than a few kilometers depth. Hence, because most of the energy release occurs at depths greater than 3 km in large earthquakes, and because earthquakes at very shallow depth do not contribute strongly to the ground motion hazard at Yucca Mountain, ground motion amplification associated with higher mode surface wave propagation from shallow sources need not be considered in development of ESF seismic design inputs.

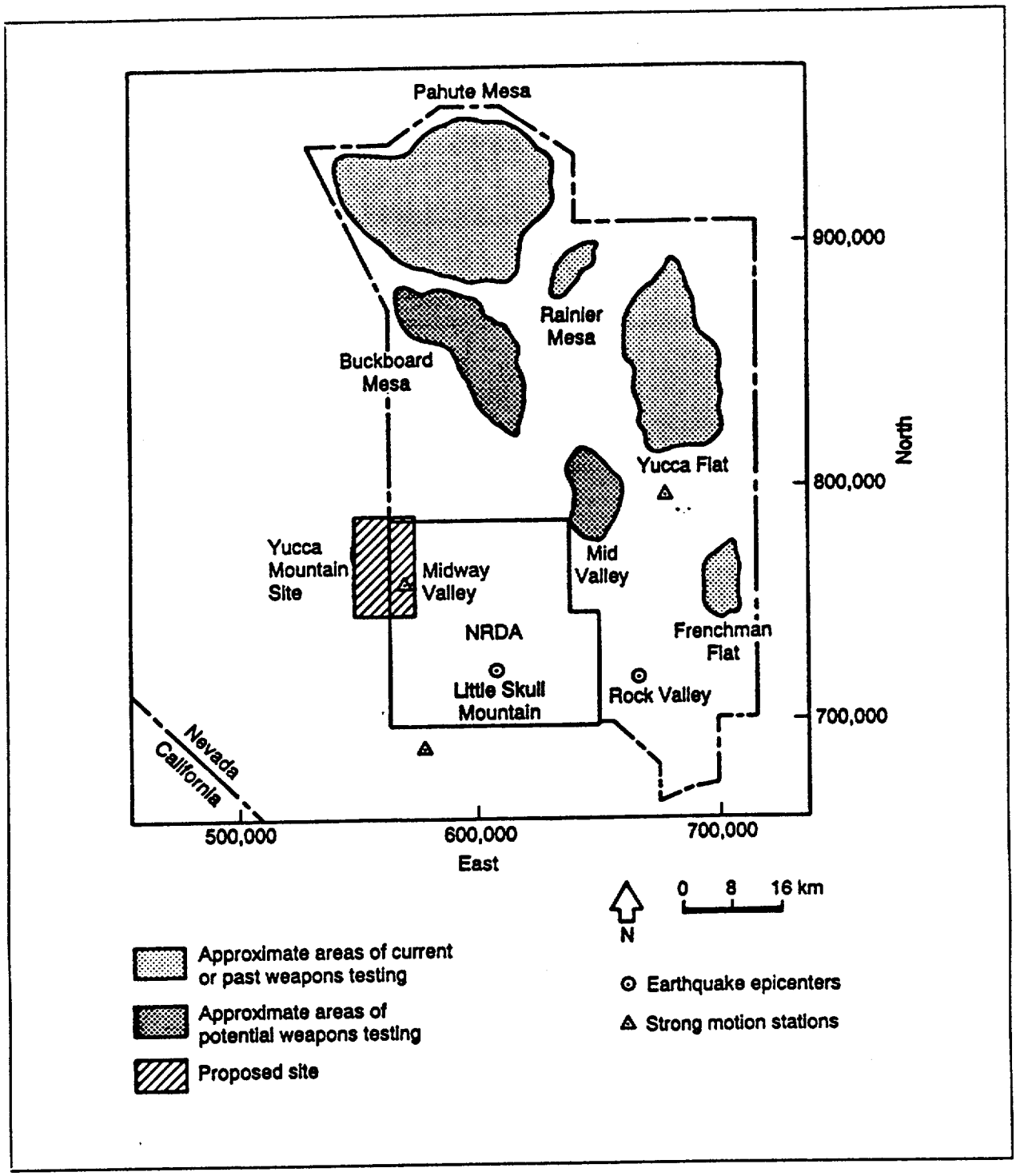

Figure B-12. Locations of strong motion recording stations and selected earthquakes in relation to the Yucca Mountain site.

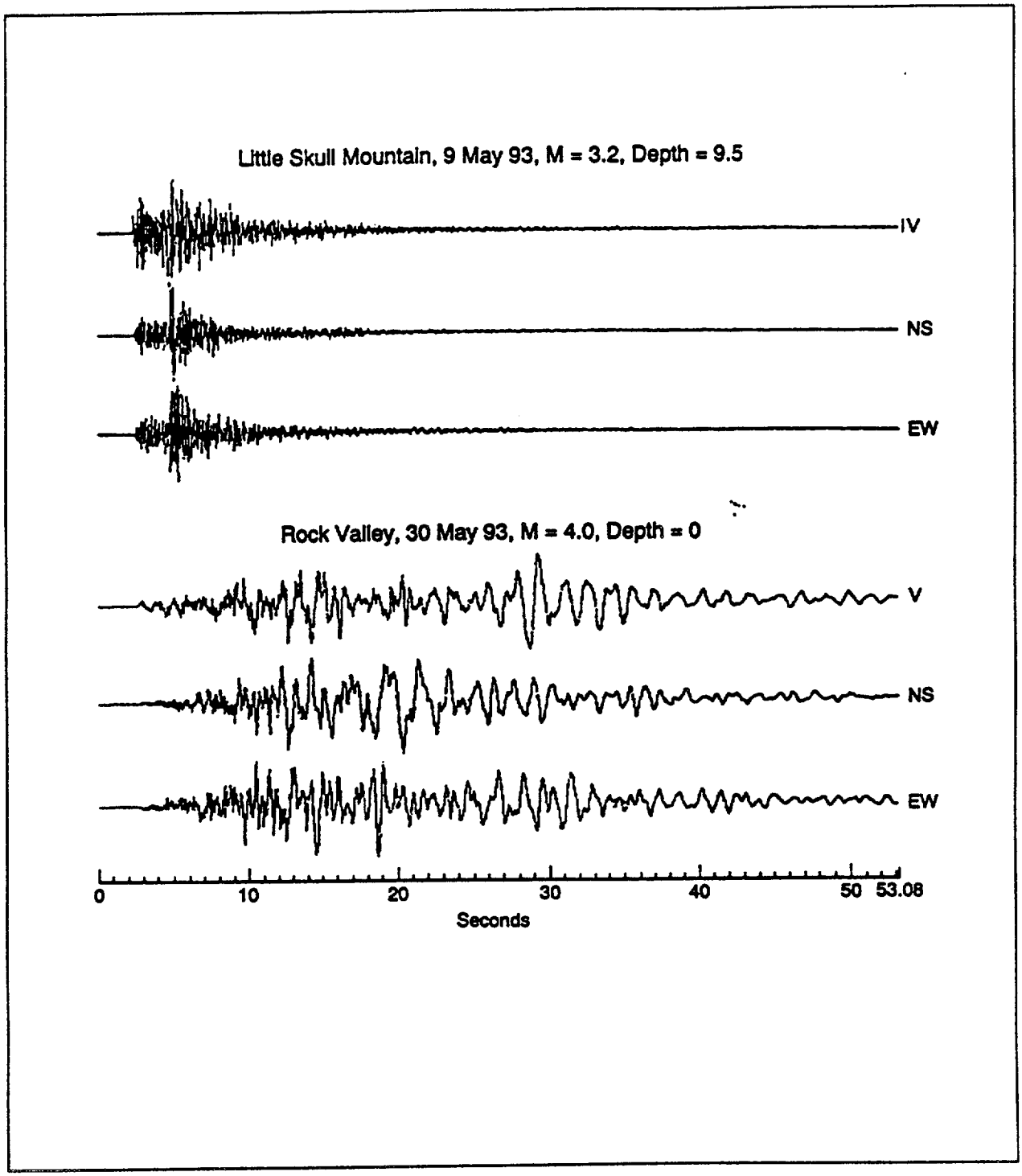

Figure B-13. Velocity time histories of a Little Skull Mountain aftershock and a Rock Valley earthquake recorded at Midway Valley.

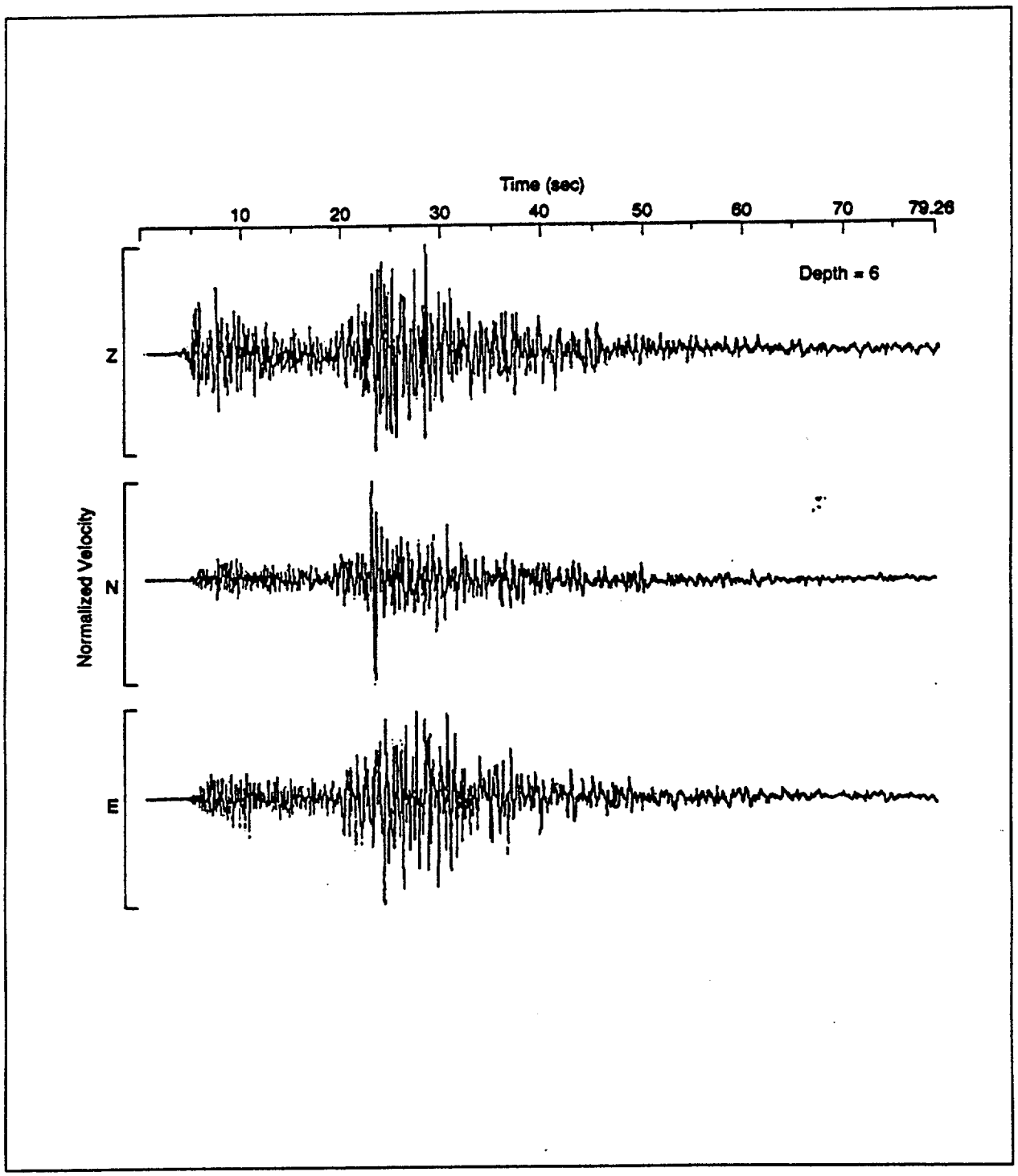

Figure B-14. Velocity time seismogram of a Eureka Valley aftershock with a depth of 6 km recorded at Midway Valley.

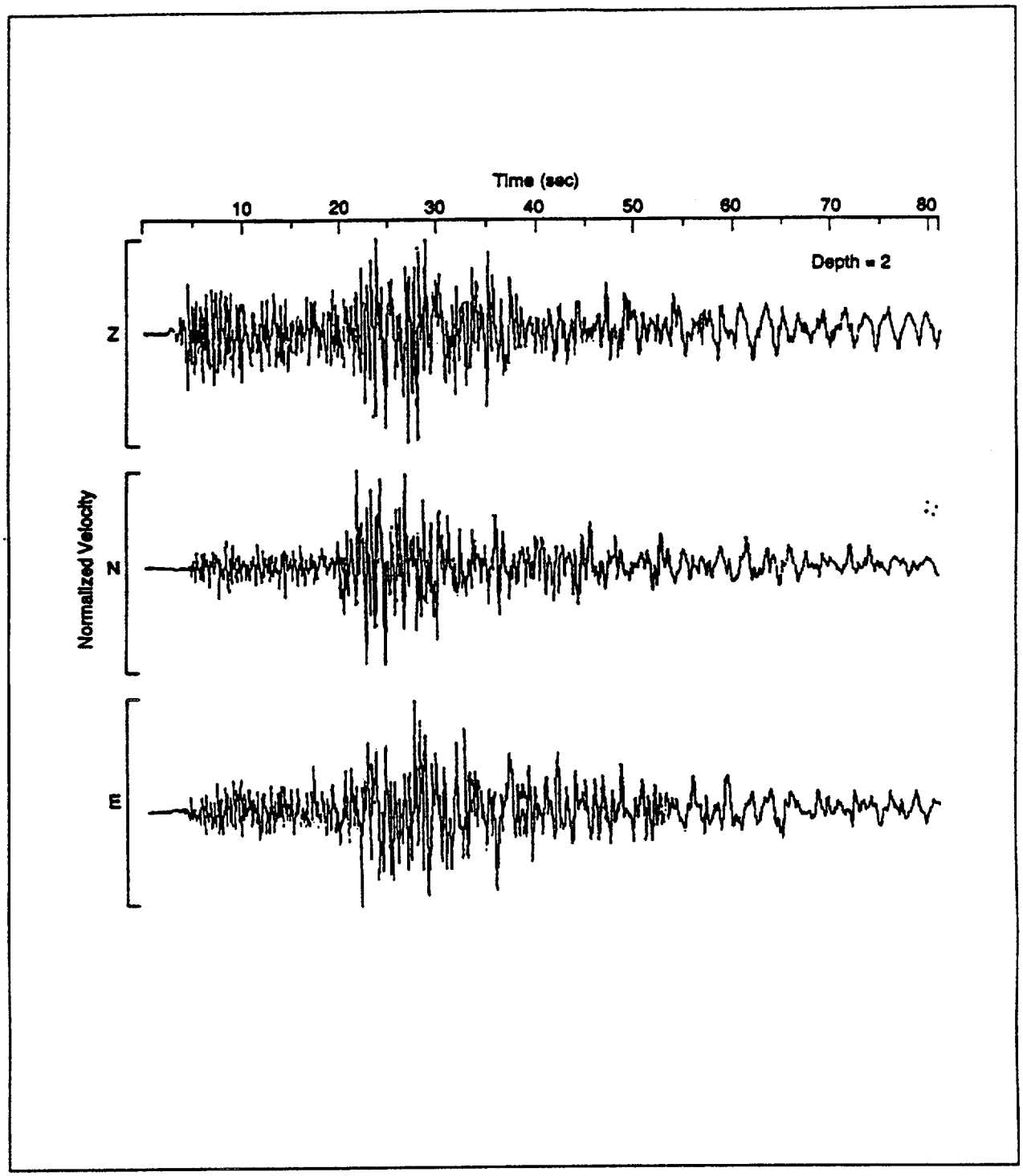

Figure B-15. Velocity seismogram of a Eureka Valley aftershock with a depth of 2 km recorded at Midway Valley.

Table B-6. List of Earthquakes Having Strong Motion Recordings Near Yucca Mountain

Location	Date	Depth (km)	Magnitude	Mechanism
Massachusetts Mtn	1971.8.5	4.3	4.3	strike-slip
Little Skull Mountain	1992.6.29	9.6	5.6	normal
Little Skull Mountain	1992.7.5	---	4.4	strike-slip
Southwestern Utah	1992.9.2	---	5.9	---
Little Skull Mountain	1992.9.7	---	3.1	---
Rock Valley	1993.5.15	---	3.6 4.0 2.8	---
Eureka Valley	1993.5.17 1993.6.3 1993.6.8	9.1 5.9 1.7	6.1 3.9 4.4	normal
EVENTS IN FIG. B-13:				
Little Skull Mountain	1993.5.9	9.5	3.2	---
Rock Valley	1993.5.30	0	4.	---

APPENDIX E REFERENCES

Abrahamson, N.A., F. Makdisi, R. Sadigh and P. Somerville (1993). Estimation of hanging wall and foot wall effects on strong ground motion, Abstract submitted to Fifth U.S. National Conference on Earthquake Engineering.

Aki, K., 1983, Seismological evidence in support of the existence of "Characteristic Earthquakes", Earthquake Notes, v. 54, p. 60-61.

Anderson, J.G., 1979, Estimating the seismicity from geological structure for seismic risk studies, Bulletin of the Seismological Society of America, v. 69, p. 135-158.

Anderson, J.G., and Hough, S.E. (1984). "A model for the shape of the Fourier amplitude spectrum of acceleration at high frequencies." *Bull. Seism. Soc. Am.*, 74, 1969-1993.

Anderson, J.G., Bodin, P., Brune, J.N., Prince, J., Singh, S.K., Quaas R., and Onate, M. (1986). "Strong ground motion from the Michoacan, Mexico, earthquake." *Science.* 223, 1043-1049.

Anderson, J.G., J.N. Brune, D. DePolo, J. Gomberg, S.C. Harmsen, M.K. Savage, A.F. Sheehan, and K.D. Smith (1993). Preliminary report: the Little Skull Mountain earthquake, June 29, 1992. In *Dynamic Analysis and Design Considerations for High-Level Nuclear Waste Repositories*, Q.A. Hossain (ed.), ASCE, New York, p. 162-168.

Arabasz, W.J., J.C. Pechmann, and E.D. Brown, 1992, "Observational seismology and the evaluation of earthquake hazards and risk in the Wasatch Front area, Utah," *in* Assessment of Regional Earthquake Hazards and Risk Along the Wasatch Front, Utah, P.L. Gori and W.W. Hays, editors, U.S. Geological Surv. Prof. Paper 1500-A-J, p. D1-D36.

Archuleta, R.J., S.H. Seale, P.V. Sangas, L.M. Baker and S.T. Swain (1992). Garner Valley downhole array of accelerometers: instrumentation and preliminary data analysis, *Bull.Seism. Soc. Am.* 82, 1592-1621.

ATC (Applied Technology Council), 1978, "Tentative Provisions for the Development of Seismic Regulations for Buildings," ATC 3-06.

Atkinson, G.M. (1984). "Attenuation of strong ground motion in Canada from a random vibrations approach." *Bull. Seism. Soc. Am.*, 74 (5), 2629-2653.

Boore, D.M. (1983). "Stochastic simulation of high-frequency ground motions based on seismological models of the radiated spectra." *Bull. Seism. Soc. Am.*, 73, 1865-1894.

Boore, D.M. (1986). "Short-period P- and S-wave radiation from large earthquakes: implications for spectral scaling relations." *Bull. Seism. Soc. Am.*, 76(1), 43-64.

Boore, D.M. and Joyner, W.B. (1984). "A note on the use of random vibration theory to predict peak amplitudes of transient signals." *Bull. Seism. Soc. Am.*, 74, 2035-2039.

Boore, D.M., and Atkinson, G.,M. (1987). "Stochastic prediction of ground motion and spectral response parameters at hard-rock sites in eastern North America." *Bull. Seism. Soc. Am.*, 77(2), 440-467.

Brune, J.N. (1970). "Tectonic stress and the spectra of seismic shear waves from earthquakes." *J. Geophys. Res.* 75, 4997-5009.

Brune, J.N. (1971). "Correction." *J. Geophys. Res.* 76, 5002.

Bucknam, R.C., S.T. Algermissen, and R.E. Anderson, 1980, "Patterns of late Quaternary faulting in western Utah and an application of in earthquake hazard evaluation," *in* Proceedings of Conference X: Earthquake Hazards Along the Wasatch and Sierra Nevada Frontal Fault Zones, J.F. Evernden, compiler, U.S. Geological Surv. Open-File Rept. 80-801, p. 299-314.

Campbell, K.W. (1990). Empirical prediction of near-source soil and soft rock ground motion for the Diablo Canyon Nuclear Power Plant Site, San Louis Obispo County, California. Report prepared for Lawrence Livermore National Laboratory, Dames & Moore, Evergreen, Colorado, 110 p.

Campbell, K.W., 1993, Empirical prediction of near-source ground motion from large earthquakes: International Workshop on Earthquake Hazard and Large Dams in the Himalaya, Indian National Trust for Art and Cultural Heritage (INTACH), New Delhi, India.

Cornell, C.A., 1968, Engineering seismic risk analysis, Bulletin of the Seismological Society of America, v. 58, p. 1583-1606.

Cornell, C.A. and S.R. Winterstein, 1986. Applicability of the Poisson earthquake occurrence model, EPRI NP-4770, Electric Power Research Institute, Palo Alto, CA.

DOE (U.S. Department of Energy), 1988, Site Characterization Plan Yucca Mountain Site, Nevada Research and Development Area, Nevada, DOE/RW-0199, Washington, D.C.

DOE (U.S. Department of Energy), 1992a, Exploratory Studies Facility Design Requirements (ESFDR), Yucca Mountain Site Characterization Project (YMP), YMP/CM-0019, Rev. 7/2/92, ICN 2.

DOE (U.S. Department of Energy), 1992b, DOE Standard: Natural Phenomena Hazards Performance Categorization Criteria for Structures, Systems, and Components, DOE-STD-1021-92, U.S. Department of Energy, Washington, D.C.

DOE (U.S. Department of Energy), 1992c, DOE Standard: Natural Phenomena Hazards Site Characterization Criteria, DOE-STD-1022-92, U.S. Department of Energy, Washington, D.C. (draft).

DOE (U.S. Department of Energy), 1992d, DOE Standard: Natural Phenomena Hazards Assessment Criteria, DOE-STD-1023-92, U.S. Department of Energy, Washington, D.C. (draft).

DOE (U.S. Department of Energy), 1992e, DOE Standard: Guidelines for Use of Probabilistic Seismic Hazard Curves at Department of Energy Sites, DOE-STD-1024-92, U.S. Department of Energy, Washington, D.C.

DOE (U.S. Department of Energy), 1994, DOE Standard: Natural Phenomena Hazards Design and Evaluation Criteria for Department of energy Facilities, DOE-STD-1020-94, U.S. Department of Energy, Washington, D.C.

Der Kiureghian, A. and Ang, A.H., 1977, A fault-rupture model for seismic risk analysis, Bulletin of the Seismological Society of America, v. 67, p. 1173-1194.

Doser, D.I., 1985, The 1983 Borah Peak, Idaho and 1959 Hebgen Lake, Montana earthquakes--Models for normal fault earthquakes in the Intermountain seismic belt, in R.S. Stein and R.C. Bucknam (eds.), Proceedings of Workshop XXVIII on the Borah Peak, Idaho, Earthquake, U.S. Geological Survey Open-File Report 85-290, p. 368-384.

Doser, D.I., 1986, Earthquake processes in the Rainbow Mountain-Fairview Peak-Dixie Valley, Nevada, region (1954-1959), Journal of Geophysical Research, v. 91, p. 12572-12586.

Doser, D.I., 1988, Source mechanisms of earthquakes in the Nevada seismic zone (1915-1943) and implications for deformation in the western Great Basin, Journal of Geophysical Research, v. 93, p. 120-143.

Doser, D.I., and R.B. Smith, 1985, Source parameters of the 28 October 1983, Borah Peak, Idaho, earthquake from body wave analysis, Bulletin of the Seismological Society of America, v. 75, p. 1041-1051.

Engdahl, E.R. and Rienhart, W.A., 1988, Seismicity map of North America: DNAG, The Geological Society of American, Scale 1:5,000,000.

Electric Power Research Institute (1993). *Guidelines for determining design basic ground motions*. Palo Alto, Calif: Electric Power Research Institute, vol. 1-5, EPRI TR-102293.

Geli, L., P.-Y. Bard, and B. Jullien (1988). The effect of topography on earthquake ground motion: a review and new results, *Bull. Seism. Soc. Am.* 78, 42-63.

Geomatrix Consultants Inc., 1993, "Earthquakes and Tectonics Expert Judgment Elicitation Project," Electric Power Research Institute, Palo Alto, CA, Report TR-102000, 55 p.

Gibson, J. D., L. E. Shepard, F. A. Kerl, F. H. Swan, and J. R. Wesling, 1990,"Synthesis of Studies for the Potential of Fault Rupture at the Proposed Surface Facilities, Yucca Mountain, Nevada," in High Level Radioactive Waste Management, Proceedings of the International Topical Meeting, April 8-12, 1990, American Nuclear Society, v. 1, pp. 109-116

Hanks, T.C. (1982). "f_{max}." *Bull. Seism. Soc. Am.*, 72, 1867-1879.

Hanks, T.C. and Kanamori, H., 1979, A moment magnitude scale, Journal of Geophysical Research, v. 84, p. 2981-2987 or 2348-2350??

Hanks, T.C. and McGuire, R.K., 1981, The character of high-frequency strong ground motion, Bulletin of the Seismological Society of America, v. 71, p. 2071-2095.

Hough, S.E., Anderson, J.G. (1988). "High-frequency spectra observed at Anza, California: Implications for Q structure." *Bull. Seism. Soc. Am.*, 78, 692-707.

Hough, S.E., Anderson, J.G., Brune, J., Vernon III, F., Berger, J., Fletcher, J., Haar, L., Hanks, T., and Baker, L. (1988). "Attenuation near Anza, California." *Bull. Seism. Soc. Am.*, 78(2), 672-691.

Idriss, I.M., 1991, Earthquake ground motions at soft soil sites: Second International Conference on Recent Advances in Geotechnical Earthquake Engineering and Soil Dynamics, v. 3, p. 2265-2272.

ICBO (International Conference of Building Officials), 1991, Uniform Building Code, Whittier, California.

Joyner, W.B. and Boore, D. M., 1988, Measurement, characterization and prediction of strong ground motion, in J.L. Von Thun (ed.), Proceedings of the Conference on Earthquake Engineering and Soil Dynamics: Recent Advances in Ground Motion Evaluation, American Society of Civil Engineers, p. 43-103.

Kajima Institute of Construction Technology (1984). Array observation of strong motion earthquake in rock.

Kulkarni, R.B., Sadigh, K., and Idriss, I.M., 1979, Probabilistic evaluation of seismic exposure, in Proceedings, Second U.S. National Conference on Earthquake Engineering, p. 90-99.

McGuire, R.K., 1974, Seismic structural response risk analysis incorporating peak response regressions on earthquake magnitude and distance, Massachusetts Institute of Technology Department of Civil Engineering/Research Report R74-51.

McGuire, R.K., 1978, FRISK: Computer program for seismic risk analysis using faults as earthquake sources, U.S. Geological Survey Open-File Report 78-1007.

Menges, C. M., G. Vadurro, R. Cress, J. Coe, and F. W. Simonds, 1993, "Stratigraphic Evidence for Multiple Small Quaternary Displacements on the Bow Ridge Fault at Northeast Yucca Mountain, Nye County, Nevada," 1993 Abstracts with Programs, Geological Soc. America, v. 25, n. 5, p. 120

Molnar, P., 1979, Earthquake recurrence intervals and plate tectonics, Bulletin of the Seismological Society of America, v. 69, p. 115-133.

Ou, G.B., and Herrmann, R.B. (1990). "A statistical model for ground motion produced by earthquakes at local and regional distance." *Bull. Seism. Soc. Am.*, 80, 1397-1417.

Papageorgiou, A.S., and K. Aki, 1983, "A specific barrier model for the quantitative description on inhomogeneous faulting and the prediction of stong ground motion: Part II. Applications," Bull. Seis. Soc. Am., v. 73, p. 953-978.

Phillips, J.S. (1991). Prediction of pseudo relative velocity response spectra at Yucca Mountain for underground nuclear explosions conducted in the Pahute Mesa testing area at the Nevada Test Site, SAND88-3032 UC-814.

Rogers, A.M., Harmsen, S.C., and Meremonte, M.E., 1987, Evaluation of the seismicity of the Southern Great Basin and its relationship to the tectonic framework of the region, U.S. Geological Survey Open-File Report 87-408.

Rogers, A.M., S.C. Harmsen, E.J. Corbett, K. Priestley, and D. dePolo, 1991, The seismicity of Nevada and some adjacent part of the Great Basin, *in* Slemmons, D.B., E.R. Engdahl, M.D. Zoback, and D.D. Blackwell, eds, Neotectonics of North America, Geological Society of America, Boulder, CO, p. 153-184.

SAIC (Science Applications Intervational Corporation), 1992, Report of Early Site Suitability Evaluation of the Potential Repository Site at Yucca Mountain, Nevada, SAIC-91/8000.

Schneider, J.F., W.J. Silva, and C. Stark, 1993, Ground motion model for the 1989 M 6.9 Loma Prieta earthquake including effects of source, path, and site, Earthquake Spectra, v. 9, p. 251-287.

Schwartz, D.P. and Coppersmith, K.J., 1984, Fault behavior and characteristic earthquakes--examples from the Wasatch and San Andreas fault zones, Journal of Geophysical Research, v. 89, p. 5681-5698.

Silva, W.J., (1976). "Body waves in a layered anelastic solid." *Bull. Seism. Soc. Am.*, 66(5), 1539-1554.

Silva, W.J. (1991). "Global characteristics and site geometry." Proceedings: *NSF/EPRI Workshop on Dynamic Soil Properties and Site Characterization.* Electric Power Res. Inst., EPRI NP-7337.

Silva, W.J. (1992). "Factors controlling strong ground motions and their associated uncertainties." *ASCE Symposium On High Level Nuclear Waste Repositories*, 132-161.

Silva, W.J., and Lee, K. (1987). *"WES RASCAL code for synthesizing earthquake ground motions."* State-of-the-Art for Assessing Earthquake Hazards in the United States, Report 24, U.S. Army Engineers Waterways Experiment Station, Misc. Paper S-73-1.

Silva, W.J., 1993, Factors controlling strong ground motion and their associated uncertainties, in Q.A. Hossain, (ed.), Dynamic Analysis and Design Considerations for High-Level Nuclear Waste Repositories, ASCE, p. 132-161.

Silva W.J. and Darragh, R.B., 1994, Engineering characterization of strong ground motion recorded at rock sites, draft final report submitted to Electric Power Research Institute, ERPI RP 2556-48.

Singh, S. and Herrmann, R.B., 1983, Regionalization of crustal coda Q in the continental United States, Journal of Geophysical Research, v. 88, p. 527-538.

Smith, R., and W. Arabasz, 1991, "Seismicity of the Intermountain seismic belt," *in* Slemmons, D.B., E.R. Engdahl, M.D. Zoback, and D.D. Blackwell, eds, Neotectonics of North America, Geological Society of America, Boulder, CO, p. 185-228.

Somerville, P.G. and R.W. Graves (1993). Conditions that give rise to unusually large long-period ground motions, Proceedings of Seminar on Seismic Isolation, Passive Energy Dissipation, and Active Control, ATC-17-1, Applied Technology Council, 1, 83-94.

Spengler, R. W., C. A. Braun, R. M. Linden, L. G. Martin, D. M. Ross-Brown, and R. L. Blackburn, 1993, "Structural Character of the Ghost Dance Fault, Yucca Mountain, Nevada," in High Level Radioactive Waste Management, Proceedings of the Fourth Annual International Conference, Las Vegas, NV, April 26-30, 1993, American Nuclear Society, pp. 653-659

Stark, C.L., Silva, W.J., Wong, I.G., and Jackson, S.M., 1992, Assessment of stress drops of normal faulting earthquakes in the Basin and Range province, Seismological Research Letters, v. 63, p. 39.

Subramanian, C.V., J.L. King, D.M. Perkins, R.W. Mudd, A.M. Richardson, J.C. Calovini, E. Van Eeckhout, and D.O. Emerson (1990). Exploratory shaft seismic design basis working group report, SAND88-1203 UC-814.

Swadley, W C, D. L. Hoover, and J. N. Rosholt, 1984, "Preliminary Report on Late Cenozoic Faulting and Stratigraphy in the Vicinity of Yucca Mountain, Nye County, Nevada," U.S. Geological Survey Open File Report 84-788, 41 p.

Toro, G.R., and McGuire, R.K. (1987). "An investigation into earthquake ground motion characteristics in eastern North America." *Bull. Seism. Soc. Am.*, 77, 468-489.

Tsai, Y.B., Brady, F.W., and Cluff, L.S., 1990, An integrated approach for characterization of ground motions in PG&E's long-term seismic program for Diablo Canyon, Proceedings, Fourth U.S. National Conference on Earthquake Engineering, v. 1, p. 597-606.

Walck, M.C., and J.S. Phillips, Two-dimensional Velocity Models for Paths from Pahute Mesa and Yucca Flat to Yucca Mountain, SAND88-3033, Sandia National Laboratories, Albuquerque, NM.

Weichert, D.H., 1980, Estimation of the earthquake recurrence parameters for unequal observation periods for different magnitudes. Bulletin of the Seismological Society of America, V. 70, p. 1337-1346.

Wells, D.L. and Coppersmith, K.J., 1994, Updated empirical relationships among magnitude, rupture length, rupture area, and surface displacement, Bulletin of the Seismological Society of America (in press).

Woodward-Clyde Consultants, 1979, Development of seismic exposure model, Report to Woodward-Clyde Consultants Professional Development Committee by R. Kulkarni, K. Sadigh and I.M. Idriss.

Working Group on California Earthquake Probabilities (Agnew, D.C., Allen, C.R., Cluff, L.S., Dieterich, J.H., Ellsworth, W.L., Keeney, R.L., Lindh, A.G., Nishenko, S.P., Schwartz, D.P., Sieh, K.E., Thatcher, W., and Wesson, R.L.), 1988, Probabilities of large earthquakes occurring in California on the San Andreas fault, U.S. Geological Survey Open-File Report 88-398, 62 p.

Working Group on California Earthquake Probabilities (Dieterich, J.H., Allen, C.R., Cluff, L.S., Cornell, C.A., Ellsworth, W.L., Johnson, L.R., Lindh, A.G., Nishenko, S.P., Scholz, C.H., Schwartz, D.P., Thatcher, W., and Williams, P.L.), 1990, Probabilities of large earthquakes in the San Francisco Bay region, California, U.S. Geological Survey Circular 1053, 51 p.

Youngs, R.R. and Coppersmith, K.J., 1985, Implications of fault slip rates and earthquake recurrence models to probabilistic seismic hazard estimates, Bulletin of the Seismological Society of America, v. 75, p. 939-964.

Youngs, R.R., Swan, F.H., III, Power, M.S., Schwartz, D.P., and Green, R.K., 1987. Probabilistic analysis of earthquake ground-shaking along the Wasatch front, Utah, in Hays, W.W., and Gori, P.L., eds., Assessment of Regional Earthquake Hazards and Risk Along the Wasatch Front, Utah: U.S. Geological Survey Professional Paper (in press).

REGULATIONS AND ORDERS

10 CFR Part 60 (Code of Federal Regulations) (1990): Title 10, Energy, Part 60, "Disposal of High-Level Radioactive Wastes in Geologic Repositories", Washington, D.C.

DOE (U.S. Department of Energy), 1993, Natural Phenomena Hazards Mitigation, Order DOE 5480.28.

EVALUATION OF EMPIRICAL ATTENUATION RELATIONS FOR EXTENSIONAL REGIME EARTHQUAKES

Presentation by
Paul Spudich, U.S. Geological Survey, Menlo Park, CA

Ground Motion Workshop #2 -
Methods, Models, and Preliminary Interpretations

Doubletree Hotel
Salt Lake City, UT

January 9, 1997

Two ways to estimate ground motions based on the extensional regime data set:

1. Develop a new ground motion prediction relation (SEA96)

2. Calculate correction factors for existing ground motion prediction relations

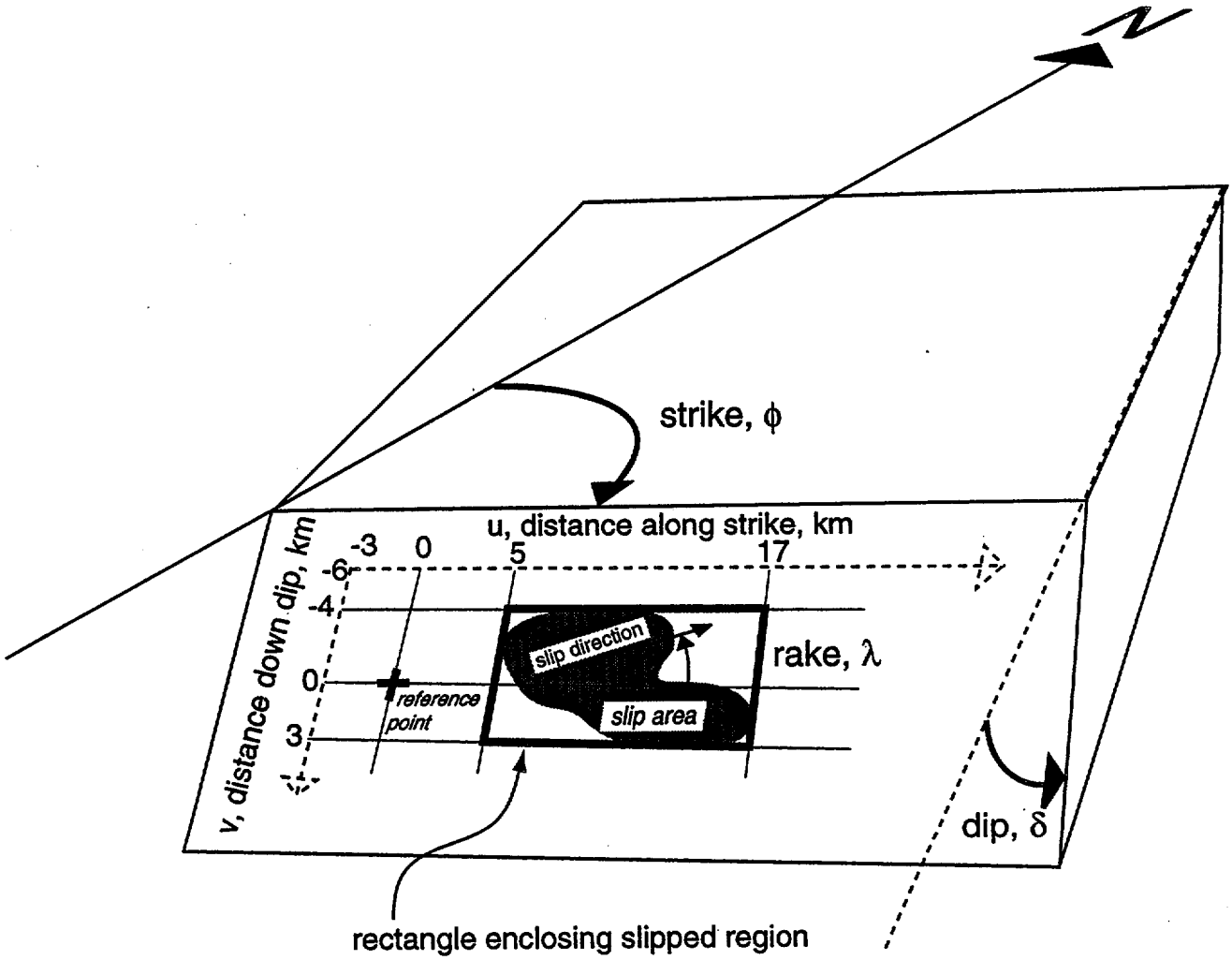
N
strike, ϕ
u, distance along strike, km
-3
0
5
17
v, distance down dip, km
-6
-4
0
3
slip direction
rake, λ
reference point
slip area
dip, δ
rectangle enclosing slipped region

GEOLOGIC SITE CONDITIONS

We characterized each site by a geologic code G=1,...,6, and by a depth to basement, when available.

Hard rock (G=1)

- plutonic igneous rocks, lava flows, welded tuffs, and metamorphic rocks (if not severely weathered)

Soft rock (G=2)

- ordinary sedimentary rocks (unless described as very hard), severely weathered rocks, pyroclastic rocks (except welded tuffs)

Rock of unknown hardness (G=0)

- (treated like soft rock in all calculations)

Deep soil (G=6)

- alluvium, sand, gravel, clay, slit, mud, fill, glacial outwash, etc, >20 m thick

Shallow soil (G=7)

- alluvium, sand, gravel, clay, slit, mud, fill, glacial outwash, etc, 5m to 20 m thick

Soil of unknown thickness (G=5)

- (treated like deep soil in all calculations)

Campbell's "depth to basement"

- depth to the top of unweathered crystalline igneous or metamorphic rock, or the depth at which P velocities of 5.0 km/s or S velocities of 3.0 km/s are reached and velocity gradients are low. *(not available for all sites)*

DEVELOPMENT OF NEW PREDICTIVE RELATIONSHIP SEA96

We used the two stage regression method of Joyner and Boore (1993, 1994) to obtain the coefficients of the following regression relation (which we have baptized *SEA96*):

$$\log_{10} Y = b_1 + b_2(M-6) + b_3(M-6)^2 + b_4 R + b_5 \log_{10} R + g\, b_6$$

where

$$R := \sqrt{r_{jb}^2 + h^2} \quad , \quad g = 0 \text{ for rock}, \quad g = 1 \text{ for soil} \quad , \quad M = \text{moment magnitude}$$

r_{jb} = closest distance to the vertical projection of the fault surface

b_2, b_4, h are coefficients determined by Boore et al. (1994)

b_1, b_5, b_6 are coefficients determined by our regression

We were forced to use b_2, b_4, and h from Boore et al. (1994) because our data set did not span a wide enough range of magnitude to determine these coefficients adequately.

Figure 3. Sample evaluations of SEA96 for M = 5.5, 6.5, 7.5, r_{bj} = 0, 100 km

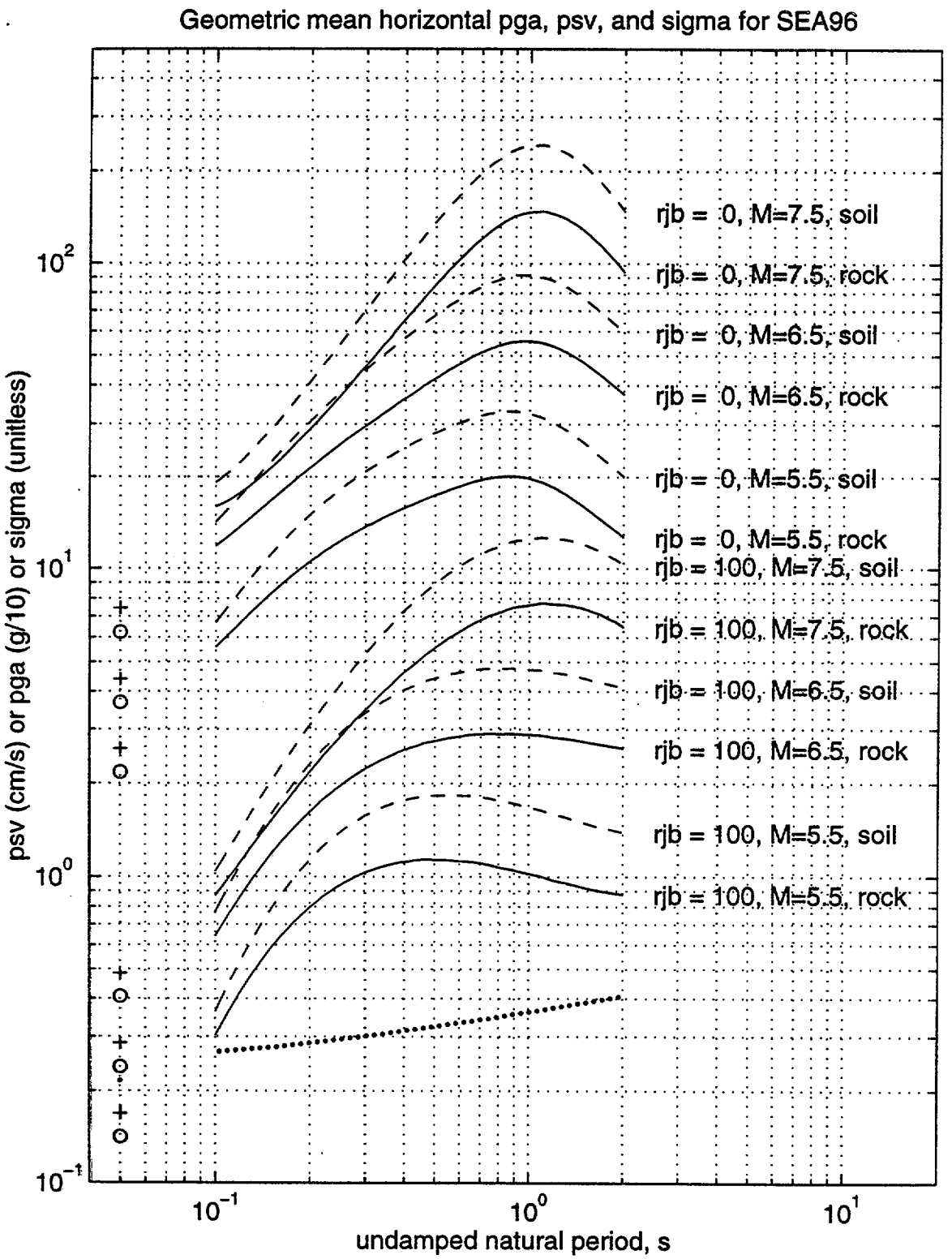

COMPARISON OF OUR EXTENSIONAL REGIME DATA WITH OTHER GROUND MOTION PREDICTION RELATIONS

We compared our data set with the following relations:

our abbrev.	*reference*
BJF94	Boore, Joyner, and Fumal (1993, 1994)
CB94	Campbell and Bozorgnia (1994)
C89 or C89/94	Campbell (1989) (scaled so its pha equals CB94 pha)
C90 or C90/94	Campbell (1990) (scaled so its pha equals CB94 pha)
C93/94	Campbell (1993) (scaled so its pha equals CB94 pha)
I93	Idriss (1991, 1993)
JB88	Joyner and Boore (1988)
SP96	Sabetta and Pugliese (1996)
S93	Sadigh et al. (1993)

Table 5: Correspondence between various authors' site classifications and the classifications used in this work.
• *indicates the combinations of Campbell's relations and site classes actually used in this report*

Authors	Predicted parameters (7) (*italic*=used in this study)	horizontal used	Our soil classes(4): rock of unknown hardness (3,6) (G=0)	hard rock (6) (G=1)	soft rock (6) (G=2)	soil of unknown thickness (G=5)	deep soil (h > 20m) (G=6)	shallow soil (5m < h < 20m) (G=7)
BJF 94	*pha, psvh*	geom. mean (5)	Vs = 620 m/s	Vs = 620 m/s	Vs = 620 m/s	Vs = 310 m/s	Vs = 310 m/s	Vs = 310 m/s
C 89 (2)	pha, *phv*, *psvh* *pza, pzv, psvz*	arith. mean	"soil/soft rock" (3)	n/a	"soil/soft rock"	•"soil/soft rock"	•"soil/soft rock"	•"soil/soft rock"
C 90	pha, *phv*, *psvh* *pza, pzv, psvz*	arith. mean	•'>10m soil or soft rock'	n/a	•'>10m soil or soft rock'	'>10m soil or soft rock'	'>10m soil or soft rock'	n/a
C 93 (1)	pha, *psah*	arith. mean	'rock'(1)	•'rock' (1)	'rock' (1)	'soil' (1)	'soil' (1)	'soil' (1)
CB 94	*pha*	geom. mean	•'soft rock'	•'hard rock'	•'soft rock'	•'alluvium'	•'alluvium'	•'alluvium'
JB 88	psvh, pha, *phv*	geom. mean (5)	'rock'	'rock'	'rock'	'soil'	'soil'	'soil'
Idriss 93	*pha, psah*	geom. mean	'rock'	'rock'	'rock'	n/a	n/a	n/a
SP 96	*pha, phv, psvh*	larger	'stiff <5m soil'	'stiff <5m soil'	'stiff <5m soil'	'deep soil, >20m soil'	'deep soil, >20m soil'	'shallow, 5-20m soil'
S 93	*pha, psah, pza, psaz*	geom. mean	'rock'	'rock'	'rock'	n/a	n/a	n/a

(1) C93 has two site catagories: "Quaternary deposits (soil)" and "Tertiary or older sedimentary, metamorphic, and igneous deposits (rock)". Campbell (written communication, 1995) says we should use this relation for psa on *hard* rock only.
(2) C89 was developed using soil data only, but stated to be appropriate for soft rock also. Campbell (written communication, 1995) says we should use this relation for psvh, pza, psvz and psaz on soil.
(3) rock of unknown hardness is assumed to be a soft rock, as true hard rock sites are relatively rare, particularly in the Western US.
(4) G is an arbitrary site code number. Numbers 3 and 4 are not used.
(5) Coefficients for the random horizontal were used, which is identical to the geometric mean. See Appendix A for $\sigma^2_{\log y}$ calculation.
(6) Sites having 5m of soil or less are considered rock sites
(7) Abbreviations: h=horizontal, z=vertical, a=acceleration, v=velocity, pza=peak vertical acceleration, psah=horizontal pseudospectral acceleration, etc ...

Table 5 of 11

- All correction factors and slope parameters were calculated for each row of the following table,
  1) for data in the 0-105 km distance range
  2) for data in the 0-20 km distance range

relation	h/z	pga	psv/ paa	pgv	hard rock G=1	soft rock G=2	unkn rock G=0	shal soil G=7	deep soil G=6	unkn soil G=5
BJF94	h	•	•		•	•	•			
BJF94	h	•	•					•	•	•
C89/94	h	•	•					•	•	•
C89	z	•	•					•	•	•
C89	h			•				•	•	•
C89	z			•				•	•	•
C90/94	h	•	•			•	•			
C90	z	•	•			•	•			
C90	h			•		•	•			
C90	z			•		•	•			
C93/94	h	•	•		•					
I93	h	•	•		•	•	•			
JB88	h			•				•	•	•
JB88	h			•				•	•	•
SP96	h	•	•		•	•	•			
SP96	h	•	•						•	•
SP96	h	•	•					•		
SP96	h			•	•	•	•			
SP96	h			•				•	•	•
S93	h	•	•		•	•	•			
S93	z	•	•					•	•	•
Sea96	h	•	•		•	•	•			
Sea96	h	•	•					•	•	•

Illustration of bias correction and dispersion correction

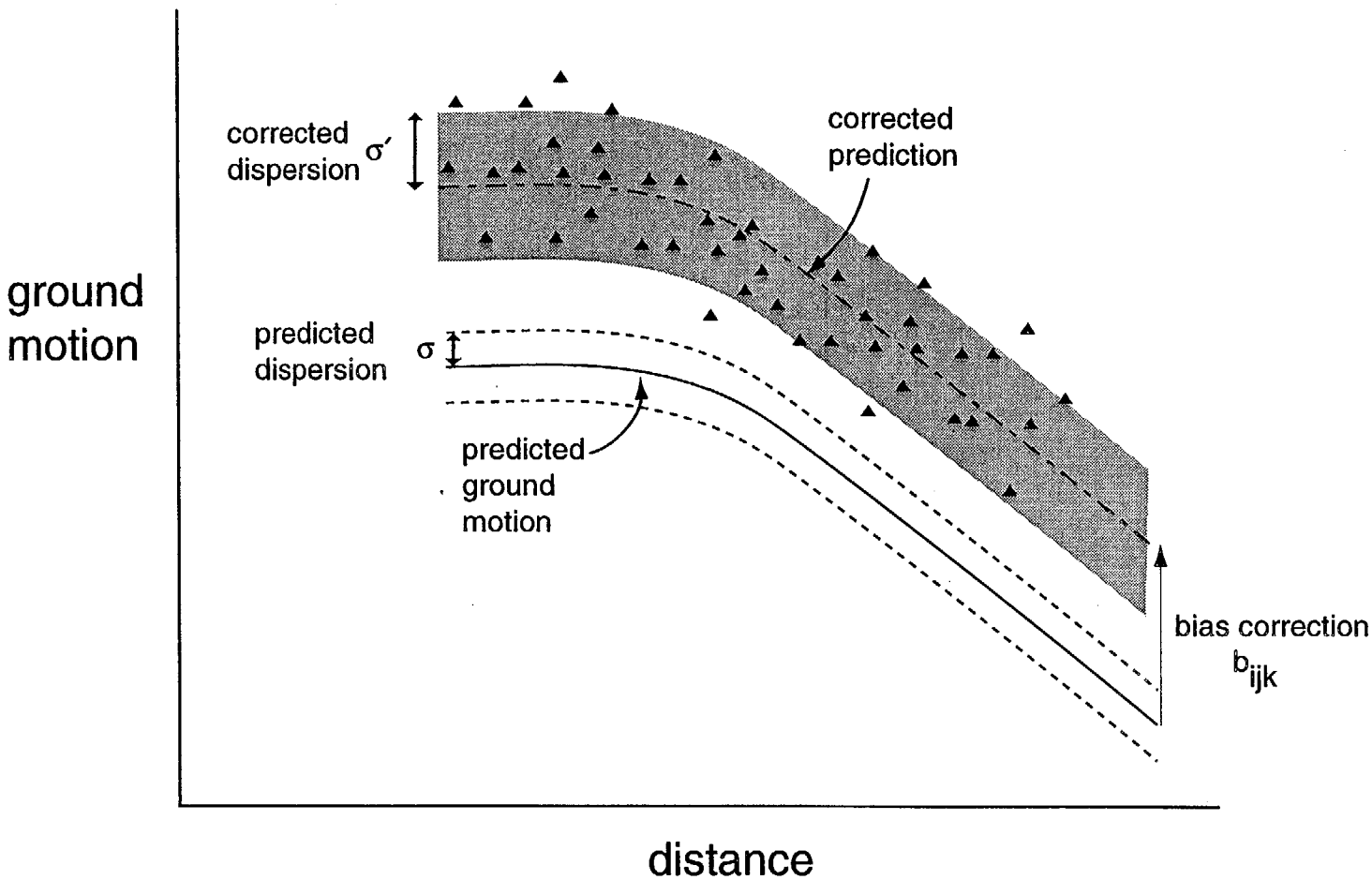

"Uncorrected" Predictive Relations

Predictive relations are of the form:

$\log(y) = f(M, R, G_i, C_j, D, F, T_k)$, where

y = ground motion parameter (e.g. pga)

M = magnitude

R = distance

D = depth to basement

F = source mechanism term (we use strike – slip always)

G_i = site geology, $i = 1, \ldots, 6$

C_j = component of motion ($j = 1$ horiz, $j = 2$ vert(z))

T_k = period, $k = 1, \ldots, m$

Predicted standard error of log(y) ("dispersion") is

$\sigma(M, pga, G_i, C_j, T_k)$

For each combination of i, j, and k (site geology, component of motion, and period) there is a population P_{ijk} of relevant data. P_{ijk} has N_{ijk} elements.

"Corrected" Predictive Relations

$$\log(y') = f(M, R, G_i, C_j, D, F, T_k) + b_{ijk}$$

where

b_{ijk} ="bias correction" for site class i,

component j, and period k

$$\sigma' := \sigma(M, pga, G_i, C_j, T_k)\, e_{ijk}$$

where

e_{ijk} ="dispersion correction" for site class i,

component j, and period k

Calculation of correction factors - bias correction b_{ijk}

Define observed residual:

$$r := \log_{10}(y_o) - \log_{10}(y_{ijk})$$

where

y_o = observed ground motion for site category i, component j, and period k

y_{ijk} = (uncorrected) predicted value of y_o

Bias correction :

$$b_{ijk} := \frac{1}{N_{ijk}} \sum_{P_{ijk}} r$$

The bias correction is the mean residual taken over all data for site category i, component j, and period k

Define demeaned residual:

$$r' := r - b_{ijk}$$

Population standard deviation of r' is:

$$\sigma_p := \left(\frac{1}{N_{ijk}} \sum_{P_{ijk}} (r')^2 \right)^{1/2}$$

Standard deviation of bias correction b_{ijk} is :

$$\sigma_b := N_{ijk}^{-1/2} \, \sigma_p$$

Calculation of correction factors - dispersion correction

Objective : determine e_{ijk} so that

$$\frac{r'}{\sigma'} \equiv \frac{r'}{\sigma\, e_{ijk}} \text{ has unit variance over } P_{ijk}$$

where

r' = demeaned residual for P_{ijk}

σ = uncorrected dispersion

σ' = corrected dispersion

$$e_{ijk} = \sqrt{v_{ijk}}$$

where

$$v_{ijk} = \text{variance of } r'/\sigma$$

$$:= \left(\frac{1}{N_{ijk}} \sum_{P_{ijk}} \left(\frac{r'}{\sigma} \right)^2 \right)$$

Significance of dispersion correction

<u>Method 1: standard deviation of standard deviation</u>

$$\sigma_e := \left(\frac{N_{ijk}-1}{2}\right)^{1/2} \frac{e_{ijk}}{N_{ijk}}$$

<u>Method 2: chi-squared test</u>

$$\text{Observed chi-squared} := \chi_o^2 = \sum_{P_{ijk}} \left(\frac{r'}{\sigma}\right)^2$$

Q statistic :

$$Q(\chi_o^2 \mid \nu) := 1 - P(\nu/2,\ \chi_o^2/2)$$

where

$P(a,x)$ is incomplete Gamma function

ν = number of degrees of freedom = $N_{ijk} - 1$

Q is the probability of obtaining, from a set of residuals drawn from a population having dispersion σ, $\chi^2 > \chi_o^2$

$Q \to 1 \Rightarrow \sigma$, predicted dispersion, is too big

$Q \to 0 \Rightarrow \sigma$, predicted dispersion, is too small

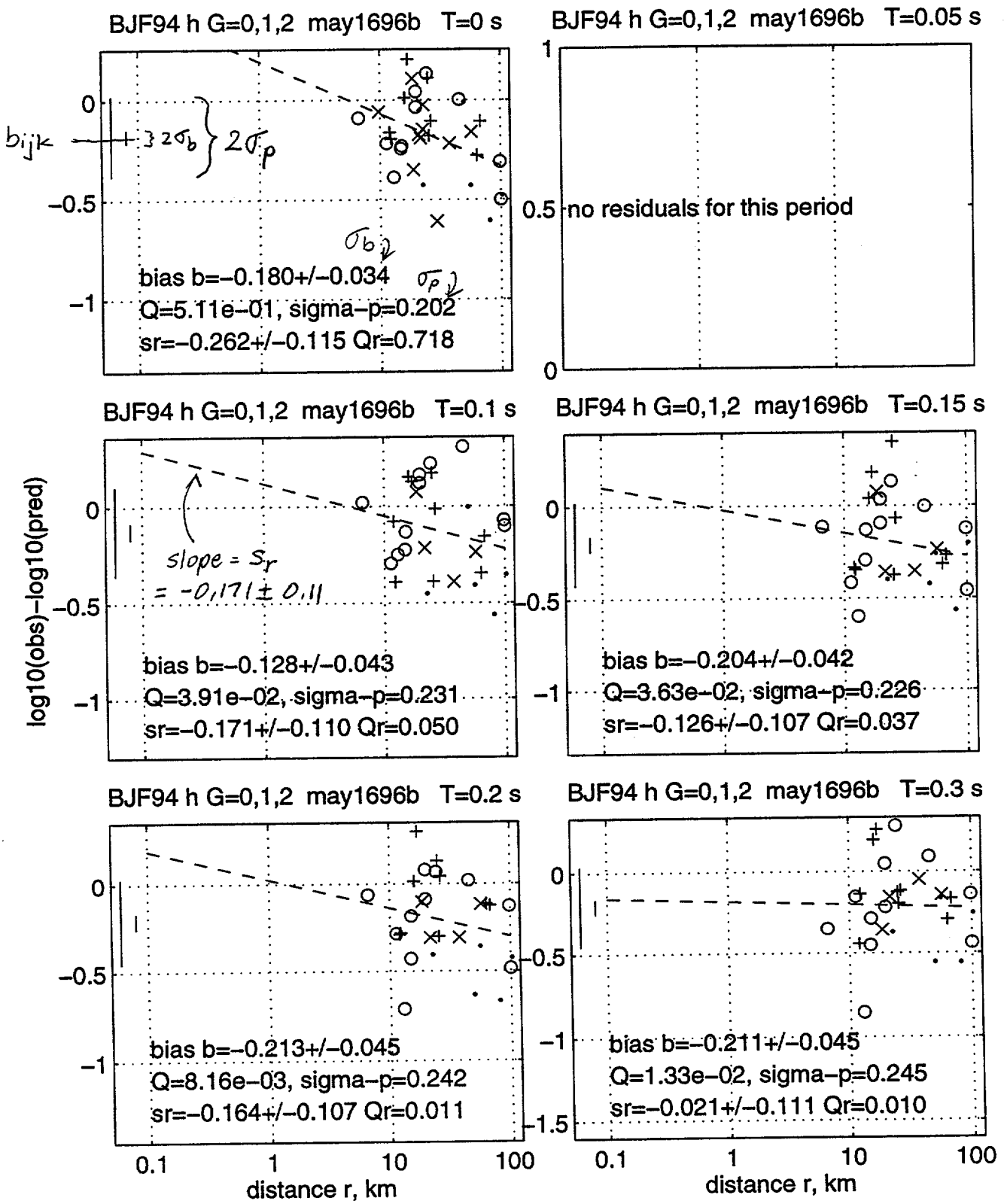

96/5/16 19:30 ymp1:[sp]may1696b1d1.eps

Table 9. Correction factors for each predictive relation, determined from data at all distances.

BJF94 h G=0,1,2 may2196b

T(s)	bijk	sigma-b	sigma-p	eijk	sigma-e	Q	N
0.00	-0.180	0.034	0.202	0.973	0.115	5.11e-01	35
0.05	-	-	-	-	-	-	0
0.10	-0.128	0.043	0.231	1.210	0.156	3.91e-02	29
0.15	-0.204	0.042	0.226	1.215	0.157	3.63e-02	29
0.20	-0.213	0.045	0.242	1.301	0.168	8.16e-03	29
0.30	-0.211	0.045	0.245	1.275	0.164	1.33e-02	29
0.40	-0.190	0.042	0.228	1.139	0.147	1.06e-01	29
0.50	-0.157	0.040	0.214	1.031	0.133	3.25e-01	29
0.75	-0.160	0.046	0.246	1.117	0.144	1.38e-01	29
1.00	-0.164	0.049	0.265	1.150	0.148	9.20e-02	29
1.50	-0.116	0.061	0.291	1.201	0.173	5.92e-02	23
2.00	-0.219	0.074	0.338	1.363	0.205	6.64e-03	21

BJF94 h G=5,6,7 may2196b

T(s)	bijk	sigma-b	sigma-p	eijk	sigma-e	Q	N
0.00	-0.083	0.021	0.204	0.981	0.072	5.55e-01	93
0.05	-	-	-	-	-	-	0
0.10	-0.040	0.024	0.225	1.179	0.088	7.34e-03	89
0.15	-0.065	0.025	0.238	1.284	0.096	8.89e-05	89
0.20	-0.087	0.026	0.247	1.330	0.099	7.97e-06	89
0.30	-0.118	0.024	0.229	1.193	0.089	4.42e-03	89
0.40	-0.139	0.026	0.245	1.224	0.091	1.28e-03	89
0.50	-0.099	0.027	0.256	1.235	0.092	8.14e-04	89
0.75	-0.110	0.034	0.318	1.443	0.108	6.46e-09	89
1.00	-0.122	0.034	0.323	1.397	0.104	1.39e-07	89
1.50	-0.084	0.035	0.322	1.329	0.102	1.39e-05	84
2.00	-0.084	0.038	0.333	1.346	0.107	1.12e-05	78

C89/94 h G=5,6,7 may2196b

T(s)	bijk	sigma-b	sigma-p	eijk	sigma-e	Q	N
0.00	-0.012	0.019	0.188	0.973	0.071	5.96e-01	93
0.05	0.090	0.022	0.195	1.021	0.081	3.45e-01	78
0.10	0.064	0.024	0.222	1.064	0.079	1.67e-01	89
0.15	0.022	0.025	0.240	1.107	0.082	6.39e-02	89
0.20	0.003	0.026	0.249	1.148	0.086	2.00e-02	89
0.30	-0.027	0.023	0.221	1.017	0.076	3.60e-01	89
0.40	-0.030	0.025	0.238	1.097	0.082	8.11e-02	89
0.50	-0.003	0.026	0.242	1.116	0.083	5.05e-02	89
0.75	-0.042	0.033	0.310	1.427	0.106	1.97e-08	89
1.00	-0.064	0.033	0.309	1.423	0.106	2.66e-08	89
1.50	-0.043	0.032	0.243	1.117	0.103	8.26e-02	58
2.00	-0.017	0.032	0.242	1.116	0.105	8.66e-02	56

C89 z G=5,6,7 may2196b

T(s)	bijk	sigma-b	sigma-p	eijk	sigma-e	Q	N
0.00	-0.008	0.024	0.223	0.904	0.068	8.78e-01	88
0.05	0.179	0.031	0.280	1.040	0.082	2.66e-01	79
0.10	-0.103	0.036	0.327	1.215	0.093	2.38e-03	84
0.15	0.023	0.028	0.257	0.956	0.073	6.71e-01	84
0.20	0.078	0.030	0.272	1.012	0.078	3.89e-01	84
0.30	0.197	0.031	0.281	1.044	0.080	2.44e-01	84
0.40	0.070	0.035	0.321	1.190	0.091	5.87e-03	84
0.50	-0.010	0.035	0.317	1.179	0.090	8.62e-03	84
0.75	-0.100	0.039	0.346	1.285	0.102	1.87e-04	79
1.00	-0.078	0.041	0.357	1.325	0.107	4.33e-05	75
1.50	-0.152	0.053	0.378	1.405	0.138	2.86e-05	51
2.00	-0.161	0.051	0.351	1.303	0.133	1.45e-03	47

C89V h G=5,6,7 may1696c

T(s)	bijk	sigma-b	sigma-p	eijk	sigma-e	Q	N
pk vel	0.026	0.026	0.200	1.168	0.107	2.67e-02	59

C89V z G=5,6,7 may1696c

T(s)	bijk	sigma-b	sigma-p	eijk	sigma-e	Q	N
pk vel	0.029	0.027	0.255	1.129	0.085	3.57e-02	88

C90/94 h G=0,2 may2196b

Slope parameters (not corrections)

<u>Distance dependence of residuals</u>

For each population P_{ijk}, we fit a straight line through residuals r as a function of $\log_{10}(R)$, where

$R = r_{rup}$ (rupture distance, used by Idriss and Sadigh et al)

r_{seis} (seismogenic distance, used by Campbell)

$\sqrt{5^2 + r_{jb}^2}$ (Joyner - Boore distance plus 5 km pseudodepth, for BJF94, JB88, SP96, and SEA96)

We obtain :

s_r = slope

σ_r = standard deviation of slope

a_r = intercept

σ_{ar} = standard deviation of intercept

$Q_r = \chi^2$ goodness of fit parameter

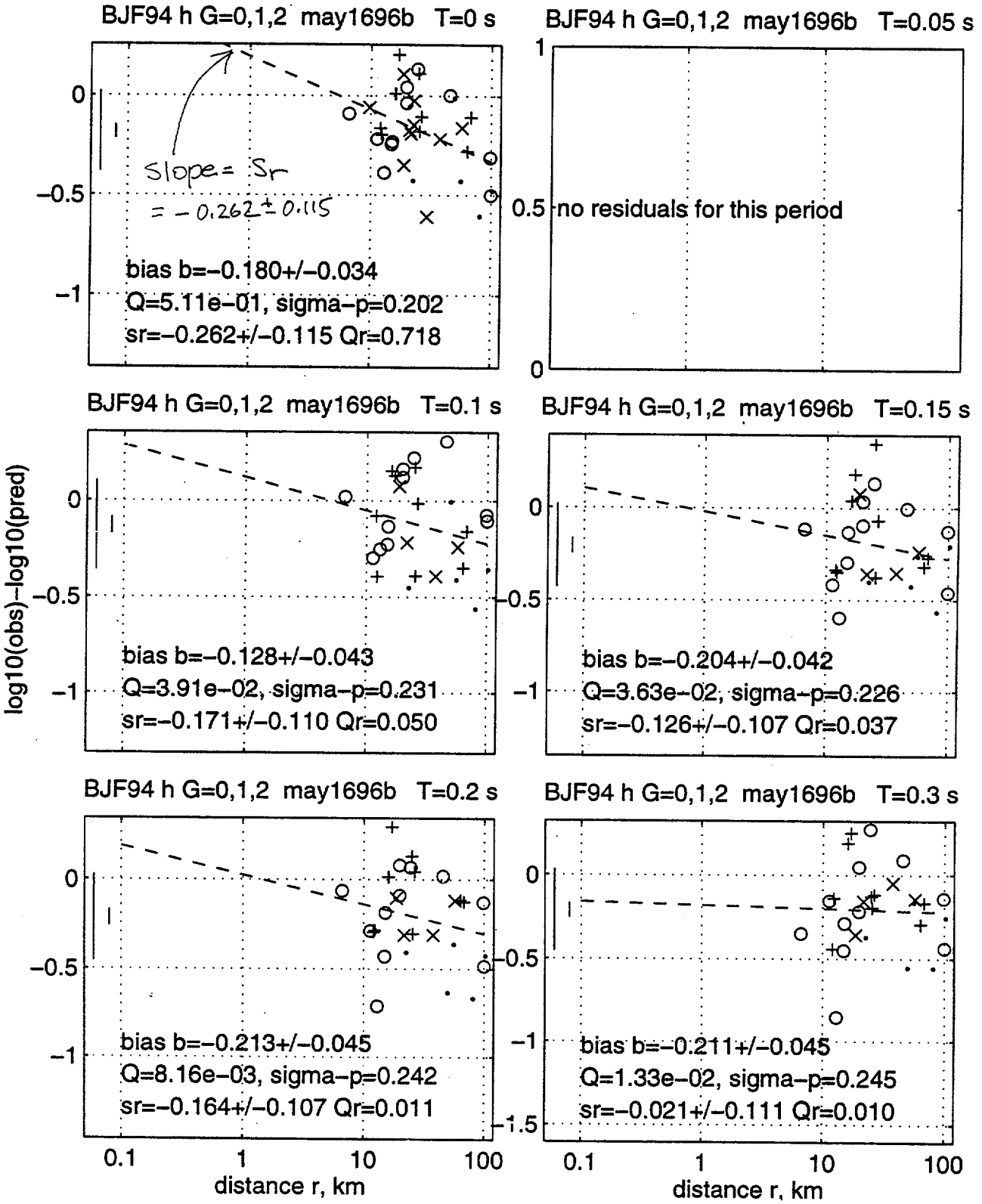

96/5/16 19:30 ymp1:[sp]may1696b1d1.eps

Table 10. Distance dependences for each predictive relation, determined from data at all distances.

BJF94 h G=0,1,2 may2196b Distance dependence

T(s)	ar	sigma-ar	sr	sigma-sr	cas	ras	Qr	N
0.00	1.93e-01	1.68e-01	-2.62e-01	1.15e-01	-1.89e-02	-0.978	7.18e-01	35
0.05	-	-	-	-	-	-	-	0
0.10	1.20e-01	1.64e-01	-1.71e-01	1.10e-01	-1.76e-02	-0.976	5.03e-02	29
0.15	-2.12e-02	1.59e-01	-1.26e-01	1.07e-01	-1.67e-02	-0.976	3.75e-02	29
0.20	2.47e-02	1.59e-01	-1.64e-01	1.07e-01	-1.67e-02	-0.976	1.05e-02	29
0.30	-1.80e-01	1.65e-01	-2.10e-02	1.11e-01	-1.78e-02	-0.976	9.67e-03	29
0.40	-1.61e-01	1.72e-01	-2.00e-02	1.15e-01	-1.93e-02	-0.976	8.47e-02	29
0.50	-1.44e-01	1.78e-01	-8.72e-03	1.20e-01	-2.07e-02	-0.976	2.79e-01	29
0.75	8.75e-02	1.89e-01	-1.70e-01	1.27e-01	-2.35e-02	-0.976	1.55e-01	29
1.00	3.62e-01	1.98e-01	-3.63e-01	1.33e-01	-2.58e-02	-0.976	2.74e-01	29
1.50	2.30e-01	2.41e-01	-2.50e-01	1.70e-01	-4.01e-02	-0.978	7.30e-02	23
2.00	1.80e-01	2.54e-01	-2.94e-01	1.83e-01	-4.54e-02	-0.977	9.36e-03	21

BJF94 h G=5,6,7 may2196b Distance dependence

T(s)	ar	sigma-ar	sr	sigma-sr	cas	ras	Qr	N
0.00	1.60e-01	7.48e-02	-2.01e-01	5.90e-02	-4.23e-03	-0.958	8.35e-01	93
0.05	-	-	-	-	-	-	-	0
0.10	9.30e-02	7.02e-02	-1.11e-01	5.63e-02	-3.79e-03	-0.958	1.15e-02	89
0.15	6.22e-02	6.82e-02	-1.07e-01	5.47e-02	-3.57e-03	-0.958	1.53e-04	89
0.20	1.63e-02	6.83e-02	-8.61e-02	5.47e-02	-3.58e-03	-0.958	1.04e-05	89
0.30	2.06e-02	7.05e-02	-1.16e-01	5.66e-02	-3.82e-03	-0.958	7.38e-03	89
0.40	-2.23e-02	7.35e-02	-9.78e-02	5.89e-02	-4.15e-03	-0.958	1.71e-03	89
0.50	3.16e-02	7.61e-02	-1.09e-01	6.10e-02	-4.45e-03	-0.958	1.19e-03	89
0.75	7.86e-02	8.10e-02	-1.58e-01	6.50e-02	-5.04e-03	-0.958	2.18e-08	89
1.00	8.32e-02	8.48e-02	-1.71e-01	6.80e-02	-5.53e-03	-0.958	4.95e-07	89
1.50	1.51e-01	9.47e-02	-2.02e-01	7.83e-02	-7.12e-03	-0.960	4.78e-05	84
2.00	3.36e-01	1.01e-01	-3.65e-01	8.43e-02	-8.18e-03	-0.961	5.78e-04	78

C89/94 h G=5,6,7 may2196b Distance dependence

T(s)	ar	sigma-ar	sr	sigma-sr	cas	ras	Qr	N
0.00	-8.65e-02	6.20e-02	5.85e-02	5.29e-02	-3.11e-03	-0.948	6.11e-01	93
0.05	4.58e-02	7.04e-02	3.90e-02	5.85e-02	-3.92e-03	-0.952	3.28e-01	78
0.10	3.31e-02	7.11e-02	2.59e-02	5.71e-02	-3.86e-03	-0.951	1.52e-01	89
0.15	-8.40e-02	7.41e-02	8.93e-02	5.94e-02	-4.19e-03	-0.951	7.38e-02	89
0.20	-1.23e-01	7.41e-02	1.07e-01	5.94e-02	-4.19e-03	-0.951	2.72e-02	89
0.30	-7.74e-02	7.41e-02	4.27e-02	5.94e-02	-4.19e-03	-0.951	3.46e-01	89
0.40	-6.15e-02	7.41e-02	2.63e-02	5.94e-02	-4.19e-03	-0.951	7.24e-02	89
0.50	-3.76e-03	7.41e-02	8.96e-04	5.94e-02	-4.19e-03	-0.951	4.34e-02	89
0.75	6.59e-02	7.41e-02	-9.15e-02	5.94e-02	-4.19e-03	-0.951	2.55e-08	89
1.00	4.38e-02	7.41e-02	-9.07e-02	5.94e-02	-4.19e-03	-0.951	3.41e-08	89
1.50	-4.34e-02	9.75e-02	6.45e-04	8.56e-02	-7.97e-03	-0.956	6.96e-02	58
2.00	-7.75e-03	9.94e-02	-8.92e-03	8.86e-02	-8.43e-03	-0.956	7.31e-02	56

C89 z G=5,6,7 may2196b Distance dependence

T(s)	ar	sigma-ar	sr	sigma-sr	cas	ras	Qr	N
0.00	-1.12e-01	8.69e-02	8.70e-02	6.92e-02	-5.73e-03	-0.953	8.89e-01	88
0.05	2.61e-01	1.00e-01	-7.01e-02	8.20e-02	-7.84e-03	-0.953	2.58e-01	79
0.10	-5.69e-01	9.68e-02	3.97e-01	7.86e-02	-7.25e-03	-0.953	1.04e-01	84
0.15	-1.86e-01	9.68e-02	1.78e-01	7.86e-02	-7.25e-03	-0.953	7.87e-01	84
0.20	-2.97e-01	9.68e-02	3.19e-01	7.86e-02	-7.25e-03	-0.953	8.36e-01	84
0.30	-2.47e-01	9.68e-02	3.78e-01	7.86e-02	-7.25e-03	-0.953	8.59e-01	84
0.40	-4.32e-01	9.68e-02	4.27e-01	7.86e-02	-7.25e-03	-0.953	2.70e-01	84
0.50	-5.24e-01	9.68e-02	4.39e-01	7.86e-02	-7.25e-03	-0.953	3.71e-01	84
0.75	-7.52e-01	1.03e-01	5.73e-01	8.67e-02	-8.55e-03	-0.956	2.11e-01	79
1.00	-6.60e-01	1.06e-01	5.18e-01	9.02e-02	-9.15e-03	-0.956	2.44e-02	75
1.50	-7.38e-01	1.29e-01	5.43e-01	1.14e-01	-1.41e-02	-0.956	5.12e-03	51
2.00	-6.72e-01	1.35e-01	4.89e-01	1.24e-01	-1.60e-02	-0.957	3.13e-02	47

C89V h G=5,6,7 may1696c Distance dependence

T(s)	ar	sigma-ar	sr	sigma-sr	cas	ras	Qr	N
pk vl	-8.05e-02	7.59e-02	9.65e-02	6.60e-02	-4.79e-03	-0.956	3.15e-02	59

C89V z G=5,6,7 may1696c Distance dependence

T(s)	ar	sigma-ar	sr	sigma-sr	cas	ras	Qr	N
pk vl	-3.78e-02	7.94e-02	5.58e-02	6.32e-02	-4.78e-03	-0.953	3.39e-02	88

C90/94 h G=0,2 may2196b Distance dependence

More slope parameters (not corrections)

<u>Magnitude dependence of residuals</u>

For each population P_{ijk}, we fit a straight line through residuals r as a function of moment magnitude, M

We obtain :

s_m = slope

σ_m = standard deviation of slope

a_m = intercept

σ_{am} = standard deviation of intercept

$Q_m = \chi^2$ goodness of fit parameter

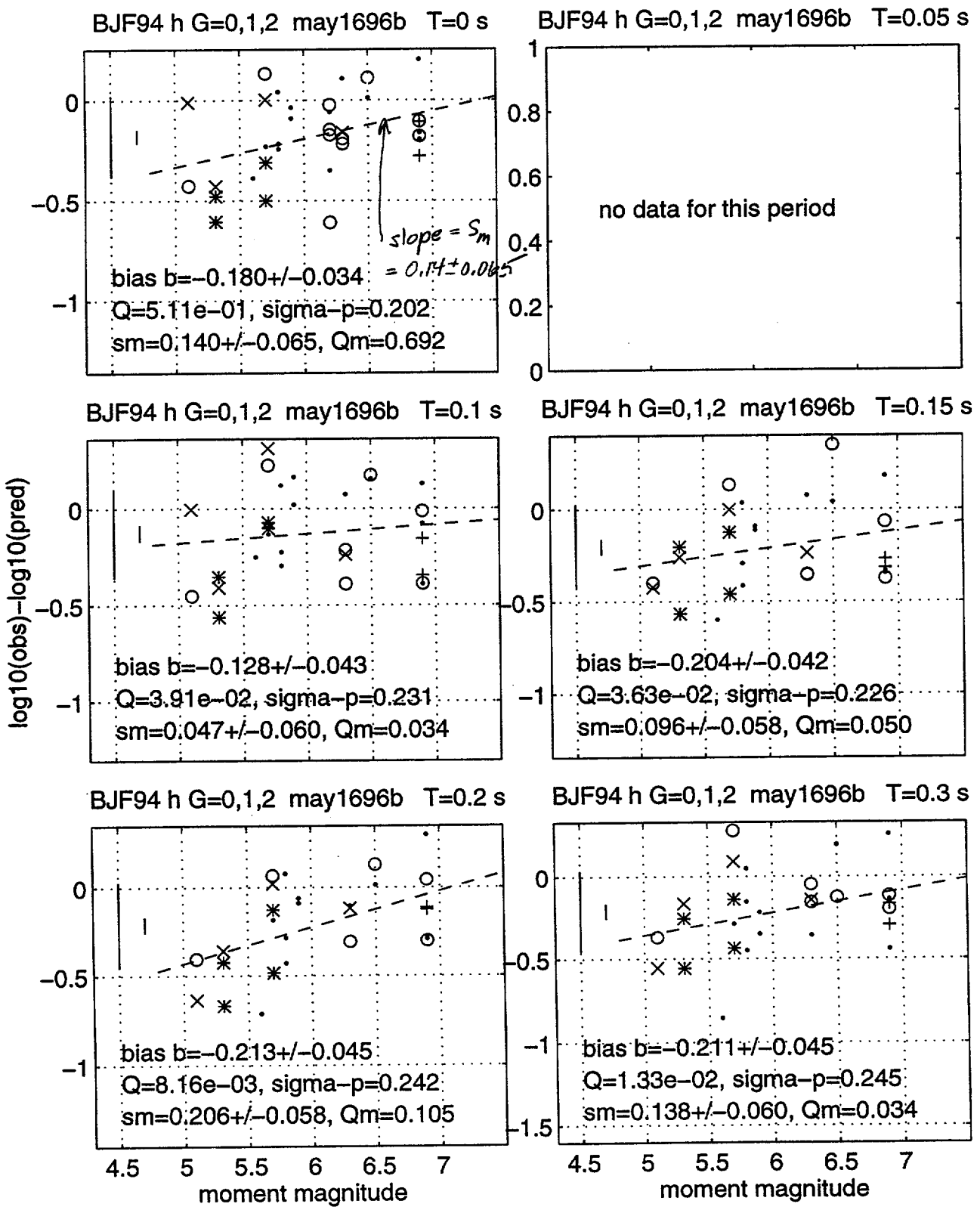

96/5/16 19:30 ymp1:[sp]may1696b1m1.eps

19D

12a

Table 11. Magnitude dependences for each predictive relation, determined from data at all distances.

BJF94 h G=0,1,2 may2196b Magnitude dependence

T(s)	am	sigma-am	sm	sigma-sm	cas	ras	Qm	N
0.00	-1.03e+00	3.96e-01	1.40e-01	6.48e-02	-2.56e-02	-0.996	6.92e-01	35
0.05	-	-	-	-	-	-	-	0
0.10	-4.10e-01	3.65e-01	4.66e-02	5.98e-02	-2.17e-02	-0.995	3.39e-02	29
0.15	-7.84e-01	3.54e-01	9.55e-02	5.81e-02	-2.05e-02	-0.995	5.00e-02	29
0.20	-1.46e+00	3.54e-01	2.06e-01	5.81e-02	-2.05e-02	-0.995	1.05e-01	29
0.30	-1.05e+00	3.66e-01	1.38e-01	6.01e-02	-2.19e-02	-0.995	3.38e-02	29
0.40	-1.19e+00	3.82e-01	1.65e-01	6.26e-02	-2.38e-02	-0.995	2.87e-01	29
0.50	-1.19e+00	3.95e-01	1.70e-01	6.49e-02	-2.55e-02	-0.995	6.32e-01	29
0.75	-1.38e+00	4.21e-01	2.01e-01	6.90e-02	-2.89e-02	-0.995	4.27e-01	29
1.00	-1.63e+00	4.40e-01	2.42e-01	7.23e-02	-3.17e-02	-0.995	4.58e-01	29
1.50	-2.23e+00	5.06e-01	3.43e-01	8.16e-02	-4.10e-02	-0.995	7.95e-01	23
2.00	-2.70e+00	5.18e-01	4.03e-01	8.36e-02	-4.30e-02	-0.995	6.71e-01	21

BJF94 h G=5,6,7 may2196b Magnitude dependence

T(s)	am	sigma-am	sm	sigma-sm	cas	ras	Qm	N
0.00	-1.01e-01	3.59e-01	2.75e-03	5.76e-02	-2.07e-02	-0.998	5.26e-01	93
0.05	-	-	-	-	-	-	-	0
0.10	8.27e-01	3.30e-01	-1.39e-01	5.29e-02	-1.74e-02	-0.998	1.84e-02	89
0.15	8.17e-01	3.21e-01	-1.42e-01	5.14e-02	-1.65e-02	-0.998	3.35e-04	89
0.20	4.37e-01	3.21e-01	-8.42e-02	5.15e-02	-1.65e-02	-0.998	1.09e-05	89
0.30	4.79e-01	3.32e-01	-9.58e-02	5.32e-02	-1.76e-02	-0.998	6.29e-03	89
0.40	5.07e-01	3.46e-01	-1.04e-01	5.54e-02	-1.91e-02	-0.998	1.97e-03	89
0.50	9.97e-01	3.58e-01	-1.76e-01	5.74e-02	-2.05e-02	-0.998	3.73e-03	89
0.75	1.13e+00	3.81e-01	-1.99e-01	6.11e-02	-2.32e-02	-0.998	7.59e-08	89
1.00	8.56e-01	3.99e-01	-1.57e-01	6.40e-02	-2.55e-02	-0.998	4.55e-07	89
1.50	9.31e-01	4.44e-01	-1.63e-01	7.10e-02	-3.15e-02	-0.998	3.45e-05	84
2.00	-1.98e-01	4.71e-01	1.81e-02	7.53e-02	-3.54e-02	-0.998	8.19e-06	78

C89/94 h G=5,6,7 may2196b Magnitude dependence

T(s)	am	sigma-am	sm	sigma-sm	cas	ras	Qm	N
0.00	7.05e-01	3.47e-01	-1.16e-01	5.53e-02	-1.91e-02	-0.998	7.01e-01	93
0.05	9.03e-01	3.73e-01	-1.31e-01	5.98e-02	-2.23e-02	-0.998	4.59e-01	78
0.10	1.14e+00	3.60e-01	-1.73e-01	5.78e-02	-2.08e-02	-0.998	3.43e-01	89
0.15	1.28e+00	3.75e-01	-2.02e-01	6.02e-02	-2.25e-02	-0.998	2.01e-01	89
0.20	8.56e-01	3.75e-01	-1.37e-01	6.02e-02	-2.25e-02	-0.998	3.61e-02	89
0.30	6.76e-01	3.75e-01	-1.13e-01	6.02e-02	-2.25e-02	-0.998	4.32e-01	89
0.40	8.56e-01	3.75e-01	-1.42e-01	6.02e-02	-2.25e-02	-0.998	1.37e-01	89
0.50	1.36e+00	3.75e-01	-2.19e-01	6.02e-02	-2.25e-02	-0.998	2.05e-01	89
0.75	1.59e+00	3.75e-01	-2.62e-01	6.02e-02	-2.25e-02	-0.998	1.79e-06	89
1.00	1.51e+00	3.75e-01	-2.53e-01	6.02e-02	-2.25e-02	-0.998	1.73e-06	89
1.50	6.57e-01	5.77e-01	-1.11e-01	9.12e-02	-5.25e-02	-0.999	8.69e-02	58
2.00	3.01e-01	5.83e-01	-5.03e-02	9.20e-02	-5.35e-02	-0.999	7.64e-02	56

C89 z G=5,6,7 may2196b Magnitude dependence

T(s)	am	sigma-am	sm	sigma-sm	cas	ras	Qm	N
0.00	1.64e+00	4.71e-01	-2.65e-01	7.56e-02	-3.55e-02	-0.998	9.87e-01	88
0.05	2.02e+00	5.43e-01	-2.97e-01	8.73e-02	-4.73e-02	-0.998	5.83e-01	79
0.10	2.38e+00	5.13e-01	-3.99e-01	8.24e-02	-4.22e-02	-0.998	8.01e-02	84
0.15	1.89e+00	5.13e-01	-3.01e-01	8.24e-02	-4.22e-02	-0.998	9.36e-01	84
0.20	1.76e+00	5.13e-01	-2.71e-01	8.24e-02	-4.22e-02	-0.998	6.90e-01	84
0.30	1.99e+00	5.13e-01	-2.89e-01	8.24e-02	-4.22e-02	-0.998	5.66e-01	84
0.40	2.13e+00	5.13e-01	-3.32e-01	8.24e-02	-4.22e-02	-0.998	6.03e-02	84
0.50	2.36e+00	5.13e-01	-3.82e-01	8.24e-02	-4.22e-02	-0.998	1.50e-01	84
0.75	2.24e+00	5.51e-01	-3.76e-01	8.82e-02	-4.85e-02	-0.998	5.45e-03	79
1.00	2.58e+00	5.72e-01	-4.25e-01	9.13e-02	-5.22e-02	-0.999	3.40e-03	75
1.50	3.16e+00	8.18e-01	-5.22e-01	1.29e-01	-1.05e-01	-0.999	1.28e-03	51
2.00	2.49e+00	8.31e-01	-4.17e-01	1.31e-01	-1.08e-01	-0.999	1.06e-02	47

C89V h G=5,6,7 may1696c Magnitude dependence

T(s)	am	sigma-am	sm	sigma-sm	cas	ras	Qm	N
pk vl	3.38e-01	4.55e-01	-4.94e-02	7.19e-02	-3.27e-02	-0.999	2.36e-02	59

C89V z G=5,6,7 may1696c Magnitude dependence

T(s)	am	sigma-am	sm	sigma-sm	cas	ras	Qm	N
pk vl	1.47e+00	4.30e-01	-2.32e-01	6.91e-02	-2.97e-02	-0.998	1.30e-01	88

C90/94 h G=0,2 may2196b Magnitude dependence

Table 12. Correction factors for each predictive relation and period, determined from data at distance less than or equal to 20 km.

BJF94 h G=0,1,2 may2196c<=20

T(s)	bijk	sigma-b	sigma-p	eijk	sigma-e	Q	N
0.00	-0.115	0.044	0.165	0.793	0.144	7.87e-01	14
0.05	-	-	-	-	-	-	0
0.10	-0.059	0.054	0.188	0.984	0.192	3.92e-01	12
0.15	-0.166	0.064	0.223	1.200	0.235	9.95e-02	12
0.20	-0.171	0.072	0.248	1.334	0.261	2.99e-02	12
0.30	-0.229	0.084	0.292	1.519	0.297	3.59e-03	12
0.40	-0.195	0.080	0.278	1.391	0.272	1.64e-02	12
0.50	-0.168	0.069	0.239	1.154	0.226	1.42e-01	12
0.75	-0.095	0.068	0.237	1.075	0.210	2.41e-01	12
1.00	-0.050	0.064	0.221	0.959	0.187	4.41e-01	12
1.50	-0.056	0.085	0.281	1.159	0.236	1.40e-01	11
2.00	-0.175	0.100	0.331	1.338	0.272	3.24e-02	11

BJF94 h G=5,6,7 may2196c<=20

T(s)	bijk	sigma-b	sigma-p	eijk	sigma-e	Q	N
0.00	-0.035	0.023	0.169	0.811	0.076	9.72e-01	56
0.05	-	-	-	-	-	-	0
0.10	-0.020	0.025	0.188	0.982	0.092	5.12e-01	56
0.15	-0.043	0.029	0.217	1.169	0.109	2.90e-02	56
0.20	-0.080	0.027	0.204	1.100	0.103	1.17e-01	56
0.30	-0.100	0.025	0.190	0.989	0.093	4.83e-01	56
0.40	-0.112	0.027	0.206	1.029	0.096	3.23e-01	56
0.50	-0.060	0.029	0.214	1.033	0.097	3.05e-01	56
0.75	-0.072	0.034	0.252	1.143	0.107	5.17e-02	56
1.00	-0.079	0.034	0.251	1.087	0.102	1.43e-01	56
1.50	-0.034	0.034	0.255	1.052	0.099	2.43e-01	55
2.00	-0.015	0.036	0.264	1.065	0.102	2.05e-01	53

C89/94 h G=5,6,7 may2196c<=20

T(s)	bijk	sigma-b	sigma-p	eijk	sigma-e	Q	N
0.00	-0.042	0.024	0.174	1.010	0.096	3.95e-01	54
0.05	0.066	0.026	0.187	0.980	0.096	5.16e-01	51
0.10	0.044	0.026	0.190	0.911	0.087	7.80e-01	54
0.15	-0.010	0.031	0.224	1.033	0.098	3.09e-01	54
0.20	-0.045	0.028	0.209	0.964	0.092	5.84e-01	54
0.30	-0.059	0.025	0.187	0.862	0.082	9.04e-01	54
0.40	-0.053	0.026	0.195	0.896	0.085	8.26e-01	54
0.50	-0.008	0.027	0.200	0.923	0.088	7.40e-01	54
0.75	-0.034	0.035	0.256	1.181	0.113	2.38e-02	54
1.00	-0.060	0.034	0.248	1.142	0.109	5.47e-02	54
1.50	-0.053	0.036	0.228	1.050	0.116	2.65e-01	40
2.00	-0.025	0.037	0.234	1.079	0.119	1.90e-01	40

C89 z G=5,6,7 may2196c<=20

T(s)	bijk	sigma-b	sigma-p	eijk	sigma-e	Q	N
0.00	-0.026	0.034	0.245	0.992	0.097	4.66e-01	51
0.05	0.200	0.040	0.282	1.047	0.105	2.63e-01	49
0.10	-0.185	0.049	0.352	1.306	0.128	9.35e-04	51
0.15	-0.021	0.039	0.276	1.027	0.101	3.33e-01	51
0.20	-0.017	0.037	0.264	0.981	0.096	5.12e-01	51
0.30	0.090	0.039	0.279	1.038	0.102	2.93e-01	51
0.40	-0.054	0.043	0.309	1.147	0.112	5.38e-02	51
0.50	-0.126	0.041	0.296	1.098	0.108	1.27e-01	51
0.75	-0.237	0.040	0.285	1.057	0.105	2.32e-01	50
1.00	-0.206	0.041	0.287	1.064	0.106	2.13e-01	49
1.50	-0.261	0.057	0.343	1.273	0.148	7.99e-03	36
2.00	-0.239	0.052	0.309	1.148	0.133	7.84e-02	36

C89V h G=5,6,7 may1696e<=20

T(s)	bijk	sigma-b	sigma-p	eijk	sigma-e	Q	N
pk vl	0.006	0.030	0.187	1.091	0.120	1.62e-01	40

C89V z G=5,6,7 may1696e<=20

T(s)	bijk	sigma-b	sigma-p	eijk	sigma-e	Q	N
pk vl	0.002	0.034	0.243	1.076	0.106	1.77e-01	51

C90/94 h G=0,2 may2196c<=20

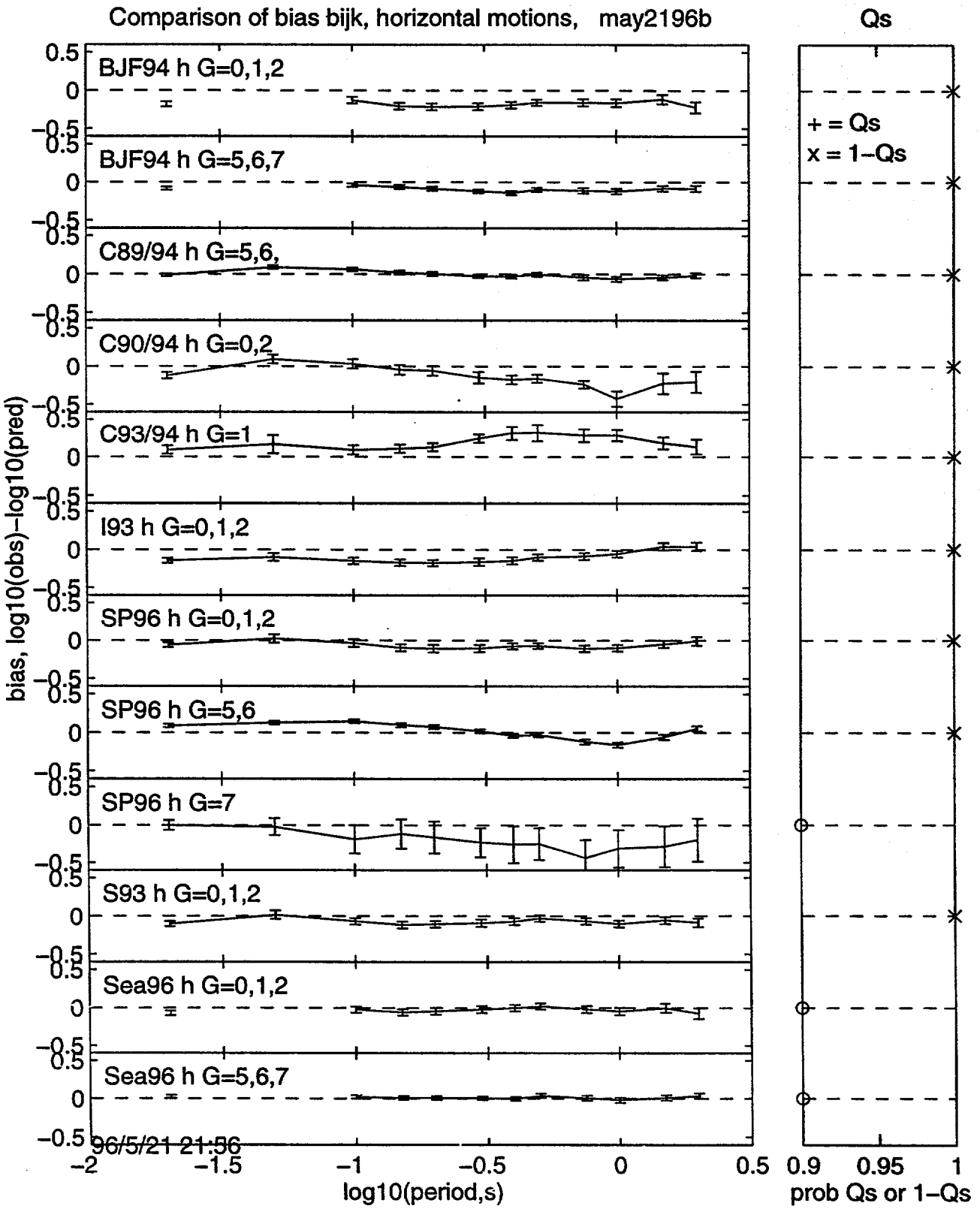
Comparison of bias bijk, horizontal motions, may2196b
Qs
BJF94 h G=0,1,2
BJF94 h G=5,6,7
C89/94 h G=5,6,
C90/94 h G=0,2
C93/94 h G=1
I93 h G=0,1,2
SP96 h G=0,1,2
SP96 h G=5,6
SP96 h G=7
S93 h G=0,1,2
Sea96 h G=0,1,2
Sea96 h G=5,6,7
+ = Qs
x = 1−Qs
bias, log10(obs)−log10(pred)
log10(period,s)
prob Qs or 1−Qs
96/5/21 21:56

16 a

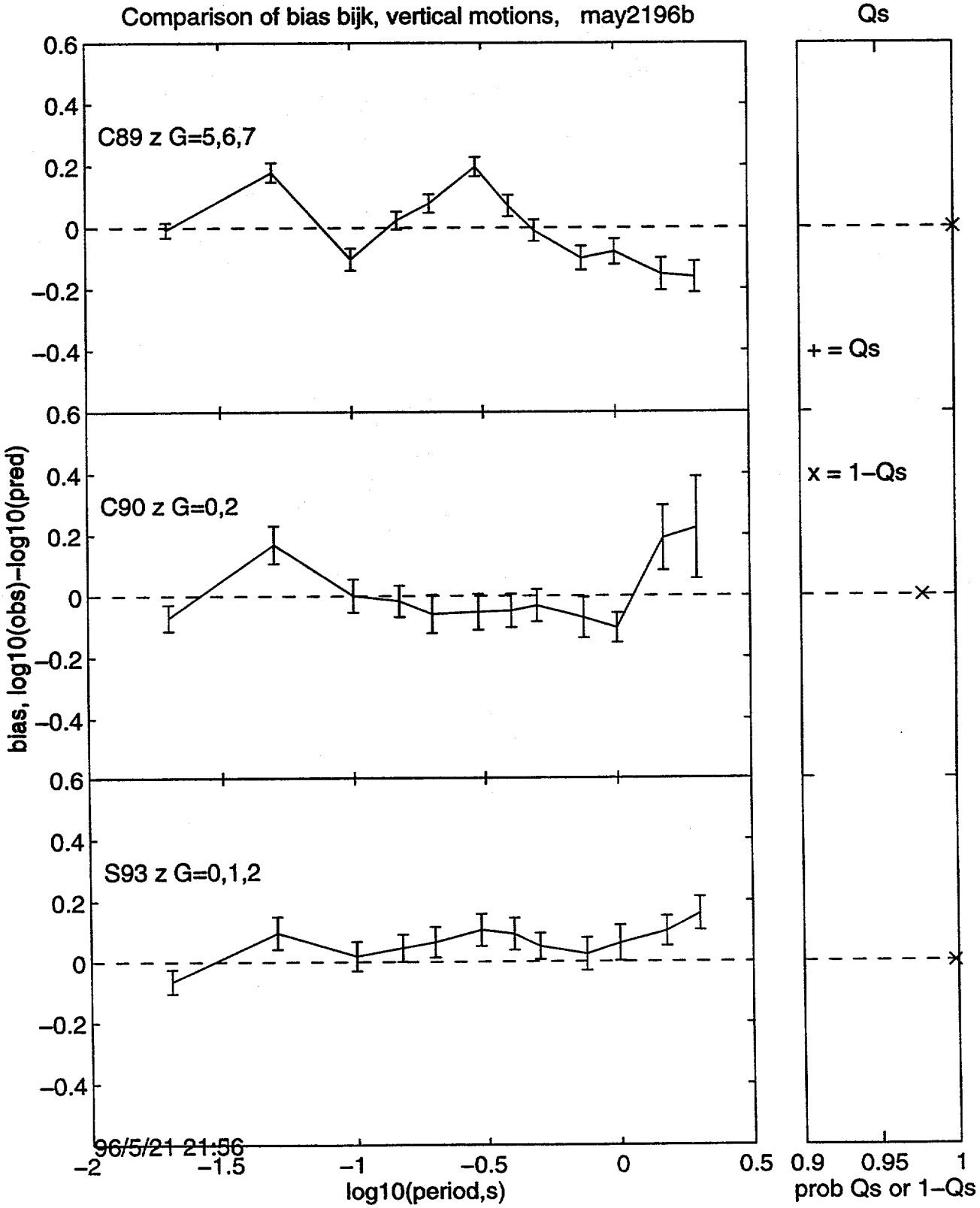
Comparison of bias bijk, vertical motions, may2196b
Qs
C89 z G=5,6,7
C90 z G=0,2
S93 z G=0,1,2
+ = Qs
x = 1−Qs
bias, log10(obs)−log10(pred)
log10(period,s)
prob Qs or 1−Qs
96/5/21 21:56
0.6
0.4
0.2
0
−0.2
−0.4
−2
−1.5
−1
−0.5
0
0.5
0.9
0.95
1

16b

Comparison of dispersion correction eijk, horizontal motions, may2196b Qs

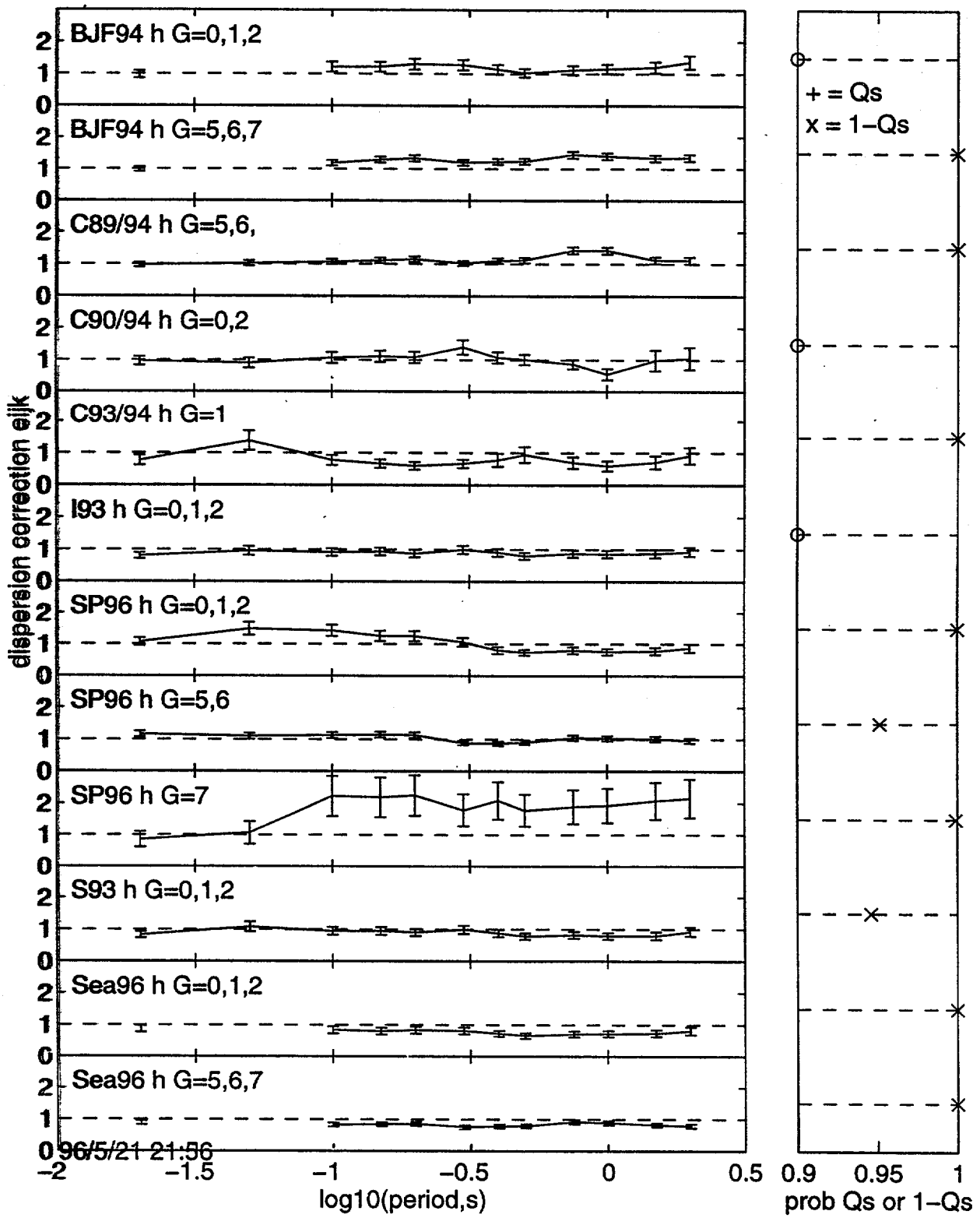

16 c

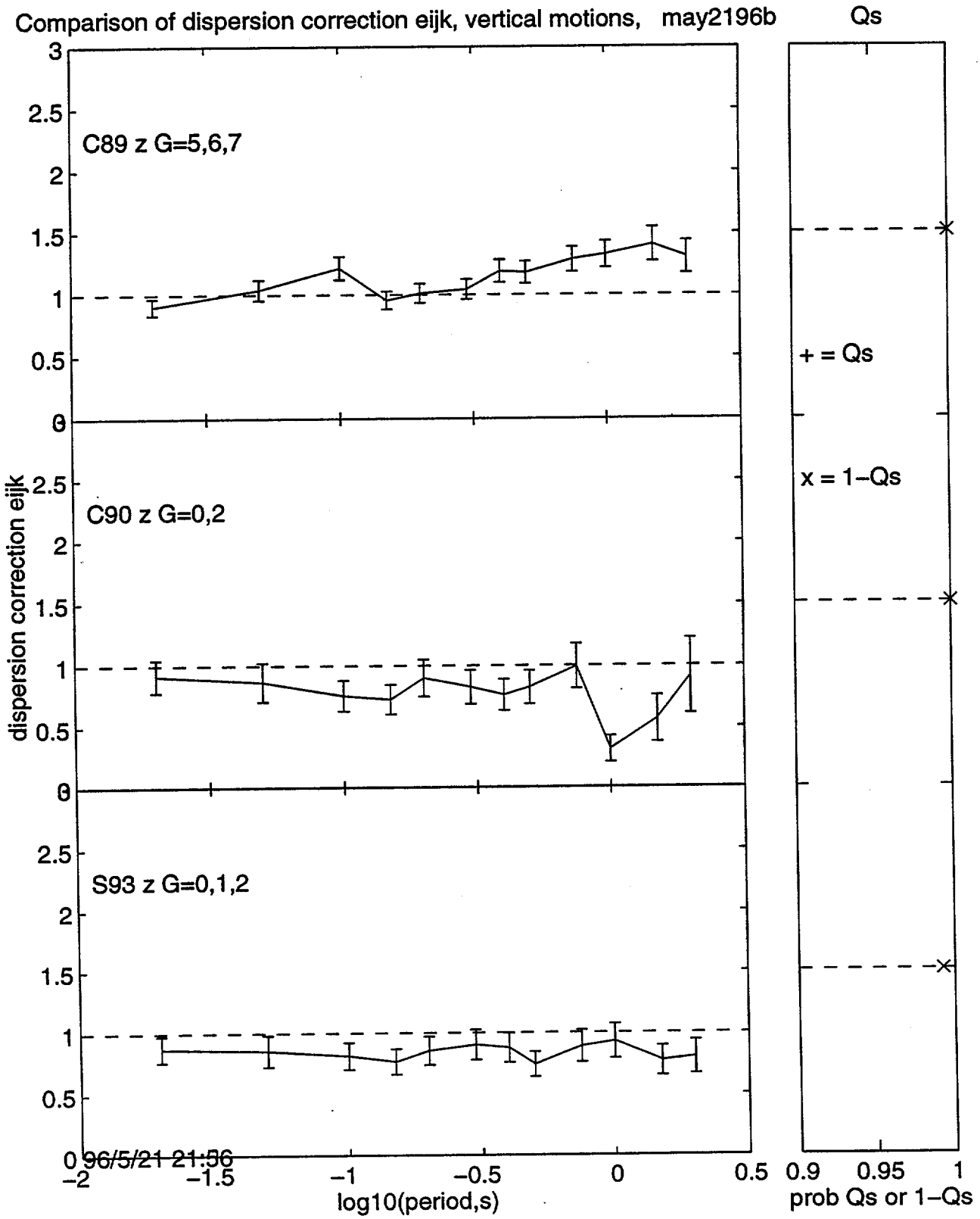
Comparison of dispersion correction eijk, vertical motions, may2196b
Qs
C89 z G=5,6,7
C90 z G=0,2
S93 z G=0,1,2
+ = Qs
x = 1−Qs
dispersion correction eijk
log10(period,s)
prob Qs or 1−Qs
96/5/21 21:56

16 d

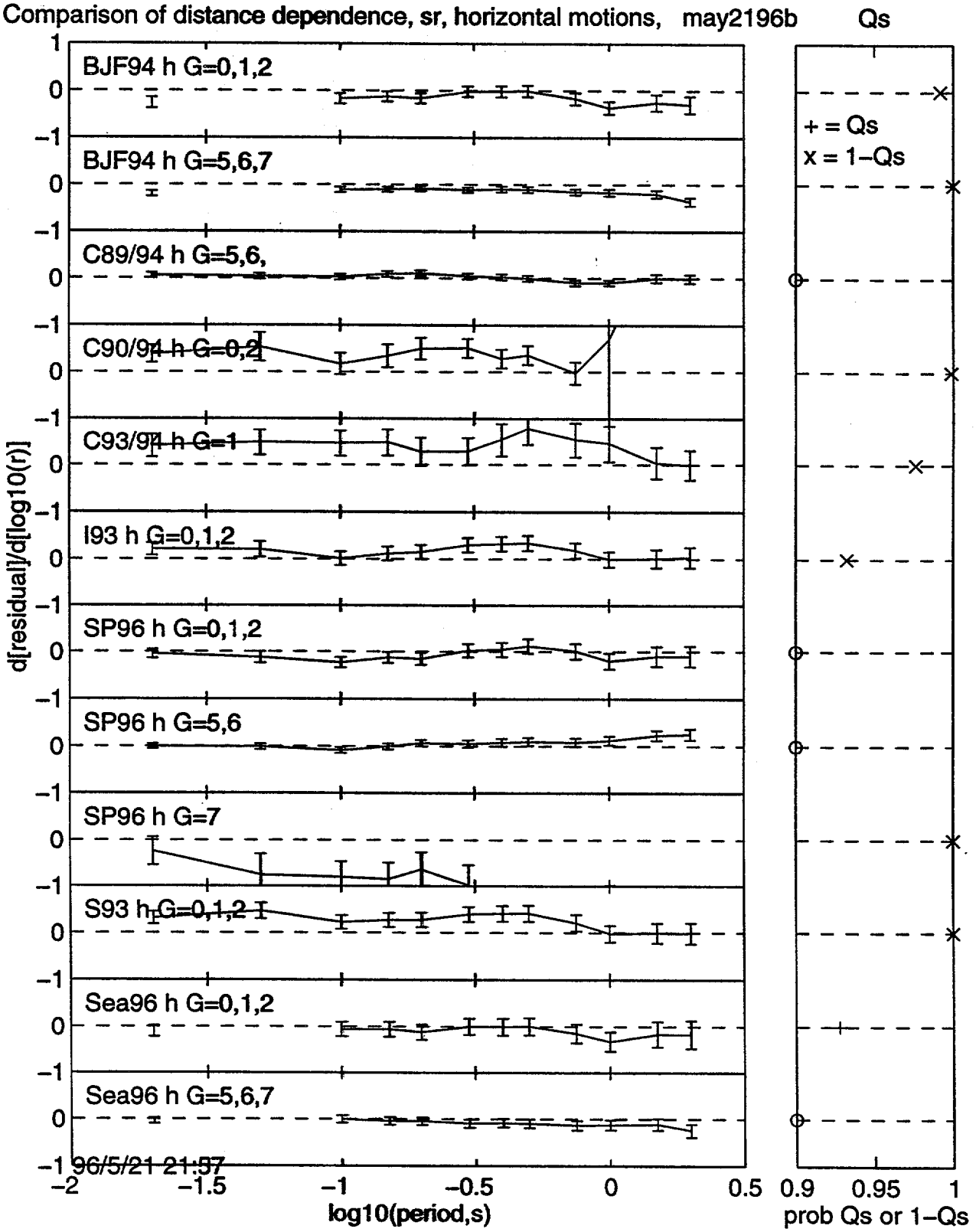
Comparison of distance dependence, sr, horizontal motions, may2196b
Qs
BJF94 h G=0,1,2
BJF94 h G=5,6,7
C89/94 h G=5,6,
C90/94 h G=0,2
C93/94 h G=1
I93 h G=0,1,2
SP96 h G=0,1,2
SP96 h G=5,6
SP96 h G=7
S93 h G=0,1,2
Sea96 h G=0,1,2
Sea96 h G=5,6,7
96/5/21 21:57
+ = Qs
x = 1−Qs
d[residual]/d[log10(r)]
log10(period,s)
prob Qs or 1−Qs

16 e

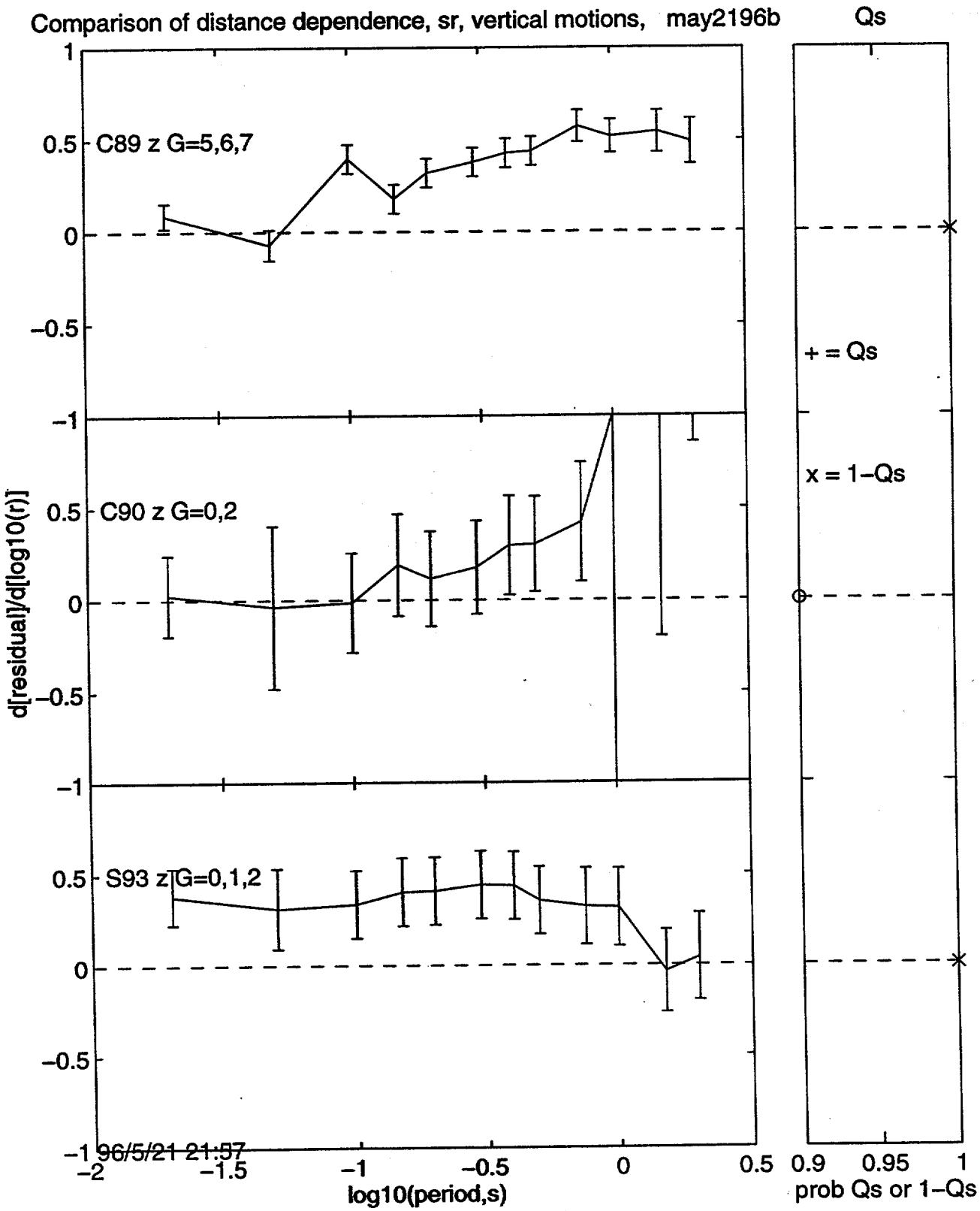
Comparison of distance dependence, sr, vertical motions, may2196b
Qs
C89 z G=5,6,7
C90 z G=0,2
S93 z G=0,1,2
+ = Qs
x = 1−Qs
d[residual]/d[log10(r)]
log10(period,s)
prob Qs or 1−Qs
96/5/21 21:57

16 f

Comparison of magnitude dependence, sm, horizontal motions, may2196b Qs

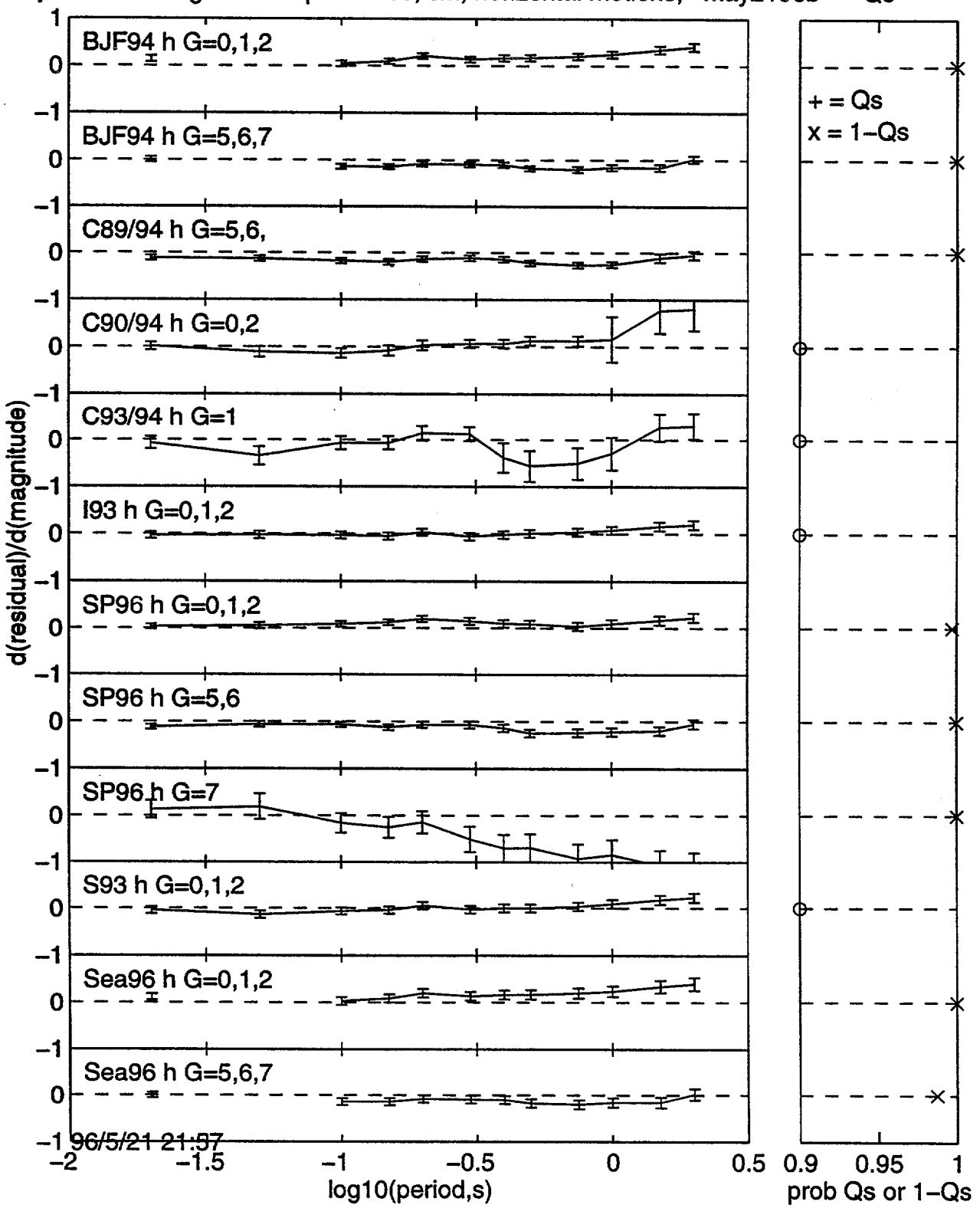

16g

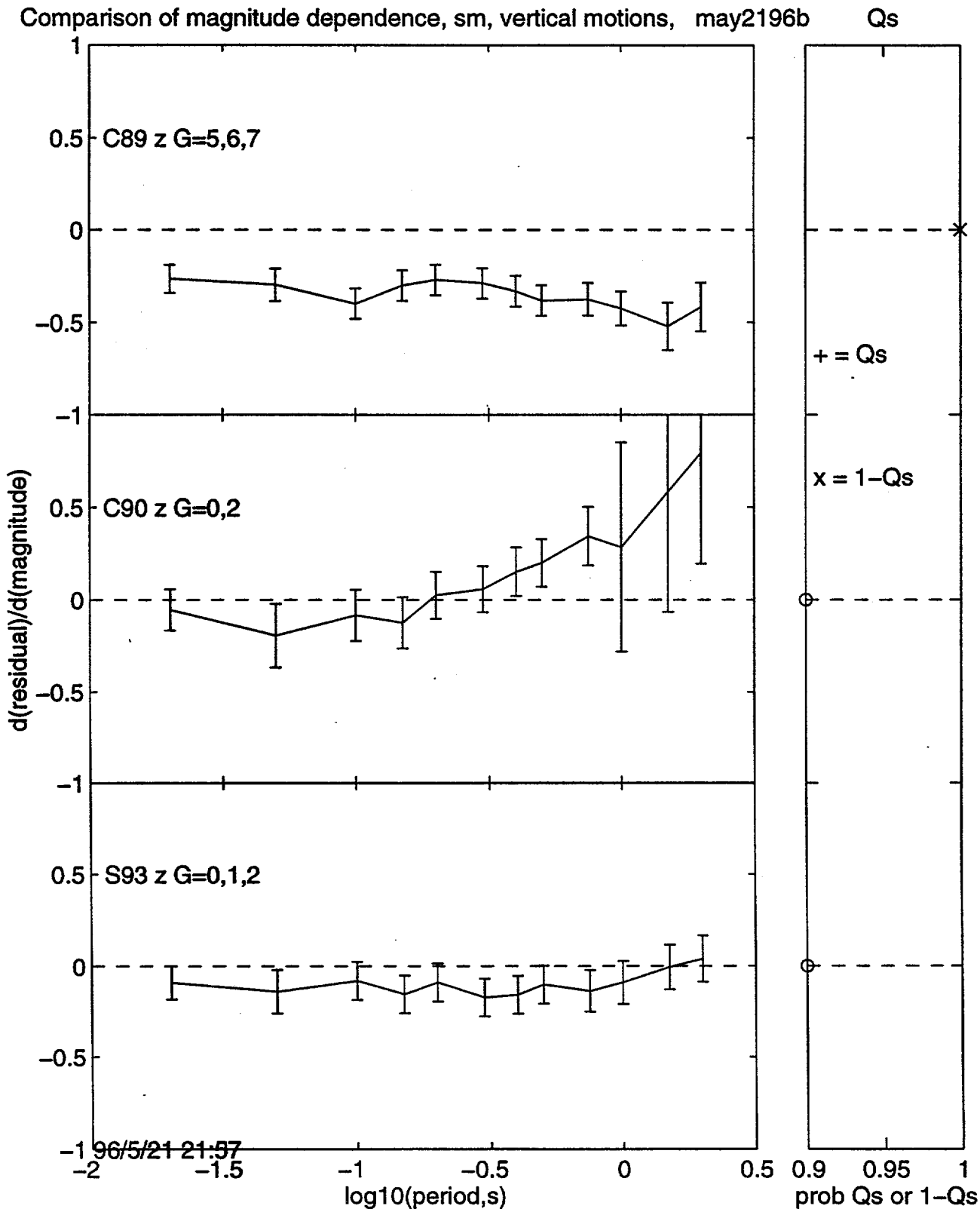
Comparison of magnitude dependence, sm, vertical motions, may2196b
Qs
C89 z G=5,6,7
C90 z G=0,2
S93 z G=0,1,2
+ = Qs
x = 1−Qs
d(residual)/d(magnitude)
log10(period,s)
prob Qs or 1−Qs
96/5/21 21:57

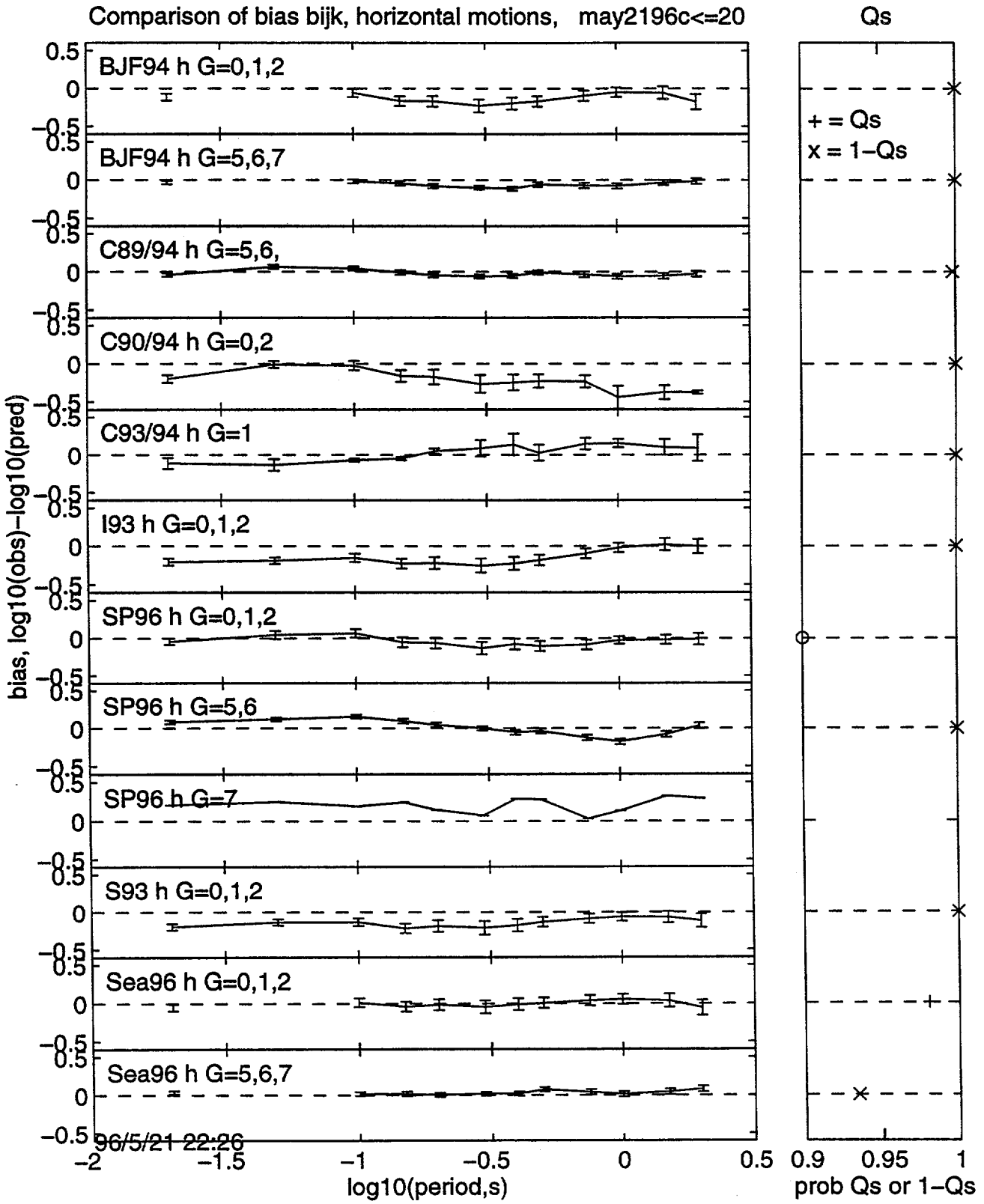
Comparison of bias bijk, horizontal motions, may2196c<=20
Qs
BJF94 h G=0,1,2
BJF94 h G=5,6,7
C89/94 h G=5,6,
C90/94 h G=0,2
C93/94 h G=1
I93 h G=0,1,2
SP96 h G=0,1,2
SP96 h G=5,6
SP96 h G=7
S93 h G=0,1,2
Sea96 h G=0,1,2
Sea96 h G=5,6,7
+ = Qs
x = 1−Qs
bias, log10(obs)−log10(pred)
log10(period,s)
prob Qs or 1−Qs
96/5/21 22:26

19a

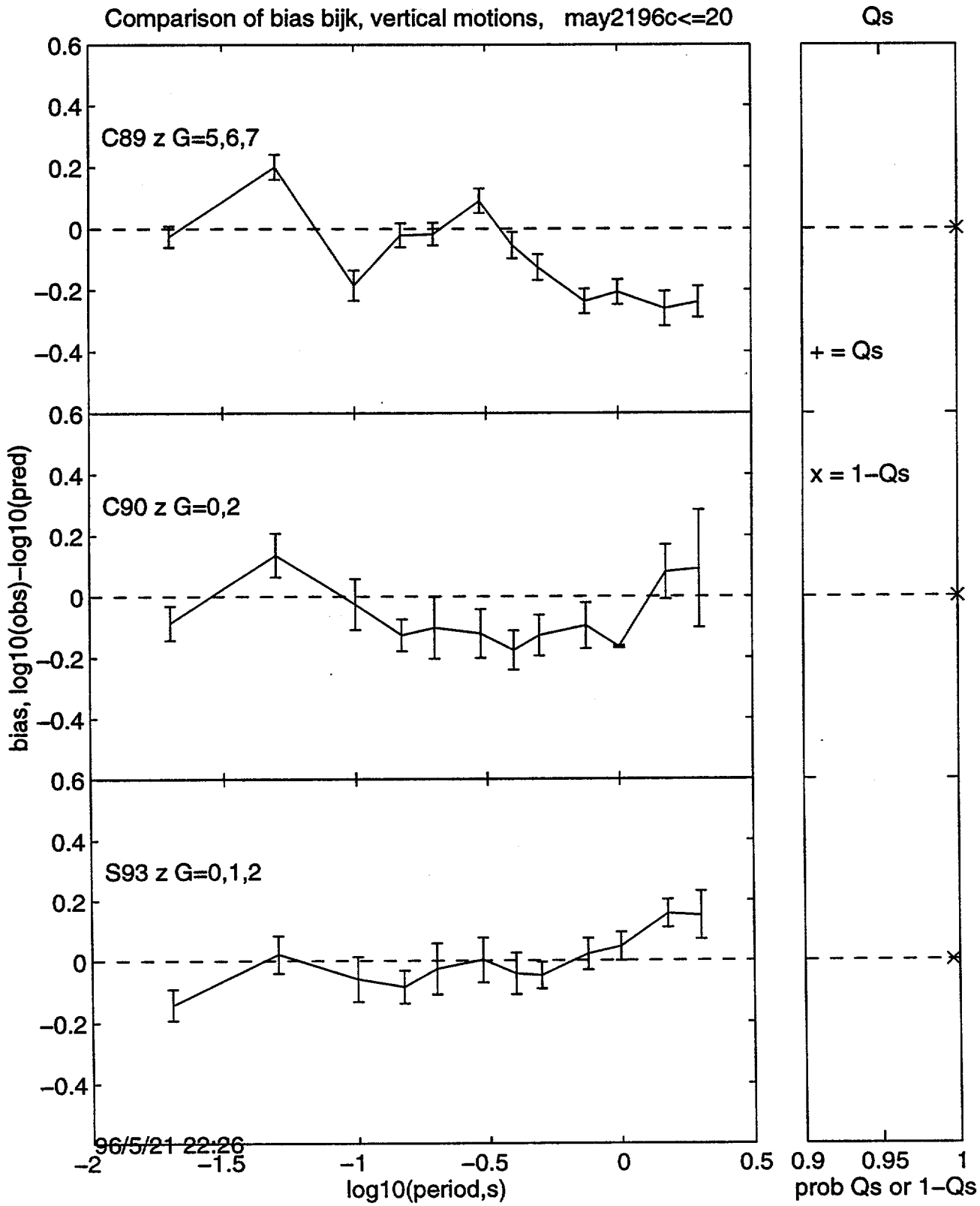
Comparison of bias bijk, vertical motions, may2196c<=20
Qs
C89 z G=5,6,7
C90 z G=0,2
S93 z G=0,1,2
+ = Qs
x = 1−Qs
bias, log10(obs)−log10(pred)
log10(period,s)
prob Qs or 1−Qs
96/5/21 22:26
0.6
0.4
0.2
0
−0.2
−0.4
−2
−1.5
−1
−0.5
0
0.5
0.9
0.95
1

196

Comparison of dispersion correction eijk, horizontal motions, may2196c<=20 Qs

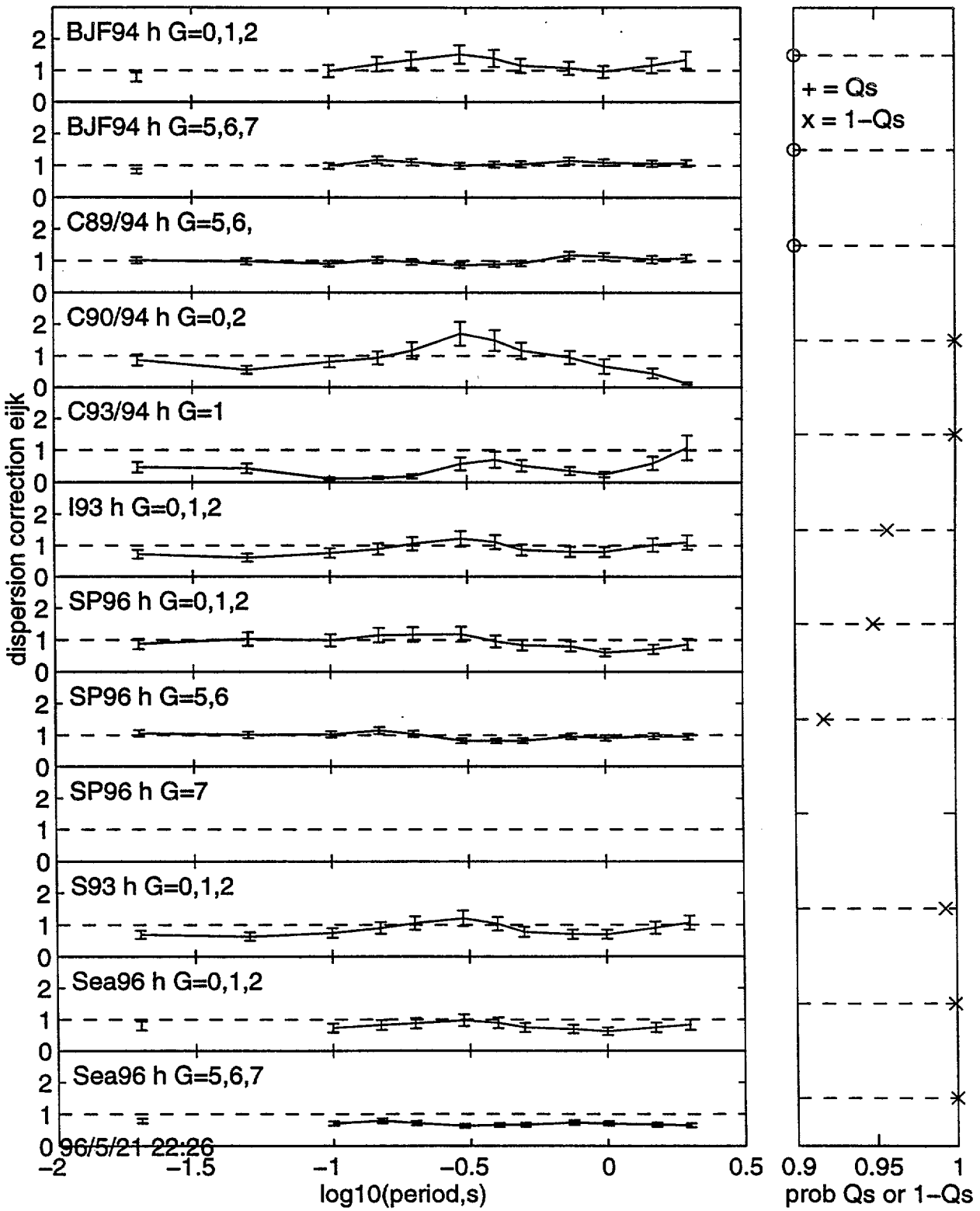

19c

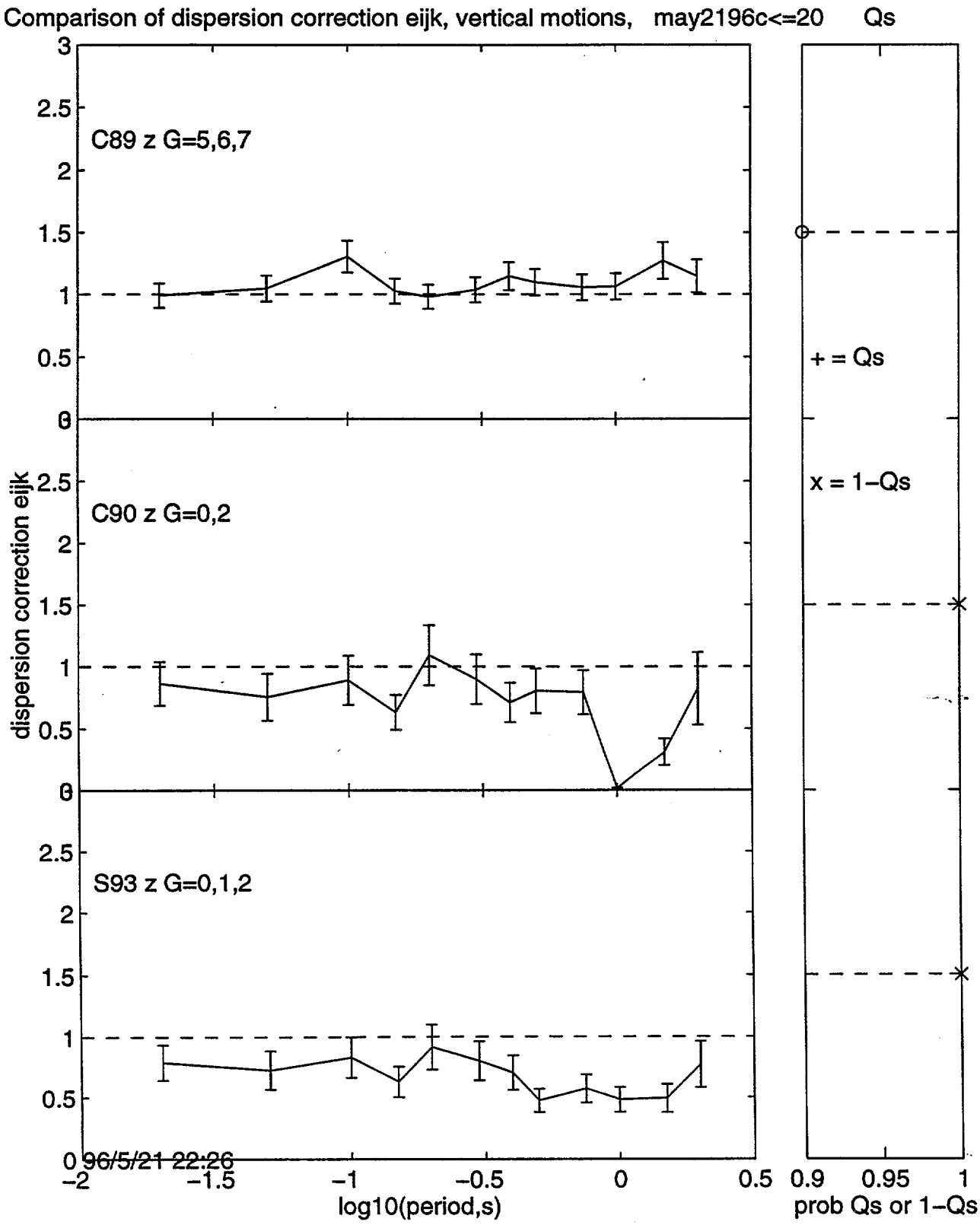
Comparison of dispersion correction eijk, vertical motions, may2196c<=20 Qs
C89 z G=5,6,7
C90 z G=0,2
S93 z G=0,1,2
dispersion correction eijk
log10(period,s)
prob Qs or 1−Qs
+ = Qs
x = 1−Qs
96/5/21 22:26

19d

Comparison of magnitude dependence, sm, horizontal motions, may2196c<=20 Qs

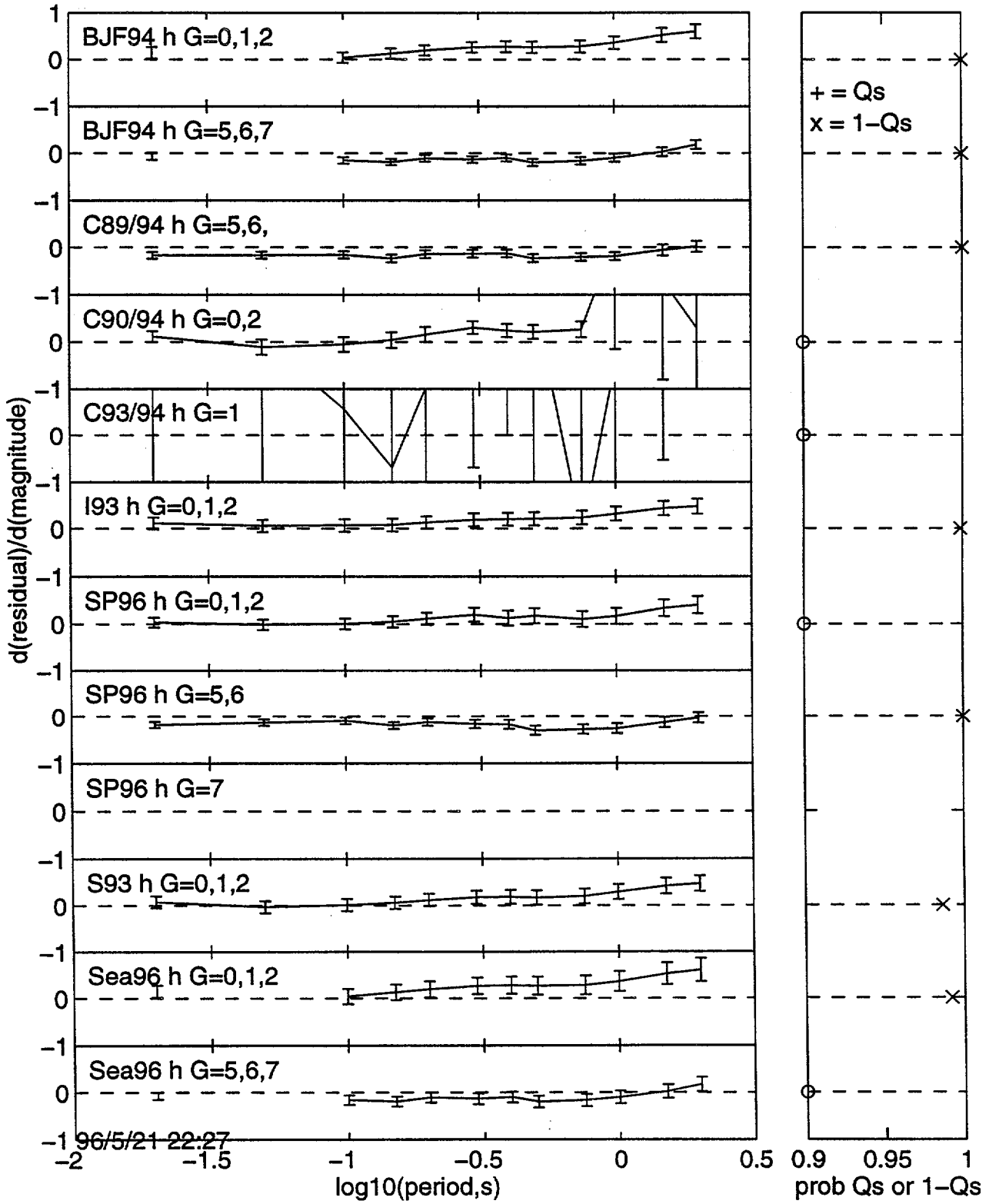

19e

Comparison of magnitude dependence, sm, vertical motions, may2196c<=20 Qs

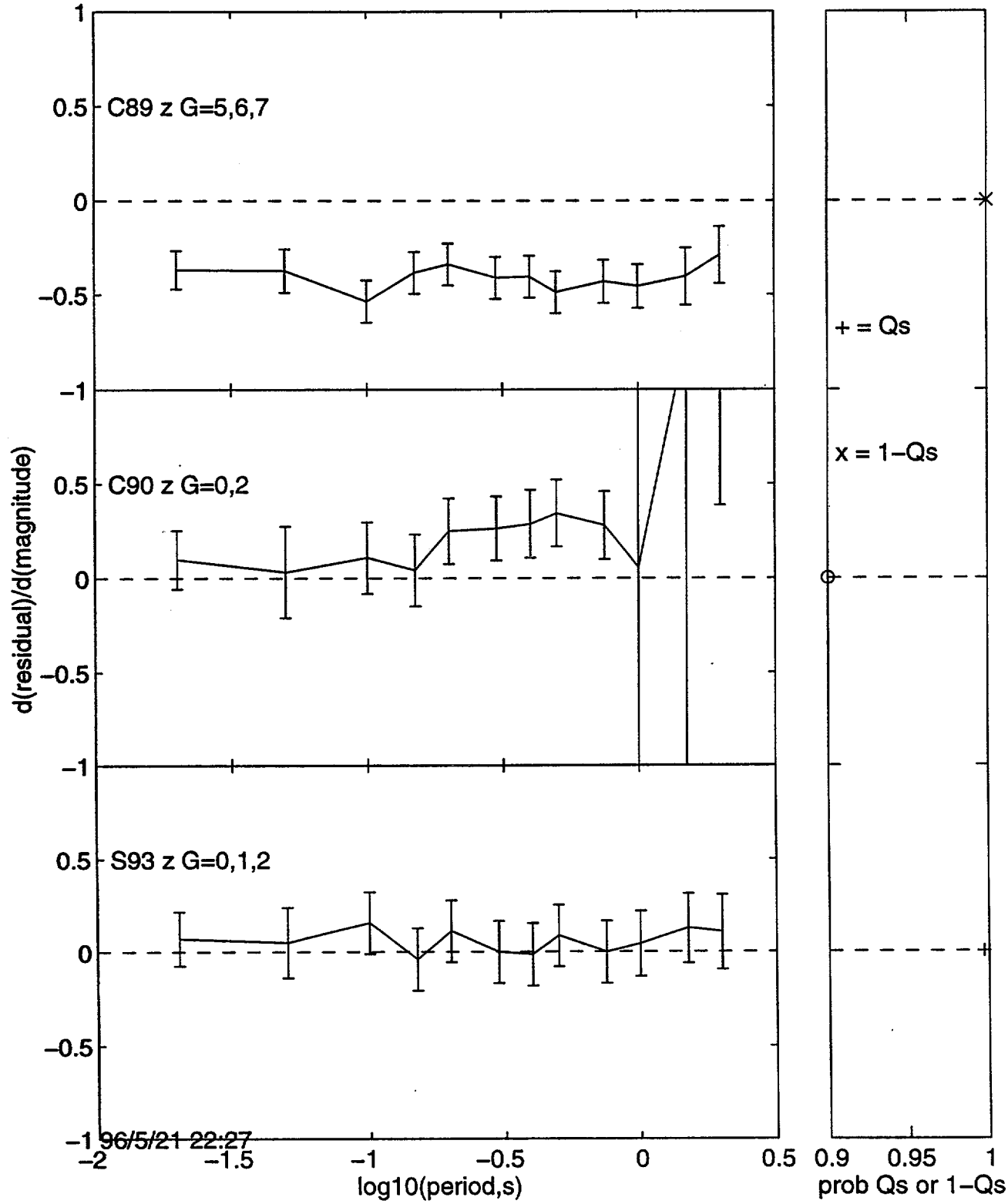

19f

Attenuation Relation for Normal Faulting Events

Norm Abrahamson

Jan 10, 1997

Approach

Compute residuals for normal faulting events (Spudich data set)
- using Abrahamson and Silva (1996) strike-slip model

Use random effects model to estimate the mean residual

Check magnitude and distance dependence of intra-event residuals

Check magnitude dependence of inter-event residuals (event terms)

Compare total standard error with previous model estimates

Data Set:
40 horizontal and 35 vertical recordings

Horizontal: All Sites, Radom Effects

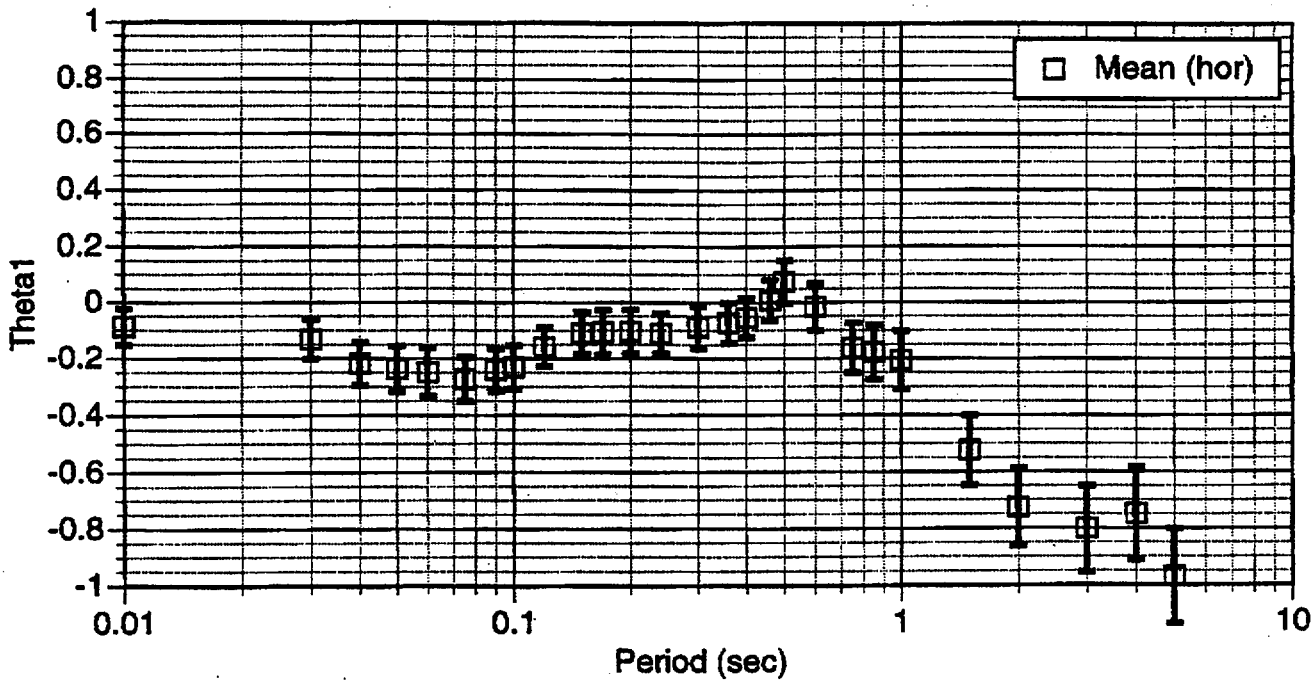

Vertical: All Sites, Random Effects

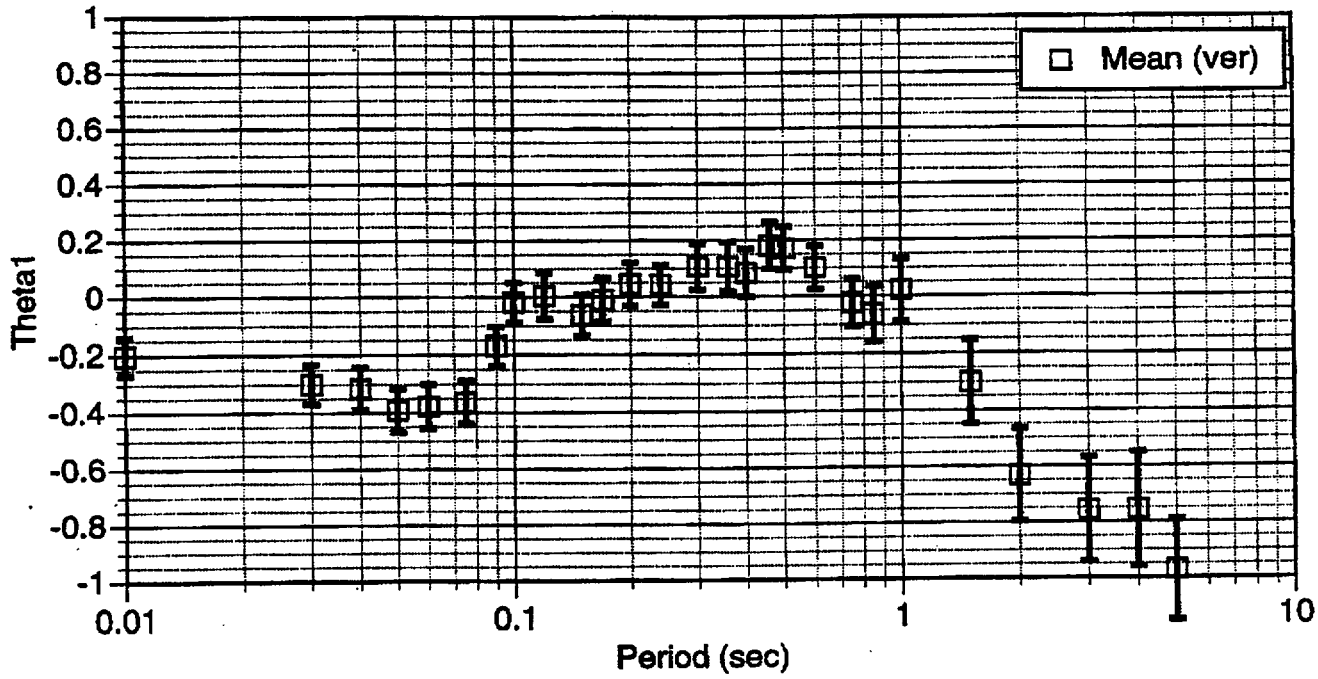

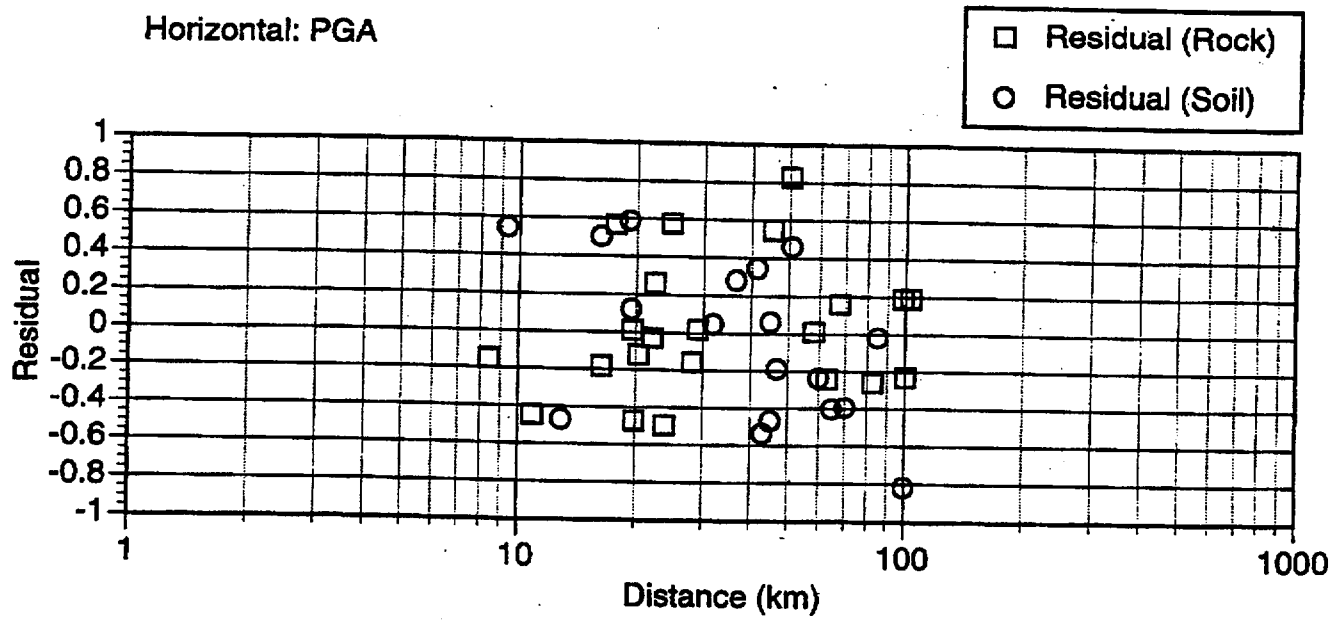
Horizontal: PGA
Residual (Rock)
Residual (Soil)
Residual
1
0.8
0.6
0.4
0.2
0
-0.2
-0.4
-0.6
-0.8
-1
1
10
100
1000
Distance (km)

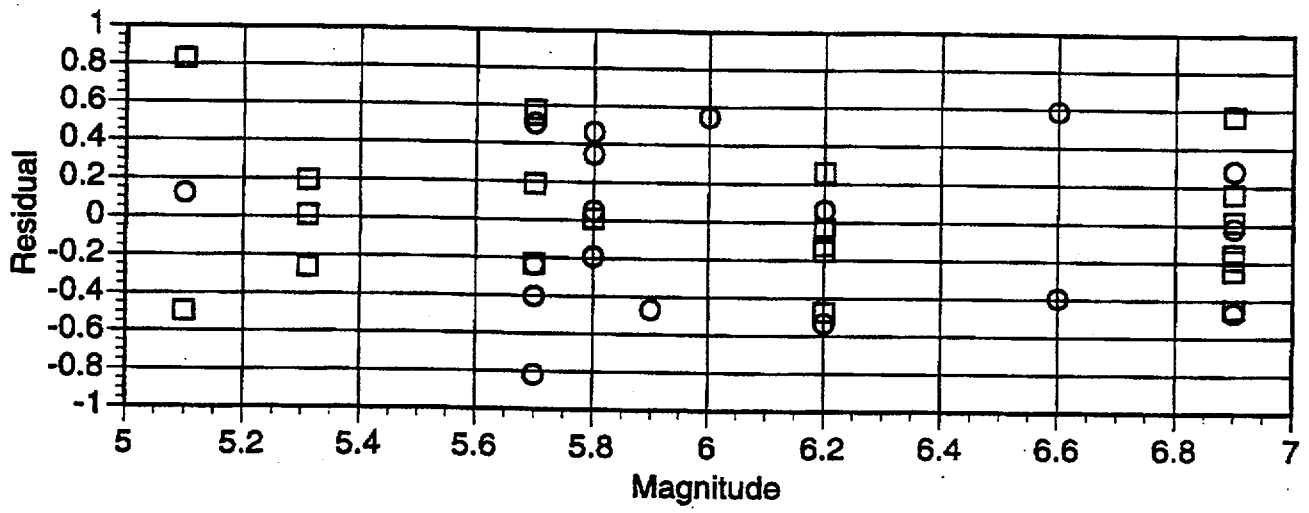
Residual
1
0.8
0.6
0.4
0.2
0
-0.2
-0.4
-0.6
-0.8
-1
5
5.2
5.4
5.6
5.8
6
6.2
6.4
6.6
6.8
7
Magnitude

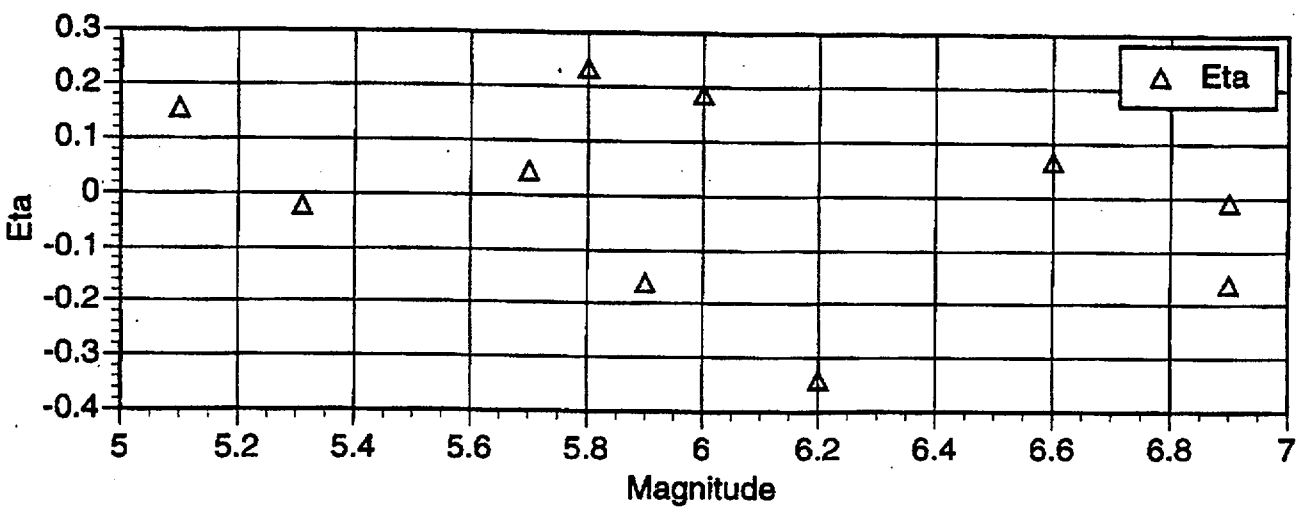
Eta
Eta
0.3
0.2
0.1
0
-0.1
-0.2
-0.3
-0.4
5
5.2
5.4
5.6
5.8
6
6.2
6.4
6.6
6.8
7
Magnitude

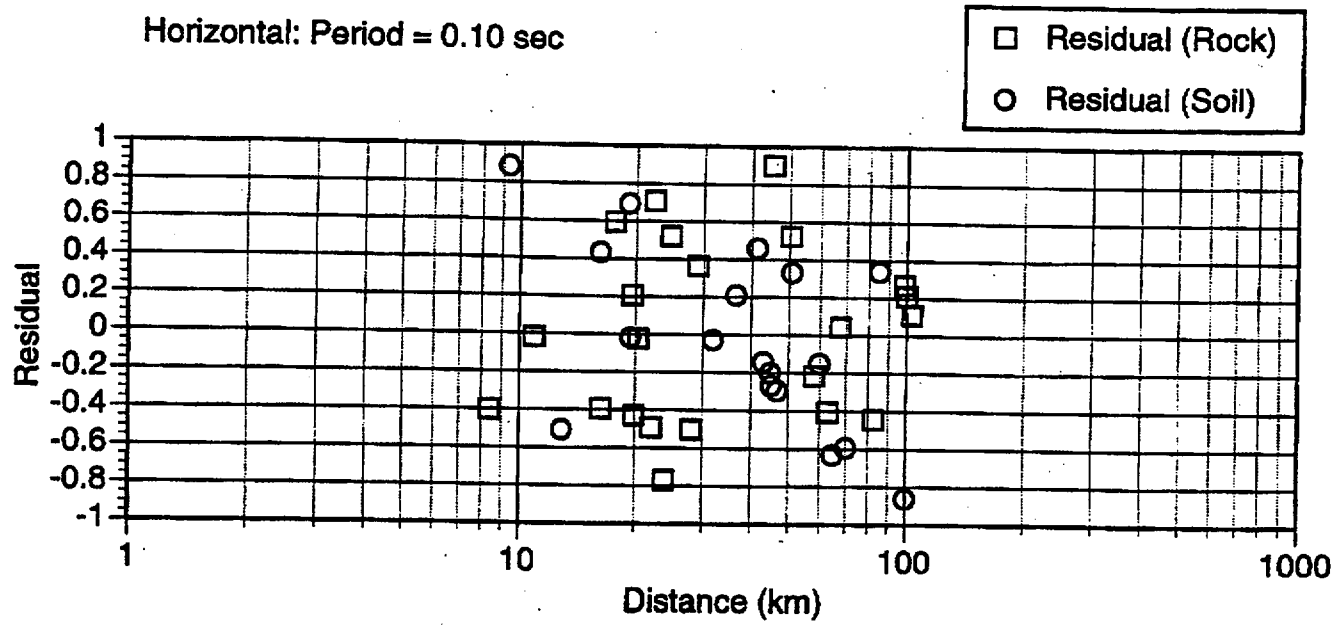
Horizontal: Period = 0.10 sec
Residual (Rock)
Residual (Soil)
Residual
Distance (km)
1
10
100
1000

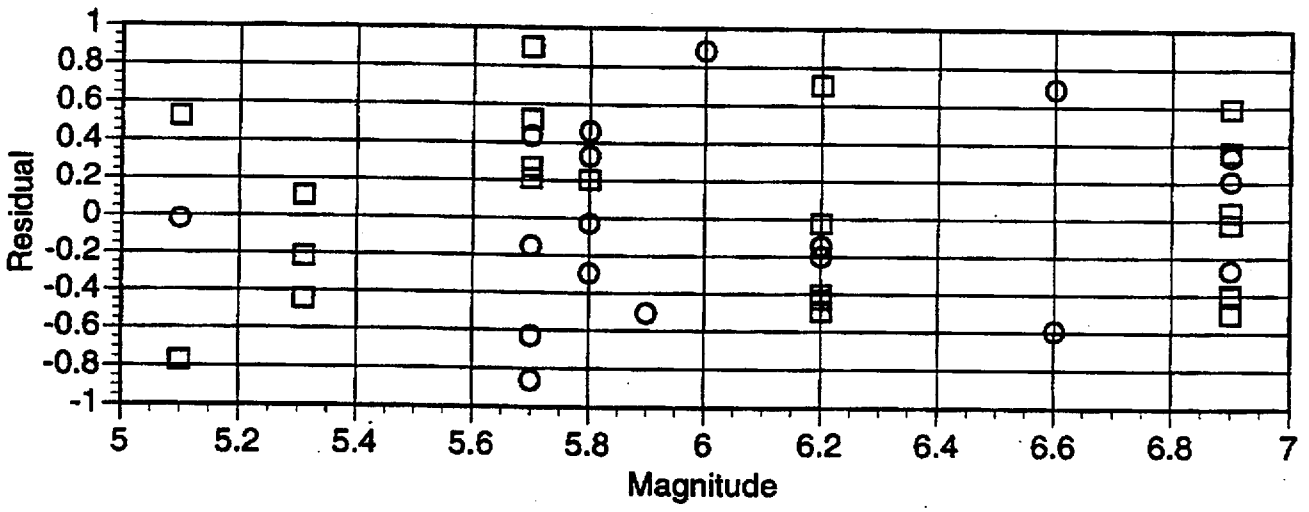
Residual
Magnitude

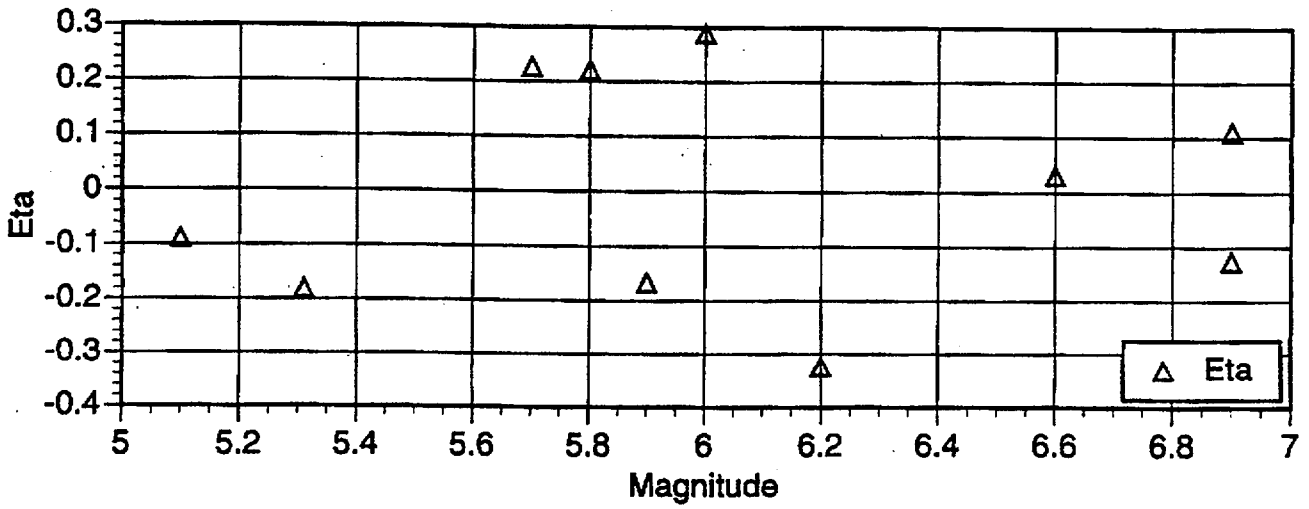
Eta
Eta
Magnitude

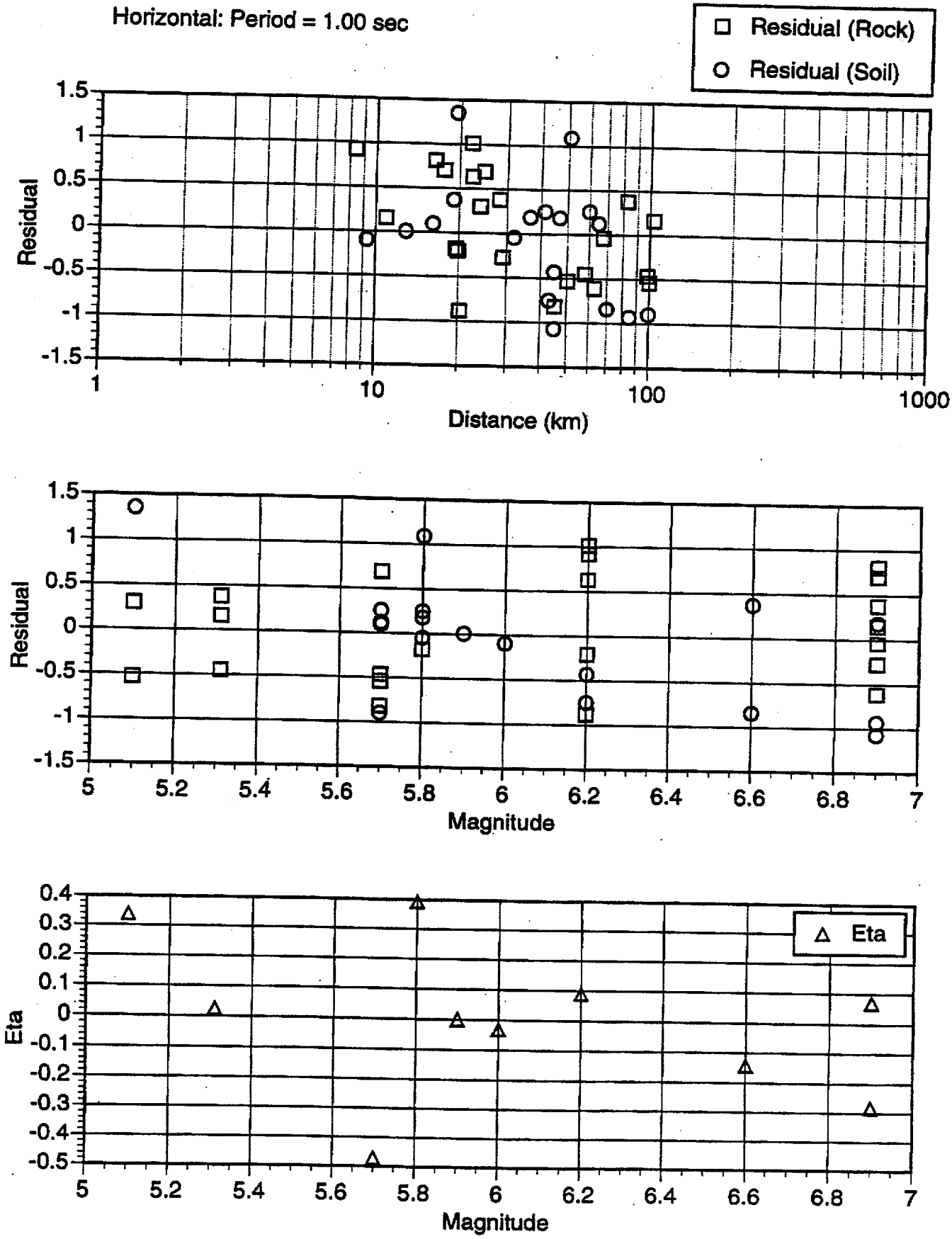
Horizontal: Period = 1.00 sec
Residual (Rock)
Residual (Soil)
Residual
Distance (km)
Residual
Magnitude
Eta
Eta
Magnitude

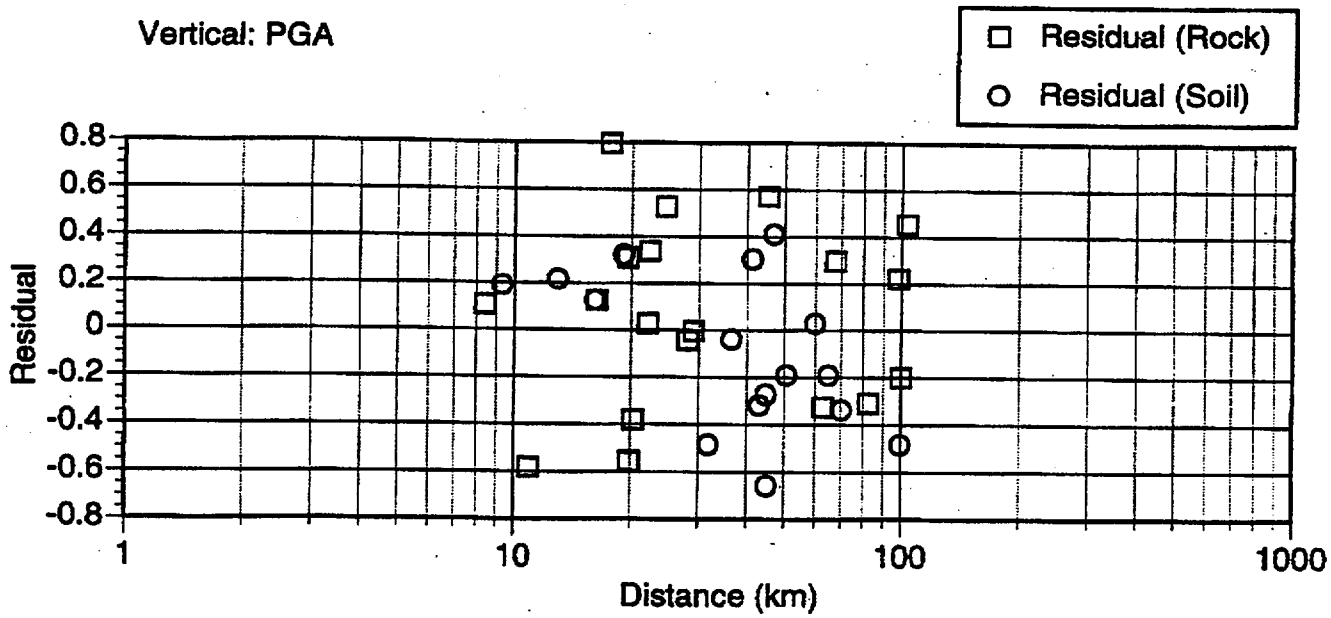
Vertical: PGA
Residual (Rock)
Residual (Soil)
Residual
0.8
0.6
0.4
0.2
0
-0.2
-0.4
-0.6
-0.8
1
10
100
1000
Distance (km)

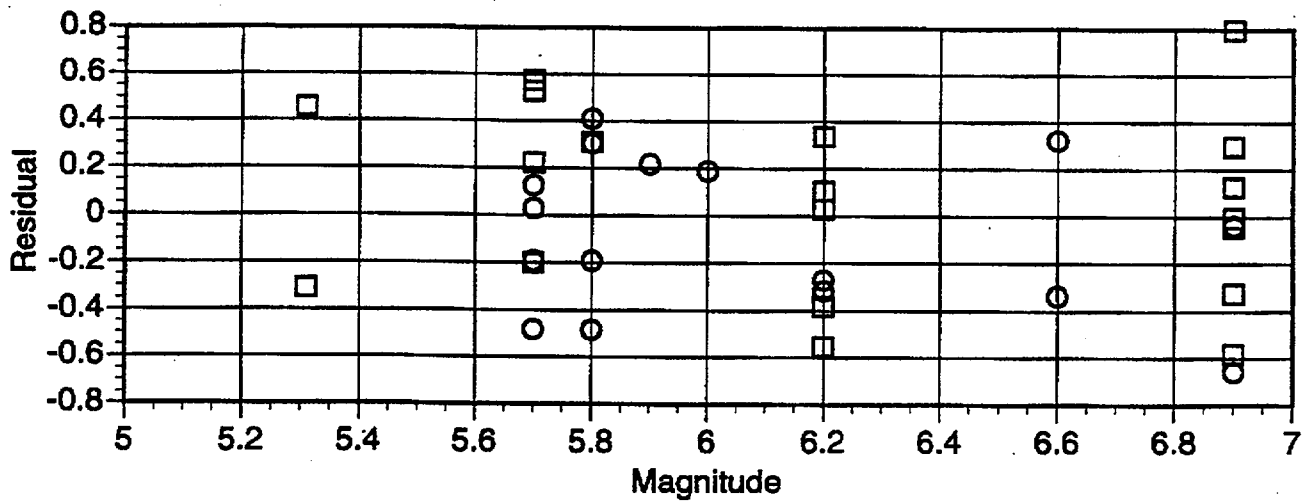
Residual
0.8
0.6
0.4
0.2
0
-0.2
-0.4
-0.6
-0.8
5
5.2
5.4
5.6
5.8
6
6.2
6.4
6.6
6.8
7
Magnitude

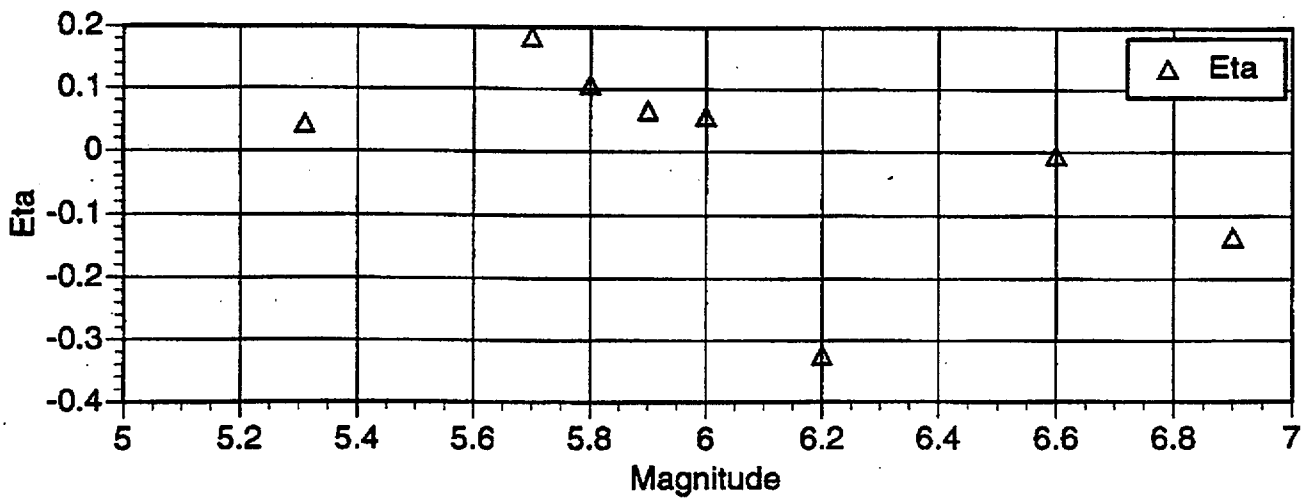
Eta
0.2
0.1
0
-0.1
-0.2
-0.3
-0.4
5
5.2
5.4
5.6
5.8
6
6.2
6.4
6.6
6.8
7
Magnitude

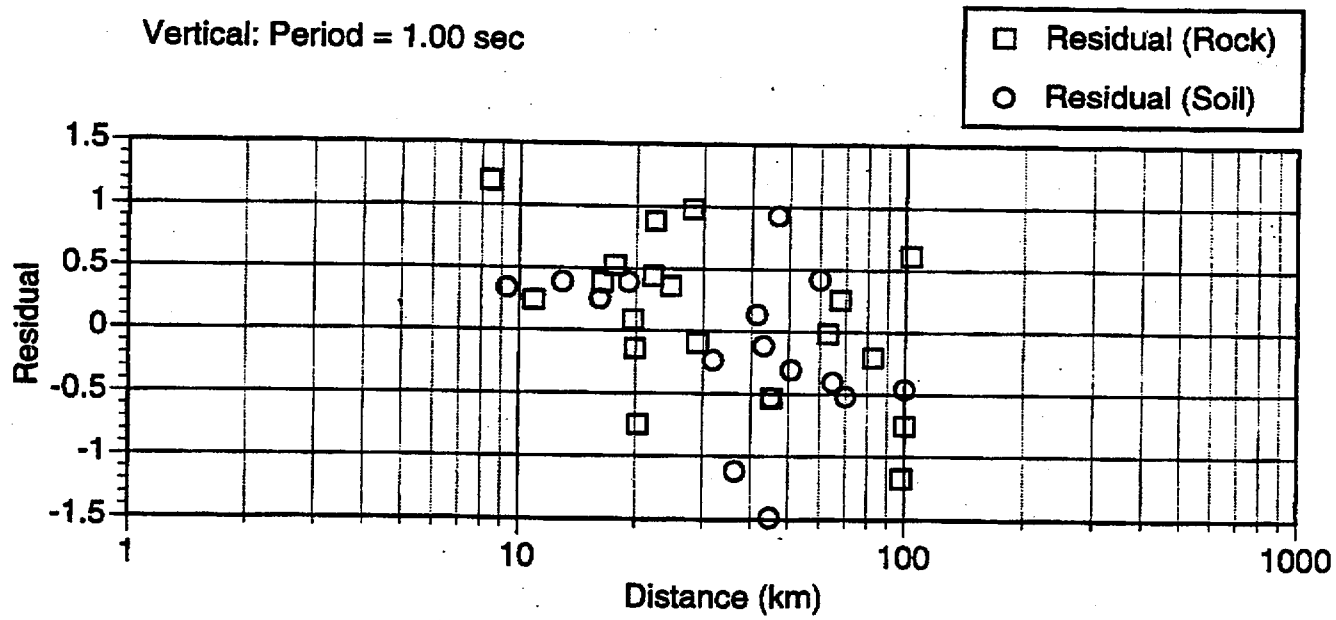
Vertical: Period = 1.00 sec
Residual (Rock)
Residual (Soil)
Residual
1.5
1
0.5
0
-0.5
-1
-1.5
1
10
100
1000
Distance (km)

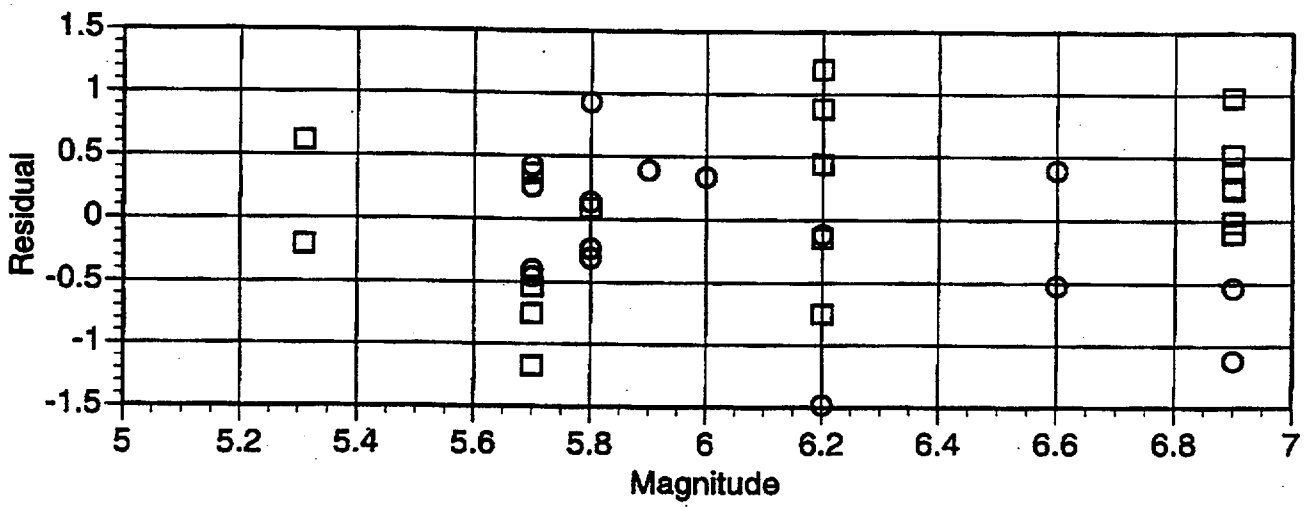
Residual
1.5
1
0.5
0
-0.5
-1
-1.5
5
5.2
5.4
5.6
5.8
6
6.2
6.4
6.6
6.8
7
Magnitude

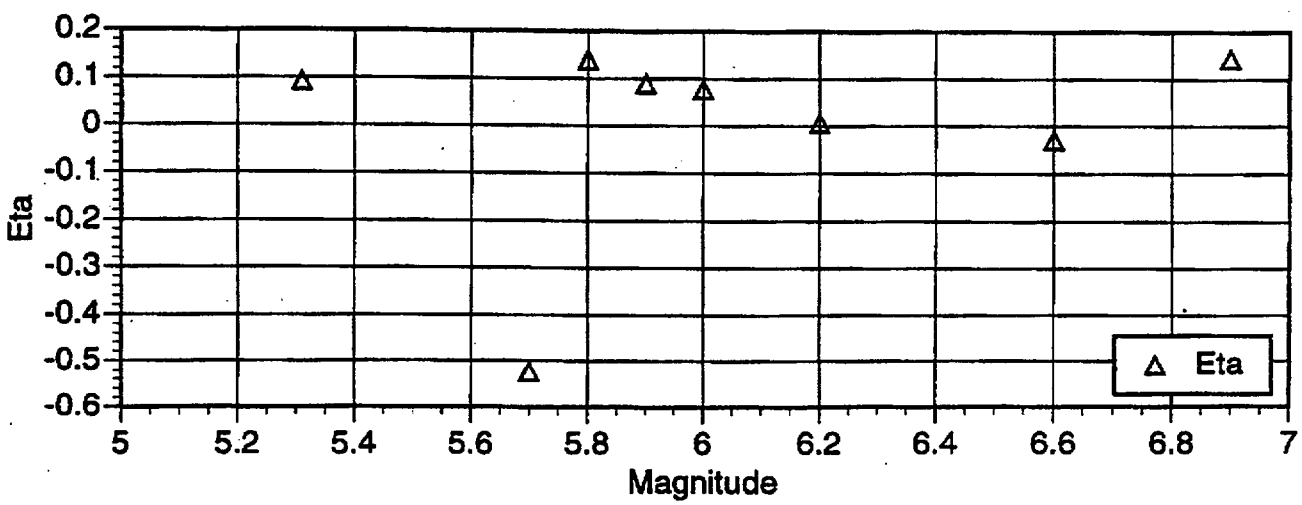
Eta
0.2
0.1
0
-0.1
-0.2
-0.3
-0.4
-0.5
-0.6
Eta
5
5.2
5.4
5.6
5.8
6
6.2
6.4
6.6
6.8
7
Magnitude

Style-of-Faulting factor for Normal Faulting Events
for Abrahamson and Silva (1996)
(in Natural Log units)

	Horiz		Vert	
Freq	Bias	σ_{Bias}	Bias	σ_{Bias}
pga	-0.087	0.065	-0.203	0.065
20.0	-0.236	0.081	-0.392	0.076
10.0	-0.231	0.078	-0.018	0.070
5.0	-0.104	0.078	0.045	0.078
2.0	0.074	0.077	0.171	0.078
1.0	-0.207	0.103	0.022	0.110
0.5	-0.726	0.136	-0.632	0.164

Standard Errors
Ave Horizontal Component

freq	sigma	tau	se sigma	se tau	cov sigma tau	total sigma	se total sigma	A&S 96 total sigma
pga	0.41	0.24	0.05	0.10	-0.00046	0.48	0.06	0.55
20	0.51	0.25	0.07	0.12	-0.00099	0.57	0.08	0.56
10	0.49	0.28	0.06	0.12	-0.00093	0.56	0.08	0.59
5	0.50	0.24	0.06	0.12	-0.00088	0.55	0.07	0.62
2	0.49	0.17	0.06	0.12	-0.00073	0.52	0.06	0.66
1	0.65	0.36	0.08	0.16	-0.00280	0.74	0.14	0.70
0.5	0.86	0.37	0.11	0.21	-0.00760	0.94	0.21	0.74

Vertical Component

freq	sigma	tau	se sigma	se tau	cov sigma tau	total sigma	se total sigma	A&S 96 total sigma
pga	0.38	0.21	0.05	0.10	-0.00035	0.43	0.05	0.55
20	0.45	0.34	0.06	0.13	-0.00080	0.56	0.10	0.56
10	0.41	0.34	0.06	0.13	-0.00059	0.53	0.09	0.59
5	0.45	0.17	0.06	0.12	-0.00057	0.48	0.06	0.62
2	0.46	0.25	0.06	0.12	-0.00071	0.52	0.07	0.66
1	0.65	0.31	0.09	0.17	-0.00270	0.72	0.14	0.70
0.5	0.97	0.39	0.13	0.25	-0.01220	1.05	0.28	0.74

Smoothed Model Coefficients

a_{14}

Freq	Horiz	Vert
PGA	-0.16	-0.25
20	-0.16	-0.25
10	-0.16	-0.13
5	-0.12	0.00
2	-0.07	0.07
1	-0.20	-0.08
2	-0.40	-0.30

Modeling Methods

Group	Method
USC	Specific Barrier Method
PEA	Stochastic Method with ω^{-2} Sub-Events
USGS	Stochastic Slip Functions Method
UNR	Composite Fractal Source Model
WCC	Broadband Green's Function Method
SCubed	Empirical Method from Nuclear Explosion Sources

Table 2.4 Selected scenario earthquakes.

Scenario	Fault	Length (km)	Width (km)	Dip	Rake	M	Dist. (km)
1	Paintbrush Canyon-Bow Ridge	14 to 15	14.2	45 to 70 W	-70 (Normal/LL)	6.31	PC: 4.5 BR: 2.5
2	Solitario Canyon	21 ± 7	14.2	58 ± 8 W	-65 ± 5 (Normal/LL)	6.48	1.0
3	Rock Valley	42	12	90 ± 5	0 to -30 (LL/dip)	6.71	~25
4	Bare Mountain	18 ± 4	14.2	45 to 70 E	-90 (Normal)	6.42	15.5
5	Furnace Creek	90 ± 10	12	90	180 (RL)	7.04	~50
6	Solitario Canyon-Fatigue Wash-Windy Wash[1]	FW: 17 WW: 25	14.2	FW: 80 to 90 WW: -50 to -60	FW: -80 to -90 WW: -70 to -90 (Normal/LL)	~6.6[2]	1.0

[1]Volcanic triggered event with 2/3 displacement on Solitario Canyon, 1/3 on Fatigue Wash and Windy Wash.

[2] Based on an average fault rupture length of 25 km.

YUCCA MOUNTAIN PROJECT

WORKSHOP 2

January 8 - 10, 1997

WALT SILVA

PACIFIC ENGINEERING and ANALYSIS

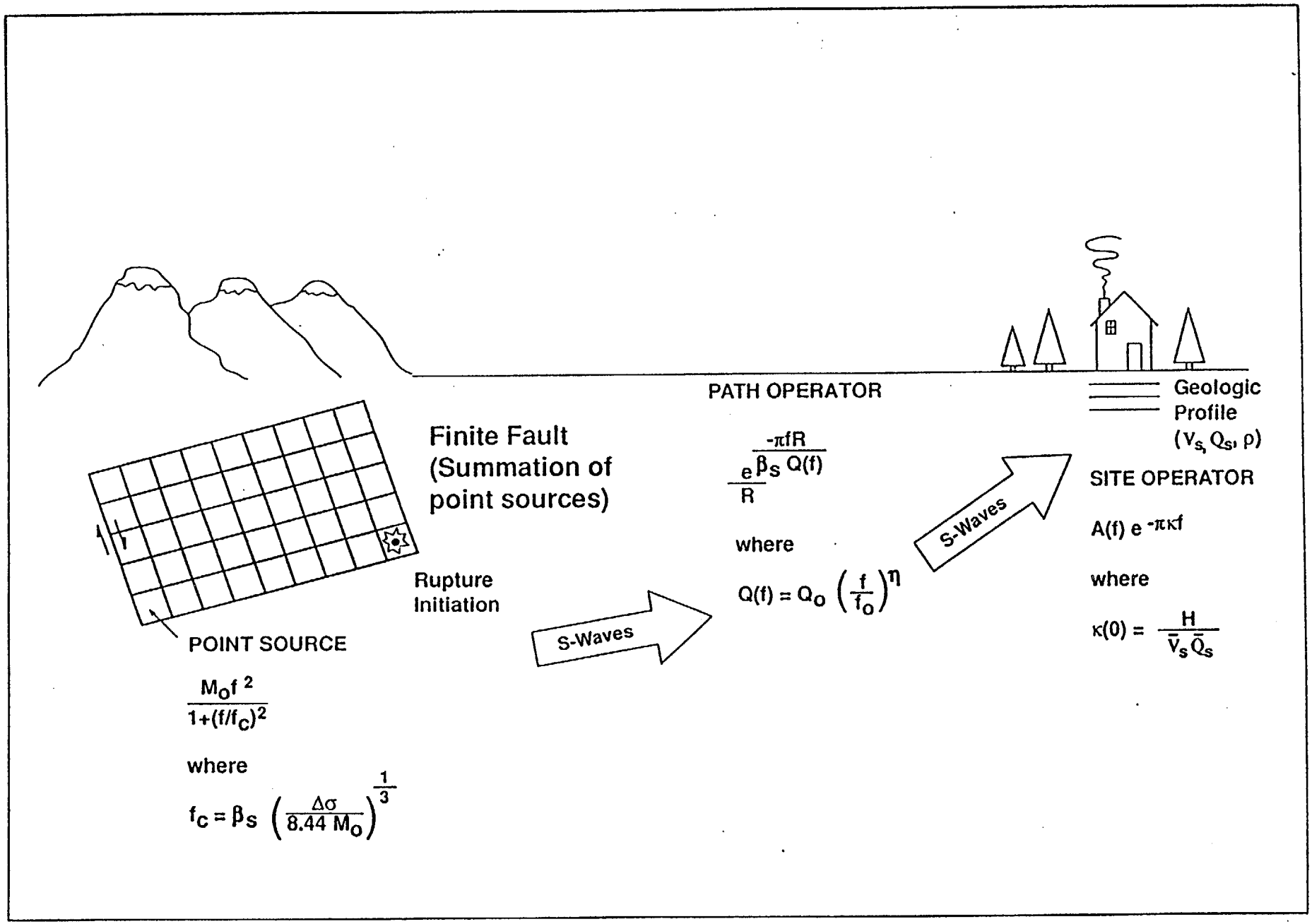

FIGURE 1. SCHEMATIC OF GROUND MOTION MODEL.

POINT SOURCE SIMULATIONS			
M	$\Delta\sigma$ (bars)	Depth (km)	Kappa (sec)
5.0	25	5	0.01
5.5	50	10	0.02
6.0	100	15	0.03
6.5	200		0.04
7.0			
7.5			
8.0			

D(km): 1, 3, 5, 10, 20, 50, 75, 100, 150, 200

$Q(f) = 250\ f^{0.4}$

Crustal Model: Regional plus local near surface

Geometrical Attenuation: $1/R$; $1/\sqrt{R}$, $R > 64$ km

Duration: $1/f_c + 0.05\ R$ ($R \geq 10$ km)

PGA Range: 10.25g - 0.0005g

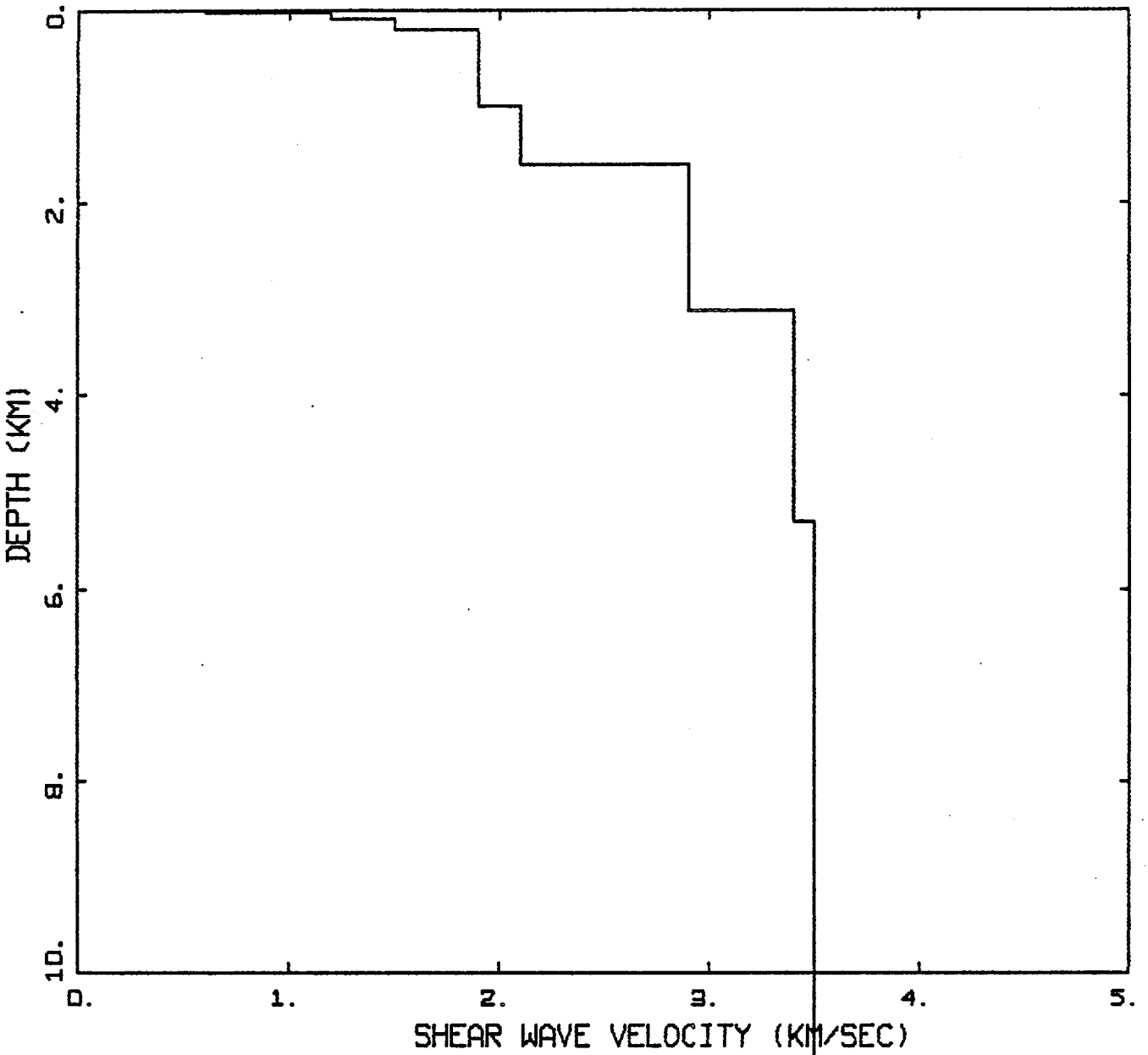

YUCCA MOUNTAIN PROFILE

LEGEND

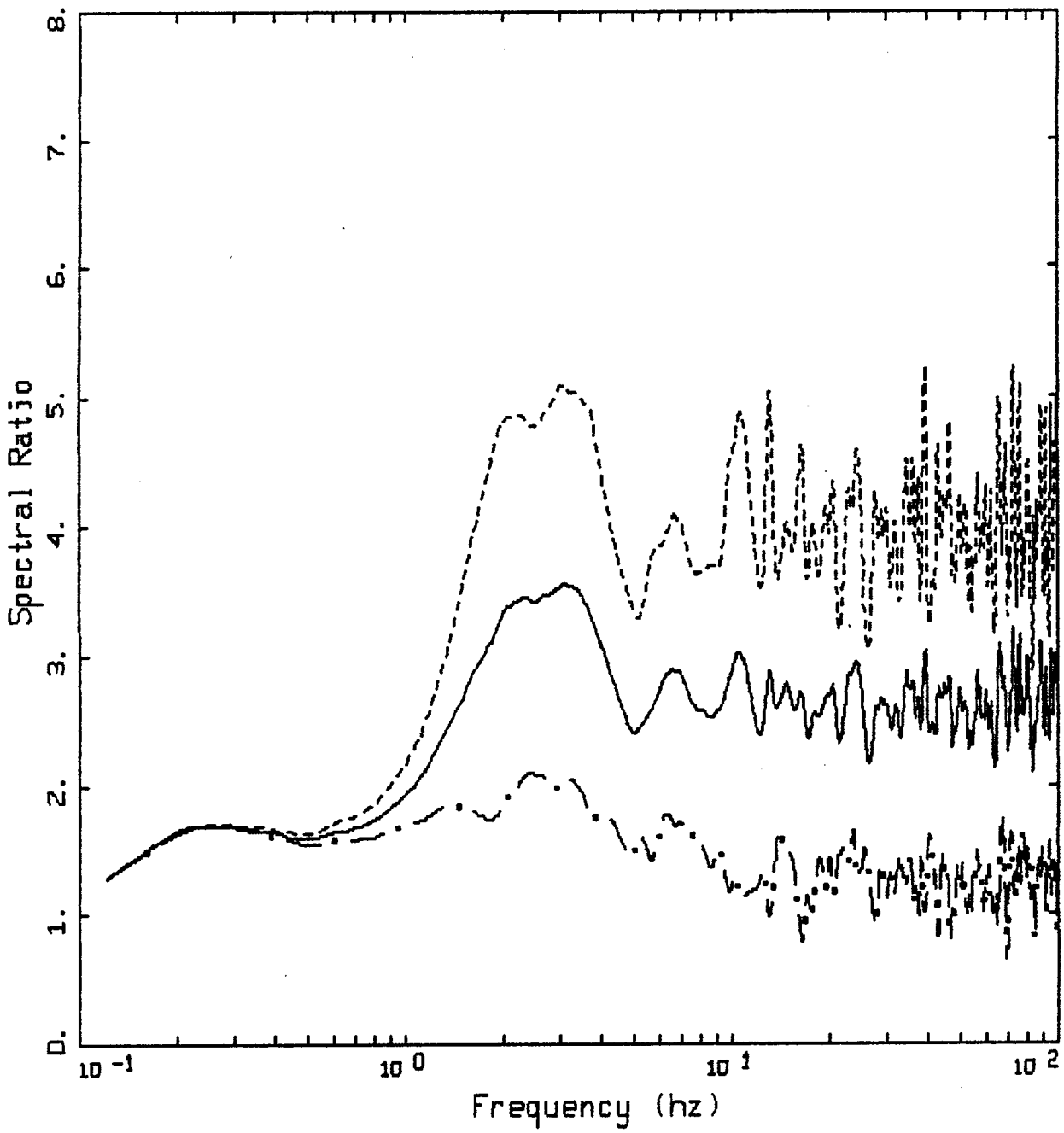

YUCCA H=8 KM OVER HALFSPACE, RANDOMIZED PROFILE
MEAN TRANSFER FUNCTION OF 30

LEGEND

----- 68TH PERCENTILE, 1 Hz SMOOTHING

——— MEAN, 1 Hz SMOOTHING

—·— 32TH PERCENTILE, 1 Hz SMOOTHING

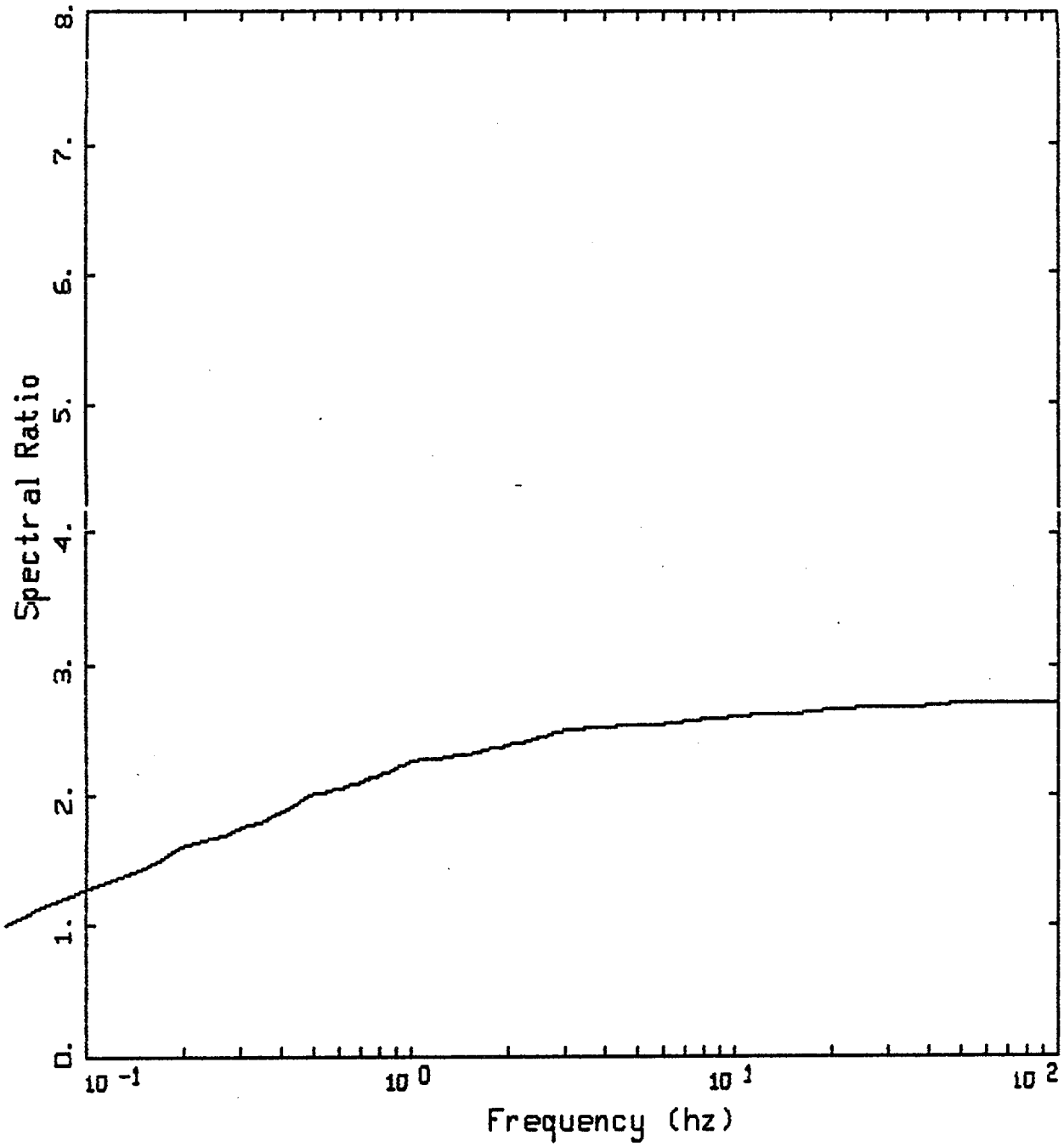

YUCCA TRANSFER FUNCTION
ROCK, SMOOTHED

LEGEND

——— SMOOTHED RATIO, FOR H = 8 KM, 10 KM, 15 KM

January 6, 1997

ATTENUATION MODEL

$$\ln(y) = C_1 + C_2 (M - 6) + C_3 (M - 6)^2 - C_4 \ln(R) - C_5 R$$

$$R = \mathrm{SQRT}(D^2 + H^2)$$

VALIDATION:

D = CLOSEST HORIZONTAL DISTANCE TO SURFACE PROJECTION

H = DEPTH TO ASPERITY ($\approx$ 8 km)

REGRESSION WEIGHTS		
Parameter		Weight
$\Delta\sigma$ (bars)		
25		0.185
50		0.630
200		0.185
Kappa (sec)		
0.01		0.185
0.02		0.630
0.03		0.185
M	H (km)	
5	5	0.80
	10	0.10
	15	0.10
6	5	0.10
	10	0.80
	15	0.10
7	5	0.10
	10	0.10
	15	0.80

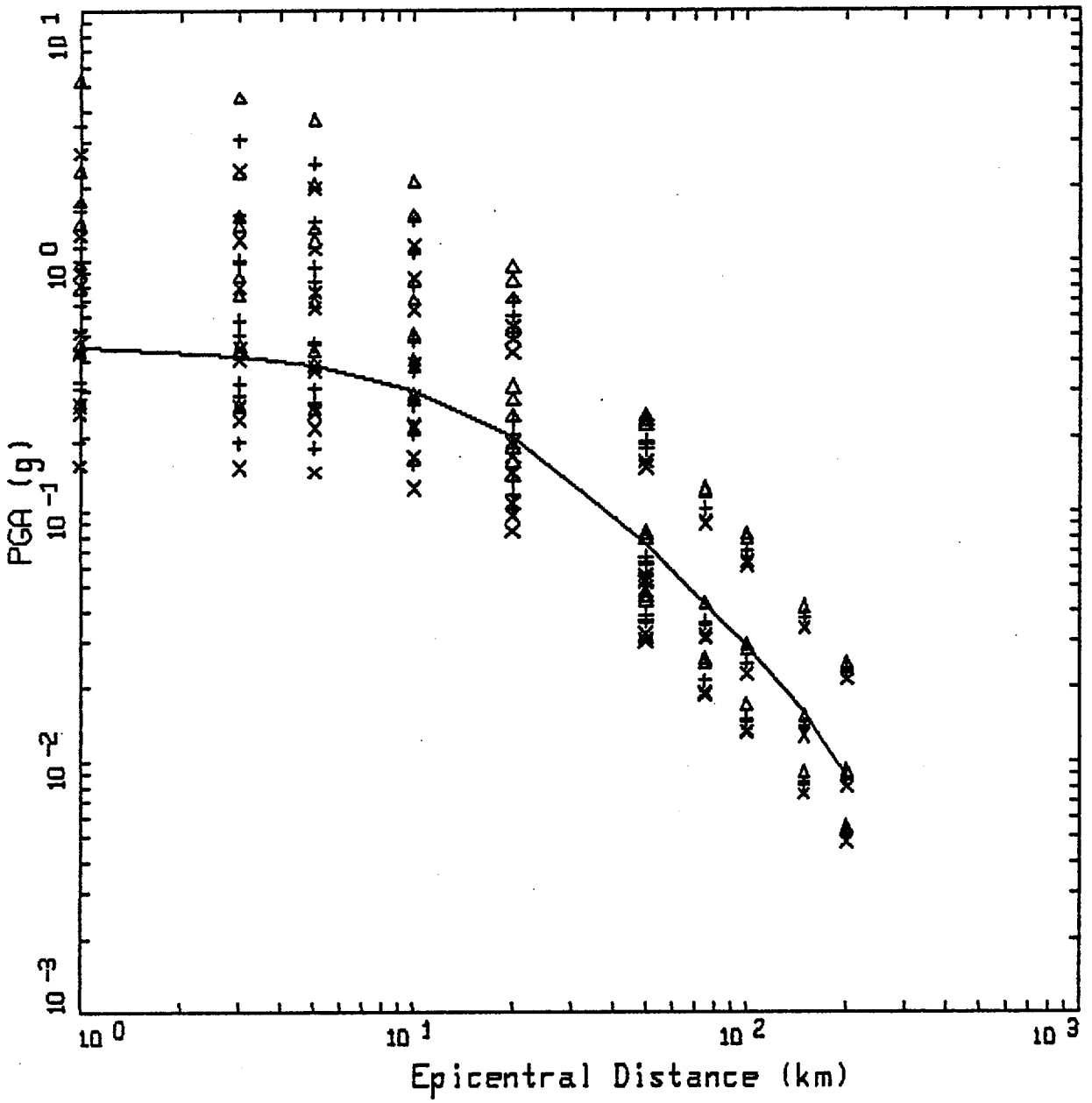

YUCCA PGA ATTENUATION
M = 7.0

LEGEND

△ DATA: PGA, KAPPA=0.01

\+ DATA: PGA, KAPPA=0.02

× DATA: PGA, KAPPA=0.03

——— REGRESSION ON DATA FOR M=7

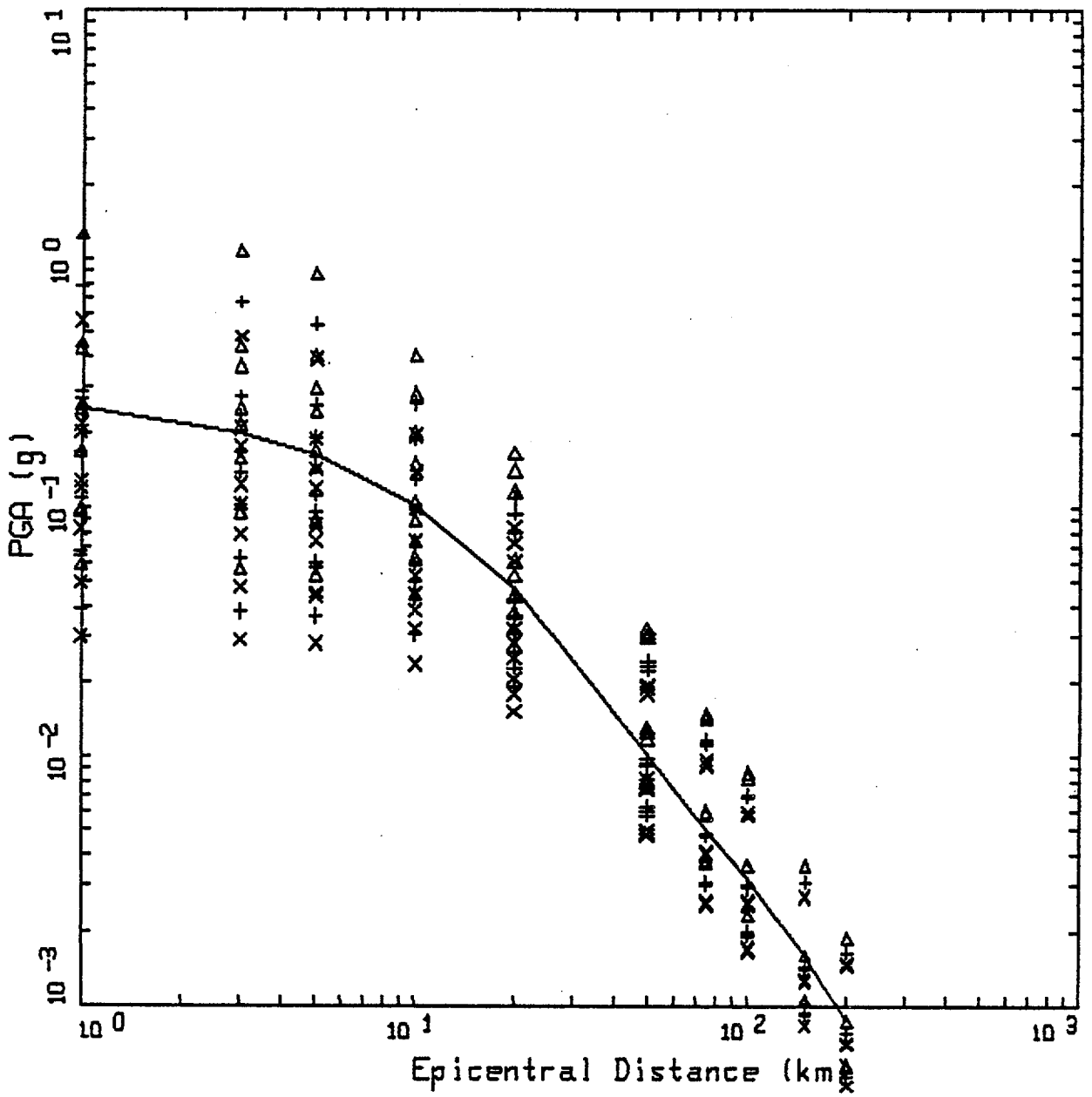

YUCCA PGA ATTENUATION
M = 5.0

LEGEND

△ DATA: PGA, KAPPA=0.01

\+ DATA: PGA, KAPPA=0.02

× DATA: PGA, KAPPA=0.03

——— REGRESSION ON DATA FOR M=5

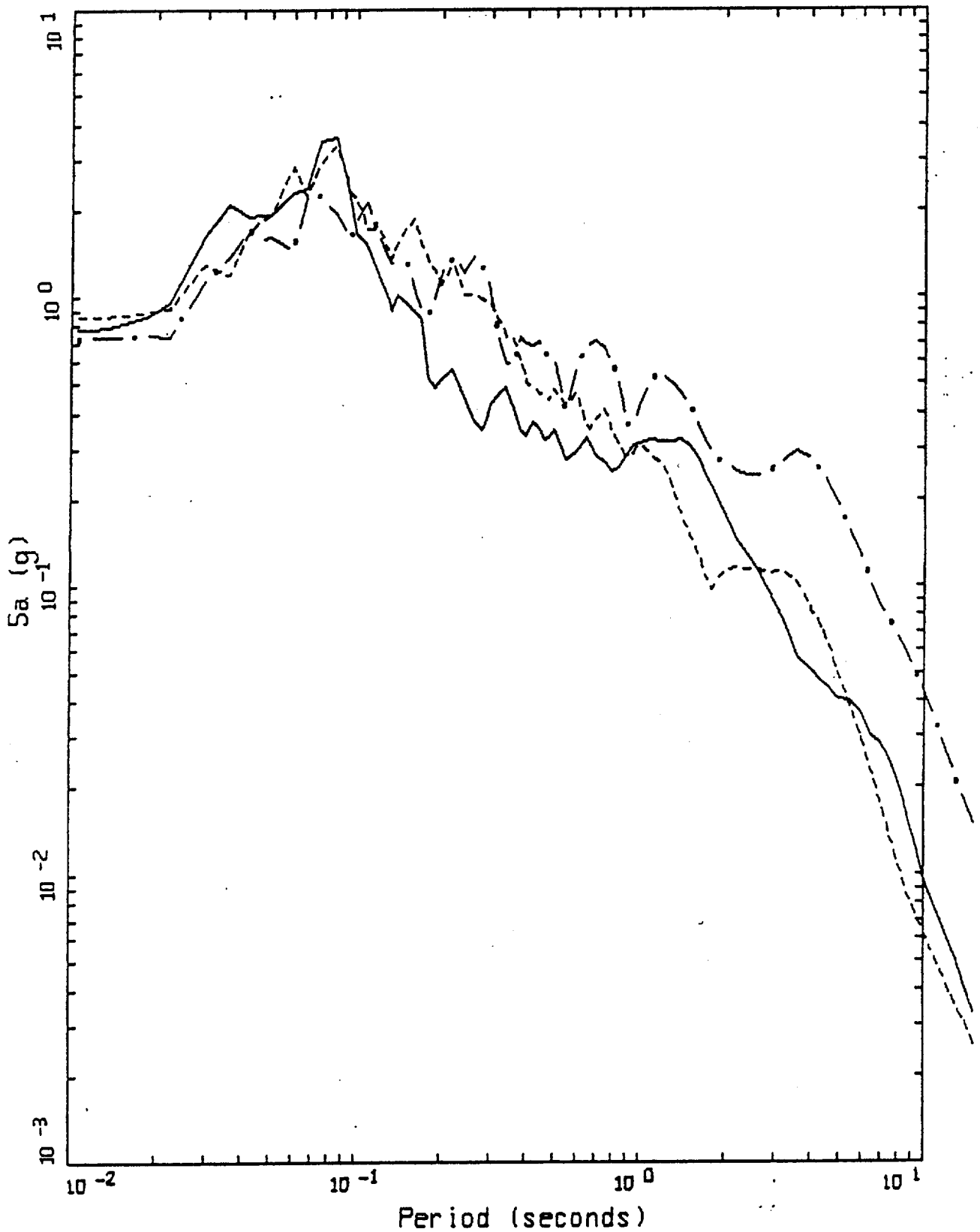

Figure 66. LANDERS 06/28/92 1158
LUCERNE

LEGEND

——— 5 %, PEER-CORRECTED DATA, COMP VRT

- - - - 5 %, PEER-CORRECTED DATA, COMP LONGITUDINAL

— · — 5 %, PEER-CORRECTED DATA, COMP TRANSVERSE

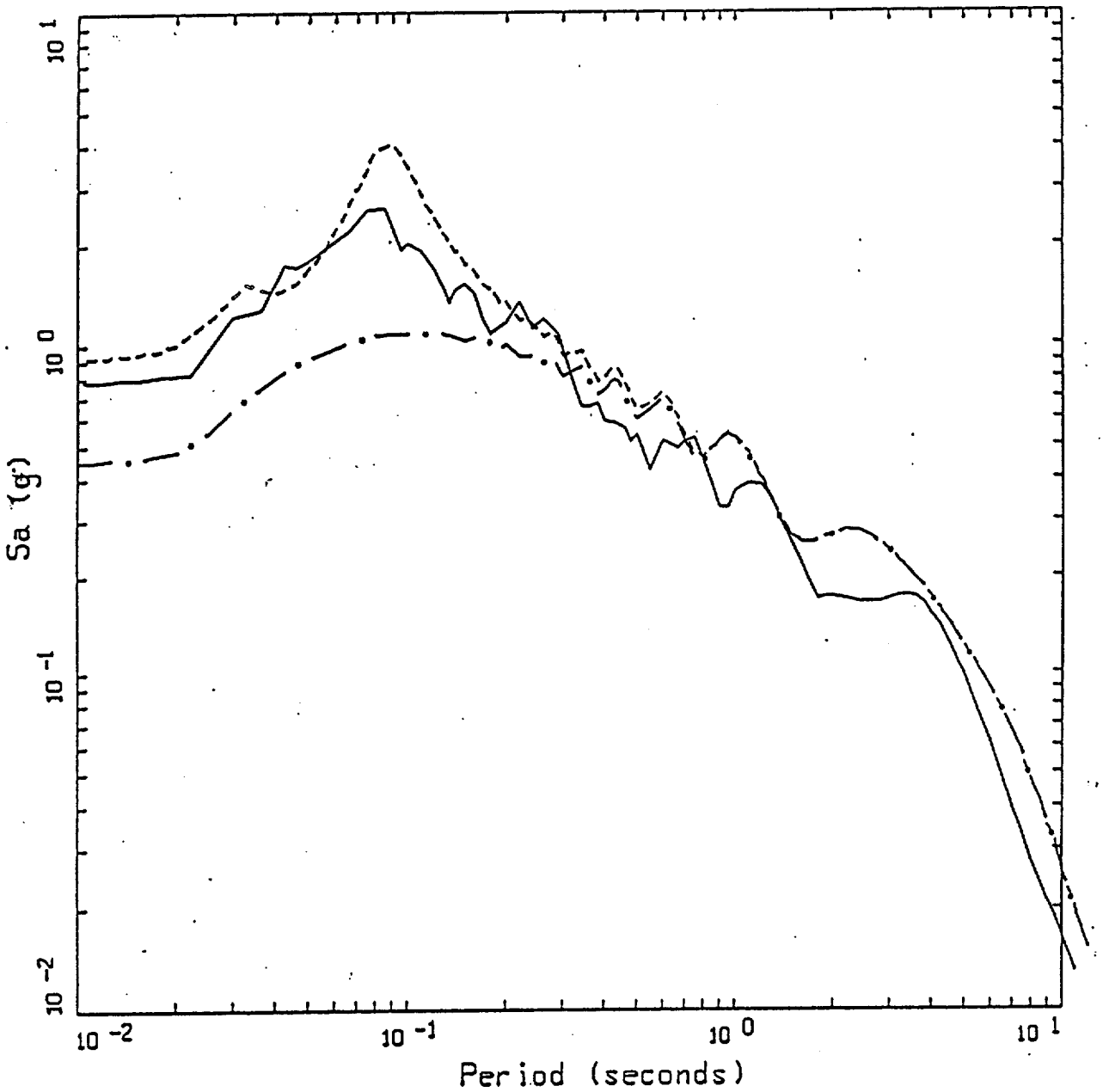

M 7.2 POINT SOURCE, H=8 KM, D=1 KM, SD=47 BARS
LUCERNE SITE

LEGEND

——— LANDERS EARTHQUAKE, M7.2, AVG OF 2 HORIZONTAL COMPONENTS

- - - - - ENA 20 FT OVER LANDERS CRUST, K=0.016 SEC, PGA=0.90 G

— · — LANDERS CRUST, K=0.020 SEC, PGA=0.45 G

Comparison of 5% damped spectral acceleration: 1992 M 7.2 Landers earthquake recordings at the shallow stiff soil site Lucern (solid line) with motion computed using a point source at a depth of 8 km and epicentral distance of 1 km. The point source stress drop is 47 bars (based on multiple site inversions). Dash-dotted line: Landers hard rock crust with a kappa of 0.02 sec. Dashed line: 20 ft stiff generic ENA soil on Landers crust with a rock kappa of 0.016 sec.

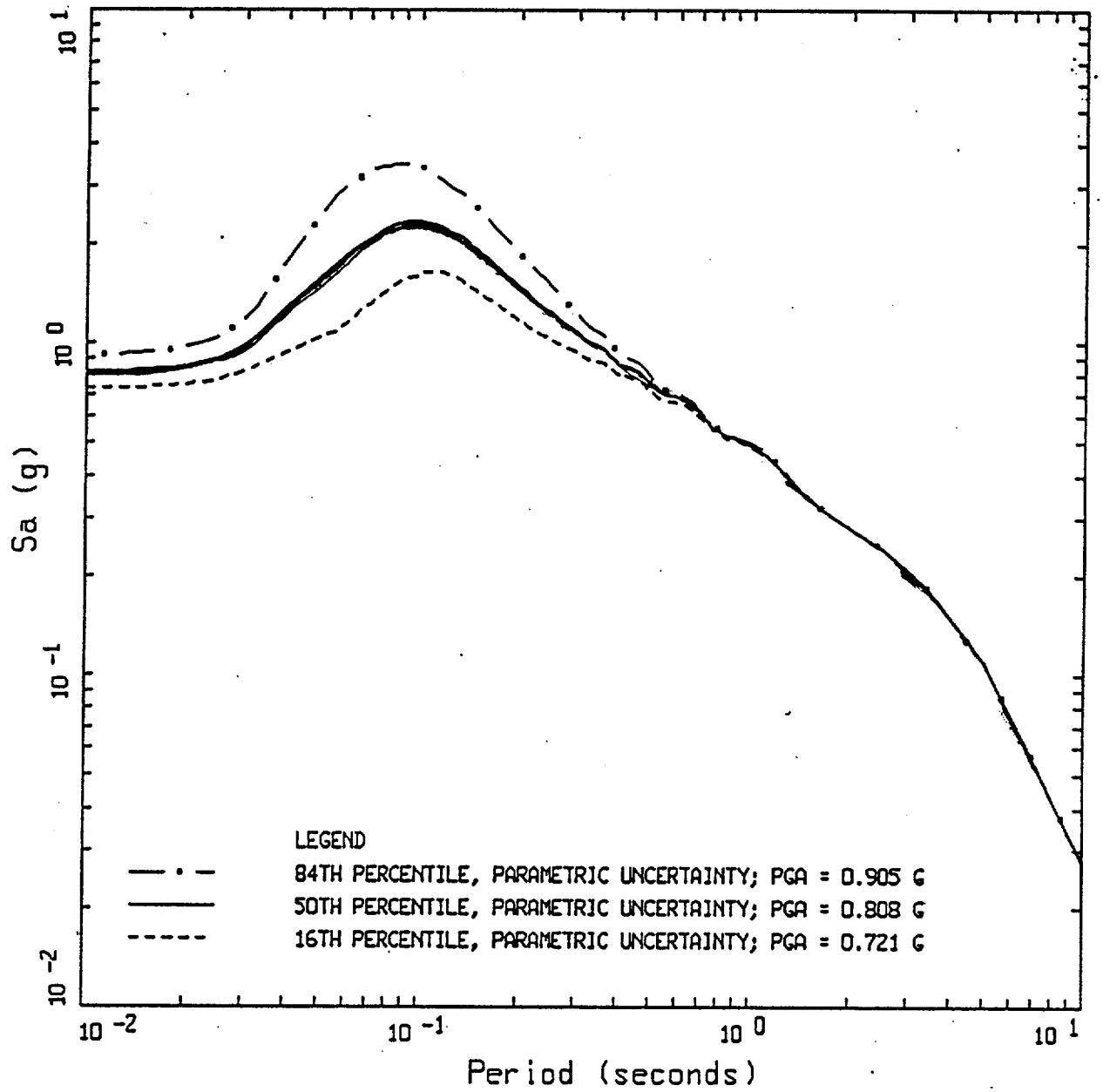

Figure 4. 5% damped spectral acceleration computed for site Lucern using the stochastic point source for a M 7.2 earthquake with a stress drop of 75 bars at an epicentral distance of 1.8 km and depth of 8 km. Median and 1-sigma estimates are based on 50 simulations using the random profiles shown in Figure 3.

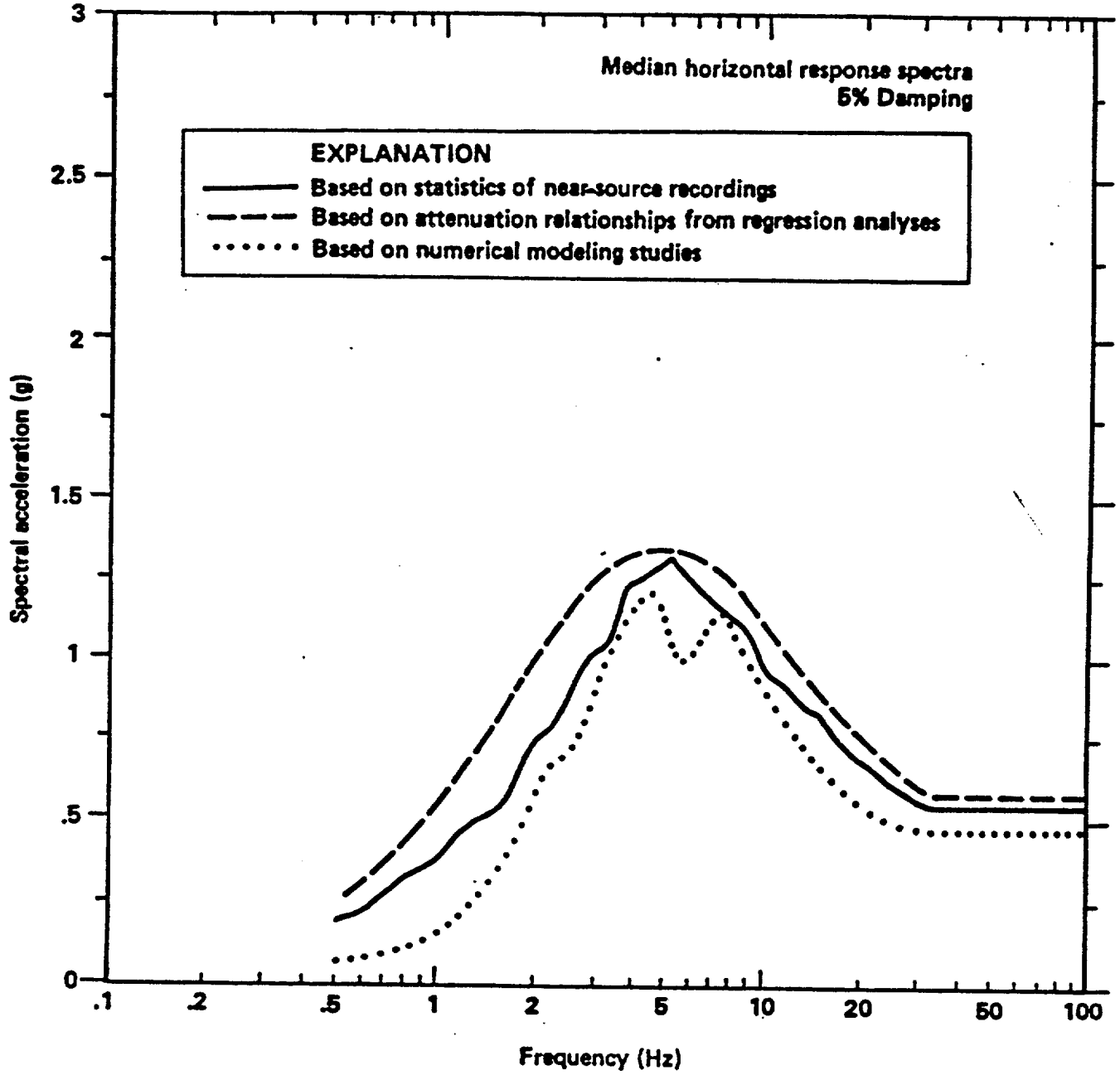

Figure 14. The Diablo Canyon site-specific median horizontal acceleration response spectra developed by PG&E, weighted for style of faulting as follows: 0.65, strike-slip; 0.30, oblique; 0.05, thrust (PG&E, 1988, Fig. 4-25).

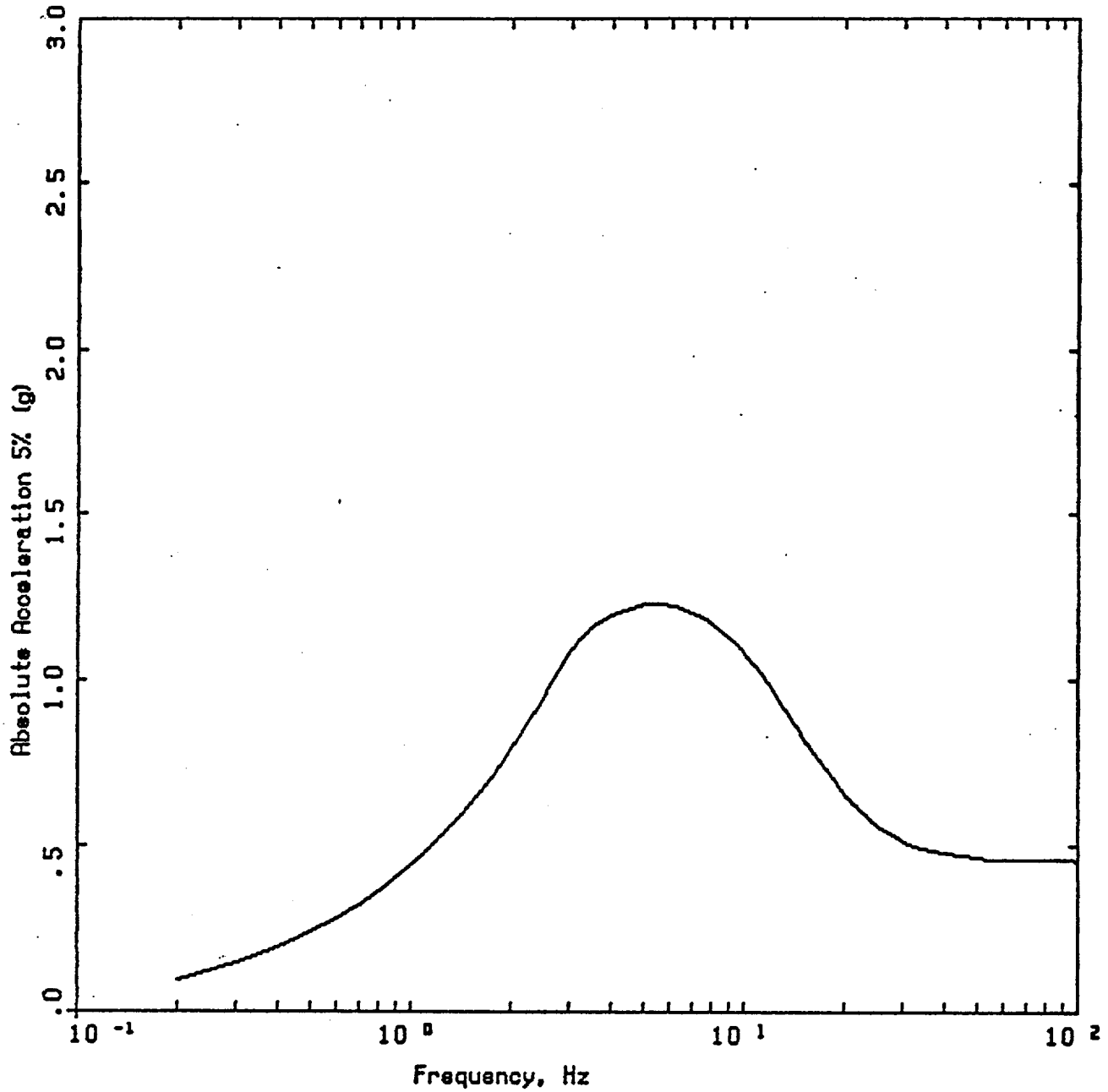

WNA ROCK M=7.2
HOSGRI EVENT

LEGEND

——— RASCALS:BLWN-RVT Spectrum Rock PGA=0.4558g PGV=51.20 cm/sec

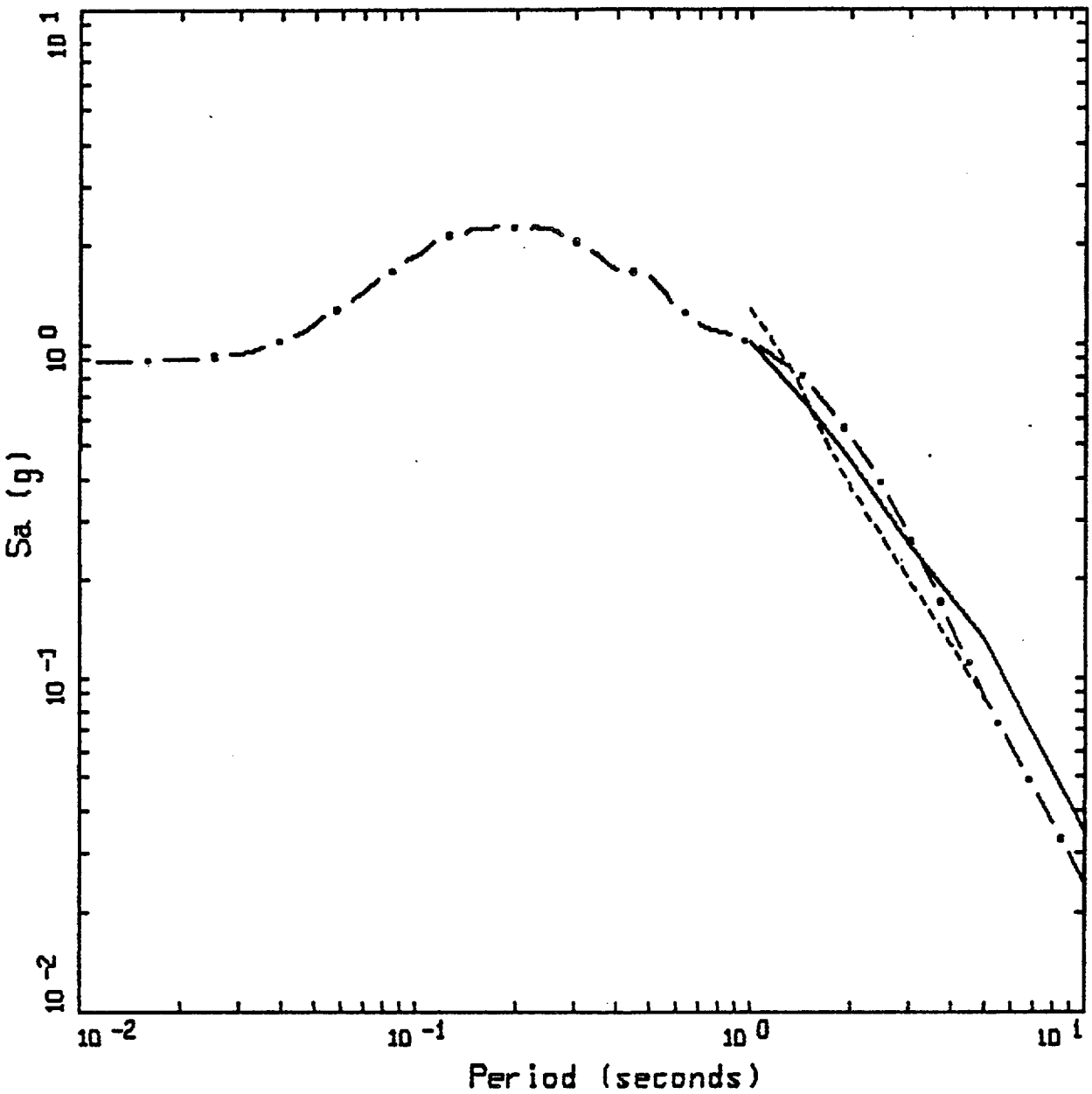

HAYWARD M 7.25 AT HEARST MINING BLDG
FAULT DISTANCE=0.25 KM, 7 SITES, 30 SLIP MODELS PER SITE

LEGEND

——— EMPIRICAL LPA

—·— MEDIAN, RVT

----- MEDIAN, DETERMINISTIC

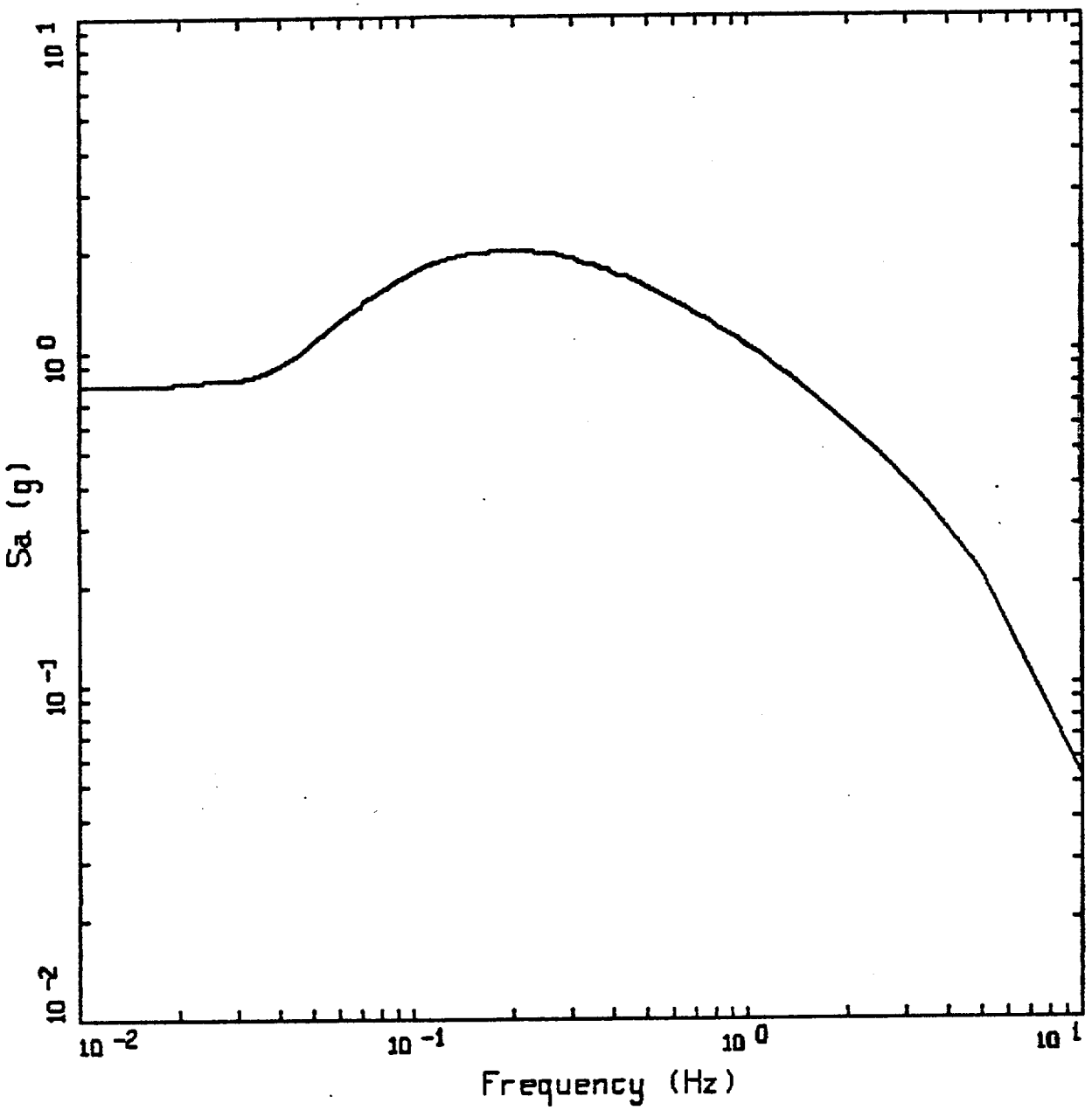

HAYWARD, M 7.25
WNA PARAMETERS

LEGEND

——— D = 0.25 KM, H = 8 KM; PGA = 0.798 G

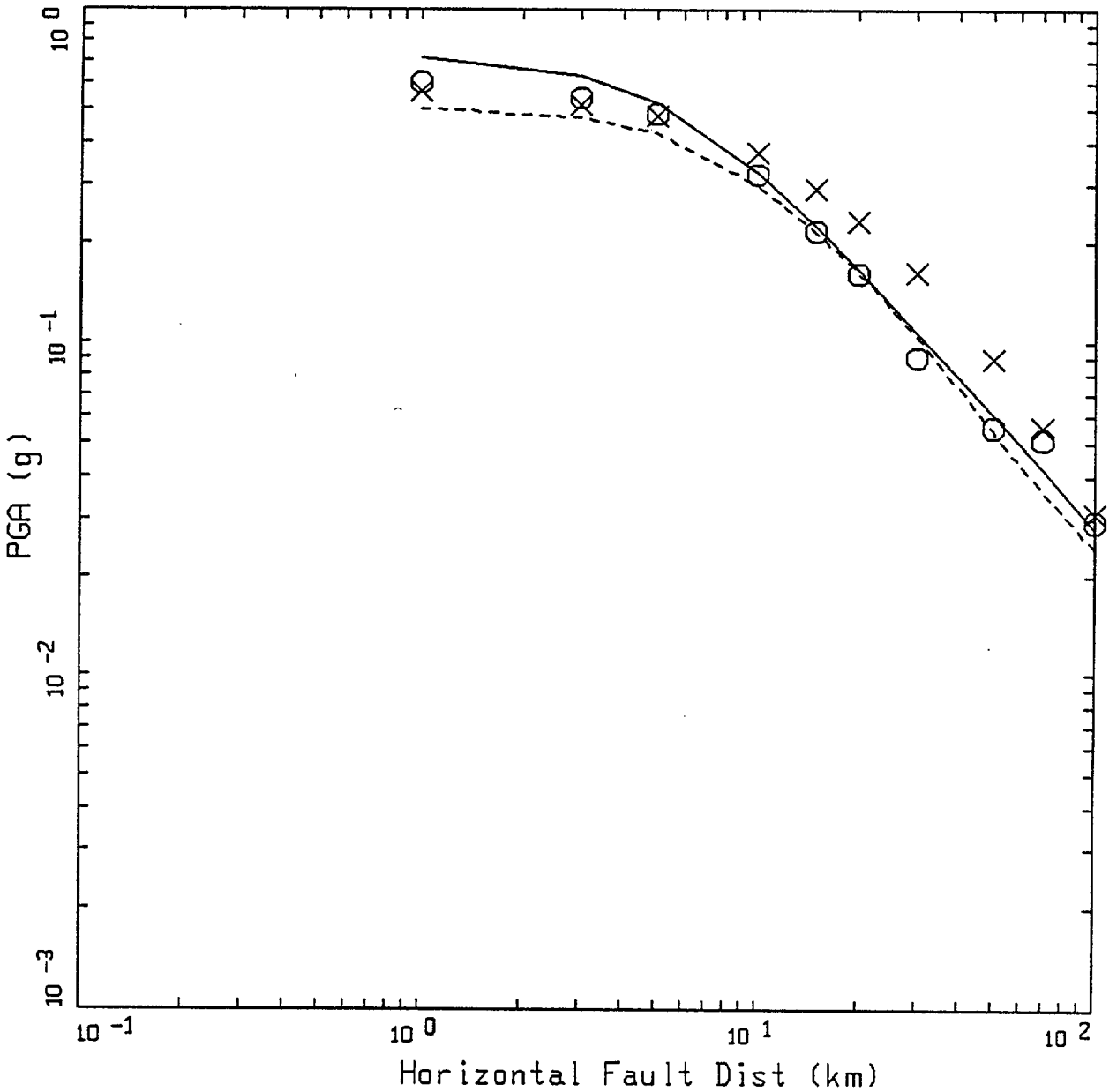

M=6.5

AVERAGE PGA ATTENUATION

LEGEND

——— EMPIRICAL

○ FINITE SOURCE: AVG OVER 11 SLIP MODELS, 11 SITES, LOMA PRIETA CRUST

× FINITE SOURCE: AVG OVER 11 SLIP MODELS, 11 SITES, LOMA PRIETA CRUST (1/R)

----- POINT SOURCE

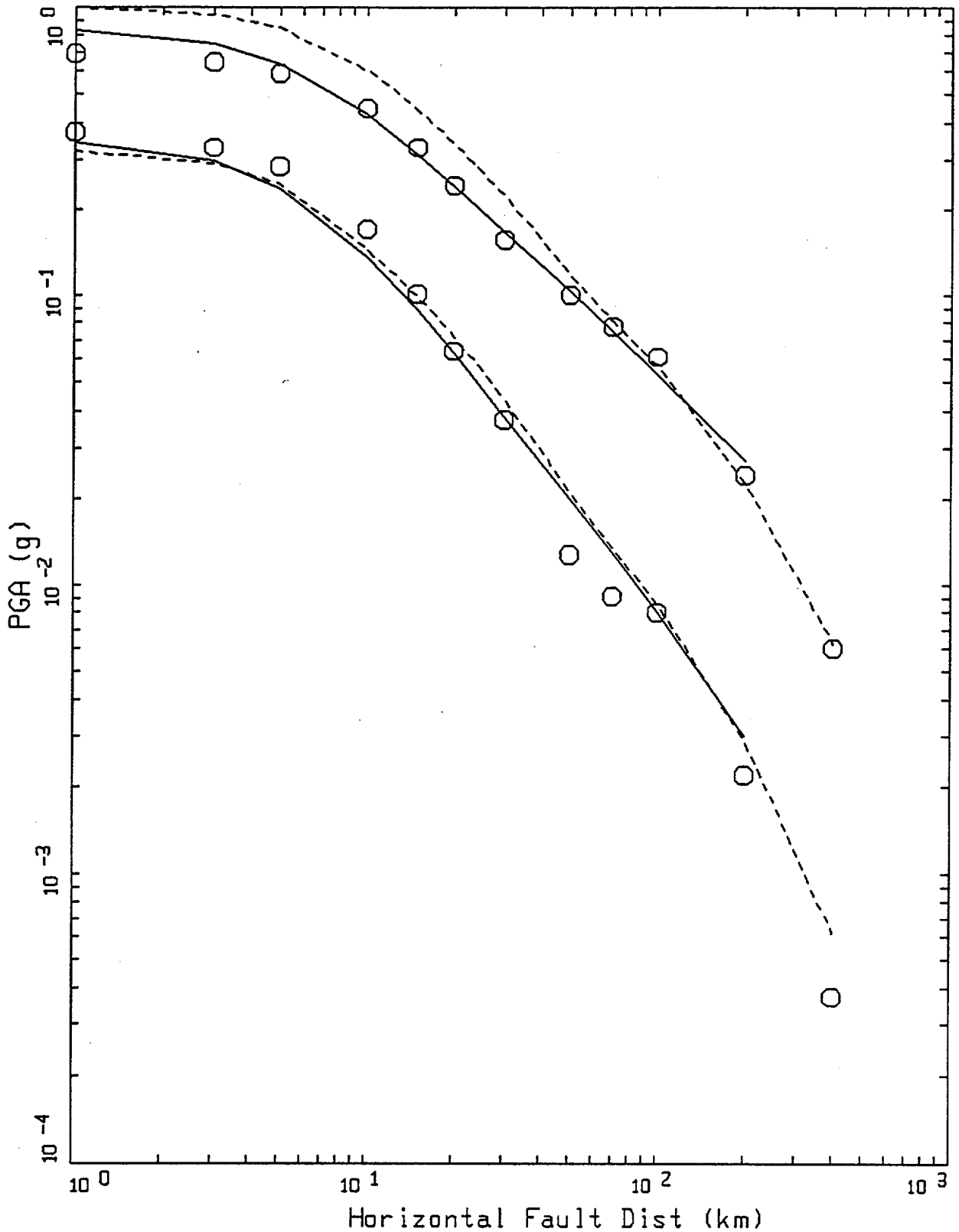

M=5.5 AND M=7.5

AVERAGE PGA ATTENUATION

LEGEND

——— EMPIRICAL

○ FINITE SOURCE: AVG OVER 11 SLIP MODELS, 11 SITES, 3 CRUSTAL MODELS

- - - - - - POINT SOURCE

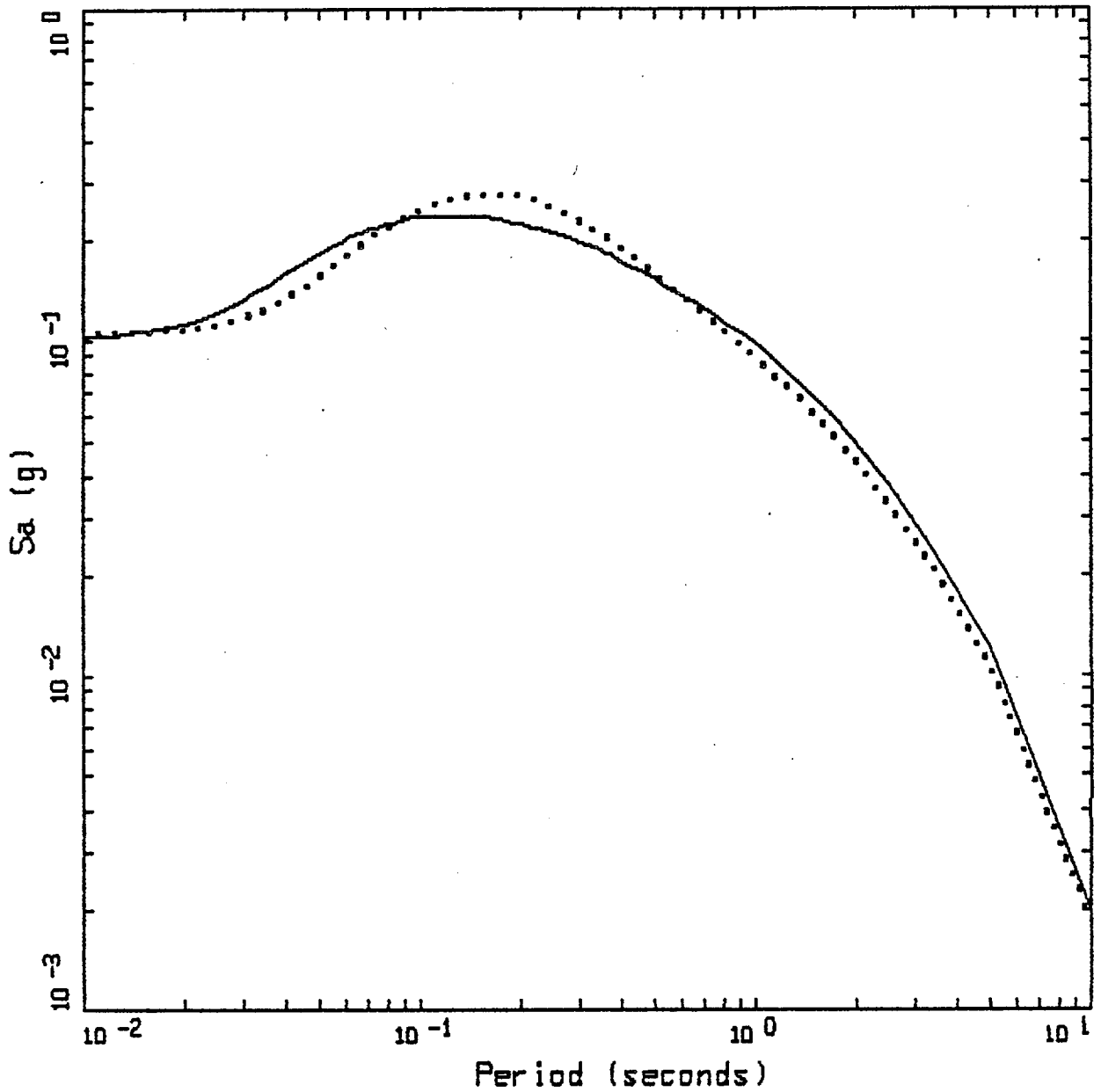

YUCCA M=6.5, D=30 KM, H=8 KM
STRESS DROP=59 BARS

LEGEND

——— 5 %, RESPONSE SPECTRA, YUCCA; PGA=1.02 g, PGV=9.06 cm/sec

.... 5 %, RESPONSE SPECTRA, WNA; PGA=1.05 g, PGV=8.39 cm/sec

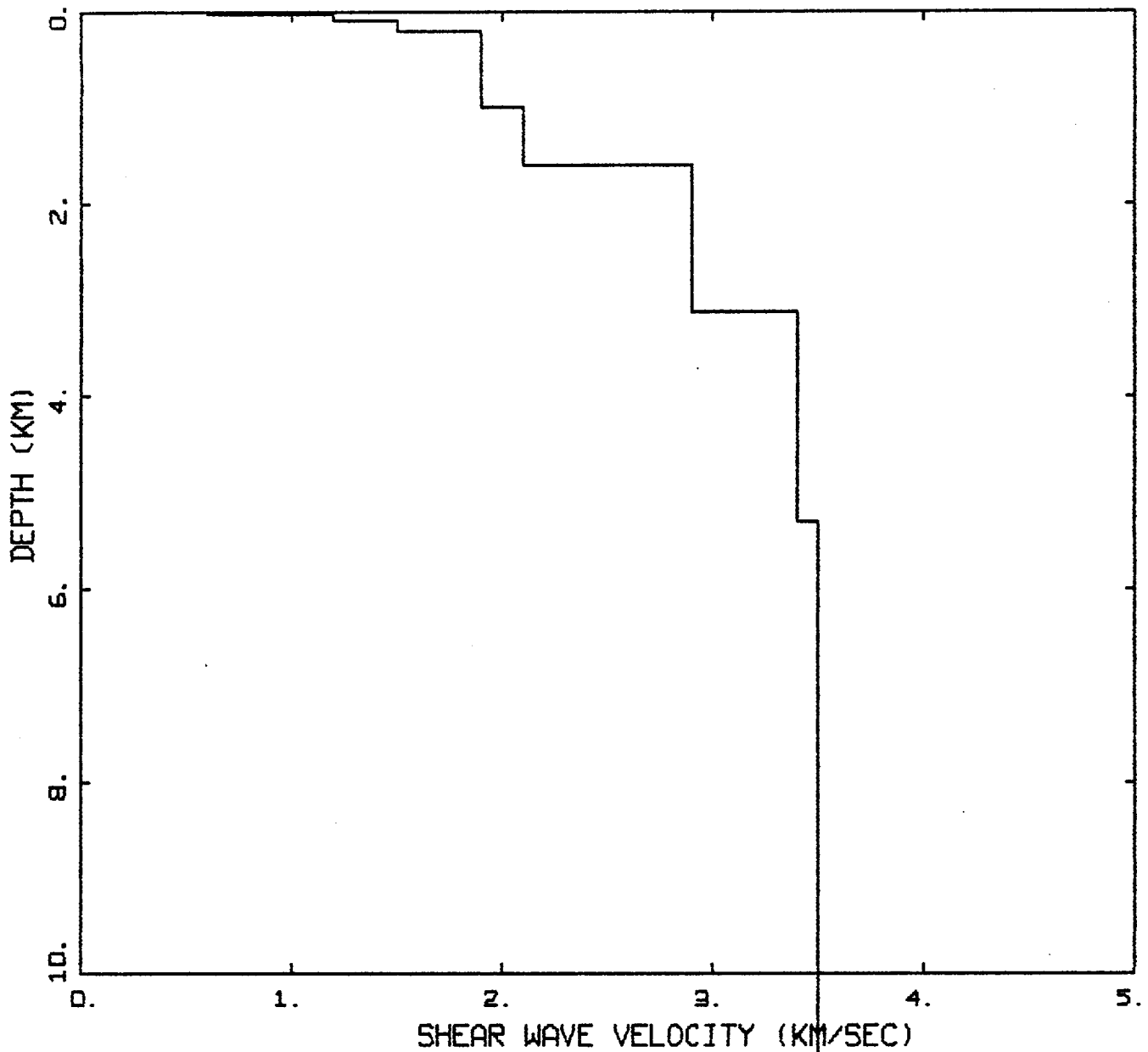

YUCCA MOUNTAIN PROFILE

LEGEND

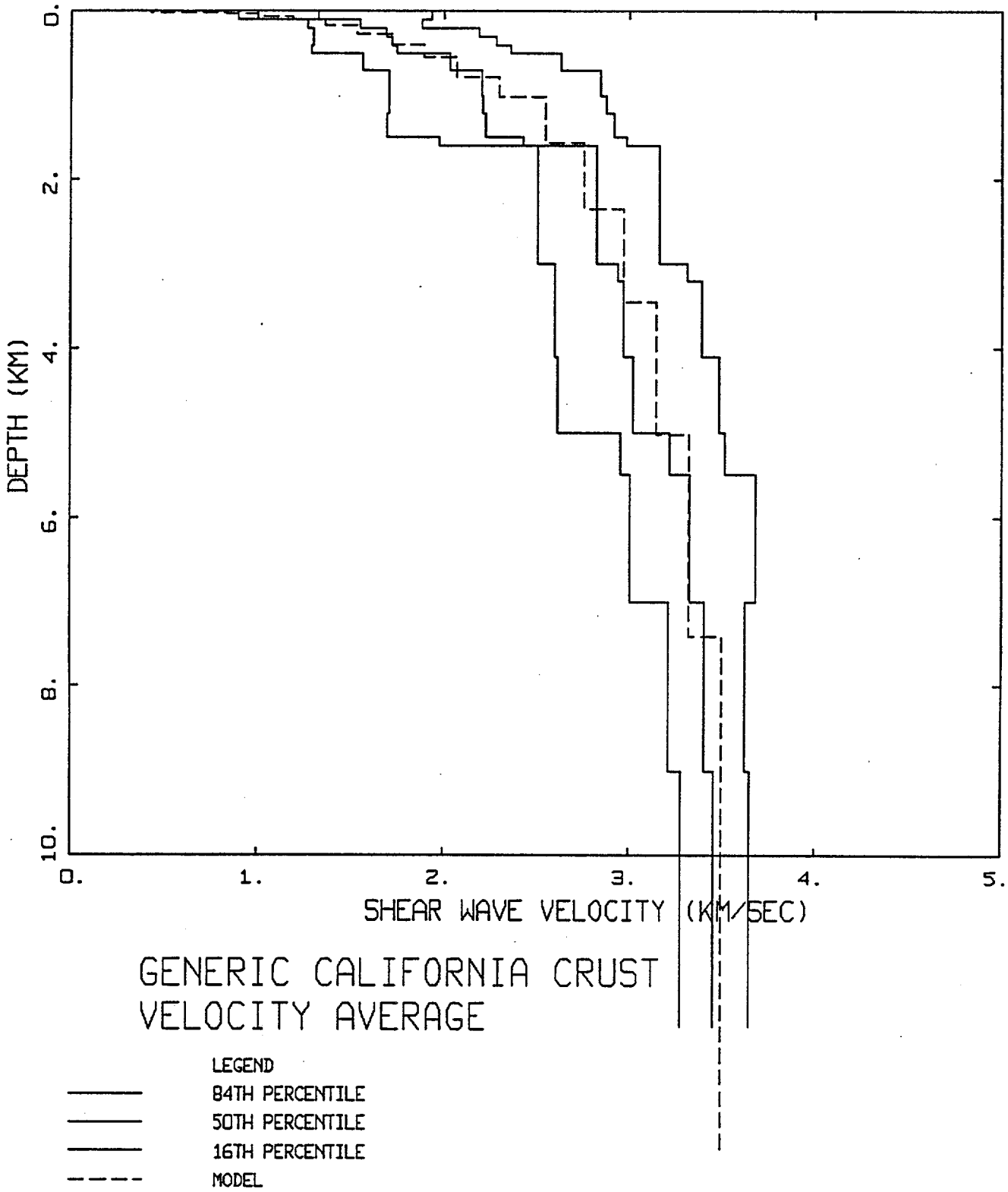
DEPTH (KM)
0.
2.
4.
6.
8.
10.
0.
1.
2.
3.
4.
5.
SHEAR WAVE VELOCITY (KM/SEC)
GENERIC CALIFORNIA CRUST
VELOCITY AVERAGE
LEGEND
84TH PERCENTILE
50TH PERCENTILE
16TH PERCENTILE
MODEL

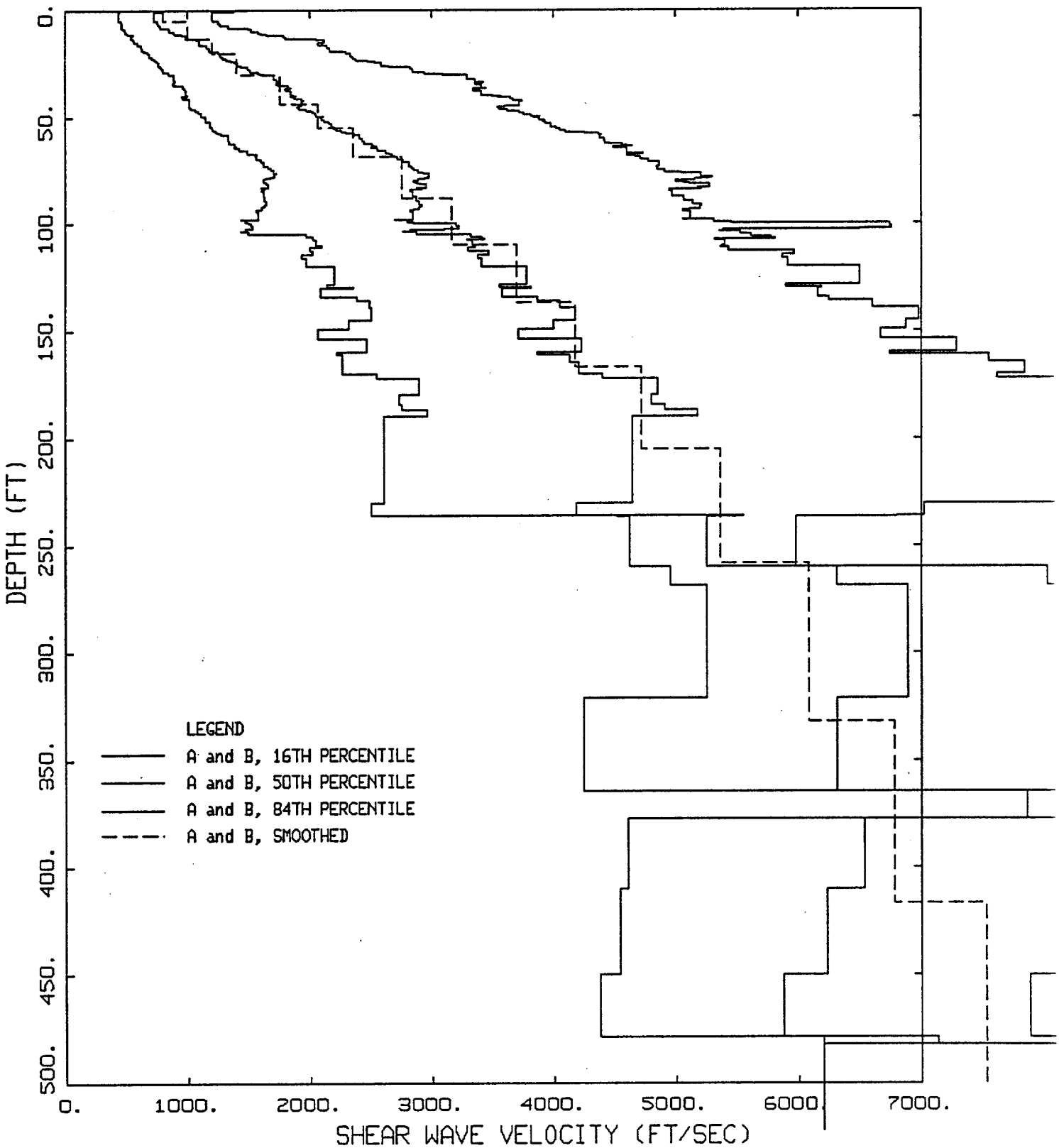

GEOMATRIX CLASS A & B

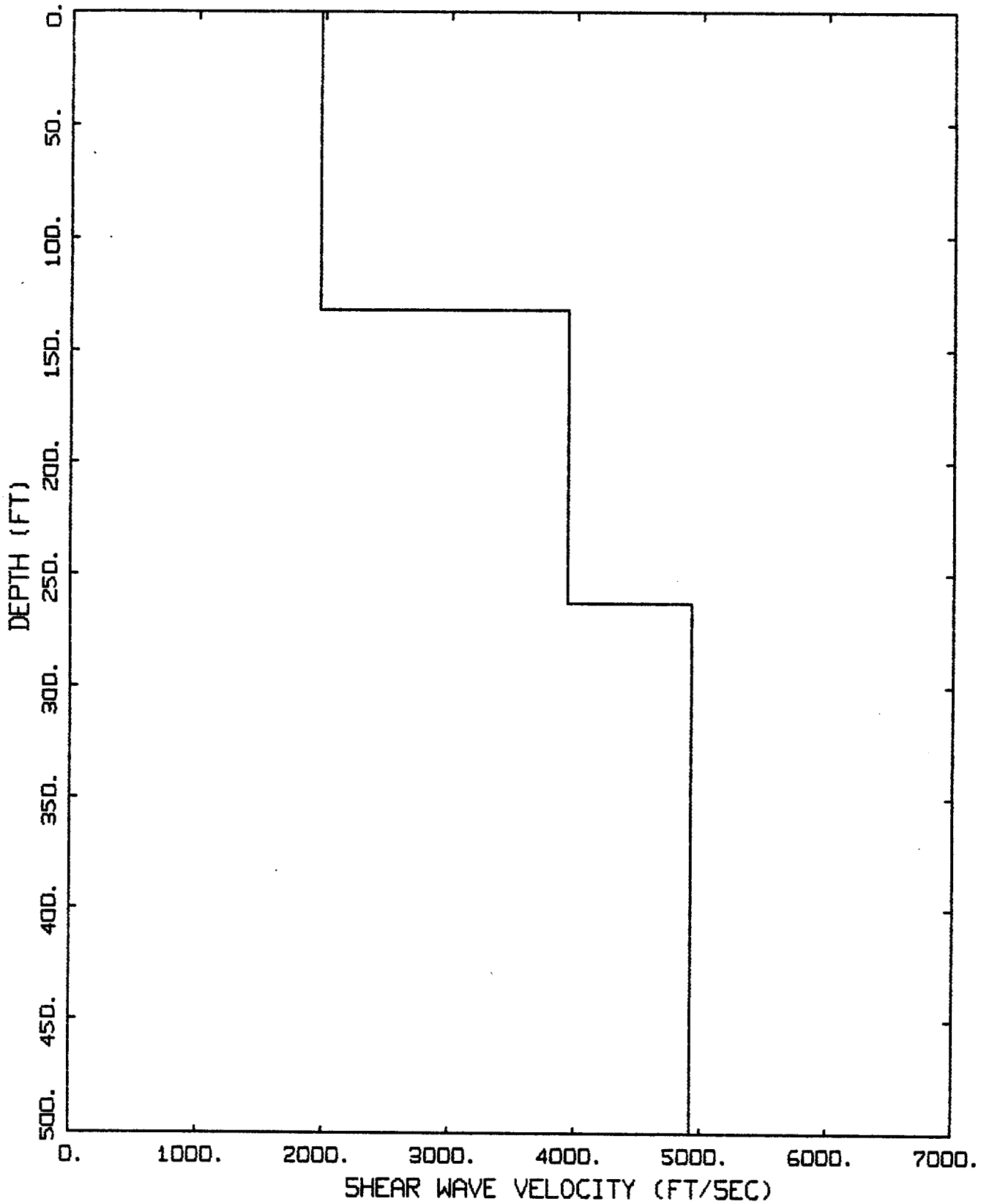

YUCCA MOUNTAIN PROFILE

LEGEND

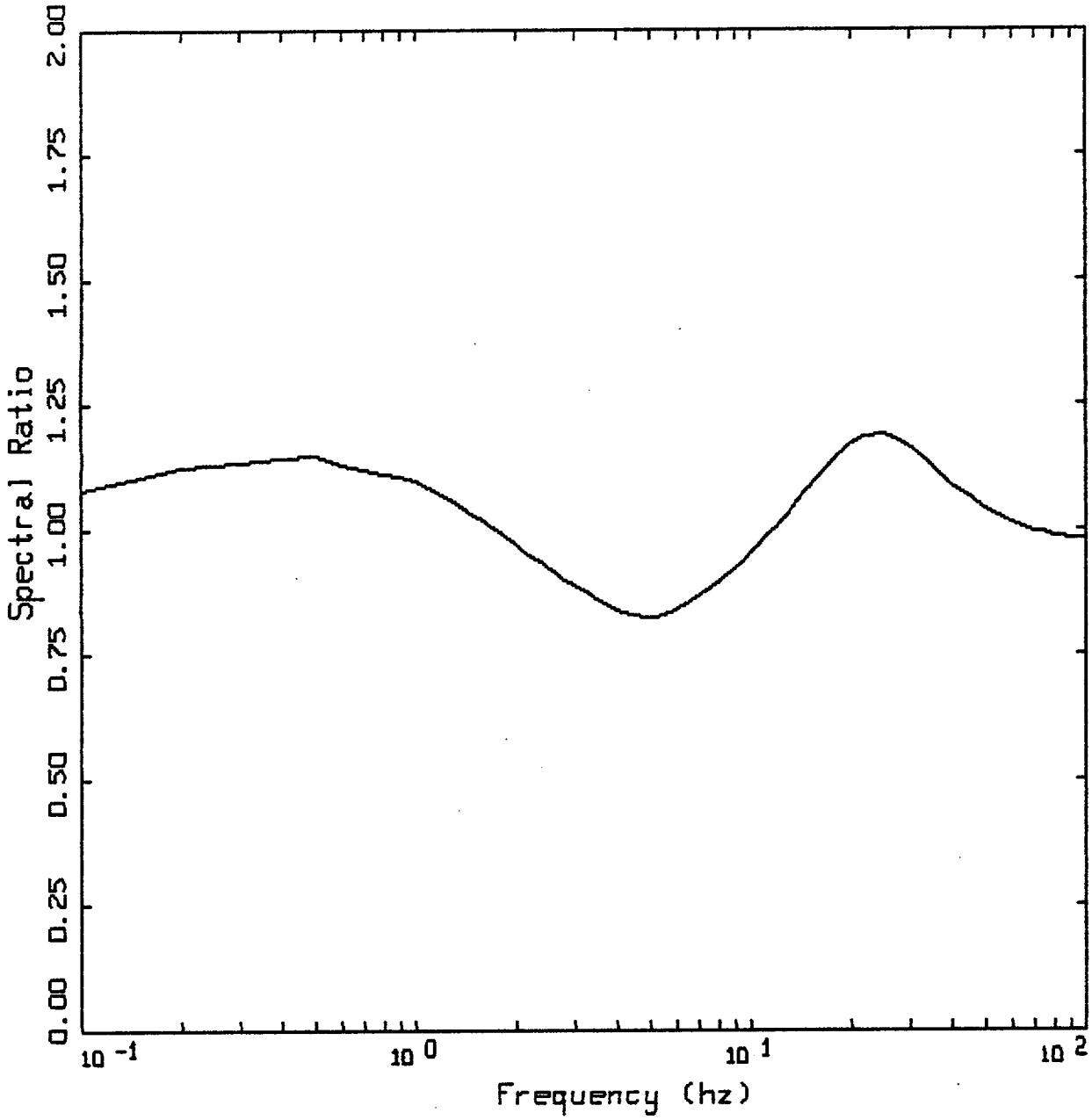

YUCCA TO WNA RESPONSE SPECTRA
TRANSFER FUNCTION

LEGEND

——— 5 %, TRANSFER FUNCTION

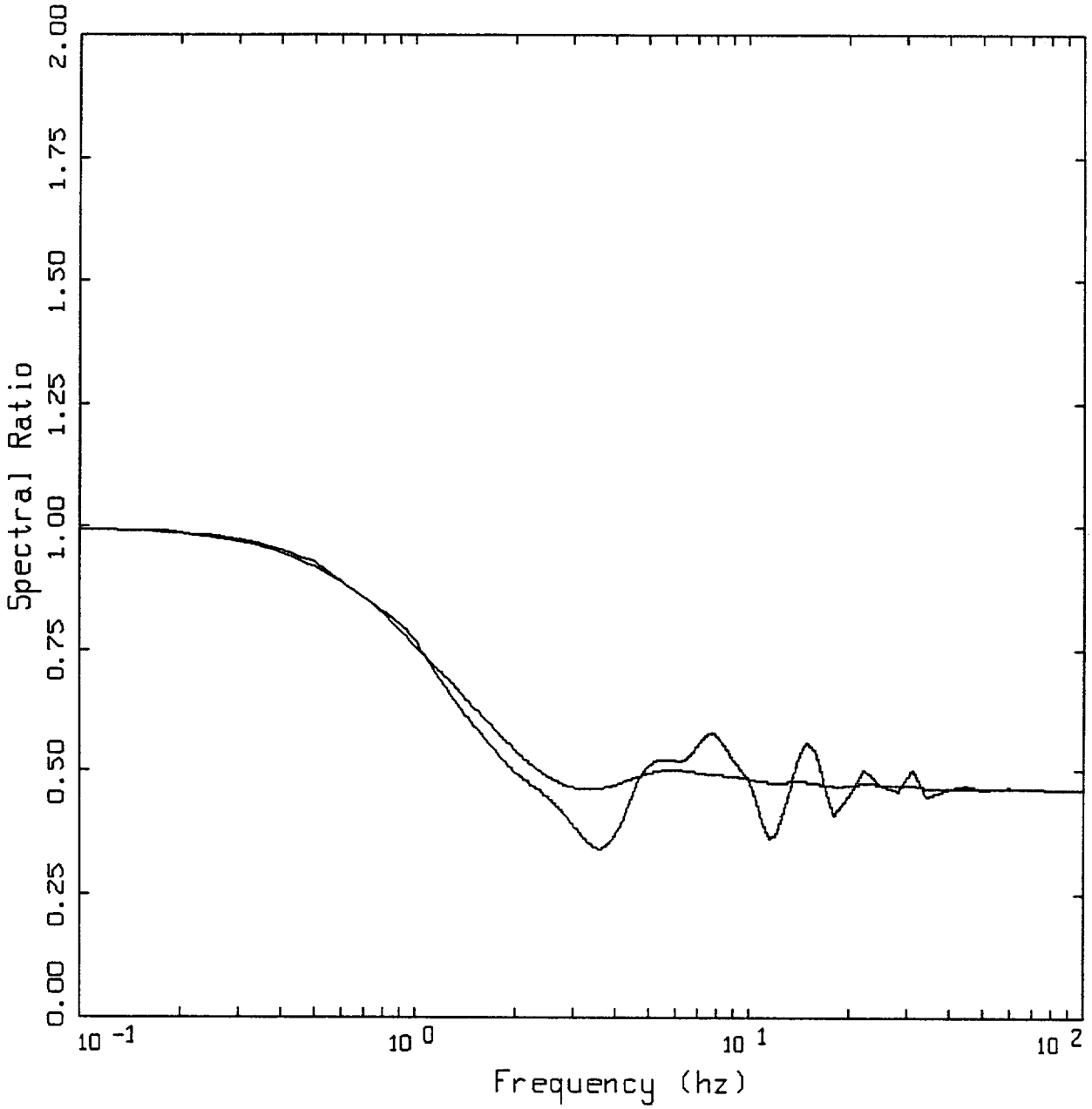

YUCCA 300M OUTCROP TO SURFACE
TRANSFER FUNCTION

LEGEND

5 %, TRANSFER FUNCTION

5 %, TRANSFER FUNCTION; 20 Hz smoothing

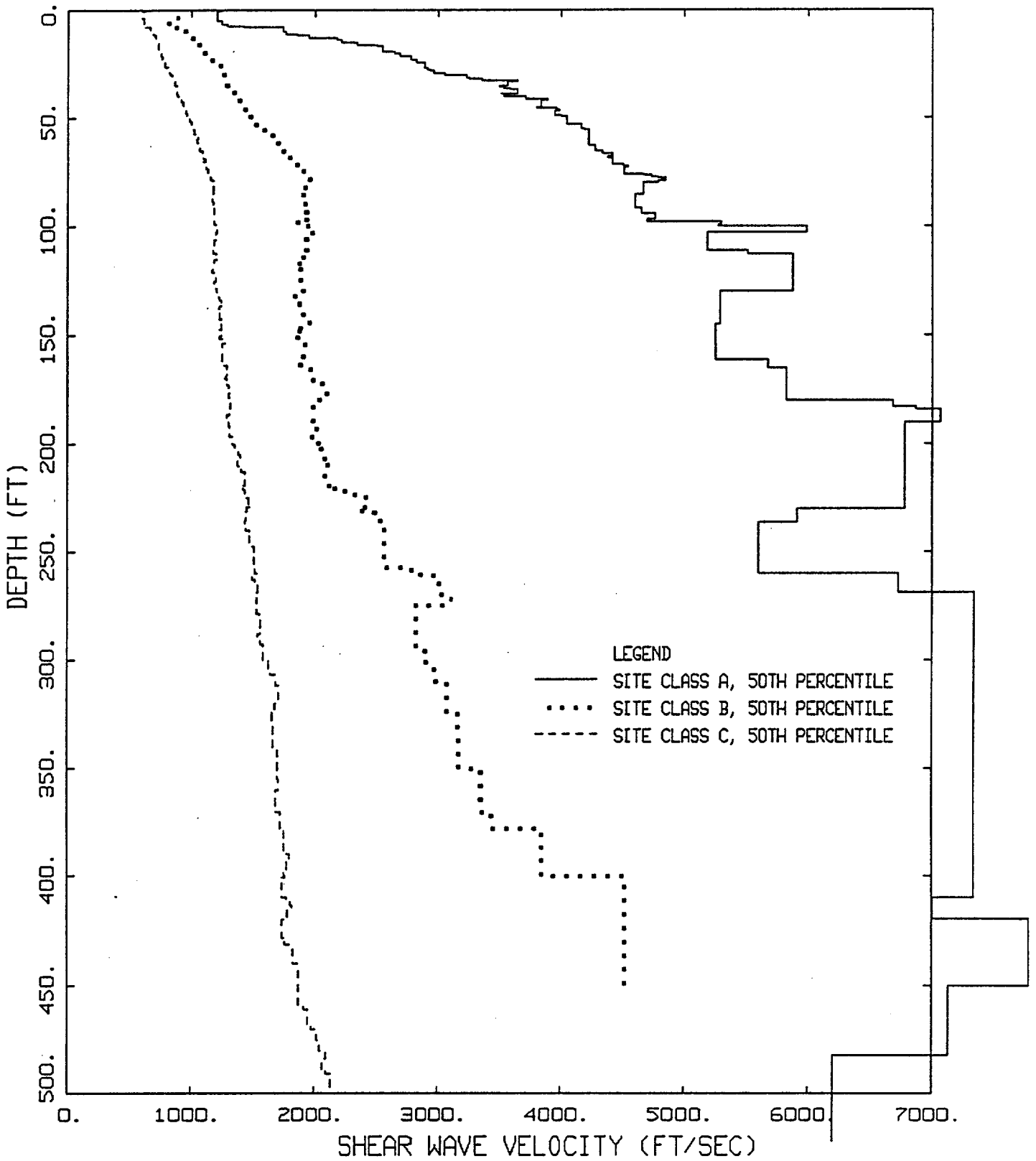

USGS SITE CLASSES
VELOCITY AVERAGE

Major Limitations

- Assumes similar near-source scaling characteristics in both regions
- Requires knowledge of earthquake, crustal, and site characteristics in both regions
- Seismological models are simplistic

EQE

PEAK GROUND ACCELERATION
Moment Magnitude 6.5 at 10 km From Surface Trace of Vertical Strike-Slip Fault

Model	Type	Site	California	Yucca Mountain					
			100 Bars	50 Bars		75 Bars		100 Bars	
			PGA (g)	Ratio	PGA (g)	Ratio	PGA (g)	Ratio	PGA (g)
Abrahamson & Silva (1997)	Empirical	Rock	0.325	1.053	0.342	1.455	0.473	1.832	0.595
Boore et al. (1997)	Empirical	V_S=620 m/s	0.193	1.053	0.203	1.455	0.281	1.832	0.354
Campbell (1997)	Empirical	Soft Rock	0.326	1.053	0.343	1.455	0.474	1.832	0.597
Idriss (1997)	Empirical	Rock	0.290	1.053	0.305	1.455	0.422	1.832	0.531
Sadigh et al. (1993)	Empirical	Rock	0.313	1.053	0.330	1.455	0.455	1.832	0.573
Spudich (1996)	Empirical	Rock	0.186	1.053	0.196	1.455	0.271	1.832	0.341
Silva	Theoretical	Site-Specific							
Zeng & Anderson	Theoretical	Site-Specific							
Chin & Aki	Theoretical	Site-Specific							
Somerville & Saikia	Theoretical	Site-Specific							
MEAN			**0.265**		**0.279**		**0.385**		**0.485**
SIGMA (EPISTEMIC)			**0.114**		**0.114**		**0.114**		**0.114**

Methodology

- Point-source BLWN model
- Regional earthquake, crustal, and site characteristics
- RVT estimate of ground motion parameters
- Scaling factors - California/Yucca Mountain
- Empirical estimate of California ground motion parameters from published attenuation relationships
- Hybrid estimate of Yucca Mountain ground motion parameters by applying regional scaling factors to California empirical ground motion estimates

EQE

Major Strengths

- Based on empirically derived near-source scaling characteristics from published attenuation relationships
- Calibrated with strong-motion recordings
- Uses basic seismological principles to derive regional scaling characteristics

EQE

HYBRID EMPIRICAL GROUND MOTION MODEL

Kenneth W. Campbell

Yucca Mountain Ground Motion Workshop #2

Salt Lake City, Utah

January 9-10, 1997

EQE

Objective

- Estimate ground motion parameters in a specific region by modifying empirical attenuation relationships developed for a different region using scaling parameters that account for differences in earthquake, crustal, and site characteristics between the two regions

EQE

PEAK GROUND ACCELERATION
Yucca Mountain Crust and Attenuation; 100 Bar Stress Drop

M_W	Distance (km)	Fault Type	PGA (g)	Sigma	
				Aleatory	Epistemic
6.5	10	Strike Slip	0.49	0.5	0.2
6.5	10	Normal (Hanging Wall)	0.62	0.5	0.2
6.5	10	Normal (Foot Wall)	0.44	0.5	0.2

PEAK GROUND ACCELERATION

Moment Magnitude 6.5 on Hanging Wall at 10 km From Surface Trace of 65° Dipping Normal Fault

Model	Type	Site	California	Yucca Mountain					
			100 Bars	50 Bars		75 Bars		100 Bars	
			PGA (g)	Ratio	PGA (g)	Ratio	PGA (g)	Ratio	PGA (g)
Abrahamson & Silva (1997)	Empirical	Rock	0.366	1.053	0.385	1.455	0.533	1.832	0.671
Boore et al. (1997)	Empirical	V_S=620 m/s	0.306	1.053	0.322	1.455	0.445	1.832	0.561
Campbell (1997)	Empirical	Soft Rock	0.371	1.053	0.391	1.455	0.540	1.832	0.680
Idriss (1997)	Empirical	Rock	0.320	1.053	0.337	1.455	0.466	1.832	0.586
Sadigh et al. (1993)	Empirical	Rock	0.346	1.053	0.364	1.455	0.503	1.832	0.634
Spudich (1996)	Empirical	Rock	0.325	1.053	0.342	1.455	0.473	1.832	0.595
Silva	Theoretical	Site-Specific							0.930
Zeng & Anderson	Theoretical	Site-Specific							0.520
Chin & Aki	Theoretical	Site-Specific							0.460
Somerville & Saikia	Theoretical	Site-Specific							0.630
MEAN			0.338		0.356		0.492		0.616
SIGMA (EPISTEMIC)			0.034		0.034		0.034		0.081

PEAK GROUND ACCELERATION
Moment Magnitude 6.5 on Foot Wall at 10 km From Surface Trace of 65° Dipping Normal Fault

Model	Type	Site	California	Yucca Mountain					
			100 Bars	50 Bars		75 Bars		100 Bars	
			PGA (g)	Ratio	PGA (g)	Ratio	PGA (g)	Ratio	PGA (g)
Abrahamson & Silva (1997)	Empirical	Rock	0.325	1.053	0.342	1.455	0.473	1.832	0.595
Boore et al. (1997)	Empirical	V_S=620 m/s	0.193	1.053	0.203	1.455	0.281	1.832	0.354
Campbell (1997)	Empirical	Soft Rock	0.297	1.053	0.313	1.455	0.432	1.832	0.544
Idriss (1997)	Empirical	Rock	0.290	1.053	0.305	1.455	0.422	1.832	0.531
Sadigh et al. (1993)	Empirical	Rock	0.313	1.053	0.330	1.455	0.455	1.832	0.573
Spudich (1996)	Empirical	Rock	0.186	1.053	0.196	1.455	0.271	1.832	0.341
Silva	Theoretical	Site-Specific							0.470
Zeng & Anderson	Theoretical	Site-Specific							0.220
Chin & Aki	Theoretical	Site-Specific							0.350
Somerville & Saikia	Theoretical	Site-Specific							0.630
MEAN			0.261		0.275		0.379		0.440
SIGMA (EPISTEMIC)			0.109		0.109		0.109		0.146

Additional Information and Background Material

Maxwell Technologies, Inc.
Federal Division
Reston Geophysics Office
11800 Sunrise Valley Drive Suite 1212
Reston, Virginia 22091

Further Results from Initial Phase of Work
As presented in previous Phase 1 workshops.

Empirical Ground Motion Prediction Goals for Yucca Mountain Repository

Objective: Use large knowledge base of strong ground motion predictions for NTS underground nuclear explosions to help establish reliable prediction capability for potential earthquake scenarios which might affect the Yucca Mountain Repository site.

Advantages:

- Experience is based on a large database (thousands of recordings) covering a range of magnitudes, distances and site conditions comparable to earthquake scenarios under consideration for the site
- Uses region-specific knowledge of attenuation
- Large database was statistically analyzed to provide specific information on uncertainty associated with ground motion predictions
- Can be used to identify potential site response problems which may affect predictions

Disadvantages:

- Uncertainties associated with defining equivalence between earthquake and explosion source term
- Mechanism differences, such as radiation pattern effects from finite sources, and focal depth differences are not accounted for

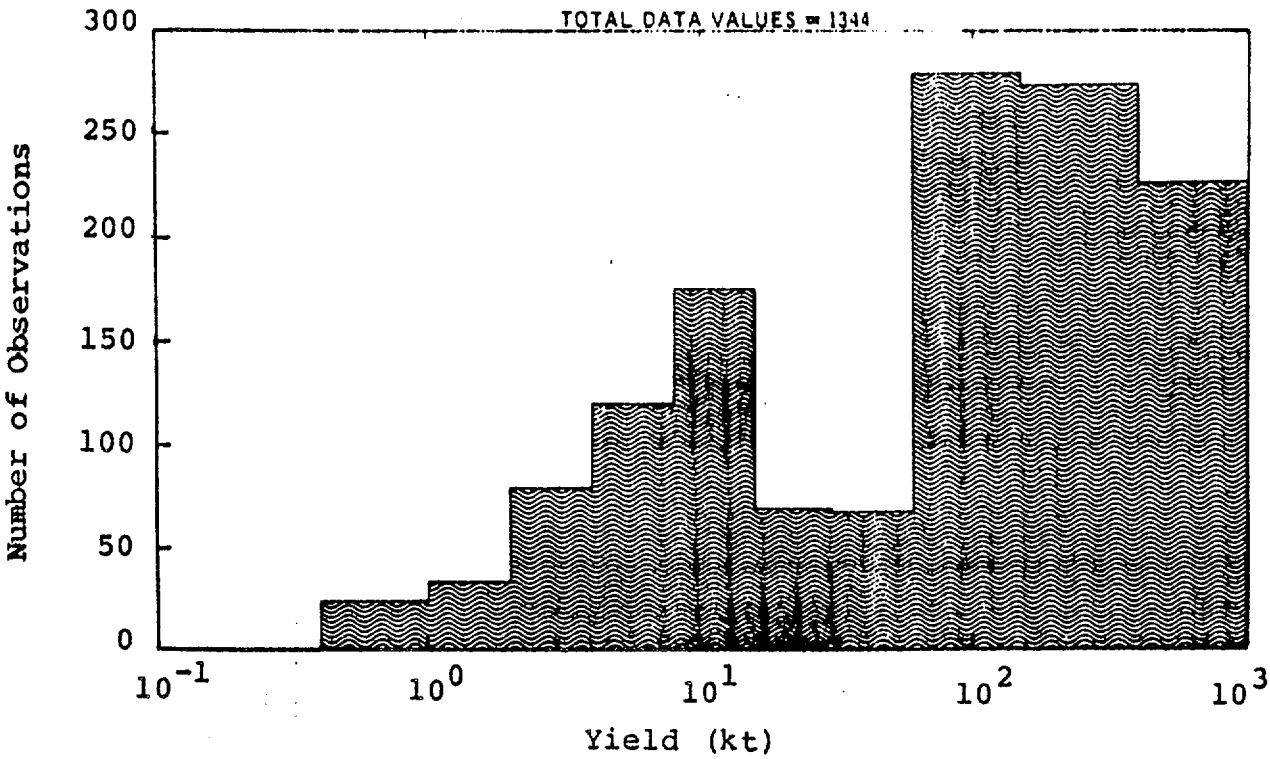

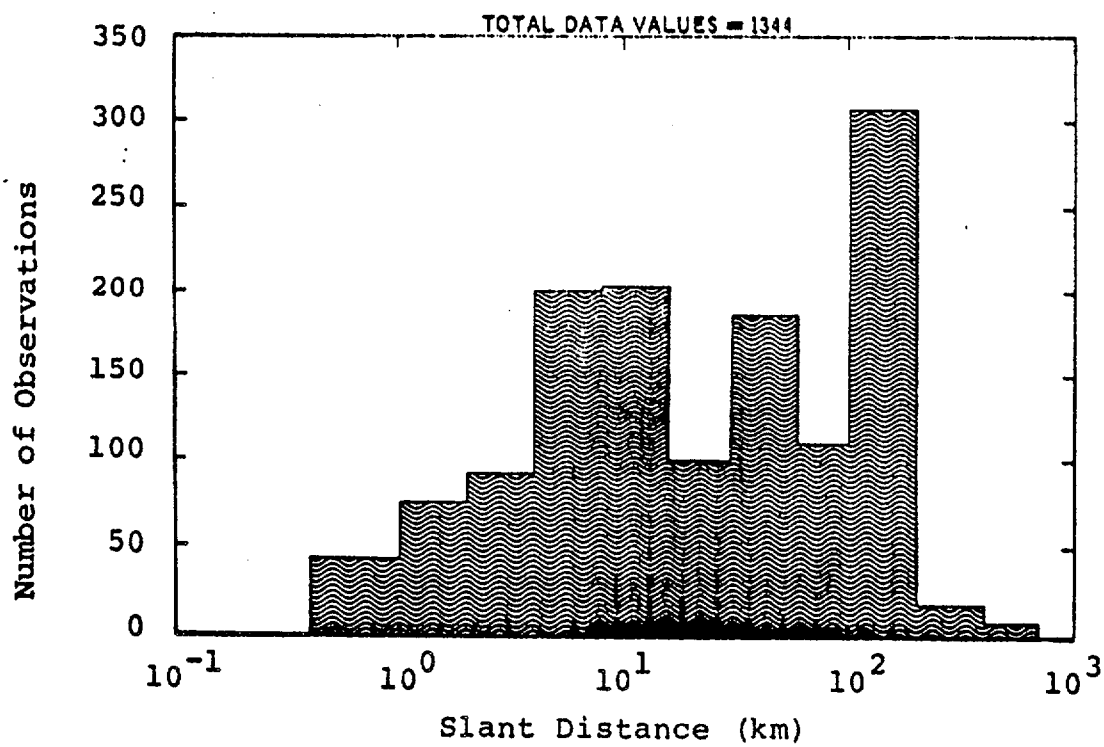

Distribution of acceleration data with respect to yield (top) and range (bottom).

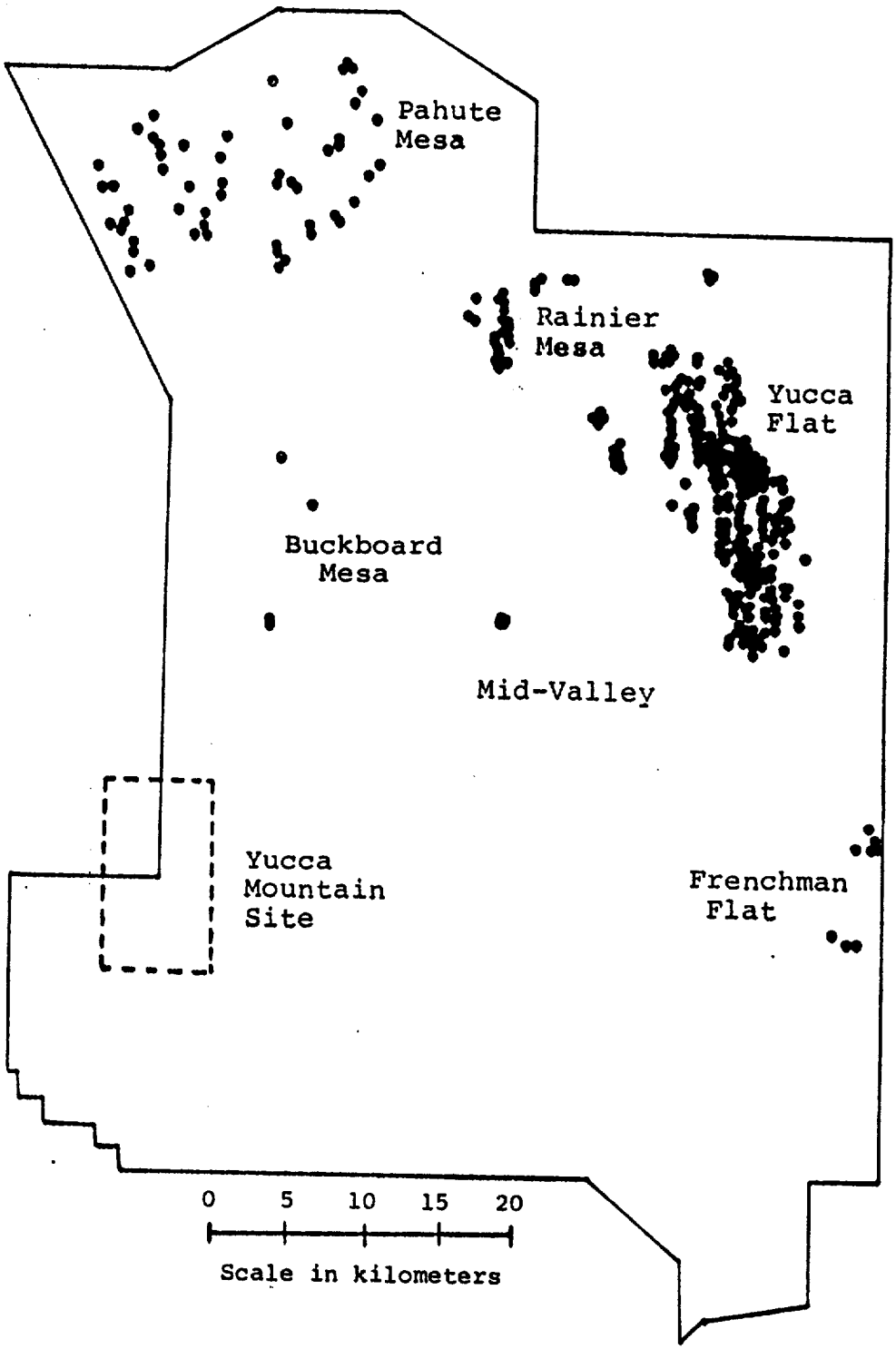

Figure 1. Locations of nuclear explosions at NTS.

Power Law Model for Ground Motion

$$A = A_0 \; W^B \cdot R^C$$

$$\log A = \log A_0 + B \log W + C \log R$$

where

A = Peak or Spectral Ground Motion Parameter

W = Explosion Yield (kiloton)

R = Range (km)

A_0, B, C = Constants Determined from Regression Analysis

Outline of Empirical Ground Motion Prediction Methodology Based on Explosion Experience

- Estimate source spectra corresponding to postulated earthquake scenarios:
  - A. Compare earthquake and explosion spectra for similar events at similar distances and stations to assess source equivalence.
  - B. Use magnitude relationships and magnitude/yield relations to determine earthquake/explosion equivalence.
  - C. Define response spectra levels at a near-source reference distance using nominal earthquake spectral scaling laws.

- Predict the PSRV ground motions:
  - A. Use the prediction relations developed from NTS experience to predict the spectra for the equivalent nuclear explosion source at the specified range of the scenario event.
  - B. Use the NTS experience to provide the attenuation adjustment to an earthquake near-source spectrum specified by other means for the scenario event.

- Assess uncertainties associated with the PSRV predictions based on NTS experience.

- Modify the spectra for site response using spectral comparisons between Yucca Mountain and average site response and other site response information.

- Assess the adequacy of predicted PSRV spectra in the light of historical earthquakes recorded near Yucca Mountain (e.g. Little Skull Mountain earthquake).

Analyses of Little Skull Mountain Earthquake Data

- Performed Regression Analysis on PSRV Spectra for Little Skull Mountain main shock.

- Estimated Frequency Dependent Attenuation Relations for Little Skull Mountain Data and Compared with NTS Explosion Experience.

- Used NTS Nuclear Explosion Experience to Predict PSRV Spectra for Equivalent Explosion Source and Compared with Little Skull Mountain Spectra and Alternative Empirical Earthquake Prediction Models.

- Reviewed Uncertainty Factors Associated with PSRV Estimates and Compared to Uncertainty in Little Skull Mountain PSRV Regression.

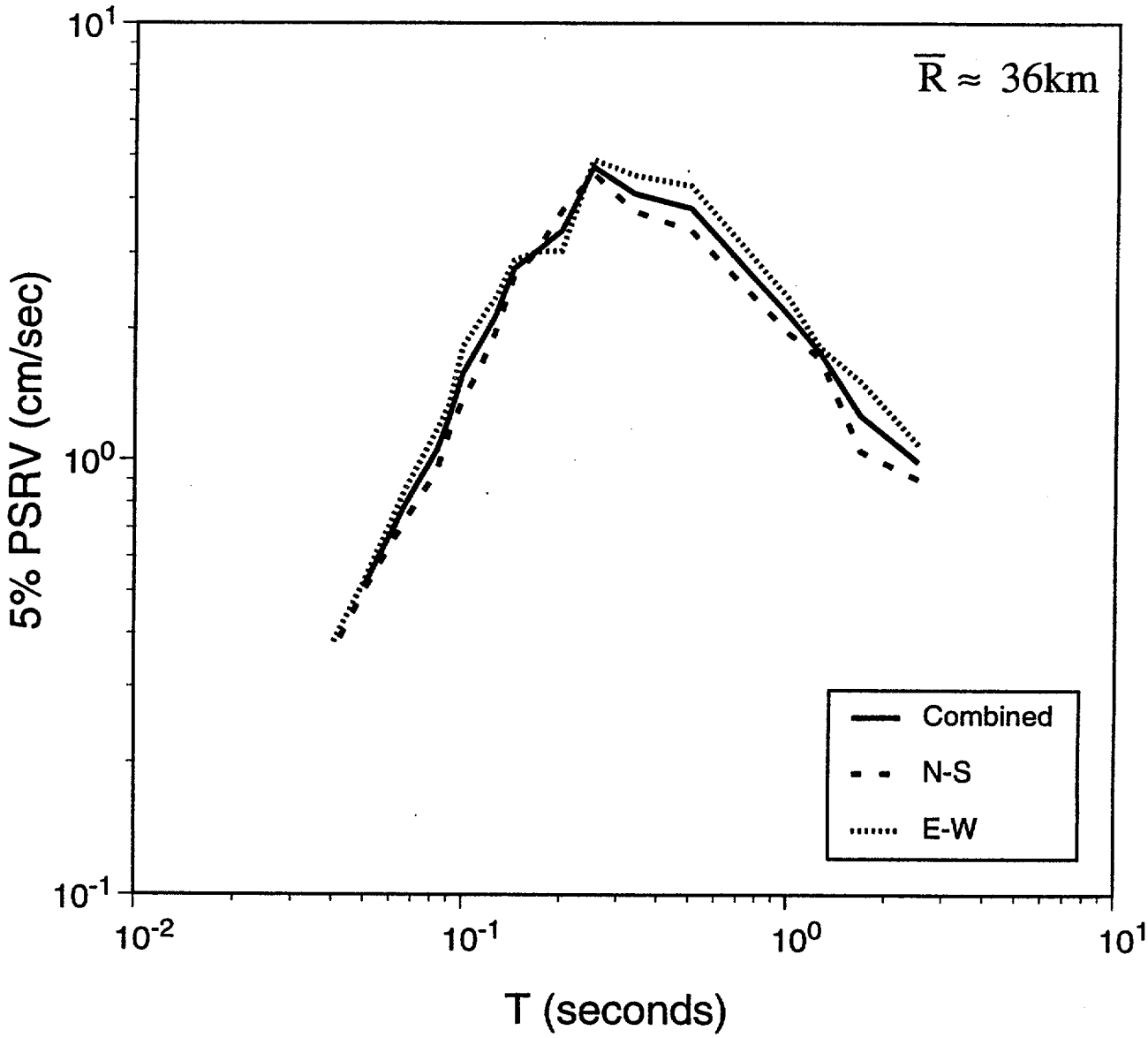

5% Damped PSRV spectra for the Little Skull Mountain earthquake projected at 36km based on regression of all horizontal component data compared with spectra based on separate regressions of each component.

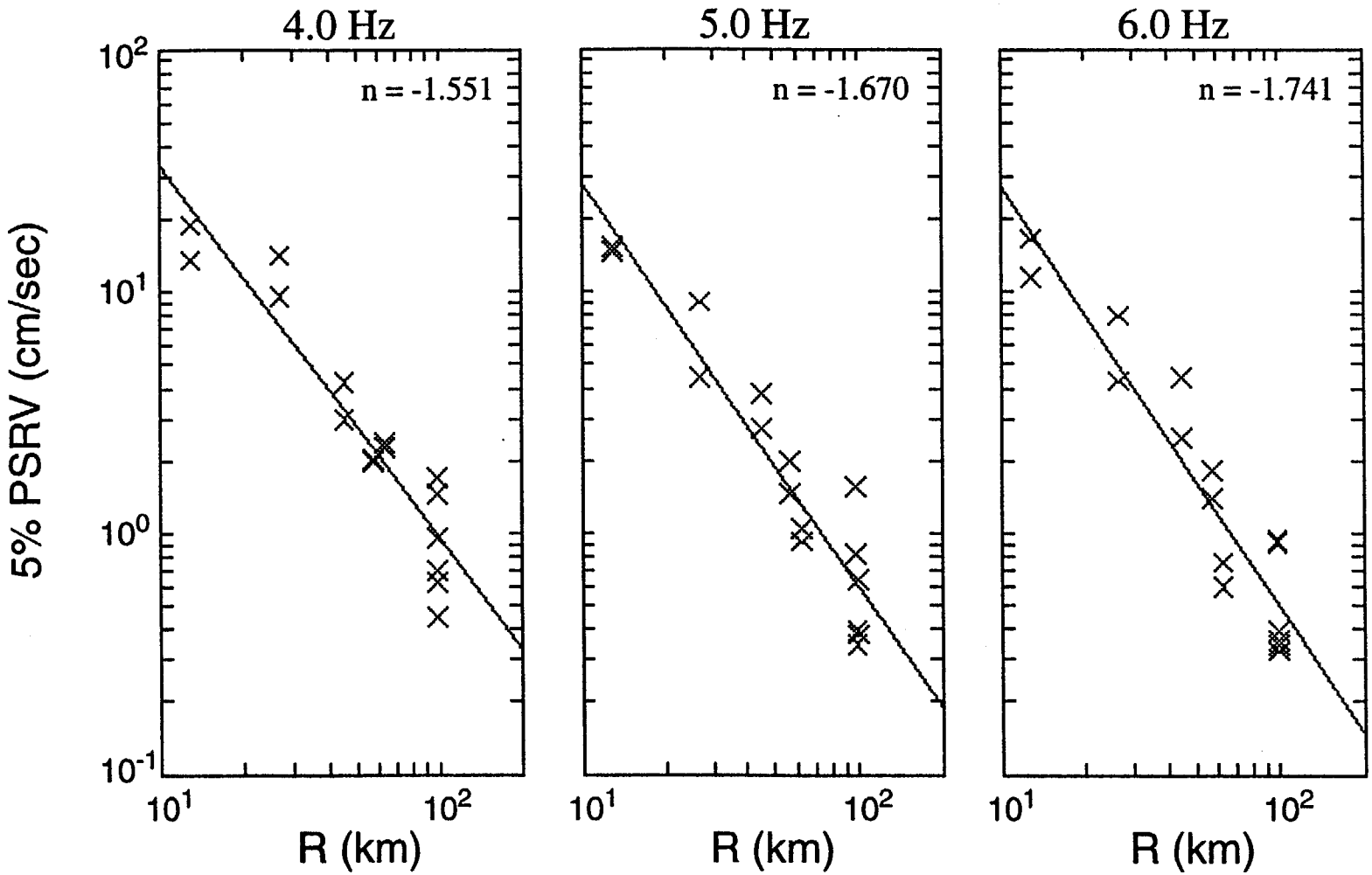

Examples of regression analyses applied to combined horizontal component PSRV spectra at individual frequencies for Little Skull Mountain earthquake. Similar analyses were performed for frequencies over a band from 0.4 Hz (2.5 sec) to 20 Hz (0.05 sec).

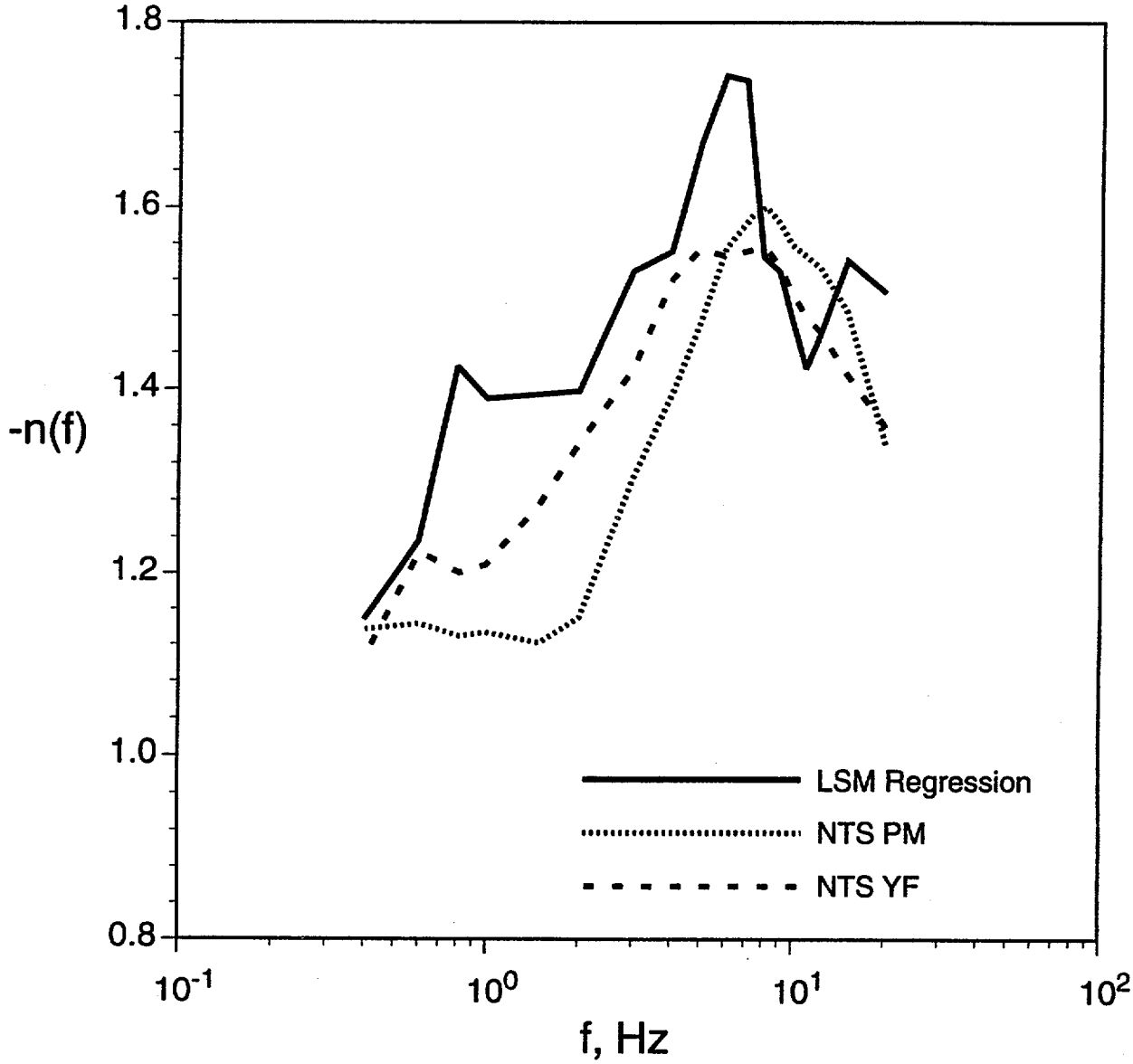

Comparison of 5% PSRV spectra attenuation exponents derived from combined regression of Little Skull Mountain horizontal components with similar regressions for nuclear explosion experience from Pahute Mesa (PM) and Yucca Flat (YF). Behavior is generally seen to be very similar. Note somewhat smoother appearance of curves for larger data samples.

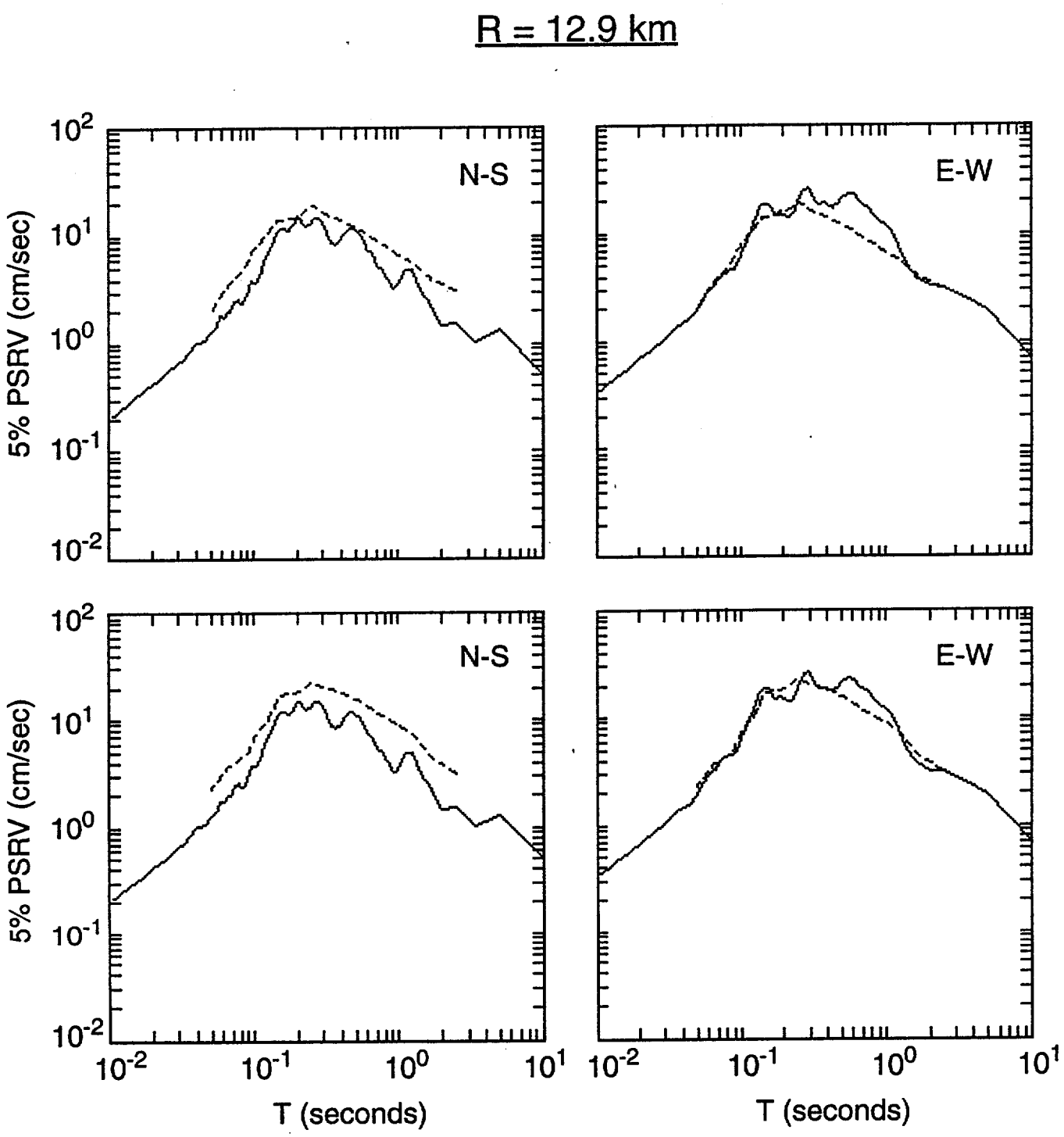

Comparison of PSRV predictions and observations at individual stations for Little Skull Mountain earthquake based on Pahute Mesa explosion attenuation experience (top) and LSM attenuation (bottom). Note fits are equally good for both attenuation relations suggesting that explosion attenuation experience can be used to predict earthquake attenuation over these ranges.

R =26.9 km

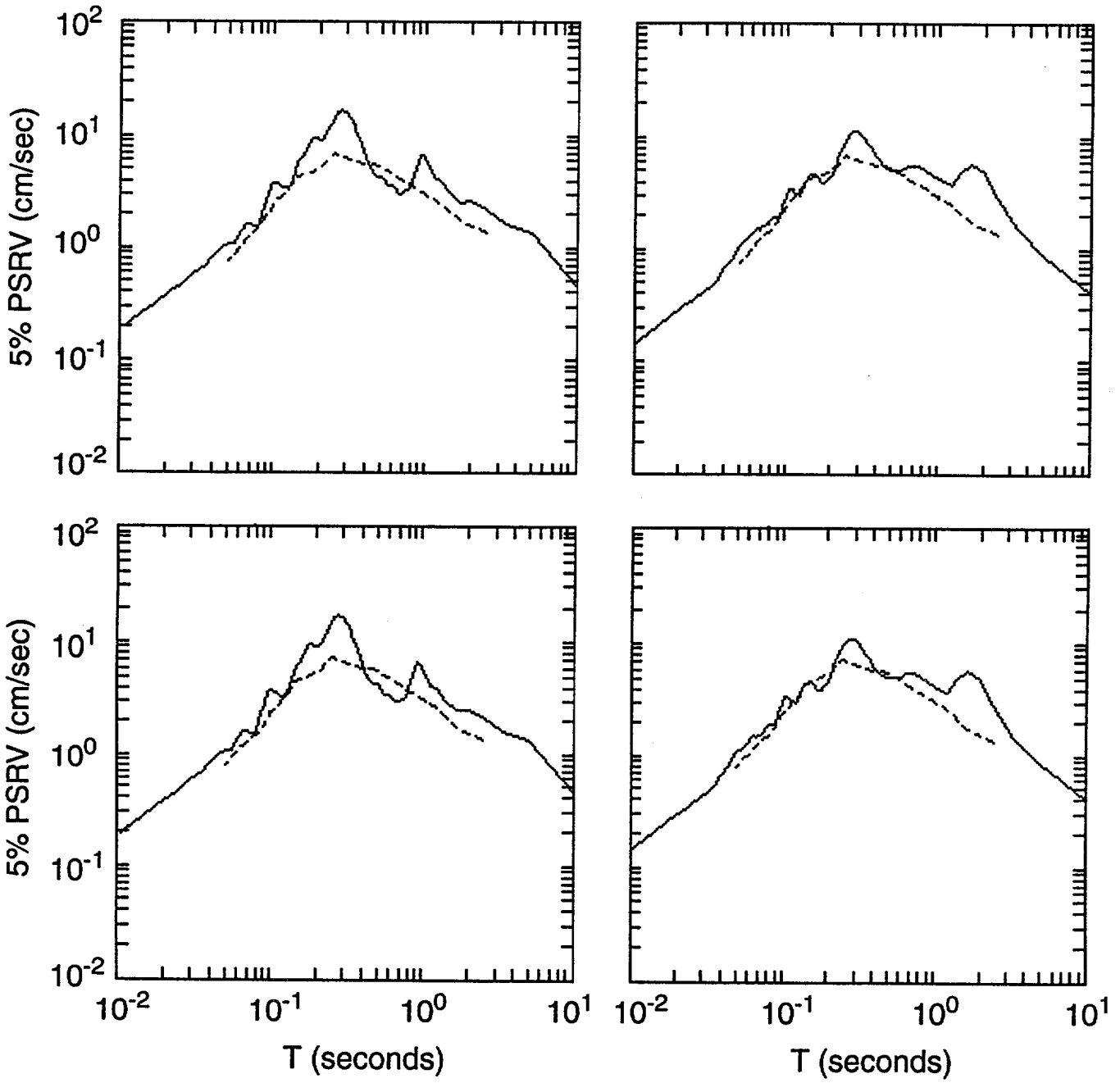

R =98.1 km

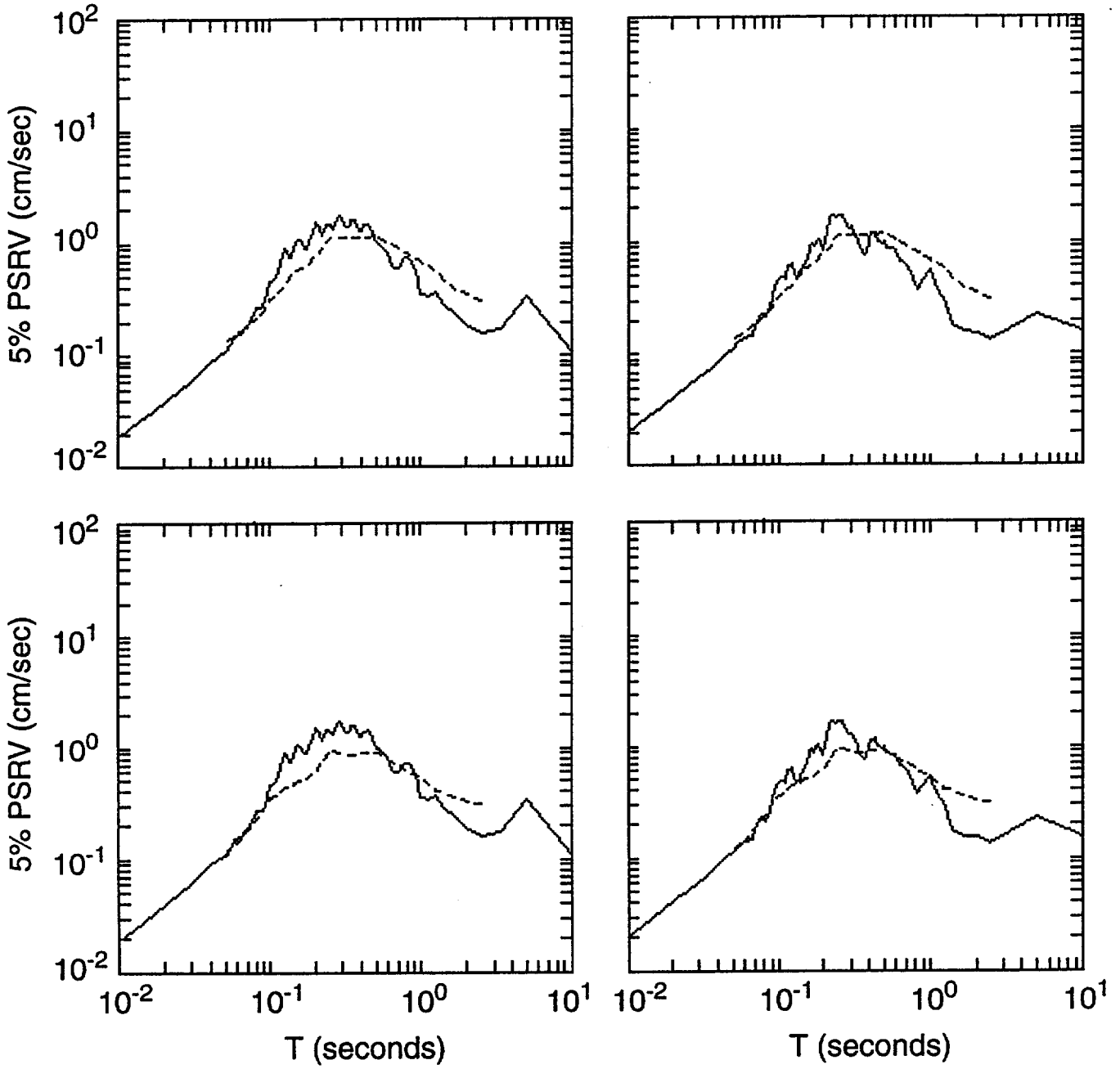

Empirical Ground Motion Predictions for Earthquakes Near NTS Based on Experience with Underground Nuclear Explosions

- Identify Nuclear Explosion Sources Equivalent to Postulated Earthquake Scenarios
- Predict the PSRV Ground Motions
- Assess Uncertainties Associated with PSRV Predictions
- Modify the Spectra for Site Response

Preliminary Procedure for Defining Earthquake/Explosion Equivalence Based on m_b/M_S Relations for Earthquakes and Explosions

Houston and Kanamori (1986) for worldwide earthquakes:

$$m_b = 0.53\ M_W + 2.7$$

$$M_W = 5.68 \longrightarrow m_b = 5.71$$

Richter (1957) for worldwide earthquakes:

$$M_S = 1.59\ m_b - 3.97$$

$$m_b = 5.71 \longrightarrow M_S = 5.11$$

Marshall (NTS Explosions):

$$M_S = 1.41 + 1.26 \log (\text{Yield})$$

$$M_S = 5.11 \longrightarrow \text{Yield} = 890\ \text{kt}$$

Murphy (NTS Explosions below water table):

$$m_b = 3.94 + 0.81 \log (\text{Yield})$$

$$\text{Yield} = 890\ \text{kt} \longrightarrow m_b = 6.32$$

Therefore, at this magnitude level:

For Earthquakes: $m_b - M_S = 0.60$

For Explosions: $m_b - M_S = 1.21$

Then, for the same M_S (i.e. same M_W):

$$m_b\ (\text{Explosion}) \approx m_b\ (\text{Earthquake}) + 0.61$$

$$m_b\ (\text{Explosion}) \approx 0.53\ M_W\ (\text{Earthquake}) + 3.31$$

So, for a $M_W = 5.68$ earthquake the explosion equivalent would have an $m_b = 6.32$ corresponding to Yield = 890 kt.

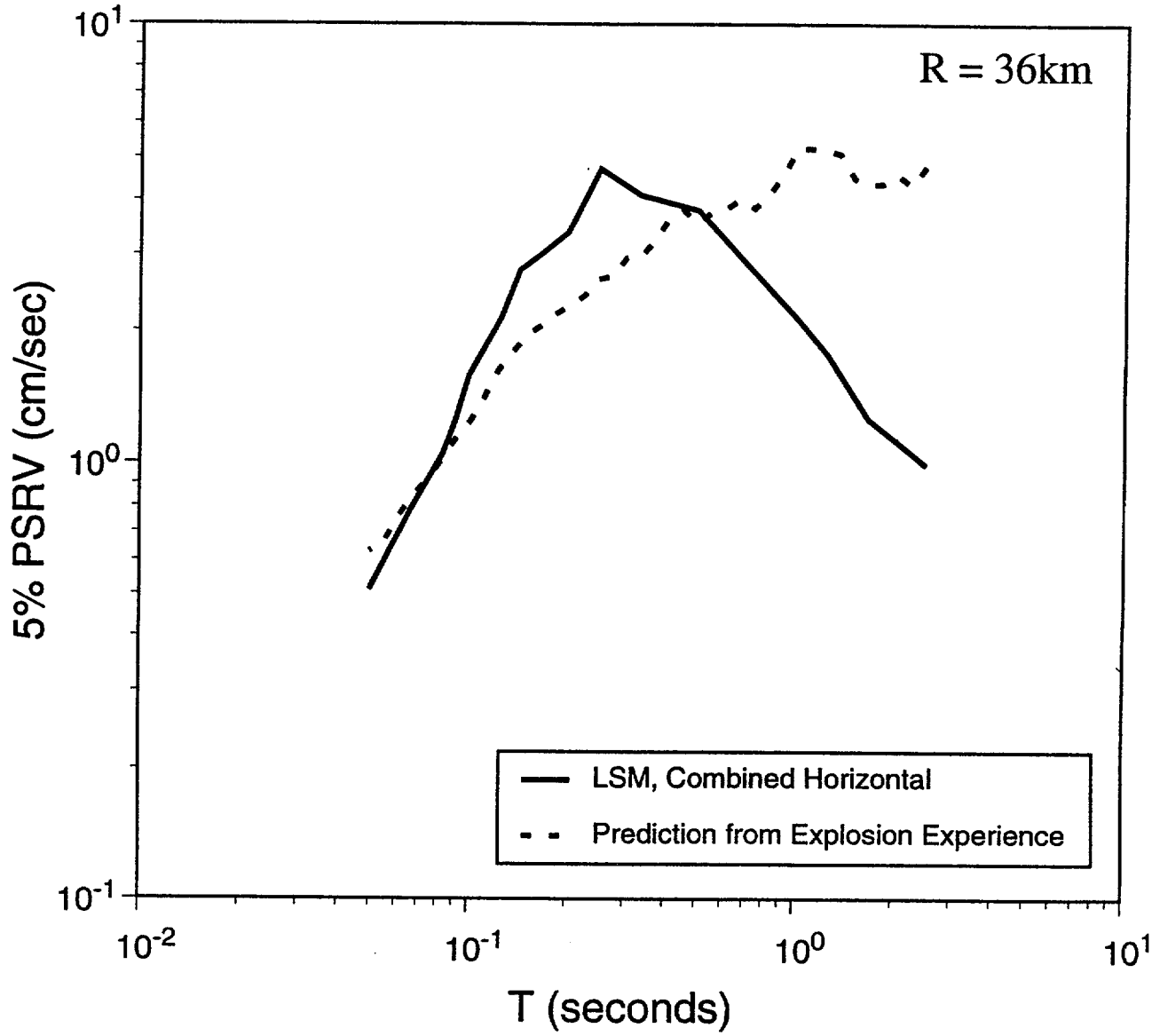

Comparison of 5% PSRV spectrum for Little Skull Mountain earthquake at 36km with prediction based on nuclear explosion experience assuming approximate equivalence of $M_W = 5.68$ earthquake and $m_b = 6.33$ (Yield = 890kt) nuclear explosion. Fit is okay on average but does not match in detail, particularly at longer periods.

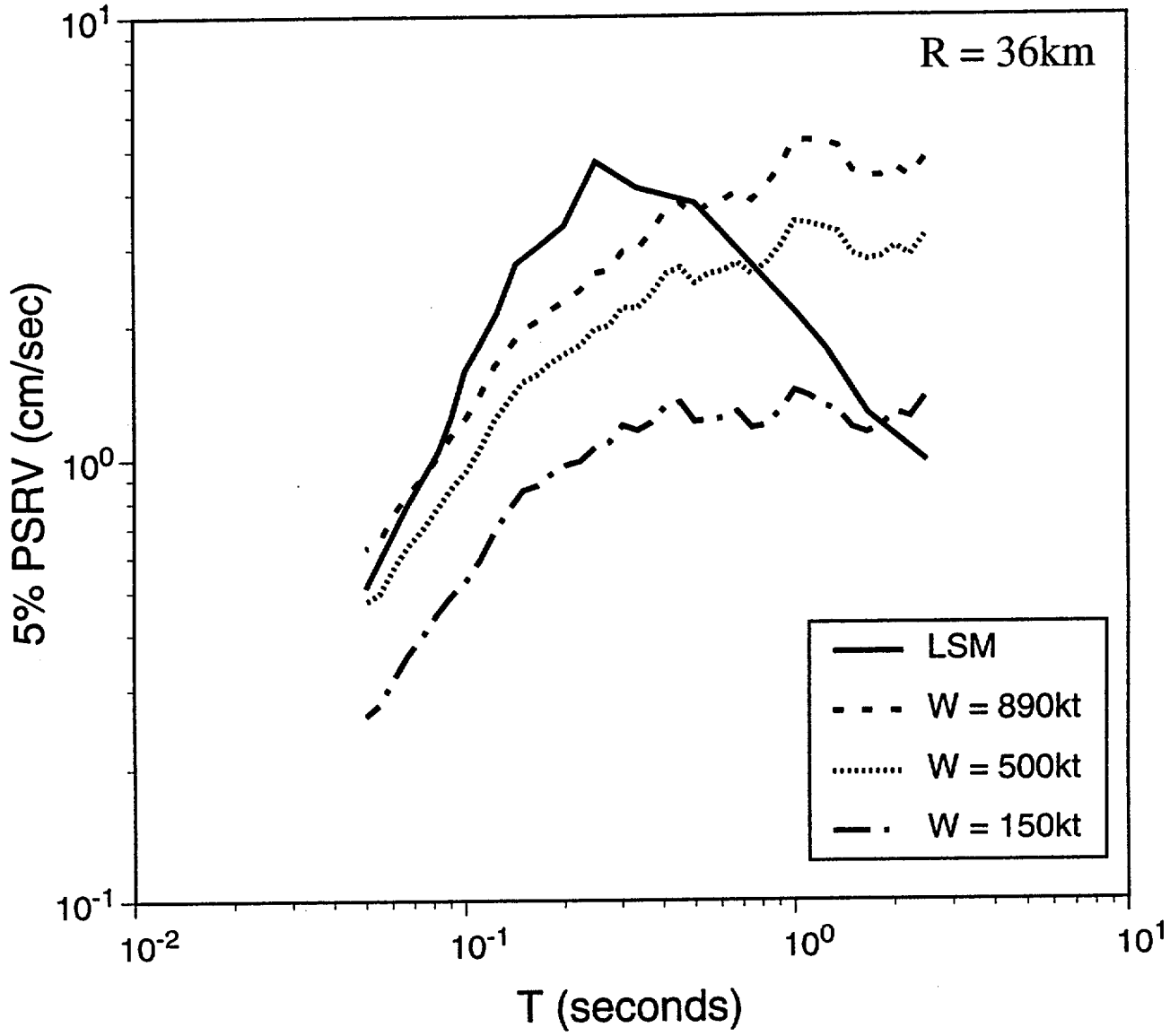

5% PSRV spectra predicted for 3 different explosion yields at R = 36km compared to PSRV spectra projected from LSM regression analysis. Lower yields show more tendency to decrease at longer period similar to behavior seen in earthquake spectral shape.

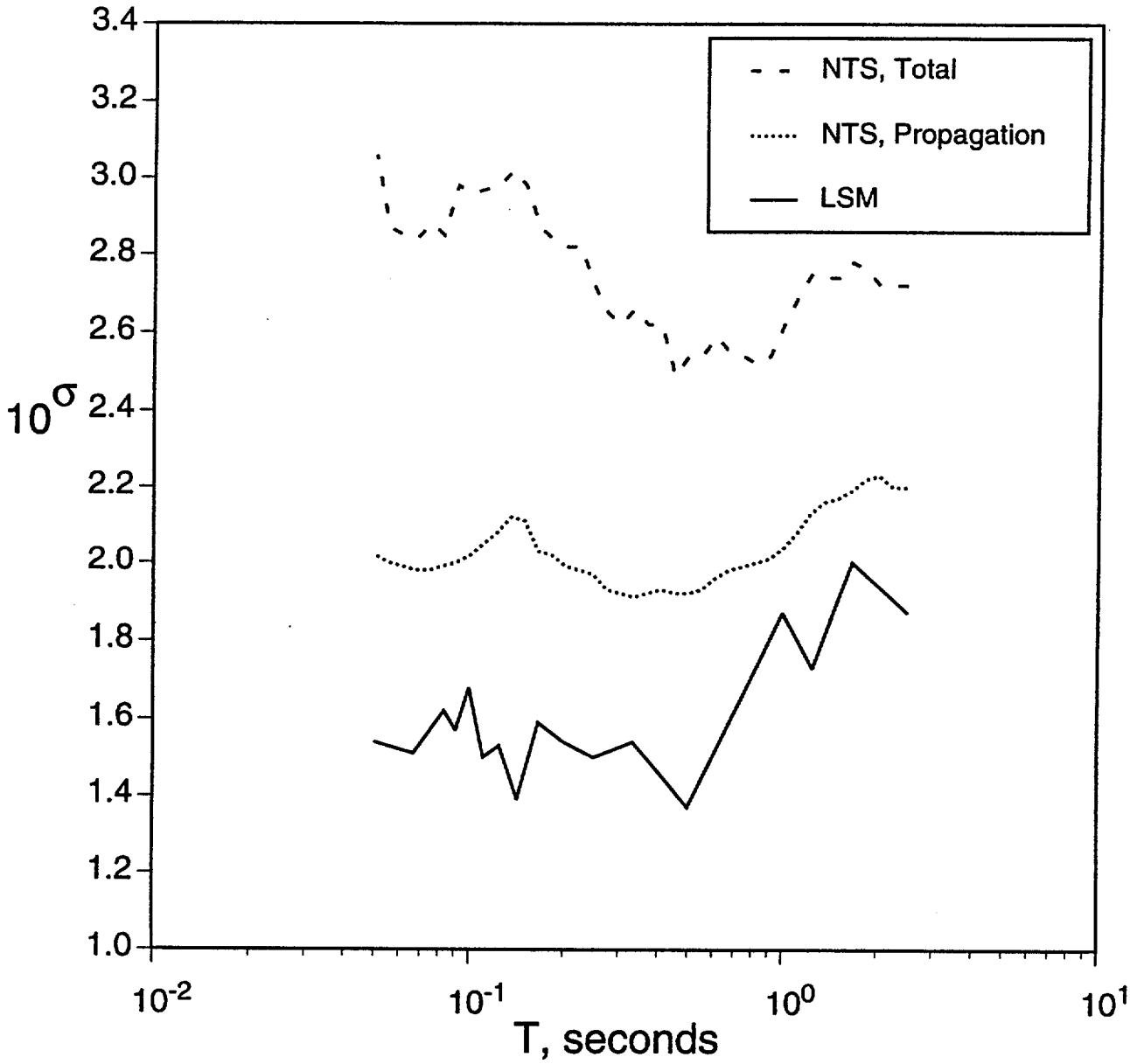

Comparison of PSRV uncertainty factors developed from regression analyses (1) for NTS explosions at Pahute Mesa for all yields, distances and stations (Total), (2) for Pahute Mesa explosions scaled to common yield for all distances and stations (Propagation), and (3) for Little Skull Mountain earthquake for all distances and stations. Note overall propagation uncertainty is roughly a factor of two.

Observations

- Results of Regression Analysis on PSRV Spectra for Little Skull Mountain Main Shock Produce Frequency Dependent Scaling Exponents Comparable to Those Based on NTS Explosion Experience.

- PSRV Spectra Predicted for Equivalent Nuclear Explosion Agree with the Average Level of Spectra Observed for the Little Skull Mountain Main Shock, but Spectral Shapes Are Notably Different.

- Alternative Empirical Earthquake Prediction Models Produce PSRV Spectral Shapes More in Agreement with the Nuclear Explosion Predictions than with Little Skull Mountain Observations.

- PSRV Spectral Shapes May Vary Significantly between Stations Based on NTS Explosion Experience.

- Uncertainty Factors Associated with PSRV Spectral Estimates Can Be Relatively Large. Station Corrections May Help, but It Could Still Be Difficult to Obtain Uncertainty Factors Much Below About Two.

Empirical Ground Motion Prediction for Specific Fault Scenarios

Objective: Apply three different empirical ground motion prediction models which utilize attenuation experience from NTS explosions to selected scenario earthquakes for the Yucca Mountain site.

THREE EMPIRICAL PREDICTION MODELS

(1) EQUIVALENT EXPLOSION WITH NTS ATTENUATION RELATIONSHIP

Using explosion with yield equivalent to Mw, apply explosion prediction relations for that yield based on NTS explosion experience to get 5 % damped PSRV spectra.

(2) GEOMATRIX/ATC SPECTRAL SHAPE WITH NTS ATTENUATION RELATIONSHIP

Use Geomatrix/ATC model to determine 5 % damped PSRV spectra at range of 10 km and apply attenuation exponents based on NTS explosion experience to extend to other distance ranges.

(3) LITTLE SKULL MOUNTAIN EARTHQUAKE SPECTRAL SHAPE WITH GEOMATRIX/ATC MAGNITUDE SCALING AND NTS ATTENUATION RELATIONSHIP

Use LSM 5 % damped PSRV spectral shape at 36 km (mean distance of LSM observations) extend to other distances using attenuation exponents based on NTS explosion experience and scale up to desired magnitude using Geomatrix/ATC model.

MODEL PARAMETERS

Base Case Normal Fault Scenarios

M_W	Distance (Slant/Hypocentral)	Scenario
6.4	6.0 km	SC, BR, PC shallow (6 km)
6.4	8.6	Intermed. shallow
6.4	9.1	PC deep (9 km)
6.2, **6.4**, 6.6	10.0	SC, BR, BM, Intermed. deep
6.2, **6.4**, 6.6	25.9	Distant deep
6.4	26.9	Distant shallow

Base Case Strike-Slip Fault Scenarios

M_W	Distance (Slant/Hypocentral)	Scenario
6.71	27.0 km	RV deep (9 km)
7.04	52.0	FC deep

Where faults are Solitario Canyon (SC), Bow Ridge (BR), Paintbrush Canyon (PC), Bare Mountain (BM), Nominal Intermediate Distance (Intermed.), Nominal Distant (Distant), Rock Valley (RV), Furnace Creek (FC).

Summary and Conclusions

- We have developed three different empirical models which take advantage of the strong motion experience base for southern Nevada based on NTS explosion experience.

- We have applied these models to investigate empirical prediction capability for the LSM earthquake and several scenario earthquakes for the Yucca Mountain site.

- Observed attenuation for the LSM earthquake is not significantly different from that based on NTS explosion experience.

- Attenuation based on NTS experience is only slightly greater than that based on the Geomatrix/ATC standard; spectral predictions are generally within a factor of two.

- Equivalent explosion spectral predictions agree surprisingly well with other prediction methods; largest differences are at periods above about 1 second.

- LSM observed spectral and predictions based on LSM spectral shape are anomalously low at long periods compared to the other empirical prediction methods.